KERNFORSCHUNGSANLAGE JÜLICH GmbH

ICANS-V

Proceedings of the 5th Meeting of the International Collaboration on Advanced Neutron Sources

Plenary Sessions and Target Station Workshops

Jülich, June 22 - 26, 1981

Editors: G. S. Bauer and D. Filges

Jül - Conf - 45
October 1981
ISSN 0344-5789

J. H. CARPENTER
Intense Pulsed Neutron Source
JAN 26 1982
Action
File

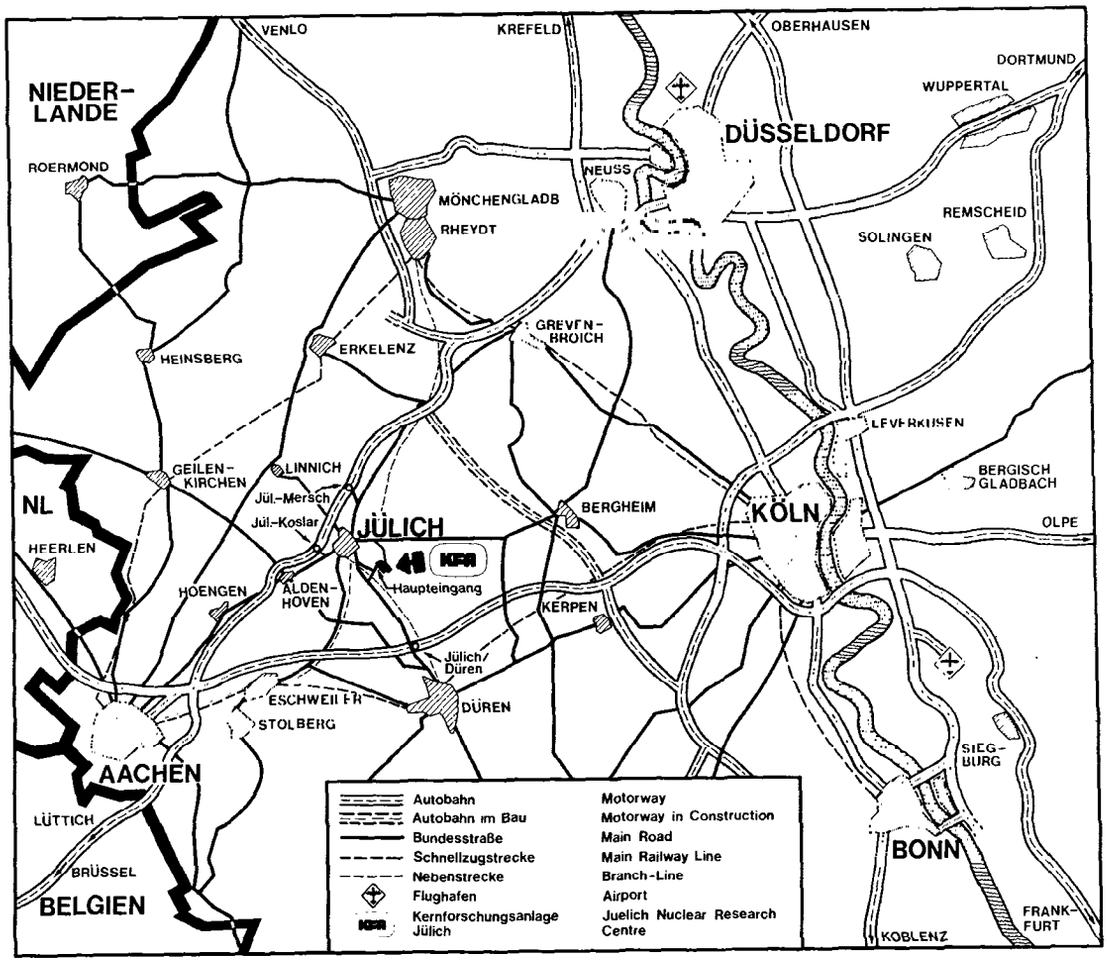

Als Manuskript gedruckt

Berichte der Kernforschungsanlage Jülich Jül - Conf - 45

Zu beziehen durch: ZENTRALBIBLIOTHEK der Kernforschungsanlage Jülich GmbH
Postfach 1913 · D-5170 Jülich (Bundesrepublik Deutschland)
Telefon: 02461/610 · Telex: 833556 kfa d

Property of Jack M. Carpenter
Please return to IPNS Library
Building 360 - Room E101

ICANS-V

Proceedings of the 5th Meeting of the International Collaboration on Advanced Neutron Sources

Plenary Sessions and Target Station Workshops

Jülich, June 22 - 26, 1981

Editors: G. S. Bauer and D. Filges

Preface

The 5th meeting of the International Collaboration on Advanced Neutron Sources (ICANS-V) was sponsored jointly by the two German research centres Kernforschungsanlage Jülich (KFA) and Kernforschungszentrum Karlsruhe (KfK), involved in the SNQ project study. It was the first meeting organized by "newcomers" in the Collaboration who joined after ICANS-III. The meeting was subdivided in two parts: The first two days were devoted to plenary sessions at KFA Jülich, featuring the traditional status reports from the vaious projects and invited review talks. These invited talks were intended to cover in a broader sense the application and specific design problems of spallation neutron source facilities. For this reason also such topics as neutrino physics, application of mesons to solid state research and materials problems in high radiation fields were included. The second half of the meeting consisted of topical workshops and discussion sessions which were held in parallel at KFA Jülich (Target Stations) and at KfK in Karlsruhe (Accelerators and Storage Rings).

The present volume of proceedings covers the plenary sessions and target workshops. It is organized in four parts:

Part A: Status reports given by the individual ICANS-member laboratories.

Part B: Manuscripts received from the invited speakers.

Part C: Topical summaries on the various workshops.

Part D: Contributed papers to the workshop sessions.

These papers have been regrouped under slightly different headings than the original workshops to account for the actual contents and for the emphasis in the discussions.

Owing to the fact that at least one member laboratory (CRNL) has the intent to promote research on the application of accelerator driven spallation reactions to breeding of nuclear fuel, one subsection (D5) has been devoted to this problem.

It is a pleasure to thank all participants, speakers and authors as well as those involved in the organization of the meeting for contributing to its success.

Jülich, october 1981

Günter S. Bauer

D. Filges

Contents

page

Part A Status reports from ICANS Laboratories and Projects

A1a The Los Alamos National Laboratory Weapons Neutron Research Facility 1
R. Woods

A1b Status of the Los Alamos Proton Storage Ring 17
R. K. Cooper and G. Spalek

A2 Present Status and Future Program of KENS 21
N. Watanabe, H. Sasaki, Y. Ishikawa, Y. Endoh and K. Inoue

A3a Status of Argonne's Intense Pulsed Neutron Source IPNS-I 33
J. M. Carpenter

A3b Improvements in the Rapid Cycling Synchrotron 53
C. W. Potts

A4 Progress report on the construction of the Spallation Neutron Source at the Rutherford & Appleton Laboratories 63
D. A. Gray

A5 Status Report on the SIN Spallation Neutron Source 73
W. E. Fischer

A6 Final Results of the German SNQ Study (abstract only) 87
H. H. Hennies

A7 Research Opportunities with Prototype Accelerators for an Accelerator Breeder 89
G. A. Bartholomew

page

Part B Invited Review Papers on Design and Uses of Spallation Neutron Source Facilities

B1 Neutron Scattering at an Intensity Modulated Neutron Source 97
R. Scherm (abstract only)

B2 Ultra-Cold Neutrons and Spallation Neutron Sources 99
R. Golub and K. Böning

B3 The Application of Intense Beams of Positive Pions and Muons in Solid-State Physics 113
A. Seeger

B4 Neutrino Physics at the Spallation Neutron Source 133
B. Zeitnitz

B5 Models and Computational Methods in the Theoretical Treatment of Spallation Neutron Sources 173
T. W. Armstrong and D. Filges

B6 High Energy Particle Spectra from Spallation Targets 215
S. Cierjacks, F. Raupp, S. D. Howe, Y. Hino, M. T. Swinhoe, M. T. Rainbow and L. Buth

B7 Radiation Effects in Targets and Structural Components of a Spallation Neutron Source 241
P. Jung

Part C Topical Summaries on Discussion Meetings

C1 Spallation and Fission in Computational Models 259
G. J. Russell

C2 Spallation Products 261
N. F. Peek

page

C3 Beam Quality 263
A. D. Taylor

C4 Radiation Effects in Targets and Structure Components 267
A. Carne

C5 Energy Deposition and Cryogenic Equipment 271
N. Watanabe and K. Böning

C6 Liquid Metal Targets 277
C. Tschalär

Part D Contributed Papers

Section 1: Target Neutronics and Target Physics

D1-1 A Comparison of High-Energy Fission Models for the HETC Transport Code - Part I: Thin Targets 281
T. W. Armstrong and D. Filges

D1-2 A Comparison of High-Energy Fission Models for the HETC Transport Code - Part II: Thick Targets 299
T. W. Armstrong, P. Cloth, D. Filges and R. D. Neef

D1-3 Differential Production Cross Sections for Charged Particles Produced by 590 MeV Proton Bombardment of Thin Metal Targets 313
S. D. Howe, S. Cierjacks, Y. Hino, F. Raupp, M. T. Rainbow, M. T. Swinhoe and L. Buth

D1-4 Neutron Production Yields and Spectra from 590 MeV Proton Bombardment of Thick Uranium Targets 333
F. Raupp, S. Cierjacks, Y. Hino, S. D. Howe, M. T. Rainbow, M. T. Swinhoe and L. Buth

D1-5 Gamma-Ray Spectrometric Product Identification and Halflife Analysis from Proton Induced Spallation and Fission Reactions of Lead and Uranium 343
W. Amian, N.F. Peek and D. J. Shadoan

D1-6 Gamma-Ray measurements of isotopes produced by 1.1 GeV protons on lead and uranium targets 355
N. F. Peek, D. J. Shadoan and W. Amian

page

Section 2: Moderator-Reflector Neutronics and Neutron Beam Characteristics

D2-1 Monte Carlo Reflector Studies for a Pulsed Neutron Source 377

A. D. Taylor

D2-2 Preliminary Neutronics of a Reflected 'T'-Shape Premoderator/Moderator for the Weapons Neutron Research Facility 389

G. J. Russell, M. M. Meier and H. Robinson

D2-3 Relative Intensities and Time Structure of Thermal Neutron Leakage from Various Moderator-Decoupler Systems for a Spallation Neutron Source 417

G. S. Bauer, J. P. Delahaye, H. Spitzer, A. D. Taylor and K. Werner

D2-4 Thermal Neutron Leakage and Time Structure Measured for Various Target-Moderator-Reflector Configurations for a Spallation Neutron Source 445

G. S. Bauer, W. E. Fischer, F. Gompf, M. Küchle, W. Reichardt and H. Spitzer

D2-5 Measurement of Time Structure and Thermal Neutron Spectra for Various Target-Moderator-Reflector Configurations of an Intensity-Modulated Spallation Neutron Source 475

G. S. Bauer, H. M. Conrad, H. Spitzer, K. Friedrich and G. Milleret

D2-6 Measurement of the High Energy Component of the Neutron Spectrum from a Moderated Source 489

Y. Hino, S. Cierjacks, S. D. Howe, M. T. Rainbow, F. Raupp, M. T. Swinhoe and L. Buth

D2-7 An Effective Inbeam Screening of Background by Choppers at a Pulsed Spallation Neutron Source 497

N. Nücker

D2-8 Measurements of Neutron Fluxes at Spallation Source Models and Bare Targets 503

V. Drüke, N. Paul and W. Litzow

page

Section 3: Cryogenic Installations

D3-1 Some Neutronic Aspects of Solid Methane Moderator System 519

K. Inoue, Y. Kiyanagi, H. Iwasa, K. Jinguji, N. Watanabe, S. Ikeda and Y. Ishikawa

D3-2 A Study on UCN Source for a Spallation Facility 525

M. Utsuro, K. Okumura and Y. Kawabata

D3-3 Feasibility Study of Low-Temperature Irradiation Facility at the German Spallation Neutron Source SNQ 539

K. Böning and R. Golub

Section 4: Target Design and Layout

D4-1 The Liquid Metal Target for the German Neutron Source (SNQ) - Status of the Theoretical and Experimental Investigations of the Target Thermo- and Fluiddynamics - 549

H. Hoffmann, M. Piesche, E. Wild, K. Marten and E. Baumgärtner

D4-2 Vertical, Convective Spallation Target at SIN 575

C. Tschalär

D4-3 Some Remarks Concerning the Use of a Rotating W-Target in a High Power Spallation Neutron Source 591

G. S. Bauer, W. Lohmann and F. Stelzer

D4-4 Remarks Concerning the Efficiency of a Booster Neutron Source 611

W. Kley

Section 5: Fertile-to-Fissile Conversion with Spallation Neutrons

D5-1 Fertile-to-Fissile and Fission Measurements for Depleted Uranium Bombared by 800-MeV Protons 621

G. J. Russell, J. S. Gilmore, H. Robinson and R. E. Prael

D5-2 Spallation in a Nuclear Energy System 641

M. Heindler

Jül-Conf-45 A1a

I C A N S - V

MEETING OF THE INTERNATIONAL COLLABORATION ON

ADVANCED NEUTRON SOURCES

June 22-26, 1981

The Los Alamos National Laboratory Weapons Neutron Research Facility

R. Woods

Los Alamos National Laboratory

Los Alamos, New Mexico 87545

Abstract

The Physical makeup is presented of the Weapons Neutron Research (WNR) facility at the Los Alamos National Laboratory with emphasis on the critical components. The operating experience is discussed including failure modes and their subsequent resolution. The present target-moderator configuration is given and plans for development and improvements.

I. INTRODUCTION

The Weapons Neutron Research (WNR) spallation neutron source began operation in 1978, and since has operated for over 7000 hours. There are few spallation neutron sources which have operated for this length of time. Because the WNR is one of the first high intensity facilities, our operating experience should be of considerable interest and value to those with similar facilities in the planning, construction, or commissioning phase.

We have experienced a variety of problems in the process of bringing the WNR to a fully operational facility to provide neutron beams for a diverse research program. In order to fully understand these problems, a brief description of the facility and certain system components follows.

The WNR utilizes 800-MeV protons from the Los Alamos Meson Physics (LAMPF) linear accelerator; the work described here will not deal with the operational aspects of the accelerator. As shown in Fig. 1, the major components of the WNR facility are: 1) the proton beam transport system, 2) the high-current target system (target 1) with its associated experiment areas and flight paths, 3) the low-current target and experiment area (target 2), and 4) the control building with areas for data gathering, including a system of computers for data acquisition and reduction.

There are two modes of operation which require different modes of beam structure. We obtain these modes by means of a chopper system in the injection beam transport line of LAMPF. The first (mode 1) produces narrow micropulses (~200 ps FWHM at the WNR target) spaced a minimum of 1 s apart; these micropulses occur under a macropulse envelope 600-μs long at a rate up to 12 Hz. The second (mode 2) produces a pulse up to 8-μs long; these pulses are separated by a 16μs window from the rest of the LAMPF macropulse and occur at a rate up to 120 Hz. In order to divert these beams out of the main beam line at the end of the linac, pulsed magnets are required to minimize interference with the beams for LAMPF experiments. For mode 1, a "slow" kicker is used which operates with a pulse over 1-ms long at repetition rates up to 12 Hz. This is a 32-turn, laminated-core magnet operating at 410 amperes and bends the 800 Mev proton beam 1.8°. Mode 2 requires a "fast" kicker which must produce a pulse which rises in 10μs and must remain flat within 0.1% for 8μs. This latter magnet is a single turn device operating at 6000 amperes and bends the proton beam 1.5°. Low-field (4 kG maximum) magnets with fixed fields completes the 90° bend to transport the proton beam toward WNR. The rest of the transport system consists of quadrupoles, steering magnets, beam position sensing devices, and vacuum equipment.

The two targets and their experiment rooms are shown on Fig. 2. They have been discussed in previous ICANS literature [1,2,3] and also later in the present conference.

The data acquisition and reduction system is shown schematically in Fig. 3. The hub of the system are two Modular Computer Corporation (MODCOMP) model IV/25 mini-computers. One serves as the host computer and services the major peripherals including magnetic tapes (MT), card reader (CRD RDR), Versatic printer-plotter (PPL), and the communication links to the satellite computers located in the data rooms. This host computer also supports a

CAMAC serial highway to the experiment areas for experiment control which is separate from data acquisition. Host computer #2 is primarily used for data acquisition, but by switching a few cables, it can take over all the functions of host #1. A typical satellite system is represented by Data Room 3 (See Fig.3). The experiments are interfaced through standard CAMAC hardware in CAMAC crates CC1, CC2 -- up to CC7. This interface is done through a special Differential Branch Driver (DBD)[4] at the computer via a branch highway cable to a Differential Branch Transceiver (DBT) located next to the CAMAC crates. Keyboard Terminals (KT) of either the hardcopy or visual display type are used for inputing commands to the computer. A separate graphics display (GD) is provided to display the experiment data.

A most versatile and powerful addition shown on the two hosts, but also available on the satellites, is the bulk memory (BM) which is controlled through our bulk memory processor (BMP)[5]. The memory is of the Mostek solid state type with a maximum capacity in one crate of 6 megabytes. The BMP utilizes bit slice integrated circuits and an 80 bit wide writeable control store microcode technique. It features a 24 bit wide architecture allowing direct addressing of up to 16 megawords and histrogramming of up to 16 million counts per channel without overflow. Coding for the BMP is also supported at the macro instruction level and the event analysis language "EVAL"[6] will be implemented in the near future.

In Fig. 3 we show our planned computer system expansion in dashed boxes. Procurement is underway for the purchase of the satellite systems for Data Rooms 1 and 2 plus the new data acquisition host a VAX 11/750. The Proton Storage Ring (PSR) VAX 11/750 will be delivered by July 1 and installed at the WNR. The two VAX computers will be coupled by a communications link, and the data acquisition VAX will be coupled to the MODCOMP IV's and to the Los Alamos Central Computing Facility.

Our present schedule calls for installation of the above computer modifications and the satellite system for Data Room 4 by this time next year. We are exploring the feasibility of some microprocessor-based computer systems for particular neutron scattering instruments.

When operating the WNR personnel control is exercised through the Personnel Safety System (PSS), and neutron radiation monitoring devices. The PSS ensures that personnel are cleared from a given area before the proton beam is transported into that area. The PSS also provides the interlocks and barriers to prevent unauthorized entry into high radiation fields. In order to leave as much of the facility as possible open to human occupancy under operating conditions, these areas are monitored for neutron radiation levels by a system of fixed and portable neutron monitoring instruments called Albatross IV's which were developed at Los Alamos. The detection system for the Albatross is a 0.25-mm-thick Ag foil wrapped around a GM tube that is located in the center of a 25-cm-diam polyethylene pseudosphere. The neutrons thermalize in the moderator and are captured by ^{109}Ag to form ^{110}Ag plus a γ-ray. The ^{110}Ag beta decays with a half-life of 24.4μs. There is also a second GM tube wrapped with tin that is used to subtract counts due to γ-rays created in the moderator and also external γ-ray fields. The β plus the γ-ray counts from the Ag wrapped GM tube and the counts from the Sn wrapped GM tube are sent to a microcomputer where they are manipulated to give the net counts due to neutrons. This information is accumulated in

bins for a predetermined time interval which can be varied between 15 sec and 8 min. This instrument was developed to respond to the pulsed nature of our source and gives a very good response over a large energy range as shown in Fig. 4. The instrument itself is shown in Fig. 5. It is a completely self contained unit with meter, an alarm level, an adjustable audible alarm, a chirping sound where the number of chirps/sec increases with increasing radiation levels, and outputs for remote monitoring and alarming. We presently utilize ten of these instruments in the main facility and outlying buildings on the long flight paths.

The control and monitoring functions for the entire facility are carried out at a single console. A computer identical to the smaller units used in the data acquisition system (MODCOMP 7830) is used for all non-safety control and monitoring. The PSS, the Albatross monitors and certain other safety related systems are hard wired independent of the computer system.

II. Operating Experience

The operating record for WNR is shown in Table I. The production time scheduled is the WNR schedule and ignores the WNR tuning time. For a facility as complicated as WNR (which relies on a sophisticated accelerator such as LAMPF) this is an excellent availability record.

The problem areas within the WNR which contributed to lost time are identified in Table II. The leading problem has been the fast kicker magnet. However, the excellent record in the most recent run cycle shows we have finally reduced the problem below the trouble threshold. The magnet itself is not the culprit, but the pulse forming network (PFN) which produces the high current pulse. The major changes we have made involve reducting or eliminating components which saw voltage or power levels close to their rated maximum. System noise in several of the timing interlock circuits also contributed to lost time by unnecessary shut downs and time spent chasing these faults. During the calendar year 1980, a lot of effort went into changing in the PFN to provide a longer pulse with better flat top characteristics (0.1%). This was very successful and led to a doubling of the pulse length to 8μs with the desired flat top.

The second item which one notices in Table II is the chopper problem we had in the early time periods. This was resolved by completely new hardware in which the chopper plates, with their helically wound copper ribbon, are better protected from melting by improperly tuned beam. The electronics feeding the chopper were also replaced. All these changes contributed to the recent excellent reliability of the chopper system.

The rest of Table II does not show any other consistent problems. The extremely good reliability of the control computer system should be noted by those planning control systems. It should also be noted that the high-current target-moderator-reflector system did not contribute at all to the WNR down time.

As mentioned earlier, because of the two target areas, the well shielded target 1, and the long flight paths (up to 200 m) with their associated experiment buildings, we try to allow human occupany in as much of the

facility as we safely can during operation. When operating, there is always at least one person on duty within the WNR (there are many more some 50 m away at the LAMPF control room within radio and telephone contact). The individual at the WNR is the designated operator responsible for all aspects of the facility including safety and personnel access. The standard operating procedure (SOP) for the facility calls for certain restrictions on human occupancy during startup or if there is a gross change in the operating conditions. This has worked very well with two notable exceptions.

The main cylindrical biological shield surrounding target 1 has been found to be extremely effective holding levels at the surface to less than 0.5 mrem/h with up to 20 μA average current on the target. However, the flight paths themselves, when open for an experiment, have created large backgrounds in the experiment area which at times render the experiment hall unoccupyable. Most of the collimating is done within the bulk shield, but effective collimation against the entire energy spectrum from even a moderated target system is difficult. The neutron "get lost" pipes and beam stops are very important in preventing the higher energy neutron component from being thermalized and then finding their way back into the room experiment and also into the experiment detector system. This appears to be one of the more significant problems for all spallation sources, and we plan to study the energy spectrum and flux in our flight paths. This will then lead to a study of the proper shielding materials and collimating methods.

The second problem is largely on outgrowth of the first; namely, personnel control within the experiment area when there is restricted access to areas near particular flight paths. Experimenters are used to unlimited access to their samples and instruments. When restrictions are forced on them because of the radiation level from an adjacent flight path, there exists a potential problem from the experimenter who is rightfully concentrating on his own problems. In most cases, we erect physical barriers such as ropes (or more effectively nets) which act as a reminder. In extreme cases, we close the shutters on a group of three flight tubes in one of our corner clusters when access is needed to anyone of the three. We believe this latter problem can be eliminated by a proper solution to the first problem.

The data acquisiton system has evolved and grown as the needs of the experiments and neutron scattering instruments have become better defined. The general advice is to provide a high level computer for each instrument. We find it to be the most cost effective to standardize on some manufacturers hardware at a high enough level to support the most sophisticated software required by the most complex instrument. This may seem wasteful in that a simpler instrument doesn't need either that level of hardware or software, however the major costs are operational rather than the initial investment. The advantage of standardizing far outway the somewhat higher initial costs. In our system, we do share the expensive peripherals such as high density magnetic tapes, line printers and plotters. This means an effective and high speed data link between central processor units.

From an experimenters viewpoint, it makes little diffrence what computer is in the other room; what experimenters interact with is some sort of terminal-keyboard system. This is an area where the efficiency of the entire facility can be enhanced by a graphics interface system with well designed hardware and software.

III. Present Status

The facility operates routinely at 10 ma peak current with a 5-μs-long proton pulse at a repetition rate up to 120. This gives an average proton current of 6μA. We have tested the beam transport and target systems at higher average currents. We believe that an average current of 20 μA can be handled without significant improvements. The neutron fluxes from these proton currents will be discussed in a later talk at this conference.

The present target-moderator-reflector assembly is shown in Fig. 6. This configuration has been worked out to best fit the needs of the experiments on the various flight paths as shown in Fig. 7. The target is W, the premoderator is H_2O, the decoupler is Gd, the moderator is high density CH_2 and the reflector is Be and CH_2.

The flexibility of the target 1 crypt allows the choice of two targets and several moderator configurations. The nuclear physics program uses a bare tantalum target and sometimes surrounded with a CH_2 moderator for enhancing the resonance region. We can switch in a matter of 30 minutes to a completely different configuration for the material science neutron scattering program.

Of interest to those about to undertake operation of such a facility is the number of personnel needed. Again let me stress that I speak only of the proton beam transport system, the target-moderator system, and the data acquisition system plus responsiblity for the entire physical facility including safety. We are presently operating with 7.5 staff and 10 technicians. Our efficiency and effectiveness would be improved with the addition of 1 staff and 2 technicians.

IV. Planned WNR Improvements

A cold moderator development program is underway to provide a cold surface as shown in Fig. 8. The reflector shape, size and material will also be improved for this configuration.

The PSR is the biggest single possible improvement to the WNR and you will hear more about that shortly. The PSR is being designed to transmit an average proton current of 100μA to the WNR, and this will necessitate improvements within the WNR itself. The beam line must transmit these large currents of H^- beam to the PSR and then transport the H^+ to the targets. There is one area in the transport system between LAMPF and the PSR which will require magnets with an increased aperture to maintain beam spill and hence component activation at the present operating level.

The major improvements required are to the target-moderator support system in target 1. The shielding above the target is not adequate to protect the magnetic components in the 90° vertical bend. We propose to replace the entire turntable mechanism which holds our 2 targets, 4 moderators, and miscellaneous components. Based on our operational experience, our target-moderator development program and the stablizing of the experiment needs, we have a much clearer idea of what is needed for the target-moderator

configuration. The improvements in this area will take all this into consideration while providing the additional shielding. Many components in this area presently maintained by hands on methods will have to be amenable to remote handling techniques. This will require extensive engineering.

The third area scheduled for improvement is additional shielding in the main experiment room for target 1. Some of this will be added to the biological shield and likewise to the neutron beam flight paths as they exit the shield. The character and location of this shielding is dependent on the solutions to the collimation and shielding problems discussed earlier.

These improvements are estimated to cost 2.7 million dollars with work commencing in October 1982 and completion commensurate with the commissioning of the PSR at 100μA.

References

1. G. A. Keyworth, Proceedings of the 4th Meeting of International Collaboration on Advanced Neutron Sources (ICANS IV) KEK, Tusukuba, October 20-24, 1980, Kens Report II, March 1981.

2. G. J. Russell, et al, Proceedings of the 4th Meeting of International Collaboration on Advanced Neutron Sources (ICANS IV) KEK, Tusukuba, October 20-24, 1980, Kens Report II, March 1981.

3. J. Eckert, et al, Proceedings of the 4th Meeting of International Collaboration on Advanced Neutron Sources (ICANS IV) KEK, Tusukuba, October 20-24, 1980, Kens Report II, March 1981.

4. D. E. McMillan, et al, "High Speed Differential Branch Highway Driver", IEEE Transactions on Nuclear Science, Vol. NS-26, No. 4, August 1979.

5. R. O. Nelson, et al, "Bulk Memory Processor for Data Acquistion", Topical Conference on Computerized Data Acquisition in Particle and Nuclear Physics, Oak Ridge, Tenn. May 28-30, 1981 [to be published in IEEE Transactions on Nuclear Science].

6. R. A. Hardekopf, et al., "Event Analysis Language For High Speed Data Acquisition", Topical Conference On Computerized Data Acquisition in Particle and Nuclear Physics, Oak Ridge, Tenn. May 28-30, 1981 [to be published in IEEE Transactions on Nuclear Science].

7. R. J. Buchanan, "Neutron Radiation Detection at Pulsed Spallation Neutron Sources", International Collaboration on Advanced Neutron Sources, Los Alamos Scientific Laboratory, ICANS III, March 10-22, 1979.

Table I WNR Operating Record 8/1/78 - 5/1/81

Production Time Scheduled	9552 hrs
Beam Time Available From LAMPF	8564 hrs
WNR In Production	7282 hrs
Overall Availability	76 %
WNR Availability	85 %
Total Charge On Tungsten Target	5.38 mA hr
Total Number of Protons Striking Target	1.2×10^{20}

Table II. Reasons for Lost Production Time At WNR

	March 4 - May 6, 1979	May 22 - August 28, 1979	November 20, 1979 January 19, 1980	January 31 - March 28, 1980	June 27 - August 24, 1980	September 4 - November 9, 1980	March 1 - April 25, 1981
Fast Kicker	62	128	64	14	132	194	
Slow Kicker			2	4			6
Chopper	64	124	4			4	
Interlocks	2			4			
Targets	54						
Vacuum		50	6				
Control Computer		16			8		2
Magnet Power Supplies			48	26			2
Miscellaneous	12	8	2	8	22	2	18
Totals	194	326	126	56	162	200	28

Figure Captions

Fig. 1 Schematic of the LAMPF-WNR

Fig. 2 Schematic of the WNR Facility

Fig. 3 The WNR Data Acquisition Computer System

Fig. 4 Front view of Albatross IV pulsed neutron survey instrument

Fig. 5 Relative response of CH_2-moderated neutron survey instruments as a function of neutron energy.

Fig. 6 The present WNR target/moderator/reflector assembly for the materials science neutron scattering program

Fig. 7 WNR flight pather configuration. Fligth paths 3, 5, 6, 7, 8, 9, and 10 are used for the material science neutron scattering programs. Flight paths 11, 12, 1 and 2 are used by the nuclear physics program.

Fig. 8 Planned WNR target/moderator/reflector assembly with a cold surface.

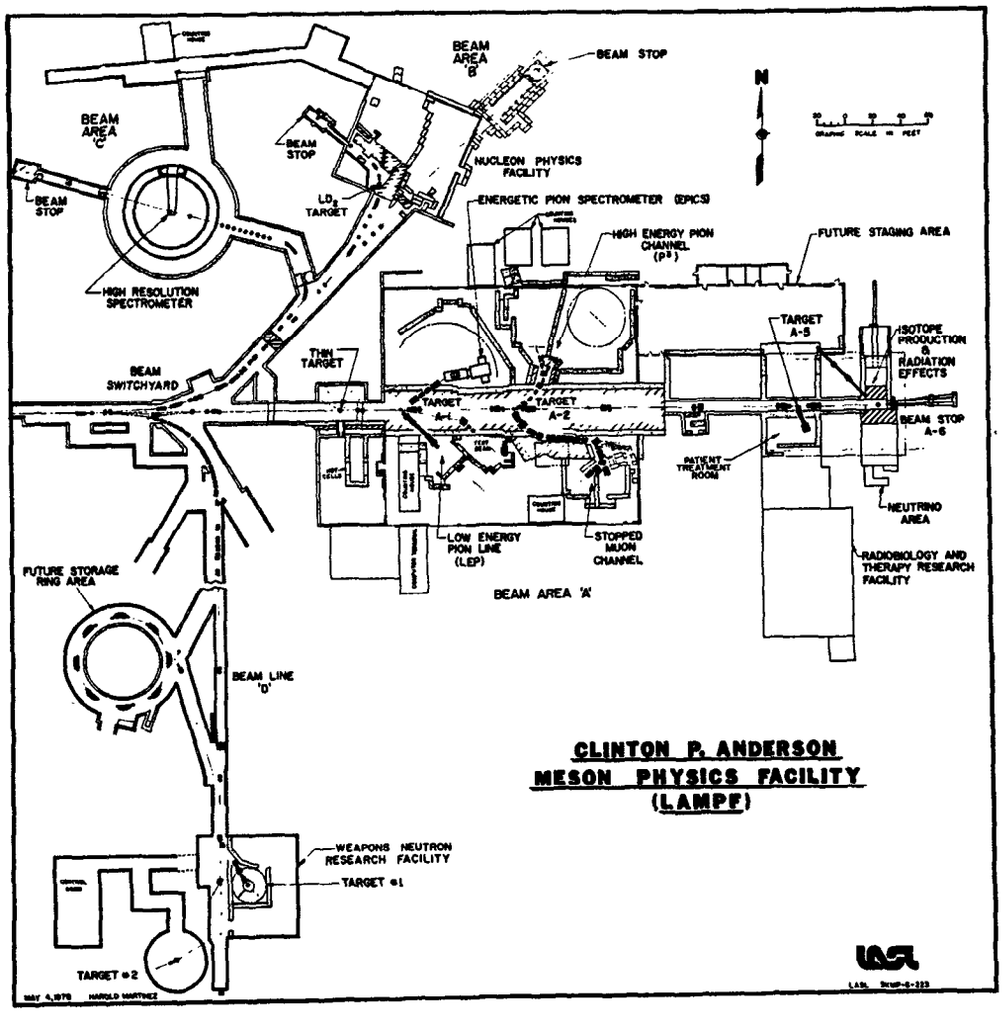
BEAM AREA 'B'
BEAM STOP
BEAM AREA 'C'
BEAM STOP
BEAM STOP
NUCLEON PHYSICS FACILITY
LD2 TARGET
ENERGETIC PION SPECTROMETER (EPICS)
HIGH ENERGY PION CHANNEL (P3)
FUTURE STAGING AREA
HIGH RESOLUTION SPECTROMETER
TARGET A-5
ISOTOPE PRODUCTION & RADIATION EFFECTS
THIN TARGET
BEAM SWITCHYARD
TARGET A-1
TARGET A-2
BEAM STOP A-6
PATIENT TREATMENT ROOM
NEUTRINO AREA
LOW ENERGY PION LINE (LEP)
STOPPED MUON CHANNEL
RADIOBIOLOGY AND THERAPY RESEARCH FACILITY
BEAM AREA 'A'
FUTURE STORAGE RING AREA
BEAM LINE 'D'
CLINTON P. ANDERSON
MESON PHYSICS FACILITY
(LAMPF)
WEAPONS NEUTRON RESEARCH FACILITY
TARGET #1
TARGET #2
N

Fig. 1

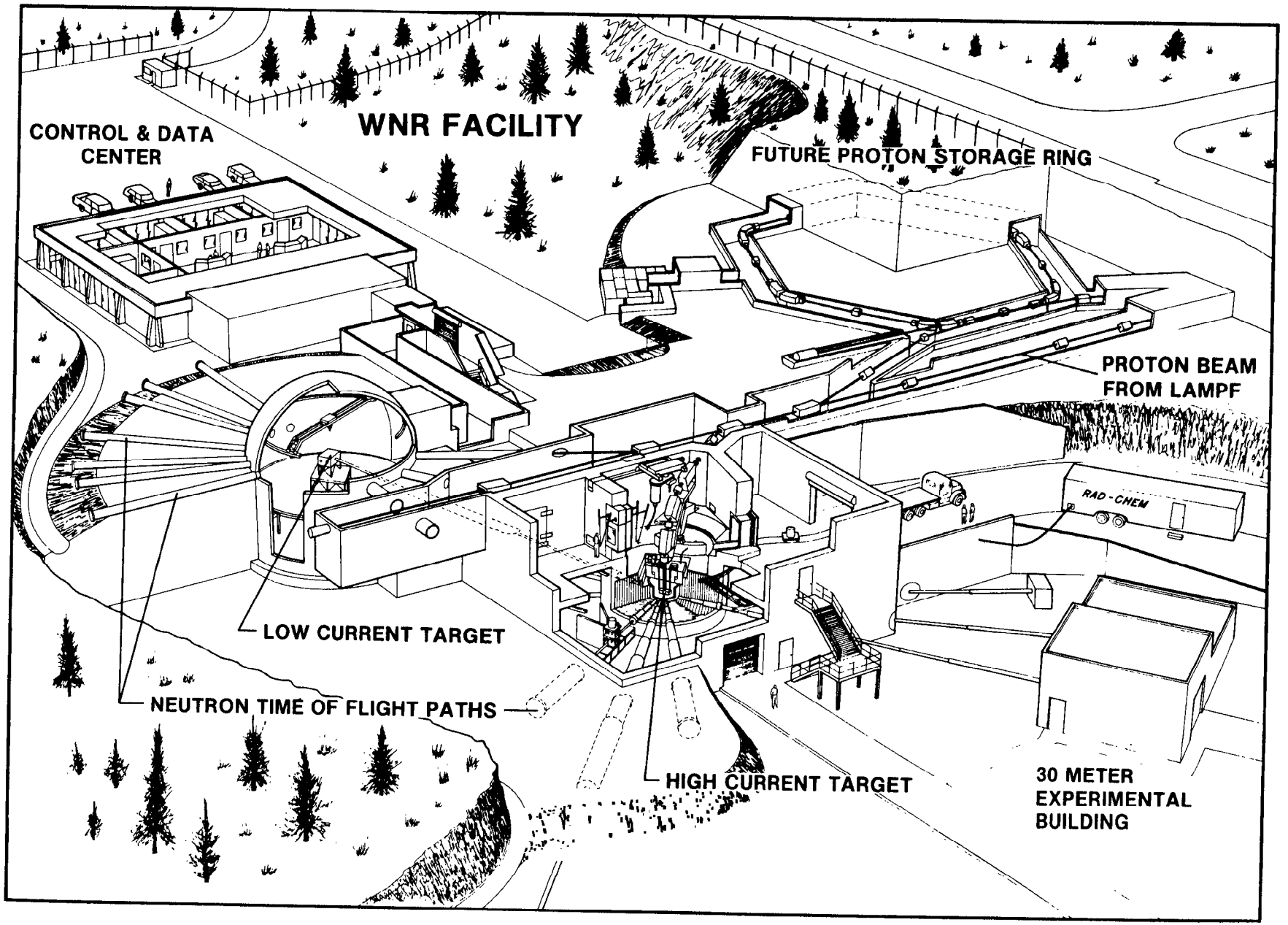
WNR FACILITY
CONTROL & DATA CENTER
FUTURE PROTON STORAGE RING
PROTON BEAM FROM LAMPF
RAD-CHEM
LOW CURRENT TARGET
NEUTRON TIME OF FLIGHT PATHS
HIGH CURRENT TARGET
30 METER EXPERIMENTAL BUILDING

Fig. 2

WNR COMPUTER SYSTEMS - PRESENT AND PROPOSED (DEM4-81)

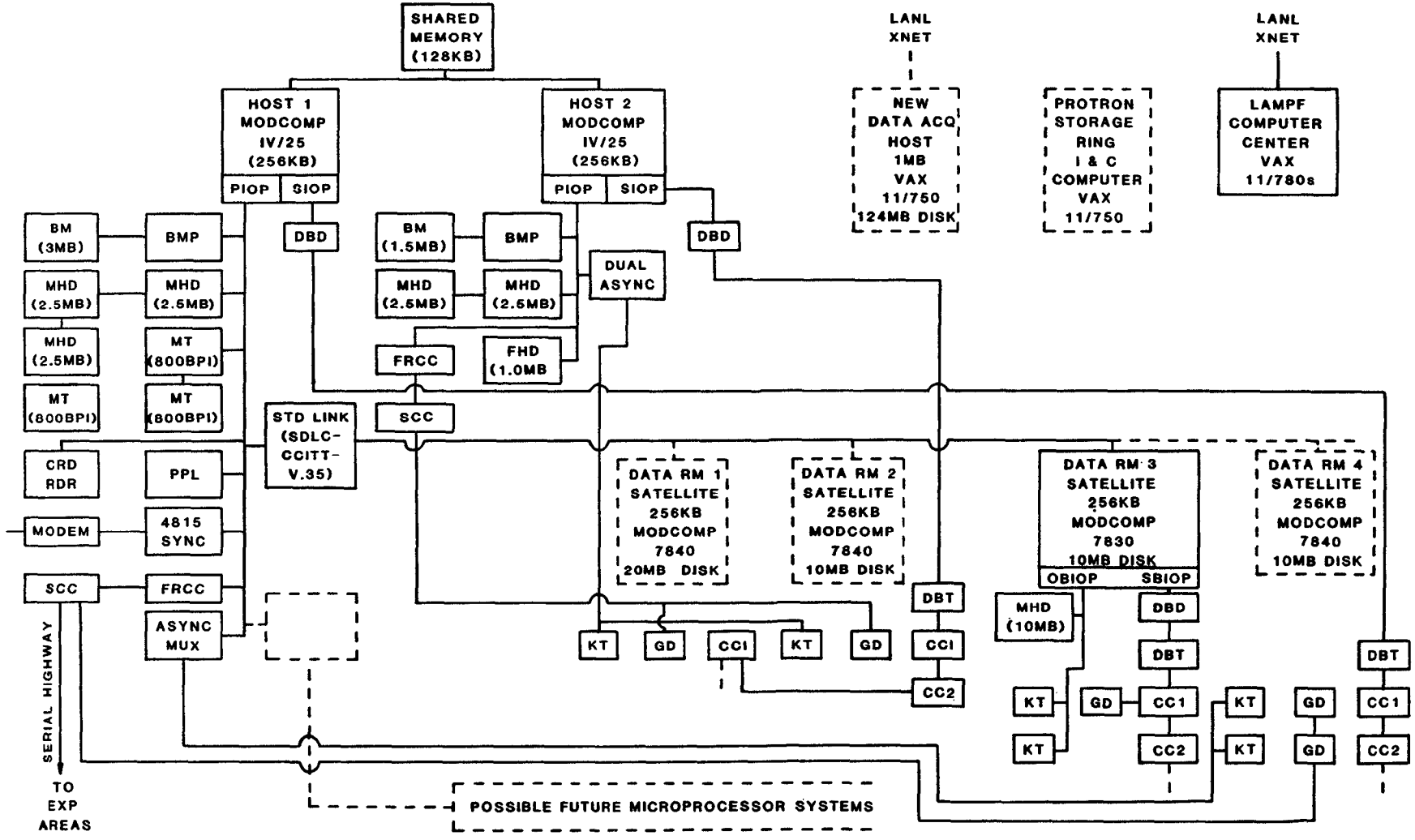

Fig. 3

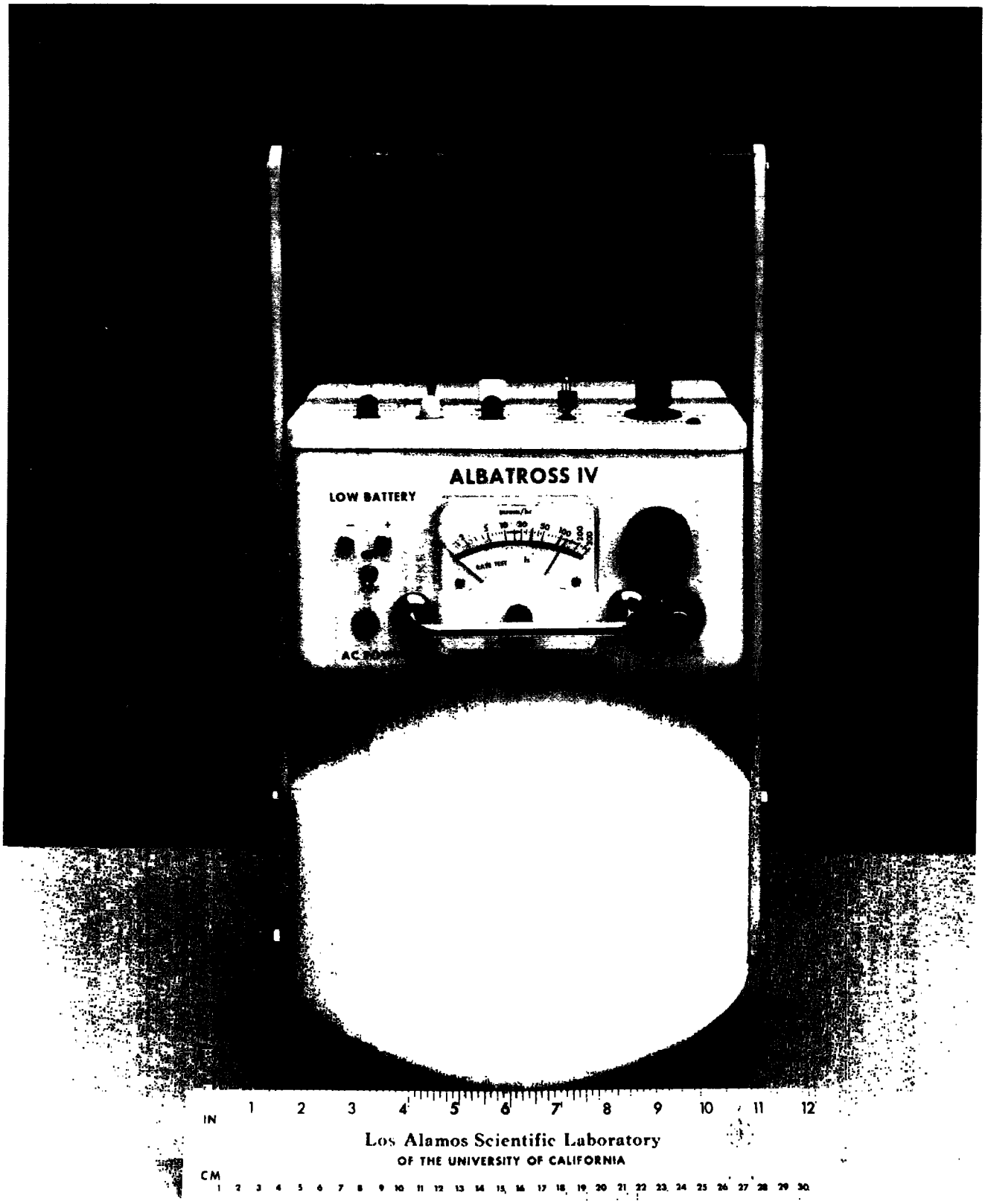
ALBATROSS IV
LOW BATTERY
IN
1 2 3 4 5 6 7 8 9 10 11 12
Los Alamos Scientific Laboratory
OF THE UNIVERSITY OF CALIFORNIA
CM

Fig. 4

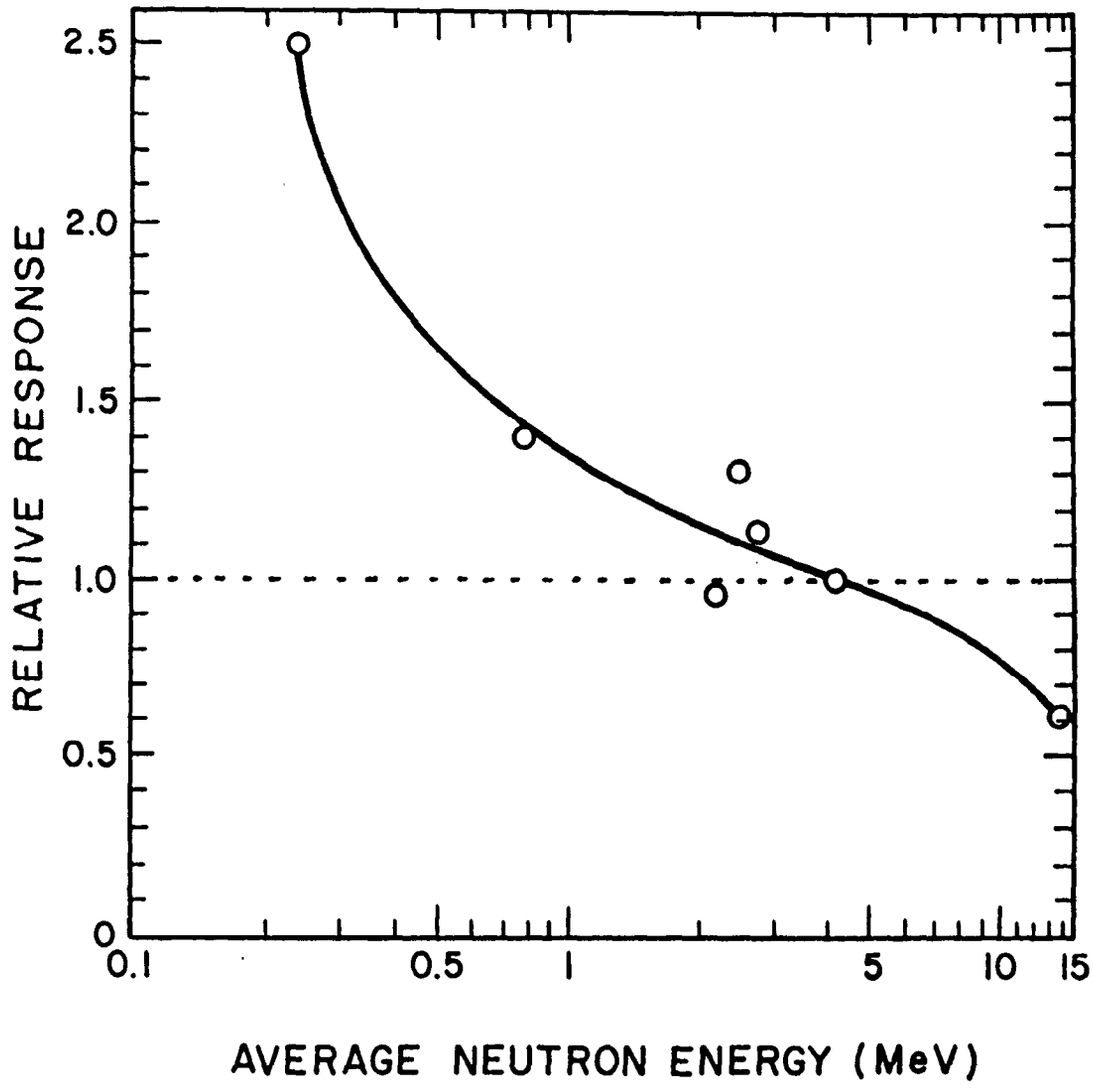

Fig. 5

Relative response of Albatross IV as a function of average neutron energy. The neutron sources used were; PuLi, PuF, ^{252}Cf, D-D, PuB, PuBe, and D-T, with average neutron energies of 0.25, 0.79, 2.2, 2.5, 2,8, 4.2, and 14 MeV, respectively.

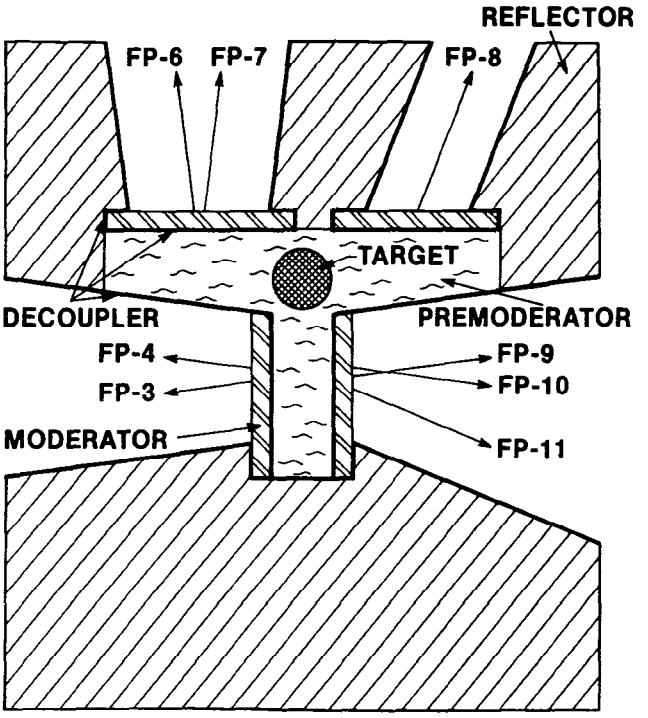

Fig. 6

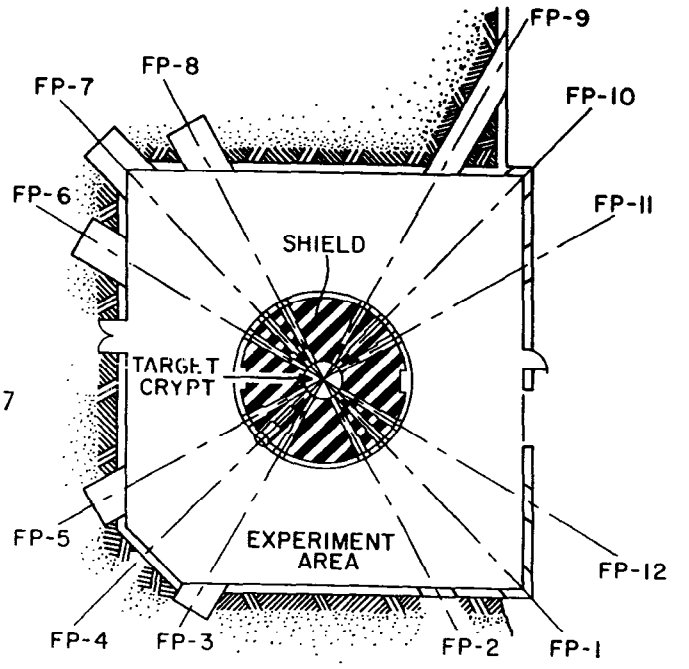

Fig. 7

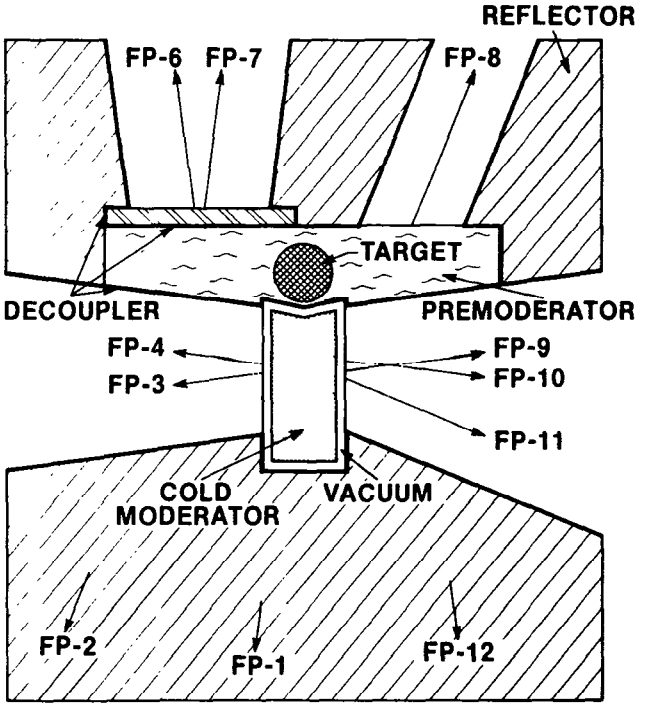

Fig. 8

I C A N S - V

MEETING OF THE INTERNATIONAL COLLABORATION ON

ADVANCED NEUTRON SOURCES

June 22-26, 1981

Status of the Los Alamos Proton Storage Ring*

Richard K. Cooper and George Spalek

Accelerator Technology Division, Los Alamos National Laboratory

Los Alamos, New Mexico

Abstract

The Proton Storage Ring for the Weapons Neutron Research Facility of the Los Alamos National Laboratory is reviewed as a construction project. The current status of construction and design is outlined.

Introduction

The purpose of this paper is not to describe the design features of the Los Alamos Proton Storage Ring (Ref. 1), but to describe the present status of the Ring as a construction project. To that end we will start by describing the status of the design and construction of the buildings, followed by the status of procurement actions, and finally we will indicate the design status of various components of the Ring.

Building Construction

A 12,500 square foot (1160 square metre) staging building is presently under construction and is scheduled for completion by July 15, 1981. This building will provide room for component fabrication and testing, as well as magnet assembly and mapping. Areas have been allocated for such activities as vacuum, low-level electronics, fast-kicker development, and 600 MHz and 3 MHz rf research and development. There will also be a machine shop in the building.

The Architect-Engineer for the project, Randy Holt and Associates of Albuquerque, New Mexico, is currently making detailed construction drawings of the Ring tunnel and the equipment building. These drawings should be complete by October 1, so that construction bids will be requested about October 15. The bids should be received by December 1 and opened December 15, so that construction of the Ring tunnel should begin in early 1982.

The Ring tunnel will be 18.5 feet (5.6 metres) wide and 12 feet (3.7 metres) high. The equipment building, which will house the power

*Work performed under the auspices of US Department of Energy.

supplies, rf sources, and general electronics, will be 90 feet square (27 metres square) and will be located above the Ring tunnel. The vertical separation from the roof of the tunnel to the floor of the equipment building will be 23.5 feet (7.2 metres) of earth and steel shielding.

Equipment Procurements

In this section we will indicate what major items have been purchased or have been put out for bids. In general those items which have been completely specified and for which complete design drawings are in hand have either been purchased or bids requested; we are not holding back any orders.

A Digital Equipment Company VAX 11/750 has been purchased as the control computer; it should arrive by July 1, 1981. Approximately 60% of all the vacuum equipment has been purchased. This percentage includes all the vacuum pumps and their controllers, valves, ion gauges, and pumping tees. The five injection line quadrupole magnets have been purchased; the power supplies for these magnets are out for bid. The bids for the Ring dipole magnets are due to be received June 15; the copper conductor for the prototype magnet coil has been purchased. The power supply specifications for the Ring dipoles are being written at this time and shortly will go out for bid. The power triodes for the transverse damper distributed amplifiers are on order. Finally, the 603.75 MHz transmitter is out for bids.

Design Status

The injection and extraction line optics, to be reported on at this conference by A. Jason, have been developed to the point where the location and size of the skew dipole magnets and the quadrupole magnets can be specified. As a result, these magnets are now in the process of being designed. The Ring focusing quadrupoles are also being designed, as are the septum magnets. The beam dump for the unstripped neutral injected beam is being designed.

Research and Development

Areas of significant research and development effort in the PSR project tend to be centered about those items which are expected to have a long lead time. Principal among these items is the fast extraction kicker, the power supply (ferrite-isolated Blumlein line) for which has recently achieved its rated voltage and repetition rate (±50 kV, 1 kA, 720 Hz). The active damper high-power electronics have been under development for several years (Ref. 2). A prototype beam position monitor (stripline electrodes) has been developed and installed in Line D for testing purposes. With an eye toward solving or alleviating the beam loading problem in the 603.75 MHz rf system some effort has been spent in developing rapid cavity detuning techniques.

Areas which have received little research effort to the present time include principally the rf bunching systems (an area of considerable concern), the beam scraper system, and the multipole magnet system. These areas are now starting to be addressed in a significant way, although our efforts could benefit greatly by the addition of experienced personnel.

References 3 through 6 are papers on PSR research and development published in the proceedings of the March 1981 National Accelerator Conference in Washington, DC.

Schedule

Presented here in tabular form is the projected schedule for the PSR:

3/83	Beneficial occupancy of Ring tunnel
6/83	Beneficial occupancy of equipment building
3/84	Line D modifications complete
6/84	PSR equipment installation complete
10/84 thru 3/85	LAMPF/Line D/WNR shutdown
3/85	PSR ready to accept beam

References

1. George P. Lawrence et al., "LASL High-Current Proton Storage Ring," Proc. of the XI Int. Conf. on High Energy Accelerators, p. 103, Geneva, Switzerland, July 1980.

2. James S. Lunsford, "Design of a Power Amplifier for the LAMPF Proton Storage Ring Transverse Damper System," IEEE Trans. on Nucl. Sci., NS-28, p. 2952, 1981.

3. E. Higgins and F. Wells, "A Beam Position Monitor System for the Proton Storage Ring at LAMPF," IEEE Trans. on Nucl. Sci., NS-28, p. 2308, 1981.

4. B. Sandberg, "A Novel Current Monitor for DC and Modulated Magnets in the Proton Storage Ring," IEEE Trans. on Nucl. Sci., NS-28, p. 2314, 1981.

5. Andrew J. Jason et al., "Neutralization of H^- Beams by Magnetic Stripping," IEEE Trans. on Nucl. Sci., NS-28, p. 2704, 1981.

6. Daniel W. Hudgings and Andrew J. Jason, "Los Alamos Proton Storage Ring Extraction System," IEEE Trans. on Nucl. Sci., NS-28, p. 2791, 1981.

Jül-Conf-45 A2

I C A N S - V
MEETING OF THE INTERNATIONAL COLLABORATION ON
ADVANCED NEUTRON SOURCES
June 22-26, 1981

Present Status and Future Program of KENS

Noboru Watanabe and Hiroshi Sasaki
National Laboratory for High Energy Physics
Oho-machi, Tsukuba-gun, Ibaraki, 305 Japan

Yoshikazu Ishikawa and Yasuo Endoh
Physics Department, Tohoku University
Sendai, 982 Japan

Kazuhiko Inoue
Department of Nuclear Engineering, Hokkaido University
Sapporo, 060 Japan

Abstract

KENS has been operated without any trouble for one year, and been open to all users in Japan from April 1981. Present paper describes present status of machine operation, research activity at KENS, spectrometers and their performances with experimental results already achieved, and future program of KENS-I' and KENS-II. KENS-I' is a project to increase the effective neutron beam intensity one order of magnitude in near future by means of the improvement of the present machine. KENS-II is a big future project which can provide hundred times higher beam intensity than KENS-I. Discussions for it have just started.

§1 Present Status of Operation

The KEK booster synchrotron has been operated successfully since the last ICANS meeting and has delivered 500 MeV proton beam to the neutron experimental facility and also to the meson facility as shown in Fig. 1.

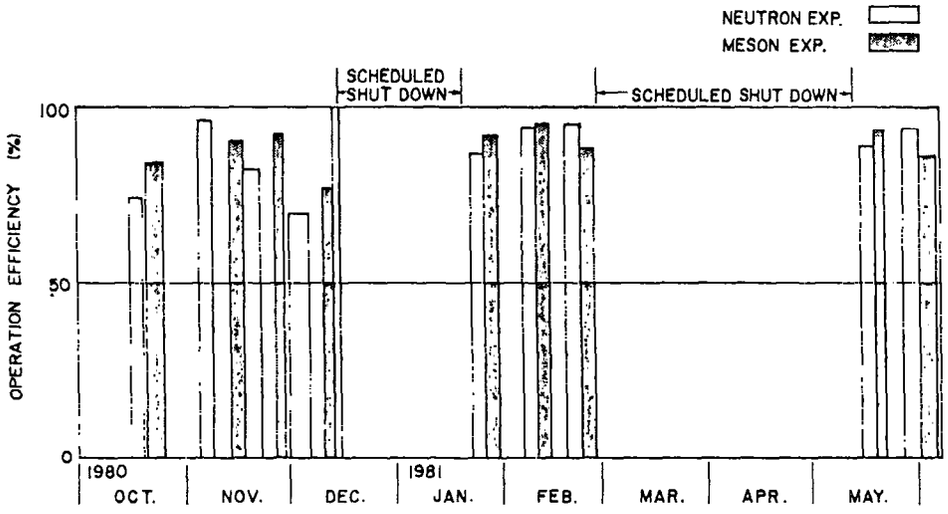

Fig. 1 Operation diagram

Neutron target as well as the cryogenic moderator have been operated without any trouble. The beam intensity of thermal neutrons obtained from the polyethylene moderator at ambient temperature is about 1.4×10^6 $n_{th}/cm^2 \cdot sec$ at the beam hole exit (4 m from the moderator). The solid methane moderator has been operated at 18.3 K and provided cold neutron beam of about 6×10^5 $n_c/cm^2 \cdot sec$ at 4 m position from the source and about 1×10^5 $n_c/cm^2 \cdot sec$ at the guide tube exit, in the time averaged values.

A remote exchange machine for the polyethylene moderator which is located below the target has been installed and has successfully changed the spent moderator to the new one.

§2 Research Activity

The KENS facility has been open to all users in Japan from this fiscal year (1981, April) and two types of proposals were accepted. One, Type I, is a project research which makes a big research group installing a spectrometer at a beam hole, while the other one, Type II, is a small research program which provides only the samples and uses the spectrometer already installed. Nine proposals are accepted as Type I (A and B, by KENS classification). They are listed in Table I.

Except RAC, all other proposals are continuation from the last year. As far as the Type-II proposals are concerned, twenty proposals are presented, in which eight proposals were accepted and all the others are on the waiting list. Since the total machine time is devided into two between the neutron and meson groups. We have already a serious problem of shortage of the neutron machine time.

Table I List of Type I Proposal

Group Name	Spectrometer	Classification	Number of Researchers
HIT	HIT	B1	11
LAM	LAM	B1	9
MAX	MAX	B1	5
SAN	SAN	B1	11
TOP	TOP	B1	9
PEN	PEN	A	9
FOX	FOX	A	5
UCN	Ultra Cold Neutron	A	6
RAC	RAC	A	5

§3 S!ectrometers and Their Performances

3.1 HIT

HIT is the total scattering spectrometer constructed to measure the precise structure factor, S(Q), of liquids and amorphous solids over a wide range of momentum transfer ($Q = 0.1 - 100\ A^{-1}$) at a higher rate of data collection[1]. The machine has fifty ^3He counters and is equipped with a sample changer which can accomodate up to six different samples. Lower angle detector banks ($2\Theta = 2 \sim 5°$) composed of annulus ^6Li glass scintillator will be equipped in this fiscal year, which are useful for Placzek correction and also provide useful data at lower Q ($Q_{min} \sim 0.05\ A^{-1}$).

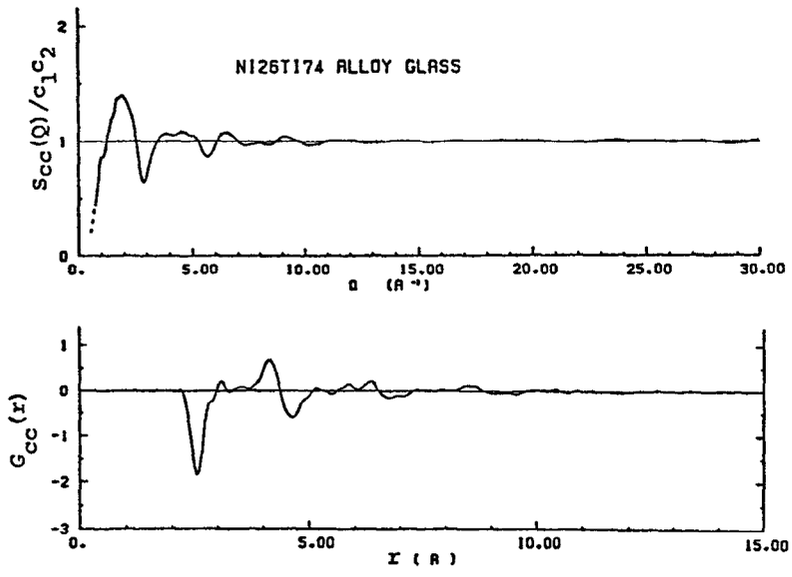

Fig. 2 $S_{cc}(Q)$ and $G_{cc}(r)$ of Ni-74at%Ti zero alloy glass

Metal-metal alloy glasses such as Pd-Zr, Cu-Ti, Ni-Zr, and Ni-Ti systems have already been measured. Particularly neutron zero alloys (<b> = 0) are interesting to make a direct observation of pure concentration-concentration correlation,. $S_{cc}(Q)$, that is the chemical short range order between unlike atoms. The observed $S_{cc}(Q)$ and transformed $G_{cc}(r)$ of Ni-74at%Ti zero alloy glass are shown in Fig. 2, which indicate that the chemical short range order clearly exists in metal-metal alloy glass[2]. HIT can perform these kinds of measurements quite easily which are very much difficult to do with the conventional method.

Higher data collection capability of the HIT makes it possible to measure many samples covering a wide range of compositions, and high Q capability can provide a highly resolved space correlation. Based on these advantages of the HIT, deuterium absorbed metal-metal alloy glasses were extensively studied in a wide range of deuterium concentration. In Fig. 3 are depicted the G(r) for $Pd_{35}Zr_{65}D_{17}$ compared with those for $Pd_{35}Zr_{65}$ glass[3]. Extra peak is clearly observed at small r in the deuterium absorbed sample which corresponds to the metal-deuteron correlation in this glass. Systematic studies are under progress.

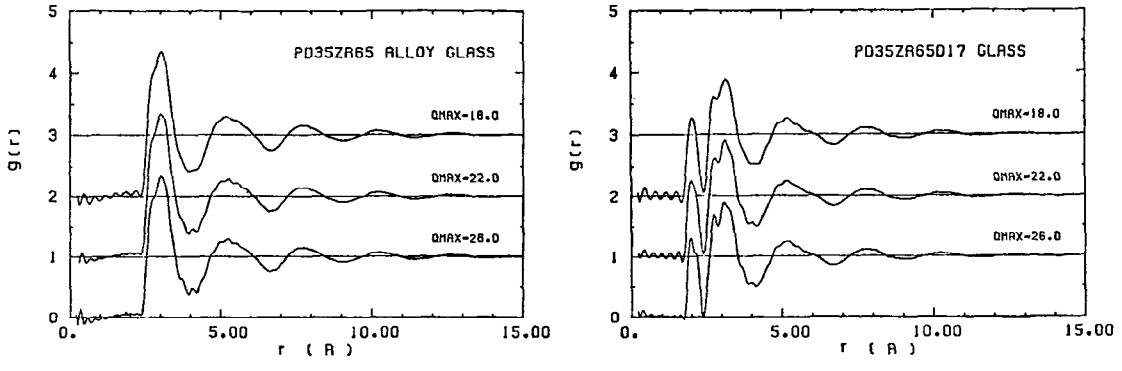

Fig. 3 G(r)'s for amorphous $Pd_{35}Zr_{65}D_{17}$ (left) and $Pd_{35}Zr_{65}$ (right)

Measurement of small and/or absorbing sample is one of the most promising field of the application. In Fig. 4 is shown the S(Q) measured for an amorphous alloy of $Ni_{60}{}^{N}B_{40}$[4] (natural boron compound, 0.4 gr in weight) to demonstrate the higher performance of the HIT for this application[4].

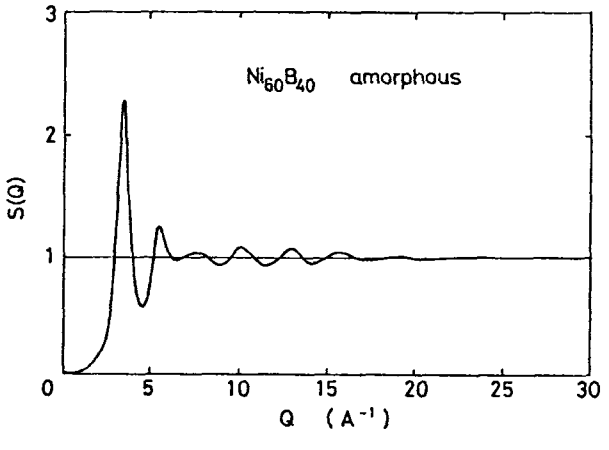

Fig. 4 S(Q) of amorphous $Ni_{60}B_{40}$ (natural boron compound, 0.4 grams)

3.2 LAM

The LAM is the inverted geometry quasielastic spectrometer with the conventional energy resolution[5]. The spectral distortion is very small due to the inverted geometry and the nearly flat cold source spectra. The signal-to-background ratio is extremely good because of the pulsed source. This spectrometer is of value in the performance of peak profile analysis in quasielastic studies. Fig. 5 shows the raw data of the quasielastic spectra recently obtained from the deuterium substituted methanols and their

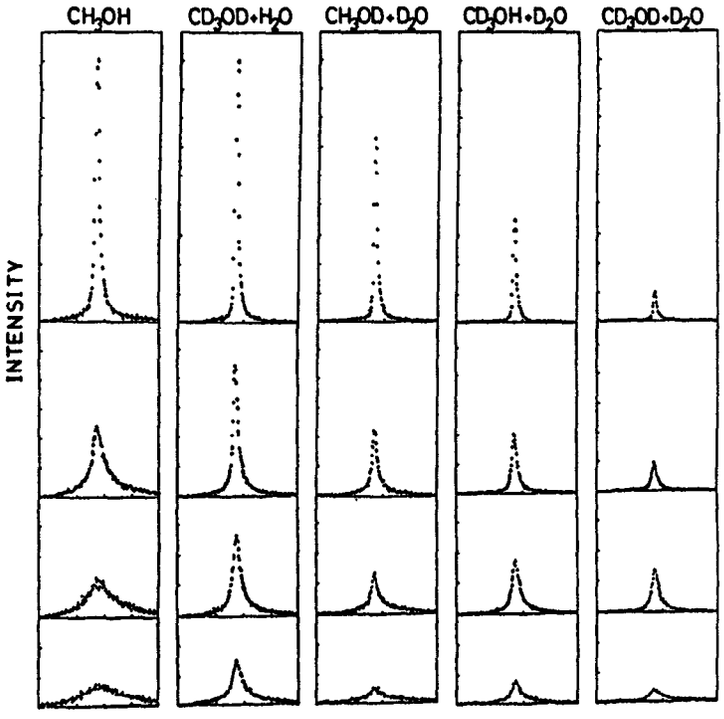

Fig. 5 Scattered spectra from the deutrium substituted methanols and their aqueous solutions measured by the LAM. From top figure to bottom one the scattering angle varies from 25° to 115°.

aqueous solutions at ambient temperature[6]. These data are useful for the investigation of the dynamical structure of the water, methanol, and their solutions. Investigations concerning the polymers and polymer solutions, some magnetic materials and hydrogen diffusion in amorphous metal also continuing.

3.3 MAX

MAX is the multi-analyzer crystal spectrometer equipped with fifteen separate analyzer crystals[7]. The spectrometer was constructed to test, first of all, the feasibility of the TOF machine for studying the collective excitations. Fig 6 is the results of scattering from a single crystal of Fe(Si) measured along [111] around the (110) reciprocal lattice point[8]. Fig. 6(a) is the TOF spectra, while Fig. 6(b) shows magnon and phonon dispersions along [110] simultaneously obtained. The broken lines are the dispersions previously obtained by triple axis spectrometers. We found the magnon scattering could be well detected up to 70 meV. The results are quite encouraging and the spectrometer would be used for studying the collective excitlation in non-equilibrium system.

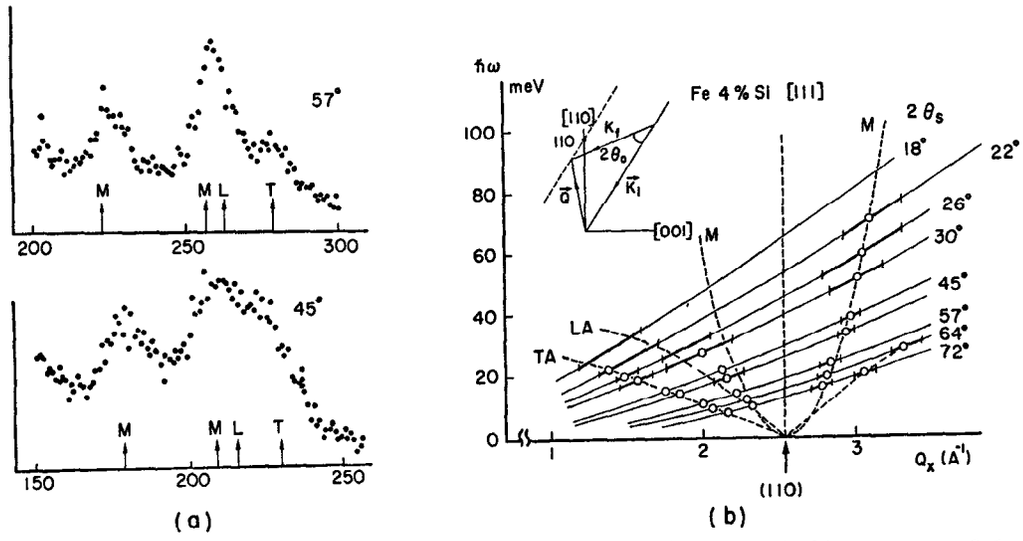

Fig. 6 Coherent scattering from a single crystal of Fe(Si) measured by MAX along [111] around the (110); (a) typical TOF spectra of scattered neutrons at selected scattering angles, (b) magnon and phonon dispersions.

3.4 SAN

SAN is the small angle scattering spectrometer equipped with a movable two dimensional PSD inside a vacuum chamber[9]. A characteristic of the spectrometer is its feasibility to measure simultaneously a wide range of momentum transfers from 3 x 10^{-3} to 4 A^{-1}. Fig. 7 is an example to demonstrate this fact, where the scattering from a Al-10%Zn-0.1%Mg is shown[10]. The low Q data is the one dimensional display of the two dimensional PSD data, while the insert to the figure is the result from a fixed counter with a scattering angle of 150°. This characteristic is particularly useful for studying non-equilibrium phenomena as spinodal decomposition or magnetic response in the spin glass systems, and the routine studies have been carried out on this field.

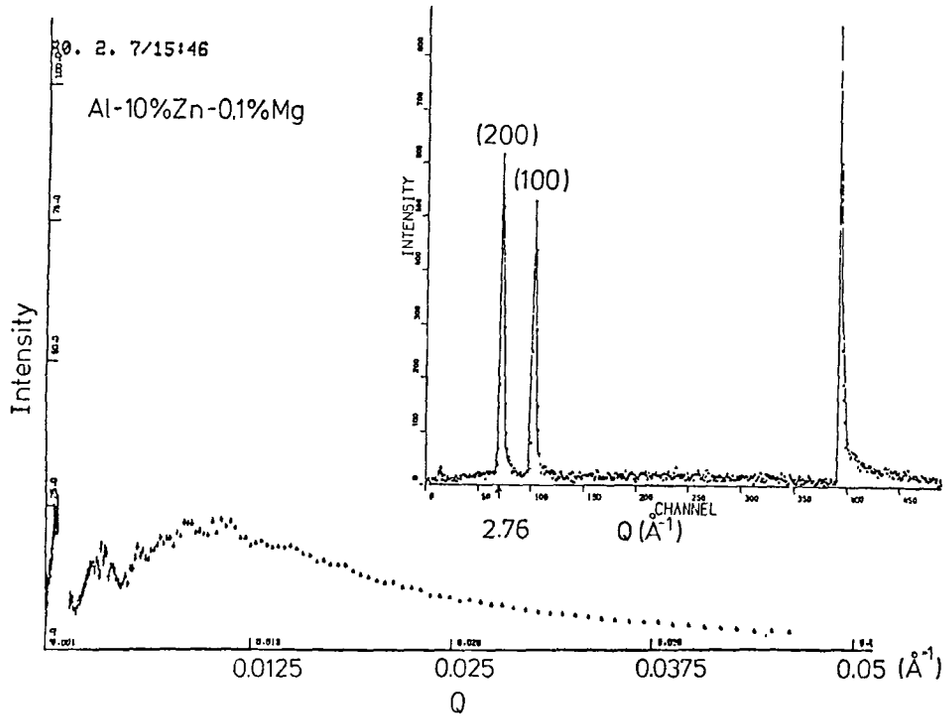

Fig. 7 Small angle scattering from a Al-10%Zn-0.1%Mg measured by SAN: insert to the figure is the results measured by a fixed conventional counter at 2Θ = 150°.

Another characteristic is its convenience for studying the single crystals. In Fig. 8 is shown the Bragg scattering from a single crystal of MnSi at 10 K with a long period of 180 A[10]. The figures correspond to the on-line display of 2D-data of satellites with Q = 0.035 in two different wave length ranges. The spectrometer could determine the wave length dependence of the satellites peaks as well as the size of the satellites from which we found a new fact that the helical structure has a shorter dimension of about 1,000 A in the screw axis compared with that in the perpendicular direction which is about 4,000 A. The extinction free intensity could also be determined.

Small angle scattering from polystyrene latex, collagen in hen and purple membrane have also been measured.

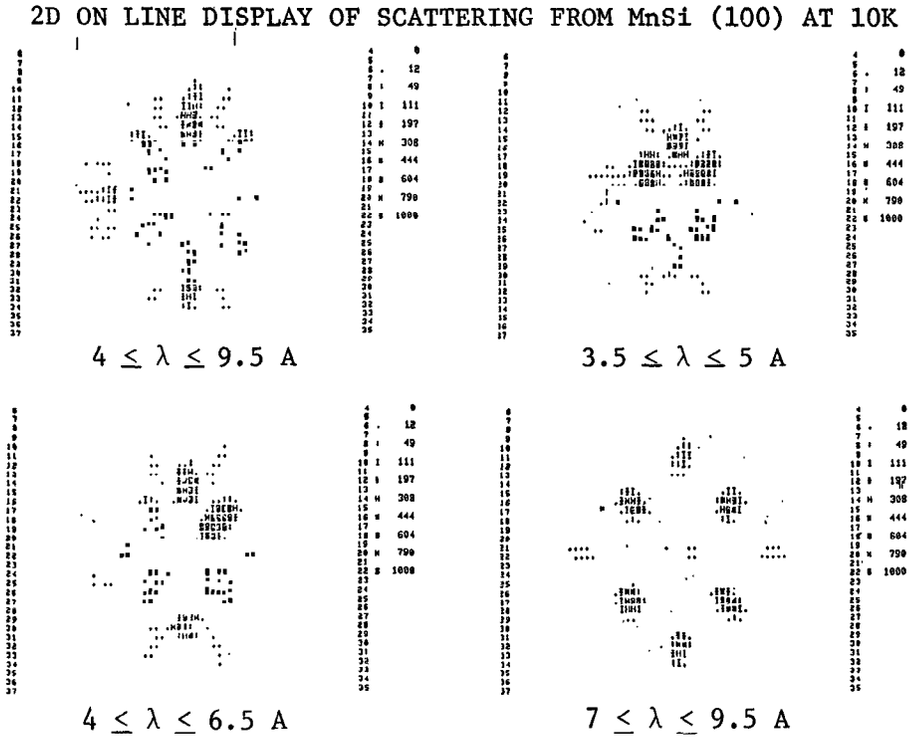

Fig. 8 Bragg scattering from a single crystal of MnSi at 10 K measured by 2D PSD of SAN in different wave length ranges.

3.5 TOP

TOP is the polarized cold neutron spectrometer utilizing total reflection from a Soller slit of Fe-Co[11]. The polarizer itself as well as the scattering apparatus was largely improved since last ICANS. A recent measurement on the polarizability using the (111) reflection of a Heusler crystal as a polarization analyzer suggests that the polarizability is more than 95 % over an entire range of wave length from 4 A to 12 A. (See Fig. 9.)

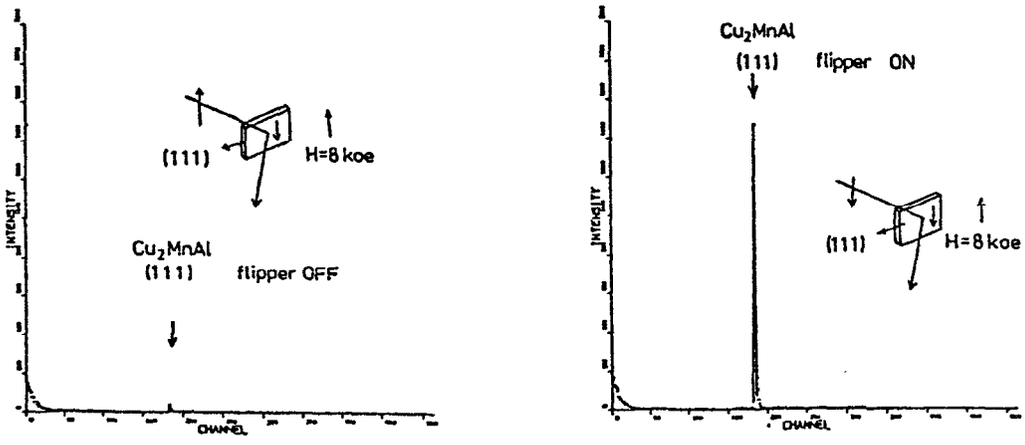

Fig. 9 Polarization dependent 111 *reflections from the Heusler analyzer for the polarizability test.*

The current studies with TOP are primarily concentrated on the small angle scattering from magnetic disordered alloys as well as magnetic bilayers. In Fig. 10 is demonstrated a typical polarization dependent TOF diffraction patterns obtained from bilayer films of Fe-Pd and Fe-Sb[12].

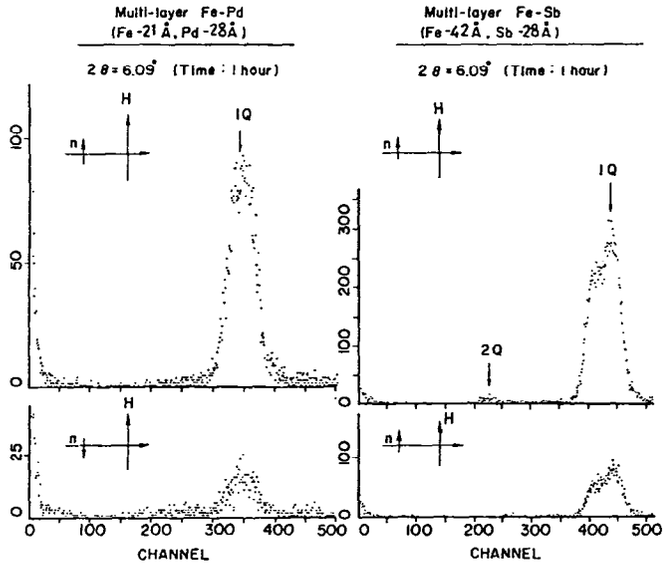

Fig. 10 Polarization dependent TOF diffraction patterns obtained from films of Fe-Pd and Fe-Sb.

3.6 PEN

PEN is the polarized epithermal neutron spectrometer designed for studying the high energy magnetic excitations. The polarization of epithermal neutrons will be achieved by using a dynamically polarized proton filter[13]. The spectrometer will be completed at the end of 1982, and the study of the polarizing process of the proton spins by means of the dynamical polarization will be started from April of 1982.

3.7 FOX

FOX is the single crystal diffractometer equipped with a conventional four circle goniometer which has been installed at H1 beam hole by the user's group at National Institute for Research in Inorganic Materials. The instrument has a conventional detector at present time which will be replaced by a position sensitive area detector in near future.

3.8 RAC

RAC is a epithermal neutron spectrometer using a resonance detector which is planned to construct in coming two fiscal years. A test set-up for various resonance detectors has been installed at H7 beam hole, and developing studies of the detector has started. Another epithermal neutron spectrometer using a crystal analyzer has been constructed and installed at the same beam hole (H7). The instrument is essentially the same to the crystal analyzer spectrometer at Tohoku linac[14] but with higher performance.

§4 Future Program

Based on the encouraging results obtained by both of the neutron and the meson groups, improvement of the present machine as well as the future plans have started to be discussed.

4.1 KENS-I'

KENS-I' is a project to increase the effective neutron beam intensity on the sample about one order of magnitude by means of the improvement of the present accelerator as well as the target station as early as possible. Following factors are under consideration and studies for that have already started.

4.1.1. Accelerator

The conversion of the injection scheme in the booster synchrotron to the charge exchange injection with H^- ions is one of the shortest way to increase the proton beam current from the booster. The developments of the ion source, the pulsed magnet for the orbit dump and its power supply, the preparation of the stripper, etc. are now in progress together with the project of the acceleration of the polarized proton beam. H^- ion beam will be delivered to the booster synchrotron in 1983. The beam intensity will be increased by a factor of two by this conversion.

4.1.2. Target-moderator-reflector Assembly

The efficiency of the present KENS target-moderator-reflector assembly is already in higher level if we compare it with those at other laboratories[15]. The reason will be as follows:

(i) The target is not diluted by the cooling channels due to the lower power dissipation.

(ii) The distances between target and moderator were minimized.

(iii) The target of the rectangular shape in the cross section was adopted which can increase the lackage of fast neutrons towards the moderators.

(iv) Solid methane moderator was adopted as the cold neutron source which can provide higher cold neutrons intensity than liquid hydrogen moderator.

In addition to the above reasons, the shorter distance between moderator and sample due to the thinner bulk shield of KENS can provide higher beam intensity at the sample position for many applications.

We believe, however, that there exist still much room for improving the efficiency of the target-moderator-reflector assembly by the further optimization. A program for it has started which includes the items below.

(i) Optimization of the moderator size under the actual boundary conditions of the existing compornents: especially the possibility

for converting the present solid methane moderator to a larger one (in lateral dimensions).

(ii) Optimal coupling (or decoupling) between target and moderator: especially the possibility for converting the present KENS solid methane moderator to a coupled one at an acceptable sacrifice of the pulse characteristics, and the possibility to reduce the thickness of the present B_4C decoupler for the polyethylene moderator which might be too thick for most applications.

(iii) Optimal shape of the moderator: various grooved moderator for both embient temperature and cold moderators.

(iv) Optimal reflector-filter: performance of the solid methane moderator with a reflector-filter of para-hydrogen or cooled beryllium.

Most opeimization studies listed above will be performed using Hokkaido linac and its cold neutron source. Some preliminary measurements were already performed at Hokkaido on a coupled and a decoupled solid methane moderators. It turned out that the beam intensity of cold neutrons from the coupled moderator was higher by about 35 percent than that from the decoupled one, while the increase in pulse width for the former was less than 15 percent[16]. This fact suggests that a higher gain factor for a couple solid methane moderator will be expected for KENS, because the reflector saving in KENS is much larger than that in Hokkaido.

We are expecting a total gain factor of, at least, 1.5 by the further optimization of the assembly.

4.1.3 Uranium Target

The convension of the present tungsten target to a depleted uranium is planned in order to increase the neutron yield by a factor of two. We believe that the rectangular shape of the present target should be conserved to keep the higher coupling efficiency between target and moderator. A Zircaloy-2 clad U alloy target is considered, which will be produced and supplied by Argonne National Laboratory. Some developments of the cladding for the rectangular shape target will, of course, be necessary in some extent. Uranium target and its cooling system should be designed for the proton beam current of several μA which might, in best case, be expected for the improved machine. We are planning to use a uranium target, at latest, in early 1984. Design studies for the heat transfer and for the thermal stress have started.

The present bulk shield of KENS-I will be adequate for KENS-I' because the measured radiation level is one third or one fourth of the regulation, and because the high energy neutron flux is proportional to the proton beam intensity, not depending upon the target material.

4.1.4. Guide Tube

The time averaged integral cold neutron flux obtained at the guide tube exit is about 1×10^5 n/cm^2•sec which is almost a half of the expected value. The reason is due to the fact that the transmittance of the guide tube was only 50 per cent[17]. Improvement of the transmittance has started which

belongs to KENS-I project rather than KENS-I', but we can expect, in best case, another gain factor of 1.6 in cold neutron intensity from the guide tube.

4.2 KENS-II

KENS-II is a big project to construct a new accelerator and a neutron scattering facility so as to make the neutron scattering research with a neutron beam intensity 100 times higher than KENS-I. Although we have made no decision on the choise between the pulsed and quasi-continuous neutron sources, the KENS group people incline for a moment on a side of the pulsed neutron source and hope to make an optimized design to achieve the desired neutron flux on the sample position with the minimum power supply. Since a big project of TRISTAN at KEK has been approved, it will be an improtant point of discussion that our new acclerator will be built as a part of the project (as an injector to the new machine) or not. Anyway, the new accelerator will be shared, at least, with the meson group. The design studies on a high intensity accelerator for the pulsed neutron source and pulsed meson source have got under way.

References

1) N. Watanabe, et al.: The High Intensity Total Scattering Spectrometer (HIT), Proc. ICANS-IV (1981) p.539.

2) T. Fukunaga, et al.: High Resolution Short-Range Structure of Metal-Metal (Pd-Zr, Ni-Ti, Cu-Ti) Alloy Glasses by Pulsed Neutron Total Scattering, to be presented in the 4th International Conf. Rapidly Quenched Metals. (Aug. 1981)

3) K. Kai, et al.: Structure Modifications of Metal-Metal (Pd-Zr, Ni-Ti, Cu-Ti) Alloy Glasses due to Hydrogen Absorption, ibid.

4) T. Fukunaga, et.al.: to be published.

5) K. Inoue, et.al.: Large Analyzer Mirror Low Energy Spectrometers LAM (KEK) and LANDAM(HU) and Electron Linac Cold Source. Proc. ICANS-IV (1981) P.592.

6) K. Inoue, et.al.: to be published.

7) K. Tajima, et.al.: Multi-Analyzer Crystal Spectrometer at KENS, Proc. ICANS-IV (1981) P.600.

8) K. Tajima, et.al.: to be published.

9) Y. Ishikawa, et.al.: Small Angle Scattering Spectrometer (KENS-SAN), Proc. ICANS-IV (1981) P.563

10) Y. Ishikawa, et.al.: to be published.

11) Y. Endoh, et.al.: Time of Flight Spectrometer with Optical Polarizer, Proc. ICANS-IV (1981) P. 609

12) Y. Endoh, et.al.: to be published.

13) S. Ishimoto: Neutron Polarization by Polarized Proton Filter, Proc. ICANS-IV (1981) P.630.

14) N. Watanabe and M. Furusaka: Time-Focussing Crystal Analyzer and Measurement of Local Modes of TaH_x, KENS Report-I (KEK Internal 80-1) (1980) P. 181.

15) N. Watanabe, et.al.: KENS Target Station, Proc. ICANS-IV (1981) P.181.

16) K. Inoue, et.al.: Some Neutronic Aspects of Solid Methane Moderator. Presented at ICANS-V (1981).

17) J. Mizuki, et.al.: Characteristics of KENS Cold Neutron Guide Tube, Proc. ICANS-IV (1981) P.521.

Jül-Conf-45

A3a

I C A N S - V
MEETING OF THE INTERNATIONAL COLLABORATION ON
ADVANCED NEUTRON SOURCES
June 22-26, 1981

Status of Argonne's Intense Pulsed Neutron Source IPNS-I

J. M. Carpenter
for the IPNS Group
Argonne National Laboratory
Argonne, Illinois
U.S.A.

Abstract

IPNS-I is approaching operational state. This report gives brief descriptions of the major components of IPNS-I, and describes the present status of each.

I. Introduction

Construction of IPNS-I is complete, and the final phases of checkout and tuneup of the accelerator, neutron generating systems and instruments are underway. This is the culmination of efforts begun with Argonne's first prototype pulsed spallation neutron source, ZING-P′ in 1974, and we are all excited.

Figures 1 and 2 show the overall layout of IPNS-I. Some small changes in instrument locations have been made since our last report. Figure 3 shows the facility at the end of May, 1981.

Since the time of the last ICANS meeting, we have seen and responded to the report of a well-publicized review of the U.S. neutron source program (the Brinkman Panel review), by which we felt threatened. The end result has been that IPNS-I will operate, although with a budget which seriously constrains operating time, and which will not allow us to pursue planned accelerator improvements to increase intensities to our original design goals. Thus our goal is now to produce 8 μA, 500 MeV proton beam on target, at 30 Hz. Operating time is envisioned to be 6 months per year, on a 24 hour per day, 12-day-on, 2-day-off schedule. We hope to improve performance of the accelerator eventually to give 12 μA, 500 MeV, 30 Hz, through experience, minor improvements and tuning.

II. Status of IPNS System Components

A. Rapid Cycling Synchrotron (RCS)

Beginning in August, 1980 after final shutdown of the ZING-P′ prototype, we have installed an extensive series of modifications of the RCS accelerator systems. (The paper of C. W. Potts, et al., in the accelerator sessions of this conference contains more details.) The table below summarizes the most important modifications:

RCS Modifications

- o Move Extraction Point
- o Install new kicker magnets and supplies
- o Install programmable octupoles and supplies*
- o Expand computer control systems
- o Strenghten shielding
- o Install new beam position diagnostics
- o Double capacity of RCS driver and predriver power supplies
- o Install new RF cavity bias system
- o Modify injection bumper system
- o Improve linac cavity cooling

* programmable sextupoles already were included.

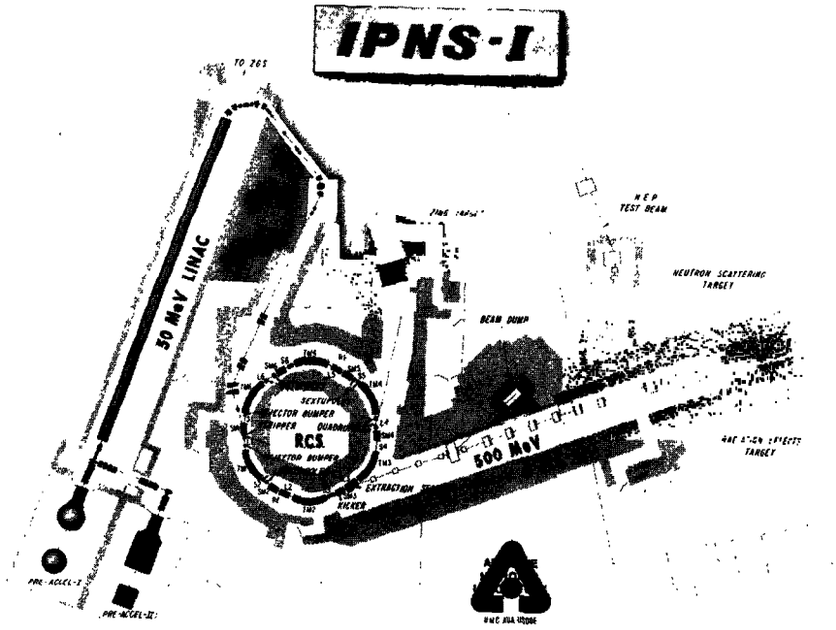

Figure 1

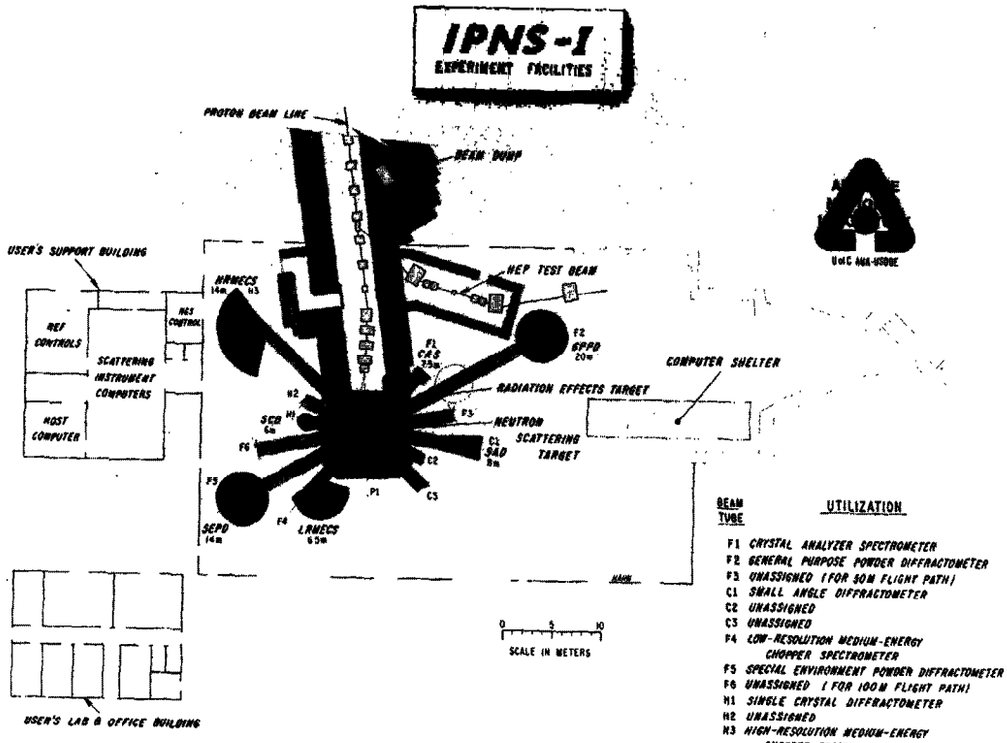

Figure 2

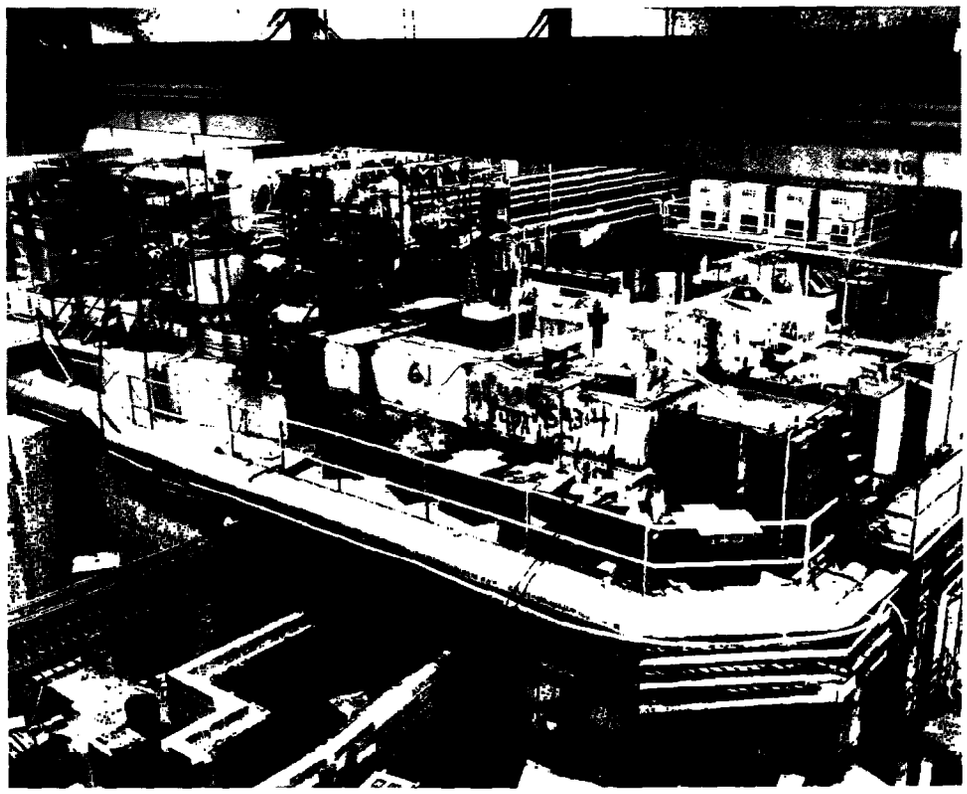

Figure 3

We completed these changes and resumed operations in a tuneup mode in April, 1981. Throughout, we found the usual large number of minor problems, and are curing them one by one. By early June 1981, we had accomplished a 18-hour run, with about 75% efficiency giving an average current of 4.5 μA of 500 MeV protons on the Radiation Effects Target of IPNS. During earlier 300 MeV operation, we delivered peak beam 20% higher than we were able prior to making these modifications.

Penning ion source development has been dropped, as have the once-intended modifications for 45 Hz operation.

B. Proton Transport System (PTS)

A new proton transport system connects the Rapid Cycling Synchrotron to the Neutron Generating System. The system includes a water-cooled graphite beam dump, which is designed as an efficient Faraday cup, and incorporates an upstream irradiation cavity. The system also provides a secondary (scattered) beam for use in testing high energy particle detectors. We adopted a very conservative design philosophy with the aim to minimize proton losses and maintain backgrounds in the experiment areas. All magnets and power supplies are second-hand components we obtained from Argonne's shutdown of ZGS as were most of the shielding steel and concrete. Ionization chamber loss monitors, beam-measuring toroids, and remotely movable segmented secondary emission monitors are distributed along the beam line to provide tuning and control information. The last magnet, a d.c. dipole, switches the beam alternatively between the two neutron generating targets.

The system is complete and, since debugging of instrumentation, has operated without any problems. We have noticed that the shield design contains a flaw in that groundshine beneath the shield walls may give personnel backgrounds greater than the design value, if proton losses are as great as 1% at any point. However, radiation surveys so far indicate no such problem.

C. Neutron Generating Systems

IPNS has two targets, one for fast-neutron irradiation experiments (the Radiation Effects Facility, REF) the other for slow-neutron beam experiments (the Neutron Scattering Facility, NSF) as shown in Figure 4. The targets shown in Figure 5 are nearly identical 25 mm x 96 mm ϕ depleted Uranium disks, clad with .5 mm thick Zircaloy-2, cooled by light water. Four of the eight disks contain thermocouples.

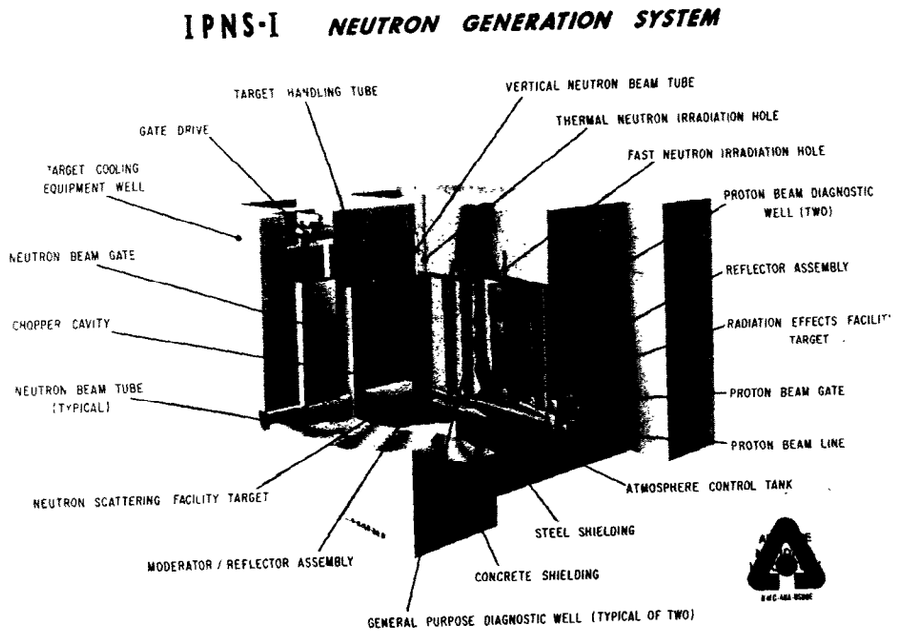

Figure 4

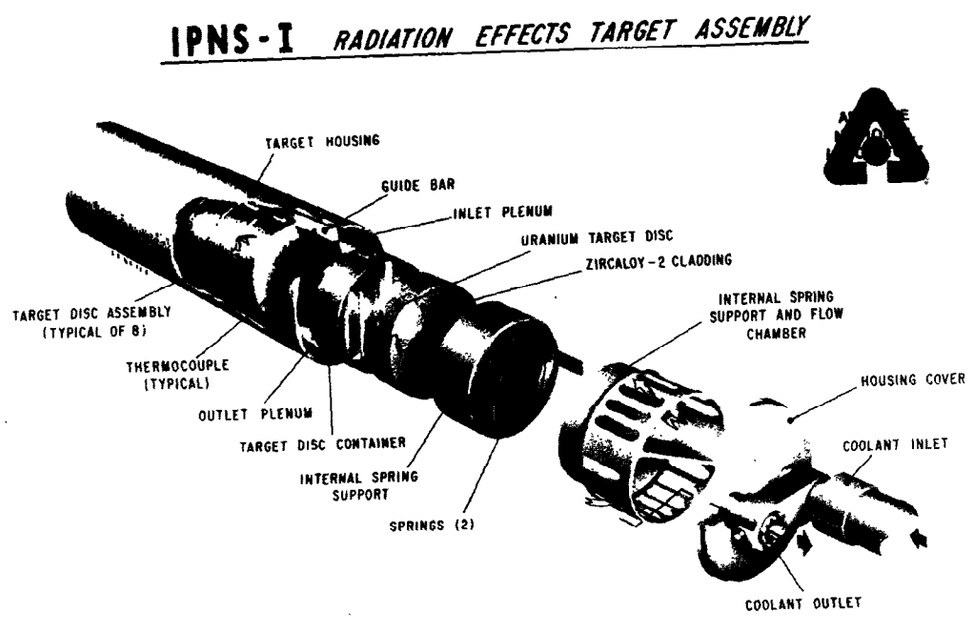

Figure 5

Aluminum-encased Pb reflectors surround the REF target, with two 50 mm ϕ vertical irradiation thimbles, and one 25 mm ϕ horizontal irradiation location. The reflectors are cooled by contact with a water cooled baseplate. Figure 6 shows the Radiation Effects Facility.

Proton beam delivered to the REF target produces the expected temperature rises in the disks; the thermal response consists of two main components, with e-folding times of about 7 sec, and 2 sec, which we have observed.

Four Beryllium-reflected moderators, two of Liquid H_2, two of Liquid CH_4, surround the Neutron Scattering Target illustrated in Figure 7. The inner Beryllium region is held at 100K to depress the thermal neutron spectrum and enable decoupling at lower energies. In the outer (300 K) Be region are two vertically-accessible thermal neutron irradiation thimbles. Pumps independently circulate cooled cryogens through the moderators. 14K He cools the hydrogen; 100K He cooled by liquid N_2 cools the methane. We have experienced a long series of problems with this complex system which are gradually being overcome. In early June, 1981, the system is not yet working and is delaying startup of the Neutron Scattering Facility. Figure 8 shows approximately the peak flux spectrum expected of the CH_4 moderator "H".

Primary shielding consists of about 4 meters of iron in an atmospheric control tank, and 2 meters of concrete. Twelve horizontal holes of approximately 30 x 45 cm^2 dimension provide neutron beams. Large iron plugs made in 4 pieces, contain 15 x 15 cm^2 channels into which collimating inserts can be placed. One-meter thick iron beam gates provide protection from direct radiation in the neutron beams when experimenters call for it. Each beam contains a vertically-accessible cavity in which to place a chopper, filter or other device. One of the gates has been modified to act as location for filters; one of the chopper cavities will contain a gate. The vertical beam contains a Ni guide tube.

Each target has its own cooling system; these can serve either target. Gross gamma activity near the demineralizer columns is continuously monitored to detect changes which may indicate target failure. Primary system water and surge-tank cover gas are periodically sampled and counted to detect abnormal activities. The monitoring and control system processes temperature and pressure data from numerous transducers in the target cooling system. The radiation around the cooling boxes is primarily .5 MeV annihilation radiation, which reaches levels around 400 mR/hr during 5 μA, 500 MeV operation.

Radiation surveys around the shield so far indicate that there are no weak spots when the Radiation Effects Target receives protons. However, contrary to our design intent, we find nearly .1 R/hr (at 5 μA, 500 MeV on the REF target) neutron dose rates above the solid-iron central shield, which we have tentatively identified as 25 KeV "iron-window" neutrons.

IPNS-I ***RADIATION EFFECTS EXPERIMENTAL ASSEMBLY***

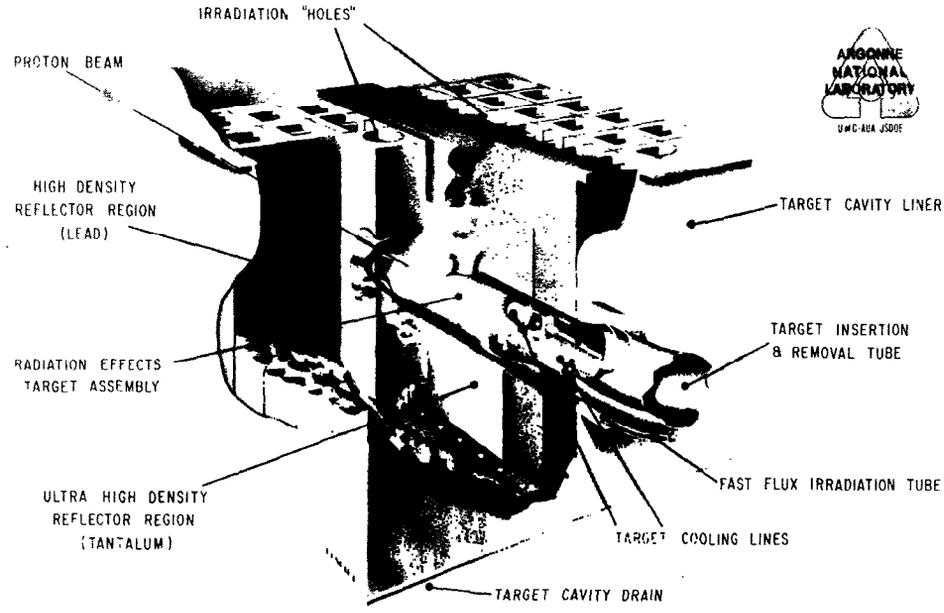

Figure 6

IPNS-I

NEUTRON SCATTERING EXPERIMENTAL ASSEMBLY

INNER REGION

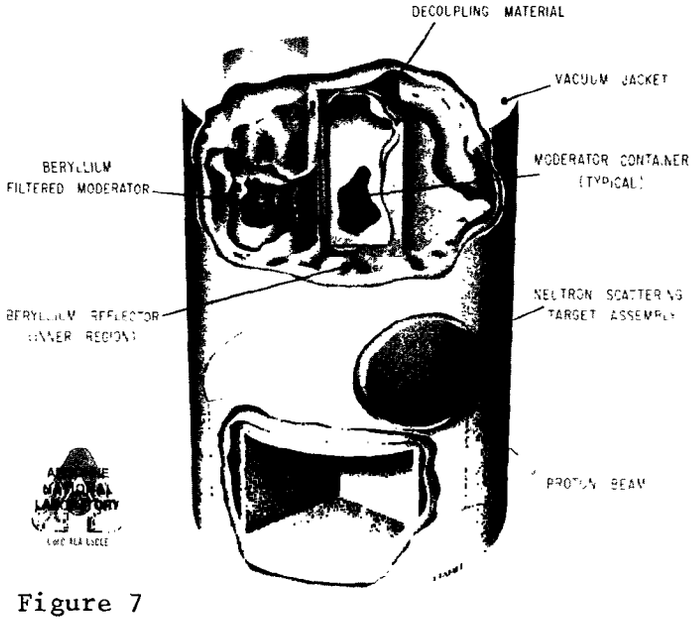

Figure 7

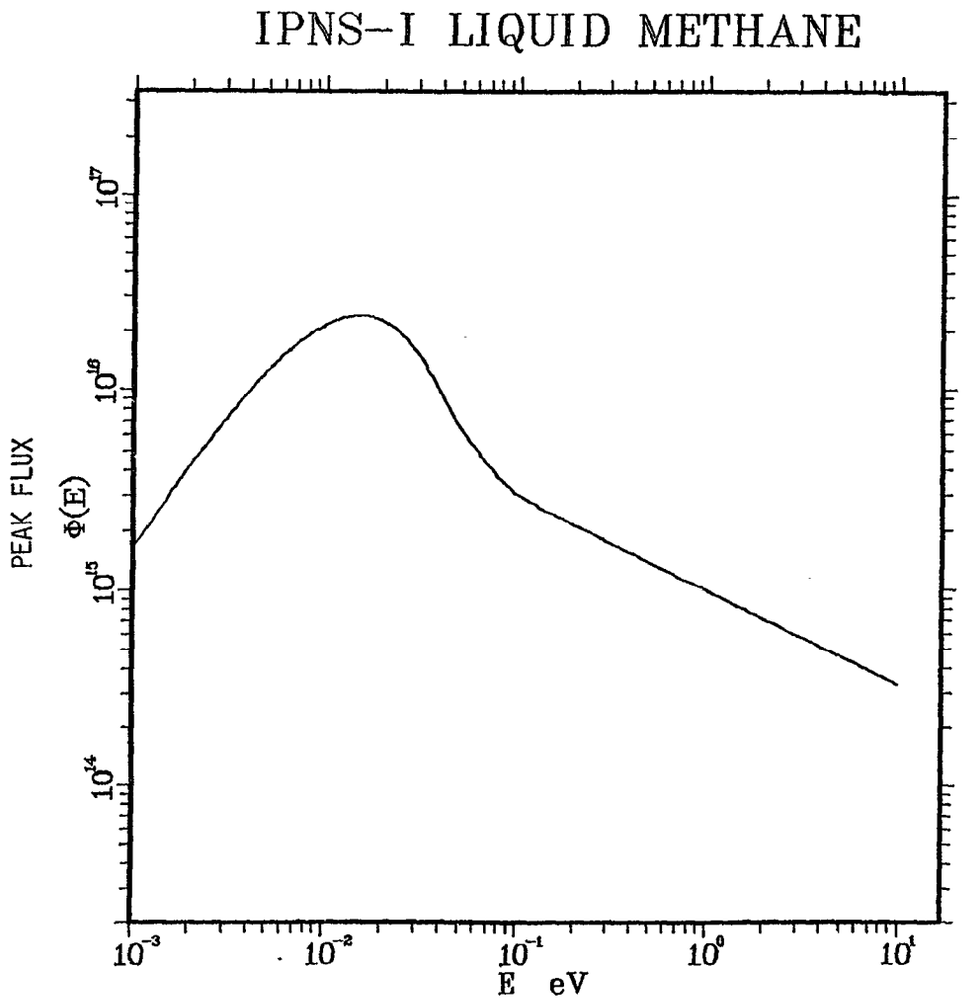

Figure 8

Spectral Temperature= 117.0
Ith/[EI(E)]|1 eV= 5.90 τ (E) $\cong$ 1.1 $\mu s/\sqrt{E_{eV}}$
EI(E)|1eV= $3.25*10^{10}$n/ster-secμamp
Frequency= 30.0
Proton Current= 8.00-μamp

D. Instruments

Two irradiation cryostats and associated equipment to maintain temperatures 4 K<T< 300 K are nearly complete. Table A summarizes features of the Radiation Effects Facilities.

Of the eventual total of seven scattering instruments, four (Special Environment Powder Diffractometer - SEPD, General Purpose Powder Diffractometer - GPPD, Single Crystal Diffractometer - SCD, and Low Resolution Medium Energy Chopper Spectrometer - LRMECS) are complete and ready for neutron beams. Figures 9, 10 and 11 show these four instruments. Tables B thru E summarizes the characteristics of the instruments.

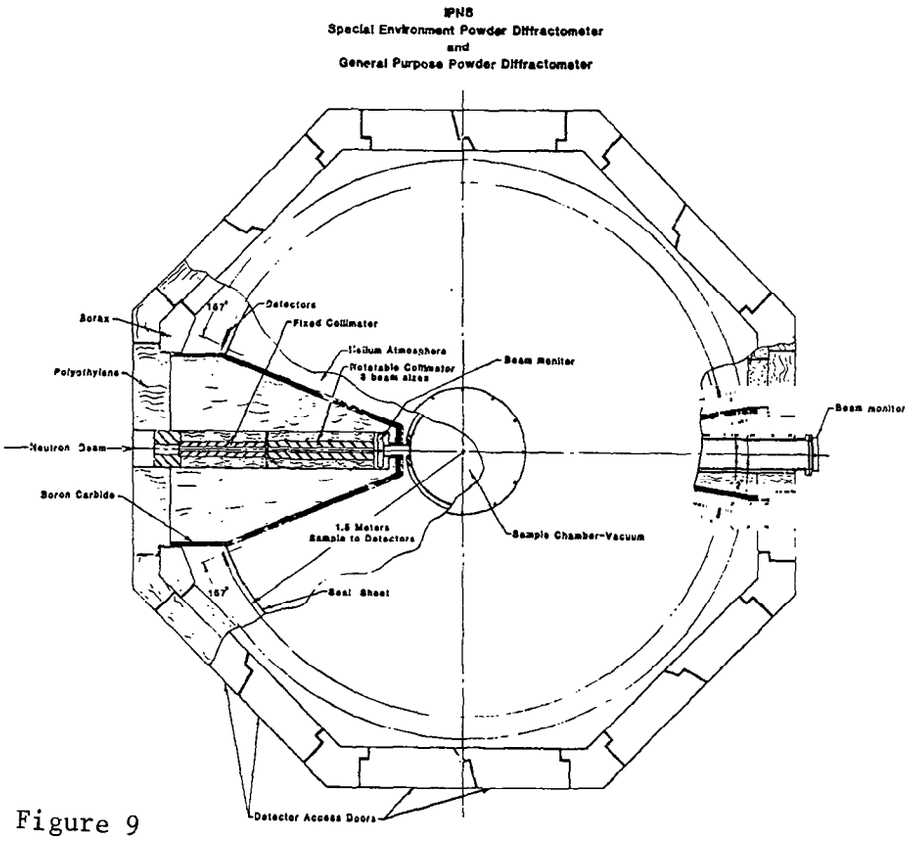

Figure 9

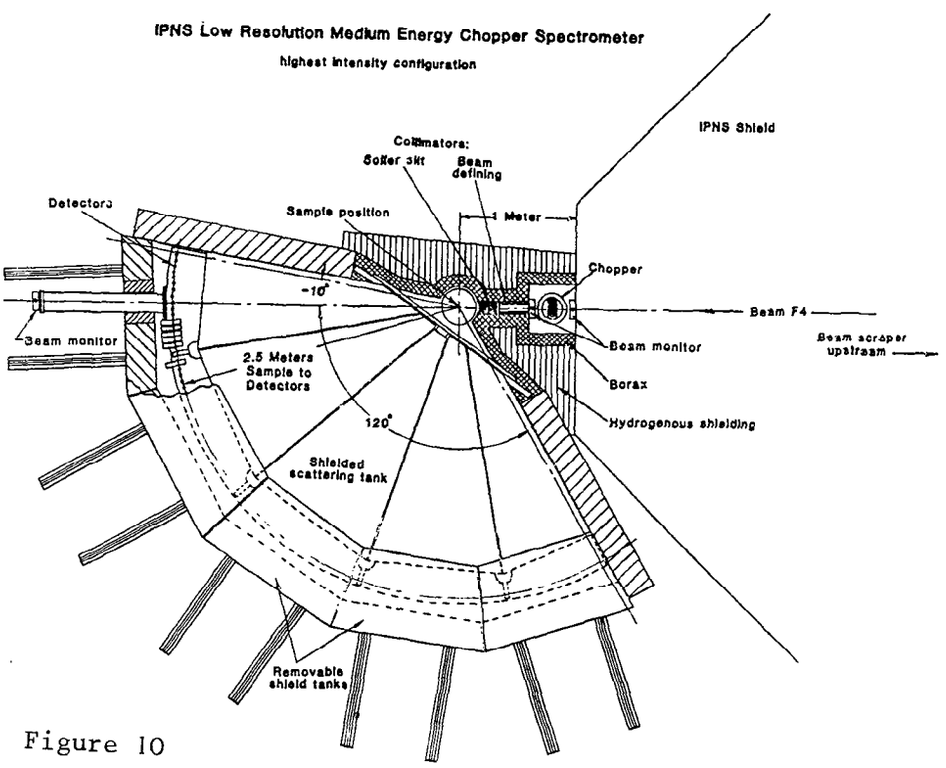

Figure 10

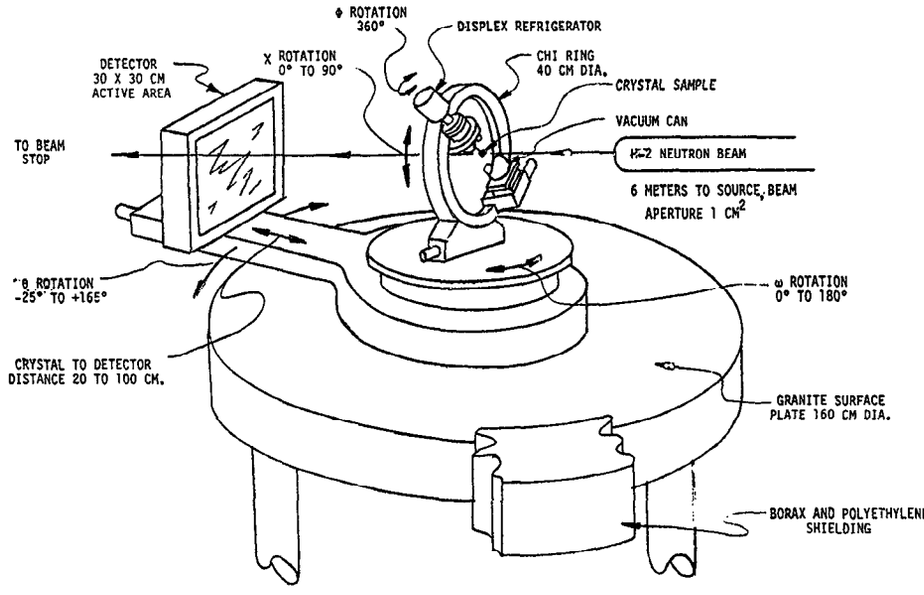

IPNS SINGLE CRYSTAL DIFFRACTOMETER

Figure 11

TABLE A - REF PARAMETERS

Time-average fast flux (E_n > 0.1 MeV)	1.5×10^{12} n/cm^{2}sec
Fast neutron pulse width	100 ns
Low-temperature holes (vertical)	
Diameter	5 cm
Temperature	4 K ≦ T ≦ 300 K
Ambient-temperature hole (horizontal)	
Diameter	3.8 cm
Temperature	∿300 K
Other environmental controls available	
Data acquisition	

TABLE B - SEPD PARAMETERS

Beam-tube assignment	F5 (liq. CH_4)
Initial flight path	14 m
Final flight path	1.5 m
Beam size	1.25 cm x 5 cm
Detectors	1.25 cm x 37.5 cm (140)
Choppers	None
Scattering angles	± 12° - 157°
Time average flux at sample (0.5Å $\leq \lambda \leq$ 5.Å)	$2.6 \times 10^5 n/cm^2$-s
Wave-vector range	0.5 - 40 $Å^{-1}$
Wave-vector resolution	0.3 - 1.0%
Special capabilities	Sample chamber, 60 cm diam x 120 cm high, able to accommodate wide variety of environmental controls; can be pumped down to 10^{-5} torr in 1 h.
Environmental controls available	Displex refrigerator, 10-300K
Data acquisition	PDP 11/34
Analysis routines available	Rietveld profile refinement (VAX 11/80)

TABLE C - GPPD PARAMETERS

Beam tube assignment	F2 (liq. CH_4)
Initial flight path	10 m <u>or</u> 20 m
Final flight path	1.5 m
Beam size	1.0 cm diam x 3.8 cm
Detectors	1.25 cm x 37.5 cm (160)
Choppers	None
Scattering angles	±30°, 60°, 90° and 150°
Time-average flux at sample (n/cm^2-sec)	1.9×10^6(10 m), 4.7×10^5 (20 m)
Wave-vector range	0.6 - 24 $Å^{-1}$
Wave-vector resolution	0.26 - 2.2%
Special capabilities	Sample chamber, 60 cm diam x 120 cm high, able to accommodate wide variety of environmental controls; can be pumped down to 10^{-5} torr in 1 h.
Environmental controls available	Displex refrigerator (10-300K)
Data acquisition	PDP 11/34
Analysis routines available	Rietveld profile refinement (VAX 11/80)

TABLE D - LRMECS PARAMETERS

Beam-tube assignment	F4 (liq. CH_4)
Initial flight path	7.5 m
Final flight path	2.5 m
Beam size	5 cm x 10 cm
Detectors	2.5 cm x 45 cm (100)
	2.5 cm x 22.5 cm (36)
	2.5 cm x 11.25 cm (24)
Choppers	
Scattering Angles	-10° to 120°
Time-average flux at sample (E_o = 0.5 eV)	2000 n/cm^{2}sec
Energy-transfer range	0 - 0.5 eV
Wave-vector range	1 - 20 Å^{-1}
Energy-transfer resolution	5%
Wave-vector resolution	2%
Special capabilities	Sample chamber, 30 cm diam, able to accommodate superconducting magnet and dilution refrigeration; can be pumped down to 10^{-4} tor in 2h.
Environmental controls available	Displex refrigerator
Analysis routines available	Reduction to S(Q,ω) (VAX 11/80)

TABLE E - SCD PARAMETERS

Beam-tube assignment	H2 (liq. CH_4)
Initial flight path	5.5 m
Final flight path	0.2 - 0.5 m
Beam size	1 cm diameter
Detectors	Anger scintillation detector 30 cm x 30 cm
Choppers	None
Scattering angles	-160° to 160°
Time-average flux on sample	
Wave-vector range	0.1 - 4 $Å^{-1}$
Wave-vector resolution	2% at 90° scattering angle
Special capabilities	Three-circle goniometer with auto-indexing procedure
Environmental controls available	Helium refrigerator
Data acquisition	PDP 11/34
Analysis routines available	Crystal structure refinement (VAX 11/80)

E. Data Acquisition System

The Data Acquisition System (DAS) is organized in a "star" configuration, with a minicomputer and data collection system for each instrument connected to a central "Host" computer through independent data lines. The Host computer is a 32-bit VAX 11/780 with a Floating Point Accelerator, 0.5 MB of memory, an RM03 67 MB Disk Drive and a TU77 125 ips dual density magnetic tape unit. It also has hard copy terminals, video terminals, graphics terminals, a Versatec Printer/Plotter and modems for remote communications. The star configuration has the advantage of independent data collection and centralized processing power and allows the more expensive peripherals to be concentrated on one machine. Most Host computer software is in FORTRAN and can be run under the VAX VMS operating system.

Each Minicomputer System has a 16 bit DEC PDP 11/34A minicomputer for experiment control and for communication with its Data Collection System and with the Host, as shown in Figure 12. The Minicomputer System software is mostly in FORTRAN and programs will execute under the RSX11M operating system. Programs and data can be stored on an RL02 10 MB capacity disk. Each Minicomputer System includes an LA120 180 character per second hard-copy terminal and a VS11 graphics terminal.

Each Data Collection System includes a CAMAC System containing a Time-Digitizer Module, a Master Clock Module, Polling Modules for the Time-Digitizers, a CAMAC Crate Controller, and optionally, a Clock Prescaler Module. The Time-Digitizer Modules have 125 nsec time resolution and have eight input channels per single-width CAMAC module. The single channel analyzers in these modules have a software controllable lower and upper discriminator levels.

Each Data Collection System also includes a Central Data Corporation Z8001 single board microcomputer and bulk memory dedicated to data collection, transformation and storage. The microcomputer accepts the digitized data from the CAMAC System and makes the real-time transformations necessary to determine which memory location in the bulk memory should be incremented for a given detected neutron.

Five front-end computers and the Host computer are installed and operating with their peripherals. We have now completed adequate software to enable experiments to be handled by the DAS and have compiled a Data Acquisition System Manual.

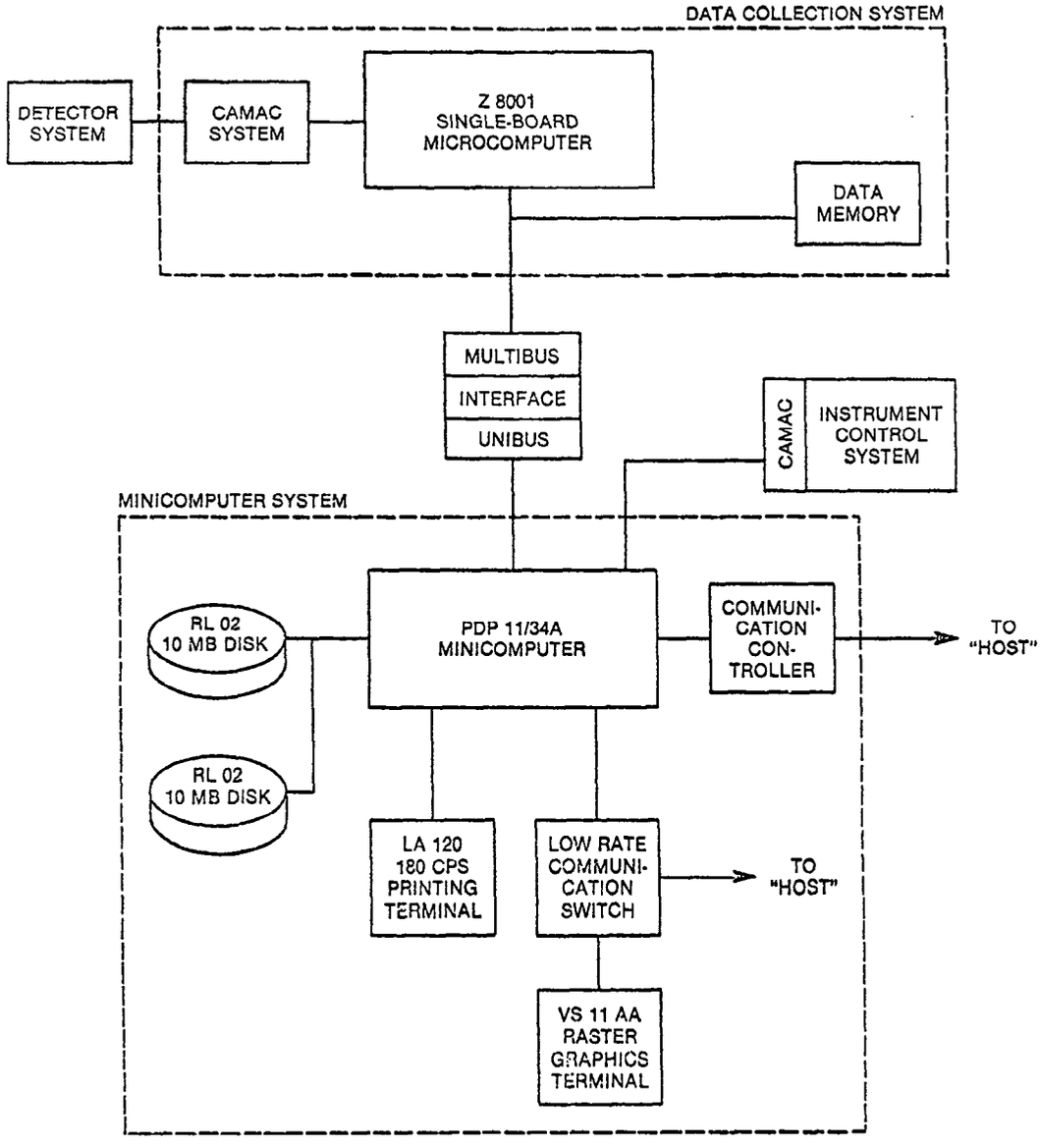
DATA COLLECTION SYSTEM
DETECTOR SYSTEM
CAMAC SYSTEM
Z 8001 SINGLE-BOARD MICROCOMPUTER
DATA MEMORY
MULTIBUS
INTERFACE
UNIBUS
CAMAC
INSTRUMENT CONTROL SYSTEM
MINICOMPUTER SYSTEM
RL 02 10 MB DISK
RL 02 10 MB DISK
PDP 11/34A MINICOMPUTER
COMMUNI-CATION CON-TROLLER
TO "HOST"
LA 120 180 CPS PRINTING TERMINAL
LOW RATE COMMUNI-CATION SWITCH
TO "HOST"
VS 11 AA RASTER GRAPHICS TERMINAL

Figure 12

III. General Items

Documents

In order to gain approval to operate IPNS-I, (not to mention, for our own purposes also) we have prepared a Safety Analysis Report (SAR). This has been reviewed and approved by all relevant Argonne and DOE bodies. (IPNS-I is designated a "non-reactor nuclear facility".) We have also generated from the SAR a working handbook of Operations Safety Requirements (OSR) which summarizes limit points, etc., for safe operation and which has also been reviewed and approved. On these bases we have full authorization to operate.

We have completed in draft form a Users' Handbook which summarizes the characteristics of the source and instruments and the available facilities. The Users' Handbook also provides information to help outside users new to Argonne Laboratory.

User Program

IPNS-I is operated as a user-oriented facility. This is not a new idea within the European neutron community, but is the first attempt in this field in the United States to provide a formal method of access to a major facility. Early this year we called for experiment proposals to be submitted for the Radiation Effects Facility, the first four scattering instruments and the uninstrumented beam tubes, for the period October, 1981 - March, 1982. We received 119 proposals, representing oversubscription of the instruments by factors between 5 and 10. The Program Committee, meeting on June 3 and 4, accepted all six special experiments, for otherwise-uninstrumented beams, and 34 neutron beam and irradiation experiments. The low rate of acceptance reflected the fact that operating time is very severely limited by funding constraints; proposals were almost all of high scientific quality. We will make another call for experiment proposals at the end of this year.

IV. Research and Development

A. Neutron Position-Sensitive Scintillation Detector(Anger Camera)

The Neutron Position-Sensitive Scintillation Detector (NPSD) is a two-dimensional neutron detector based on the principle of the highly-evolved medical gamma ray imaging device, the "Anger" camera. We have described the principles and results of prototype tests earlier. However, a larger version is nearing completion which is 30 x 30 cm overall, uses 2-mm-thick ^{6}Li-loaded, cerium-activated GA-20 (NE905) glass, and 49 2"/square RCA S83003E photomultipliers.

Resolution is 3.mm (measured on the 20 cm ϕ prototype). Pulse height resolution is 14%. The efficiency is expected to be 60% at λ = .5 Å, and over 95% at λ = 1.8 Å. Position stability with respect to temperature variation is less than 0.05 mm/°C. Pulse-pair resolution (includes digitizing ((9 bits))) time is less than 5 μsec.

The first model is to be used in the Single Crystal Diffractometer. We hope later to provide similar detectors for the Small Angle Diffractometer and for epithermal neutron radiography.

B. Compact Preamplifier

We have developed a compact, charge sensitive preamplifier for IPNS instruments which is housed in a 5 x 7.5 x 2 cm^3 brass box and costs $85.00 per unit to produce. The small physical size is attributable to the circuit layout and the low (2500 volt) operating voltage of the ^3He detectors being used in IPNS instruments. This allows small, 3 KV DC filter capacitors to be used. Two integrated circuits perform the work of the 5 or 6 discrete components found in more conventional preamps. Savings result from reduced assembly time. Gain varies among the preamps within approximate range ± 25%; we account for this in the single channel analyzer limits.

The small size and weight of this preamplifier allows it to be mounted directly to closely-packed detectors. This factor is further advantageous for reducing noise pickup in cabling between preamp and detector. We have built 600 of these preamplifiers.

Conclusion

IPNS-I will be the most powerful pulsed spallation neutron source for the next several years. We look forward enthusiastically to its imminent startup, confident that IPNS-I, together with the sources elsewhere, will provide significant advances in the scientific applications and technical development of pulsed spallation neutron sources.

I C A N S - V

MEETING OF THE INTERNATIONAL COLLABORATION ON

ADVANCED NEUTRON SOURCES

June 22-26, 1981

Improvements in the Rapid Cycling Synchrotron*

Charles W. Potts

Argonne National Laboratory

Argonne, Illinois 60439 USA

Abstract

The Rapid Cycling Synchrotron[1] (RCS), originally designed as an injection energy booster for the Zero Gradient Synchrotron (ZGS), operated under constraints imposed by ZGS operation until December 1979. Once these restraints were removed, the RCS made rapid strides toward its near-term goals of 8 μA of protons for Argonne National Laboratory's (ANL) Intense Pulsed Neutron Source (IPNS) program. Reliable 30 Hz operation was achieved in the spring of 1980 with beams as high as 2×10^{12} protons per pulse and weekly average intensities of over 6 μA on target. These gains resulted from better injection matching, more efficient RF turn-on and dynamic chromaticity control. A high intensity small diameter synchrotron, such as the RCS, has special problems with loss control which dictate prudence during intensity improvement activities. Additional improvements were made to the machine starting in August of 1980 while the extraction magnets were relocated for operation with the IPNS-I target. These improvements have now been completed. Startup of the accelerator is now underway, and it is clear that these modifications have resulted in a radioactively cleaner operation. It is too early to evaluate the effects of the improvements on intensity and reliability, but a single pulse extracted intensity of 2.4×10^{12} protons has been achieved, a 20% increase. The studies and equipment leading to the intensity gains are discussed.

*Work supported by the U.S. Department of Energy.

The submitted manuscript has been authored by a contractor of the U. S. Government under contract No. W-31-109-ENG-38. Accordingly, the U. S. Government retains a nonexclusive, royalty-free license to publish or reproduce the published form of this contribution, or allow others to do so, for U. S. Government purposes.

Introduction

Figure 1 shows the configuration of the IPNS-I spallation neutron facility.[2] It will come into operation in July of 1981 as a national user-oriented facility intended to be used for neutron scattering studies 75% of the time and radiation effect studies 25% of the time. A high energy physics test beam is also provided. In this facility, a fast burst (90 ns) of 500 MeV protons from the RCS is slammed into a uranium target 30 times per second. Resulting spallation and fission neutrons travel down 12 neutron beam lines to users' instruments. A prototype target (ZING-P'), Fig. 1, was the recipient of the protons in 1979 and 1980. The neutrons from ZING-P' were used for target yield studies, moderator material and arrangement studies as well as neutron science. Some 55 publishable neutron scattering measurements were made after the RCS came into a production mode in the summer of 1980.

The trials of turning-on and improving a new machine with scientific users waiting with high expectations is old hat to most of the readers. Normally, however, the users have some previous accelerator user experience and are, therefore, somewhat tolerant of the foibles of synchrotrons. In the case of the RCS, however, the users are reactor oriented and become somewhat irate when the published intensity, energy, and reliability are not available within a few months after startup. Fortunately, the accelerator made dramatic progress in intensity and reliability during the summer 1980 run and the needed rapport was developed between users and operators, and a viable scientific program seems to be on the horizon.

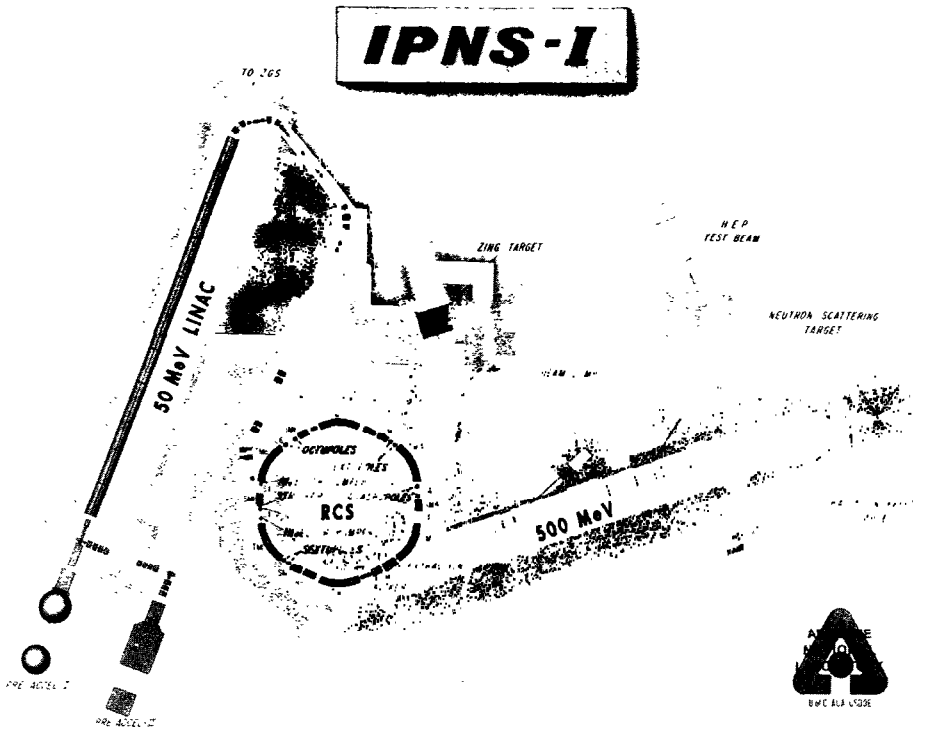

Fig. 1. IPNS-I Accelerator System

The goals of the RCS have long been to deliver 20 μA of 500 MeV protons to a target with 90% operating reliability. Numerous review panels have not seriously questioned the ability of the RCS to meet the 20 μA goal. Neutron science reviews have, however, questioned whether the national neutron science budget can support a dedicated facility like IPNS-I. This is a complicated, many-faceted question which may take quite awhile to answer. Lower goals are compatible with a lower budget and the goals have now been changed to 8 to 10 μA. As Table I indicates, the RCS has made tremendous progress since 1978 and the new lower goals will be achieved in 1981.

Table I

	1978	1979	1980
Scheduled Operating Time	2681 hours	3976 hours	2569.2 hours
Actual Operating Time	1796 hours	2928 hours	2187.8 hours
Operating Efficiency	67%	73.6%	85.2%
Total Protons on Target	0.294×10^{20}	1.06×10^{20}	2.25×10^{20}
Total Pulses on Target	0.43×10^{8}	1.13×10^{8}	1.98×10^{8}
Average Beam Current	0.73 μA	1.61 μA	4.72 μA

The remainder of this paper will present, in chronological order, what improvements were made to achieve these results. It is of great importance to realize that in some of 1979 and most of 1980, the beam intensity was limited somewhat by fears concerning heating and thermal cycling of the prototype uranium target. One certainly must not be fooled into thinking that the target was the only limit. The operators of a small radius fast-cycling synchrotron, without extensively prepared remote handling apparatus, must always consider beam loss control as a prime goal if the synchrotron is to be kept repairable. The gentle positive slope of the beam current vs. time in Fig. 2 was planned as accelerator problems and uranium target worries were slowly worked out in unison. Some of the peak numbers such as 10 μA and 2.4×10^{12} protons per pulse were short-term accomplishments that could not be sustained over long periods because of beam losses, but they do provide input as to the synchrotron's overall capability.

Operation in 1979

The RCS time-shared the 50 MeV linac with the ZGS, usually in a mode of 3 seconds RCS to 1 second ZGS. Programmable bending and focussing magnets made the ZGS H^+ polarized proton operation and the H^- operation of the linac compatible. The operating frequency of the RCS was limited to 15 Hz due to possible damage to the linac when operated at 30 Hz. No one expected major damage, but even two or three weeks of lost operation was considered vital to the high energy polarized beam which was shutting down permanently at ANL in October.

This was a very productive period for the RCS physicists. Approximately 20 hours per week were dedicated to machine studies. Many of the

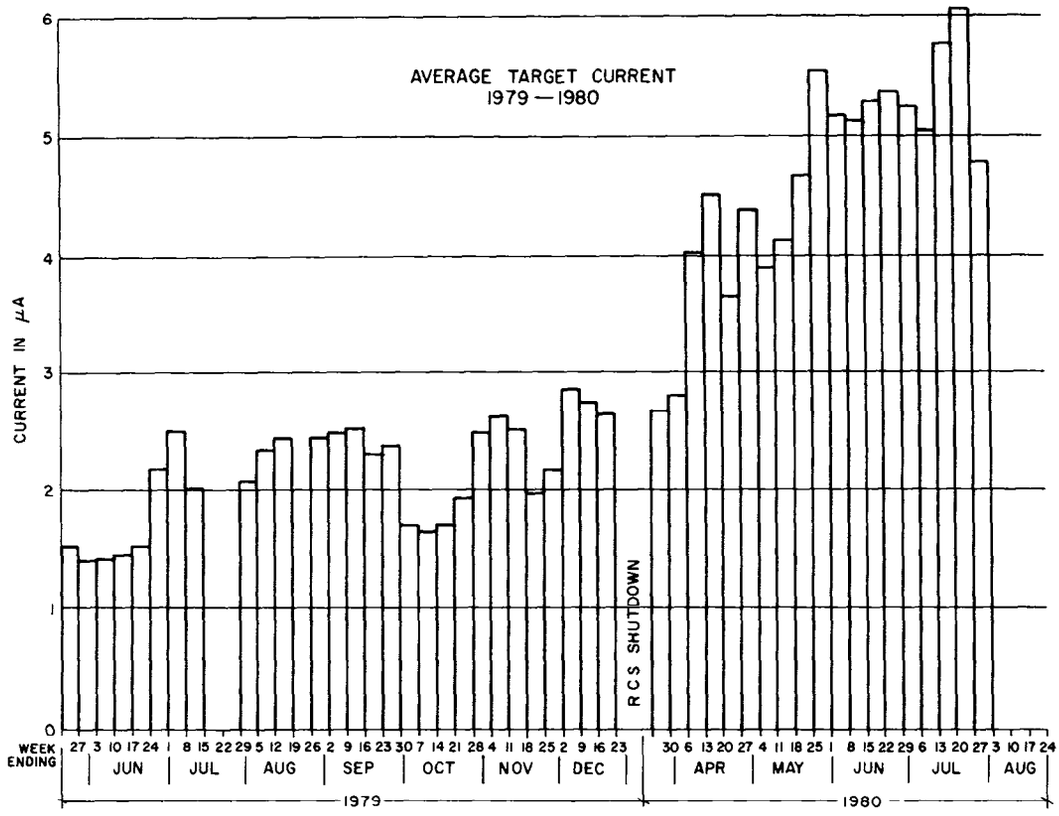

Fig. 2. Weekly Average Beam Current on Target

beam problems uncovered during this period are still being addressed although some were corrected in the spring of 1980 with gratifying results. Studies found that the 500 MeV beam was too large for efficient extraction due to "head-tail" instability.[3] Tune measurements disclosed dynamic reversal of the chromaticity at 350 MeV. Extraction was studied at 200 MeV, and it was noted that 100% of the accelerated beam could be extracted. The extraction kick was insufficient to kick out the wide 500 MeV beam created by the "head-tail" instability. The 500 MeV extraction efficiency was about 65%. A temporary compromise of 300 MeV operation was chosen to get fairly good neutron yield while still providing a radioactively clean extraction efficiency of over 90%.

High radiation levels were detected at the 50 MeV end of the linac. This resulted from gas stripped H^0 and H^+ particles. Appropriate shielding was added. Quantitative measurements were made later of H^0 and H^+ production as a function of linac tank pressure.[4] These measurements show that H^0 and H^+ production is proportional to residual gas pressure as expected.

This was a beneficial time for the users also as neutron yield measurements were made in tungsten, tantalum, and uranium targets. The results agreed fairly well with computer predictions, and uranium was chosen as the target material in the IPNS-I monolith for neutron scattering and radiation damage work. Tantalum backup targets were also built. A uranium target was then installed in the ZING-P' monolith for operation

until August of 1980. While this target was only a few pounds of uranium, numerous safety reviews, ad hoc committees, and some 30 target interlocks gave the accelerator operators some new concerns.

One of the more ambitious accomplishments was phase locking the accelerator to a crystal controlled neutron chopper.[5] From the accelerator standpoint this is like the "tail wagging the dog," but it works! Extensive modifications were made in the controls and capacitor bank of the ring magnet power supply of the synchrotron to automatically keep the parallel tuned portion of the system in resonance as the chopper clock forced the system slightly off the power main's frequency. This kept the magnet field stable as it drifted in respect to the power line frequency. An added modification allowed the chopper to control the extraction time of the beam as early as 100 μs before the peak energy and as late as 100 μs after. If the chopper did not call for extraction by the later time, the beam was extracted for the benefit of the other users while the chopper missed that particular pulse. It was found that the chopper and machine were synched within this 200 μs window over 95% of the time. The size of the 200 μs window was chosen experimentally by studying extraction and transport losses for off-nominal energy extraction.

Reliability during this period was not good. The pulsed septum magnet was the real Achilles' heel. It was a 30-inch long conventional 4-turn thin septum magnet. Several different versions of this magnet failed with the best lasting 10^8 pulses. Failure required a lengthy cool-down before repair. The extraction kicker magnet system provided more than its share of failures through high voltage cable breakdowns which often destroyed low level electronics as well.

Once the ZGS was shut down in October of 1979 restrictions on linac operating frequency were lifted, but insufficient data existed to begin 30 Hz operation at once. The ZGS authorities graciously allowed use of half the ZGS main ring magnet system and its beam diagnostics as a spectrometer for analysis of behavior in the linac beam running at 30 Hz. At the same time the linac tank was instrumented for temperature measurements at various points. When the linac was run at 30 Hz with RF on for long enough to accommodate 120 μs beam pulses, some hot spots were noted on uncooled tuning balls. These had grown leaky over the years and the water was shut off, which was acceptable during low power operation. A very clever design provided cooling for these leaky units, but construction and installation of these cooling adapters took over two months. Thirty-hertz operation was tried again in mid-December, but because of kicker magnet power supply problems it was not successful, although short-term currents of 5 μA were achieved.

1980 Modification and Operation

From January until the third week of March the machine was off for improvement. The most extensive was the installation of a new transformer septum magnet[6] that provided one-half the bend of the old magnet. A more standard dc septum provided the remainder. In addition, two small vertical and one small horizontal trimming magnets were designed and built to better

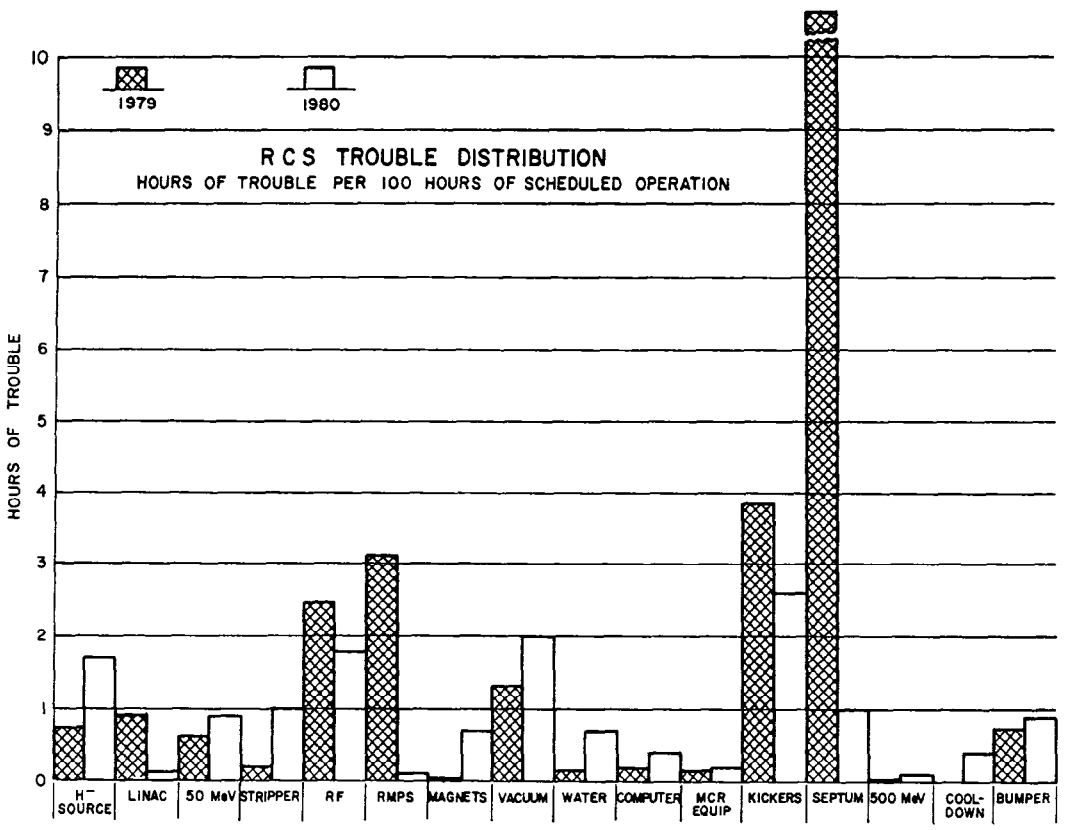

Fig. 3. Comparison of RCS Trouble Distribution for 1979 and 1980

match the machine to the target transport line. Significant improvements were made in protecting the low level electronics in the kicker magnet power supplies, and cable termination problems were solved. These two efforts made great improvements in the operating reliability of these systems, as can be seen from comparing the 1979 and 1980 system reliability data in Fig. 3. Several other modifications were added to improve beam output and beam handling efficiency. Programmable linear amplifier power supplies were provided for dynamic chromaticity adjustment. Preamplifier improvements were made in the RF system to improve dynamic range and automatic gain control (AGC) response. Ninety percent of the complicated 50 MeV transport line from the linac to synchrotron was wire orbitted, and the beam diagnostics were realigned for better injection matching. A 750 keV proton beam chopper was constructed to give the machine synchronous injection capability. One look at Fig. 2 from April through July 1980 should convince the reader that these modifications were, on the whole, quite successful. It was during this running period that 30 Hz operation became routine. The reader should bear in mind that this running was carried out with the ratio of beam on target to 50 MeV beam delivered to the synchrotron at 70% or better.

Machine physics studies continued during this running period, more problems noted, some corrections made and some longer range plans formulated. A disturbing coupling between proton beam noise and the ring magnet power supply was discovered and partially corrected. This was particularly troublesome when the accelerator was running in synchronism

with a neutron beam chopper. Two-turn extraction, 500 MeV acceleration, and the effects of space charge distribution were among the more common topics. The most troublesome aspect of beam acceleration was, and remains, an instability which occurs at intensities of over 1.5×10^{12} protons per pulse for about the last 6 ms of the acceleration cycle. It seems to be longitudinal in nature since there is a great deal of bucket size modulation. A "head-tail" instability has been noted at this time in the acceleration cycle. This instability causes about 3% amplitude modulation in the RF amplitude envelope. Several theories have been considered concerning this instability: (1) Oscillation in the AGC loops of the RF system; (2) Oscillations in the loop that phase locks the two RF cavities together; (3) Coupling between the dc position feedback loop and the bandpass beam phase compensation loop; (4) A microwave instability generated by beam coupling to the eddy current shields in the accelerator; (5) A microwave instability caused by the lack of symmetry in the straight sections. This instability has been controlled during 300 MeV operation with extracted beams up to 2.4×10^{12} protons by very judicious injection and careful chromaticity adjustment, but it cannot be said to be operational at 30 Hz at these intensities due to extensive beam losses.

Conversion for Operation into IPNS-I Target Monolith

The accelerator was shut down August 4, 1980, to begin the attachment of a new proton transport system (PTS) to carry the beam to the IPNS-I target monolith. From the accelerator standpoint, additional work was required as may be seen in Fig. 4. The extraction straight section containing the septum magnets has been moved from the L-4 to L-3 straight section; a set of quadrupoles was moved from the L-3 to L-4 straight section; a longer fast kicker magnet has been installed in the S-3 straight section; extensive shielding additions totaling 450 tons of concrete have been added over the extraction straight section.

Several system modifications and additions were completed during the time of IPNS-I conversion. These items should improve beam handling, beam intensity and operating reliability. The most ambitious of these has been complete reconstruction of the fast kicker extraction system. A new magnet and power supply[7] have been designed and constructed to provide efficient 500 MeV extraction. Four separate thyratron switching power supplies each drive 1/4 turn of a 75 cm long ferrite magnet. Each 1/4 turn is terminated in 7 Ω and the system is operated at 62 kV. The peak switched power is over 0.5 gigawatts. The four supplies must fire within 2 ns of each other. So far, the system works quite well. Measurements with the proton beam indicate the kick angles are as predicted.

Octupole magnets[8] driven by programmable 30 kW linear transistor amplifiers have been added to the synchrotron. Betatron tune measurements indicate that these magnets perform as predicted; however, they have not as yet shown the ability to control beam instabilities. Less than four hours of machine time has been spent in applying them to instability correction studies, so prospects for their success are still bright. The injection bumper power supply was modified extensively to up its duty

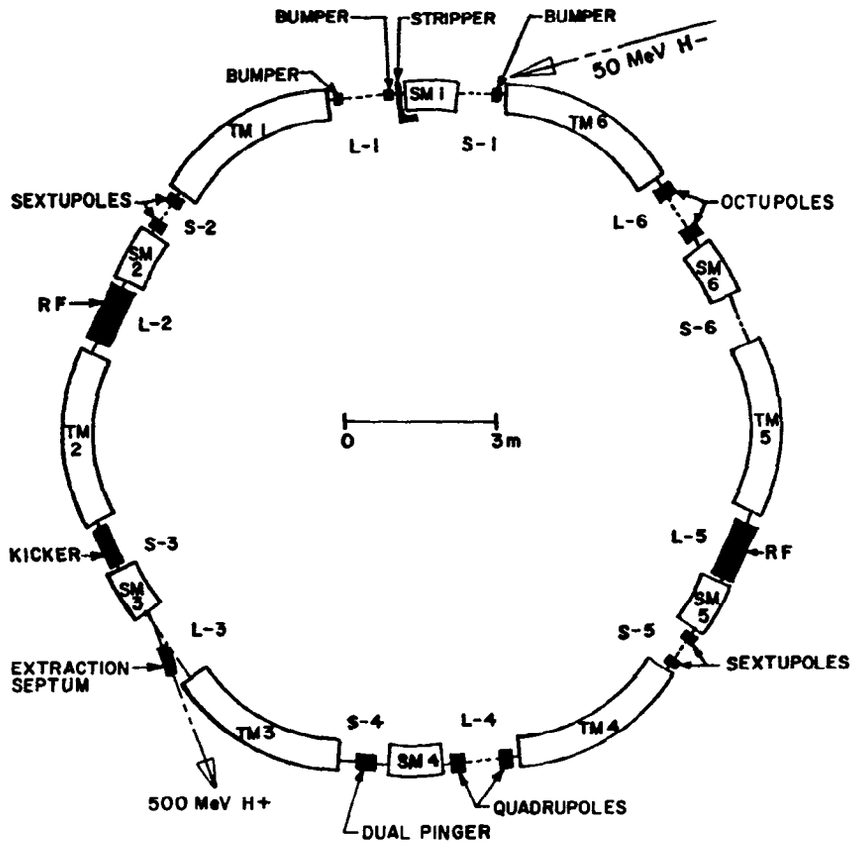

Fig. 4. RCS Component Arrangement

cycle by 50%, provide faster injection slewing and greater waveform flexibility, as well as improved accessibility for repair.

Linear transistor amplifiers control the dynamic impedance of the RF cavities by magnetically modulating the inductance as the RF frequency sweeps from 2 to 5 MHz during the beam acceleration cycle. These amplifiers are part of the cavity bias system (CBS). New CBS amplifiers have been constructed and installed which increase the corner frequency of this system from 800 Hz to 10 kHz. It is hoped that better cavity impedance control will improve many aspects of the dynamic RF performance, in particular, better cavity-to-cavity tracking and better AGC control, since both the phase and magnitude of the load impedance seen by the amplifier are more constant. The synchrotron oscillation frequency of the beam varies from 4 to 7 kHz during the machine cycle. The potential problem of having the CBS response span this frequency was recognized. In fact, studies have shown that beam losses do increase when CBS response corners above 3 kHz, so the response is limited there.

Extensive changes have been completed on the RCS computer control system with an Eclipse AP-130 replacing a NOVA 210. The greatly augmented capacity is used to interact with machine studies,[9] provide more flexible parameter monitoring and readout to control and monitor the new proton transport line to the IPNS-I target. It also monitors all the parameters required for cooling and radioactivity control of both the neutron

scattering and radiation effect targets and is part of the protective shutdown system.

The accelerator physics team remeasured both the injection and extraction orbits during the IPNS-I installation shutdown. They recommended changes in nominal injection angle and extraction apertures. These changes were carried out with what seems, at this time, to be excellent results. Beam output to input ratios have improved from 70% to 85%. Radiation outside shielded areas has decreased by factors of at least 5 and in some places by a factor as high as 20. Of course, shielding improvements and improved extraction kick have also helped.

Linac and Ion Source

One does not expect that a 1 Hz linac and a 1 Hz H^- ion source will easily operate at 30 Hz, but they have performed suprisingly well. The linac, with the beam pulse width restricted to 70 μs or less, has performed flawlessly thus far. Modifications in tank water flow, tuning ball cooling and oscillator cavity cooling have been necessary. The ion source, with similar power restrictions, has done well with grid life being the limiting factor. With pulse widths under 60 μs, grids last about six weeks.

The previously mentioned fiscal problem has brought a two-year program of ion source development to a halt. A Penning discharge type H^- ion source was beginning to show promise.[10] This work has completely stopped. Linac operating personnel are working to adapt a 15 Hz magnetron type source to 30 Hz operation. This will be a very modestly financed program and does not have a high probability of success for that reason. A new or improved ion source is generally regarded as one of the easiest ways to improve RCS beam intensity.

Foil Life

The stripping foils used in the RCS are made of poly-paraxylene.[11] They are 3000 to 4500 Å (60 μg/cm^2) thick with a 400 Å coating of aluminum deposited on them. Considerable work has been done on nonstressed mounting of these foils with satisfying results, but the aluminum coating has been the most effective factor in extending their life to millions of beam pulses. The aluminum coating allows a bleed-off of charge and also allows for an even distribution of charge. Noncoated foils tend to contract when protons pass through them.

The injected current on the RCS is typically 5 mA for 60 μs. The way this beam is injected determines the number of passes the recirculating beam makes through a foil. This obviously has a significant, but unquantified, effect on foil life. The RCS has a remotely controlled foil changer which can hold 50 foils in its magazine. For reasons that are unclear, a new foil survives best if it is "conditioned" for an hour or so at 5 Hz before applying beam at 30 Hz. Foils usually last about 10 million pulses.

Conclusions

Great strides have been made since the 1978 commissioning. Weekly average beam currents have gone from less than 1 μA to over 6 μA, weeks with over 15 million extracted pulses have been recorded and reliability has jumped from 67% to 85%. Peak intensities of 2.4 x 10^{12} protons per pulse and a 24-hour average of 7.6 μA has been attained. Much remains to be done. Five-hundred MeV operation must be reliably demonstrated. Firm control of beam losses must be maintained and stable financing would help.

Acknowledgments

In a survey paper of this type the work of many must be acknowledged. To acknowledge some would slight others. Thanks to everybody who helped. You know who you are.

References

1. Rauchas, A. V., Brumwell, F. R., and Volk, G. J., "Commissioning of the Argonne Intense Pulsed Neutron Source (IPNS-I) Accelerator," IEEE Trans. Nucl. Sci., Vol. NS-26, No. 3, p. 3006 (June 1979).
2. Carpenter, J. M., Blewitt, T. H., Price, D. L., and Werner, S. A., "Pulsed Spallation Neutron Sources," Physics Today, Vol. 32, No. 12, p. 42 (December 1979).
3. Cho, Y. and Rauchas, A. V., "Observations and Cure of Head-Tail Effect in the Argonne Rapid Cycling Synchrotron," IEEE Trans. Nucl. Sci., Vol. NS-28, No. 3, p. 2585 (June 1981).
4. Cho, Y., Madsen, J., Shin, S.-A., and Stipp, V., "Measurements of H^0 and H^+ Ion Yields During H^- Acceleration in a 50-MeV Linac," IEEE Trans. Nucl. Sci., Vol. NS-28, No. 3, p. 2888 (June 1981).
5. Praeg, W., McGhee, D., and Volk, G., "Phase Lock of Rapid Cycling Synchrotron and Neutron Choppers," IEEE Trans. Nucl. Sci., Vol. NS-28, No. 3, p. 2171 (June 1981).
6. Foss, M., Thompson, K., and Praeg, W., "A Transformer Septum Magnet," IEEE Trans. Nucl. Sci., Vol. NS-26, No. 3, p. 4024 (June 1979).
7. Suddeth, D. E. and Volk, G. J., "The Rapid Cycling Synchrotron Extraction Kicker Magnet Drive System," IEEE Trans. Nucl. Sci., Vol. NS-28, No. 3, p. 3017 (June 1981).
8. Potts, C., Faber, M., Gunderson, G., Knott, M., and Voss, D., "Tune Control Improvements on the Rapid Cycling Synchrotron," IEEE Trans. Nucl. Sci., Vol. NS-28, No. 3, p. 3020 (June 1981).
9. Rauchas, A. V., Brumwell, F. R., Cho, Y., Czyz, W. S., Gunderson, G.R., Knott, M. J., Suddeth, D. E., and Volk, G. J., "Betatron Tune Measurement at the Argonne Rapid Cycling Synchrotron," IEEE Trans. Nucl. Sci., Vol. NS-28, No. 3, p. 2331 (June 1981).
10. Moffett, D. R. and Barner, R. L., "An Intense H^- Source for the IPNS-I Rapid Cycling Synchrotron," IEEE Trans. Nucl. Sci., Vol. NS-28, No. 3, p. 2678 (June 1981).
11. Poly-paraxylene film developed by Carbide Chemicals and Plastics, Research and Development Department, Bound Brook, New Jersey.

Jül-Conf-45

A4

I C A N S - V

MEETING OF THE INTERNATIONAL COLLABORATION ON

ADVANCED NEUTRON SOURCES

June 22-26, 1981

Progress report on the construction of the Spallation Neutron Source at the Rutherford & Appleton Laboratories

D A Gray

Rutherford & Appleton Laboratories
Chilton, Didcot, Oxfordshire, UK

Abstract

This report is an update of the report given by G Manning at ICANS IV, KEK, in October 1980. The proceedings of that meeting give details of the specifications for the SNS and the financial and programme expectations for the project.

The SNS programme is proceeding well. Although there have been delays in producing some of the equipment, these do not appear to prejudice the time-scale being aimed for.

1. INTRODUCTION

This report is an update of the report given by G Manning at ICANS IV, KEK, in October 1980. The proceedings of that meeting give details of the specifications for the SNS and the financial and programme expectations for the project.

2. FINANCE

The financial approvals for capital have been updated and are now £14.405M for the machine and target station and £2.179M for the first seven instruments, all at 1.10.80 prices. The update is purely for inflation; no real extra cost is involved. This money does not include money for staff or for research and development items. The allocation to cover all costs for the SNS for the current financial year is £7.42M. This is about £0.5M less than that indicated in G Manning's last report. We aim to try to keep to the programme.

Approximately £6.2M worth of capital equipment has been ordered for the machine (out of £11.4M) and £0.25M on the target station (out of £3.0M). Only £150K has been committed on the instruments.

3. PROGRESS

An outline of progress on different parts of the facility is given below.

3.1 Civil Engineering and Services

All civil works for the synchrotron room and for the RF power supply have been completed on schedule. This work included the filling of a trench and provision of supports for the foundations for the ring and the provision of a flat floor inside and outside the ring to provide easy access for maintenance.

The mechanical services, such as cooling and ventilation, formerly used on Nimrod are being refurbished and installation of services in the ring building has started. Components for the electrical distribution system, eg transformers and switchgear, already available are being installed in places to meet their new task.

3.2 Injection

Updating of the cooling systems on the 4 tanks of the 70 MeV linac has been completed. Tank 1 has been fed with full RF power at 50 Hz using the new modulator feeding the original RF power tube. Conditioning was very quick. Presumably the improved vacuum conditions resulting from using the installation of turbomolecular pumps rather than diffusion pumps provide the reason why problems with multipactoring did not recur.

Tanks 1 and 4 and the drift tubes in them have been realigned.

The pre-injector voltage polarity has been reversed together with that of the 'bouncer' which compensates for voltage droop during the pulse.

Work on the ion source has concentrated on obtaining reproducible and reliable results at close to full duty cycle. Currents of 33 mA of H^- have been regularly produced. This work is discussed in the Accelerator session by P Gear. We aim to have a 655 kV H^- beam by September.

Good progress has been made in the development of the stripping foil as C Planner reports in the Accelerator session. Foils of 12 cm x 3 cm with 50 $\mu g/cm^2$ thickness of Alumina with one 12 cm edge unsupported have been produced.

3.3 Synchrotron ring magnets

As reported in October, all magnets for the 10 superperiods are on order. The 20 doublet quadrupoles have been delivered. There is good coincidence of the magnetic centre with the geometric centre. The trim quadrupoles which permit shift of Q-value during injection and acceleration have been tested and are also within specification.

The prototype singlet quadrupole is expected soon. The prototype dipole magnet will probably be one year late. There have been problems of gluing together the laminations into wedge-shaped blocks which are then put together to form the top and bottom yokes. The method so far used has been to coat the laminations with a wedge of epoxy resin which is then cured to B-stage using ultra-violet light. The laminations are then dry-stacked into a jig where they are heated and the end shape controlled under pressure. There have been problems with obtaining the correct heating so that the outer epoxy does not cure before the inner has softened and also with uneven pressures.

An alternative method is being investigated which would use laminations with dimples to obtain the wedge with vacuum impregnation of resin. The prototype coils and the first base are available.

3.4 Magnet power supplies

The choke and capacitors for the main ring resonant power supply have been installed. The DC bias supply has been delivered. The make-up supply will use a DC motor driving an alternator. Control of the speed through the DC motor will enable operation either locked to the mains at 50 Hz or a fixed frequency, eg 53 or 47 Hz. This later mode may be necessary for the operation of linked choppers for fine shaping of the neutron pulse.

3.5 Main ring vacuum

Following the successful testing of the 3 different prototype ceramic chambers, production is in full swing. The manufacturer of the ceramic sections has delivered all the components for the 2 types of quadrupole chamber including flanges. Six of the 10 3m chambers for the doublet and trim quadrupole module have been glued up using the glass-bonding technique. One chamber in the middle of the production run cracked for a reason not ascertained. Otherwise the production has gone well. The first production set of sections for the 36° 5m chamber for the dipole magnet is available at the manufacturers. We shall change over to making this type of chamber to prove that the successful prototype was not just a fluke. The smaller chambers for correction magnets have been ordered as have the metal sections of chamber not subjected to magnetic fields.

All vacuum pumps have been delivered.

3.6 RF shields

Detailed design of the RF shields which fit inside the ceramic chambers is in hand. These present a low RF impedance to the beam to reduce destructive RF voltages seen by the beam. Final dimensions for beam size and aperture have been determined which take into account the expected shape of the fall-off of magnetic field at the edge of the dipole magnets.

3.7 Main ring RF system

A complete prototype RF system has now been built up and is ready for testing. The cavity itself was somewhat delayed by late delivery of the initial batch of copper discs for cooling the ferrite. There was also some delay in delivery of ceramic-metal components forming the two accelerating gaps in the cavity. The prototype RF amplifier which is removable as a unit and plugs into the cavity is ready for test into a dummy load.

As far as the production RF components are concerned, the 6 anode power supplies and the bias supplies are being manufactured. All the ferrite for the cavities has been delivered and properties measured. All is within specification. The properties will determine the position in the ferrite stack. All the cooling rings have also been delivered.

The design of the low power RF is proceeding well. Six more prototypes remain to be made of the 50 or so circuits required.

3.8 Diagnostics

The position monitors have been designed. The electronic head units for these have been completed. The mechanical components will be ordered in a few months. The special co-axial cable required will be ordered very soon.

A prototype intensity monitor is under construction. The measurement of beam profile presents a very difficult problem. A method based on measuring ions produced by the proton reaction with residual gas molecules has been evolved. To measure the betatron frequency of the circulating protons the protons will be perturbed transversely and the resultant oscillations measured. A prototype system has been successfully built and tested.

The design of special diagnostics required in the injection straight have yet to be integrated with the injection straight design.

3.9 Extraction

Significant progress has been achieved since the last report. The kicker magnet rise time has now been reduced to below the 220 ns spacing between the 2 bunches.

3.10 Beam loss protection

A full description of the scheme was given in the last report. Development of the hardware is proceeding.

3.11 Extracted proton beam line

The DC septum magnet design is being developed using existing magnets powered from the final power supply which is already installed. Design of the second vertical bending magnet is continuing. Part of the shielding for the EPB tunnel has been installed.

3.12 Target station

A description of the target station was given by A Carne in the ICANS-IV proceedings. As indicated in that paper, there were difficulties in obtaining satisfactory cladding of the uranium target plates with Zircaloy-2. An order has now been placed for work which will use the hot isostatic pressure bonding technique.

The decision to have a $20^{o}K$ moderator has been reconfirmed. In addition, there will be two ambient temperature moderators and one at $77^{o}K$.

The target assembly is mounted in a cylindrical vessel 3.2 m diameter by 3.8 m high which provides a contained helium atmosphere at reduced pressure. The detailed engineering design is about 70% complete. The target vessel has 18 double skinned aluminium windows for the neutron beams. The design of these windows and their remote handling equipment has been carried to the proof-of-feasibility stage.

The energy deposition in the shutter system has been calculated to be 13 kW. This heat will be removed by flowing air, to be exhausted via the extracted beam line shielding enclosure into the magnet hall. Design of the shutters proceeds and the vertical movement will be provided by mechanical jacks.

The outer bulk shielding will contain 75% iron and 25% concrete. The iron will be in the form of large blocks of former Nimrod shielding. A large milling machine has been installed in Hall 3 for machining the blocks to the required shape. The bulk shield will contain inserts, fabricated from steel plate, which contain apertures in which the neutron beams will be mounted. The order for the inserts has been placed.

The target station plinth provides shielding under the target and a stable common foundation for the bulk shield and remote handling facility. It consists of a reinforced concrete tank with a waterproof membrane and contains 3 layers of Nimrod magnet sectors and pole pieces and on top a 0.18 m reinforced concrete plate. A double-walled stainless steel drain has been installed to connect eventually the void vessel to the underground shielded dump tanks. Steel plates which form the base for the shutter system have been manufactured and are currently being installed, together with a central survey pillar.

Major dimensions of the remote handling cell have been determined and design of the interior is continuing. The main areas of study have been use of the manipulators (the first pair of which has been delivered), design of the target storage wells, recess doors and ventilation.

A mock-up remote handling cell has been built to study in detail the problems of handling the components of the target assembly. Prototype components and handling fixtures have been made.

The first of the two zinc bromide windows for the remote handling cell has been ordered. This window will be used firstly in the mock-up cell.

A first draft of the Target Station Safety Assessment has been prepared for discussion purposes. In addition to satisfying the more conventional requirements the assessment has aimed to show that:

a) The overall target station design takes proper account of the principal hazards, ionising radiation and radioactivity, and that we are able to meet our statutory obligations under Radiation Protection legislation.

b) Under extreme fault conditions, such as a target melt-down, the release of radioactivity will be contained in a closed volume.

c) The release of activity into the raw water supply (and hence dispersal to the environment) would require the breaking of three physical barriers. This is backed up by continuous monitoring of activity levels and the ability to safely isolate the target.

3.13 Controls

Work on both the software and hardware continues. The satellite computer for the injector system has been installed and will be used for the 665 keV beam commissioning in September.

3.14 Experimental instruments

The SNS project provides for 15 instruments, 14 of which have been identified and 7 have received approval for construction. Of these 7, the Liquids and Amorphous Materials Diffractometer (LAD) and the High Throughput Inelastic Spectrometer (HTIS) are being built for installation on the Harwell linac. The main shielding tank for LAD has been delivered and all other components are on order. It should be installed at the linac in the summer of 1981. Detailed design is complete for HTIS and the majority of the components ordered, in particular the beryllium for the filter. The latter will not be delivered before the autumn of 1981 and is on the critical path for the project, which will be completed in the Spring of 1982.

Detailed design is complete for the following 3 instruments:

1. High Intensity Powder Diffractometer
2. High Resolution Powder Diffractometer
3. High Energy Transfer Spectrometer

Manufacture of these now awaits provision of funding.

No further work has been done yet on the remaining 2 of the 7 approved instruments; the Low Q Diffractometer and the quasi-elastic instrument IRIS.

The state of the remaining 7 instruments is as follows:

1. Small Angle Neutron Diffractometer for Liquid and Amorphous Samples (SANDALS) - outline design and cost estimates are complete.

2. Medium Energy Transfer Spectrometer (MET) - outline design is at an early stage.

3. Single Crystal Diffractometer (SCD) - completion of outline design awaits experience on the linac which will decide the type of detector.

4. Polarised Neutron Spectrometer (POLARIS) - the major components of this instrument, two polarising filters, are being funded by the NBR Programme. One filter is well proven and the dilution refrigerator for the second has been commissioned. Final design of the SNS instrument awaits experience on the linac.

5. Constant Q Spectrometer (CONQ) - design of the SNS instrument will depend on experience gained with the existing linac instrument.

6. High Symmetry Spectrometer (HYSYM) - design awaits the results of a test experiment on the linac.

7. eV Spectrometer (EVS) - again, the design of the SNS instrument will use experience gained from experiments on the linac.

Work has begun on the scientific specification of SNS beam collimators and beam stops.

A technical trawl was carried out early in 1980 of possible suppliers for the PUNCH Computing System for instrument control, data collection and data reduction. No further work will be done until funds are available.

4. OTHER USES OF THE SNS

There is interest in other uses of the SNS. The status of these is given below:

4.1 Intermediate Target Station in the EPB

The design of the system that transports the proton beam to the SNS Target Station has been made so that an intermediate focus can be produced 22m upstream of the SNS target. If no target is placed at this focus the full beam will be delivered to the SNS target with no deterioration.

If a target of 5 cm of carbon is placed at the intermediate focus 12% of the protons will interact in the target and the rest will be delivered to the SNS target with a slight increase in the beam divergence and a slight decrease in energy - the neutron yield would be reduced by 15%. Adequate shielding must be provided around the intermediate target to reduce radiation to below the tolerance levels for biological and experimental purposes.

Secondary beams can be formed from particles produced at this intermediate target. Two such beams are a pion beam for biomedical experiments and a muon beam for either muon spin rotation experiments for use in condensed matter research or for studies of rare muon decays.

A proposal has been made to the Medical Research Council and SERC for the construction of a pion beam for biomedical research at an estimated cost of £1.2M. The MRC has agreed to pay half of the £78K required to carry out work on the construction of the shielding for the EPB and the beam transport equipment to keep open the option for the construction of the pion beam and the muon beam. The SERC has agreed to provide the other half of the money.

4.2 Neutrino Facility

A cavern has been constructed below floor level adjacent to the SNS Target Station.

A Letter of Intent has been produced proposing to construct a detector and to carry out neutrino experiments using the SNS. A group from Karlsruhe is also considering a proposal to undertake neutrino experiments on the SNS and this may involve increasing the size of the neutrino cavern.

The neutrino experiments are completely compatible with neutron experiments and will in no way interfere with the requirements of the neutron beam exploitation.

4.3 Irradiation Facilities

An investigation has been made of the possibilities of using the 70 MeV beam from the linac for isotope production. The cost of these studies was covered by the Radiochemical Centre at Amersham. They have decided not to request us to proceed with the implementation of the resulting plan at this stage. Further possibilities of using the small neutral beam formed when the H^- beam passes through the stripping foil, or other parasitic possibilities, may be investigated at a later stage.

There is also the possibility of providing fast neutron irradiation facilities close to the SNS target. This is of interest to study radiation damage of materials relevant to fusion and/or fission energy sources. The Energy Committee of the SERC has agreed to provide £30K for the provision of an access tube in the Target Station to permit the option for an irradiation facility to be kept open.

If this facility is provided it will be compatible with the neutron beam use of the SNS.

4.4 Charged Particle Test Beam for HEP

A study is in hand to provide a charged particle test beam in Hall 1 for use by high energy physics teams. The beam will be formed using particles produced by beam lost in the SNS Machine Room during acceleration or extraction.

Every attempt will be made to minimise the beam lost and under no circumstances will beam be deliberately lost to increase the test beam intensity. The requirements of the test beam are not stringent and it is virtually certain that there will be no difficulty in meeting the needs - it is not possible to be completely certain until we operate the SNS.

The Nuclear Physics Board of SERC will pay for any expenditure required for this test beam and the facility will be parasitic on normal SNS operation.

4.5 Use of the SNS for accelerator studies relevant for heavy ion fusion

Many groups throughout the world have been investigating the possibility of achieving controlled fusion as an energy source by using beams of energetic heavy ions to compress hollow pellets of dimensions of a few millimetres containing deuterium and tritium. The studies indicate that the ions need to be singly charged uranium of 10-20 GeV energy. These particles have the same velocity as protons of about 70 MeV. These paper studies indicate that beams have to be produced that are very intense and have to be tightly compressed in time and space. The space charge effects are very large and experimental verification is needed to prove that the required compression can be achieved. The cost of a suitable 10-20 GeV heavy ion accelerator is extremely high (>> £10^8) and hence it is necessary to make studies using a suitable scaled model. The SNS with the 70 MeV injected beam is a perfect model and is uniquely suitable for all the existing or planned accelerators.

RAL has recently held an international Workshop to consider the possibilities of using the SNS for these model studies relevant for heavy ion inertial confinement. RAL proposed a programme costing about £1.6M over a period of about 5 years. The Workshop supported the proposed programme and many laboratories expressed interest in participating.

The requirements for the SNS are believed to be compatible with normal SNS use but require about 12 days per year of dedicated use of the SNS. It is unlikely that normal SNS operations will be able to use all of the available time because of financial constraints so it is probable that the dedicated time could be given without conflicting with normal SNS utilisation.

It is intended to develop this programme as a formal proposal.

5. CONCLUSION

The SNS programme is proceeding well. Although there have been delays in producing some of the equipment, these do not appear to prejudice the time-scale being aimed for.

Jül-Conf-45 A5

I C A N S - V
MEETING OF THE INTERNATIONAL COLLABORATION ON
ADVANCED NEUTRON SOURCES
June 22 - 26, 1981
at Kernforschungsanlage Jülich

Status Report on the SIN Spallation Neutron Source

Walter E. Fischer
Swiss Institute for Nuclear Research (SIN)
5234 Villigen, Switzerland

Abstract

This status report describes the general layout of the planned SIN spallation neutron source. In the description of the technical concept we emphasize the version using natural convection of the liquid metal target. In the second part of the report we discuss the neutronics, based on results of mock-up experiments. Furthermore, beam tube arrangements and proposed spectrometers are presented.

Layout

Figure 1 shows the general layout of the SIN accelerator system and of the experimental hall with the two meson target stations. The injector II with its pre-injector (Cockcroft-Walton) can be seen at the north side of the hall. With this injector 2 mA beam currents of 590 MeV protons can finally be expected. The position of the planned spallation neutron source will be south-east of the main experimental hall, in the prolongation of the primary proton beam. This site is illustrated in Fig. 2 which also shows the extended experimental hall. The south-east hall is reserved for the neutron source and the experimental areas with thermal neutrons and the "guide-hall" for experiments with cold neutrons.

Technical Concept

The SIN spallation neutron source will use the principle of a liquid heavy-metal target (Pb/Bi-eutectics). Either of the two following cooling concepts may be applied:

1) forced convection - horizontal target

2) natural convection - tilted or vertical target (beam entering from below)

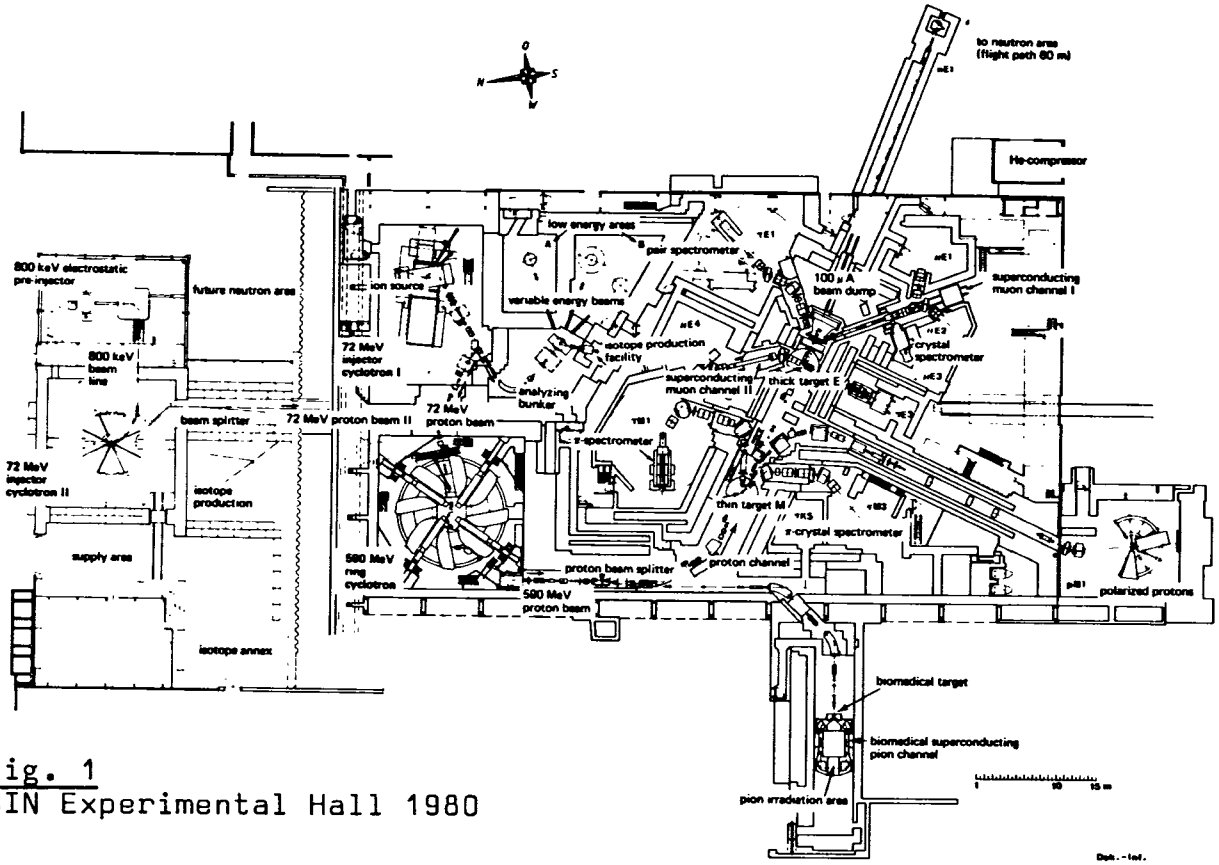

Fig. 1
SIN Experimental Hall 1980

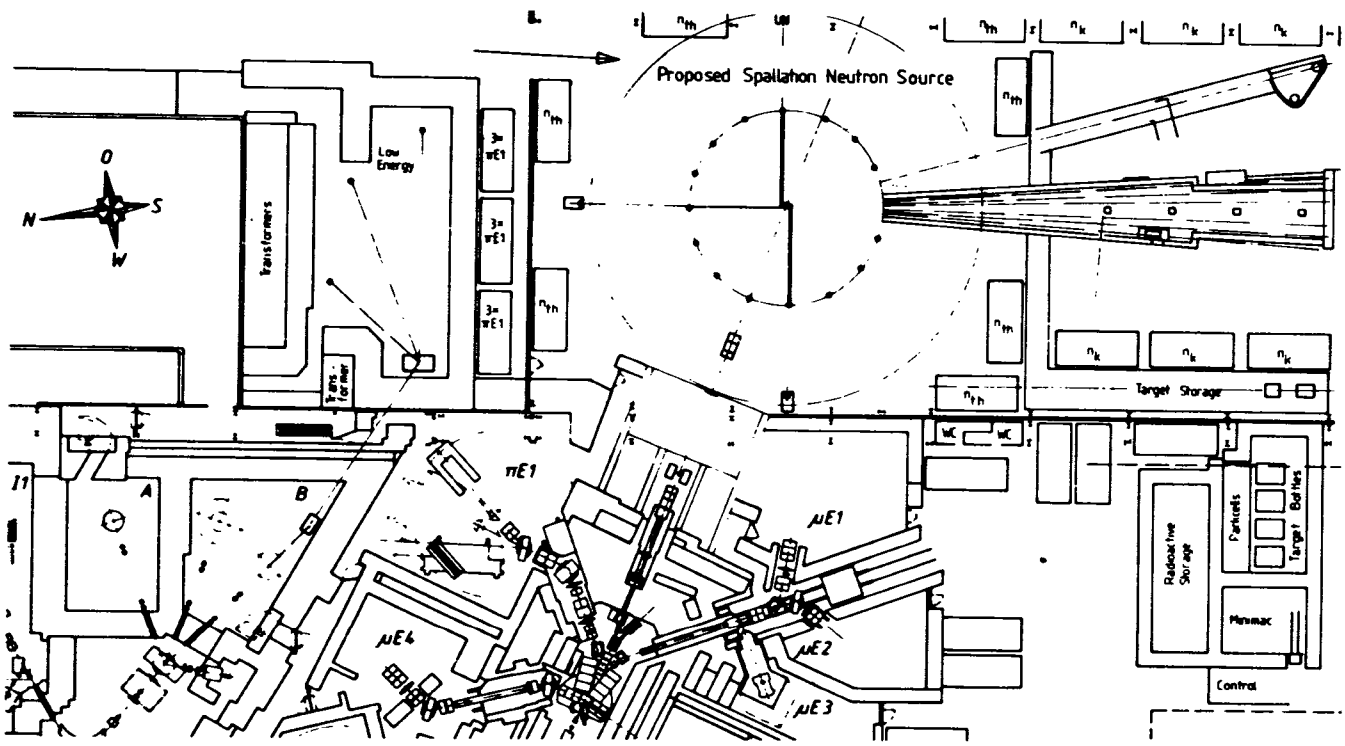

Fig. 2
Experimental Hall including the planned neutron hall

The first concept has been discussed at ICANS III and IV[1]. In this report we shall restrict the discussion to the second concept[2]. A somewhat schematical view of a vertical spallation source arrangement is shown in Fig. 3

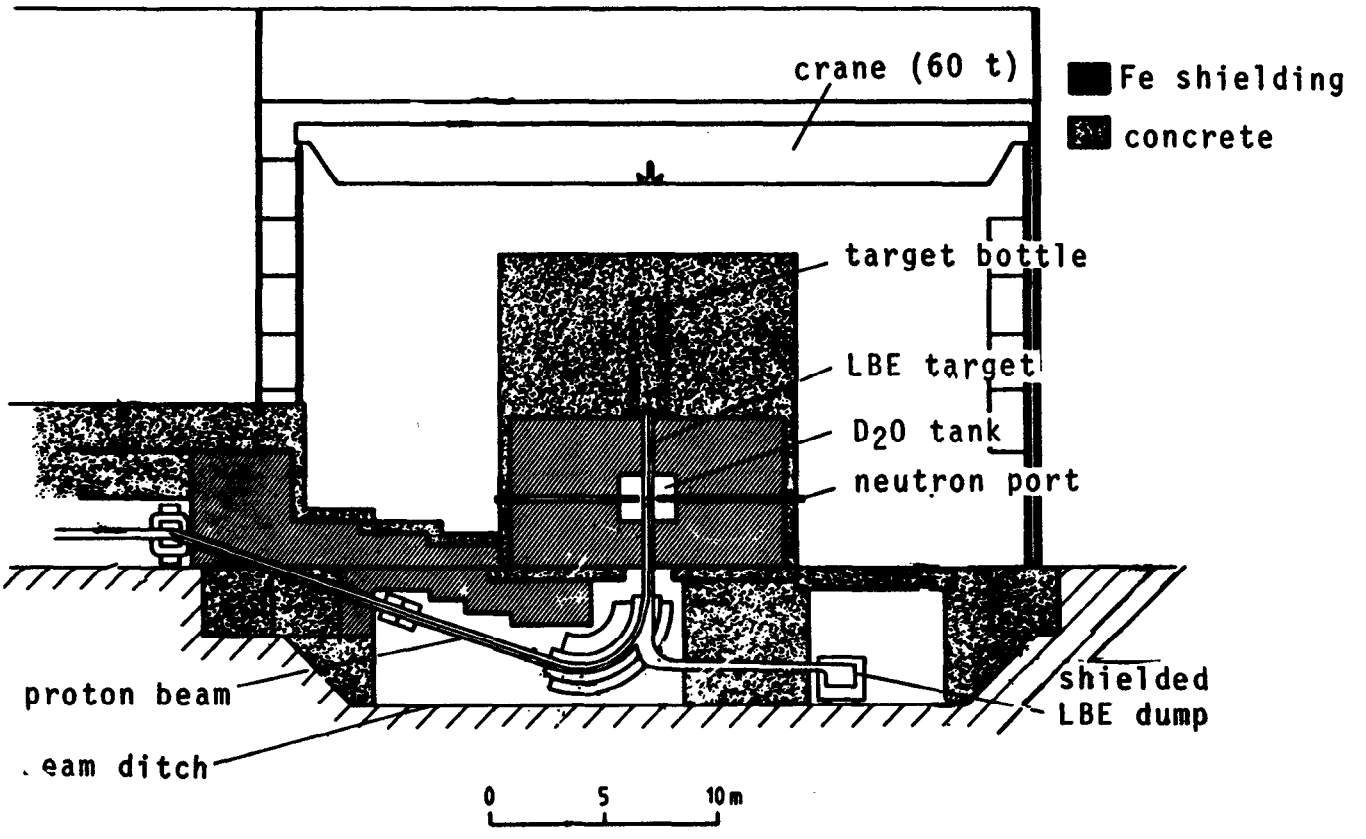

Fig. 3
Schematic view of the vertical version of the spallation neutron source

A critical component for both versions of a convective liquid metal target is the beam window. The power density dumped in the window can however be diluted up to a certain extent. Contrary to a pulsed spallation source with its small hydrogen moderators which require a high neutron source density in the target, the continuous source may accept a more spread beam without strong penalty. The coupling of the source to the moderator is always good. Furthermore, yield measurements at a cylindrical target with fixed diameter and variable cross section of the proton beam showed that up to a ratio of the beam target radius of 0.5 the decrease of the neutron yield is less than 20 %. Nevertheless, radiation damage tests at possible beam window materials are very essential. One of these tests is described below:

Window material	Reactor - graphite
	Thickness D = 3 mm
	Diameter Ø = 2 cm

Beam current and size 100 µA (590 MeV protons) within 0.3 cm^2 corresponding to a current density of 333 $\mu A/cm^2$

This piece of graphite was exposed to the beam for 200 hrs. at a temperature of T ≈ 1200° C. After this load of 67 $mA \cdot h/cm^2$ no macroscopic damage was observed. This probe should now still be investigated microscopically and exposed to strength tests. If these tests turn out to be successful, such a window has a fair chance to survive longer than 1600 hrs. with a beam current of 2 mA and a beam diameter of 4 cm. Stronger radiation tests on graphite materials will be mentioned by Ch. Tschalär in his discussion contribution[3]. Further tests with the window material in contact with Pb/Bi of the target ought to be done.

Let us now discuss the conception of the liquid metal target with natural convection as a cooling mechanism. Figure 4 shows a schematic view of the target. The vertical target will be described in the contribution to this meeting by Ch. Tschalär. I restrict the discussion in this status report to the tilted version.

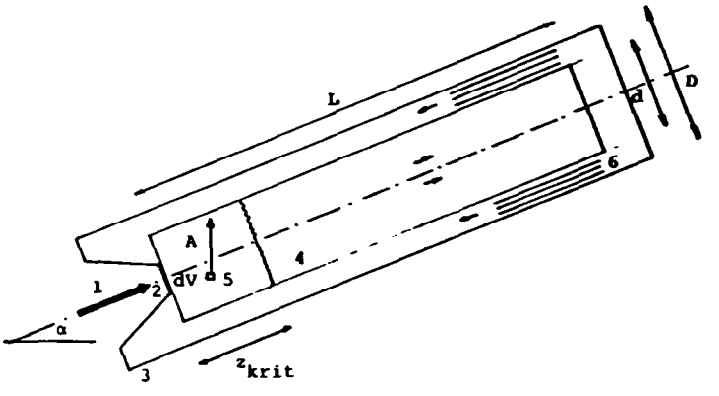

Fig. 4
Liquid metal target - tilted version - using natural convection

In the stationary case the flow of the liquid metal is dominated by the rise along the target axis towards the heat exchanger. This flow is driven by the buoyancy force

$$\rho g \beta \Delta T \cdot V \cdot \sin\alpha$$

ρ: density of Pb/Bi eutectics; $-1/\rho \cdot \delta\rho/\delta T = \beta$: thermal expansion coefficient; α: target tilt angle as indicated in Fig. 4; V: volume of the target.

A simple one-dimensional consideration for turbulent flow caused by a 1 MW proton beam leads for a head of 2 m to a flow rate of 4 l/sec. and a temperature rise of ∿ 200° C. This is indeed a very comfortable situation. However, the really critical situation appears during the start-up phase. A 1 MW beam drives the target temperature in the stopping re-

gion from 130° C up to the boiling point of 1670° C within 1 sec. if the liquid stays at rest. On the other hand, the 30 cm deep, heated region needs about 8 sec. to be moved out of the beam stopping area by the buoyancy force in the start-up situation. This demonstrates the rather large inertia of this system. In order to circumvent this difficulty, the beam power may be increased gradually - a procedure more adequate to certain parts of the accelerator system (rf-system) in any case.

A more thorough investigation of the fluid dynamics shows however that a target design is possible which does not even rely upon such a procedure. If outside the heated beam cross section there is ample target material available for a transversal convection during the starting phase, overheating can be avoided.

Figure 5 shows the time development of the temperature profiles in the vertical symmetry plane of the target. This and the following figures are the results of the solution of the Navier-Stoker- and Heat Conduction equations. The problem is treated in the Boussineq approximation i.e., incompressibility and constant density are assumed apart from the driving buoyancy force of course. For the code available, a quadratic cross section of the target containment (l = 19.2 cm) was more convenient. Furthermore a constant temperature (130° C) at the target boundary has been assumed. The case of an adiabatic boundary will be presented in another report.

The results for this case can be interpreted in the following manner. Two vertical vortices to the left and right side

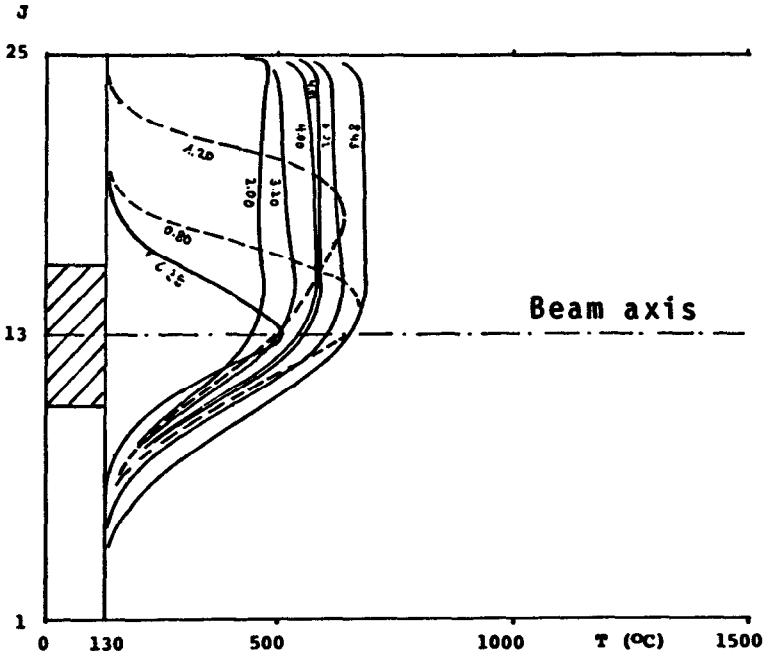

Fig. 5
Time development of the temperature profile in the vertical symmetry plane

of the beam axis transport the heated material to the upper cooled target boundary. The cooled material then flows down along the boundary and is drawn up again into the center. The isothermal field through a cross section of the target, shown in Fig. 6, may visualize the situation more clearly. At this very first moment the convection of the liquid metal along the target axis is not yet important. After about 8 sec., however, this motion has come into full action - the material has moved out of the heated region - and the flow and temperature pattern remains stationary. Figure 7 describes the time development of the maximal temperature in the system. This temperature remains far below the boiling point even during the start-up phase. After 7 sec. the spatial position of the point with maximal temperature remains fixed. At this time the up-drift along the target is activated and the heat exchanger stabilizes the temperature.

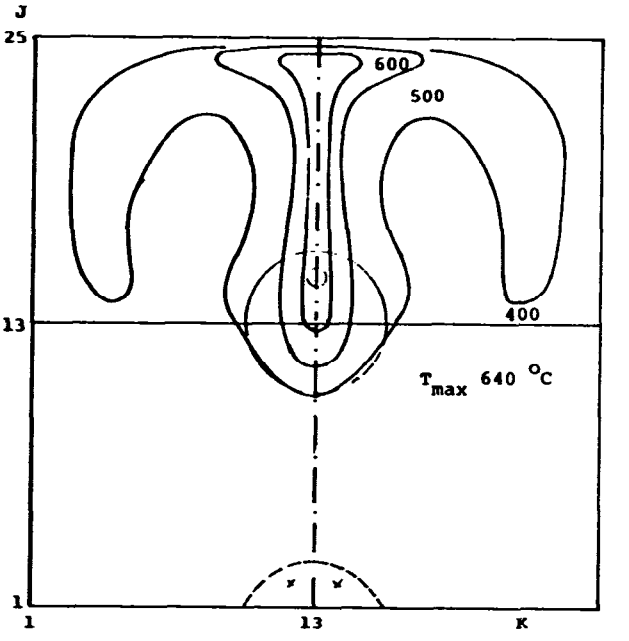

Fig. 6
Isothermal field after 8 sec.

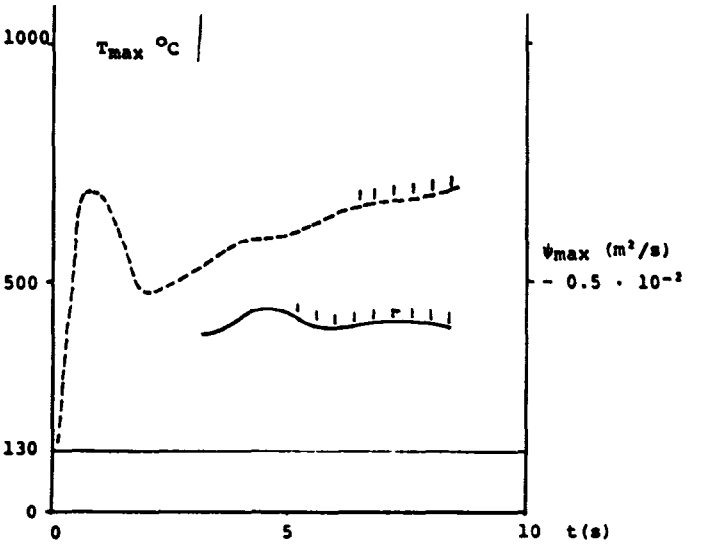

Fig. 7
Time development of the maximal temperature in the target. The lower curve is the time dependence of the maximal value of the streaming function.

Neutronics

Figure 8 shows three models of a neutron source which were considered in the mock-up experiment at SIN by the Jülich - Karlsruhe - SIN collaboration. The first two models have been investigated mainly in view of the German SNQ-project, and will not be discussed further in this report. The third model is relevant for the planned SIN source. The neutron flux in the D_2O was measured with Dy-foil activation and with BF_3-counters mounted inside snorkels. The two independent measurements are consistent. Through the beam tube, indicated in Fig. 8, a beam of thermal neutrons was extracted from the system. The counting rate from this beam, together with the proton beam monitors,

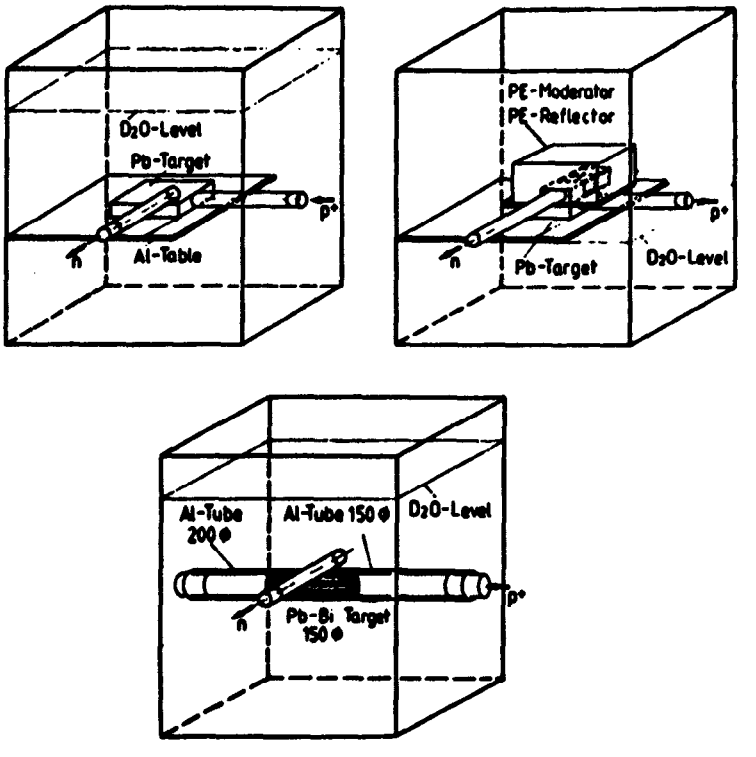

Fig. 8
Models considered in the mock-up experiment at SIN for neutronics investigations

served as one of the absolute calibrations of the neutron flux in the moderator. The results indicate that a thermal flux of $9 \cdot 10^{13}$ n/cm^2 sec. at the tube nose in the moderator can be realized for 1 mA primary proton beam current at 590 MeV. This calibration agrees with the gauge of the Dy-measurements with an uranium probe.

The results of this flux measurements are represented in Fig. 9. The position of the target is below the z-axis with its

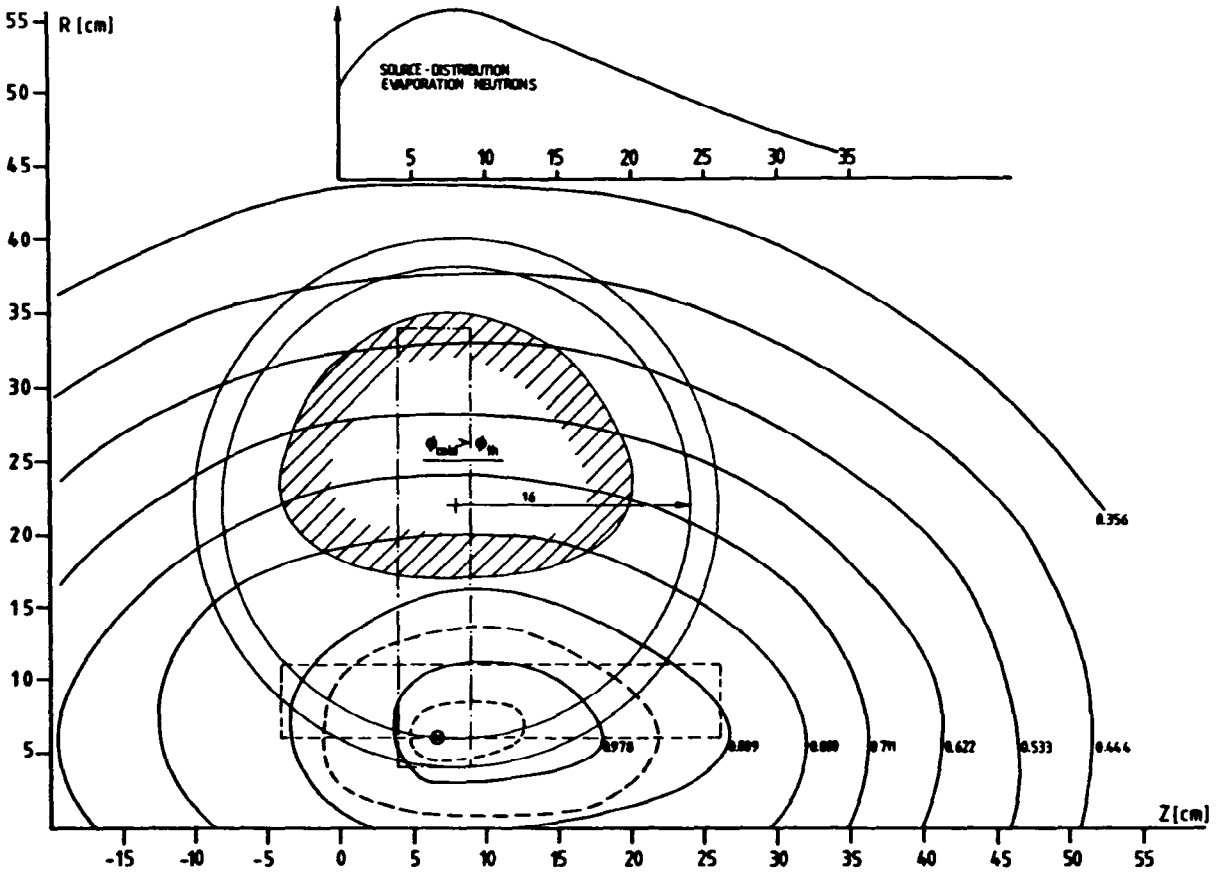

Fig. 9
Flux distribution for thermal neutrons in the D_2O-reflector

front end at z = 0 cm. The proton beam comes in from the left side below the z-axis. The whole system is cylindrically symmetric around the target center line which is 10 cm below the z-axis. In the (r, z) frame are drawn the lines of an equal flux for thermal neutrons.

The numbers at the equi-flux lines signify the thermal flux in units of maximal flux which is situated at the point (6 cm, 7 cm). In the upper small frame of Fig. 9 is indicated the source distribution of evaporation neutrons at the surface of the target, measured by activation of Rh-foils.

Using this flux distribution for thermal neutrons in the D_2O-reflector, we may find the optimal position of the cold source as well as position and size of the neutron tubes for the extraction of thermal neutrons. The sphere drawn in Fig. 9 indicates the possible position of the containment of a liquid D_2 (20° K) source. Neutron guides would look towards the hatched region of the cold source. The nuclear heating of the

source at this position is estimated to be about 2.5 kW for a proton beam current of 2 mA.

In the same figure we have drawn the cross section of a slit beam hole for thermal neutrons - the one parallel to the z-axis in the suitable position for a vertical target, the other for a horizontal (tilted) target. From these positions of the beam tubes and the flux distribution we realize that the hole for the vertical target version couples somewhat better to the neutron flux. The average flux over the beam hole cross sections are

$\bar{\phi} = 0.75\ \phi_{max}$ for the horizontal version

$\bar{\phi} = 0.9\ \phi_{max}$ for the vertical version

Beam Tubes and Instrumentation

Figure 10 shows a possible arrangement of beam tubes and the cold source for the horizontal - or tilted - target version. (The target tilt is not indicated in the figure.) The reflector volume above the target is reserved for the cold source, the corresponding beam tubes and the connections to the guides for the cold neutrons. The thermal neutrons will be extracted through beam tubes, all situated below the target. All beam tubes are in a tangential position with respect to the target. Figure 11 gives an idea about the distribution of spectrometers at the spallation neutron source with the arrangement of beam tubes just presented in Fig. 10. The monochromator shielding may be partly inserted into the main shield, depending on the angular range needed by the particular spectrometer.

It may be interesting to compare this beam tube arrangement with the one which seems to be feasible for the vertical target version. The set-up, shown in Fig. 12, should be understood as a maximal possible set. The actual number of tubes may be rather smaller and should be subject to negotiations with the potential users.

We would like to give finally some estimates of the flux for thermal neutrons at the monochromator of a typical beam tube. It is assumed that a vertical focussing monochromator allows us to accept a beam with divergencies

0.5^{o} horizontal
3.0^{o} vertical.

The corresponding slit tube has the dimensions 5x30 cm^2. According to our knowledge of the target yield and the flux distribution in the reflector we expect from a Pb/Bi target of the

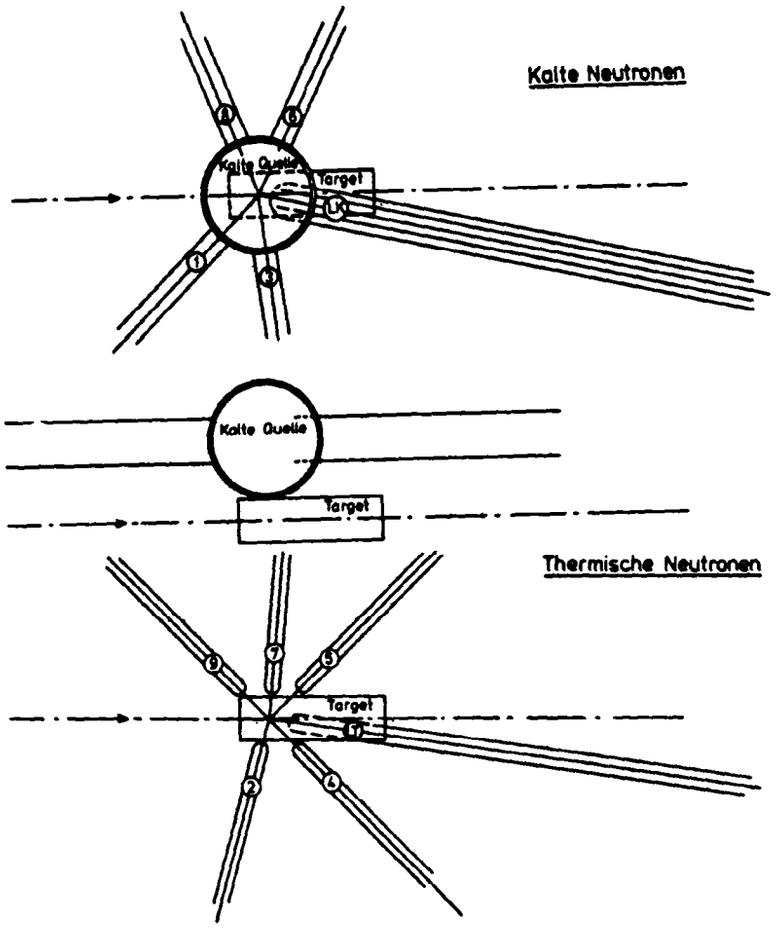

Fig. 10
Possible arrangement of beam tubes for the horizontal or tilted target version.

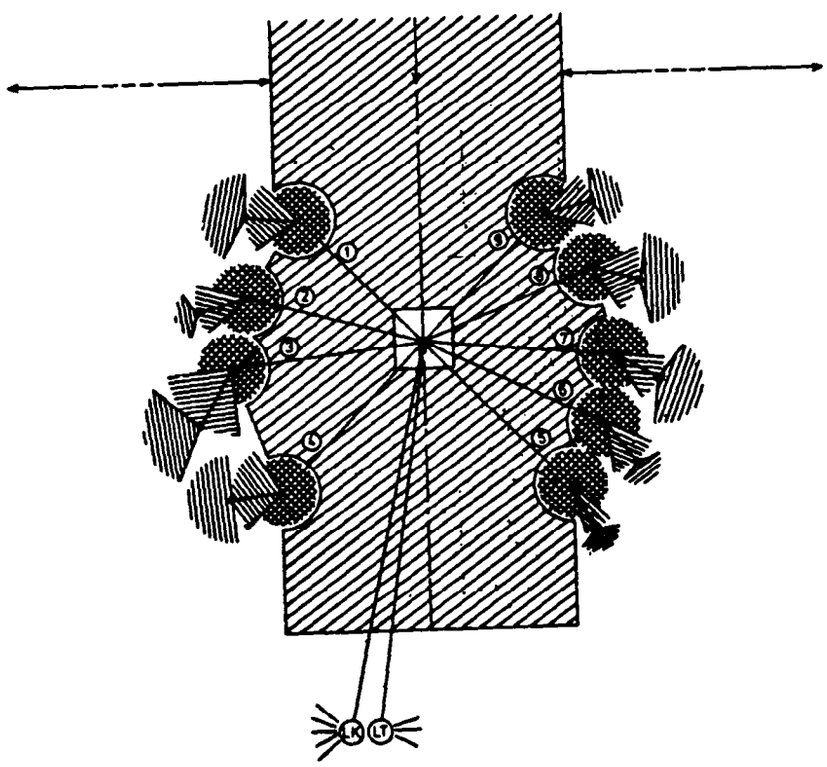

Fig. 11
Distribution of spectrometers with the arrangement of beam tubes shown in Fig. 10

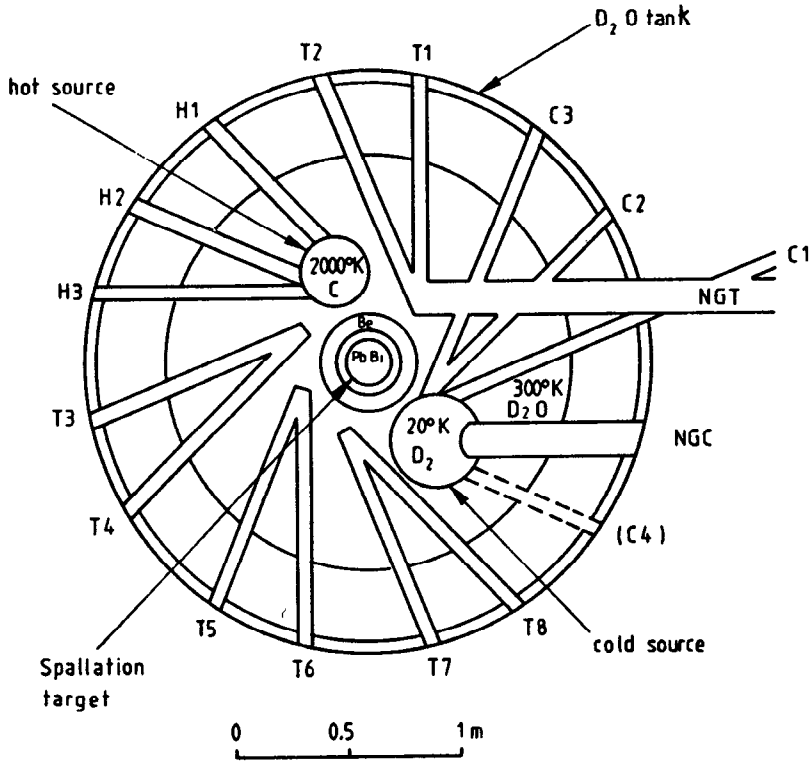

Fig. 12
Maximal possible set of beam tubes in the vertical version of the spallation neutron source.

horizontal version

45°	$1.3 \cdot 10^9$ n/cm^2 sec. mA
135°	$1.8 \cdot 10^9$ n/cm^2 sec. mA

depending on the direction of the beam tube with respect to the beam axis (different shield thickness!). For the vertical target concept the flux at the monochromator is

$$1.9 \cdot 10^9 \text{ n/cm}^2 \text{ sec. mA}$$

independent of the beam tube direction.

Table I shows the instrumentation, which would be installed at the beam ports of the version presented in Fig. 10 and Fig. 11. The instruments are labeled with the numbers of the beam hole (see Fig. 10), where the spectrometer is supposed to be placed. This instrumentation is based on an evaluation of long-term research projects made in 1978, proposed by five study groups for

structure research
solid state physics
chemistry
biology
material research

Since then, no new aspects appeared which could have modified the planning of the scientific exploitation of this neutron

Table I

Phase 1 : 1987		
2 Triple-Axis Spectrometer	1, 7	
1 Two-Axis Spectrometer	6	
1 Four-Circle Spectrometer	2	
1 Powder-Diffractometer	3	
Phase 2 : 1988		
1 Small Angle Scattering Spectrometer	LK1,	cold source (guide)
1 Spectrometer for Polarized Neutrons	9	
1 Triple-Axis Spectrometer	8	
Phase 3 : 1989		
1 Back-Scattering Spectrometer	LK2	cold source (guide)
1 Triple-Axis Spectrometer	4	
1 Four-Circle Spectrometer	5	
Phase 4 : 1990		
1 Powder-Diffractometer	LT1)	at thermal
1 Triple-Axis Spectrometer	LT2)	guides

source.

The beam tubes could essentially be exploited by national requirements; at the neutron guides some capacity for international participation would still be available. The potential concerning the number of beam ports would, however, be larger at the vertical version of the neutron source.

References

1) W.E. Fischer, W. Joho, Ch. Tschalär, B. Sigg, H. Rauch, Studie über eine kontinuierliche Spallations-Neutronen-Quelle am SIN
SIN-internal Report (1978)

Ch. Tschalär,
Spallation Neutron Source at SIN / Technical Concept
SIN Report TM-37-13 (1980)

See also SIN contributions to ICANS III and IV

2) Ch. Tschalär,
Free Convection Liquid Metal Target
Proc. ICANS IV, Tsukuba, Oct. 1980

H.P. Weiss,
Konvektive Kühlung einer Spallations-Neutronenquelle,
Untersuchung der instationären Anlaufphase, Teil I und II,
INNOVENT Zürich AG (1980/81)

3) Ch. Tschalär,
These Proceedings

4) G.S. Bauer, E.W. Fischer, F. Gompf, M. Küchle,
W. Reichardt, H. Spitzer,
Thermal Neutron Leakage and Time Structure for Various
Target-Moderator-Reflector Configurations for a Spallation
Neutron Source (1981)

V. Drücke, N. Paul, G.S. Bauer, H. Spitzer,
Measurement of Thermal Neutron Flux Distribution for
Various Target-Moderator Configurations for a Spallation
Neutron Source by Activation of Dy-Foils,
Realisierungsstudie zur Spallations-Neutronenquelle,
Teil IIIa, Band 2 (1981)

Jül-Conf-45 A-6

I C A N S - V

MEETING OF THE INTERNATIONAL COLLABORATION ON

ADVANCED NEUTRON SOURCES

June 22-26, 1981

Final Results of the German SNQ Study

H. H. Hennies

Kernforschungszentrum Karlsruhe

Vorstand

D-7500 Karlsruhe, Postfach 3640

Extended Abstract*

The SNQ project study, carried out jointly by Kernforschungsanlage Jülich and Kernforschungszentrum Karlsruhe has been completed in May 1981 as planned. The report was prepared in three parts: part I (available as report Jül Spez 113/ KfK 3175)** gives a general description of the project and its scientific motivation; part II is a more detailed record of the technical concept and related research results; part III is a collection of appendices containing original papers and reports and is meant to serve as a basis for the future work on the project.

The main characteristics of the project have already been presented at the ICANS-IV meeting in Tsukuba in 1980 by W. Klose (report KENS-II), with many details given in contributed papers to both, ICANS-IV and the present meeting. We have considered a basic concept (reference design) and several possible future options. In its basic configuration, the source is designed to reach a time average thermal neutron flux of $7 \cdot 10^{14}$ $cm^{-2}s^{-1}$ and a peak flux of $1.3 \cdot 10^{16}$ $cm^{-2}s^{-1}$ at 100 Hz repetition rate, which would make it superior to all existing neutron sources for beam hole research. The proposal includes a 1.1 GeV, 5 mA time average linear accelerator consisting of an Alvarez type low energy part and a disc-and-washer type high energy accelerating structure which operates at a peak current of 100 mA and at RF-frequencies of 108 (Alvarez) and 324 MHz (daw). The target material is proposed to be lead initially. It will be arranged on a 2.5 m diameter wheel rotating at 0.5 rps, to reduce the heat load and radiation damage of the target. The proton beam will impinge on the circumference of the wheel at right angles to its axis. Provisions are proposed for neutron scattering (thermal and cold neutron source) irradiation facilities, neutrino physics, nuclear physics and meson research. With its time

average beam power of 5.5 MW and peak proton current of 100 mA the facility is a major step forward from existing machines in accelerator development as well as target power. However, the study has shown with a high degree of confidence, that this step is feasible within reasonably small extrapolations from proven technologies. Options for future extensions include: increase in proton beam power up to 11 MW time average, use of uranium as target material, addition of a proton pulse compressor to provide pulses of 0,7 μs duration at 66 A and construction of a second target station designed for pulsed neutron work mainly in the epithermal energy range. The estimated cost (in 1980 money) for the basic configuration is 680 million German Marks and another 130 million for the proton pulse compressor. We expect a decision from the government to go ahead with a detailed design study and hardware tests early in 1982. The projected time scale includes a further development period of little less than two years and about eight years of construction time if adequate funding can be provided.

* A full paper will be available from the author.

** This report is in German. The following reports in English are available upon request:

G.S. Bauer and J.E. Vetter "The German Project of a High Power Spallation Neutron Source for Fundamental Research" preprint of a paper to be published in the IIASA-Pergamon Press Conference Proceedings series

J.E. Vetter (ed). "The Basic Concept of the SNQ Linear Accelerator", report KfK 3180 B

G. Schaffer, ed. "IKOR, An Isochronous Pulse Compressor Ring for Proton Beams" report Jül-Spez-114.

I C A N S - V

MEETING OF THE INTERNATIONAL COLLABORATION ON

ADVANCED NEUTRON SOURCES

June 22-26, 1981

RESEARCH OPPORTUNITIES WITH PROTOTYPE ACCELERATORS FOR AN ACCELERATOR BREEDER

G.A. Bartholomew

Atomic Energy of Canada Limited
Research Company
Chalk River Nuclear Laboratories
Chalk River, Ontario K0J 1J0

Abstract

Three stages of the prototype cw proton accelerator required to develop a pilot accelerator breeder provide opportunities for neutron research. New spallation yield measurements at 100 MeV in Pb, together with known yields above 400 MeV confirm that the second stage device, a 70 mA 200 MeV linac, coupled to a Pb-Bi target could provide beam tube fluxes of $\approx 10^{15}$ cm^{-2} s^{-1}. The pilot breeder is visualized to be located in a nuclear energy centre whence users might enjoy reduced costs owing to shared use of the accelerators, cheaper electricity and the possibility of output heat reclammation.

RESEARCH OPPORTUNITIES WITH PROTOTYPE ACCELERATORS FOR AN ACCELERATOR BREEDER

G.A. Bartholomew

As many in the audience will know, CRNL has not had the same goals in R and D for intense accelerator neutron sources as other laboratories in ICANS. The other laboratories have been interested in developing neutron sources primarily for fundamental research while in recent years we have been interested in developing them for accelerator breeding of fissile fuel[1]). I would like to tell you in what directions our planning is leading us as from this different vantage point. Although our thinking in spallation sources for research goes back to ING, we have only in the last year or two begun to think seriously of such sources as opportunities arising ready made from our accelerator breeder program and our concepts are still not very detailed. At Karlsruhe Dr. Chidley will describe our current accelerator development work. For some years we have also done target neutron yield and blanket fissile yield studies in collaboration with Dr. Thorson and others at TRIUMF and in the last year there has been a small scale effort on liquid-metal target concepts.

By way of background, let me mention that Canada is in the rather unique position in its nuclear power program in not needing a fast breeder reactor to extend its fissile fuel supply. With the CANDU reactor we could meet electricity needs for a very long time on the thorium fuel cycle[2]). In principle, the CANDU-thorium reactor could operate as a thermal breeder with a breeding ratio of unity but in practice it would be more economic to use some "topping enrichment" from outside the cycle. Extra fissile material would also be needed as initial inventory to start new reactors to expand the system. One can foresee a time when it may be economic to produce this makeup fissile material by means of a local auxiliary breeder and in a review just completed at CRNL we have confirmed our view that the accelerator breeder is, for us, the leading option to fill this role. So we visualize the accelerator breeder as a relatively small auxiliary supply system working in conjunction, or symbiosis, with a very much larger system of thermal reactors which will be the same CANDU advanced converter reactors we now have.

It has been determined[3]) that an optimized accelerator breeder would require a 1 GeV proton accelerator at 300 mA cw (Table 1). The beam would bombard a lead bismuth target surrounded by a blanket of fertile material and would produce something like 3 kg per day of fissile material. This is all I want to say about the breeder itself because I want to concentrate on opportunities presented by the prototype accelerators that will be needed to develop the accelerator breeder.

Three major steps are foreseen in building the technological base for the electronuclear breeder demonstration plant as portrayed in Fig. 1. The first step is the zero-energy breeder accelerator (ZEBRA) which would produce the full accelerator-breeder beam current but at only 1% of the final energy. This is visualized as a laboratory test accelerator located at CRNL. It would be very much an experimental

TABLE 1 PARAMETERS OF ACCELERATOR BREEDER

Energy	1 GeV
Beam Current	300 mA protons cw
Accelerator	0-50 keV injector 0.050-2 MeV RFQ 2-200 MeV DTL 200-1000 MeV coupled-cavity
Target	Pb-Bi (distributed)
Blanket	uranium or thorium
Target/Blanket Power	1800 MWth
RF Power	370 MW
Fissile Output (80% availability)	≈3 kg/day

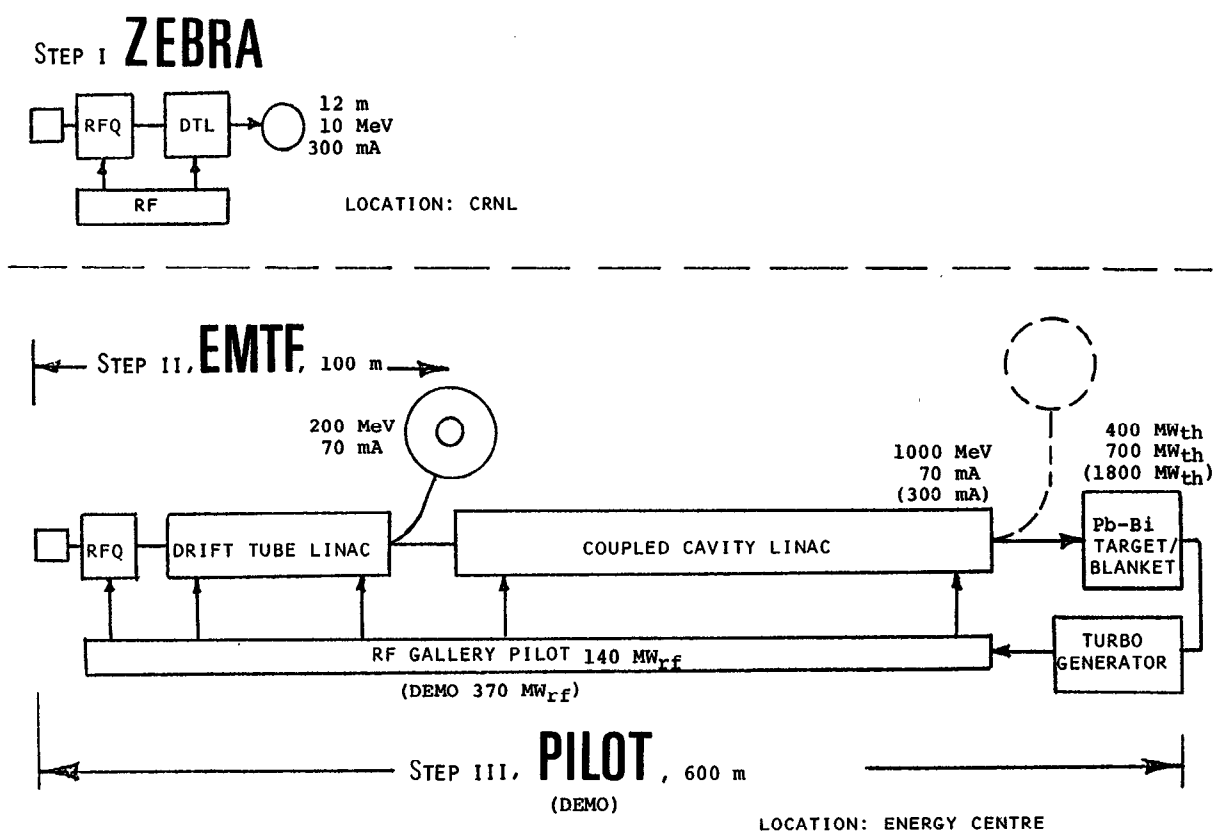

Fig. 1 Schematic representation of three modular steps in development of accelerator breeder from Zero Energy Breeder Accelerator (ZEBRA) to Electronuclear Materials Test Facility (EMTF) to PILOT Breeder. Subsequent upgrading from PILOT to DEMO would be accomplished by increasing the radiofrequency power.

prototype heavily instrumented to diagnose accelerator performance at high currents and low energy; this would be its main reason for existence. ZEBRA would involve an ion source and injector to about 50 keV, then a radiofrequency quadrupole to 2 MeV followed by a drift tube linac to 10 MeV. I will return to the output and possible experimental uses later.

The second step is an Electronuclear Materials Test Facility (EMTF) which, as indicated in Fig. 1, would accelerate a 70 mA proton beam to 200 MeV. This facility is envisaged to be located within the exclusion area of a nuclear energy centre because it is planned ultimately that it would be the front end of a full-demonstration breeder and the breeder would be best located near fuel reprocessing and storage facilities and also near the turbo generators of a CANDU station all of which we envisage to be located in the energy centre. However at the EMTF stage the beam would be stopped in a Pb-Bi target to form a neutron source. The beam parameters were chosen to give a thermal neutron flux of $\approx 10^{15}$ cm^{-2} s^{-1}. The accelerator might be planned so that 200 MeV is the transition energy between the drift-tube linac section and the coupled-cavity section. I will return to target characteristics in a moment.

In the third or PILOT stage the EMTF accelerator would be extended to 1000 MeV and 70 mA. This beam is considered the minimum to provide a full demonstration of the accelerator breeder target-blanket system, in particular to test performance at heat fluxes and neutron fluxes of interest to the reactor physicists and fuel engineers who would develop the blanket. It would be advantageous at this stage to reclaim the power developed in the target and blanket which might be of the order of 700 MW - the exact value would depend on the equilibrium fissile concentration permitted in the blanket. Beam splitting could be arranged to maintain both the EMTF and PILOT in service at the same time. By uprating the 200 MeV section to deliver 140 mA both could enjoy a 70 mA beam.

In later stages the rf supply of the pilot plant would be uprated to deliver the full 300 mA current required of a demonstration breeder plant and again I would think ways can be found to accommodate the research interests at the same time.

The facility represented by the broken line from the output of the 1 GeV accelerator in Fig. 1 would be a possible addition that would allow the 70 mA beam to be used, with a suitably uprated target of course, to provide a superb cw neutron source[4]) for research with a thermal flux of about 10^{16} cm^{-2} s^{-1}. We do not stress this possibility in present planning because it is too far in the future.

There is an obvious disadvantage in mixing the functions of a neutron source for research and a prototype breeder facility of interest to a utility. However, because the breeder is a pilot or demonstration device such a marriage may be rather more tolerable than attempting to share facilities with a fully committed commercial breeder. There could be compensating advantages, for example, in reduced operating costs for the research device because of close proximity to the power station and support services.

Now to return to ZEBRA one has to build a beam dump for 3 MW in any case and perhaps an argument could be made to go a bit further and install a falling liquid-lithium-stream target of a type similar to that for the Fusion Materials Irradiation Test (FMIT)[5]. We have not done a detailed design but we feel it may be possible to dissipate 3 MW with a flow of some 15-20 m/s in a jet several times thicker than the proton range (0.27 cm) in lithium. This flow may not be enough to prevent some vapour formation and cavitation by the beam, but it should be possible to arrange not to burn right through the Li jet. The proton beam would be about 10 cm in diameter to distribute the heat. The Li(p,n) yield at 10 MeV is known[6]) to an accuracy of about 4%; for 300 mA the total yield is 5.6×10^{15} ns^{-1} over 4π. This source would have a white spectrum and would not be pulsed, which makes it unattractive for cross section measurements. However, there are likely to be some applications in radiation damage, activation analysis, and isotope production. Of course, one would also gain valuable experience with liquid metal systems.

In the case of the EMTF source, we first thought of using a Li target here also because it would have simplified the heat dissipation problem. In fact our first plan called for a 100 MeV EMTF with 300 mA beam onto a Li target. However the accelerator will cost the same and will produce twice the yield at 200 MeV 70 mA, i.e. half the beam power, if we use a lead-bismuth target. One could not use a lead target at 100 MeV 300 mA because the range is only about 1.5 cm in lead and the power density in the metal becomes too high. At 200 MeV, the range in lead is about 5 cm. We envisage some kind of falling Pb-Bi stream but have not settled on the geometry; it could be cylindrical or rectangular. In simple calculations assuming a 10 cm diameter proton beam, the 14 MW heat deposition can be removed with a 15 m/s flow rate. The neutrons would be moderated to thermal energies and there would be space for a number of beam tubes in the high flux region.

When we started to study EMTF prospects as a neutron source we found that the total neutron yields for proton energies in the range from 25 MeV to 400 MeV were not measured for lead and other heavy metals. Only in this last month, as a direct result of our requirement an integrated yield measurement at 100 MeV has been carried out by a collaboration of CRNL and McGill University scientists using the McGill cyclotron[7]). The technique employed was quite standard, involving a large water bath in which are placed gold foils to give an integral flux measurement from which, and a measurement of the beam current, one calculates the yield. The lead target in the experiment was 5 cm in diameter and 1.5 cm thick. The Pb yield between 25 and 400 MeV was previously only known from calculations using the NMTC code[8]). The yield curve is shown in Fig. 2. Data points from previous results are shown above 400 MeV. The new results from McGill confirm the calculated yield at 100 MeV and therefore greatly improve confidence in the yield calculated for 200 MeV. The estimated yield at 200 MeV is $\approx 9 \times 10^{18}$ ns^{-1} A^{-1} from which the thermal flux from EMTF can be estimated to be $\approx 10^{15}$ cm^{-2} s^{-1} at 5 cm from the 5 cm target diameter surface in a water moderator. At the target surface the flux is $\approx 2 \times 10^{15}$ $cm^{-2}.s^{-1}$. We have not tried to fix the geometries or moderators for this system at this stage.

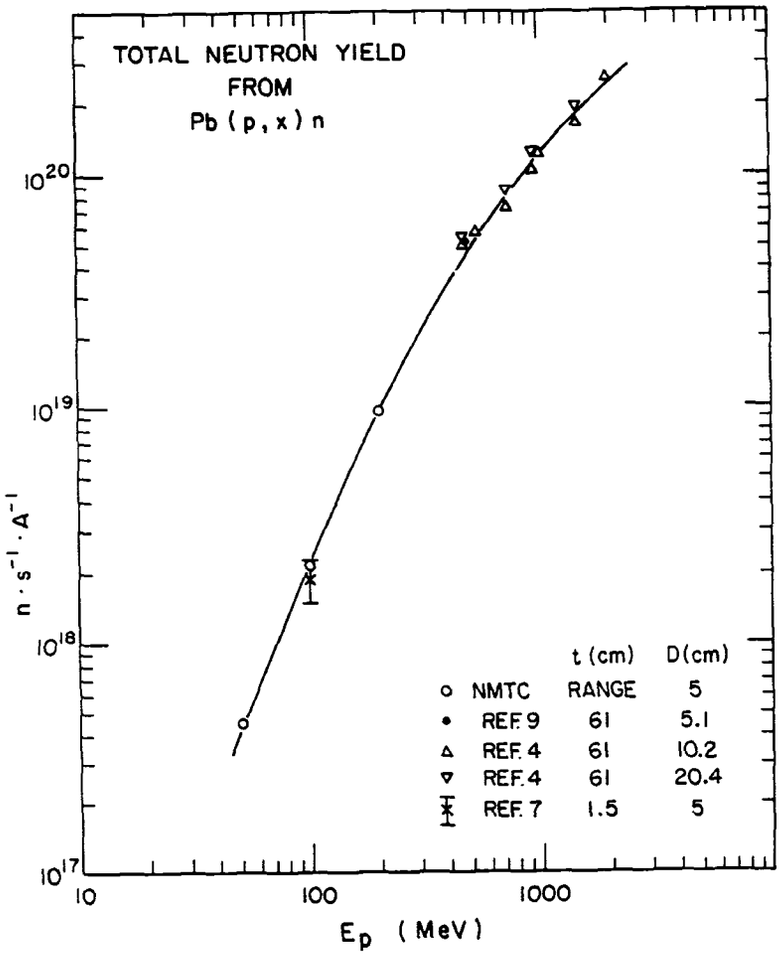

Fig. 2 Total neutron yield from bombardment of lead with protons. The recent experiment at 100 MeV (ref. 7) confirms the NMTC calculation at that energy.

Some uses of EMTF are listed in Table II. I should emphasize that one of the main justifications for EMTF is to study materials problems associated with the accelerator-breeder target/blanket assembly. For this purpose the spallation spectrum at 200 MeV is near ideal since its shape at low energies is a close approximation to the evaporation spectrum from 1 GeV protons; only the high energy cascade tail above 200 MeV is missing.

TABLE II EMTF USES

A. Programmatic:

1. neutron source with intensity and spectrum needed for testing of accelerator breeder target/blanket materials
2. liquid Pb-Bi target design and operating experience
3. accelerator tests cw, to 200 MeV

B. Spin-Off

1. high-flux ($\approx 10^{15} cm^{-2} s^{-1}$) steady state thermal neutron source for neutron solid state research
2. industrial opportunities in new liquid metal technology, new materials, new cooling systems, new components
3. complementary neutron damage studies for fusion
4. isotope production by fast neutrons
5. intense proton beam applications

In practical tests with the EMTF target one would be limited by practical flow rates of the liquid metal and by desire to avoid turbulent flow conditions caused by excessive vapour formation in the body of the metal. Of course several ICANS projects will provide valuable experience in high power targets. With EMTF there would be incentive to explore even more extreme conditions and press beyond 70 mA to breeder-type targets. You will realize of course that the target for a breeder would not necessarily be one useful for a high flux application; a breeder target might consist of a large number of jets and the proton beam would probably be widely spread to accommodate the heat load and to provide the distributed source required for the blanket. Experiments with a liquid lithium target system at 200 MeV energy might also be substituted in EMTF if desirable. Incidentally it is planned to extend the McGill total neutron yield experiments at 100 MeV to lithium and other targets.

Finally, I should mention that we do not yet have approval to build ZEBRA. We are still in a pre-ZEBRA development phase. We hope to obtain approval to build ZEBRA in 1983-84 and begin tests with it about 1987-89. The earliest we can imagine building EMTF is 1991-92 with first beam in 1995. We are not at this stage considering details of any neutron sources for research that might become available in later stages of the accelerator breeder development.

REFERENCES

1. Accelerator Breeder Concept, G.A. Bartholomew, J.S. Fraser and P.M. Garvey, Atomic Energy of Canada Limited, Report AECL-6363 and International Nuclear Fuel Cycle Evaluation, Report INFCE/WG.8/Can/Doc1 (1978).

2. Prospects of Self-Sufficient Equilibrium Thorium Cycles in CANDU Reactors, E. Critoph, S. Bannerjee, F.W. Barclay, D. Hamel, M.S. Milgram and J.I. Veeder, Atomic Energy of Canada Limited, Report AECL-5501 (1976).

3. High Current Proton Linear Accelerator and Nuclear Power, P.R. Tunnicliffe, B.G. Chidley and J.S. Fraser, Proc. 1976 Proton Linear Accelerator Conference, Atomic Energy of Canada Limited, Report AECL-5677 (1976).

4. The AECL Study for an Intense Neutron Generator, G.A. Bartholomew and P.R. Tunnicliffe eds., Atomic Energy of Canada Limited, Report AECL-2600 (1966).

5. Review of Accelerator Development at LASL Relevant to Intense Neutron Sources, R.A. Jameson, Los Alamos National Laboratory, Report LA-UR-80-2724 (1980).

6. M.A. Atta and M.C. Scott, J. Nucl. Energy 27(1973)875.

7. M.A. Lone, R.B. Moore, A. Okazaki, J.M. Robson, D.C. Santry, B.M. Townes, R.T. Jones, J.K.P. Lee, private communication (1981).

8. The Nucleon-Meson Transport Code NMTC, W.A. Coleman and T.W. Armstrong, Oak Ridge National Laboratory, Report ORNL-4606 (1970).

9. Neutron Production in Thick Targets of Lead, Thorium, and Uranium Bombarded by 480 MeV Protons, J.S. Fraser, P.M. Garvey, J.C.D. Milton, F.M. Kiely, I.M. Thorson and B.D. Pate, Proc. Symp. on Neutron Cross-Sections from 10 to 50 MeV, Brookhaven, 1980, Vol. 1, Brookhaven National Laboratory, Report BNL-NCS-51245 (1980).

Jül-Conf-45 B1

I C A N S - V

MEETING OF THE INTERNATIONAL COLLABORATION ON

ADVANCED NEUTRON SOURCES

June 22-26, 1981

Neutron Scattering at an Intensity Modulated Neutron Source

R. Scherm

Physikalisch-Technische Bundesanstalt

D-3300 Braunschweig, Bundesallee 100

Abstract

The performance of an intensity modulated neutron source like the SNQ with respect to any particular neutron scattering experiment depends on the peak neutron flux and on the fraction of time during which useful information is collected by the detector. In this respect we can distinguish different classes of instruments. Steady state-type instruments like diffractometers and triple axes machines utilize essentially the time average flux only, but can profit from the time structure by gating the detector against background and higher order monochromator reflections. Time of flight instruments use the peak neutron flux. A third class of instruments, most of which will be newly developped or will be suitable modifications of existing ones, will operate quasi-continuously on a variing neutron wavelength and thus effectively see the peak flux over a long period of time (say 50% duty cycle).

Jül-Conf-45

B2

I C A N S - V

MEETING OF THE INTERNATIONAL COLLABORATION ON

ADVANCED NEUTRON SOURCES

June 22-26, 1981

Ultra-Cold Neutrons and Spallation Neutron Sources

R.Golub and K.Böning

Physics Department

Technische Universität München

8046 Garching

Abstract

We present a brief introduction to the field of Ultra-Cold neutron (UCN) research including a review of the properties of UCN and some current and future applications.

We then discuss two types of UCN source suitable for use in connection with spallation neutron sources - "Doppler shifter" and "Superthermal" UCN sources

1) Properties of UCN

Ultra-cold neutrons (UCN) are neutrons with energies so low (a few times 10^{-7} ev) that they are totally reflected from many materials. While reflecting from a surface the UCN penetrate 100 or more Angstroms into the material. The loss probability per reflection depends on the material and the condition of the surface and ranges from 10^{-3} to 10^{-5} for selected materials. These properties mean that UCN can be stored in bottles made of selected materials for periods of time exceeding 100 seconds and perhaps approaching 1,000 seconds (the neutron decay lifetime) and open up a wide range of interesting applications.

2) Applications of UCN

a. The search for a neutron electric dipole moment (edm)

At the present time this is perhaps the UCN application which is being most energetically pursued. Groups at the ILL, Argonne National Laboratory, Leningrad and Dubna have all put many manyears of effort into this experiment. The search for the neutron electric dipole moment is interesting because the existence of an edm would be direct evidence for time-reversal violation outside the K^{o}-meson system. The present best experimental limit corresponds to an edm $\leq 6 \times 10^{-25}$ e-cm is the result of a UCN experiment at Leningrad.
It is expected that the observation of a neutron edm will make a clear distinction between the superweak theory on the one hand, and the other theories (e.g. spontaneous T violation, unified theories of the weak and electromagnetic interactions) which have been proposed to account for the T violation.

The UCN densities expected from the sources discussed below are so large compared to currently available densities that the UCN density should no longer be a limiting factor on the experimental sensitivity which will undoubtedly be limited by magnetic field fluctuations. With such high UCN densities it will certainly be advantageous to push the UCN technique to its limit using superconducting magnetic shields and other aspects of low temperature technology. However the presence of the large iron radiation shield at SNQ may cause some perturbations to the magnetic environment.

b. Neutron β-decay

At present the neutron lifetime is only known to an accuracy of about 1 %. A more accurate determination of the neutron lifetime would improve our knowledge of the weak interaction constants appearing in the theory of β-decay, which are currently determined by a fit to a large number of measurements of β-decays of nuclei and elementary particles. There would also be an improvement in our knowledge of the radiative corrections to the β-decays. The knowledge of several of these theoretical parameters is currently limited by the 1 % accuracy of the neutron β- decay lifetime (1,2).

Classical methods of measuring the neutron lifetime involve separate detectors a) to measure the neutron density in the apparatus and b) either

electron or proton detectors to measure the decay rate. Thus the measurement requires knowledge of the absolute efficiencies of a neutron and a charged particle detector. By using stored UCN the measurement can be carried out with a single detector whose absolute efficiency is not required.

This experiment has been actively pursued for several years by the group at Bonn (3) who are hoping to measure the lifetime of UCN stored in a magnetic bottle. The UCN will be produced by downscattering in liquid Helium similar to the UCN source discussed below.

UCN can also be used to study asymmetries in the β-decay of polarized neutrons and may prove useful for studying parity violation in (n, γ) reactions.

c. Material Studies with UCN

UCN have the unique property that they penetrate surfaces to depths of a few hundred Angstroms. The depth of penetration is a function of neutron energy as well as the density and composition of the material surface. The loss rate of UCN on a surface is also a function of these parameters. Thus the loss rate of a surface will be altered by the presence of a layer of oxide or film of other material on the surface and UCN will provide a unique way of studying such films.

The above properties suggest several interesting applications for UCN. For example one could study the depth of penetration of ions into a surface as a function of ion energy. After ion bombardment the surface will be exposed to the UCN which, penetrating to the depth of the implanted ions, will indicate the presence of the ions by the characteristic γ-rays resulting from (n, γ) reactions. With the high UCN densities expected from the "new generation" of sources it should be possible to obtain profiles for cases where the implantations are carried out with negligible surface damage and at low concentrations of the implanted ions.

UCN can be used for inelastic scattering studies of materials in several ways. For energy transfers large compared to the UCN energy, UCN can be upscattered from the surface region (or from the bulk of those samples which are penetrated by UCN) and the energy spectrum of the upscattered neutrons can be measured. Although this will have the disadvantage that only the region of the ω-Q plane that lies along the $\omega \propto Q^2$ curve of the free neutron is accessible, the technique may allow measurements which are impossible by other methods. For example UCN stored in liquid Helium will be upscattered as a result of interactions with the phonons and rotons at a rate which is temperature dependent. A measurement of the spectrum of the upscattered neutrons would provide information on $S(Q,\omega)$ in a region far from the phonon resonance at unprecedented levels of sensitivity - mean free paths of kilometers for 5 m/sec UCN. Such experiments seem to be impossible by any other technique and have become more interesting in the light of recent experimental and theoretical results. In addition one can study excitations in thin Helium films by a similar technique.

There is also the possibility of accelerating the UCN gas to $\lambda \sim 100 \div 200$ Å in order to do scattering experiments. One method to accomplish this is to gradually accelerate a container filled with UCN. When the container

is suddenly stopped the neutrons will continue (through the walls of the container) with an average velocity given by the velocity of the container before deceleration. The advantage of such a scheme derives from the very high phase space density available in the UCN source.

Somewhat related to this is the possibility of accelerating the UCN stored in liquid Helium by means of a strong monochromatic phonon beam or perhaps a shock wave in the Helium. In addition to the possibility of producing an intense burst of approximately monoenergetic neutrons the latter approach may provide an interesting method for studying shock waves in the superfluid Helium.

Another method of using UCN to study condensed matter is by means of a UCN spectrometer such as the gravity spectrometer constructed by Steyerl (fig. 1). This offers the possibility of very high energy resolution ($\sim$10 neV) in the Q range of $10^{-3} \div 3 \times 10^{-2}$ Å^{-1}. Such a spectrometer could be used to study slow dynamics in biological systems, hyperfine splittings, magneto-crystalline anisotropies, lowlying rotational states and hindered rotations in very large molecules and the slow critical fluctuations close to a phase transition, in particular magnetic phase transitions.

Elastic scattering of UCN can be used to study inhomogeneities in materials and transmission of UCN to study thin films.

d. UCN optics

Steyerl and his co-workers have allready demonstrated the operation of an achromatic Fresnel lens for UCN. Such work can be expected to lead to the development of a UCN microscope with a resolution of perhaps 1 μ. A prototype with a resolution of a few hundred microns is currently under construction (fig. 2). The advantage of such an instrument would be based on the different scattering properties of materials for neutrons as compared to other radiations, e.g. a UCN microscope is expected to be useful for studying the distribution of Hydrogen in a given sample.

Recent experiments at Garching have studied quasi-bound states in one-dimensional potentials produced by multi-layer structures. One could extend this work by constructing a UCN Fabry-Perot interferometer and studying transitions between different bound levels induced by an oscillating magnetic field as proposed by Steyerl. This would demonstrate the operation of the time dependent Schroedinger equation in an almost macroscopic system ($\sim 10^3$ Å).

3) New Generation UCN Sources

While existing UCN sources provide densities of at most 1 UCN/cm^3, new neutron sources (e.g. spallation neutron sources) now being planned or constructed open up several possibilities for producing UCN densities on the order of 10^3 UCN/cm^3 or perhaps even significantly greater.

One type of "new generation" UCN source ("Doppler shifter" UCN source) is based on the slowing down of faster neutrons as a result of reflection from a reflector which is moving in the direction of the neutrons. Such a

device would be placed at the end of a guide tube looking at a "cold" Hydrogen or Deuterium source and would produce a UCN density which is limited by Liouville's theorem to correspond to the phase space density in the peak of the pulse in the cold source since the UCN are admitted to a storage vessel by means of a shutter which opens in phase with the neutron pulse.

Two methods of realizing such a UCN source have been proposed. One makes use of the total reflection phenomena from a moving curved surface and produces UCN by slowing down 50 m/sec neutrons (Steyerl turbine). The second uses Bragg reflection from a moving crystal and requires 400 m/sec neutrons as an input; such a device has been constructed at Argonne. Both devices are expected to provide similar UCN densities which are estimated to be about 3×10^3 UCN/cm^3 at SNQ, produced outside the radiation shield at a position suitable for experiments.

The second general type of UCN source ("superthermal source") is based on the slowing down of 400 m/sec neutrons as a result of the emission of phonons by the neutrons (inelastic down-scattering) in superfluid liquid He^4. The Helium is contained in a vessel suitable for storing UCN so that the UCN, once produced, remain in the source until they are removed as the result of interactions with the Helium or the walls. The steady state UCN density in the source then depends on the production rate and the loss rate. After a time on the order of the UCN storage time the UCN density approaches its steady state value and this high density UCN "gas" can be extracted by means of a valve which would be opened to release the UCN. This device is not limited by Liouville's theorem which applies to the complete system - neutrons and phonons - and not to the neutrons alone.

Such a source, installed 70 cm from the bottom of the SNQ D_2O tank is expected to produce densities $\sim 4 \times 10^5$ UCN/cm^3 in the source. In order to be useful, for most experiments the UCN will have to be transported from the source to an apparatus outside the spallation source radiation shield, a process which will introduce some losses.

Steady state currents can be extracted from the UCN storage bottles in both of the sources under consideration (the Helium source and the Doppler shifter source) by fitting the bottle with an outlet port. In both cases the currents available would be proportional to the saturation densities in the sources so the comparisons we give here are also applicable to the case of scattering experiments.

The gain in available density expected from these "new generation" sources in comparison with existing sources is so great that one can expect that an entirely new range of research applications with UCN will be opened.

4) Doppler Shifter UCN Source (4)

A sketch of the apparatus as realized at the Argonne Spallation neutron source is shown in fig. 3. Neutrons (400 m/sec) are transported from a liquid Hydrogen moderator through a 5 m long vertical guide tube. After leaving the guide the neutrons are reflected from a moving crystal which

leaves them with a very small velocity after the reflection. The result is a cloud of UCN some of which move into the UCN guide tube which is kept closed by a slotted rotating disc except during the time when the neutron pulse is approaching the UCN guide.

This synchronous opening and closing of the guide allows the UCN density in the guide to build up (in principle) to that corresponding to the phase space density in the peak of the pulse.

Since the phase space density for a Maxwellian spectrum corresponding to total flux ϕ_o is given by:

$$n(v_o) = \phi_o \, e^{-(v_o/v_T)^2} (2\pi \cdot 100 \, v_T^4)^{-1} \quad n \cdot cm^{-3} (m/s)^{-3} \qquad (1)$$

v_T = thermal velocity - m/sec

v_o = velocity of incident neutrons

the maximum UCN density available with this technique is:

$$\rho_{UCN} = \hat{n}(v_o) \left[\frac{4}{3} \pi v_c^3 \right] \qquad (2)$$

where v_c is the maximum UCN velocity that can be stored and $\hat{n}(v_o)$ is the phase space density corresponding to the peak of the neutron pulse, because the reflection from the moving crystal ideally shifts the velocity without changing the phase space density.

However because of inefficiencies due to crystal reflectivity, pulse broadening, etc, the UCN density produced is expected to be only 10 % of (2).

In addition the Bragg scattering process distorts the sphere in velocity space so that only a disc around the equator of the sphere is populated. This reduces the expected UCN density by a further factor of 6 as confirmed by experiment and Monte-Carlo calculations, but perhaps some of this can be recovered by a suitable angular collimator at the input of the UCN guide.

5) The "superthermal" UCN source using superfluid He^4

a. Production of UCN by down scattering in liquid Helium

If a volume of Helium is exposed to a flux of neutrons there will be a production of UCN given by

$$P_{UCN} = \frac{d\phi(E^*)}{dE} E_{lim} \frac{4}{3} \left[\sqrt{\frac{E_{lim}}{E^*}} \right] S(k^*) \, N \sigma_o \quad UCN/sec/cm^3 \qquad (3)$$

where E_{lim} is the limiting energy for UCN storage

$E_{lim} = 2{,}5 \times 10^{-7}$ eV

$= 2{,}9 \times 10^{-3}$ K for Beryllium

N is the density of Helim atoms in the liquid = $2{,}18 \times 10^{22}/cm^3$

σ_0 is the free atom coherent scattering length = 1.1 barns

E* is the critical energy for UCN production by phonon emission

$$E^* = \hbar\, \omega_0\, (k^*) = \hbar^2\, k^{*2} / 2\, m \qquad (4)$$

$$E^* = 12\ K$$

where ω_0 (k) is the phonon dispersion curve for liquid Helium

S(k*) = 0.1 is the one phonon structure factor and

$d\phi/_{dE}$ (E*) is the energy spectrum of the incident neutrons evaluated at E*

Putting in the numbers we find from (3)

$$P_{UCN} = \frac{d\phi(E^*)}{dE} \quad 1{,}44 \times 10^{-7} \quad UCN/sec/cm^3 \qquad (5)$$

For a Maxwell Spectrum at temperature T

$$\frac{d\phi}{dE} = \phi_{th} \frac{E}{T^2} e^{-E/T} \qquad (6)$$

where ϕ_{th} is the total thermal flux. Thus

$$P_{UCN} = 1{,}92 \times 10^{-11}\ \phi_{th} \quad \text{for } T = 300°K \qquad (7)$$

b. Saturation steady state UCN density in the Source

Given the production rate P_{UCN}, the saturation density of UCN is given by

$$\rho_{UCN} = P_{UCN}\, \tau \qquad (8)$$

where τ is the storage time of UCN in the Helium containing vessel

$$\frac{1}{\tau} = \frac{1}{\tau_{He}} + \frac{1}{\tau_{abs}} + \frac{1}{\tau_{wall}} + \frac{1}{\tau_{\beta}} \qquad (9)$$

τ_{He}, the relaxation time for upscattering of UCN in the Helium.

τ_{abs} is the absorption time ($\to \infty$) in He^4

τ_{wall} is the relaxation time for wall losses

and $\tau_{\beta} = 10^3$ sec is the ß-decay lifetime.

According to calculations τ_{He} = 4000 sec at 0.6 K

and = 500 sec at 0.8 K

6) Comparison of UCN Sources

From equations (1) and (2) we can write the UCN density from the Doppler shifter source as

$$\rho_{Dop} = \frac{\bar{\phi}_o\ (Eo)}{\eta}\ \frac{(\Delta E)}{v_o}\left(\frac{\Delta\Omega_{Dop}}{4\pi}\right) \tag{10}$$

where η is the duty cycle of the neutron pulses ($\bar{\phi}/\eta$ is the peak flux $\hat{\phi}$)

$$\Delta E = (2/3)\ m\, v_o\, v_c \tag{11}$$

and $(\Delta\Omega_{Dop}/4\pi) = (1/4)\ (v_c/v_o)^2 = 7.6 \times 10^{-5}$ (12)

for v_c = 7 m/sec, v_o = 400 m/sec.

From equations (3) and (8) we can write

$$\rho_{He} = \Sigma_o\ (\Delta E)\ \bar{\phi}_o\ (E_o)\ \tau\ (\Delta\Omega_{He})/4\pi \tag{13}$$

with Δ E defined by (11) and

$$\Sigma_o = N\ \sigma_b\ S\ (k^*)\ (k_c/k^*)^2 = 4 \times 10^{-7} cm^{-1} \tag{14}$$

Thus if both sources were placed at the end of the same guide tube the ratio of UCN densities produced would be

$$\rho_{He}/\rho_{Dop} = \Sigma_o\, v_o\, \tau\, \eta\, (\Delta\Omega_{He}/\Delta\Omega_{Dop}) \tag{15}$$

In the case when the solid angle for the Helium source is limited by the guide $\Delta\Omega_{He} = \Delta\Omega_{Dop}$

and $$\rho_{He}/\rho_{Dop} = \Sigma_o\, v_o\, \tau\, \eta \tag{16}$$

$$= 0.8 \times 10^{-2}\, \tau\eta = 3.2\,\eta$$

(if we take τ = 400 sec)

for the case when the Doppler shifter source gives the maximum output allowable by Liouville's theorem.

However we have seen above that the density produced by the Doppler shifter source must be reduced by an unavoidable factor of 10 so that (16) becomes

$$\rho_{He}/\rho_{Dop} = 32\,\eta \tag{17}$$

Now at Argonne $\eta \simeq 1/165$ so the Doppler shifter source would appear to be slightly better while at SNQ $\eta \sim 1/12$

However the real advantage of the Helium source (at a spallation neutron source) becomes apparent when we consider that while $(\Delta\Omega)_{Dop}$ is limited by the mechanism of total reflection to be given by (12), $(\Delta\Omega)_{He}$ is only determined by the geometric arrangement of the UCN

source relative to the primary neutron source.

For a practical case on the SNQ (fig.4) we have $(\Delta\Omega)_{He}/4\pi = 0.27$
or $(\Delta\Omega)_{He}/(\Delta\Omega)_{Dop} = 350$

in a position where there is an acceptable heat input to the Helium container.

Because the cold source supplying the guide tube for the Doppler shifter source can be in a higher flux, and can be larger and hence more efficient than the cold source supplying the "Superthermal" Helium source we have $\eta_{eff} = 10^{-2}$ for SNQ

and (17) becomes

$$\rho_{He}/\rho_{Dop} = 32 \times 10^{-2} \times 350 = 110$$

This figure applies only to the UCN produced inside the Helium, so it must be reduced by the losses associated with extraction of the UCN from the Helium to a position where they can be used for experiments. It seems reasonable to suppose that these losses can be kept below a factor of ten so that the "Superthermal" Helium source can offer significantly increased UCN densities if the engineering problems associated with its construction can be overcome.

References

1) Blin-Stoyle, Fundamental Interactions and the Nucleus, North Holland, 1973

2) Kropf and Paul - Z. Phys. 267,129 (1974)

3) Kügler, Paul, and Trinks - Phys.Letts.72B,422 (1978)

4) Brun etal Phys.Letts 75A,223 (1980)

5) Steyerl Z.Phys. B30,231 (1978)

6) Steyerl and Hermann, (1981) Private Communication

Fig.1 a) ω, Q space showing region accessible to UCN scattering
b) UCN inelastic scattering spectrometer [5]

a)

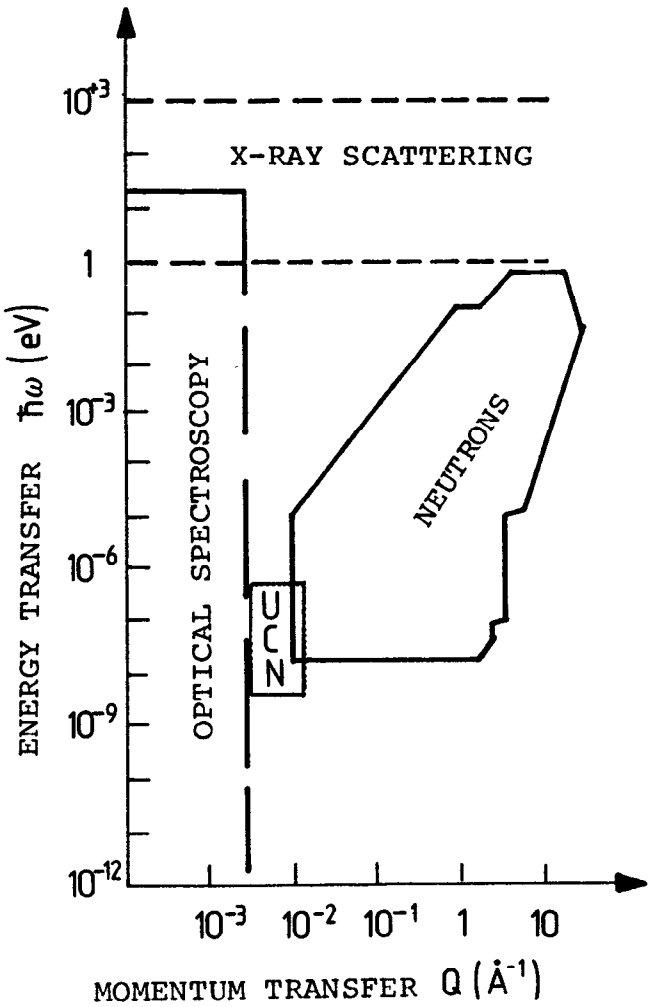

b)

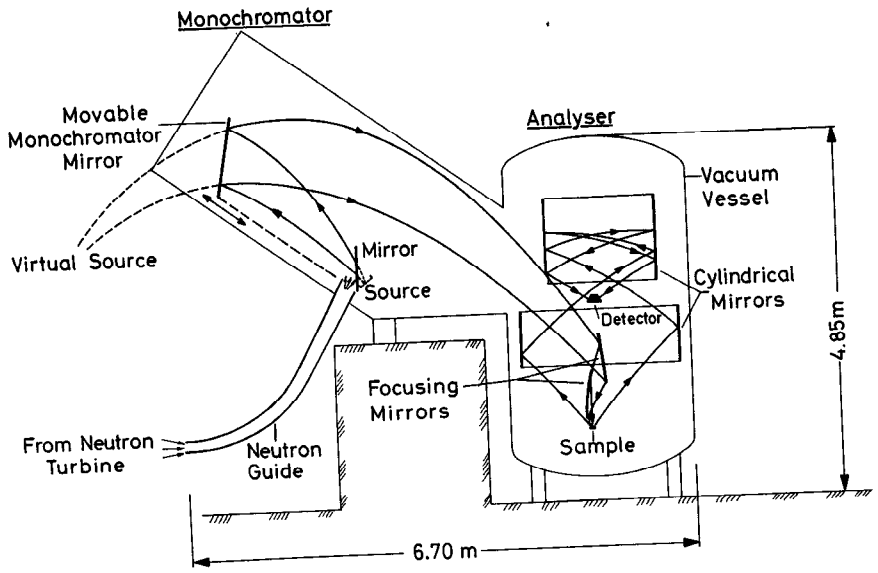

Fig. 2 Neutron microscope using UCN (6)

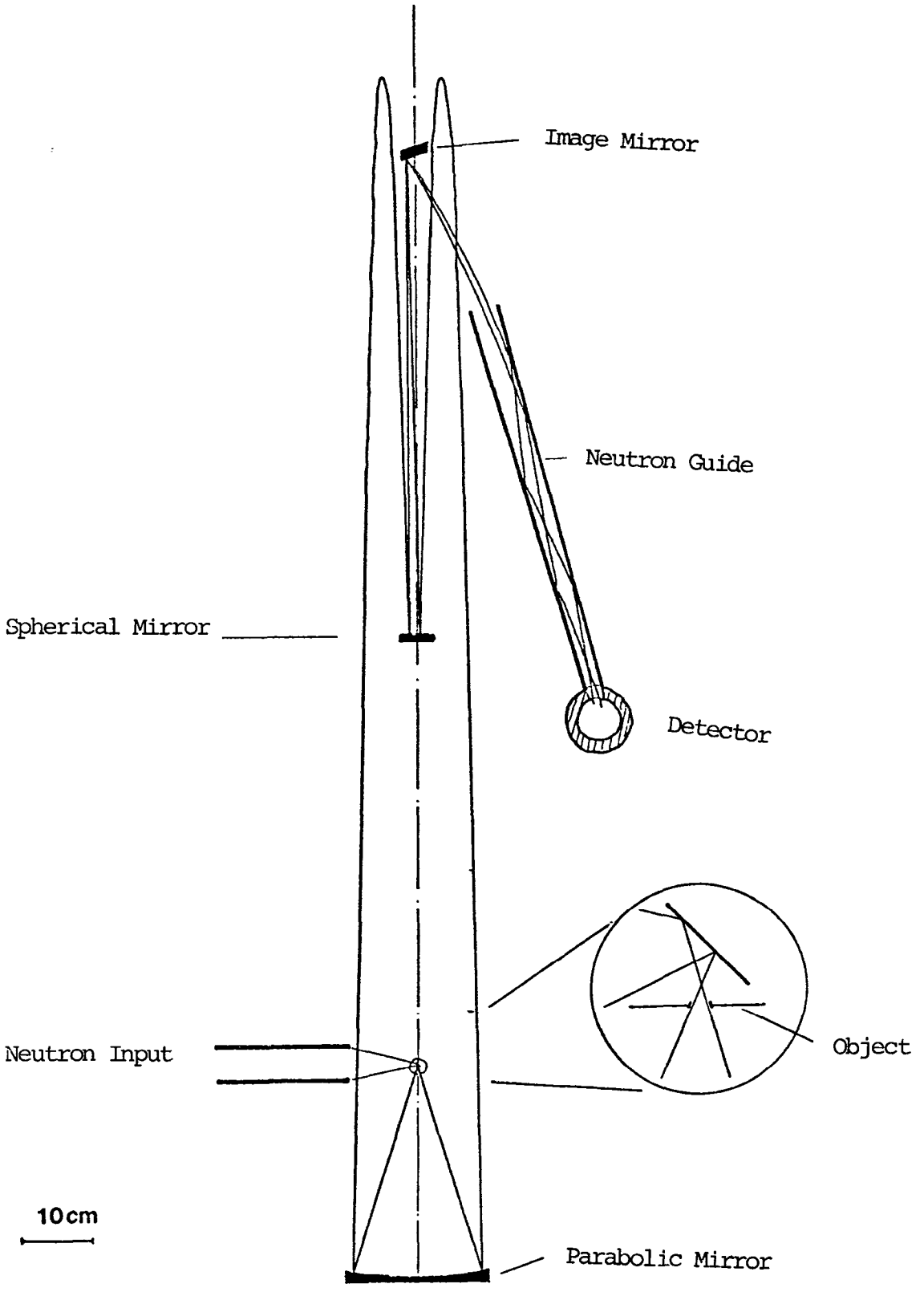

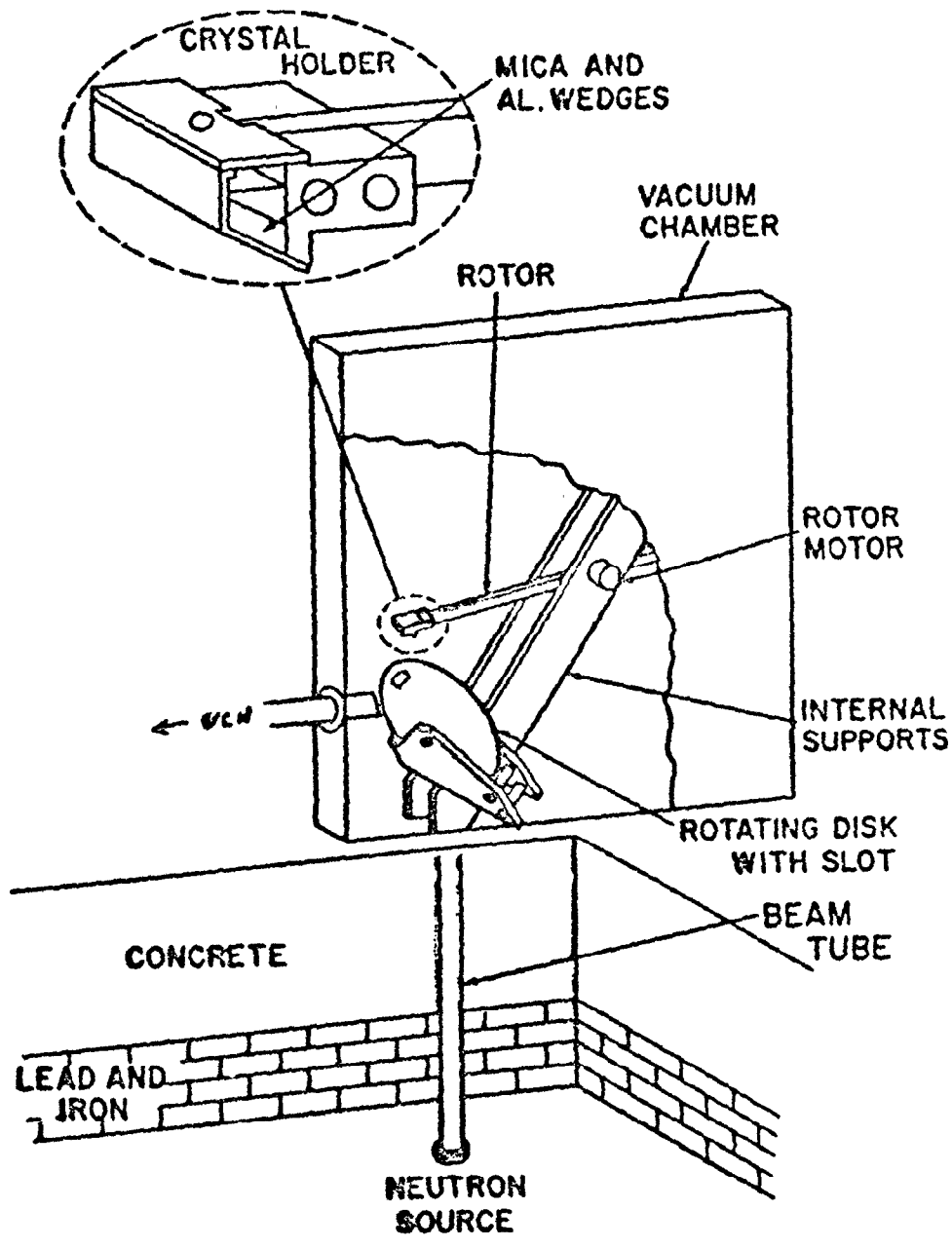

Fig. 3 Doppler shifter UCN source using rotating crystal as realized at Argonne (4)

Fig. 4 Superthermal UCN source proposed for SNQ

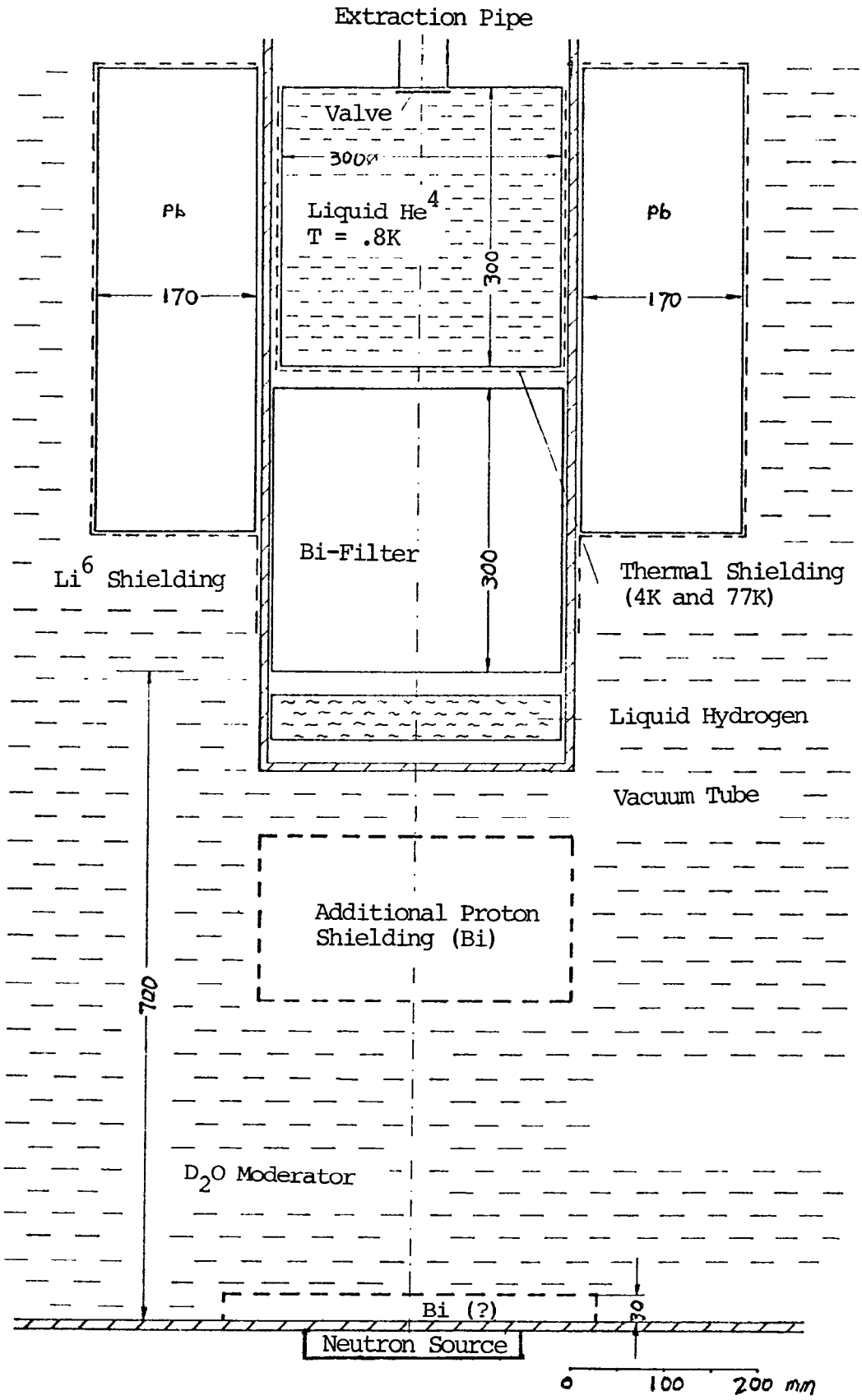

Jül-Conf-45

B3

I C A N S - V

MEETING OF THE INTERNATIONAL COLLABORATION ON

ADVANCED NEUTRON SOURCES

June 22-26, 1981

The Application of Intense Beams of Positive Pions and Muons in Solid-State Physics

Alfred Seeger

Max-Planck-Institut für Metallforschung, Institut für Physik, Stuttgart, and Universität Stuttgart, Institut für theoretische und angewandte Physik, Postfach 80 06 65, D - 7000 Stuttgart 80, Germany.

Abstract. It is pointed out that while the proton accelerator requirements for meson factories and for spallation sources are very similar, the target requirements (thin targets of light nuclei for π-meson (pion) production, thick targets of very heavy nuclei for spallation) are complimentary. It is therefore possible to use, with very little interference, the same proton beam for neutron production by the spallation process and pion production. From the pion decay muon beams may be obtained. The muon and pion beams of a high-intensity spallation installation may possess properties that make them extremely interesting for solid-state (and neutrino) physics. This is particularly true for beams with appropriate time structures, namely pulse lengths Δt_1 that are short compared with the lifetimes $\tau_{\pi^\pm}=2.6\cdot 10^{-8}$ s or $\tau_\mu=2.2\cdot 10^{-6}$ s, and periods Δt_2 that are long compared with these lifetimes.

The present paper outlines the basic physics of positively charged pions and muons and of their behaviour in condensed matter. This behaviour may be studied by two quite different techniques, viz. lattice steering (channelling) of the positive muons (μ^+) resulting from the π^+ decay or of the relativistic positrons (e^+) resulting from the μ^+ decay, and muon spin rotation (μSR). Both π^+/μ^+ and μ^+/e^+ lattice steering have recently been demonstrated experimentally. The lattice-steering techniques have the advantage that they are universally applicable. With more intense μ^+ and π^+ beams of suitable time structure the time-differential versions of the lattice-steering techniques are very promising for the study of crystal defects that can be decorated by π^+ and μ^+.

μSR constitutes a well established technique based on the non-conservation of parity in Weak Interactions. It may be applied to a wide variety of materials with suitable magnetic properties. These include nuclear magnetism, ferro- and antiferromagnetism, spin polarization of conduction electrons, orbital magnetism of electrons in superconductors with non-homogeneous magnetic structures, and muonium atoms. So far the great majority of the μSR experiments were done in the so-called individual time-differential mode. When stronger beams with suitable time structures become available, resonance and collective-mode μSR methods will give access to problems that could not be investigated with the classical μSR methods.

1. Introduction

Muons (originally called mesotrons or μ-mesons) and pions (π-mesons) were discovered in the study of the cosmic radiation. Incoming high-energy protons react in the upper atmosphere with light nuclei and produce positively charged (π^+), neutral (π^0), and negatively charged (π^-) pions together with heavier particle such as K mesons etc.. The neutral pions decay very rapidly mainly into two γ quanta (lifetime at rest $\tau_{\pi^0}=8.4\cdot 10^{-16}$ s). They have so far not found any application in condensed-matter physics and will not be discussed here further. The charged pions decay with a much longer rest lifetime $\tau_{\pi^\pm}=2.60\cdot 10^{-8}$ s through a so-called semi-leptonic decay

$$\pi^{\mp} \rightarrow \mu^{\mp} + \begin{cases}\bar{\nu}_\mu \\ \nu_\mu\end{cases} \qquad (1)$$

into muons (μ^-, μ^+) and muon (anti-) neutrinos (ν_μ, $\bar{\nu}_\mu$). The muons (lifetime at rest $\tau_\mu=2.197\cdot 10^{-6}$ s) are sufficiently long-lived for many of them to reach (with the help of the relativistic time dilatation) the ground level of the Earth. The cosmic-ray intensity at ground level is almost entirely due to high-energy muons (Fig. 1, upper left-hand corner).

In meson factories the processes occurring in the cosmic radiation are reproduced, though on different energy and intensity scales. Protons from accelerators with typical energies between about 0.5 and 1.1 GeV fall on thin targets of light nuclei (e.g., Be or graphite), where π^+, π^0, and π^- are generated. At the time of the foundation of CERN (~ 1950) the largest accelerators conceived were mainly planned for the production of π-mesons to be used in nuclear and elementary-particle physics. Since then the development of the large proton accelerators has branched into that of high-energy accelerators, aiming at higher and higher energies, usually at the cost of intensity, and that of "middle-energy" accelerators or meson factories, whose purpose is to provide intense beams of charged pions and muons. The three meson factories in operation are SIN (Schweizerisches Institut für Nuklearforschung = Swiss Institute of Nuclear Research, Villigen, Aargau, Switzerland), LAMPF (Los Alamos Meson Physics Facility, Los Alamos, New Mexico, USA), and TRIUMF (Tri-University Meson Facility, Vancouver, Canada). An intermediate place is occupied by the booster machines of high-energy proton accelerators, which may operate in energy and intensity ranges comparable to those of the meson factories or at least of meson factorettes such as those at CERN, Dubna and Gatchina (USSR). At one of them, viz. the Japanese high-energy physics laboratory KEK at Tsukuba, Ibaraki, Japan, the Booster Meson facility BOOM has recently gone into operation [1,2].

The proton accelerators of spallation neutron sources work in the same energy range as meson factories and should produce, in order for the spallation sources to be competitive with high-flux reactors, proton currents which are comparable with or larger than those of the existing meson factories. In spallation sources the neutrons are produced in thick targets of very heavy nuclei (e.g., Pb-Bi, U). This means that while the accelerator requirements for spallation sources and meson factories are essentially the same with regard to proton energy and intensity (time structure will be considered separately below), the target requirements are complementary. It is thus feasible to use simultaneously and with little interference the same proton beam for both the production of neutrons by the spallation process and the generation of intense beams of charged pions and, through the decay reaction (1), of muons (comp. Fig. 1). In view of the very widespread and rapidly growing applications of pions and muons this is an extremely interesting possibility. Without going into further detail we mention that according to (1) intense

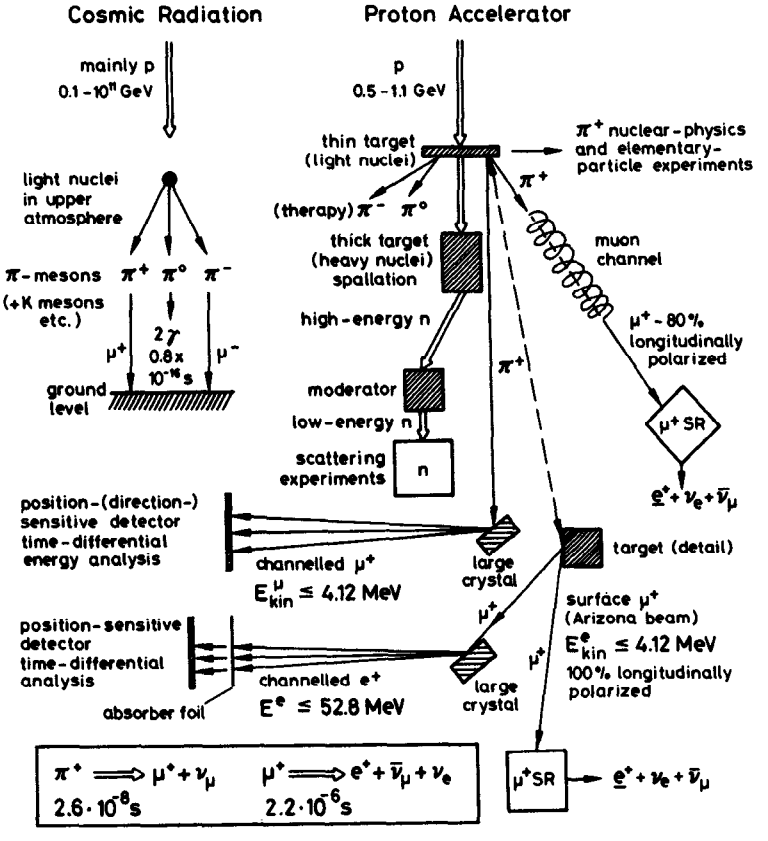

Fig. 1: Generation and Investigation of π^+ and μ^+

pion beams are also copious sources of muon neutrinos, so that the possibility just described holds also great promise for neutrino physics [3].

The present paper will concentrate on the use of positive pions and muons in solid state physics, emphasizing the new possibilities that will be opened up if very intense and/or pulsed beams become available. Fig. 1 gives a survey of the main configurations envisaged and discussed in detail below. We should nevertheless like to draw attention to just one application of negative pions, viz. their use in cancer therapy [4]. This development (in the view of the present author of enormous future potential) has recently been started at LAMPF and SIN and might be greatly accelerated by the availability of more intense beams.

2. Basic Physics

Since (1) is a two-body decay, in the pion rest system the muons obtained from (1) possess a fixed energy (corresponding to kinetic energy E^{μ}_{kin}=4.12 MeV, linear momentum p^{μ} =29.79 MeV/c, and velocity v^{μ}=0.27 c). Pions are spinless particles. Since by their nature neutrinos are 100 % left-handed polarized, conservation of angular momentum demands that in the π^+ rest system the μ^+ generated by (1) are 100 % left-handed polarized, too (Fig. 2). (This is opposite to the "natural" polarization of anti-leptons such as μ^+ and e^+, and hence the reason why only $1.2 \cdot 10^{-4}$ of the π^+ decay into positrons e^+ rather than into positive muons.)

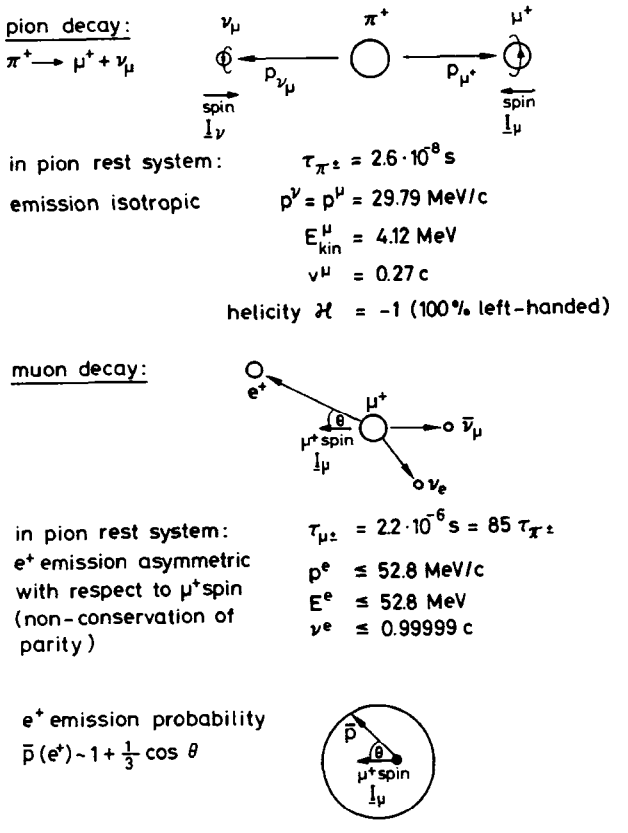

Fig. 2: Decay of positive muons and pions

Positive muons decay according to the leptonic reaction (β-decay)

$$\mu^+ \rightarrow e^+ + \bar{\nu}_\mu + \nu_e \quad , \tag{2}$$

where ν_e denotes the electron neutrino. The decay positrons possess an energy spectrum with maximum values (in the μ^+ rest system) $E^e_{max} = 52.8$ MeV, $p^e_{max} = 52.8$ MeV/c and $v^e_{max} = 0.99999$ c. Because of parity non-conservation the emission probability of the positrons is asymmetric with respect to the direction of the muon spin $\underline{I}_\mu$. Averaged over all positron energies its angular dependence is given by (comp. Fig. 2)

$$\bar{p}(e^+) \propto 1 + \frac{1}{3} \cos\theta \quad . \tag{3}$$

This permits us to study, by observing the directional distribution of the decay positrons, the muon polarization at the time of the decay and to obtain, on account of the coupling between spin and magnetic moment of the muons, information on the "magnetic history" of the muons. This is the basic idea of the μSR (Muon Spin Rotation) technqiue, which was already employed in the work [5] establishing the parity non-conservation in (2) and which has since found wide application in nuclear, atomic, and solid-state physics [6-8] as well as in chemistry [9] and biophysics [10].

Like neutrons, μ^+ and π^+ may be used as probes for the study of condensed matter. In contrast to neutrons, however, μ^+ and π^+ interact with their environment predominantly through the electrostatic interaction and are in this respect analoguous to positrons [11]. This has two important

thermalization:	10^{-12}s-10^{-14}s $\ll \tau_{e^+}, \tau_{\pi^\pm}, \tau_\mu$		
principal interaction:	electrostatic ⟶ interstitial sites trapping at defects Mu "atom" formation		
diffusion:	strongly mass-dependent (isotope effect) may lead to trapping at defects		
information transmitted in decay or annihilation:	e^+	μ^+	π^+
	e^- charge and momentum density (e^+ lifetime, angular correlation, Doppler broadening)	"magnetic history" (μSR)	
		location in crystal (lattice steering: blocking or flux enhancement)	
interpretation:	involved	direct	

Fig. 3: Positively charged probes in condensed matter

consequences. First, in condensed matter positive pions and muons as well as positrons are slowed down to thermal velocities ("thermalized") in times that are short compared with their lifetimes. With respect to their kinetic and potential energy they are hence most of the time in thermal equilibrium with their environment. This means that they constitute indeed, like neutrons but for different reasons, well-defined probes. Second, the Coulomb repulsion by the nuclei keeps the positively charged probes as far away for the nuclei as possible[1]. In perfect crystals this leads to the localization of the probes in lattice interstices. In imperfect crystals, in addition bound states may be formed at sites where nuclei are missing (e.g., vacancies) or where extra space is available (e.g., on the dilation side of edge dislocations).

In thermal equilibrium π^+ and μ^+ diffuse by hopping from interstice to interstice. If their diffusivity D^+ is high enough, they may be trapped at imperfections providing bound states for them. Because of the ratio of 85 in their mean lifetimes the probability that this occurs is much higher for μ^+ than for π^+ under otherwise equal conditions. This may be used to determine the mass dependence (isotope effect) of the diffusivity of point particles of unit positive charge (mass ratios proton: pion:muon $m_p : m_{\pi^\pm} : m_\mu = 1 : 1/7 : 1/9$), which is of great interest for the theory of quantum diffusion in crystals [12-14] and for a deeper understanding of hydrogen diffusion.

As indicated in Fig. 3 the information on location and trapping of the probes is transmitted by the decay or annihilation products, in the case of

[1] In the case of positive pions this suppresses the Strong Interaction of these hadrons with the nuclei. During the implantation the suppression is achieved by keeping the pion momenta at or below about 150 MeV/c and thus below the pion-nucleon resonances.

π^+ by the μ^+, in the case of μ^+ by the e^+, and in the case of e^+ by the annihilation γ's (usually in the 2γ-annihilation mode). With regard to the ease of interpretation of this information big differences between the three probes exist. Since in the case of positrons the behaviour of the probes in condensed matter and the annihilation process are determind by the same interaction (viz. the electromagnetic interaction) the quantitative interpretation of the information transmitted by the annihilation γ's requires rather involved calculations. These are made particularly difficult by the fact that electrons and positrons possess the same mass, so that the recoil of the probes has to be allowed for and the usual approximations in the electron theory of "impurities" in crystals become inapplicable. The situation is much simpler for muons and pions, since the decay reactions (1) or (2) are controlled by the Weak Interaction and therefore (for all practical purposes) independent of the electrostatic interaction which governs the behaviour of the probes in condensed matter. The latter is many orders of magnitude stronger than the interaction between the magnetic moments of the muons and those of the constituents of matter - nuclei and electrons - so that the tracing of the "magnetic history" of the muons by the μSR technique (see Sect. 3) does not interfere with their behaviour as charged probes.

The situation is even more striking for the other technqiue that can be used to obtain formation on μ^+ or π^+ in crystals, i.e. the lattice steering of the charged decay products e^+ or μ^+ [15] (see Sect. 4). Here the "message" carried by the decay particles is accumulated only after the decay and disappearance of the probes, so that any interference with their behaviour is impossible.

The combination of the properties just described with the fact that the diffusivities of μ^+ and π^+ can be varied within fairly wide limits by varying the temperature makes these particles ideal probes, in particular for "decorating" defects in crystalline solids [11]. It is true that on account of their larger masses the diffusivities of μ^+ and π^+ are substantially smaller than those of positrons, but this is compensated by their much longer lifetimes. (Typical positron lifetimes in metals are about $2\cdot 10^{-10}$ s.)

3. The μ^+SR Techniques

The various μSR techniques all make use of three basic facts, namely (i) that muons possess a magnetic moment (of a magnitude 4.65 times that of the neutron, corresponding to a gyromagnetic ratio $\gamma_\mu = 8.516\cdot 10^8\ T^{-1}s^{-1}$), (ii) that they are generated according to (1) with longitudinal polarization, and (iii) that the polarization at the time of decay may be detected by observing the directional distribution of the positrons from the decay reaction (2). μSR is similar to NMR (Nuclear Magnetic Resonance) or EPR (Electron Paramagnetic Resonance) but much simpler in several respects. Because of (ii) high magnetic fields in order to produce a detectable polarization are not needed. Because of (iii) changes in the polarization may be detected without having to employ high-frequency radiation. Moreover, the theoretical interpretation is often much more straightforward than in NMR, since the interaction between muon spins is completely negligible on account of the extremely small number of muons in the samples at any one time.

In the discussion of the various μ^+SR techniques it is convenient to distinguish between transverse measurements, in which the average field $\underline{B}_\mu$ acting on the magnetic moments of the muons is perpendicular to the muon polarization $\underline{P}$, and longitudinal measurements, in which the muon polarization precesses in the plane perpendicular to $\underline{B}_\mu$ with the angular velocity

$$\omega_\mu = \gamma_\mu B_\mu \quad . \qquad (4)$$

The transverse polarization P_2, that is the polarization component perpendicular to $\underline{B}_\mu$, stays constant if all muon moments experience the same magnetic field. If this is not the case, the muon spins may precess at somewhat different angular velocities, and the transverse polarization P_2 "relaxes" gradually towards its equilibrium value zero. This may be described by the transverse relaxation function

$$R_2(t) \equiv P_2(t)/P_2(0) \quad , \tag{5}$$

where $P_2(t)$ is the transverse polarization of an ensemble of thermalized muons at time t after thermalisation.

A longitudinal field $\underline{B}_\mu$ gives rise to Zeeman levels separated by

$$\Delta E = \hbar\omega_\mu \quad , \tag{6}$$

where ω_μ is given by (4). Transitions between the Zeeman levels are introduced by magnetic fields with circular frequency ω_μ and non-vanishing component perpendicular to the muon polarization. Such time-dependent fields may either be external fields, or may result from different magnetic fields at different muon sites, so that diffusing muons experience magnetic fields that vary with time.

The relaxation of the initial longitudinal polarization $P_1(0)$ of a muon ensemble to its equilibrium value P_1^{eq} may be described by means of a longitudinal relaxation function $R_1(t)$:

$$R_1(t) = \frac{P_1(t) - P_1^{eq}}{P_1(0) - P_1^{eq}} \quad . \tag{7}$$

If we consider transitions between the Zeeman levels of the μ^+ only, we are dealing with a two-level system. Hence the longitudinal relaxation function has, to a very good approximation, the form

$$R_1(t) = \exp(-\Gamma_1 t) \quad , \tag{8}$$

so that the information obtainable from longitudinal relaxation measurements is contained in the field and temperature dependence of the longitudinal relaxation rate Γ_1. By contrast, the functional form of the transverse relaxation function $R_2(t)$ depends on the type of magnetic interaction involved and on the motion of the muons. Important special cases are the exponential function

$$R_2(t) = \exp(-\Gamma_2 t) \quad , \tag{9}$$

which is usually encountered when the muons diffuse very rapidly, and the Gaussian

$$R_2(t) = \exp(-\Gamma_o t) \quad , \tag{10}$$

which is characteristic for immobile muons and a Gaussian distribution of the magnetic fields at the muon sites [16,17].

How are precession or Zeeman frequencies ω_μ and relaxation functions $R_i(t)$ measured? As indicated in Fig. 4, the available techniques may be grouped into the individual mode, the collective mode, and the high-frequency or resonance technique, in which an external high-frequency field is employed.

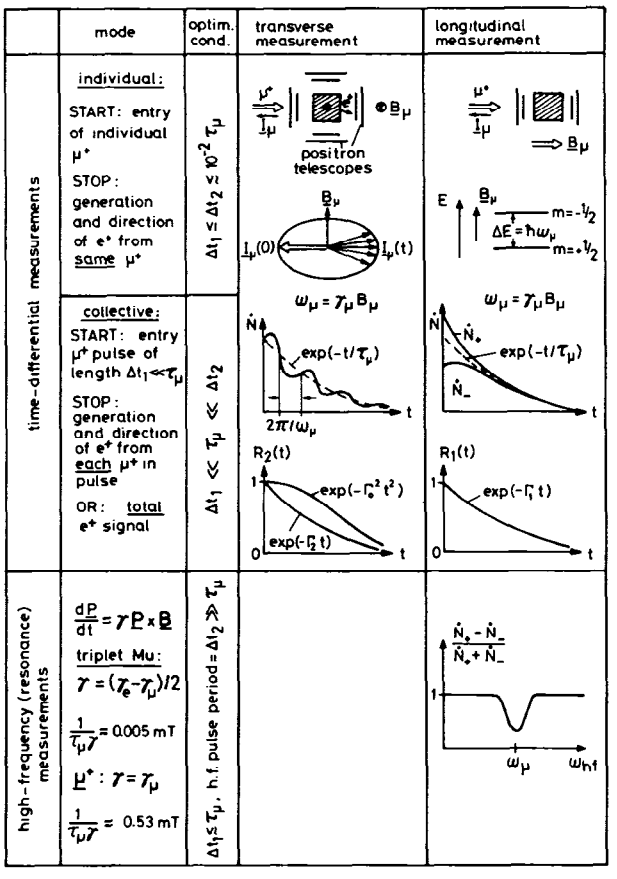

Fig.4: μ^+SR techniques

In the individual mode (which is the one used by most groups in the field and responsible for most of the μSR results so far obtained) the entry and the decay times of individual muons as well as the directions in which the decay positrons emerge are recorded. From the observation of many such events [typically $(1 - 30)\cdot 10^6$] the decay rate $\dot{N}_j$ in each of the so-called positron telescopes (scintillation counters) is recorded as a function of the time difference between entry and exit (Fig. 4). From this information the relaxation functions (and in the transverse case also the precession frequency ω_μ) may be obtained. A prerequisit of the method is that with high probability there is only one muon in the sample at any one time (unless one uses counters which enable him to differentiate between different parts of the sample from which the positrons are coming). This limits sharply the rate at which useful events can be accumulated and, because of stability problems, also the smallest relaxation rate that can be detected. At the present time this limit appears to be $\Gamma_2 \approx 1/10\tau_\mu \approx 0.05\cdot 10^{-6}\,s^{-1}$.

The collective mode requires pulsed muon beams. If the pulse length Δt_1 is small compared with the muon lifetime τ_μ and if the repetition period Δt_2 of the pulses is much longer than τ_μ, it is possible to use the collective entry of the muons of a pulse as zero-time signal. The decay times and the directions of positron emission may either be determined as in the individual mode with the help of positron telescopes and fast electronics by the time-differential technique, or "macroscopically" by measuring in a Cerenkov counter the superposition of all delayed events following a muon burst [2]. In the collective mode there is no inherent limit to the rate of data accumulation. It is therefore feasible to detect substantially smaller relaxation rates and precession frequencies than in the individual mode simply because

there may be more muons that live long enough. The use of pulsed beams is particularly advantageous in longitudinal measurements, where the elimination of the background constitutes a serious problem when continous μ^+ beams are employed. The main disadvantage of the collective measurements is that they are not suited for the study of fast relaxation processes or rapid muon spin precession.[2)]

Of course, the advantages of the collective mode can only be fully realized if the muon beams not only possess the right time structure and high fluxes within the muon pulses but also a sufficiently large average flux. In this regard it should be notes that because of the exponential time law of the muon β-decay the minimum relaxation rates or precession frequencies that may be still be detected increases only logarithmically with the muon flux.

Collective-mode measurements have recently been performed at BOOM with $\Delta t_1 = 5\cdot 10^{-8}$s, $\Delta t_2 = 5\cdot 10^{-2}$s, and $3.5\cdot 10^4$ μ^+ per pulse [2]. It has indeed been possible to obtain a preliminary relaxation rate $\Gamma_2 \gtrsim 10^{-8}\,s^{-1}$ for indium at 393 K, a quantity that due to its smallness could not be reliably determined in earlier individual-mode measurements.

The high-frequency or resonance μSR technique comes closest to the familiar NMR or EPR techniques [16,17]. An external hf field with a non-vanishing magnetic component perpendicular to the muon polarization $\underline{P}$ induces transitions between the Zeeman levels if its circular frequency ω_{hf} satisfies the condition $\omega_{hf} \approx \omega_\mu$. The muon-spin reversals associated with these transitions reduce the asymmetry $(\dot{N}_+ - \dot{N}_-)/(\dot{N}_+ + \dot{N}_-)$ between the counting rates $\dot{N}_+$ in the positron telescopes in the direction of $\underline{P}$ and $\dot{N}_-$ in those in the opposite direction. By sweeping the frequency ω_{hf} or by varying the applied magnetic field $\underline{B}_{appl}$ and hence the energy difference ΔE we may determine the resonance conditions and thus obtain the spectrum of Zeeman frequencies ω_μ^j.

Resonance measurements have been carried out on the triplet state of muonium atoms Mu = (μ^+e^-) [18]. In this state electron and muon spins are parallel, so that the system behaves as a spin-one particle with gyromagnetic ratio $(\gamma_e - \gamma_\mu)/2$, where $\gamma_e = 1760.8\cdot 10^8\ s^{-1}T^{-1}$ denotes the electron gyromagnetic ratio. The physical situation may be described qualitatively by saying that the torque exerted on the spin momentum is not determined by the magnetic moment of the muon but by the much larger magnetic moment of the electron. It is therefore not particularly difficult to achieve the hf field strength necessary to reverse the muon spins within times of the order of magnitude of the muon lifetime.

From the practical point of view the situation is quite different if we attempt to study "naked" μ^+ or negative muonium ions $Mu^- = (\mu^+e^-e^-)$ by means of the resonance technique. Then the hf field has to act directly on the magnetic moments of the muons. The hf field strengths required for the spin reversal are now larger by a factor 10^2 than in the triplet Mu case. Under otherwise equal conditions (same frequency and sample volume) this means that the hf power would have to be increased by a factor of 10^4. The problem of

2) The shortest relaxation times or spin precession periods that can be measured in the collective mode are determined by the time interval Δt_o over which the muons coming from the same pulse enter the sample. Δt_o may be made shorter than Δt_1 by letting the muons pass through time-dependent magnetic fields arranged in such a way that the paths of muons generated at the beginning of the pulse are longer than those generated towards the end. The compression of a pulse of muons with v^μ=0.27c by $1\cdot 10^{-7}$s requires a path difference of 8 m.

supplying and cooling away the necessary power is very much reduced if the muon beam is pulsed with a period $\Delta t_2 >> \tau_\mu$, since then the high-frequency field needs to be applied only as long as the sample still contains a detectable number of muons. On the other hand, there is no limitation to the number of muons that may be present in the sample at any one time. This means that in the resonance technique best use is made of the muons and of the hf energy if the muons are produced in intense pulses of length $\Delta t_1 \lesssim \tau_\mu$ and if both the muon and the hf pulses possess long periods $\Delta t_2 >> \tau_\mu$. Similar considerations hold for the effects of laser light on μSR, which are of interest for the study of muonium atoms in non-metallic materials.

A μSR resonance facility satisfying the above requirements has recently been installed at BOOM [2]. A radio-frequency field with a peak power of about 20 kW is applied during 10^{-4} s after each muon beam burst. As a first application of the facility the μ^+ resonance in H_2O was detected by irradiating at a fixed frequency of $20 \cdot 10^6$ Hz and sweeping the magnetic fields. It should be emphasized, however, that in the resonance technique the use of pulsed muon beams is not essential but merely a matter of economy. A letter of intent for μ^+ spin resonance experiments at SIN (where $\Delta t_1 << \Delta t_2 << \tau_\mu$) has been submitted by a Stuttgart–Heidelberg collaboration in November 1979.

All μSR techniques require magnetic interactions between the magnetic moments of the implanted muons and the host material. As indicated in Table I, the possible interactions may be divided into five major groups. Table I lists examples of the materials that might be investigated through the various interactions, of the physical quantities that may be observed, and of the information that may be gained from the measurements. The multitude of existing possibilities forbids a systematic discussion in this paper. We have to confine ourselves to a few remarks on each of the five interactions.

I) The dipolar interaction between the nuclear magnetic moments and the muon magnetic moments is rather weak. Longitudinal or transverse relaxation rates that can be investigated with good precision require a high abundance of nuclei with large magnetic moments. Fortunately a large number of elements satisfy these requirements. Quite detailed information on the behaviour of muons may be obtained through the dependence of the transverse rate on the crystallographic direction of the applied field $\underline{B}_{appl}$. A particularly interesting possibilitiy is the use as analytical tool for detecting and characterizing intrinsic or extrinsic (impurity) defects capable of trapping positive muons [19,20].

II) The interaction of magnetic moments of d- and f- electrons with those of muons is the strongest of the interactions considered in Table I. Its consequences for μSR measurements are strongly dependent not only on the magnetic structure of the material (ferromagnetic, antiferromagnetic, ferrimagnetic, strongly paramagnetic ions in diamagnetic or weakly paramagnetic hosts) but also on its crystallographic structure and the symmetry of the sites occupied by the μ^+ [8,21,22]. In many cases the strength of the interaction allows us to carry out measurements on internal fields, muon diffusion, and muon trapping over much wider temperatures ranges than is feasible with other techniques [21,23].

III) From the theoretical point of view the contact interaction between conduction electrons and muon spins is just a special case of the interaction between electron and muon magnetic moments. The practical manifestations, however, are quite different from those of II). Because of the Pauli principle

Magnetic Interaction	Examples	Observations	Information to be Gained
nuclear magnetic moments	Li, ..,Cs,Be,Al,In,Cu Co,As,Bi,V,Nb,Ta	longitudinal or transverse relaxation	μ^+ location, lattice distorsion around μ^+, μ^+ diffusion, study of defects and trace impurities
magnetic moments of d- or f- electrons	Fe,Ni,Co,Gd,Cr,Mn, Dy,Fe_3O_4	$B_\mu = \omega_\mu/\gamma_\mu$, longitudinal or transverse relaxation	internal magnetic fields, μ^+ diffusion over wide T range, trapping at defects
contact interaction with conduction electrons	normal metals, ferromagnets	Knight-shift $B_\mu = \omega_\mu/\gamma_\mu$	local density of states, conduction-electron spin polarization, trapping at defects
orbital magnetism of conduction electrons	Type I + II superconductors	$B_\mu = \omega_\mu/\gamma_\mu$ transverse relaxation	fast low-temperature diffusion of μ^+, B_μ distribution, flux-line flow
Mu = (μ^+e^-): hyperfine interaction	semiconductors insulators gases	ω_μ^j, longitudinal or transverse relaxation	Mu chemistry, reaction rates, simulation of H behaviour, isotope effects

Table I: Magnetic Interaction in μ^+SR Applications

the spin polarizability and hence the Knight shift in normal metals is very small. By means of a special stroboscopic μSR technqiue [24] in many "normal" metals the muon Knight shift may be determined more accurately than is possible for the hydrogen Knight shift. In this way interesting information on the electronic structure of point-charge impurities in normal metals has been obtained [25]. In ferromagnetic metals there exists a spontaneous spin polarization of the conduction electrons which gives rise to the so-called Fermi field acting on the muon magnetic moments. Whereas neutron diffraction can give information on the spin polarization of conduction electrons in ideal ferromagnetic metals [26], the information obtainable from μSR measurements pertains to the presence of positive point charges and is thus complementary to the neutron-diffraction information.

IV) The interaction between the muon magnetic moments and the orbital magnetism of conduction electrons in superconductors may be used to study the magnetic field distribution in magnetically inhomogeneous superconducting states, i.e. in the intermediate or in the mixed state [27]. Particularly interesting possibilities exist in the mixed state of Type-II superconductors, where the very fast low-temperature diffusion of muons in pure Type-II superconductors may be studied [28,29] and where information on the flow of flux lines may be obtained.

V) In materials in which muonium atoms Mu = (μ^+e^-) are formed the hyperfine interaction between the muon spin and that of the bound electron is usually the most important magnetic interaction of the muons. This interaction may be employed in a wide variety of ways in order to obtain information on the physics and chemistry of the host material. The study of the magnetic properties of Mu atoms has given rise to a field of its own, muonium chemistry [9].

4. Lattice Steering ("Channelling")

The basic ideas of the lattice-steering technique, which is applicable to both reactions (1) and (2), are indicated in Fig. 5. For simplicity we shall first describe the technique as based on reaction (1), briefly called π^+/μ^+ lattice steering or channelling, and subsequently discuss the differences between π^+/μ^+ and μ^+/e^+ lattice steering.

Suppose that the implanted positive pions are located on interstitial sites in an otherwise perfect crystal. Then the monoenergetic positive muons emitted into one of the open "channels" going out from the π^+ sites along the low-index crystallographic directions undergo sequences of correlated repulsive small-angle collisions with the nuclei bordering the channel. They keep the direction of the μ^+ propagation, on the average, parallel to the channel direction (Fig. 5, top). This "lattice steering" effect leads to a flux-enhancement in the channel directions compared to random directions, in which the μ^+ are deflected by large-angle scattering.

The crystallographic directions in which the flux enhancement may be observed in position-sensitive detectors placed sufficiently far from the sample depend on the interstitial sites on which the emitting particles are located, so that from observations in different crystallographic directions these sites may be deduced. Moreover, from the precise shape of the enhancement profile one may draw conclusions on the spatial distribution of the emission probability, i.e. on the quantum-mechanical and thermal vibration amplitudes of the π^+ in their interstices.

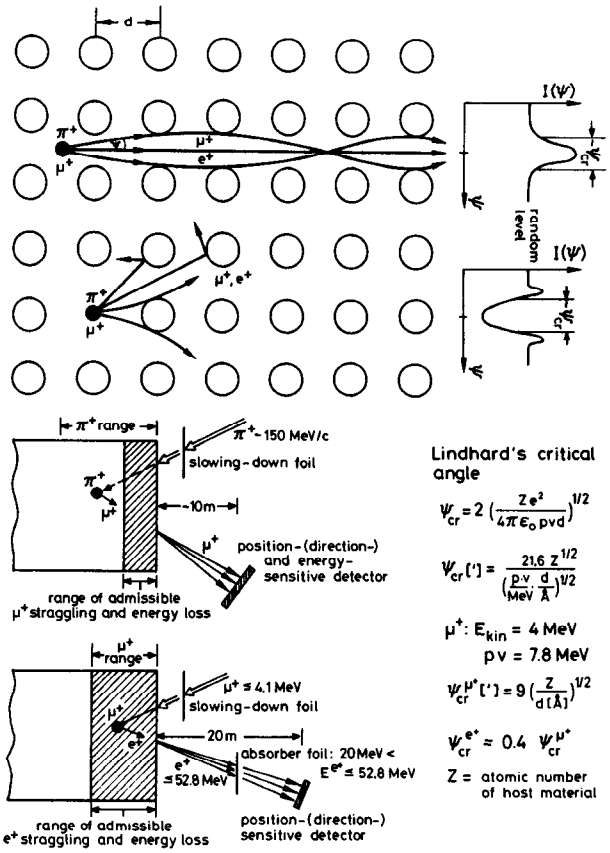

Fig.5: Lattice steering of μ^+ and e^+

In those directions in which the emitted particles encounter an entire row of atoms, the phenomenon of blocking takes place. As indicated in Fig. 5, this results in a diminuition of the muon flux relative to that observed in a random direction. If the μ^+ are located on substitutional sites because they have been trapped in vacancies, the blocking phenomenon occurs in all major crystallographic direction. Thus vacancies (and, provided observations in a sufficient number of crystallographic directions are available, also divacancies, etc.) may be monitored fairly directly by this "decoration" technique.

The angular range around a crystallographic direction in which the information on the location of the probes is contained may be estimated from Lindhard's critical angle [30,31]

$$\psi_{cr} = 2(Z\, e^2/4\pi\, \varepsilon_o\, p\, v\, d)^{1/2} \quad , \qquad (11)$$

where Z denotes the atomic number of the host material, e the elementary electric charge, $\varepsilon_o = 8.85 \cdot 10^{-12}$ A s $V^{-1} m^{-1}$, p and v linear momentum and velocity of the particles undergoing channelling (assumed to have unit charge), and d the interatomic distance in the channelling direction. For positive muons emitted by pions at rest (11) becomes

$$\psi_{cr} = 9\, \left(\frac{Z}{d/\mathring{A}}\right)^{1/2} \quad , \qquad (12)$$

where ψ_{cr} is measured in angular minutes. This means that for medium heavy elements the solid angle within which the lattice-steering phenomenon takes place is comparable with that under which the full Moon is seen from the Earth. The information on the pion location is thus carried by a very small fraction of the muons that are emitted, so that lattice-steering experiments, informative and easy to interprete as they are, require large pion fluxes.

Closer inspection shows that the fraction of "useful" μ^+ is even smaller than might appear from the preceding estimate. The small-angle scattering of channelled particles by conduction and valence electrons leads to an increase of $\langle\Delta\psi^2\rangle$ proportional to the distance travelled by the channelled particles ($\Delta\psi$ = deviation of the propagation direction from the channel axis). It is thus necessary to limit the depth from which the particles are emitted. Since in the case of π^+/μ^+ lattice steering the channelled particles are originally

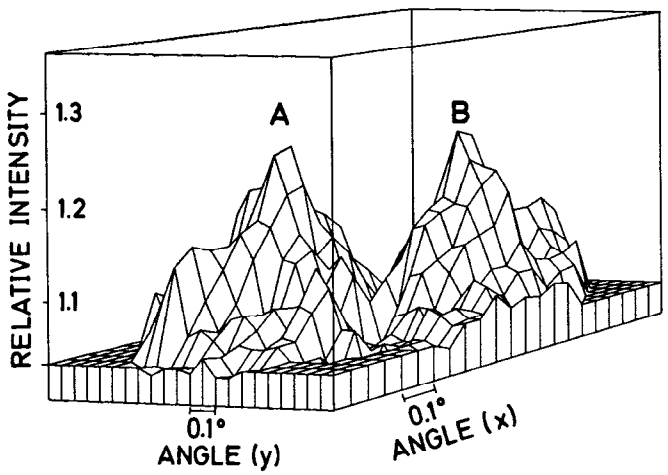

Fig.6: Flux enhancement of positive muons emitted in <100> directions from thermalized π^+ in a tantalum single crystal at 200 K (x,y = coordinates on position-sensitive detector).

monoenergetic and since their energy loss, too, is proportional to the distance travelled, this can be done by counting only particles whose kinetic energies lie above a certain threshold.

The first π^+/μ^+ lattice-steering experiments have recently been performed on tantalum single crystals by Maier et al. [15,32,33]. Fig. 5 indicates schematically the experimental arrangement employed. Because of the short pion lifetime linear momentum and velocity of the π^+ were chosen close to the highest values admissable from the point of view of nuclear reaction cross-sections (cf.footnote1).By means of a degrader foil the pions were slowed down in front of the sample so that they were deposited close to the specimen surface. Fig. 6 shows two flux-enhancement patterns A and B obtained in these experiments [33]. Two patterns rather than just one were observed because the sample was rotated with respect to the beam in order to eliminate the characteristics of the position-sensitive detector. The separation of the two peaks agrees with the angle of rotation. The width of the flux-enhancement peak corresponds to the theoretical expectations.

Experiments on μ^+/e^+ lattice steering, in which the muons serve as the probe and the e^+ undergo channelling, present several additional problems: (i) Generally speaking, the available μ^+ fluxes are smaller than the π^+ fluxes. (ii) The quantity $p \cdot v$, which according to (11) determines the critical angle for channelling, is smaller for e^+ from (2) than for μ^+ from (1)[3] Hence in μ^+/e^+ lattice steering the critical angles are smaller than those of π^+/μ^+ channelling and the demands on the perfection of the crystals used as samples accordingly higher. In addition, the fraction of the particles carrying the lattice-steering information becomes even smaller than in π^+/μ^+ experiments. (iii) Since the e^+ emitted by μ^+ are not monoenergetic, the depth limitation necessary to keep the straggling effect below a critical level cannot be achieved by energy selection but must be done by limiting the depth at which the μ^+ are implanted.

An experimental arrangement for a μ^+/e^+ lattice-steering experiment is shown in Fig. 5 (bottom). It makes use of the fact that from π^+ stopped near the surface of the proton target a well-collimated beam of so-called surface muons with kinetic energies $E^{\mu}_{kin} \leq 4.12$ MeV ("Arizona beam") may be obtained. The experimental difficulties described above have been overcome in recent experiments of Maier et al. on Au [34], in which μ^+/e^+ lattice steering was demonstrated for the first time. In these experiments the surface muons were

[3] At the upper end of the e^+ spectrum we have $p^e v^e = 53$ MeV, which is to be compared with $p^{\mu} v^{\mu} = 8.0$ MeV.

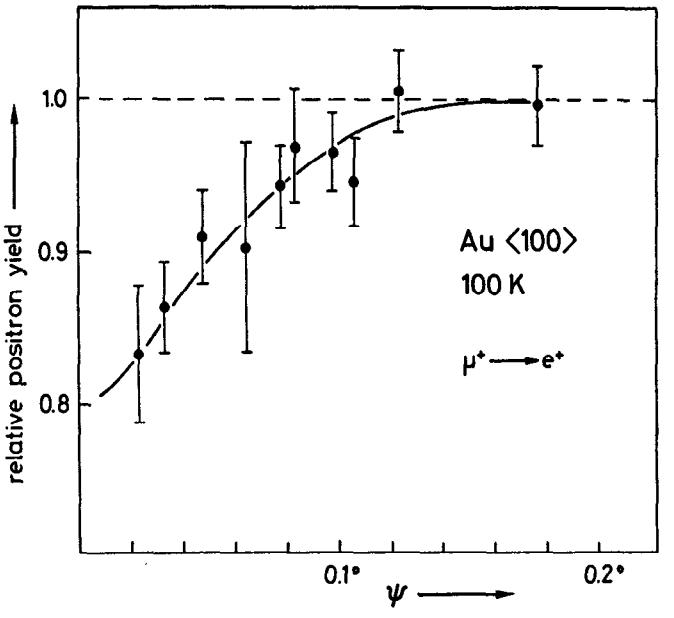

Fig.7: Blocking of positrons emitted in a <100>direction from thermalized μ^+ in gold single crystal at 100 K (averaged over angle around <100>).

slowed down by means of a polyethylene foil to such an extent that virtually all muons were stopped in a surface layer of 20 μm depth. The low-energy part of the positron spectrum was cut off by means of an Al foil, so that only positrons with energies exceeding 20 MeV were recorded in the position-sensitive detector. Fig. 7 shows a blocking pattern obtained at 100 K on an Au crystal along one of the cube directions. It is in agreement with the view that μ^+ in face-centred cubic metals preferentially occupy octahedral interstices.

We emphasize that the lattice-steering techniques are not confined to any particular type of chemical bond nor - in contrast to μSR - to specific magnetic properties. It is this generality with regard to the materials to be investigated that makes the lattice-steering method very promising for the future. It does, however, require single crystals of good quality and sufficient size. The know-how of growing such crystals is available for a large number of materials. We expect that in the years to come further progress in crystal growing and in the application of the lattice-steering technique will go hand in hand.

5. Beams and Time Structure.

Let us return to Fig. 1, where the main uses of a future combined spallation- meson-production facility are indicated. The charged pions produced in a thin target of light nuclei may be utilized either directly for biomedical applications and for elementary-particle, nuclear, atomic, and solid-state physics, or for the production of muon beams.

Muon beams may be obtained either from pions decaying at rest or from pions decaying in flight. In the first case the muons are emitted from pions that have been stopped near the surface of the proton target. The μ^+ beams produced in this way are known as "surface-muon beams" or (for historical reasons [35]) as "Arizona beams". Such beams possess the attractive feature that they are virtually 100 % longitudinally polarized. The kinetic energy of the muons, E^{μ}_{kin}, varies between zero and 4.12 MeV. This means that the penetration of the muons is small and that low-density targets (gases and vapors!) as well as very thin samples may be investigated. Furthermore, because of the low E^{μ}_{kin} values Arizona beams are very useful if one wishes to implant the muons only near the sample surface. Examples for this are the μ^+/e^+ lattice-steering experiments discussed in Sect. 4 or the investigation of near-surface radiation damage produced by ion or electron bombardment.

A definite drawback of the surface muons is that because of their small linear momenta (p^{μ} < 30 MeV/c) they are easily deflected by transverse magnetic fields. This makes it difficult to carry out transverse μSR measurements in

applied fields exceeding, say, 0.1 T. This weakness can be remedied by means of a spin rotator, a combination of magnetic and strong electric fields that rotates the muon spin by 90° with respect to the muon momentum and thus gives us transversely polarized beams. The geometry of transverse μSR experiments can be arranged in such a way that beams with transverse polarization are not deflected by the applied magnetic field. A low momentum beam with transverse polarization would also be of great help for μ^+/e^+ lattice-steering experiments, since then full advantage could be taken of the fact that in (2) the asymmetry of the positron emission depends on the positron energy and that the emission of low-energy positrons opposite to the muon spin direction is suppressed. In all future Arizona-beam installations provisions should be made for setting up a spin rotator, which necessarily is several meters long.

In order to obtain polarized muons from pions in flight one needs a so-called muon channel. In the case of SIN and BOOM this consists of a superconducting solenoid, in which the spiralling path of the pions is so long that virtually all of them decay in the channel. In this way high-momentum muon beams with very little pion and positron contamination have been achieved. However, because of the so-called kinematic depolarization [36] the polarization of high-momentum beams is necessarily smaller than that of Arizona beams and amounts in practice to not more than 0.75 - 0.80 . The kinematic depolarization is due to the fact that a muon beam extracted in the laboratory system in, say, backward direction from the flight direction of the pions contains a certain fraction of muons that have been emitted in the forward direction as seen from the pion rest system and which hence in the laboratory system possess the "wrong" spin direction.

So far the only application of positive pions outside of nuclear and elementary-particle physics is the π^+/μ^+ lattice steering described in Sect. 4. In this application the π^+ should be implanted into the samples at energies as low as possible in order to keep the path of the emerging μ^+ inside the samples short. On the other hand, in order not to loose too many pions by decay the pion velocity and hence the pion energy should be as high as possible. The distance over which the fraction e^{-1} of pions with velocity c/4 have not yet decayed is only 2 m. In the experiments on Ta performed at SIN [15,33] a flux of $2 \cdot 10^8 \pi^+/s$ at a momentum p^π = 150 MeV/c was available. This resulted in 8 counts per second in the useful ranges of direction and energy. Under these conditions, which by present standards must be considered quite favourable, about 5 hours were required in order to obtain the information contained in Fig. 6.

The two important time constants in the physics of pions and muons are the lifetimes $\tau_{\pi^\pm} = 2.6 \cdot 10^{-8}$ s and $\tau_\mu = 2.2 \cdot 10^{-6}$ s. From this it follows that interesting time structures are $\Delta t_1 \ll \tau_{\pi^\pm} \ll \Delta t_2$ for pion beams and $\Delta t_1 \ll \tau_\mu \ll \Delta t_2$ for muon beams. The time-structure requirements for pulsed μSR measurements have been discussed in Sect. 3. In the following we add some remarks on the use of beams with the above time structures for the study of pion and muon trapping at crystal defects by means of time-differential lattice steering.

In order to reach defects at which they may be trapped, thermalized pions and muons must diffuse a certain distance. An estimate of the time t it takes till the fraction e^{-1} is trapped (neglecting the possibility of detrapping) by an atomic concentration C of defects with capture radius r_o is given by

$$t = V_A / 4\pi \, r_o \, C \, D^+ \quad , \qquad (13)$$

where D^+ denotes the diffusivity of the positively charged probes and V_A the atomic volume. The majority of the probes that decay at times short compared to (13) will do so at interstitial sites in a perfect lattice environment and will give rise to the corresponding flux-enhancement pattern, whereas those which decay at times longer than (13) are likely to have been trapped. The flux-enhancement and blocking patterns should then be those of the trapping sites.

Using pulses with lengths Δt_1 satisfying one of the above conditions as collective entry signals we may record the lattice-steering patterns as a function of the time the probes have spent in the sample. If the trapping time t is comparable with the lifetime of the probes this allows us to obtain in the same run the patterns both of the free and the trapped probes. From this the trapping time t and, with the help of (13), the quantity $r_0 C D^+$ may be derived. For a fixed defect concentration it will thus be possible to deduce the temperature dependence of D^+. Alternatively, if D^+ is known, one may determine $r_0 C$ experimentally.

The possibility just described is particularly attractive in view of the fact that the ratio of the muon to the pion lifetime is 85 and that the diffusion coefficients of the two probes are not expected to be too different. The combination of π^+/μ^+ and μ^+/e^+ lattice steering should enable us to follow variations of D^+ or C over almost four powers of ten.

The normal operation conditions of SIN are $\Delta t_1 = 1\cdot 10^{-9}$s and $\Delta t_2 = 2\cdot 10^{-8}$s. This means that they satisfy $\Delta t_1 \ll \tau_{\pi\pm}$ but not $\tau_{\pi\pm} \ll \Delta t_2$. However, at the cost of reducing the average pion flux to one third it is possible to operate the SIN accelerator at $\Delta t_2 = 5.9\cdot 10^{-8}$s, corresponding to $t_2/\tau_{\pi\pm}=2.3$. Under these conditions the time-differential π^+/μ^+ lattice-steering experiment described above appears feasible, although the time structure is not ideal and a single run is expected to take more than 24 hours. After the increase of the π^+ flux foreseen in a few years from now [37] it should be possible to perform time-differential π^+/μ^+ experiments routinely at SIN.

With the present facilities at SIN a <u>non-time-differential μ^+/e^+ lattice-steering experiment</u> would take about a factor of ten longer than the corresponding π^+/μ^+ experiment if the same statistical accuracy is to be achieved. This means that it goes beyond what can be routinely done now but that routine experiments should become feasible after the SIN extension program is completed.

To the writers knowledge, at present there is nowhere a realistic possibility to perform <u>time-differential μ^+/e^+ lattice-steering experiments</u>. However, an accelerator with an average 1.1 GeV proton current of 5 mA and time structure $\Delta t_1 = 1.5\cdot 10^{-7}$s and $\Delta t_2 = 2\cdot 10^{-2}$s as it is under discussion for the German neutron spallation source would provide close-to-ideal conditions for setting up such experiments. This would allow us to reach the "ultimate goal" of the application of positive pions and muons to solid-state physics, namely the possibility to perform μSR and time-differential μ^+/e^+ lattice-steering experiments on the same samples and thus to obtain experimental information in unprecedented completeness and detail on crystal defects capable of trapping muons.

Fig. 8 summarizes our discussions on flux strength and time-structure[4)].

[4)] In Fig. 4 the interrupted lines mean that the time structure inside the lines is advantageous but not necessary.

time structure	direct current	$\Delta t_1 \ll \tau_\mu \ll \Delta t_2$	$\Delta t_1 \ll \tau_{\pi^\pm} \ll \Delta t_2$	comments
increasing μ^+ or π^+ flux	individual time-differential μSR (trans., long.)			classical technique, only marginal improvements possible
		high-frequency μSR, coupling through e⁻spin (Mu)		time structure desirable but not necessary
	π^+/μ^+ lattice steering			demonstrated at SIN
		high-frequency μSR, coupling through μ^+spin (long.)		feasible at SIN (S-HD letter of intent) and BOOM
		collective time-differential μSR (trans., long.)		principal technique at BOOM (Japan)
			time-differential π^+/μ^+ lattice steering	feasible at SIN, requires larger π^+ flux
	μ^+/e^+ lattice steering			demonstr. at SIN, larger flux required
		time-differential μ^+/e^+ lattice steering		much larger fluxes than available required
		t.-d. μ^+/e^+ lattice steering + μSR on same sample		"ULTIMATE" AIM

Fig. 8: Time-structure and flux requirements for μSR and lattice steering

The "classical" individual-mode μSR makes best use of the muons produced if a direct current of muons is available. (Direct current in this context means that $\Delta t_2 \ll \tau_\mu$, so that from the point of view of muon physics SIN is a direct current facility[5].) As explained in Sect. 3 the count rates that can be achieved in this mode are sharply limited, so that a further increase in the muon flux will only give marginal improvements (e.g., narrower momentum range of the beams, higher polarization of high-momentum beams, possiblity to use smaller samples). All other techniques, however, will gain from higher muon and pion fluxes, most strikingly so the lattice-steering experiments in which the count-rate is strictly and without limitation proportional to the particle flux.

The various techniques have been arranged in Fig. 8 roughly in the sequence of increasing flux required. Only the first two techniques may be said to be in good shape with the present facilities. All other techniques will substantially profit from future increases in intensity or, as the time-differential μ^+/e^+ experiments, will only become possible when fluxes at least one order of magnitude higher than those of to-day will be available.

[5] An exception is the stroboscopic μSR technique [24] mentioned in Sect. 3, which does make use of the finiteness of Δt_2.

Acknowledgment

The author acknowledges numerous stimulating discussion with Dr. K. Maier.

References

[1] K. Nagamine, Hyperfine Interactions 8, 787 (1981)
[2] UT - MSL Newsletter (Meson Science Laboratory, University of Tokyo) No. 1 (1981)
[3] B. Zeitnitz, this conference
[4] J.-P. Blaser, Physikal. Blätter 35, 576 (1959)
[5] R.L. Garwin, L.M. Lederman, and M. Weinreich, Phys. Rev. 105, 1415 (1957)
[6] V.W. Hughes and C.S. Wu (eds.), Muon Physics, Vol. I-III, Academic Press, New York 1975-77
[7] A. Schenck, Positive Muons and Muonium in Matter, in: Exotic Atoms (ed. by G. Fiorentini and G. Torelli), p. 355, Laboratori Nazionali die Frascati 1977
[8] A. Seeger, Positive Muons as Light Isotopes of Hydrogen, in: Hydrogen in Metals I (ed. by G. Alefeld and J. Völkl), p. 349, Springer, Berlin–Heidelberg–New York 1978
[9] P.W. Percival, Radiochimica Acta 26, 1 (1979)
[10] C. Bucci, P.R. Crippa, G.M. de Munari, G. Guidi, M. Manfredi, R. Tedeschi, A. Vecli, and P. Podini, Hyperfine Interactions 6, 425 (1979)
[11] A. Seeger, Positron Annihilation (ed. by R.R. Hasiguti and K. Fujiwara), p. 771, The Japan Institute of Metals, Sendai 1979
[12] C.P. Flynn and A.M. Stoneham, Phys. Rev. B 1, 3966 (1970)
[13] Yu. Kagan and M.I. Klinger, J.Phys. C, 7, 2791 (1974)
[14] H. Teichler and A. Seeger, Phys. Letters 82A, 91 (1981)
[15] K. Maier, G. Flik, A. Seeger, D. Herlach, H. Rempp, G. Jünemann, and H.-D. Carstanjen, Nucl. Instr. and Meth. in Phys. Res. (Proc. 9th Intern. Conf. on Atomic Collisions in Solids), in the press
[16] A. Abragam, The Principles of Nuclear Magnetism, Clarendon Press, Oxford 1961
[17] C.P. Slichter, Principles of Magnetic Resonance, 2nd ed., Springer, Berlin–Heidelberg–New York 1980
[18] V.W. Hughes, Exotic Atoms '79 (ed. by K. Crowe, J. Duclos, G. Fiorentini, and Gabriele Torelli) p. 3, Plenum Press, New York and London, 1980
[19] A. Seeger, Phys. Letters 53 A, 324 (1975)
[20] A. Seeger, Proceedings 5th Intern. Symposium on High-Purity Materials in Science and Technology (ed. by J. Morgenthal and H. Oppermann), Akademie der Wissenschaften der DDR, Dresden 1980
[21] A.B. Denison, H. Graf, W. Kündig, and P.F. Meier, Helv. Phys. Acta 52, 460 (1979)
[22] A. Seeger and P. Monachesi, to be submitted to Phil. Mag.
[23] E. Yagi, H. Bossy, K.-P. Döring, M. Gladisch, D. Herlach, H. Matsui, H. Orth, G. zu Putlitz, A. Seeger, and J. Vetter, Hyperfine Interactions 8, 553 (1981)
[24] M. Camani, F.N. Gygax, E. Klempt, W. Rüegg, A. Schenck, H. Schilling, R. Schulze, and H. Wolf, Phys. Letters 77 B, 326 (1978)
[25] A. Schenck, Hyperfine Interactions 4, 282 (1978)
[26] C.G. Shull, Magnetic and Inelastic Scattering of Neutrons by Metals (Metallurgical Society Conferences Vol. 43, ed. by T.J. Rowland and P.A. Beck) p. 15, Gordon and Breach, New York–London–Paris 1968

[27] M. Gladisch, D. Herlach, H. Metz, H. Orth, G. zu Putlitz, A. Seeger H. Teichler, W. Wahl, and M. Wigand, Hyperfine Interactions 6, 109 (1979)
[28] A. Seeger, Phys. Letters 74A, 259 (1979)
[29] E.H. Brandt and A. Seeger, to be published
[30] J. Lindhard, Mat.Fys.Medd.Dan.Vid.Selsk. 34, No.14 (1965)
[31] E. Uggerhøj, Phys. Letters 22, 382 (1966)
[32] K. Maier, Nuclear Physics Methods in Materials Research (ed. by K. Bethge, H. Baumann, H. Jex, and F. Rausch) p. 264, Vieweg, Braunschweig-Wiesbaden 1980
[33] K. Maier, G. Flik, D. Herlach, G. Jünemann, H. Rempp, A. Seeger, and H.-D. Carstanjen, Phys. Letters 83A, 341 (1981)
[34] K. Maier, G. Flik, D. Herlach, G. Jünemann, A. Seeger, and H.-D. Carstanjen, Phys. Letters, in the press
[35] A.E. Pifer, T. Bowen, and K.R. Kendall, Nucl. Instr. Meth. 135, 39 (1976)
[36] A.O. Weissenberg, Muons, North-Holland, Amsterdam 1967
[37] Alpine Medium-Energy Physics Workshop (Arolla 1980), Schweizerisches Institut für Nuklearforschung, Villigen 1981

Jül-Conf-45 B4

I C A N S - V
MEETING OF THE INTERNATIONAL COLLABORATION ON
ADVANCED NEUTRON SOURCES
June 22-26, 1981

Neutrino Physics at the Spallation Neutron Source

B. Zeitnitz
Kernforschungszentrum Karlsruhe
Institut für Kern- und Teilchenphysik
7500 Karlsruhe, Postfach 3640
Federal Republic of Germany

Abstract

The advantages which the new high intensity neutron spallation sources will offer for neutrino physics are discussed. The experimental area planned for neutrino measurements at the SNQ (Spallations-Neutronen-Quelle) is presented. An experiment to search for neutrino oscillations $\nu_\mu \leftrightarrow \nu_e$ is proposed.

Autorized reprint of the report KfK-3155

I. INTRODUCTION

During the last years interest in the physics of neutrinos has substantially grown. Especially in the context of successful application of gauge theories and quark models the new weak interaction theories have led to new questions concerning the elementary properties of the neutrinos. The interest in possible "anomalous" properties of the neutrinos has been further stimulated by the discrepancy existing between the measured and the calculated numbers of neutrinos from the sun.

An explanation of the deficit of solar neutrinos may be possible by assuming that the neutrinos have a small but finite mass. The second assumption is then plausible that this mass differs for the different kinds of neutrino: $(\nu_e, \nu_\mu, \nu_\tau)$. However, this opens up the possibility that neutrinos transform into each other. In principle. this transformation could be either a reversible process by so-called oscillations or by decay /1/.

If the interaction violates muon number conservation and if the neutrinos of the electron and of the muon have different masses, this leads e.g. to the oscillation: $\nu_e \leftrightarrow \nu_\mu$ and to the decay $\nu_\mu \rightarrow \nu_e + \gamma$ (assuming $m_{\nu_\mu} > m_{\nu_e}$). The lifetime can be estimated to $\tau > 5 \cdot 10^{11}$ years /1/. Therefore, the decay of neutrinos cannot be observed in the laboratory.

The oscillation of particles to particles (and antiparticles to antiparticles, respectively) has been recently termed also "flavour oscillation". The reason is that in the unified theory of weak and electromagnetic interactions lepton flavours have been introduced by analogy with quark flavours. According to their helicity the leptons are combined into a doublet and a singlet each:

For example:

$$L = \begin{pmatrix} \nu_L \\ e_L^- \end{pmatrix}; \qquad R = e_{\bar{R}}$$

(L = left handed; R = right handed).

In total, this gives the following doublets:

$$\begin{pmatrix} \nu_e \\ e^- \end{pmatrix}; \begin{pmatrix} \nu_\mu \\ \mu^- \end{pmatrix}; \begin{pmatrix} \nu_\tau \\ \tau^- \end{pmatrix}$$

$$\begin{pmatrix} \bar{\nu} \\ e^+ \end{pmatrix} \begin{pmatrix} \bar{\nu}_\mu \\ \mu^+ \end{pmatrix} \begin{pmatrix} \bar{\nu}_\tau \\ \tau^+ \end{pmatrix} \qquad (1)$$

$\nu_\tau(\bar{\nu}_\tau)$ has not yet been unambiguously detected in the experiment, Moreover, the mass of the τ-particle of 1.8 GeV/c^2 lies beyond the range of energies accessible at the spallation neutron source. Therefore, only the particles of the first four doublets will be considered in this paper.

For zero-mass particles mixing of different states of helicity and different doublet assignments (lepton flavours) is not possible. Also, besides the conservation of the lepton number, there is a separate conservation of the muon number. In the weak interactions in vertical direction in (1) e.g. for the ν_e - e^- coupling exchange of the so-called $W^\pm$ boson is assumed to take place. However, because of its great mass, this boson could not yet been detected in experiment. The proof of interactions by "neutral currents" (e.g. ν_μ - e^--coupling) has been one of the great discoveries in the past years. As a consequence, the existence of a (likewise very heavy) electrically neutral exchange particle Z_0 is predicted.Experiments aiming at

the direct proof of the existence of $W^{\pm}$ and Z_0 can be performed only in high energy physics. However, quite a number of very fundamental questions can be studied particularly well by means of the very high neutrino fluxes to be generated at the planned SNQ spallation neutron source.

In this context the interactions in the horizontal direction in (1) will be of special interest. The interest at the time being concentrates on studies of the transitions $\nu_e \leftrightarrow \nu_\mu$; $\bar{\nu}_e \leftrightarrow \bar{\nu}_\mu$ (flavour oscillations) but also on possible particle-antiparticle oscillations: $\nu_e \leftrightarrow \bar{\nu}_e$; $\nu_\mu \leftrightarrow \bar{\nu}_\mu$; $\nu_e \leftrightarrow \bar{\nu}_\mu$ etc..

Such studies could provide information about possible mass differences and violations of the conservation numbers. But more accurate measurements on neutrino coupling to other leptons continue to be equally important. For instance, measurements with good statistics of elastic neutrino scattering from electrons may serve this purpose, viz. $\nu + e \rightarrow \nu + e$. A particularly interesting process is the elastic scattering of mu-neutrinos from electrons: $\nu_\mu + e^- \rightarrow \nu_\mu + e^-$ or $\bar{\nu}_\mu + e^- \rightarrow \bar{\nu}_\mu + e^-$. Studying this fundamental reaction yields clear information about the weak neutral coupling of the electron. The results allow to make comparisons with theory in a very direct manner, e.g., the determination of the Weinberg angle /3,4,5,6/. The existence of $\nu_e + e \rightarrow \nu_e + e$ could not be even proven until now.

Besides the study of neutrino interaction with other leptons, coupling to hadrons offers some interest. Coupling constants and form factors both for charged and neutral interactions could be derived from suitable experiments /7,8/. An interesting field of activities not covered so far by experiments is the defined excitation of nuclear levels by neutrino scattering. Firstly, the nucleus is used as a microscopic laboratory with a defined spin-isospin with a view to determine coupling constants in a selective way and largely model independent. Secondly, nuclear matrix elements can be measured for light nuclei. The excitation by mu-neutrinos would offer particular interest. The reason is that this interaction allows to excite the nuclei

merely by neutral current coupling. The combination of the results of such measurements with corresponding (in most cases already known) numerical values from β-decay, electron scattering and γ-decay of energy levels of nuclei would allow detailed testing of the unified theory of electromagnetic and weak interactions. If, however, this theory is supposed to be valid, the nuclear matrix elements are obtained practically independent of the model. A number of articles and proposals have been published during recent years about this field of "nuclear physics involving neutral currents". A comprehensive description has been furnished by T.W.Donnelly and R.D.Peccei /9/. The new high-intensity accelerators with a time structure suitable for separation of the mu-neutrinos will enable us for the first time to perform such experiments. An interesting example would be the inelastic excitation of the $(1^+,1)$ 15.11 MeV level in ^{12}C by mu-neutrinos:

$$^{12}C(\nu_\mu,\nu'_\mu)^{12}C^* \ (0^+0 \rightarrow 1^+1,\ 15.11\ \text{MeV})$$

Since the level in ^{12}C decays into the ground state by 95%, the 15.11 MeV γ-ray constitutes a clear signature for excitation of a nucleus by neutral current. Since the spin and the isospin are defined, measurement of the integral cross section for this reaction would already be appropriate for the selective determination of the isovector part of the neutral current. The integral cross section at neutrino energies below approximately 100 MeV is obtained as /9/:

$$\sigma'_{\nu\nu} = \text{const.}\ |\langle 1;1\ ||L||\ 0;0\rangle|^2\ (E_\nu - 15.11)^2 C_Q^2 \qquad (2)$$

where E_ν is the neutrino energy in MeV. The reduced matrix element is the same as that occurring in the calculation of the β-decay rate (see p.47 of /9/):

$$\omega_{\beta\,\pm} = \frac{4}{3\pi^2}\, G^2\, f^{\pm} \cdot |\langle 1;1\ ||L||\ 0;0\rangle^2| \qquad (3)$$

Introducing (3) into (2) and use of the measured ß-decay rates gives independent of the nuclear model:

$$\sigma'_{\nu\nu} = 1.08\cdot 10^{-38}\,\frac{(E_\nu - 15.11)^2}{M_N^2}\cdot C_Q^2\ \mathrm{cm}^2 \qquad (4)$$

where C_Q^2 is a coupling constant for isovector axial coupling. Very different values are obtained for this cross section for different gauge theories. This is demonstrated in Fig.1. Supposing that the WSGIM-model is correct, we have $C_Q^2=1$ ($C_Q^2=\frac{1}{4}$ for the b-quark model). With this assumption, an integral inelastic scattering cross section of $\sigma_{\nu_\mu\ \nu'_\mu} = 2.5\cdot 10^{-42}\ \mathrm{cm}^2$ is obtained for the mu-neutrinos from the SNQ spallation neutron source (beam stop E_ν = 30 MeV). With adequate shielding and a suitable time structure this extremely small cross section could be measured within one week of measuring time at the proposed SNQ spallation neutron source, the statistical accuracy being better than $\pm$ 10% (for 1 mA averaged proton current).

The desired extension of the unified theories of interaction might lead to the postulation that light scalar gauge bosons exist /10,11/. In the meantime, H.Faissner has reported about first experimental indications of the existence of such semi-weak interacting spin-zero particles having a mass m_a = (300 $\pm$ 50)KeV /12,13/. Given an adequate time structure, investigations including such particles could be performed at a high-intensity spallation neutron source in parallel with neutrino physics investigations and in the same experimental hall, using similar or the same detectors /2/.

The importance of neutrino experiments at high-intensity proton accelerators at medium energies have been discussed intensively by several authors in recent years; see /8,9,14/. During the past months, detailed proposals have been submitted for experiments to be performed at LAMPF /6,15,16,17/.

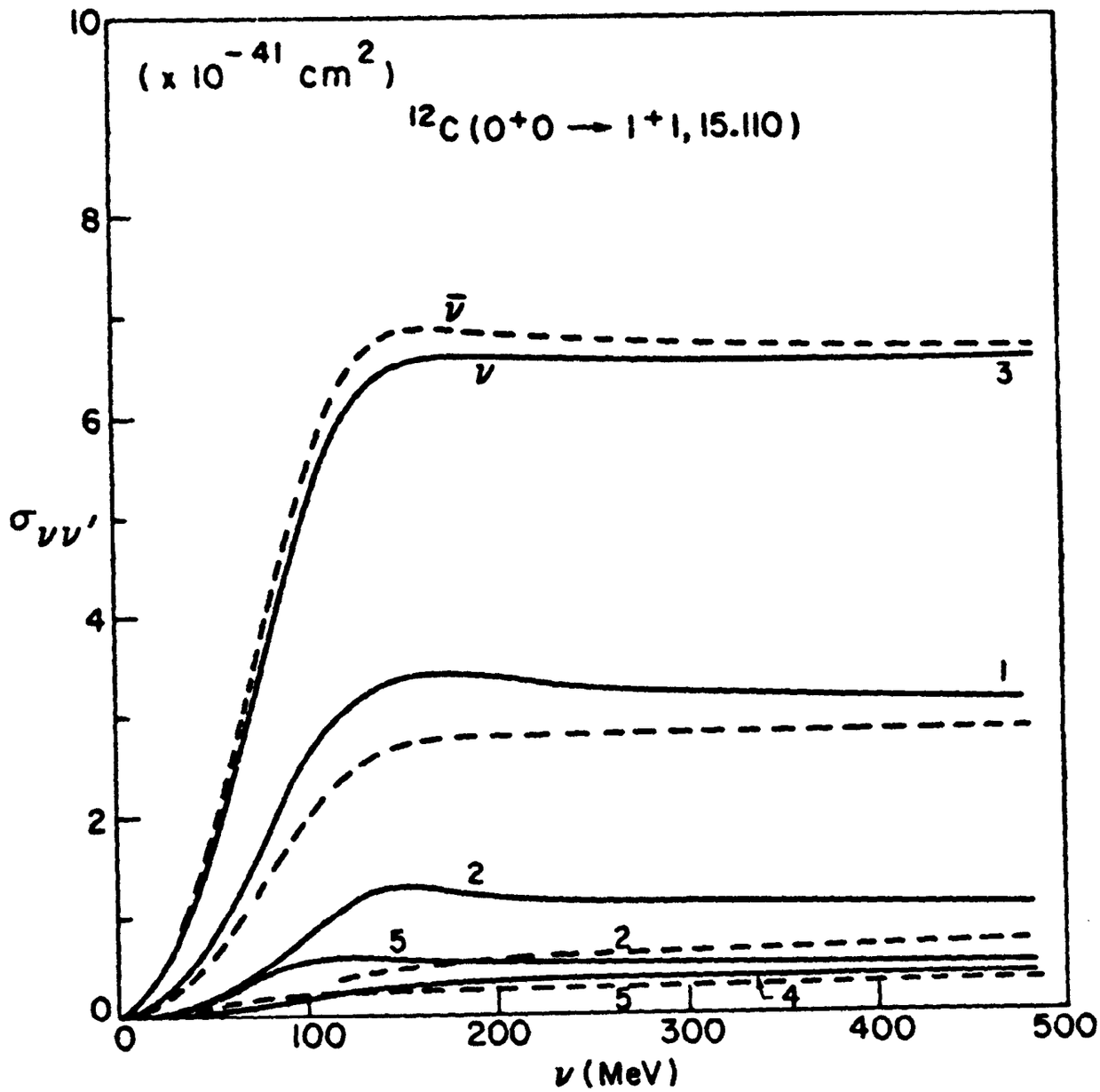

Fig.1: Cross sections for inelastic neutrino scattering from ^{12}C (15.1 MeV) for different quark models 1 - 5 (taken from /9/). 1: WSGIM; 2: b-quark

It is evident from all these publications that this type of neutrino physics is on the way to become a field of research for several working groups. Thanks to the extremely high neutrino fluxes to be generated at the high-intensity proton accelerators already under construction and planned, respectively, work on the weak neutral currents nowadays considered as rather exotic could develop into a standard discipline of modern nuclear and particle physics.

The great advantages which the facility proposed in this study would offer for neutrino physics, will be explained by way of example in the following chapters. The computations required in this context, part of them very extensive, were carried out as a collaboration of the Karlsruhe Nuclear Research Center and the Oak Ridge National Laboratory by T.Gabriel (ORNL) and J.Wilczynski (KfK). A comprehensive presentation of the methods and results will be published soon /18/.

II. NEUTRINOS FROM THE SPALLATION NEUTRON SOURCE (Beamstop Neutrinos)

The protons do not only give rise to the production of neutrons in the spallation target. At the same time a considerable number of pions π^+ (and π^-) is produced which emit neutrinos while decaying. Fig.2 shows the calculated number of π^+ particles produced per stopped proton for different target materials as a function of the proton injection energy /18/. It can be noted that in our case with E_p = 1100 MeV and lead as the target material: N_{π^+}/N_p = 0.13(3).

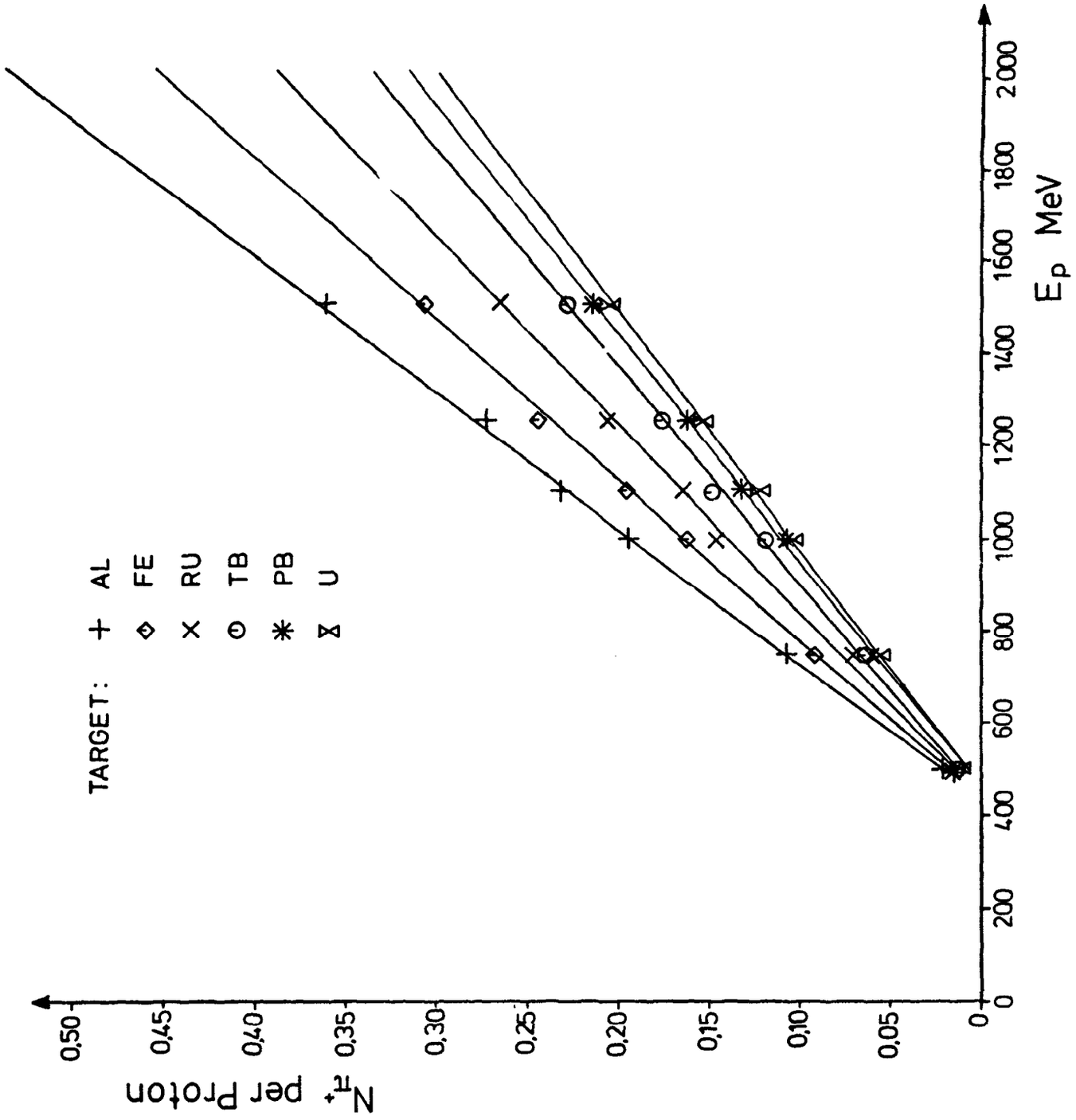

Fig.2: Yields of pions (π^+) per stopped proton for different target materials

The pions are very quickly stopped (10^{-10} s) still in the target zone so that only a small fraction of about $5 \cdot 10^{-3}$ decay while on flight. Whilst the negative pions, when at rest, are captured by nuclei and finally absorbed, the positive pions, with a life time τ = 26 ns, decay into a positive muon and a muon neutrino. This means that, practically, only the positive pions and the positive muons play a role at the SNQ spallation neutron source. The muon with a life time τ = 2.2 µs subsequently decays into a positron and (because of conservation of the lepton and muon numbers) into an electron neutrino and a muon antineutrino. Thus, we have

$$\pi^+ \rightarrow \mu^+ + \nu_\mu \qquad \tau = 26.03 \times 10^{-9}\ \mathrm{s} \qquad (5)$$

$$\mu^+ \rightarrow e^+ + \nu_e + \bar{\nu}_\mu \qquad \tau = 2.197 \times 10^{-6}\ \mathrm{s} \qquad (6)$$

Since the pion at rest decays into two particles, the muon neutrinos from (5) have a constant energy E_{ν_μ} = 29.79 MeV. By contrast, continuous distributions with an end energy of 52.83 MeV are obtained for the neutrinos produced by the three-particle decay (6). Fig.3 shows the respective energy distributions. Since the decays take place with the particles at rest, the intensities of all three kinds of neutrino are equal and isotropic in space. The source strengths given in Fig.3 were calculated for an averaged proton current $\bar{I}_p$ = 1 mA. For each kind of neutrino and the desired parameters of the spallation neutron source E_p = 1100 MeV and $\bar{I}_p$ = 5 mA an averaged source strength is obtained of

$$\bar{Q}_\nu = 3 \times 4.1 \times 10^{15}/\mathrm{s}. \qquad (7)$$

This means that the facility would be the most powerful source for the three kinds of neutrino $\nu_\mu, \nu_e, \bar{\nu}_\mu$.

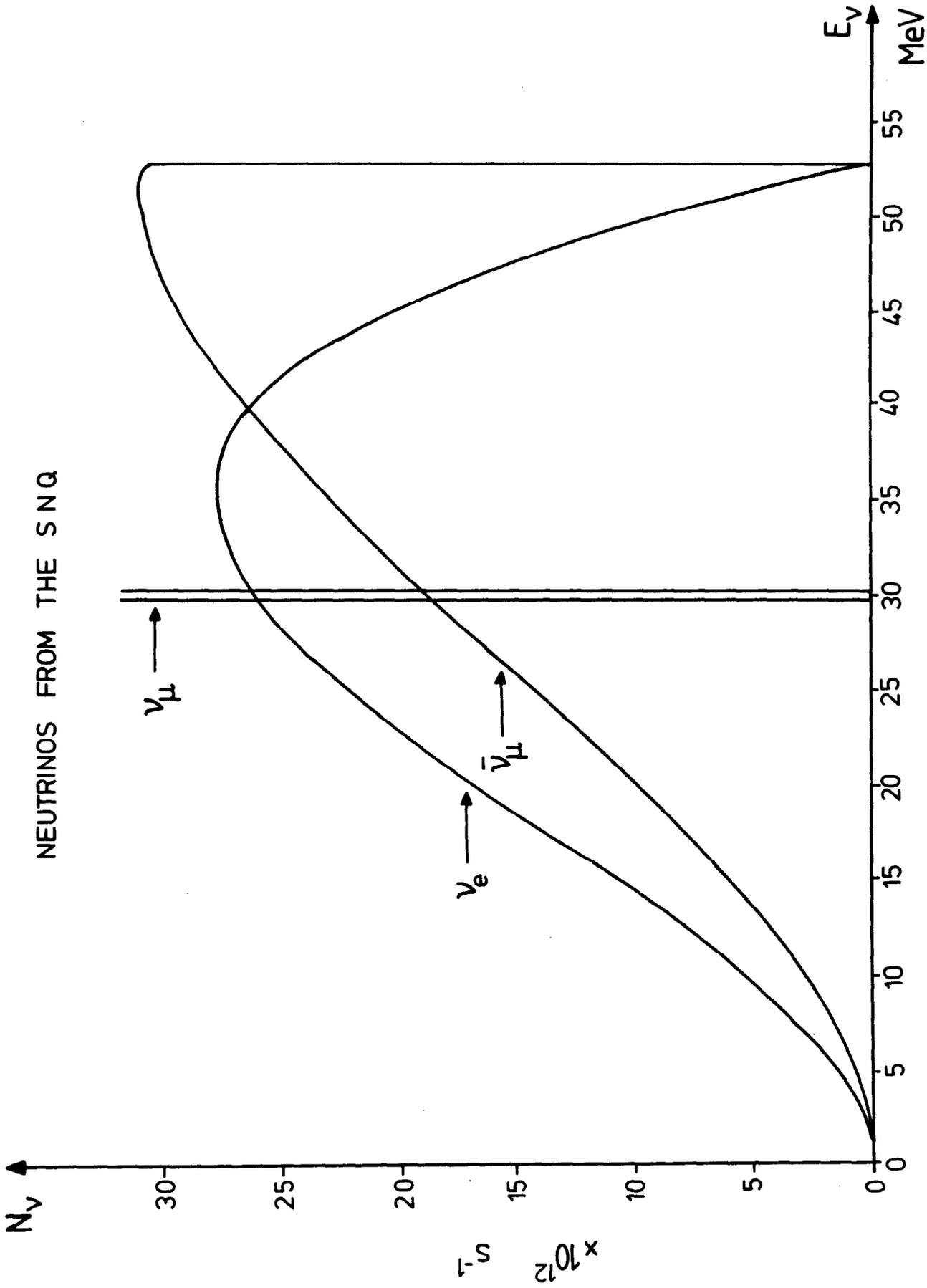

Fig.3: Energy distributions of the neutrinos generated at the SNQ spallation neutron source (beamstop). The total numbers of all three kinds of neutrino are equal. The indicated source strengths apply to 1 mA averaged proton current for E_p=1100 MeV

This source can be utilized for distances from about 6 m on, where it will appear practically as a point source yielding a flux of

$$\varphi_\nu = \frac{Q_\nu}{4\pi r^2} \tag{8}$$

$$\varphi_\nu = 3 \times \frac{3.2\times10^{10}}{r^2}\ \mathrm{cm}^{-2}\ \mathrm{s}^{-1} \tag{9}$$

(r in m).

However, in future experiments involving neutrinos not only a high average flux but likewise a suitable time structure and the highest possible peak flux will play a role. There are three main reasons for this requirement:

1. Most of the experiments which will be of interest also after some years need separation of the different kinds of neutrino. For this purpose, the very different lifetimes of pion and muon decay can be utilized provided a suitable time structure of the beam. This problem will be treated more comprehensively later in this paper.

2. On account of the very small cross sections in neutrino experiments, the number of background events originating from continuous sources (cosmic rays, detector noise, etc.) must be kept extremely low. Therefore, the smallest possible duty cycle of the beam should be aimed at.

3. Background events from the source reaching the detector even through a very thick shielding are produced mainly by neutrons. The slow part of the spectrum of neutrons can be eliminated by time of flight measurements.

II.1 Dependence on Time of the Neutrino Flux

For a rectangular pulse of the proton beam with the pulse duration t_p the time dependencies of the neutrino source strengths indicated by the expressions (10) to (13) are obtained

in accordance with the different lifetimes τ_π and τ_μ of the pions and muons generated (cf. also /19/):
For the source flux of the mu-neutrinos ν_μ from the π^+-decay:

$$\varphi_{\nu_\mu} = Q_0 \left(1-e^{-\frac{t}{\tau_\pi}}\right) \qquad t \leq t_p \tag{10}$$

$$\varphi_{\nu_\mu} = Q_0 \left(e^{\frac{t_p}{\tau_\pi}} -1\right) e^{-\frac{t}{\tau_\pi}} \qquad t \geq t_p \tag{11}$$

For the source flux of the electron neutrinos φ_{ν_e} (identical with that of mu-antineutrinos $\varphi_{\bar{\nu}_\mu}$) we obtain in good approximation ($\tau_\mu >> \tau_\pi$):

$$\varphi_{\nu_e} = Q_0 \frac{t_p}{(t_p+\tau_\pi)\ \tau_\mu} \cdot t \cdot e^{-\frac{t}{\tau_\mu}} \qquad t \leq t_p+\tau_\pi \tag{12}$$

$$\varphi_{\nu_e} = Q_0 \frac{t_p}{\tau_\mu} e^{-\frac{t}{\tau_\mu}} \qquad t \geq t_p+\tau_\pi \tag{13}$$

where

$$Q_0 = 0.133 \frac{6.24 \times 10^{15}}{f \cdot t_p} \text{ mA}^{-1}\ \text{s}^{-1} \tag{14}$$

f = pulse frequency in Hz

t_p = pulse length of the protons in s.

Fig.4 shows this time dependence of the neutrino source fluxes for the practical example of a proton pulse length of t_p = 200 ns with a repetition frequency of 100 Hz, i.e. for $Q_0 = 4.15 \times 10^{19}$ mA^{-1} s^{-1}. (The unit mA relates to the averaged proton current).

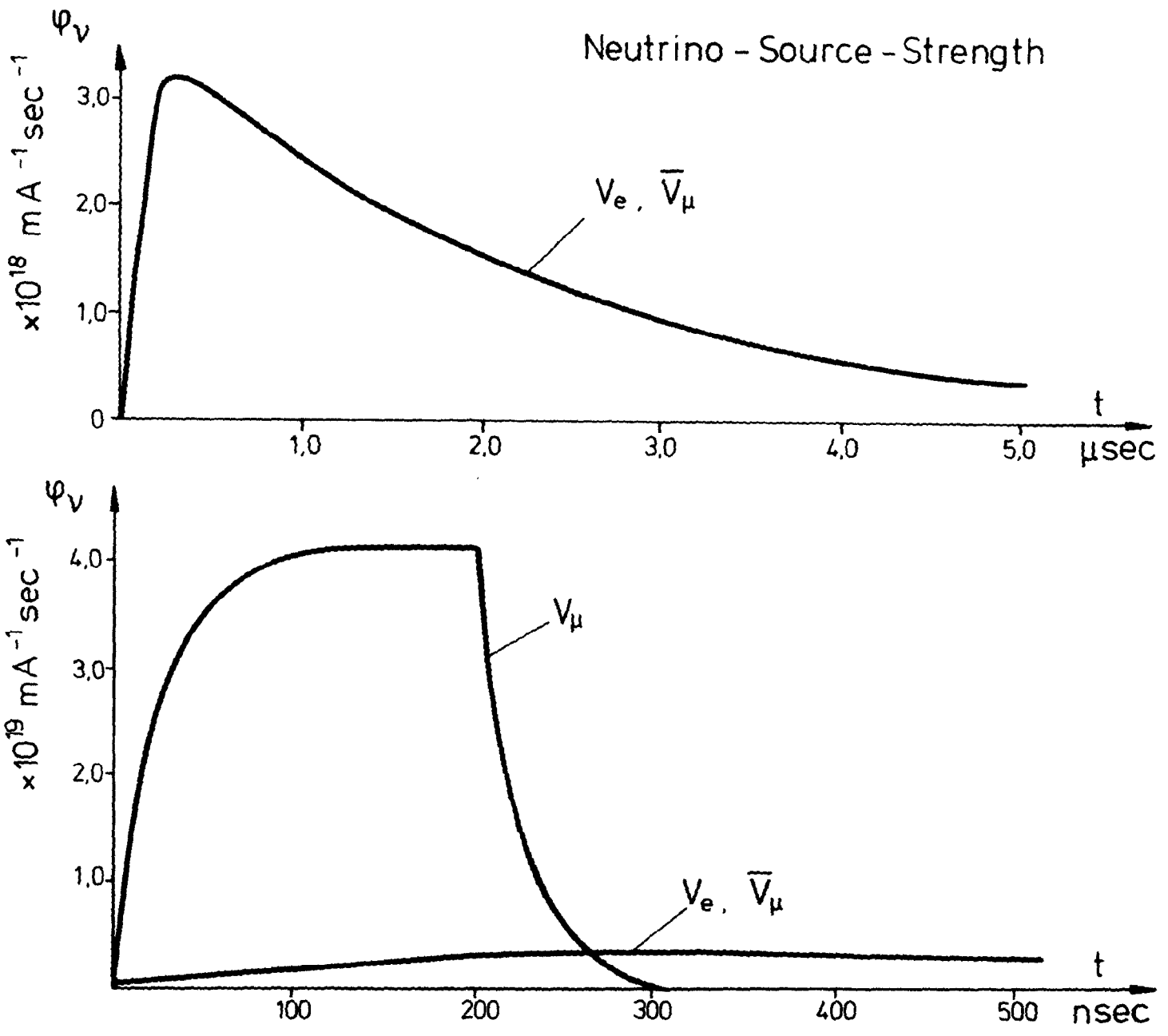

Fig.4: Time dependence of the neutrino source fluxes at the SNQ spallation neutron source (t_p = 200 ns, $\bar{I}_p$ = 1 mA, f = 100 Hz)

As has been expected, saturation of the mu-neutrino source strength φ_{ν_μ} is attained already after about t = 100 ns. Since the muons have a much longer lifetime, the fluxes of the electron- and muonantineutrinos φ_{ν_e} and $\varphi_{\bar{\nu}_\mu}$ are still much smaller at that time. Thus, the optimum pulse length for the separation in terms of time of ν_μ is about 50 ns. However, for most of the experiments the total intensity attainable is equally important as the degree of separation. The ideal case of a pulse length t_p = 50 ns with the averaged proton current of 5 mA maintained at the same time (at f = 100 Hz), would require a peak current of 1000 A. However, since this would probably exceed the existing technical and financial limits (see chapter dealing with the storage rings), compromises must be made. A closer study of the conditions prevailing in some interesting experiments shows (see example of neutrino oscillation, chapter IV) that a pulse length of about 200 ns with an averaged current of about 1 mA would still be a good compromise. The source has to be compared with the facilities planned for construction in the next years at the Rutherford Laboratory in the United Kingdom and at LAMPF in the USA.

Since the proton energies of these competing accelerators lie at about 800 MeV, the neutrino intensities in these facilities will be lower by the factor 1.9 for the same current level (see Fig.2). On the whole, it can be supposed that an accelerator with an energy of E_p = 1100 MeV, a time structure of about t_p < 200 ns for f = 100 Hz and, at the same time, I_p = 1 to 5 mA, will be an extremely interesting source of neutrinos ν_μ, ν_e and $\bar{\nu}_\mu$, even in about ten years. Since the high peak intensity will be of major importance, it can be assumed that such a facility would be unrivaled for a long period of time.

The desired time structure with the simultaneous conservation of the mean intensity can be attained only by bunching with a storage ring. Therefore, a storage ring would be of particular interest for neutrino physics.

In case a storage ring will not be available in the initial phase, the required time structure of the beam could be achieved in the meantime by a compromise associated with loss in intensity. One could, e.g., think of a prepulse group ahead of the main pulse, as shown in Fig.5. Depending on the purpose of the experiment, the pulse length t_p could be varied from the ion source of the accelerator. The minimum interval between two beam pulses is about 10 μs because of the necessary reduction in the number of μ-decays. With a good time structure (useful pulse: t_p = 200 ns, pulse interval t = 10 μs) and a peak current of 100 mA ($\bar{I}_p$ = 5 mA for t_p = 0.5 ms) this would yield an averaged current $\bar{I}_p$ = 100 μA which could still be utilized for neutrino physics. Consequently, the facility would just be competitive with the planned facility at the Rutherford Laboratory as regards its mean neutrino flux. The accelerator at the Rutherford Laboratory will produce double pulses at a frequency of 50 Hz. The duration of each single pulse will only be 100 ns. However, the second pulse arrives as early as 250 ns after the first. The averaged current will be $\bar{I}_p$ = 200 μA at an energy of 800 MeV. This means that the mean intensity which can be used for neutrino physics will attain roughly the same level in both accelerators, even without a storage ring. However, the duty cycle, which is very important in suppressing the continuous cosmic background, is less favourable in the proposed interim solution. For the experiments with mu-neutrinos to be performed at the Rutherford accelerator this duty cycle will be $2\cdot10^{-5}$ as compared with $1\cdot10^{-3}$ in our interim solution. In experiments involving electron and muon antineutrinos a duty cycle of about $1\cdot10^{-3}$ could be expected as compared with $5\cdot10^{-2}$ in our facility.

Here the advantages are evident which would be derived from installation of a storage ring. The values of the duty cycle of the Rutherford accelerator, i.e., $2\cdot10^{-5}$ and $1\cdot10^{-3}$, respectively, could also be attained in our facility if the storage ring were used. At the same time, the neutrino intensities would be higher by nearly a factor 50.

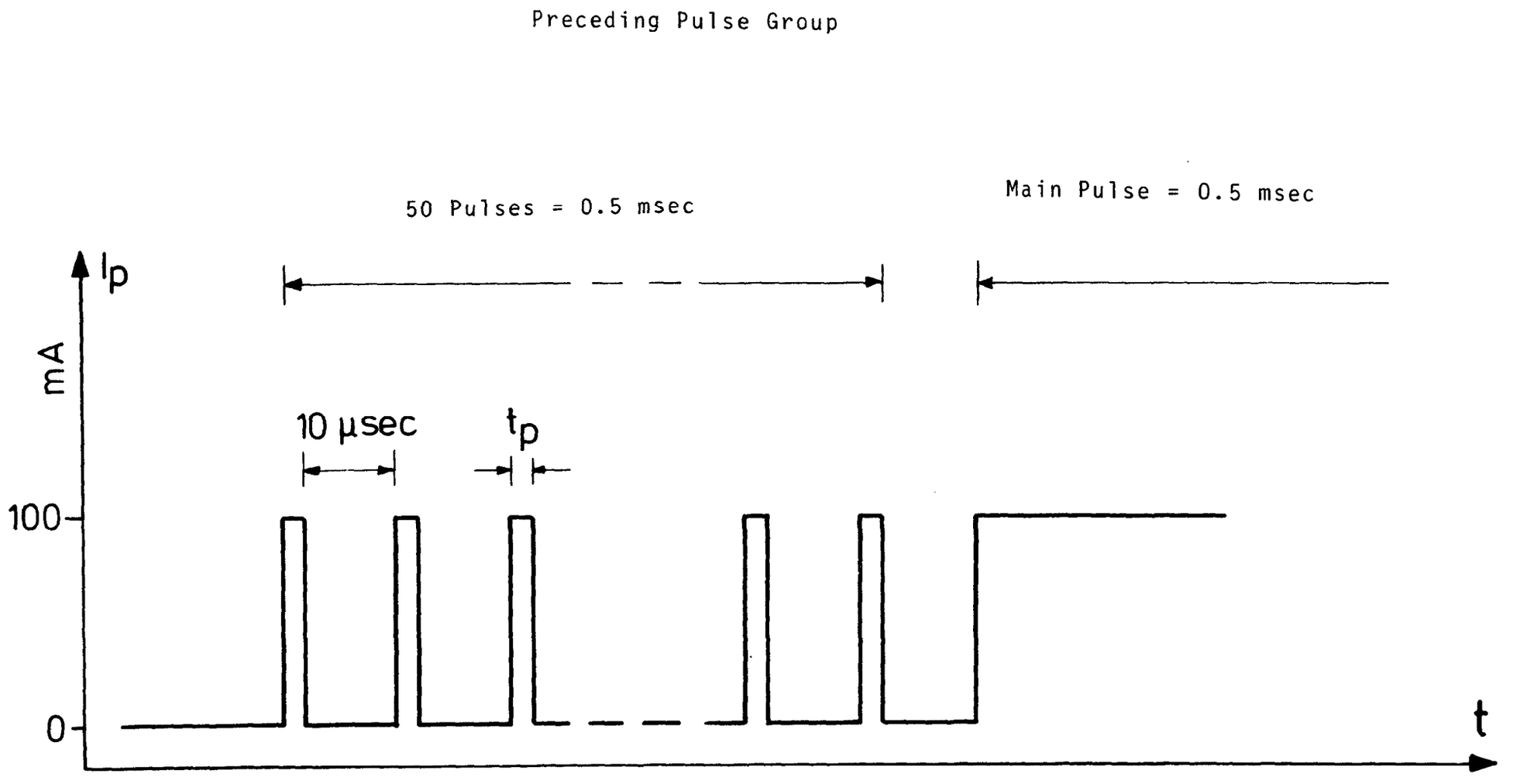

Fig.5: Time structure of the beam for a preceding neutrino pulse group. Interim solution before a storage ring has been provided

Obviously, a comparison of the interim solution proposed by us with the proton storage ring (PSR) planned to be built at Los Alamos in 1985 will lead to less favorable results. At Los Alamos an averaged proton current I_p = 100 μA is to be achieved for a duty cycle of $3 \cdot 10^{-6}$. The proton energy will be 800 MeV. This means that the mean neutrino intensity in our facility would be higher by a factor 2 already if the interim solution were adopted. However, a disadvantage is that the duty cycle would be poorer by a factor 1000 for mu-neutrino experiments (500 for ν_e and $\bar{\nu}_\mu$ experiments).

Another accelerator for planned neutrino physics experiments is already under construction in Moscow. It is intended to provide also a proton storage ring at some later date which will deliver an averaged current of about 500 μA, although at 600 MeV only. A comparison of our interim solution with the facility in Moscow also shows that we would just be competitive as regards the mean neutrino intensity, but not as regards the duty cycle.

For a number of neutrino experiments still of some interest, a larger duty cycle could be compensated initially by better shielding and by extra expenditure for the neutrino detectors. However, experiments on neutrino-electron scattering would become very difficult. With respect to all experiments the storage ring would result in an additional considerable improvement of the quality of results. This will be demonstrated in more detail in chapter IV by the example of measurement of $\nu_\mu \leftrightarrow \nu_e$ oscillations.

The utilization of neutrinos generated during flight while the pions decay has not been discussed here because this would require an expensive decay channel provided at an external beam. However, if such a beam was available for other purposes, above all those experiments could be performed which require higher neutrino energies. They include neutrino disappearance experiments involving muons, e.g., $\nu_\mu + {}^{12}C \rightarrow \mu^- + {}^{12}N$ etc. /8,15,16/. The cross sections for inelastic neutrino scattering continue to

grow by the square of neutrino energy up to about 100 MeV (see Fig.1). However, the extent of practical utilization of this advantage depends on many details of equipment and operation of the facility.

The great advantage offered by the utilization of the pions stopped in the spallation source is that they are available anyway so that the neutrino experiments can be performed simultaneously over extended periods of time and without noticeably impairing the solid state physics experiments.

III. PROPOSAL FOR AN EXPERIMENTAL AREA IN WHICH NEUTRINO MEASUREMENTS COULD BE PERFORMED AT THE SNQ SPALLATION NEUTRON SOURCE

Neutrino experiments are difficult mainly for the reason that the probability of detecting strong or electromagnetic interacting background radiations are higher by 10 to 20 orders of magnitude than they are for neutrinos characterized by weak interaction. The total cross sections listed in Table 1, which are typical of beamstop neutrinos, have to be compared with the total cross sections for capturing thermalized background neutrons from the source or also with that of muons originating in cosmic rays. Therefore, a facility in which neutrino experiments are to be performed, must be very well shielded both against the source and against cosmic rays. In addition,all sources of continuous residual background radiation (cosmic rays, natural radioactivity, noise, etc.) must be suppressed as much as possible by a small duty cycle accompanied by a high peak intensity of the neutrino source. The requirements on the time structure have

Table 1: Cross Sections and Counting Rates Typical for Neutrinos at the SNQ Spallation Neutron Source

Reaction	Mean Energy MeV	σ_{tot} (cm^2)	Counting Rate* $(day,mA,to)^{-1}$	Remarks
$\nu_e + d \rightarrow p + p + e^-$	37	$5 \cdot 10^{-41}$	29	
$\nu_e + {}^{12}C \rightarrow e^- + {}^{12}N11ms$	37	$1.5 \cdot 10^{-41}$	2.9	WSGIM theory
$\nu_e + e^- \rightarrow \nu_e + e^-$	37	$6 \cdot 10^{-43}$	0.74	V-A theory
$\nu_\mu + e^- \rightarrow \nu_\mu + e^-$	30	$5 \cdot 10^{-44}$	0.062	
$\nu_\mu + {}^{12}C \rightarrow \nu'_\mu + {}^{12}C^*(15.1)$	30	$2.5 \cdot 10^{-42}$	0.48	WSGIM theory
$\nu_\mu + {}^{6}Li \rightarrow \nu'_\mu + {}^{6}Li^*(3.56)$	30	$1.5 \cdot 10^{-41}$	5.7	

*Counting rates at 12 m distance from the neutron source.
Target electrons per ton of organic scintillator.

already been discussed in the preceding chapters. To achieve also a sufficient separation in time, a beam pulse length of less than about 200 ns must be realized with at least about 10 μs intervals between the pulses (see Fig.4).

In order to be able to measure the extremely small cross sections listed in Table 1 within a reasonable period of time, we need a correspondingly great target. The target nuclei or target electrons should, if possible, also be part of the detector for the respective signature of the neutrino reaction. Depending on the problem, different types of detector will be necessary in order to comply with these requirements. The large detectors currently used today in elementary particle physics cannot be simply taken over. The main reason is that the energy available as a signature for beam stop neutrinos is much lower than the energy in neutrino experiments at high-enery accelerators. Related to electrons in the detector the energies for interesting cases lie below about 20 MeV, for the major part of nuclear physics signatures (γ-transitions and β^- (β^+) emissions) even well below 10 MeV. On the other hand, the background both from the source and from cosmic rays increases roughly exponentially towards the smaller energies. For these reasons neutrino experiments at the beam stop have been performed until now only for energies between 25 and 50 MeV /20,21/. Only going down to energies between 3 and 20 MeV offers the possibility of nuclear physics signatures. This would allow for the first time to perform a great number of interesting experiments which could employ over a long period two to three research groups.

The calculations of shielding and background already mentioned above resulted in the proposal of the two detector regions shown in Fig.6. It can be easily seen that the shielding conditions are most favourable for the detector region I (ring bunker below the spallation source).

The calculated total background in that region is lower by a factor of five than in the detector region II. Therefore,

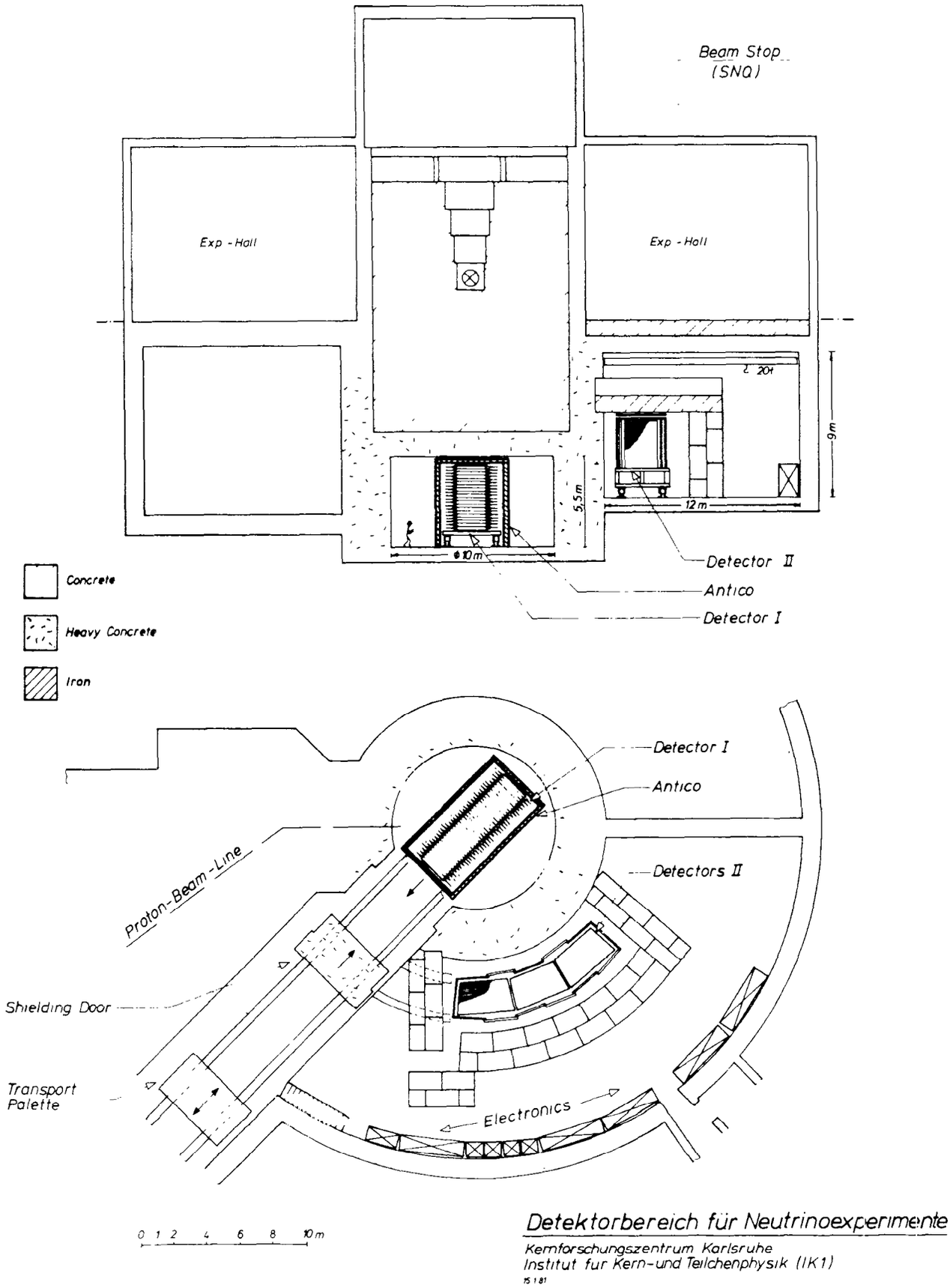

Fig.6: Proposal for the neutrino facility at the spallation source

it is particularly well suited for measurements with low γ- or electron energies. To be able to study the situation in quantitative terms we have selected a practical example of a detector placed in the region I. The target is formed by the ^{12}C nuclei in an organic scintillator. The scintillator is divided into segments consisting of elements of 1.5 m length each with a square cross section of 20 x 20 cm. Each element is supplied with one photomultiplier on both ends. This permits local resolution of about 10 cm along the element. Moreover, the requirement of coincidence of the two photomultipliers acts as an additional noise suppression. To obtain reasonable measuring time, about 50 tons of detector material are necessary.

With these requirements fulfilled,the following numbers of events are expected per mA of averaged current (see also Table 1):

$\nu_\mu + {}^{12}C \rightarrow \nu'_\mu + {}^{12}C^{\dagger}$(15.1 MeV): 24 events/day

$\nu_e + {}^{12}C \rightarrow e^- + {}^{12}N$ -18 MeV: 145 events/day

$\downarrow$

$e^+ + {}^{12}C$+18 MeV

$\nu_e + e^- \rightarrow \nu_e + e^-$: 35 events/day

$\nu_\mu + e^- \rightarrow \nu_\mu + e^-$: 3 events/day

Thus, if one wishes to study mu-neutrino-electron scattering, the total background in an interval of about 10 to 25 MeV must not exceed about one event/day. As shown by the computations, this requirement can be fulfilled with a suitabele time structure at the SNQ spallation neutron source:

1. Background from the spallation neutron source

   The background from the SNQ spallation neutron source at the location of the detector I after having passed through 8 m iron and 1 m borated high-density concrete is shown in Figs. 7 to 9. Details will be presented in /18/. Within the interesting range between approximately 10 - 25 MeV (related to electron energies in the scintillator) a flux in the detector due to background events caused by fast neutrons of about $2 \cdot 10^{-12}/(cm^2 s\ mA)$ is obtained at the SNQ spallation neutron source. For our 50 ton scintillator this means 0.02 event per day per mA. Consequently, the background of the SNQ spallation neutron source can be reduced to negligible values through shielding.

2. The high-energy muon component of cosmic rays is much more penetrating. It can be sufficiently reduced only by combination of a passive with an active shielding. Therefore, in the detector region I, two separate anticoincidence counters will be provided in addition to a passive detector shielding consisting of 20 cm thick iron plates (or a similar lead shielding). After a muon (or electron) has passed through these counters, the whole detector is switched to be insensitive for about 25 µs. In addition it can be made insensitive by the topmost segment layer and by about 10 cm surface layer at the ends of the segments.

More detailed investigations /18/ have shown that a suppression factor of about 10^{-5} by anticoincidence should be possible. In the proposal for an experiment at LAMPF, submitted by T.Y.Ling et al. /16/, even a value of $3 \cdot 10^{-6}$ is assumed for a similar anticoincidence shielding. Disturbing background from cosmic rays is mainly produced by the bremsstrahlung of the muons (or the electrons following them) near the detector shielding. The neutral radiation (true neutrals) still passing through the detector shielding (20 cm iron) is less intense by a factor 10^5 than the bremsstrahlung generated there by muons. Therefore, further

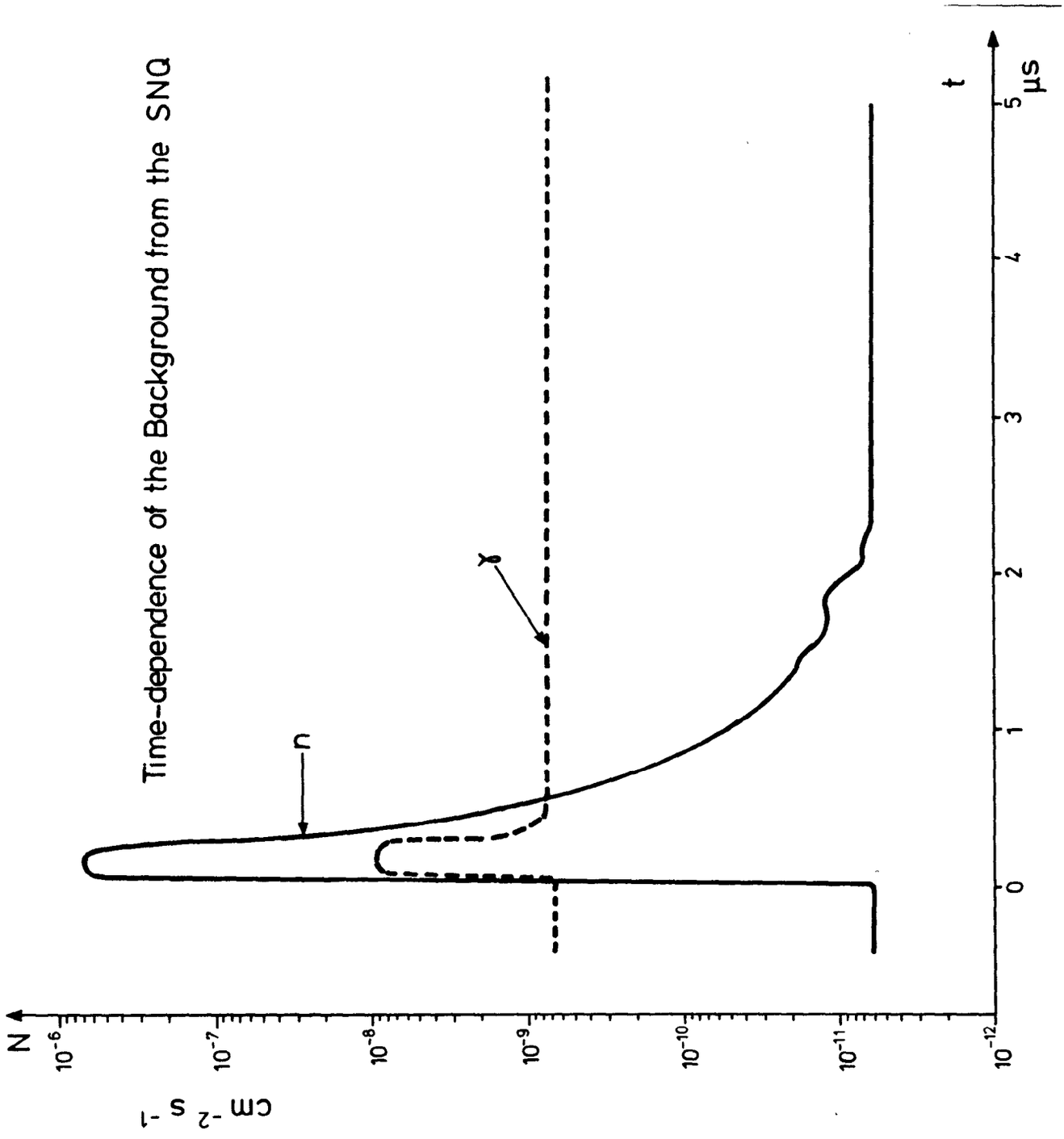

Fig.7: Time dependence of the background from the SNQ spallation neutron source (gammas, neutrons) for $\bar{I}_p$ = 1 mA

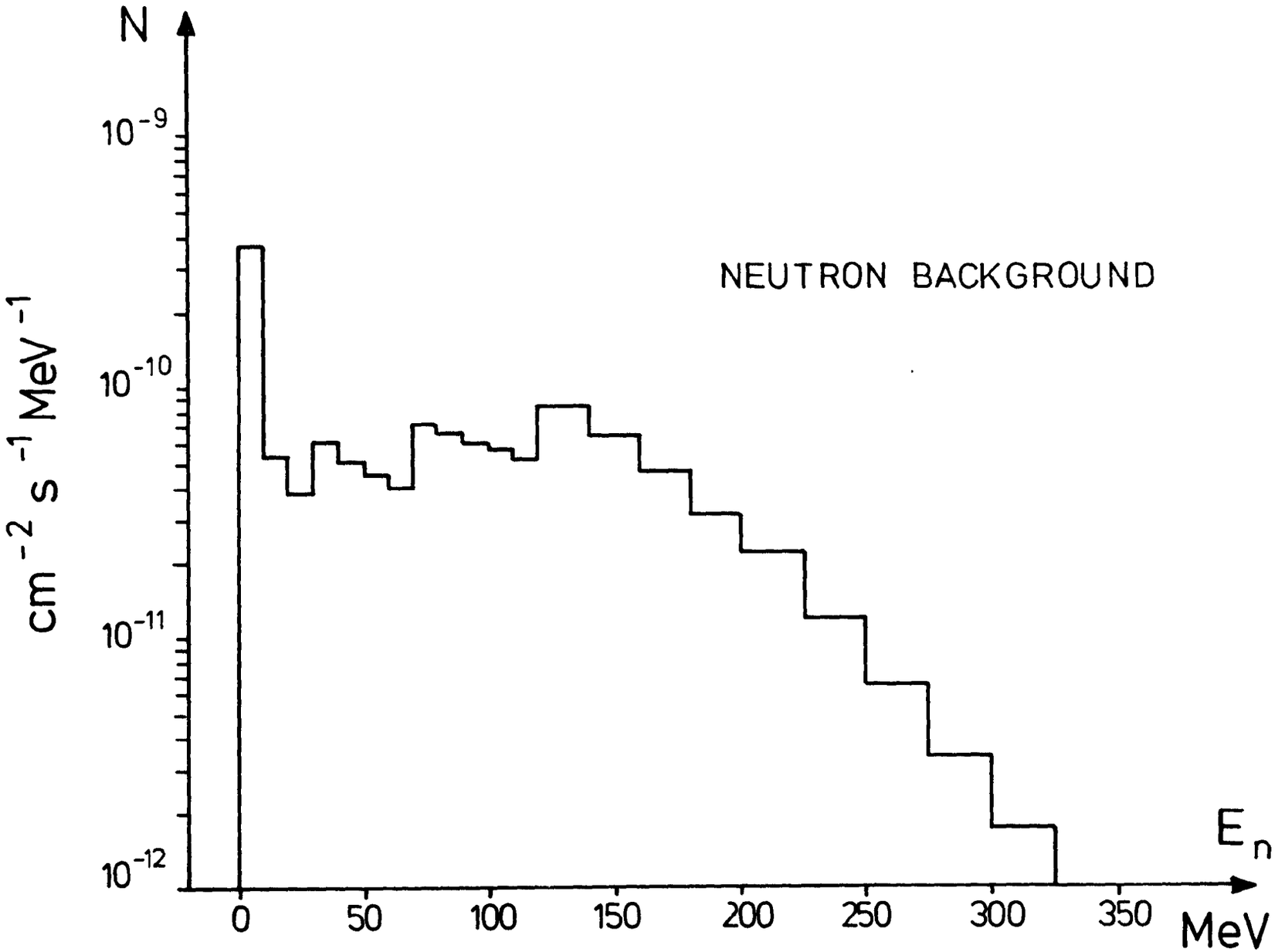

Fig.8: Energy dependence of the neutron background from the SNQ spallation neutron source for $\bar{I}_p$ = 1 mA

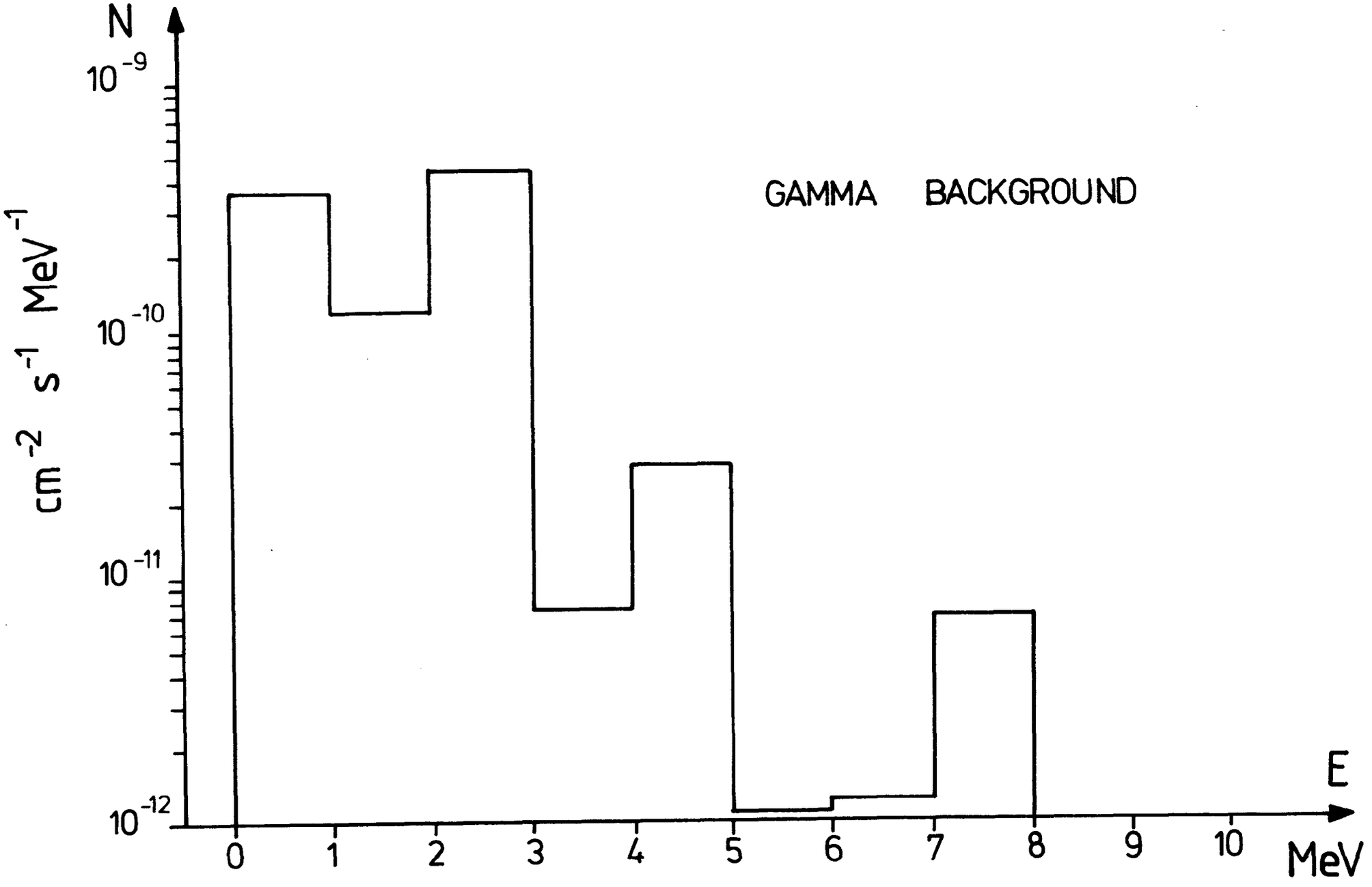

Fig.9: Energy dependence of the gamma background from the SNQ spllation neutron source

optimization of the geometry of the passive and active detector shieldings might be rewarding.

Fig.10 shows the bremsstrahlung background in the detector I converted into electron energies in the scintillator, plotted versus the energy. The individual components are discussed in /18/. The background intensities are higher by approximately the factor three for the detector region II.

For our range of energies of 10 - 25 MeV the cosmic background yields $N_U = 1.5 \cdot 10^6$ events per day, leaving out of consideration the anticoincidence and the duty cycle. With an anticoincidence suppression factor of 10^{-5} we, therefore, expect $N_U = 15 \cdot DF$ per day (DF = duty factor). Consequently, even for the proposed interim solution ($DF = 5 \cdot 10^{-2}$) a background rate of less than 1 event per day can still be expected.

This would be comparable with the rate for neutrino-electron scattering: From Table 1 a rate of 3.7/day is calculated for $\nu_e + e^- \rightarrow \nu_e + e^-$ and 0.3/day for $\nu_\mu + e^- \rightarrow \nu_\mu + e^-$ (based on the averaged current 100 μA attained in the proposed interim solution). In the presence of a storage ring the expected counting rates would be higher by a factor 50 while the background would still be strongly reduced. It is worth mentioning in this context that so far not even the existence of the reaction $\nu_e + e^- \rightarrow \nu_e + e^-$ has been proved.

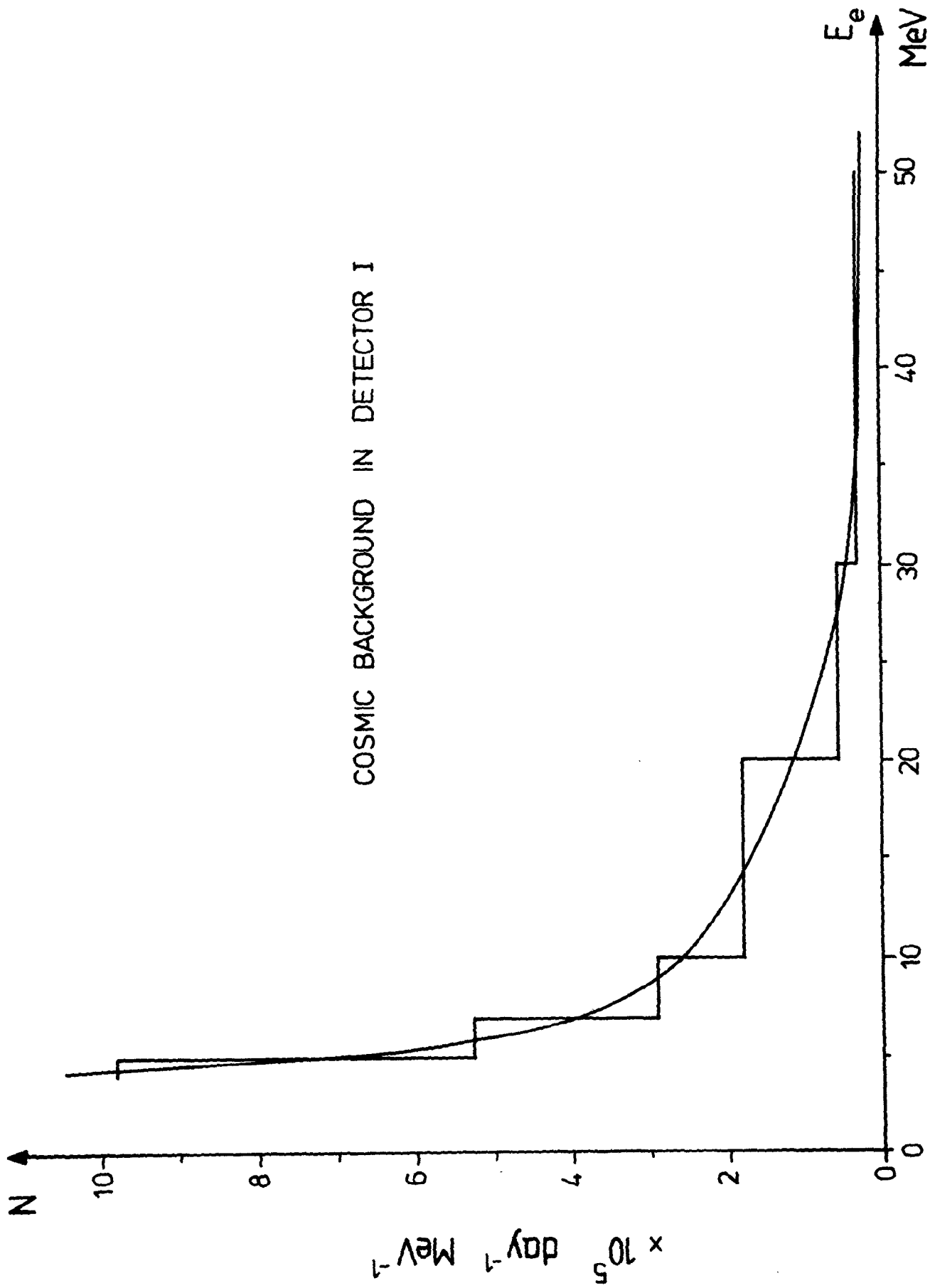

Fig.10: Energy dependence of the cosmic background measured in the detector I

IV. PROPOSAL FOR AN EXPERIMENT TO SEARCH NEUTRINO OSCILLATIONS $\nu_\mu \leftrightarrow \nu_e$ AT THE SPALLATION NEUTRON SOURCE

To demonstrate the extraordinary possibilities for neutrino physics at a high-intensity spallation neutron source associated with a good time structure an experiment will be proposed below for observation of neutrino oscillations $\nu_\mu \leftrightarrow \nu_e$.

If the physical neutrinos ν_μ and ν_e are formed by superposition of two fundamental neutrinos ν_1 and ν_2 having defined masses m_1 and m_2, oscillations $\nu_\mu \leftrightarrow \nu_e$ can occur /1/. ν_μ and ν_e in this case are no longer stationary states, nor do they have defined masses.

The mixture is described by:

$$\nu_e = \nu_1 \cdot \cos\Theta + \nu_2 \cdot \sin\Theta$$

$$\nu_\mu = -\nu_1 \cdot \sin\Theta + \nu_2 \cdot \cos\Theta$$

where Θ is the mixing angle still unknown. If at the time $t = 0$ a pure beam $|\nu_e>$ or $|\nu_\mu>$ starts, a combination of both kinds of neutrino will be found at the time $t = t$. In this case, the probability of transition in terms of quantum mechanics can be calculated as usual /1/. For a constant energy, conversion is possible from time dependence into flight path dependence. This gives for the transition probability:

$$P(x) = \sin^2 2\Theta \cdot \sin^2 \left(\frac{\pi \cdot \delta m^2}{2.48 \cdot E_\nu} \cdot x\right) \quad \text{for } \nu_\mu \rightarrow \nu_e$$

$$P'(x) = 1 - P(x) \quad \text{for } \nu_e \rightarrow \nu_\mu \qquad (15)$$

where Θ = mixing angle, $\delta m^2 = |m_1 - m_2|^2$ in eV^2, E_ν = neutrino energy in MeV, x = distance from the source in m.

We now assume a source pulsed according to Fig.4 i.e., a pulse length of t_p = 200 ns. As shown by Eqs.(10) to (13), the number of muon neutrinos at the source is much greater in the range < 200 ns than the number of electron neutrinos, whilst in the range > 200 ns we find almost exclusively electron neutrinos (except for the muon antineutrinos). This fact can be utilized to define a ratio of measurable counting rates which reacts very sensitively to the oscillation $\nu_\mu \leftrightarrow \nu_e$ but which, on the other hand, is insensitive to instabilities and other systematic errors.

We firstly set up the following counting rates applicable to the reactions with the ^{12}C nuclei in the detector I (50 t scintillator):

$$N_\nu(1) = \frac{\varphi_\nu \cdot N(^{12}C)}{4\pi \cdot 100^2}$$

$$N(^{12}C) = 2.51 \cdot 10^{30} \text{ (target nuclei in the detector)}$$

The expected counting rates at the distance x in meters from the source will then be:

$$N_{\nu_\mu}(x) = \frac{\sigma_{\nu_\mu}}{x^2}(N_{\nu_\mu}(1) \cdot (1-P(x)) + N_{\nu_e}(1) \cdot P(x))$$

$$N_{\nu_e}(x) = \frac{\sigma_{\nu_e}}{x^2}(N_{\nu_e}(1) \cdot (1-P(x)) + N_{\nu_\mu}(1) \cdot P(x)) \qquad (16)$$

For simplification the energy of the mu-neutrinos and of the electron neutrinos will be assumed to be $\langle E_\nu \rangle$ = 30 MeV, σ_{ν_μ} and σ_{ν_e} are the total cross sections:

σ_{ν_μ} for $\nu_\mu + {}^{12}C \rightarrow \nu_\mu' + {}^{12}C^+(15.1)$; σ_{ν_e} for $\nu_e + {}^{12}C \rightarrow e^- + {}^{12}N$

Assuming a proton pulse duration of t_p = 200 ns we now make a distinction between two counting rates each. For the time interval between t = 0 and t = t_p = 200 ns we mark the counting rates from (16) with the index <. For the neutrinos generated after this time interval (200 ns to 8 μs) the index > is used. Inserting numerical values yields:

$$N^{<}_{\nu_\mu}(x) = \frac{1}{x^2}\,(3346(1-P(x))+345\cdot P(x))$$

$$N^{>}_{\nu_\mu}(x) = \frac{1}{x^2}\,(175(1-P(x))+3146\cdot P(x))$$

$$N^{<}_{\nu_e}(x) = \frac{1}{x^2}\,(2067(1-P(x))+20074\cdot P(x)) \qquad (17)$$

$$N^{>}_{\nu_e}(x) = \frac{1}{x^2}\,(18875(1-P(x))+1049\cdot P(x))$$

The numerical values relate to 1 mA averaged current over a period of one day (24 hours) and with 50 to of ^{12}C in the target.

For $\langle E_\nu \rangle$ = 30 MeV it follows from Eq. (15):

$$P(x) = \sin^2 2\Theta\cdot\sin^2(0.042\cdot\delta m^2\cdot x) \qquad (18)$$

and assuming maximum mixing ($\sin^2 2\Theta = 1$):

$$P(x) = \sin^2 (0.042\cdot\delta m^2\cdot x) \qquad (19)$$

From equation (19) follows that for $\delta m^2\cdot x \leq 1$ (e.g. δm^2 = 0.1 eV^2; x=10 m)the transition probability gets proportional to $\delta m^4\cdot x^2$. Thus, the number of converted neutrinos at the distance x ist approximately:

$$N \sim \frac{1}{x^2}\cdot\delta m^4\cdot x^2 = \delta m^4 = \text{constant.}$$

Using the counting rates in (17), the following ratio can be defined:*

$$R(x) = \frac{N^{<}_{\nu_\mu}(x) - N^{<}_{\nu_e}(x) + N^{>}_{\nu_e}(x)}{N^{<}_{\nu_e}(x) + N^{>}_{\nu_e}(x)} \qquad (20)$$

The number $N^{>}_{\nu_\mu}(x)$ was not used because it is difficult to measure. Introducing (17) into (20) gives:

$$R(x) = \frac{20154 - 39883 \cdot P(x)}{20942 + 181 \cdot P(x)} \qquad (21)$$

It can be noticed that the denominator is practically independent of x. Therefore, it can be determined with the smallest possible statistical error for a small distance. If one introduces in addition (19) into (21), one obtains:

$$R(x) = 0.962 - 1.904 \sin^2 (0.042 \cdot \delta m^2 \cdot x) \qquad (22)$$

Since $1 - \sin^2\alpha = \cos 2\alpha$, the following expression applies approximately:

$$R(x) \approx \cos (0.084 \cdot \delta m^2 \cdot x) \qquad (23)$$

The expression (23) reflects the fact that $\tau_\pi << \tau_\mu$. If the number of mu-neutrinos abruptly became zero after the time interval t_p, (23) would apply exactly.

Since in one detector the counting rates in (20) can be measured simultanesously for the same number of target nuclei, the ratio R(x) is relatively insensitive to systematic errors. The statistical error of R(x) can be estimated by:

$$\Delta R(x) \approx \pm \frac{1}{N(x)} \sqrt{R(x) \cdot N(x) + N_U} \qquad (24)$$

---

* see addendum, Appendix A

where N(x) is the denominator of (21) which can be determined with a small error and N_U is the (cosmic) background rate which can be measured conveniently during the beam intervals. As has been shown in chapter III, $N_U \approx 1$/day can be expected.

Fig.11 is a plot of R(x) (x = 12 m, 60 m and 120 m) versus the square of the mass difference. The error bars represent statistical errors to be expected for an averaged current of 1 mA and a duration of measurement period of one year (300 days). A widely used reference variable is the smallest still measureable mass difference for a maximum mixture. This minimum mass difference can be read from Fig.12.

It appears that for an averaged current of 5 mA the lower limit of the still measureable mass difference of neutrinos lies at $\delta m^2(\min) = 0.03\ eV^2$. However, this extremely small value can be attained only in the presence of a storage ring. The minimum values roughly depend on the square root of the averaged proton current at the spallation neutron source. One obtains e.g. $\delta m^2(\min) = 0.06;\ 0.2\ eV^2$ for $\bar{I}_p = 1;\ 0.1$ mA.

These numbers must be compared with the limit of $\delta m^2 \approx 1\ eV^2$ obtained from very lengthy and difficult high-energy and reactor experiments /15,22,23/. Even with the proposed interim solution with $\bar{I}_p = 100\ \mu A$, this value could be measured at the spallation neutron source within about ten days of measurement time with an error of only about $\pm\ 0.25\ eV^2$.

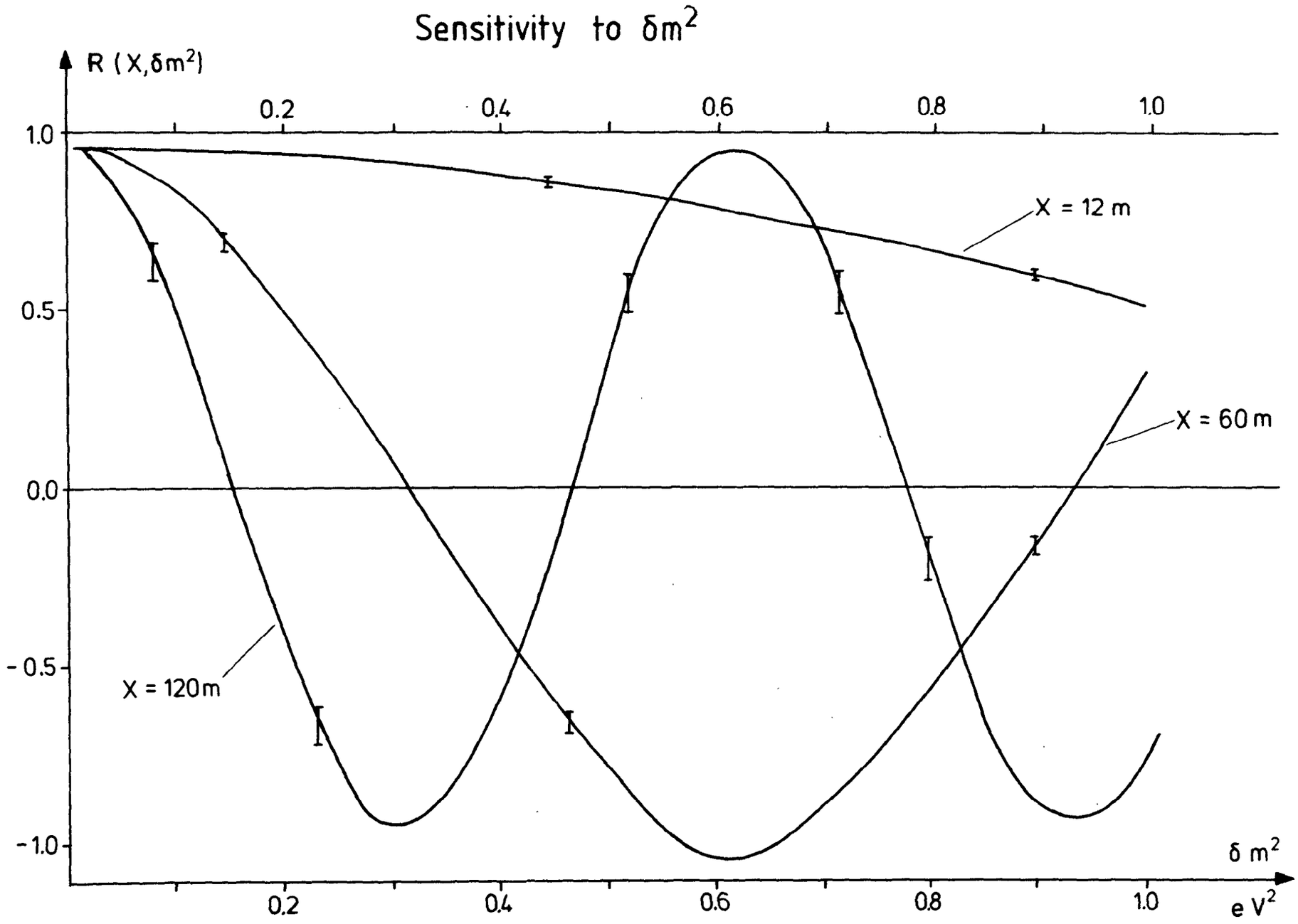

Fig.11: Dependence of the ratio R(x) on the mass difference of the neutrinos for different distances from the source. The error bars apply to a period of measurement of one year at 1 mA proton current

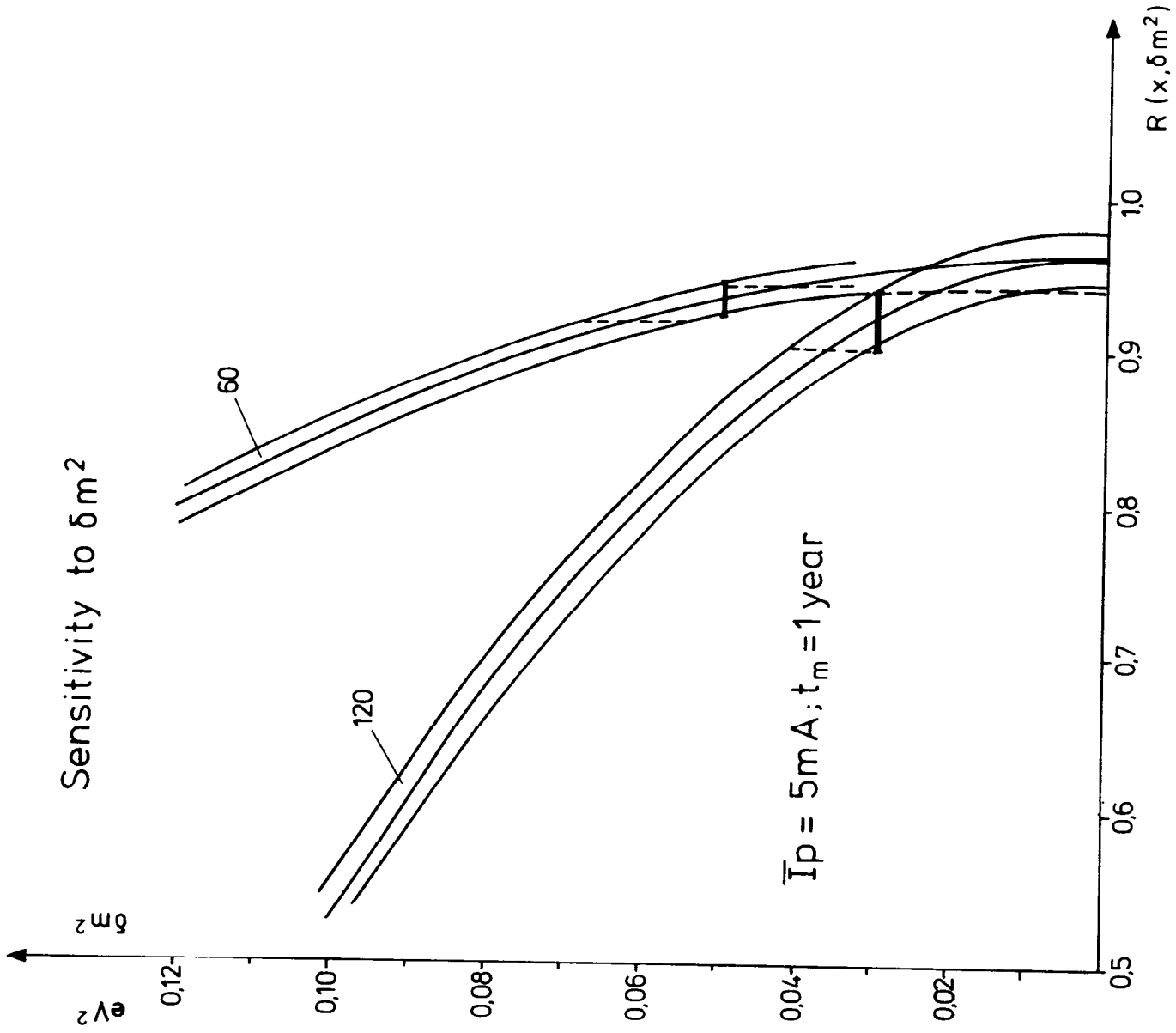

Fig.12: Sensitivity of the ratio R(x) to δm^2 for the distance 120 and 60 m for a period of measurement of one year at 5 mA averaged current.

REFERENCES

1. For a review, see
S.Bilenky and B.Pontecorvo
Phys.Reports 41, 225 (1978)

2. H.Faissner
Experimente zur schwachen und halbschwachen Wechselwirkung an der 1.1 GeV Spallationsquelle (Januar 1981)
Priv. Communication and to be published

3. S.Weinberg
Phys.Rev. Lett.19 (1967) 1264
A.Salam
Elementary particle theory (Stockholm 1969)

4. H.Faissner et al.
Phys.Rev.Lett. 41(1978) 213

5. N.Armenise et al.
Phys.Lett. 86B (1979) 225

6. H.Chen, F.Reines
A Study of Neutrino Electron Elastic Scattering at LAMPF,
Status Report UCI-Neutrino No.39, UCLA, Irvine (April 1980)

7. Conf.Rep. Neutrino "78", Purdue University (1979)

8. Proc. Intermediate Energy Physics at LAMPF, Neutrino-Induced Interactions, Paneldiscussion P-3, Los Alamos Publ., LA-8335-C, Vol.1-3, 1979

9. T.W.Donnelly and R.D.Peccei
Neutral Current Effects in Nuclei, Phys.Rep. 50 (1979) 1-85

10. T.W.Donnelly et al.
Phys.Rev. D18 (1979) 1607

11. S.Weinberg
Phys.Rev.Lett 40 (1978) 223

12. H.Faissner
Neutrino "80", Erice (in press)

13. H.Faissner et al.
Phys.Lett., to be published

14. C.J.Batty, K.Green
Some Additional and Alternative Uses of the Spallation Neutron Source. Report Rutherford Lab. RL-78-018/A, 1978

15. T.Bowles, T.Dombeck and R.Burman
A Search for Oscillations using Muon-Neutrinos, LAMPF-Proposal Nr.638 (1980)

16. T.Y.Ling et al.
A Search for Neutrino-Oscillations at LAMPF, Report of the Ohio State University and LASL (1980)

17. H.H.Chen
Use of the UCI/LASL Detector to Search for Neutrino Oscillations. Report UCLA Irvine UCI-Neutrino No.44 (1980)

18. T.Gabriel, J.Wilczynski and B.Zeitnitz
Neutrinophysics at an Intense Spallation Neutron Source II KfK-Report, to be published

19. H.Fischer
Neutrinoflüsse aus dem Pion-Zerfall und dem Müon-Zerfall bei verschiedenen Pion-Pulslängen; Feasibility Studie zur Spallationsneutronenquelle, Speicherring S.
(Private Mitteilung)

20. S.E.Willis et al.
Neutrino Experiment to Test the Nature of Muon-Number Conservation, Phys.Rev.Lett. 44 (1980) 522
see also errata: Phys.Rev.Lett. 45 (1980) 1370

21. S.E.Willis
Thesis, LASL-Report LA-8030-T (1980)

22. V.Barger
Talk at Neutrino Mass Mini-Conference, Telemark, Wisconsin, University of Wisconsin, Preprint COO-881-135 (1980)

23. H.Kwon
Talk at Neutrino Mass Mini-Conference, Telemark
F.Boehm et al.
Cal.Inst.of Tech., Preprint 5P-80-115 (1980)

B.Zeitnitz, June 1981

Addendum to KfK-Report 3155, page 32

Neutrino Physics at the Spallation Neutron Source

In the meantime there was some discussion on the "best" ratio of numbers to be extracted from the proposed measurements. Indeed, the number $N^{<}_{\nu_\mu}(x)$ as defined in eq.(17) (and used in eq.(20)) is not directly measureable. The reason is that the neutrinos "oscillated" from ν_μ to ν_e will give a neutral current contribution to inelastic scattering from ^{12}C which cannot be separated experimentally.

Therefore, if one wants to avoid recalculated numbers in eq.(20) one should use separate ratios like:

$$R_1(x) = \frac{N^{>}_{\nu_e}(x) - N^{<}_{\nu_e}(x)}{N^{>}_{\nu_e}(x) + N^{<}_{\nu_e}(x)} \; ; \; R_2(x) = \frac{N^{<}_{\nu_e}(x)}{N^{<}_{\nu_\mu+\nu_e}(x)} \quad \text{etc.}$$

Using the information of $R_1(x)$ only, the equivalent of eq.(23) is:

$$R_1(x) \approx 0.8 \cdot \cos(0.084 \cdot \delta m^2 \cdot x)$$

Therefore, the following arguments in the paper stay essentially valid already for that part of the experimental information used in $R_1(x)$.

Jül-Conf-45 B5

I C A N S - V
MEETING OF THE INTERNATIONAL COLLABORATION ON
ADVANCED NEUTRON SOURCES
June 22-26, 1981

MODELS AND COMPUTATIONAL METHODS IN THE THEORETICAL TREATMENT OF SPALLATION NEUTRON SOURCES

T.W. Armstrong* and D. Filges

Kernforschungsanlage Jülich GmbH
Inst. f. Reaktorentwicklung
Postfach 1913
D-5170 Jülich
Federal Republic of Germany

*Consultant
P.O. Box 2807
La Jolla, California 92038, U.S.A.

Abstract:

The main aims of this review paper are: 1) to give an overview of the theoretical methods and physics models that are currently being applied in investigating various aspects of spallation neutron sources, 2) to illustrate the capabilities of present methodology with a few sample applications, and 3) to summarize some preliminary results of model validation studies that are in progress.

1. INTRODUCTION

For spallation neutron source applications, we are interested in theoretical methods that are capable of predicting a variety of different quantities related to radiation fields produced by proton beams (≈0.5 - 1 GeV) and their associated effects, both in the vicinity of the target station and from beam losses which occur in the accelerator (Table 1). It is also desirable that such calculational models be sufficiently general to allow investigations of potential applications of spallation sources for purposes in addition to providing an intense low-energy neutron source (e.g., utilization as irradiation facility for radiation effects research, high-energy nuclear physics studies, research related to transmutation and power generation, etc.) To satisfy these needs requires rather general calculational methods which can incorporate numerous physics modules for treating the various types of interaction mechanisms that take place, and which are capable of accommodating complex geometries and material configurations. This necessarily leads to large Monte Carlo computer codes, which is the type of calculational method considered in this paper.

For spallation source applications, there are basically four categories of particle interactions which must be taken into account when high-energy proton beams bombard thick targets: 1) atomic processes, 2) high-energy ($\gtrsim$15 MeV) nonelastic nuclear collisions ("spallation"), 3) pion and muon decay, and 4) the effects of low-energy ($\lesssim$15 MeV) neutron interactions. For the proton beam energy range of interest, the secondary particles produced in a single spallation collision proceed to undergo subsequent collisions, generating a multiplicity of particles inside the target material, which is illustrated schematically in Fig. 1. This process is generally referred to as a "hadronic cascade", since it is the hadrons (in this case: neutrons, protons, and charged-pions) which are effective in the "radiation transport" through the target material. The phenomenology involved has been studied previously in a number of different application areas (e.g. /1/).

Thus, we are interested in theoretical methods which can predict the details of such hadronic cascades in thick targets of various compositions and geometries. There are essentially three hadronic transport computer codes that have been written which are capable of detailed predictions: the code of Barashenkov, et al. (Dubna, USSR) /2/, the Ranft code (Karl-Marx Univ., GDR) /3/, and the HETC code /4/. In all of the current studies related to spallation neutron source facilities, HETC (or an earlier version called NMTC /5/) is the code that has been used, and it is this code which is discussed here.

Some basic features of the HETC code are summarized in Table 2. The main HETC physics models are discussed in the next section; further details can be found in /6/ and /7/.

2. MODELS AND COMPUTATIONAL METHODS

2.1 HETC Code: Physics Models

The methods used in HETC for treating atomic interactions are outlined in Table 3. These interactions are described using rather standard formulae and procedures, and the physics uncertainties are small, so they will not be discussed in detail here.

The most difficult step in the prediction of hadronic cascades lies in determining the description (energy, angle, and multiplicity) of the secondary particles resulting from spallation collisions, and this is the source of the largest physics uncertainties in hadronic cascade predictions. In HETC, a theoretical model is used, the intranuclear-cascade-evaporation (INCE) model, in which the spallation collision is considered to proceed in two phases: 1) a "fast" phase, in which the incident particle interacts with individual nucleons inside the nucleus, producing a particle cascade inside the nucleus, and 2) a "slow" phase, in which the remaining nuclear excitation energy is distributed among all nucleons and dissipated by further

particle emission. This second phase can be described by applying a statistical evaporation model.

Intranuclear Cascade Model

The INC model, as implemented in the form of a computer code (MECC-7) by Bertini, et al. /8/ is incorporated as a subroutine in the HETC code. The major steps of the calculation are summarized in Figure 2; further details are given in /8/ and /9/.

For pion production (production threshold ~400 MeV), the Sterheimer-Lindenbaum isobar model /10/ is used, in which nucleon-nucleon or pion-nucleon collisions inside the nucleus are assumed to form an "isobar", or excited nucleon system. To determine the energy and direction of pions and nucleons emitted by the isobar, empirically determined angular distributions are specified.

The main input data required for applying the INC model are free particle-particle cross sections. Twenty-two cross sections sets, based on measured data, are input to the HETC code (Table 4). With these particle-particle cross sections and the INC model, collision products for essentially any type of target nucleus can be computed for spallation collisions which occur during the hadronic cascade. This is an important feature of the HETC calculational approach because particle-nucleus data, over the wide parameter range needed for spallation neutron source applications, is not available experimentally.

Evaporation Model

The residual mass number, charge number, and residual excitation energy after the INC are used as input for an evaporation calculation to determine further particle emission. The basic theory is that of Weisskopf /11/ as implemented by Gutherie /12/. The output of this phase of the calculation is emitted particle spectra (neutrons, protons, deuterons, tritons, ^{3}He, and alpha particles), the

type (A and Z) of residual nucleus and its recoil energy, and the final excitation energy, which is assumed to be released by γ-ray emission.

High-Energy Fission

For high energies ($\gtrsim$100 MeV) and high-mass target nuclei, there is competition between evaporation and fission at each step of the nuclear de-excitation process. For example, for collisions with uranium, fission occurs about 80% of the time at the some stage in the de-excitation chain. Statistical models can be applied to determine the parameters for the fission fragments immediately after fission, and the usual evaporation model applied to determine post-fission particle emission from each fragment (Fig. 3). Recently, several high-energy fission models have been developed for use in the HETC code /13-16/. (Calculations have recently been made at KFA to compare several of these models; this work is discussed in separate papers.)

HETC Treatment of Pion and Muon Decay

Neutral pions have a very short half-life (Table 5) and are assumed to decay at the spallation collision site where created. At the beam energies applicable for spallation neutron sources ($\lesssim$ 1 GeV), neutral pion production is small, and the decay γ-rays are normally neglected.

For charged pions "in-flight" (i.e., before coming to rest due to ionization energy losses), both decay and nuclear collisions are taken into account. Positively charged pions which come to rest are assumed to decay. Negatively charged pions which stop may be selected to decay or undergo nuclear capture, depending on the setting of an input option; the appropriate choice depends upon the density of the target material.

Pion decay in-flight is determined by defining a "macroscopic decay cross section", which is analogus to the

macroscopic cross section used for nuclear collisions (Table 5). The relative probability of decay versus collsion is then selected according to the magnitude of these two cross sections.

If the option is specified that negative charged pions become captured when stopped, the capture products are computed using the INCE model, with the initial excitation corresponding to the rest-mass energy of 140 MeV. For media containing more than one (non-hydrogen) element, the identity of the capturing nucleus is selected proportional to the electron density of the element in the mixture.

2.2 Low-Energy Neutron Transport and Analysis (10^{-5} eV-15 MeV)

The INCE model discussed above is not applicable to low-energy ($\lesssim$15 MeV) nuclear collisions. Charged particles produced $\lesssim$15 MeV in spallation collisions have short ranges and predominately come to rest before having further nuclear collisions, so usually only the low-energy neutrons produced need to be further transported. The inapplicability of the theoretical INCE model to low-energy neutron collisions is not a problem because there are large data bases of experimental nuclear cross sections available for low-energy neutrons for a wide range of target nuclei as result of extensive fission reactor and fusion research, so it is not necessary to resort to a theoretical collision model as at higher energies. Furthermore, for low-energy neutrons, there have been numerous transport computer codes developed and tested. The HETC code provides a complete descriptiion (energy, angle, and spatial distributions) of the low-energy neutrons produced in spallation collisions, which allows HETC to be coupled with any of the available low-energy transport codes.

General Requirements

A rather detailed treatment of the low-energy neutron transport is required (Table 6) since we are, in general, interested in accurate predictions of the spatial,

time, and spectral dependence. Thus, while there is some choice of low-energy transport codes which can be coupled with HETC for spallation neutron source applications, some consideration must be given to insure that the particular code and options used have the features and physics treatments for the particular results of interest.

Low-Energy Transport Codes

There are two basic types of low-energy neutron and gamma-ray transport codes that have been developed (Table 7): a) those that numerically solve the Boltzman transport equation by quadrature (discrete ordinates codes), and b) those that use stochastic methods (Monte Carlo codes). For applications where target geometries can be adequately simulated in one or two dimensions, the discrete ordinates codes usually require less computation time, especially in obtaining time-dependent results. The Monte Carlo codes are capable of simulating very complex, three dimensional target configurations. Both types of codes can be interfaced with HETC.

For the low-energy transport calculations related to the German SNQ study, the MORSE code /17/ has been used because of its general capabilities and because several useful analysis codes are available for use with MORSE. Also, MORSE is a "coupled" neutron/gamma-ray transport code-i.e., the gamma-rays created during the neutron transport from $(n,n'\gamma)$ and (n,γ) reactions are also transported, which is important for heating estimates. Other codes that have been used for spallation neutron source applications are O5R and TIMOC (at Rutherford and Appleton Laboratories for the SNS) /18,19/ and VIM (at Argonne for the IPNS).

Analysis Codes

Some features of support codes that are available for interfacing with the radiation transport codes for special analyses and results are listed in Table 8. The

SIMPEL code /20/ is a rather general analysis code that has been written at KFA to provide various results of interest from the events which occur during the HETC transport calculation.

Cross Section Codes

Cross section generation codes are used to: a) read the neutron and gamma-ray cross section data at discrete energy values from data bases and output them in a multigroup format compatible with requirements of the low-energy transport codes, and b) generate from the data bases specific "response functions" (e.g., kerma factors for obtaining energy deposition), which can then be folded with the flux spectra computed by the transport codes to obtain particular results of interest. Examples of such codes which are used at KFA are given in Table 9.

Cross Section Libraries

Evaluated cross-section data bases for neutrons and gamma-rays which are maintained at KFA and applicable to spallation neutron source applications are indicated in Table 10. For the SNQ study /21/, we have used two libraries. The EPR library has been used for energy deposition calculations since this is a coupled library and allows the heating from gamma-rays to be taken into account. However, the EPR library contains only one thermal neutron group. Therefore, for computing detailed neutron spectra from the moderators, we have used the RSYST-53 library, which has a fine group structure at low neutron energies (26 groups below 1 eV) and allows upscattering.

2.3 Summary of Calculational Proceedure

The major steps of a general calculational proceedure, using the state-of-the-art computer codes discussed above, for making theoretical estimates related to spallation neutron source applications are summarized in Fig 4, and this is the basic method that has been usd in the SNQ study /21/.

The main physics input data required are: a) particle-particle ((n,n),(n,p),(π,p),etc.) cross sections and nuclear masses for the high-energy transport, and b) low-energy (≲15 MeV) neutron and gamma-ray cross sections, which can be obtained from extensive measurements and data bases created from fission and fusion research.

Two Monte Carlo radiation transport models are used, one for the transport of high-energy (≳15 MeV) hadrons and muons and one for low-energy (≲15 MeV) neutron and gamma-ray transport. The high-energy model treats atomic interactions, particle-nucleus collisions, and particle decay. A theoretical model is used to obtain the secondary particles created in high-energy nuclear collisions, and this is the largest source of uncertainty in such predictions. While not a necessity, it is very convenient to have common geometry modules as part of both transport codes so that the same geometry and material descriptions can be used as input. For the version of the HETC code used at KFA, a "combinatorial geometry" module has been incorporated, which allows complex three dimensional target configurations to be simulated using logical commands to "combine" various simple bodies. This is the same type of geometry module contained in the standard version of the MORSE code.

The output of the transport calculations is mainly a stored data set (on disk or magnetic tape) containing a record of all "events" (nuclear collision, material boundary crossings, etc.) which occurred during each particle "history" of the Monte Carlo transport computation. Separate "analysis" codes are then used to read these data and compute various problem-dependent results of interest. While these codes are usually simple conceptually, and in a sense perform only "numerical bookkeeping" tasks, they can, in practice, be rather large and represent a substantial part of the overall programming time required.

While the method outlined in Fig. 4 is rather time consuming to carry out, both in terms of programming effort

and computer time, it has general capabilities for target and beam parameter simulation, and it can provide essentially all of the physics output quantities of interest for spallation neutron source studies.

3. EXAMPLES OF MODEL APPLICATIONS: SNQ STUDY

The calculational method described above has been applied recently as part of a German study (designated SNQ, for "Spallations Neutronen Quelle") to investigate the feasibility of spallation neutron sources for obtaining intense thermal neutron beams for solid state physics research. A report describing these calculations for the SNQ target station has recently been written /21/, and some initial results were presented previously at the ICANS-IV Meeting /22/. Here, we present only a few of these results as example applications of the models.

3.1 Target Configuration and Beam Parameters

The target configuration was simulated in the calculations as shown in Fig 5. All of the components indicated were modeled in three-dimensions, with all major material regions accounted for. The beam parameters assumed and the type of results computed are given in Table 11.

3.2 Example Results

Table 12 gives the calculated thermal flux values from the water moderator at several locations. The calculated flux value at the end of the 6 meter long beam tube has also been converted to an "equivalent isotropic flux", which is a commonly used basis for comparison in relating the neutrons measured at the end of a beam tube to the magnitude of the thermal neutron source. As indicated, the calculations predict fluxes slightly higher than the goal set for the SNQ reference design. The time -averaged thermal neutron flux in the D_2O tank (at a distance of ≈10-20 cm from the tank bottom (corresponding to the spatial maximum) is computed to be 7.0×10^{14}n cm^{-2} s^{-1} for 5mA average beam current.

While the SNQ reference design contains lead as the spallation material, a few calculations have been made for uranium also. Table 13 compares the target heating for lead and uranium for both the average energy deposition rate (i.e., time-averaged over the beam pulse structure) and the peak deposition rate (during a single pulse). For lead the average heating rate (inside the volume of the target "wheel") is about one-half of the incident beam power of 5.5 megawatts, with U-238 a factor ≈ 4 higher, and natural uranium a factor of ≈ 6 higher. The ratio of peak heating rates for uranium compared to lead are less than the ratios for the average heating rates. This is because of the different spatial distributions for the heating due to the different relative contributions of high-energy particles and low-energy neutrons.

The mass distributions for Pb and U-238 as target materials are shown in Fig. 6. These results correspond to the number of residual nuclei produced, over the total target material region, having a given mass number, and include both stable and radioactive nuclides. These results were computed using the HETC code for the high-energy spallation and fission products (incorporating the model of Atchison /13/ to obtain mass distributions of fission fragments from U-238 high-energy fissioning) and the MORSE and ORIGEN /23/ codes to obtain the mass distributions for low-energy ($\lesssim 15$ MeV) fissioning. Also shown in Fig. 6 is the small amount of spallation products from the oxygen of the coolant water and the aluminum cladding contained in the target material region. The main point from Fig. 6 is that the induced radioactivity from a uraniun target is inherently larger (roughly a factor of 10) than for a lead target because of both high-energy and low-energy fissioning, and the production of particular radioactive species can be very different due to the different product mass distributions.

4. MODEL VALIDATIONS

Table 14 lists experiments that have been carried out for spallation neutron source investigations, and a brief indication of the quantities measured, target materials considered, and proton beam energies used /19,25-30/. For all of the experiments, comparisons have been made with HETC (or NMTC) code calculations; a summary of most of these comparisons is given in /21/. As part of the SNQ feasibility study, a series of experiments (Table 15) has been carried out to provide data for arriving at a reference design and to provide more extensive data for model validation. The data analyses and theoretical predictions for comparisons are not yet completed, but some preliminary comparisons have been made /21/, and a few of the results are summarized here.

Bauer, et al. /24/ have made measurements of the thermal neutrons at the end of a beam tube for 600-MeV proton bombardment using a geometry and material configuration (Table 16) which is close to the reference design model (shown previously in Fig. 5) assumed for the SNQ calculations discussed above in Section 3. For comparison with the calculations, we assume that the experiment for a 600-MeV beam energy when normalized to 10 mA beam current is approximately equivalent to the calculated beam parameters of 1100 MeV and 5 mA. (Theory and measurements show that, in this energy range, neutron production is proportional to beam energy.) A comparison of the measured and calculated thermal neutron fluxes (in terms of equivalent isotropic flux) for both H_2O and D_2O moderators is shown in Table 16. (The calculated values are the same as given previously in Table 12.) The agreement for this single comparison (within about 10%) is perhaps better than generally expected from present state-of-the-art theoretical methods. Nevertheless, this comparison provides some confidence in the calculations made for the SNQ reference design configuration model for one of the important quantities (thermal neutron output) related to assessing physics feasibility.

As part of the SNQ study, Cierjacks and co-workers of KfK have measured the neutron spectra escaping at various angles from thick, bare targets bombarded by high-energy proton beams /31/. For one case (measured spectrum at 90 degrees from a bare, cylindrical lead target 10 cm diameter and 60 cm long, 590-MeV proton beam), we have made HETC and MORSE calculations for comparison (Fig. 7). The theoretical predictions substantially underpredict the neutron spectrum at high energies (e.g., factor of about 5 at 100 MeV). (Initial comparisons with measurements of Cierjacks et al. for thin targets show a similar trend at high energies /32/) The thermal neutron fluxes in the moderators are not essentially affected by this high-energy region of the spectrum. However, high-energy neutrons are important for shielding estimates and in predicting the heating of components near the target wheel (e.g., cold-source heating). Additional calculations and comparisons are planned to try to resolve what is presently an apparently large discrepancy between theory and experiment.

Other code validation comparisons being made in the SNQ study are discussed in /21/, and a summary of the present status is given in Table 17. Also, preliminary results related to the evaluation of high-energy fission models for use in the HETC code are reported in /33/ and /34/.

5. PRESENT STATUS OF THEORETICAL MODELS FOR SPALLATION NEUTRON SOURCE APPLICATIONS

To put the present status of theoretical methods in perspective, Fig. 8 indicates the major theoretical and experimental events which have taken place. The computer codes being used today were developed some years ago, primarily for studying accelerator shielding and the shielding of manned spacecraft from cosmic radiation. However, the codes were sufficiently general to be applicable to neutron spallation source problems, and are being used for these purposes today in their original form.

Experimentally, some measurements of neutron spectra were made in the design of the WNR facility at Los Alamos, but the main experimental data for guidance in spallation source design until recently were the Cosmotron target yield data of Fraser et al. /25/, which were taken over 15 years ago. On this time scale, only rather recently have data become available from various spallation source projects to allow any extensive evaluations of the theoretical models.

To date, several theoretical/experimental comparisons have been made and definitive quantitative evaluations and weaknessess of the theory are emerging, but no modifications of the models have yet been made.

Hopefully, this research will continue to better define the theoretical uncertainties and to identify particular features of the present models which can be updated and improved. This should then allow accurate theoretical models to be applied for assessing, and optimizing, spallation neutron source performance, and to be used as reliable computational tools to aid in the engineering design and safety analyses of such facilities.

REFERENCES

1. T.W. Armstrong, "Introduction to Hadronic Cascades", Chapter 18 in Computer Techniques in Radiation Transport and Dosimetry, W.R. Nelson and T.M. Jenkins (Editors), Plenum Press, New York, (1980).

2. V.S. Barashenkov, N.M. Sobolevskii, and V.D. Toneev, "The Penetration of Beams of High-Energy Particles Through Thick Layers of Material", Atomnaya Energiya 32, 217 (1972).

3. J. Ranft, "Estimation of Radiation Problems Around High Energy Accelerators Using Calculations of the Hadronic Cascade in Matter", Particle Accelerators 3, 129 (1972).

4. T.W. Armstrong and K.C. Chandler, "HETC - A High Energy Transport Code", Nucl. Sci. and Engr. 49, 110 (1972).

5. W.A. Coleman and T.W. Armstrong, "NMTC - A Nucleon - Meson Transport Code", Nucl. Sci. and Engr. 43, 353 (1971).

6. T.W. Armstrong, "The HETC Hadronic Cascade Code", Chapter 23 in Computer Techniques in Radiation Transport and Dosimetry, W.R. Nelson and T.M. Jenkins (Editors), Plenum Press, New York, (1980).

7. T.W. Armstrong, R.G. Alsmiller, Jr., K.C. Chandler, and B.L. Bishop, "Monte Carlo Calculations of High-Energy Nucleon-Meson Cascades and Comparison with Experiment", Nucl. Sci. Engr. 49, 82 (1972).

8. H.W. Bertini, Phys. Rev. 188, 1711 (1969).

9. T.W. Armstrong, "The Intranuclear Cascade Evaporation Model", Chapter 20 in Computer Techniques in Radiation Transport and Dosimetry, W.R. Nelson and T.M. Jenkins (Editors), Plenum Press, New York, (1980).

10. R.M. Sternheimer and S.J. Lindenbaum, Phys. Rev. 123, 333 (1961).

11. V. Weisskopf, Phys. Rev. 52, 295 (1937).

12. M.P. Guthrie, "EVAP-4: Another Modification of a Code to Calculate Particle Evaporation from Excited Compound Nuclei", ORNL-TM-3119 (1970).

13. F. Atchison, "Spallation and Fission in Heavy Metal Nuclei Under Medium Energy Proton Bombardment", Proc. of Mtg. on Targets for Neutron Beam Spallation Sources (G.S. Bauer, Ed.), Jülich, W. Germany, Jül-Conf-34, (January 1980).

14. F.S. Alsmiller, et al., " Calculated Particle Production Spectra and Multiplicities from Nucleon-Fissile Element Collisions at Medium Energies", Proc. of the International Conference on Nuclear Cross Sections for Technology, Knoxville, Tennessee, (October 22-26, 1979).

15. H. Takahashi, "Fission Reaction in High-Energy Proton Cascade", Symposium on Neutron Cross-Sections from 10 to 50 MeV, Brookhaven National Laboratory, Upton, N.Y. (May 12-14,1980)

16. Y. Nakahara, "Studies of High-Energy Spallation and Fission Reactions", ICANS-IV Meeting, KEK National Laboratory for High-Energy Physics, Tsukuba, Japan (October 20-24, 1980).

17. M.B. Emmett, "The MORSE Monte Carlo Radiation Transport Code System", ORNL-4972 (1975).

18. F. Atchison, "A Theoretical Study of a Target Reflector and Moderator Assembly for SNS", Rutherford and Appleton Laboratories, RL-81-006, April 1981.

19. A.D Taylor, "Neutron Transport from Targets to Moderators", Meeting on Targets for Neutron Beam Spallation Souces (G.S. Bauer, Ed.), Julich, W. Germany, Jül-Conf-34, (January 1980).

20. SIMPEL "Analyse-Code zur Auswertung von HETC Ereignisfolgen", (KFA-Bericht in Vorbereitung).

21. T.W. Armstrong, P. Cloth, D. Filges, and R.D. Neef, "Theoretical Target Physics Studies for the SNQ Spallation Neutron Source", Jul-Spez-120, July 1981.

22. D. Filges, et al., "Theoretical Studies Related to Spallation Target Physics", Proc. of the 4th Meeting of International Collaboration on Advanced Neutron Sources (ICANS-IV), KEK National Laboratory for High Energy Physics, Tsukuba, Japan, Oct. 20-24, 1980.

23. M.J. Bell, "ORIGEN - The ORNL Isotope Generation and Depletion Code", ORNL-43628 (May 1973).

24. G.S. Bauer, "Layout of the Target Station for the German High Power Spallation Neutron Source Project", ICANS-IV Meeting, KEK National Laboratory for High Energy Physics, Tsukuba, Japan (October 20-24, 1980).

25. J.S. Fraser, et al.: "Neutron Production in Thick Targets Bombarded by High Energy Protons", Phy. in Canada 21,17 (1965).

26. G.A. Bartholomew and P.R. Tunnicliffe (Editors): "The AECL Study for an Intense Neutron-Generator (Technical Details)", Atomic Energy of Conada Limited, Chalk River, Ontario, AECL-2600, (July 1966).

27. L.R. Veeser, R.R. Fullwood, A.A. Robba, and E.R. Shunk, "Neutrons Produced by 740-MeV Protons on Uranium", Nucl. Instr. Meth. 117, 509 (1974).

28. J.M. Carpenter, et al., "Summary of Results from the ZING-P' Pulsed Neutron Source", Proc. of the 4th Meeting of International Collaboration on Advanced Neutron Sources (ICANS-IV), KEK National Laboratory for High Energy Physics, Tsukuba, Japan, Oct. 20-24, 1980.

29. G.J. Russell, et al., "Measurements of Spallation Target-Moderator Reflector Neutronics at the Weapons Neutron Research Facility", Proc. of the 4th Meeting of the International Collaboration on Advanced Neutron Sources (ICANS-IV), KEK National Laboratory for High Energy Physics, Tsukuba, Japan, Oct. 20-24, 1980.

30. P. Garvey, "Neutron Production by Spallation in Heavy Metal Targets, Experiments and Calculations", Meeting on Targets for Neutron Beam Spallation Sources (G.S. Bauer, Ed.), Jülich, W. Germany, Jül-Conf-34, (January 1980).

31. S. Cierjacks, M.T. Rainbow, M.T. Swinhoe, and L. Buth, "Messung der absoluten Ausbeuten und Spektren schneller Neutronen und sekundarer Protonen aus Spallationsreaktionen am Pb und U", Primarbericht, Kernforschungszentrum Karlsruhe (1980).

32. S. Cierjacks, et al., "High Energy Particle Spectra from Spallation Targets", ICANS-V Meeting on the International Cooperation on Advanced Neutron Sources, Jülich, W. Germany, June 22-26, 1981.

33. D. Filges et al., "High-Energy Fission Models for the HETC Code: Thick-Target Comparisons", ICANS-V Meeting on the International Cooperation on Advanced Neutron Sources, Julich, W. Germany, June 22-26, 1981.

34. T.W. Armstrong and D. Filges, "High-Energy Fission Models for the HETC Code: Thin Target Comparisons", ICANS-V Meeting on the International Cooperation on Advanced Neutron Sources, Jülich, W. Germany, June 22-26, 1981.

Table 1. Requirements of Calculational Methods

- Predictions of Interest:

  - Target Station
    - neutron spectra
    - heating
    - activation
    - shielding requirements
    - material damage, etc.

  - Accelerator
    - radiation fields
    - component activation

  - Other
    - assessments for additional potential applications (nuclear physics research, radiation effects, transmutation, etc.)

- Requires:
  - general calulational methods (in terms output, materials, geometry, beam parameters)

- Which leads to:
  - large Monte Carlo computer codes

Table 2. Overview of HETC Code

Name:	HETC (High-Energy Radiation Transport Code)
Particles Transported:	Neutrons (≲15 Mev), Protons, $\pi^{\pm}$, $\mu^{\pm}$
Mechanisms Included:	Ionization and Excitation Multiple Coulomb Scattering Range Straggling Pion and Muon Decay Nuclear Interactions High-Energy Fission
Calculational Method:	Monte Carlo
Nuclear Collision Model:	Intranuclear-Cascade-Evaporation
Geometry:	Three Dimensional
Materials Allowed:	Essentially Arbitrary

Table 3. Treatment of Atomic Interactions in HETC Code

- Ionization

  Bethe-Bloch Formula

- Ranges

  Numerical integration of stopping powers

- Range Straggling

  Gaussian stopping distribution

- Coulomb Scattering

  Fermi joint distribution for angular and lateral spread

  Rutherford single-scattering formula

Table 4. Cross Section Input Required for INC Model

Reactions

n-p	differential
π^+-p	absorption
π^o-p	absorption
p-p	differential
p-p	single pion production
p-p	double pion production
n-p	single pion production
n-p	double pion production
π^+-p	single pion production
π^o-p	single pion production
π^--p	single pion production
π^o-n	single pion production
π^o-p	elastic
π^o-n	elastic
π^--p	charge exchange
π^--p	elastic
p-p	elastic
n-p	elastic
π^+-p	differential
π^--p	differential
π^--p	differential charge exchange
π^o-p	differential

Energy Range

n and p reactions: 0-3500 MeV
pion reactions : 0-2500 MeV

Table 5. Pion, Muon Decay

1. Decay Properties:

particle	mean lifetime τ_0 (sec)	$c\,\tau_0$ (m)	decay mode
π^+	2.6×10^{-8}	7.8	$\pi^+ \rightarrow \mu^+ + \nu$
π^-	2.6×10^{-8}	7.8	$\pi^- \rightarrow \mu^- + \nu$
π^0	0.8×10^{-16}	$\sim 10^{-8}$	$\pi^0 \rightarrow \gamma + \gamma$
$\mu^\pm$	2.2×10^{-6}	~660.	$\mu^\pm \rightarrow e^\pm + \nu + \bar{\nu}$

2. HETC Treatment

	"in-flight" collisions	"in-flight" decay	"at rest" collisions	"at rest" decay
π^+	✓	✓	–	✓
π^-	✓	✓	✓ or	✓
$\mu^\pm$	–	✓	–	✓
π^0	("immediate decay")			

3. "Decay Cross Section"

- $\tau \equiv \gamma\,\tau_0$, $\gamma \equiv [1-(v/c)^2]^{-\frac{1}{2}}$
- $\lambda_{decay} = v\tau = v\gamma\tau_0 \equiv$ decay m.f.p

$\Longrightarrow \Sigma_D(E) = 1/\lambda_{decay}$ ≡ "macroscopic decay cross section"

4. π^- Capture at Rest

- Enter INCE Routines with:
  - E_{kin} = 1 MeV
  - $E^* \approx 140$ MeV = E_0^π (π rest energy)
- Capture Nucleus:
  - $p_i \propto N_i Z_i$

Table 6. General Requirements of Low-Energy Radiation Transport Code for Spallation Neutron Sources

- Transport of neutrons and gamma-rays created in neutron collisions (coupled neutron-gamma transport)
- Anisotropic scattering
- Time dependence
- Source and eigenvalue (fission source, or combined) problems
- Solution in either the forward or adjoint mode
- Use of multigroup cross sections sets or point cross sections
- Upscattering at thermal energies
- Geometry modules same as in high energy transport and analysis (in general: three-dimensional)

Table 7. Codes Available for Low-Energy Neutron and Gamma-ray Transport

- Discrete Ordinates Codes

  (solution of Boltzmann Equation by quadrature)

  - ANISN : 1-D geomerties
  - DOT : 2-D geometries
  - TDA : time-dependent ANISN
  - TIMEX : similar to TDA

- Monte Carlo Codes

  (solution of Boltzmann Equation by stochastic methods)

  - MCNP (LASL)
  - MORSE-CG (ORNL)
  - O5R (ORNL) : earlier version of MORSE
  - TIMOC (BNL)
  - VIM (ANL)

Table 8. Support Codes for Analysis

- SIMPEL-KFA (HETC)
  - 3-D Geometry, Combinatorial
  - All particle fluxes, currents and spectra
  - Energy deposition
  - Residual nuclei distribution
  - Special options for detailed spatial analysis without new HETC runs

- MAGIC (HETC, MORSE)
  - Residual nuclei production
  - Spatial distribution of gamma sources
  - Prompt doses
  - Time-dependent gamma doses

- RECOIL (MORSE)
  - Radiation damage parameters as dpa rates and production rates (H,He)

- DOMINO (MORSE, DOT)
  - Interface between DOT-IV and MORSE for boundary source tapes

- ORIGEN (HETC, SIMPEL)
  - Depletion code for build-up and decay of HETC nuclide production rates

Table 9. Cross Section Generation Codes

- AMPX (ORNL)

  Modular system for n/γ-libraries

  from data in ENDF format

- RSYST (KFA)

  Modular system for n-libraries

  with a special 126-group thermal library

  (3.0 eV - 10^{-5} eV)

- MACK-IV (ORNL)

  Calculation of nuclear response functions

  from nuclear data in ENDF format

  (e.g., kerma factors, displacements

  (n,2n), (n,3n), (n,γ), (n,p), (n,f), etc.)

Table 10. Evaluated Cross Section Libraries

- EPR-Lib (ORNL)
  - Coupled 100-group neutron, 21-group gamma-ray cross sections (ENDF/B-IV) (14.9 MeV - 10^{-4} eV)

- THERM-126 (KFA)
  - 126-group neutron library (3.0 eV - 10^{-5} eV), with all important moderator materials

- RSYST-53 (KFA)
  - 53-group neutron library (14.9 MeV- 10^{-5} eV) with 26 neutron groups below 1 eV

- HELLO (ORNL)
  - coupled 47 neutron, 21 gamma-ray group cross section (60 MeV - 10^{-4} eV)

- VITAMIN-C (ORNL)
  - Coupled 171 neutron, 36 gamma-ray group cross sections (17.3 MeV - 10^{-4} eV)

- MACKLIB-IV (ORNL)
  - 171 neutron, 36 gamma-ray group nuclear response function library (ENDF/B-IV)

Table 11. Theoretical Predictions for SNQ Reference Design Target

- Beam Parmeters Assumed:
  - E_0 = 1100 MeV
  - $\bar{I}$ = 5 mA (3.1 x 10^{16} protons/sec)
  - $\hat{I}$ = 100 mA (6.2 x 10^{17} protons/sec)
  - Pulse Width = 0.5 milliseconds
  - Repetition Rate = 100 pulses/sec
  - Beam Profile: FWHM = 4.0 cm
- Target Model Assumed:
  - Target Composition

    Pb : "spallation material"

    Al : cladding

    H_2O : coolant
  - "Hybrid" Configuration

    D_2O: "slow" moderator

    H_2O : "fast" moderator
  - 3-D Simulated Mockup
- Calculated Results:
  - Neutron output + γ-output
  - Heating and cooling requirements
  - Induced radioactivity
  - Radiation environments for initial estimates of:

    Materials damage

    Shielding

Table 12. Calculated Thermal Neutron Fluxes from Fast Moderator

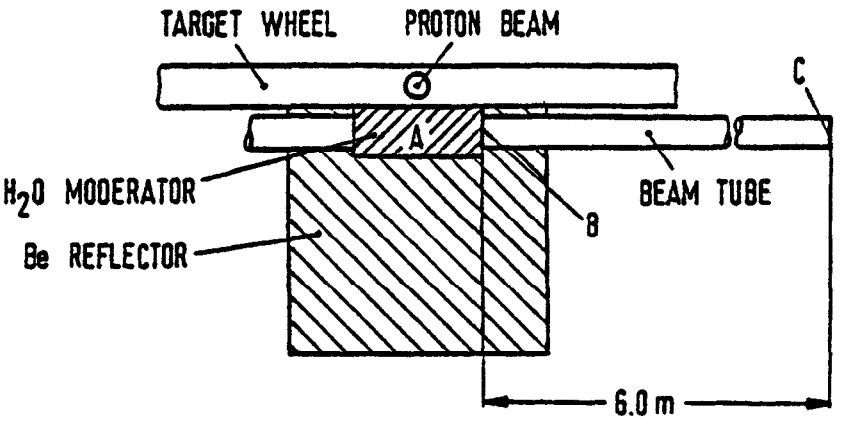

Position	Thermal Neutron Flux		
	ϕ'th (a) (n/cm^2-p)	$\bar{\phi}$th (b) (n/cm^2-s)	$\hat{\phi}$th (c) (n/cm^2-s)
A	2.0×10^{-2}	6.2×10^{14}	1.2×10^{16}
B	3.1×10^{-3}	9.7×10^{13}	1.9×10^{15}
C	2.2×10^{-7}	6.9×10^{9}	1.4×10^{11}
"EIF" (d)		7.9×10^{14}	1.6×10^{16}
"EIF" Design Goal		6.0×10^{14}	1.2×10^{16}

(a) Neutron fluence per beam proton

(b) Average neutron flux for $\bar{I}$ = 5 milliamperes

(c) Peak neutron flux for $\hat{I}$ = 100 milliamperes

(d) "EIF" = "Equivalent Isotropic Flux"

Table 13. Comparison of Heating for Lead versus Uranium as Target Material, SNQ Reference Design Geometry, 1100-MeV Protons

	Pb	U-238	Natural U
1. Total Deposition in Target (MeV)			
- HET (a)	542	945	945
- MORSE (b)	29	1140	2540
- Total	571	2085	3485
2. Total Deposition/1100 MeV	0.52	1.90	3.17
3. Total Deposition Relative to Pb	1.0	3.7	6.1
4. Peak Deposition (MeV/cm^3-proton)			
- HET (a)	1.20	2.45	2.45
- MORSE (b)	0	0.55	0.76
- Total	1.20	3.00	3.21
5. Peak Deposition (kW/cm^3), for I = 100 mA	120	300	321
6. Peak Deposition Relative to Pb	1.0	2.5	2.7

(a) From the effects of high-energy particle transport (all charged particles and neutrons > 15 MeV)

(b) From the effects of low-energy (≤15 MeV) neutron and gamma-ray transport

Table 14. Experimental/Theoretical Studies Related to Spallation Neutron Sources

1. Cosmotron Experiments (CRNL/ORNL ~1965)
   - target yields / U, Pb, Sn, Be / 540, 960, 1470 MeV

2. LASL (WNR design exp.) (Fullwood, et al., ~1971)
   - neutron spectra / bare U / 800 MeV

3. NIMROD (MUSTA experiments) (RL, late 70's)
   - neutron spectra / U + moderator + reflector /

4. Argonne (~1980)
   - neutron spectra / U + PE, H / 300, 500 MeV
   - neutron spectra / Ta, U; Pb reflector / 500 MeV
   - energy deposition / U, W / 300,500 MeV

5. FERFICON Experiments (on going)
   - target yields: U, Th, Pb, etc.
   - isotope production
     E = 480 (CRNL/TRIUMF)
     E = 800 (LASL)

6. LASL (on going)
   - E = 800 MeV
   - different neutron spectra / thin targets: U, Pb, In, Cu, Al
   - neutron spectra / moderator-reflector assemblies

7. SNQ (in progress)

Table 15. Experiments for Code Validation Related to SNQ Study

- Thin and Thick Targets
- Bare and with Moderators
- Target Materials: Mainly Pb and U
- E_0 : 600 and 1100 MeV
- Types of Measurements
  - target yields (n/p)
  - particle spectra from targets
  - neutron spatial distribution in moderators
  - time dependence of thermal flux
  - isotope production

Table 16. Theoretical / Experimental Comparisons

1. Experimental Configuration :

(Measurements of Bauer, et al. /24/)

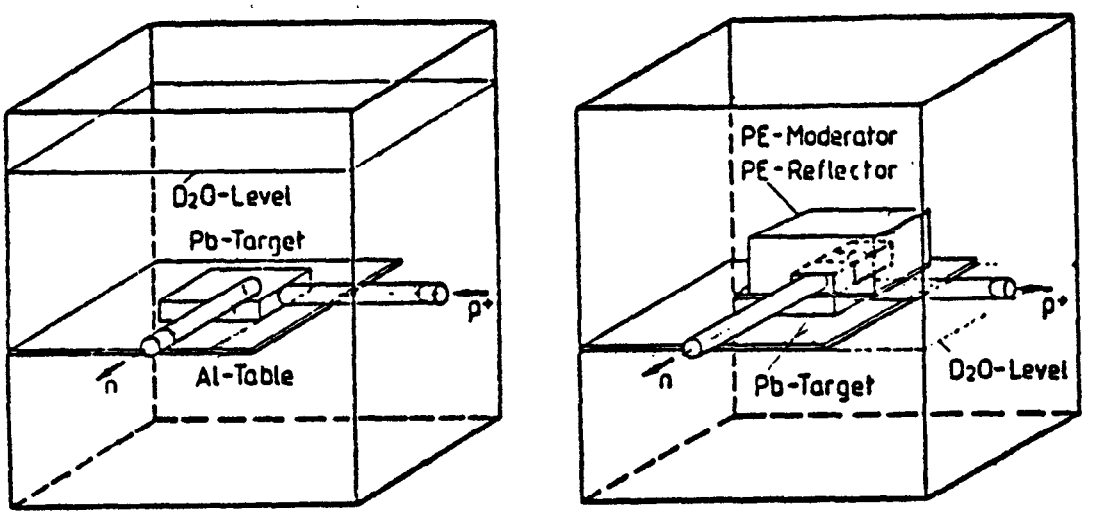

E_0 = 600 MeV

($\bar{I}$ = 10 mA)

2. Theoretical Configuration:

"Reference Design"

E_0 = 1100 MeV, $\bar{I}$ = 5 mA

3. Results

Moderator	Average Thermal Flux (n $cm^{-2}s^{-1}$)		Ratio
	Theory	Experiment	(Theo./Exp.)
D_2O	7.0×10^{14}	7.3×10^{14}	0.96
H_2O	7.9×10^{14}	7.1×10^{14}	1.11

Table 17. Experiments and Code Validations Related to SNQ Project

Case	Quantity Compared	Theoretical/Experimental Agreement
1. SNQ "Reference Design" Geometry, 600 MeV Lead Target	Thermal flux at end of beam tube	Excellent: agreement within ≈10% for both D_2O and H_2O moderators
2. "	Rh foil activation within moderators	(not yet compared)
3. SNQ "Reference Design" geometry, 600 MeV Uranium Target	Thermal flux at end of beam tube	(not yet compared)
4. "	Rh foil activation within moderators	(not yet compared)
5. Bare Pb and U, 600 and 1100 MeV	Rh foil activation	Comparisons made for 600 MeV, Pb-good agreement for relative spatial distribution (≈10-15%)
6. Pb-Bi target, H_2O moderator, 600 MeV	Spatial distribution of dysprosium reaction rate	Good agreement for relative spatial distribution (≈20%)
7. Bare Pb, 600 MeV	High-energy neutron leakage spectra, 1 MeV to 600 MeV	Poor at high energies, e.g. factor of 5 difference at 100 MeV
8. Thick Pb target 1100 MeV	Production of various isotopes of Bi, Pb, Tl and Hg	Preliminary comparisons only; Fair agreement (within factor ~2)
9. Thick U-target, 1100 MeV	Isotope production	(not yet compared)
10. Thin targets of various materials, 600 MeV	Neutron and charged particle spectra	(not yet compared)

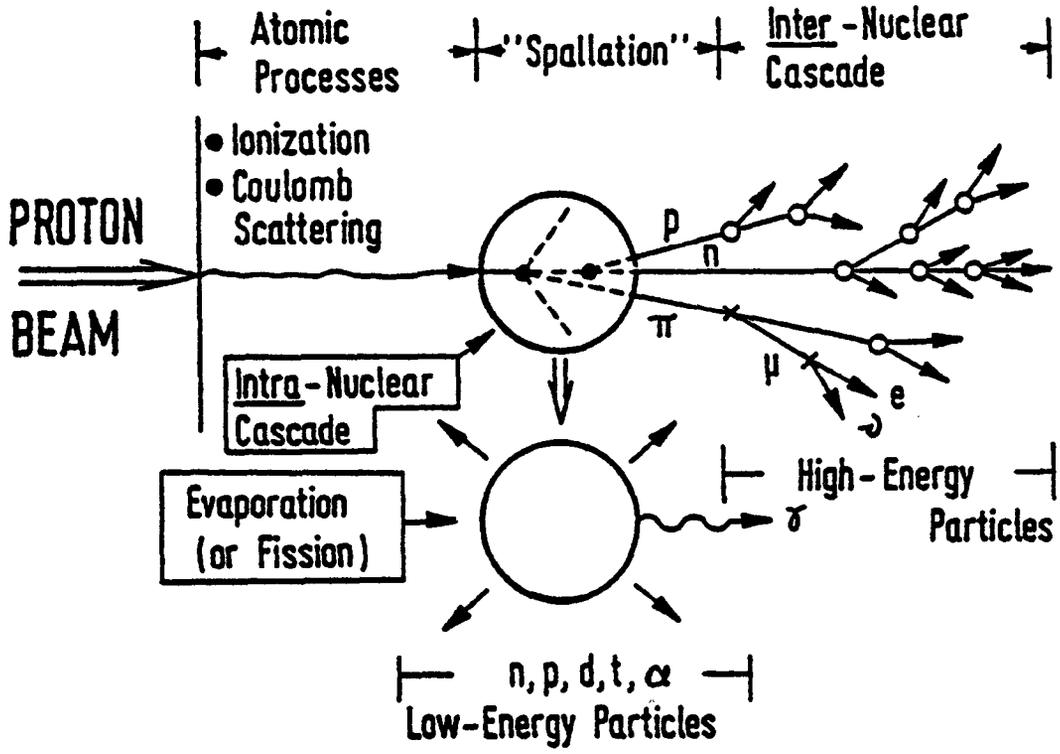

Figure 1. Interaction mechanisms produced by high-energy proton bombardment of thick targets.

Figure 2. Basic Features of Intranuclear Cascade Model Used to Treat Spallation Collisions

1. Entry into nucleus:

   -select uniformly over projected area

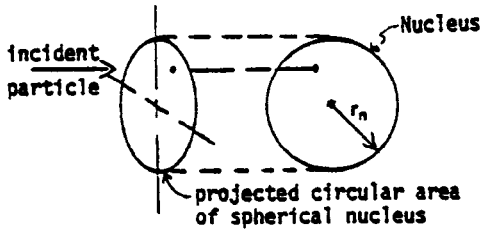

2. Nucleon Density Inside Nucleus:

   • 3-Region Approximation.

   • $[n/p]_{\text{each region}} = [(A-Z)/Z]_{\text{whole nucleus}}$

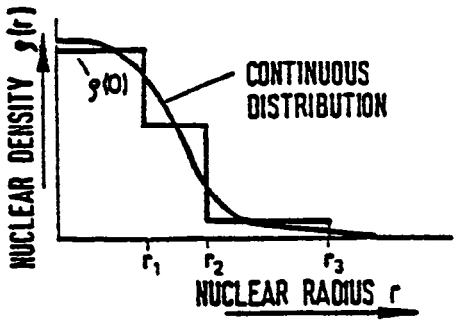

3. Nucleon Momenta:

   • Assume Fermi distribution,

   $$f(p) = cp^2$$

   • Normalization,

   $$\int_0^{p_f} f(p)\,dp = \begin{Bmatrix} n_i \\ p_i \end{Bmatrix} \text{ in each region}$$

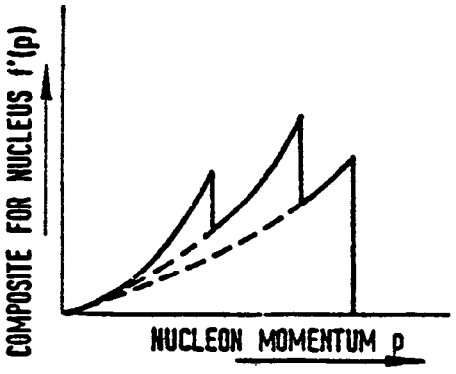

4. Nucleon Potential Energies:

   • $-V = E_f + BE$

   $BE = 7$ MeV

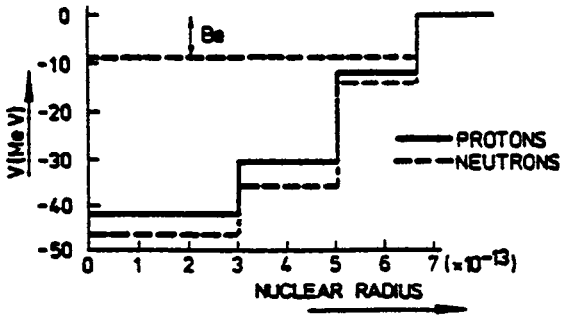

5. Cross Section Needed:

   • nucleon-nucleon
   • pion-nucleon

6. Exclusion Principle:

   -reject outcome if state filled

7. Outcome of INC:

   • $E, \overline{\Omega}$ of emitted particles: $n, p, \pi^+, \pi^\circ, \pi^-$
   • residual E^*
   • residual A, Z of nucleus

Figure 3. High-Energy Fission Model

Consider as 4-step process:

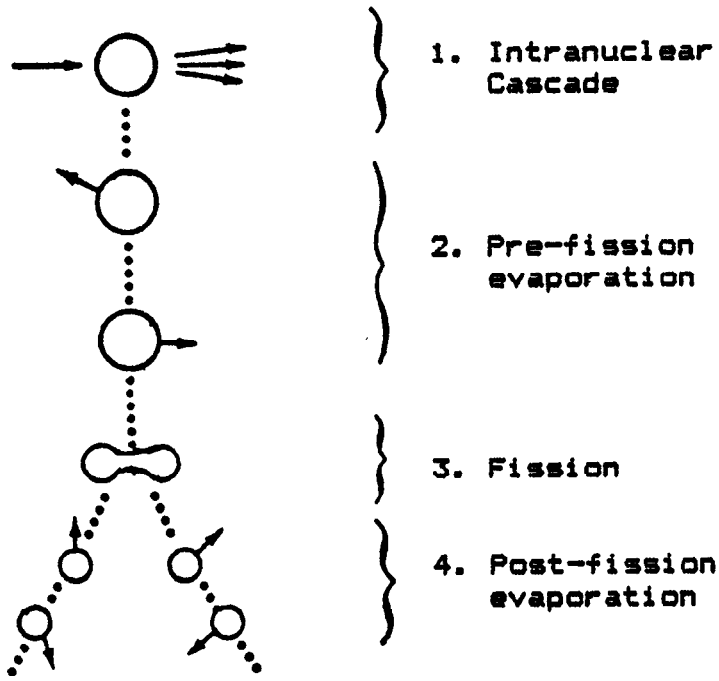

Must determine:

a. Fission probability at each step of de-excitation:

$$P_f(E^*,A,Z) \approx P_f(A,Z) \equiv (\Gamma_n/\Gamma_f + 1)^{-1}$$

b. Parameters for fission products at fission:

E_1^* , E_2^* : excitation energies

E_1 , E_2 : kinetic energies

Z_1 , Z_2 : charge numbers

A_1 , A_2 : mass numbers

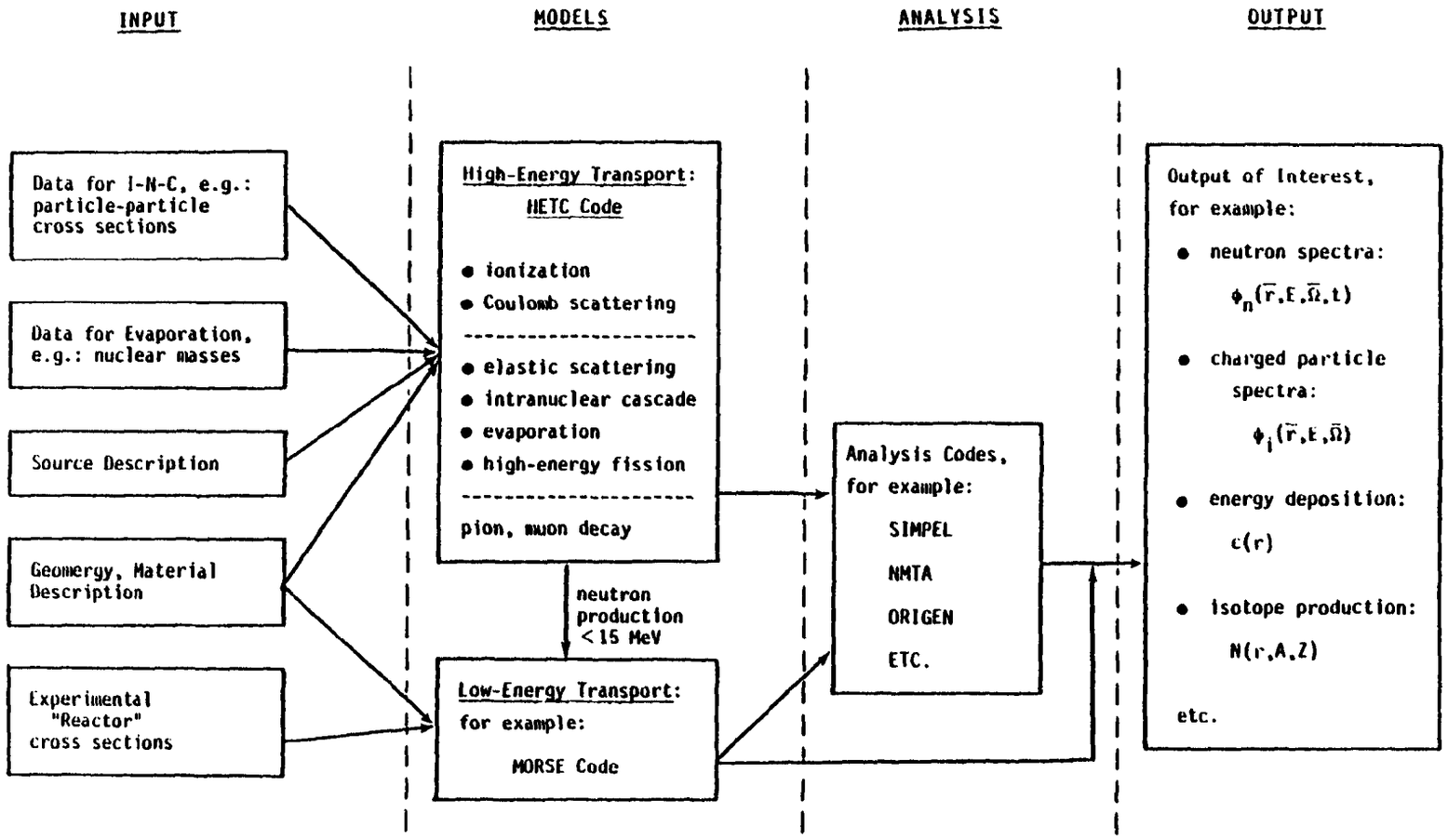

Figure 4. General Calculational Proceedure for Spallation Neutron Sources

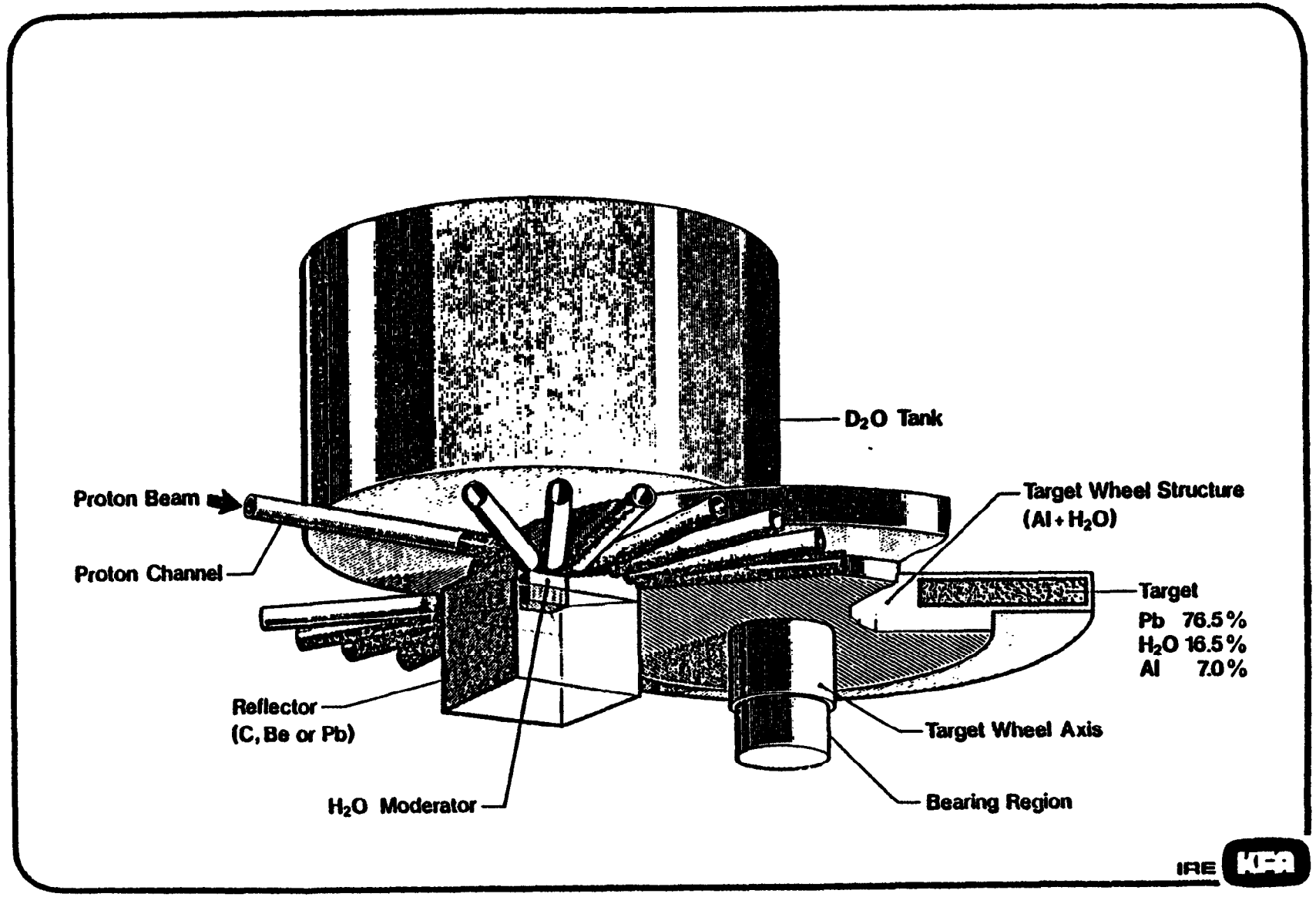

Figure 5. Three-dimensional computer model of SNQ target used for calculaions.

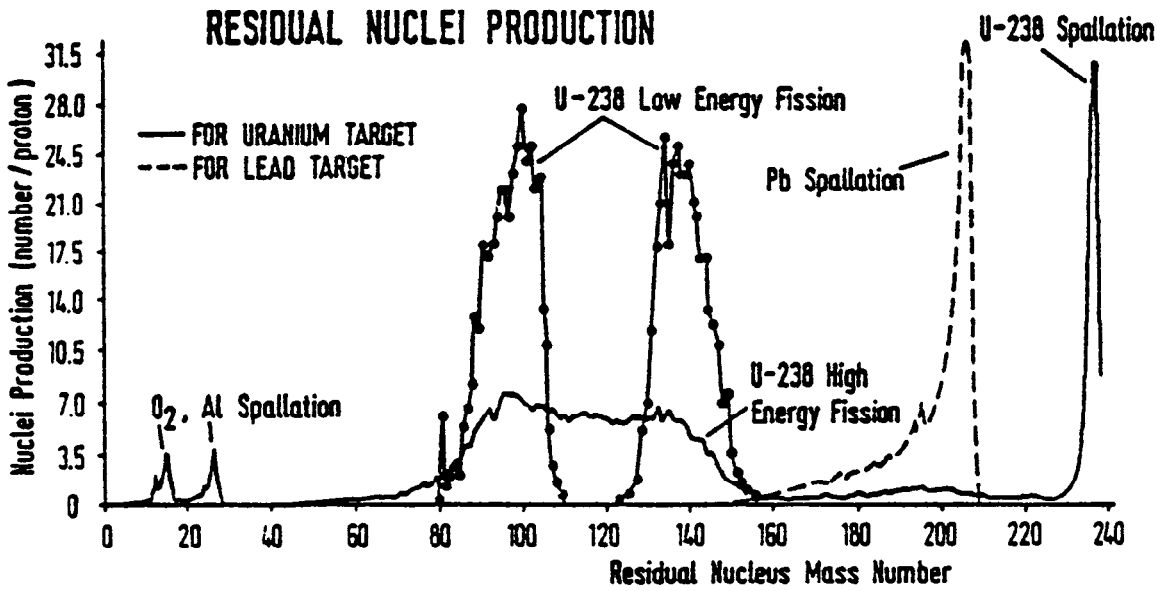

Figure 6. Mass distributions of isotopes produced for Pb and for U-238 as target materials, SNQ reference design target geometry, 1100-MeV proton beam.

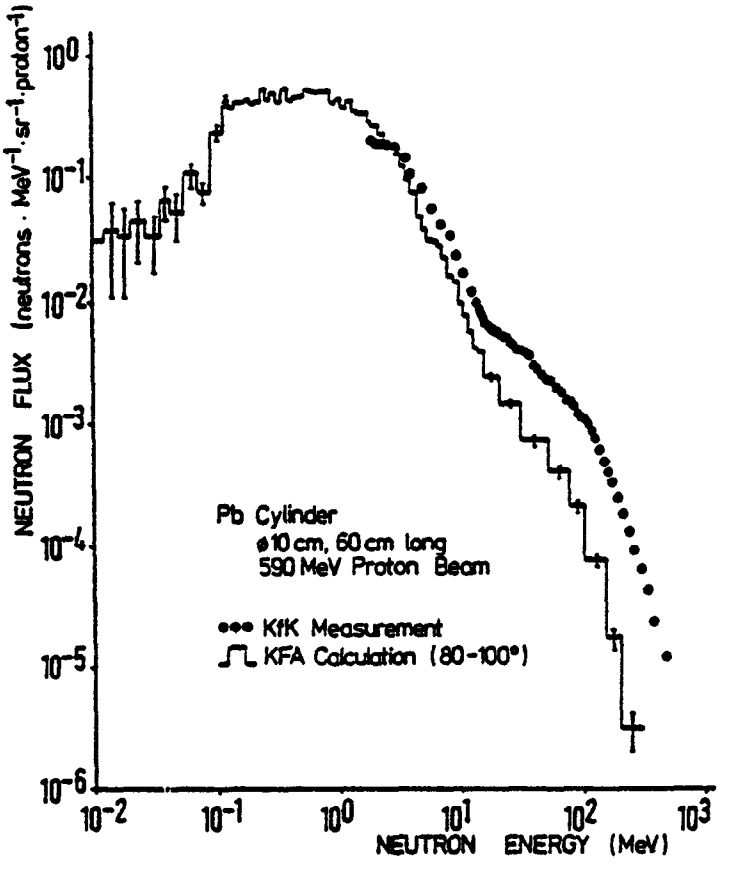

Figure 7. Comparison of calculated /21/ and measured /31/ neutron leakage spectrum at 90° (summed over 0-35 cm target length).

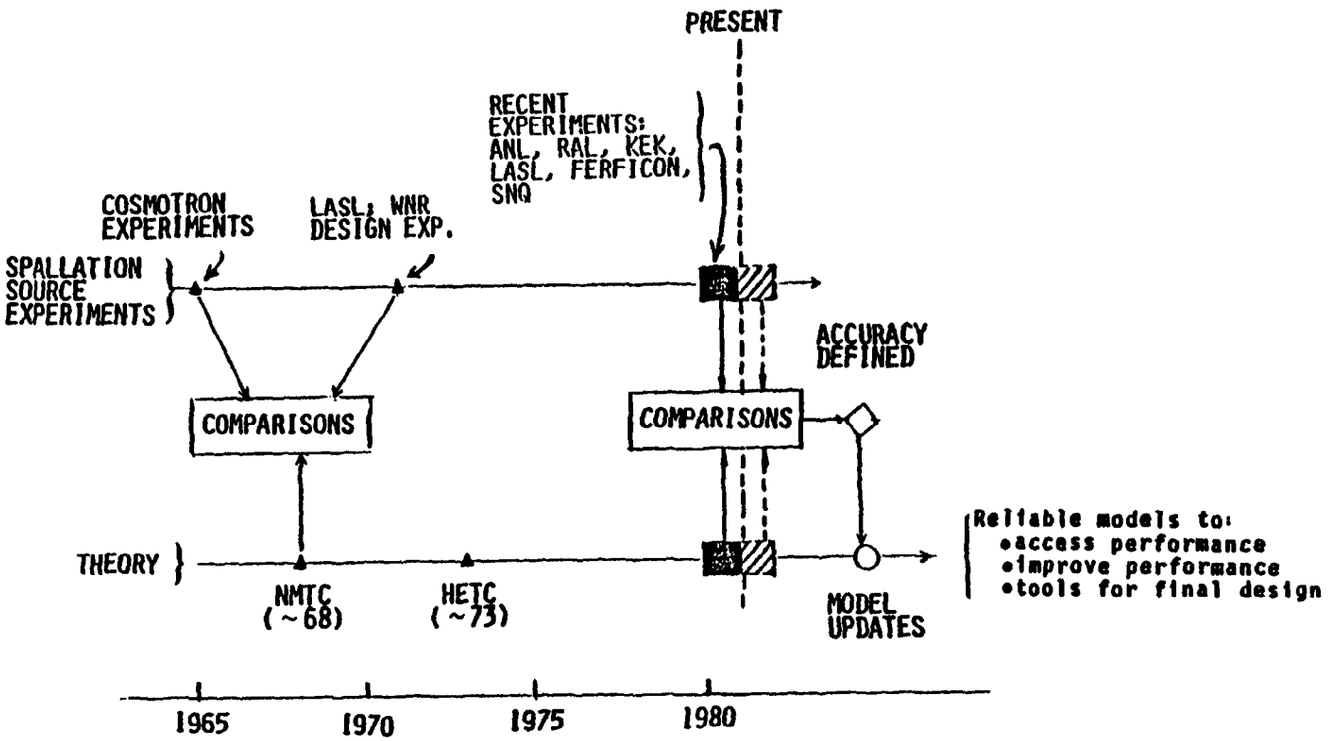

Figure 8. Present Status of Validation of Theoretical Models for Spallation Neutron Source Applications.

Jül-Conf-45 B6

I C A N S - V

MEETING OF THE INTERNATIONAL COLLABORATION ON

ADVANCED NEUTRON SOURCES

June 22-26, 1981

High Energy Particle Spectra from Spallation Targets

S. Cierjacks, F. Raupp, S.D.Howe, Y. Hino, M.T. Swinhoe,
M.T. Rainbow and L. Buth

Kernforschungszentrum Karlsruhe
Institut für Kernphysik
7500 Karlsruhe, Postfach 3640
Federal Republic of Germany

Abstract:

The experimental program of high energy spectra measurements performed in conjunction with the feasibility study for a German spallation source is surveyed. This program included the measurement of angular and depth dependent neutron and charged-particle yields and spectra from thick targets, the determination of high energy neutron spectra associated with moderated beams and the measurements of neutron and charged-particle production cross sections from various thin targets by 590 and 1100 MeV protons. Since absolute measurements of neutron data depend on the accurate knowledge of the neutron detection efficiency of scintillation counters, auxiliary measurements of this quantity were performed in the neutron region 50 to 450 MeV.

1. INTRODUCTION

High energy particle spectra from spallation targets by 590 and 1100 MeV protons were measured as part of the project study for a German spallation neutron source. In this context depth and angular dependent yields and spectra of neutrons and charged-particles leaking out from thick bare metal targets were of primary interest. The accurate knowledge of these quantities is an important prerequisite for a realistic estimate of the specifications of a spallation source, because the bare target data determine all

subsequent particle transport in the moderator and the reflector of a particular target assembly.

In parallel to the study of yields and spectra from the bare target also the spectra of the fast neutrons were measured which are scattered in the moderator and which are emitted together with the thermal neutrons through the beam holes of a shielded target assembly. Since for this type of measurements the time-of-flight method was not applicable, a new technique was employed which is based on spectrum unfolding of analog data. A large fraction of fast neutrons in a moderated neutron beam may cause shielding problems and can cause additional undesirable background in some experiments with thermal and epithermal neutrons.

Beginning of this year additional experiments were started to measure neutron and charged-particle production cross sections from thin spallation targets covering a wide range of masses from carbon to uranium. The measurements of differential production cross sections aimes at a better understanding of the spallation process and can be used to test the nuclear models underlying the existing high-energy transport codes such as the High-Energy Nucleon-Meson Transport Code, HETC (1).
A final auxiliary program concerned the experimental determination of neutron detection efficiencies at high energies. While reliable data are well established below $\sim$ 70 MeV from various experiments and calculations, detection efficiencies above that energy rely almost completely on Monte Carlo calculations for this quantity.

2. HIGH ENERGY PARTICLE YIELDS AND SPECTRA FROM THICK TARGETS

2.1 Experimental Details

The measurements were performed at the SIN cyclotron providing 590 MeV protons and at the LNS synchrotron providing 1100 MeV protons. A schematic view of the target-detector arrangement as used for the SIN experiments is shown in Fig. 1. The proton beam was focussed to 2 cm diameter onto the cylindrical lead target. This was composed of twelve cylindrical blocks, each 5 cm long and 10 cm in diameter, to give an overall length of 60 cm. Time-of-flight

measurements of the neutrons produced were made using the cyclotron microstructure pulsing at 16.9 MHz repetition rate and of < 0.2 ns pulse width.

Neutrons emitted from the target at 30°, 90° and 150° were detected at the exit of a $\sim$ 1 m long iron collimator. Depth dependent measurements of neutron spectra were made by moving the target along the beam axis, so that the individual blocks were opposite the collimator entrance. The principal detector was a 3 cm thick, 4,5 cm diameter, NE 213 liquid scintillator employing n-γ pulse-shape discrimination (PSD). In order to remove pulses from charged particles also produced in the target, a 5 mm thick plastic scintillator placed in front of the principal detector was used as a veto counter. (While neutron and γ-rays produce in general a signal in only one of the detectors, charged particles from the target are characterized by signals in both counters).

Background measurements at 90° were performed with the target block opposite the collimator entrance removed. For 30° and 150° shaped wedges were used to give the relevant background contribution.

The experimental arrangement at SATURNE was similar to that shown in Fig.1. But, due to the lower pulse repetition rate of 7.3 MHz for the SATURNE machine a longer flight path of 3 m was employed. In this case an auxiliary iron collimator, 0.5 m thick, was placed in front of the neutron detector.

Data accumulation was accomplished in a 4-parameter mode. A block diagram of the electronics is shown in Fig. 2: The pulse-height signal from the liquid scintillator was split into two amplifier channels, one with ten times the gain of the other. This was necessary to cover the large total dynamic range and the expanded threshold region (an accurate measurement of the effective detector threshold is an important prerequisite for a precise detector efficiency determination). The timing signal of the neutron detector served three functions:

1. It started the main TAC which provided the neutron time-of-flight via ADC 4. This TAC was stopped by a timing signal derived from the cyclotron r.f.
2. It provided the input signals for the n-γ pulse-shape discrimination circuit providing an identification signal which went to ADC 3.

3. It was used in conjunction with the fast signal from the veto detector to generate a master trigger signal which notified the computer that a neutron or a γ-event occured and that the gates to the ADCs should be opened.

The contents of the four ADCs were stored event-by-event on magnetic tape for subsequent off-line data processing. The number of master triggers applied to the computer was recorded and used in conjunction with the number of accepted events to evaluate dead-time effects.

At the SIN the proton current was measured throughout the experiment by a proton beam monitor (see Fig. 1). This monitor consisted of a carbon scatterer placed in the incident proton beam. Scattered protons were detected by a pair of thin plastic scintillators which operated in coincidence. The monitor was calibrated with respect to absolute proton flux by counting individual protons in the direct beam with a third thin plastic scintillator at sufficiently reduced current. The proton-current measurement at SATURNE was accomplished by three different detector systems:

1. A proton telescope counter similar to that used at SIN,
2. an ionization chamber and
3. a secondary electron emission chamber.

All three systems were calibrated simultanously by carbon activation employing the well known $^{12}C\ (p,x)^{11}C$ activation cross section.

2.2 Off-Line Data Processing

The analysis of neutron yields and spectra began with the separation of neutron and γ events by a consideration of 2-dimensional arrays of pulse height versus "pulse shape discrimination time". Excluding γ-events from further analysis the neutron events from the corresponding background runs were then substracted. These data were subsequently sorted into suitable time-of-flight bins and their corresponding energies calculated relativistically according to the time of occurence of the prompt γ- peak.
In typical time-of-flight measurements a single overlap in part of the neutron time-of-flight spectrum was admitted. Seperation of the response due to high energy neutrons from that due to low energy neutrons was

achieved by linear extrapolation of the high energy pulse height response down to the bias level. The error associated with this procedure is small because of the largely different shapes of the corresponding distributions.

The contents of each time bin were integrated and the results divided by the detection efficiency of the NE 213 neutron detector. The Monte Carlo Code of Stanton as modified by Cecil et. al. (2) was used to calculate the required efficiency. The shape of the pulse height spectra produced by the code were in good agreement with the measured spectra in the various time bins. This was the case even when the ranges of charged particles produced in the detector are greater than the detector dimensions. This fact in conjunction with experimental tests of the original code in various laboratories up to 70 MeV (3) and with own measurements between 50 and 450 MeV (compare section 5) gives confidence in the operation of the code.

The data were finally scaled by the solid angle subtended by the detector, the energy bin width, the dead time correction factor and the number of incident protons to produce the absolute neutron yields as neutrons per proton, per steradian, per MeV and per cm^2 target surface. Finally the results for various distances into the target were added to produce the absolute angular dependent neutron yield from the whole target. The measured neutron spectra were corrected for the measured time resolution of the system using the second derivative method (4).

2.3 Results

Fig. 3 shows a typical spectrum measurement obtained for lead with 590 MeV protons. This result represents the sum of the 90° depth-dependent spectra for the whole target length. This spectrum exhibits the well known two-component shape originating from contributions of evaporation processes and direct cascade reactions (the latter of which produces the broad shoulder around 50 MeV). In Fig. 3 the measured 90° spectrum is compared to a recent calculation performed at KFA Jülich (5). The calculational method is based on the 3-dimensional "High Energy Nucleon-Meson Transport Code, HETC" (1). As can be seen from this comparison the calculations produce at the present time much softer spectra than observed in the measurements.

Three depth dependant neutron spectra obtained from a thick uranium target by 590 MeV protons are shown in Fig. 4 (6). They correspond to the neutron yields obtained at 90° to the incident proton beam and 2.5, 7.5 and 12.5 cm depths into the target. The upper curve and the two lower curves were measured in two different runs at the SIN involving different pulse repetition rates. Therefore, the detector threshold was set to a much higher value in the two bottom curves than in the top curve. It can be seen from the upper yield curve that the uranium spectrum is significantly softer than the respective lead spectrum (comp. Fig. 3). This together with the by a factor of two higher n/p value provides an additional advantage, when uranium is used as the primary target for a moderated source, because a largerfraction of the total neutron spectrum is moderated.

The spectral distribution of neutrons emitted at 90° from a 2.5 cm average target depths of a thick lead target is shown in Fig. 5 for 590 MeV and 1100 MeV proton energy. Except for the higher energy limit of the spectrum and the by a factor of 1.3 higher n/p value for 1100 MeV proton energy both spectra are very similar.

The difference for incident proton energies of 590 MeV and 1100 MeV is more pronounced for the spectra of secondary protons emitted at 90° from thick lead targets as shown in Fig. 6. These data were also taken for an average target depth of 2.5 ± 2 cm. The high fraction of high energy protons, particularly for 1100 MeV incident beam energy may have some implications for the installation of a cold neutron source. Thus it could be worthwhile for the sake of a lower heat deposition to choose a larger diameter for the primary target.

3. MEASUREMENTS OF THE HIGH ENERGY COMPONENT OF THE NEUTRON SPECTRUM FROM A MODERATED SOURCE

The neutron spectrum from a moderated source covers the energy range from thermal to hundreds of MeV. The range of interest for these measurements of the "high energy" part of the spectrum includes all those neutrons above a few MeV. Even though time-of-flight measurements of fast neutron spectra would have been most desirable, this method was not applicable at the SIN

cyclotron and the SATURNE accelerator where the only useful pulse comes from the machine microstructure. This time structure is much too narrow compared with the large time spread associated with the moderation process and so an unfolding method was necessary.

The moderated source studied at the SIN was a 15 cm diameter heavy metal target (lead or uranium) in a cubic tank (of side 2 m) of light water. The detector, an 8.9 cm thick NE 213 scintillator, was placed approximately 8 m from the target at 30° to the incident beam direction. The collimator defined a region above the bare target so that neutrons coming directly from the target could not be seen. The same electronics and data recording system were used as for bare target measurements described above, with the omission of the time-of-flight parameter. The general target configuration used at Saturne is shown in Fig. 7. The primary target was a large 50 by 50 cm, 10 cm high, heavy metal block (lead or uranium). The centre part which was directly hit by the proton beam was composed of alternately arranged plates of metal, polyethelene and aluminum, in order to simulate a realistic spallation neutron target design. The polyethylene and the aluminum represented the coolant and the structural material. A polyethylene moderator was placed on top of the primary target and surrounded by a 20 cm thick reflector (lead or beryllium).

The results obtained for the four described target configurations are shown in Fig. 8. These were obtained by rectangularly unfolding the pulse height distributions of the detector and are normalized to 5 mA and 10 mA, for 1100 MeV and 590 MeV protons respectively, at a distance of 6 m from the target. It can be seen that the distributions are very similar for lead and uranium targets. The sharp cut-off of the spectra above about 100 MeV is mainly due to a combined effect of the small detector size and the adopted simplified unfolding method. With respect to the detector only a commercial 8.9 cm long liquid scintillator was available during the early phase of the program. In such a detector very high energy particles are not completely stopped. The simplified method of rectangular unfolding was applied mainly because it allowed a quick data analysis while providing a rather good estimate of the total number of fast neutrons and the spectrum below ~100 MeV as verified by computer simulations of the experiments (7).

The disadvantage of the described unfolding method which underestimates the fraction of high energy neutrons was avoided in a recent experiment which employed a self-built, 30 cm long, liquid scintillator and an iterative method of spectrum unfolding (8). In this experiment the earlier measurement on the lead-polyethelene-lead target configuration was repeated. A comparison of the results obtained with the two methods is shown in Fig. 9. In order to enhance the differences in the two methods only the smoothed lines drawn through the original data points are shown in this diagram. It can be seen that both unfolding methods give the same spectrum below about 50 MeV and approximately the same integral number of neutrons. However, the spectrum above 50 MeV is increasingly distorted with increasing energy when the previous unfolding method is applied.

4. PARTICLE PRODUCTION CROSS SECTION MEASUREMENTS

4.1 Neutron Production Cross Sections

Neutron production cross sections of C, Al, Fe, In, Ta, Pb and U by 590 MeV were measured at the SIN at angles of 30°, 90° and 150°. In this case the same collimator arrangement as shown in Fig. 1 was used. Thin metal plates of 10x10 cm, a few mm thick, were used as neutron targets. The proton beam was focussed to 1 cm onto the centre of the target. Data aquisition and data analysis was analogous to that involved for the thick sample measurements. A first result of these measurements is shown in Fig. 10. The measured differential production cross section is compared with a recent HETC calculation performed by Armstrong et al. (9). The measured and calculated absolute cross sections are in excellent agreement below ~20 MeV. In the cascade region the calculations give much lower values than the measurements similar as for the thick target yields. In view of the discrepancies between measured and calculated values it was intresting to compare our results also with previous measurements performed at 800 MeV in Los Alamos (10). Even though both measurements are not directly comparable there is an obvious similarity of the spectrum shapes in the cascade region. The sligthly smaller cross section at the very high energy end of the spectrum may at least be partly explained by the larger observation angle for the Los Alamos experiment.

4.2 Charged-Particle Production Cross Sections

Charged-particle production cross sections can be measured with the same apparatus as that used for neutrons. In this case the liquid scintillator is operated in coincidence with the adjoint thin plastic scintillator (comp. Fig. 1). The identification of different charged particles must be accomplished by their specific energy losses in the main detector. This can be done by consideration of the two-dimensional arrays of pulse-height versus particle time-of-flight. The theoretical relationship between energy deposition and particle time-of-flight is shown in Fig. 11. The given relationship applies for a detector of the size used for our experiments. For this detector the range of the particles with the utmost possible energy is much larger than the detector size. Therefore all individual curves peak at those energies where the the particle range in the detector is equal to the detector length. Above the maximum the monotonic decrease with energy is caused by the decreasing specific energy loss over the fixed detector length. It is obvious from Fig. 11 that the difference in the various curves allows good particle separation over most of the total energy range. It is also advantageous that the particle spectra for deuterons, tritons and α-particles drop rapidly with energy, so that even the crossing areas for different particles don't cause major problems in the off-line analysis of raw data. Thus only the separation of pions and very high energetic protons remains comparatively problematic. A typical result obtained by the described type of analysis is shown in Fig. 12. This exhibits the relative charged -particle spectra observed from a thin lead target by bombardment with 590 MeV protons. Besides secondary protons also deuterons, tritons, α-particles and charged pions were measured. For the sake of clarity the pion spectrum was not included in this diagram. Since the displayed lead data stemmed from an early orientational run no absolute production cross sections were calculated.

Extensive charged-particle production cross section measurements have recently been performed for 590 MeV protons at the SIN. In these experiments an "open geometry" was used. This was possible, because room-scattered background events are severely reduced by the telescope-type of measurement which is strongly directional selective. Due to the high particle threshold caused by the plastic coincidence counter flight paths of up to 4 m could be em-

ployed without causing any time overlap from successive machine pulses. Various charged-particle results which have been obtained from the recent SIN experiment are presented in a workshop contribution of this conference (11).

5. MEASUREMENTS OF NEUTRON DETECTION EFFICIENCIES

As stated in section 1 absolute neutron spectrum measurements require an accurate knowledge of the detection efficiency for the employed neutron detectors. For neutron energies below 70 MeV various codes have been established in the past which provide accurate predictions of typically 5 - 10% This was verified by numerous comparisons of code predictions with experimental efficiency determinations (3). However, to our knowledge the only measurement up to 225 MeV is that of Mc Donald et al. (12) which shows partly rather poor agreement with Monte Carlo code predictions of Cecil et al.(2). Therefore, auxiliary measurements were carried out at the SIN to determine the detection efficiency for our neutron detecor in the energy range from 50 MeV to 450 MeV. For this purpose the neutron facility of the Freiburg University group was employed. A schematic diagram of the experimental arrangement used for the efficiency determination is shown in Fig. 13. The primary neutrons were produced by 590 MeV protons incident on a 9 cm thick beryllium target. The neutron spectrum provided by this source at an angle of 3° exhibits a pronounced peak between 470 and 570 MeV. Only this part of the neutron spectrum was used for our experiment. A narrow neutron beam was produced by several collimators placed at different positions along the 60 m long flight path. Charged-particles and γ-rays were removed from the incident neutron beam by cleaning magnets and an 8 cm long γ-filter in the beam line. The elastic scattering of the neutrons in a liquid hydrogen target was used to determine the detection efficiency by means of the associated particle method. Since the elastic scattering in the hydrogen target produces equal numbers of protons and neutrons, the detector efficiency can be derived by the number of detected neutrons related with the number of protons measured in the kinematically related solid angle. The selection of neutrons in a narrow energy band was accomplished from proton time-of-flight measurements with the two proton detectors. For variation of the neutron detection energy measurements were made at different scattering angles.

The results obtained from our efficiency measurements are shown in Fig. 14. The detection efficiency for the 4.5 cm diameter, 3 cm thick, NE 213 liquid scintillator was determined for three different thresholds of 0.6, 4.2 and 17.5 MeV electron energy (MeV_{ee}). The corresponding efficiencies predicted by the Cecil code are in good agreement with the measured values. Only for the 17.5 MeV_{ee} threshold the two data points above 300 MeV are systematically higher than the predictions which could be due to the fact that the code of Cecil does not include pion production.

6. CONCLUSION

The experimental program persued during the last two years in conjunction with the project study for a German spallation neutron source has provided a large number of accurate high energy spectra results. These results together with recent neutron production cross section measurements from Los Alamos have revealed some significant inconsistencies with existing theoretical model calculations, particularily in the cascade energy region. It appears,therefore, worthwhile to intensify specific comparisons of experimental results and model calculations. Apart from thick target yields and spectra absolute neutron and charged-particle production cross section measurements provide a useful tool to efficiently test the underlying nuclear models used in existing high energy nucleon-meson transport codes.

The authors acknowledge the help provided during the measurements by the SIN staff,especially Dr. W. Fischer and Dr C.Tschalär, and by the LNS staff, particularily Dr. F.Faure, Dr.G. Milleret and Dr. J. Siret

REFERENCES

1. HETC - ORNL - 4744 (Oak Ridge National Laboratory)
2. R.A.Cecil, B.D. Anderson and R.Mady, Nucl. Instr. and Meth.161,439(1979)
3. N.R. Stanton, Report, COO-1545-92 (1971)
4. H.W.Schmitt, W.E. Kiker and C.W. Williams, Phys Rev.B137,837(1965)
5. D. Filges,P. Cloth, R.D.Neef,G. Sterzenbach, Contr. to Spallation Source Meeting, Bad Königstein, 18-20 March 1980

6. F. Raupp, S. Cierjacks, Y. Hino, S.D. Howe, M.T. Rainbow, M.T. Swinhoe, L. Buth, contribution to this conference
7. S. Cierjacks, M.T. Rainbow, M.T. Swinhoe, L. Buth, KfK-Report, KfK 3097B, Dec 1980
8. Y. Hino, S. Cierjacks, S.D. Howe, F. Raupp, M.T. Rainbow, M.T. Swinhoe, L. Buth, contribution to this conference
9. T.W. Armstrong, private communication
10. S.D. Howe, PhD Thesis, Kansas State University, 1980
11. S.D. Howe, S. Cierjacks, Y.Hino, F. Raupp, M.T.Rainbow, M.T. Swinhoe, L. Buth, contribution to this conference
12. W.J. Mc Donald, A. Anderson, L. Antonuk, W.K. Dawson, D.A. Hutchson, P.Kitching, C.A. Miller, D.M. Sheppard, Nucl. Instr. Meth. 166,187 (1979)

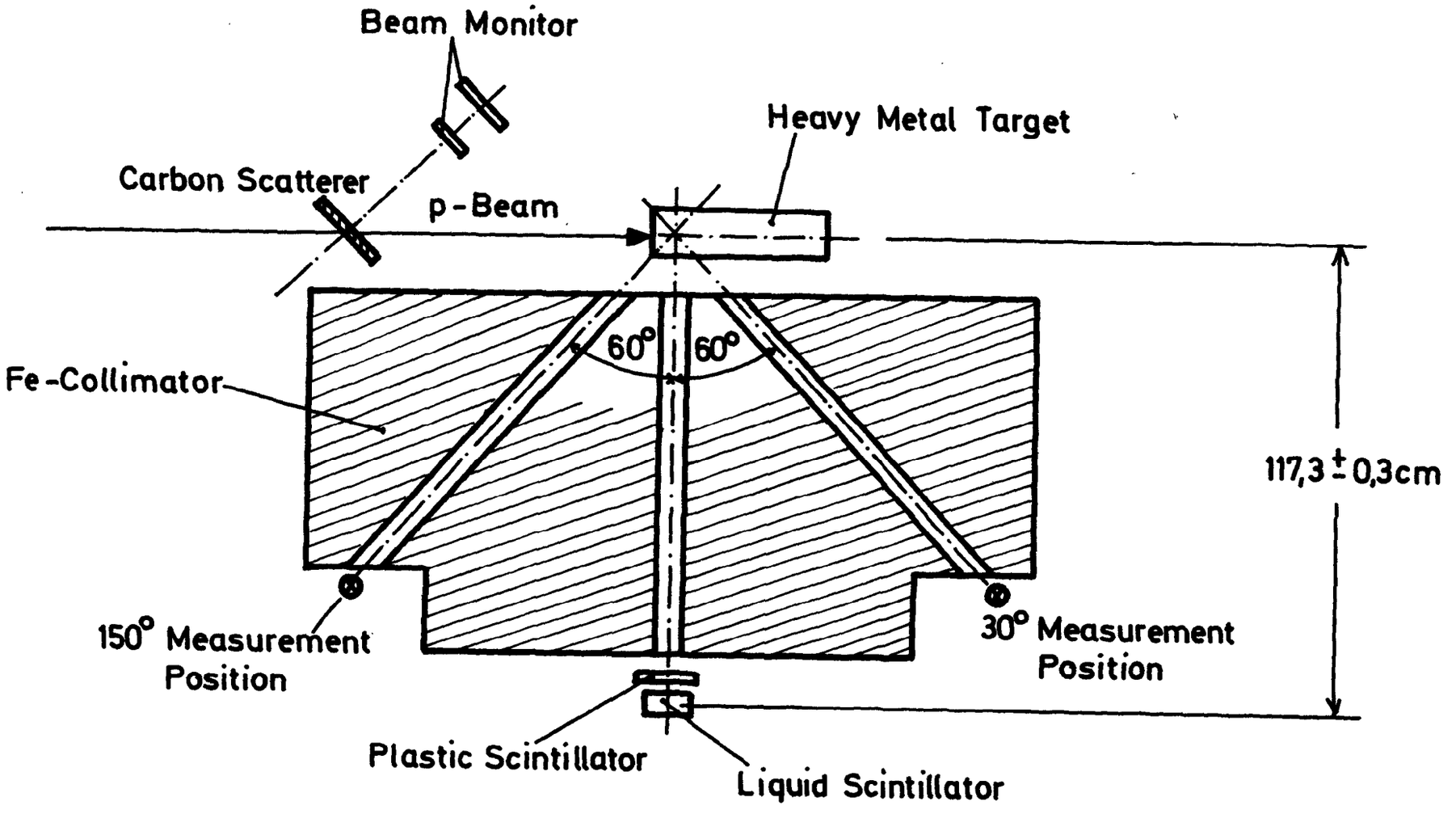

Figure 1 - Schematic diagram of the experimental arrangement used for the SIN time-of-flight experiments

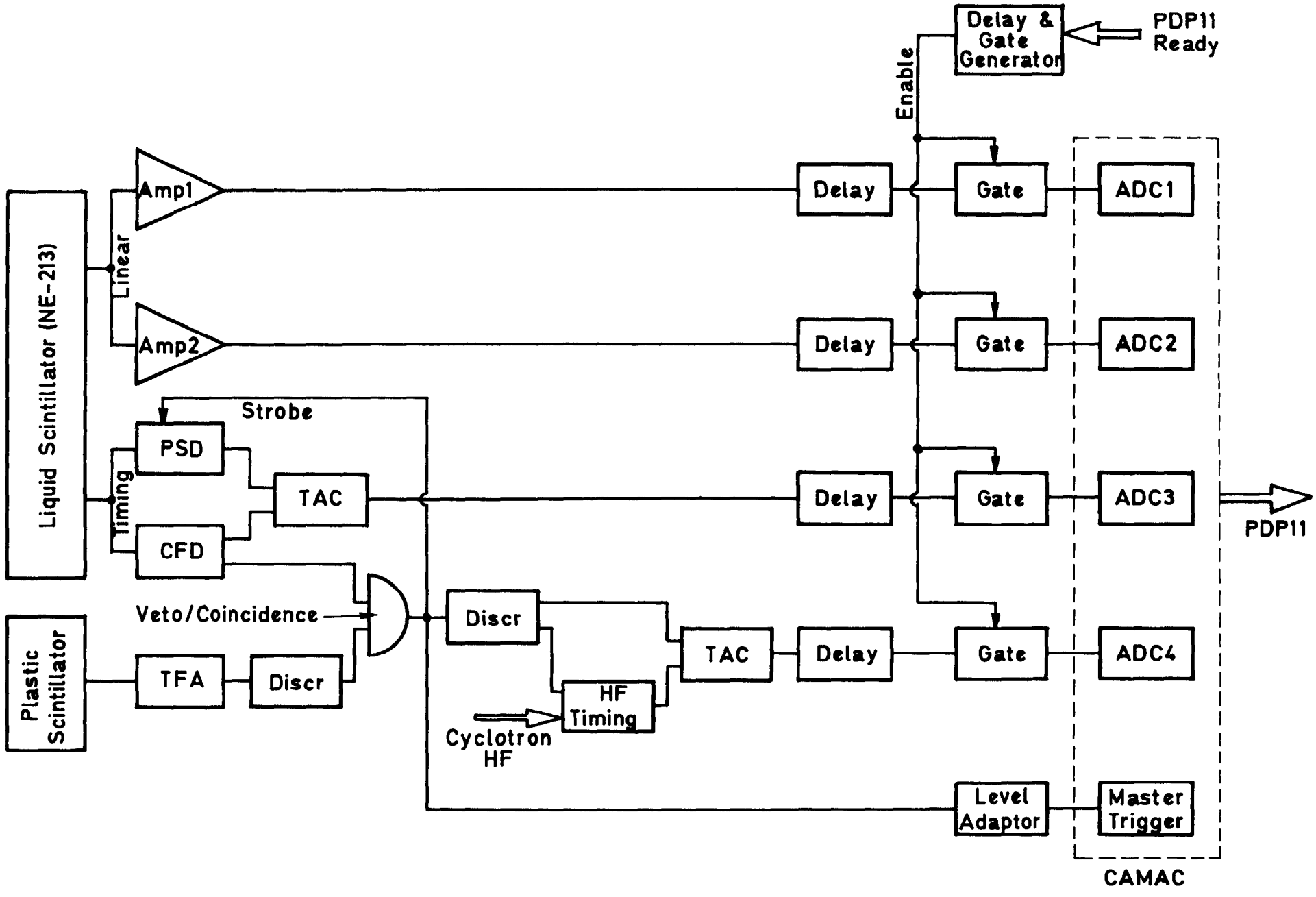

Figure 2 - Simplified circuit diagram of the electronics used in the time-of-flight experiments

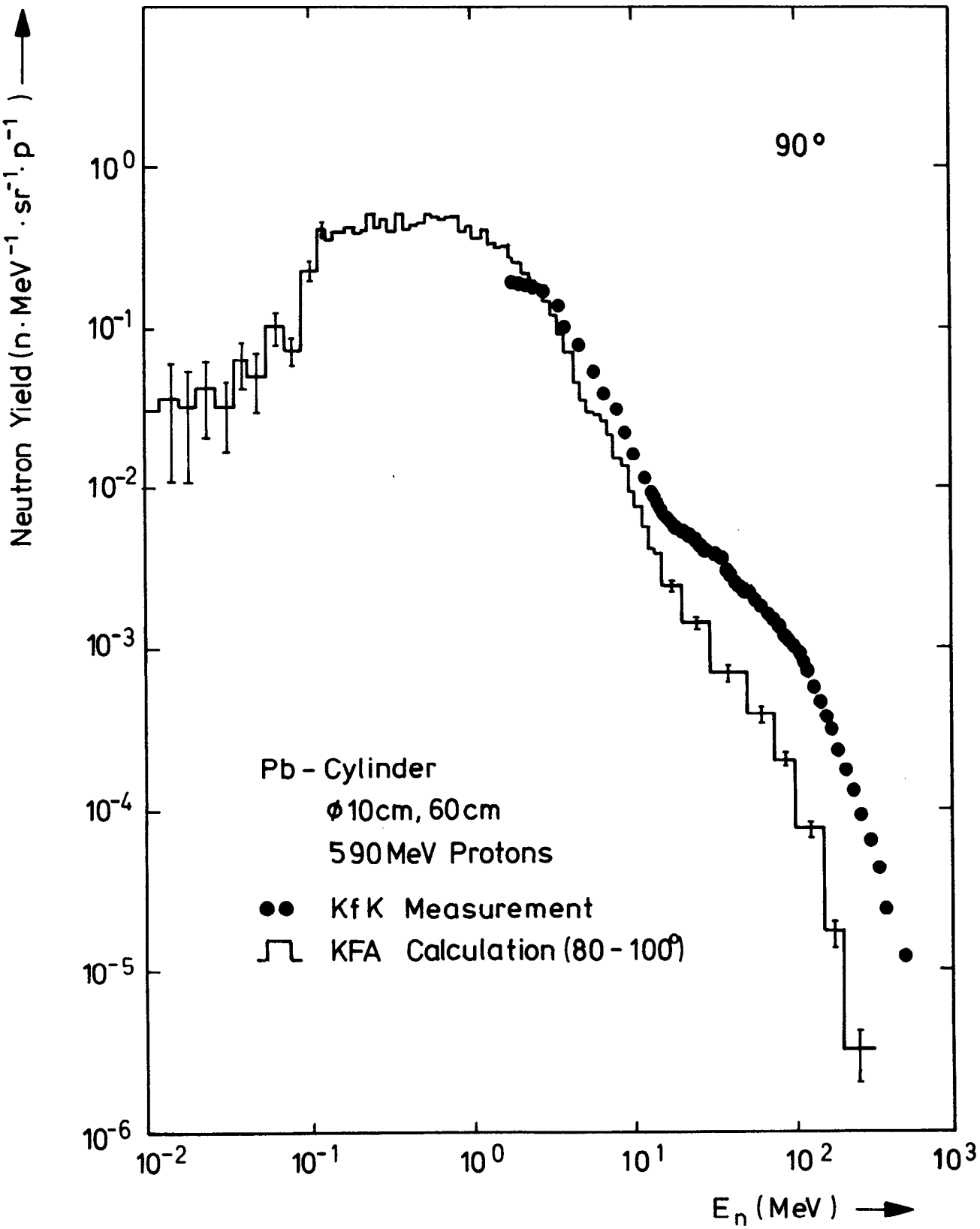

Figure 3 - Measured and calculated neutron spectra from a thick lead target at 90° for an incident proton energy of 590 MeV

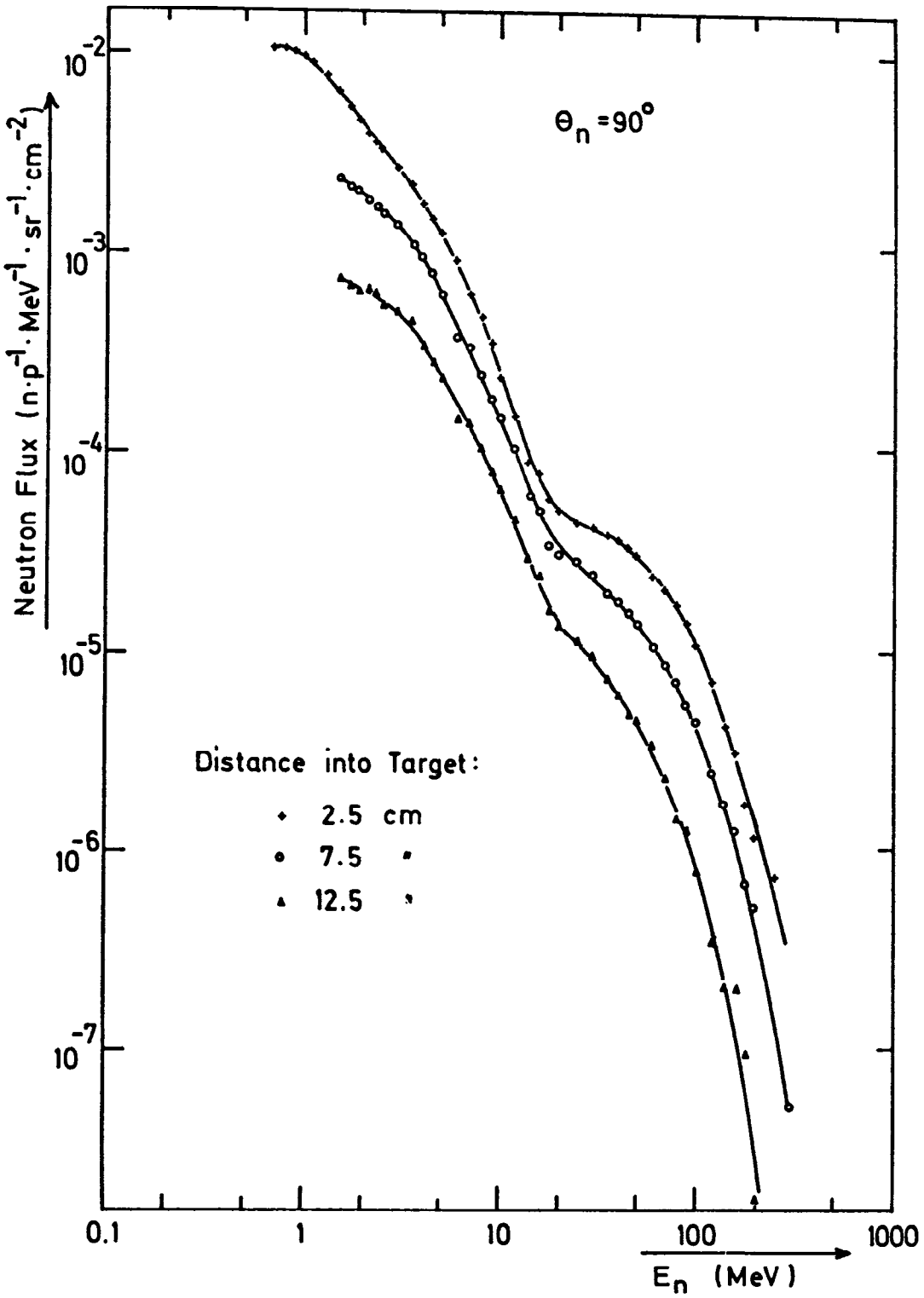

Figure 4 - Differential spectra of neutrons emitted at 90° from the first three blocks of a thick, 10x10 cm, uranium target for an incident proton energy of 590 MeV. Given data refer only to neutrons coming from the effective target volume

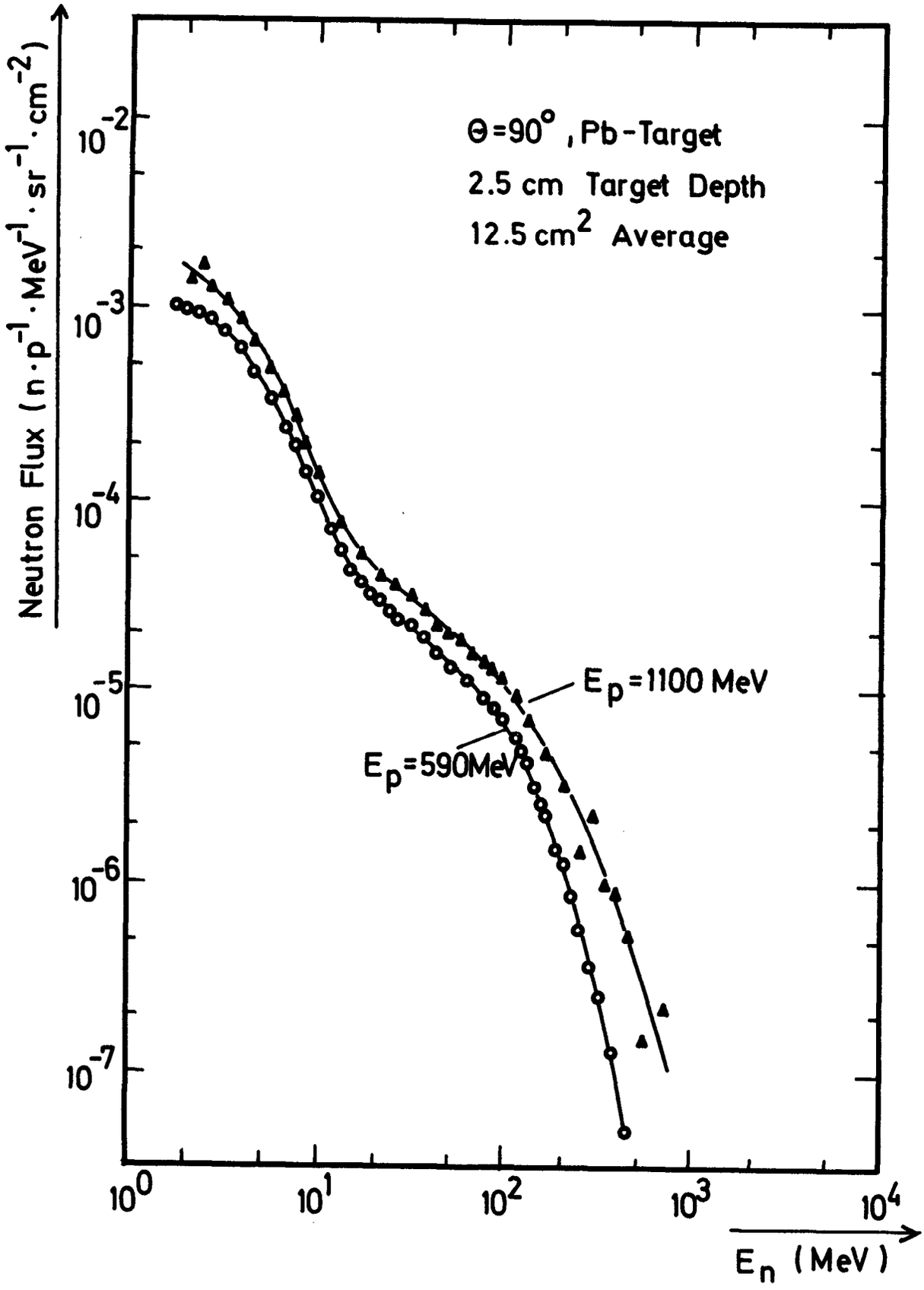

Figure 5 - Differential spectra of neutrons emitted from the first 5 cm block of a thick, 10 cm diam, lead target for incident protons of 590 and 1100 MeV. Given data refer only to neutrons coming from the effective target volume

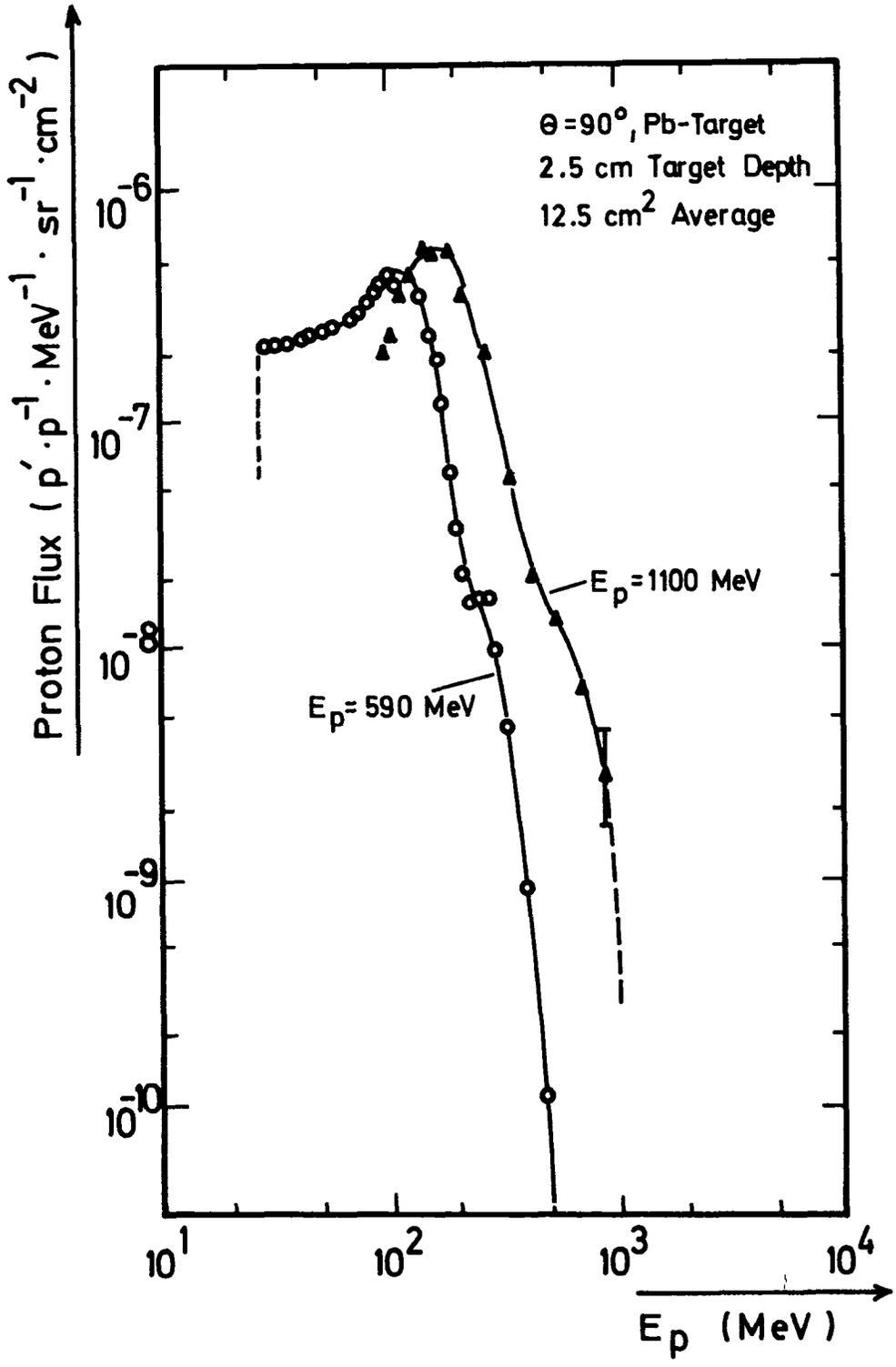

Figure 6 - Differntial spectra of protons emitted from the first 5 cm block of a thick, 10 cm diam, lead target for incident protons of 590 and 1100 MeV. Given data refer only to protons coming from the effective target volume

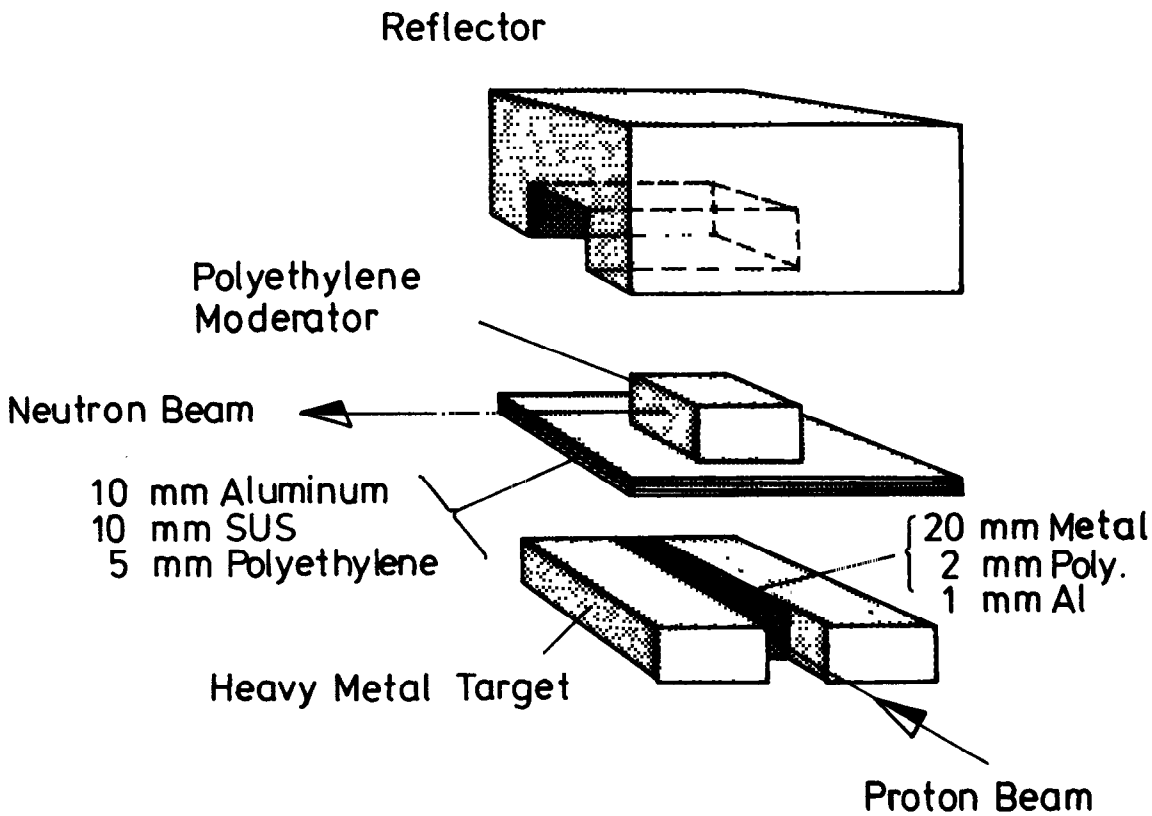

Figure 7 - Geometric arrangement of the target configurations (disassembled) studied at the SATURNE accelerator

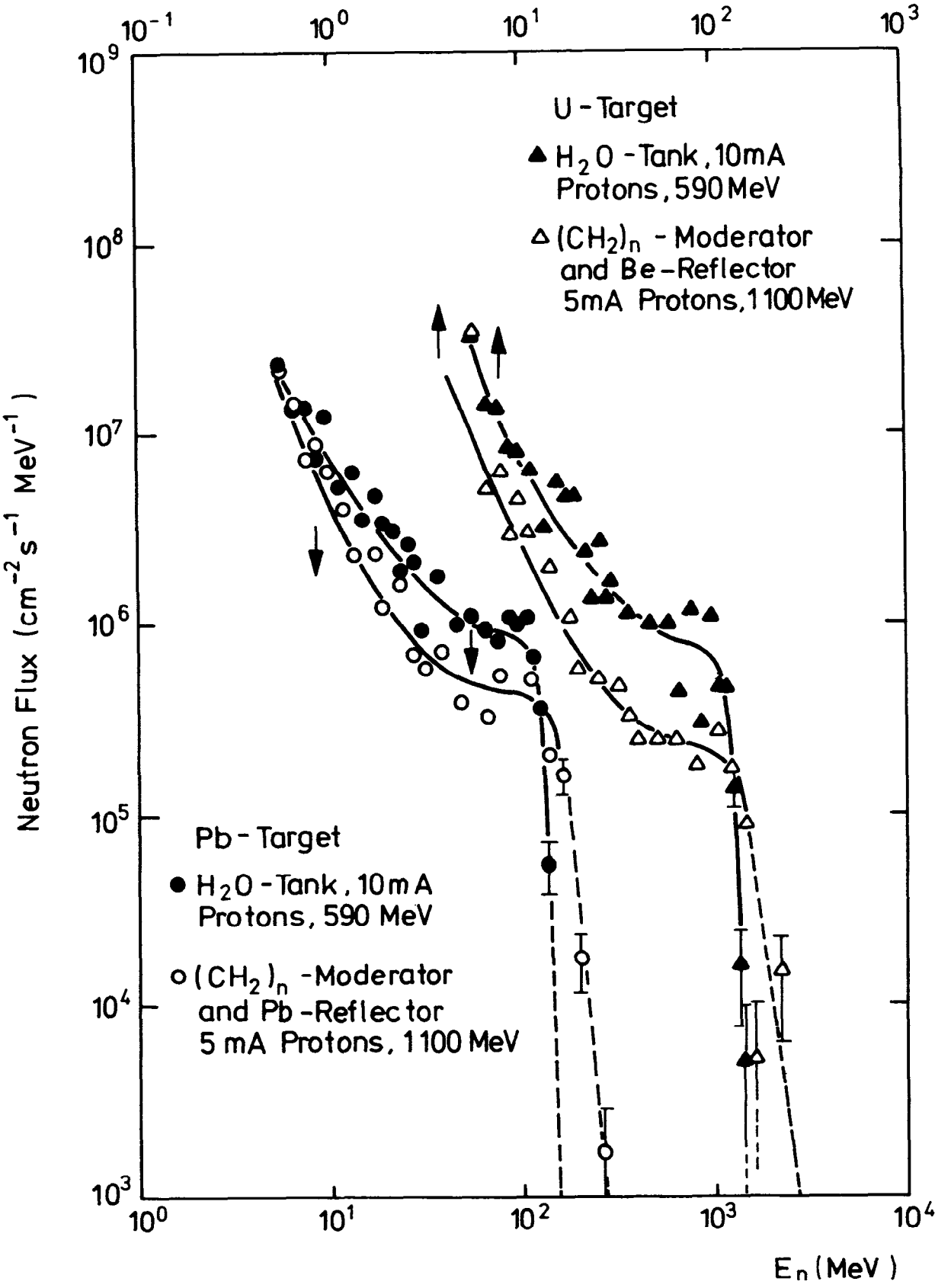

Figure 8 - High energy neutron spectra from moderated sources for several target configurations bombarded by 590 and 1100 MeV protons

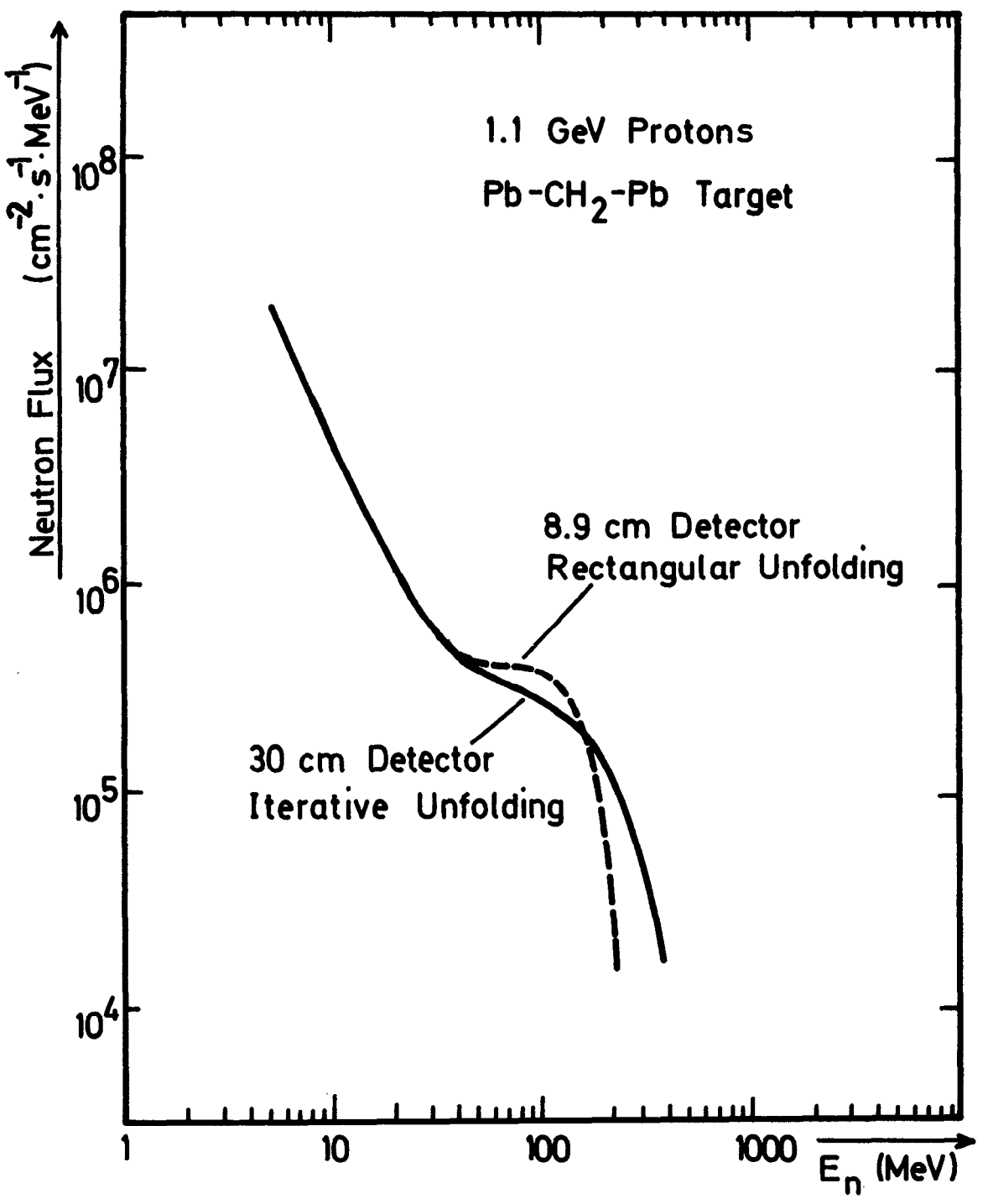

Figure 9 - Comparison of a spectrum measurement with a commercial, 8.9 cm long, liquid scintillator and rectangular unfolding and with an improved, 30 cm long, detector and iterative spectrum unfolding

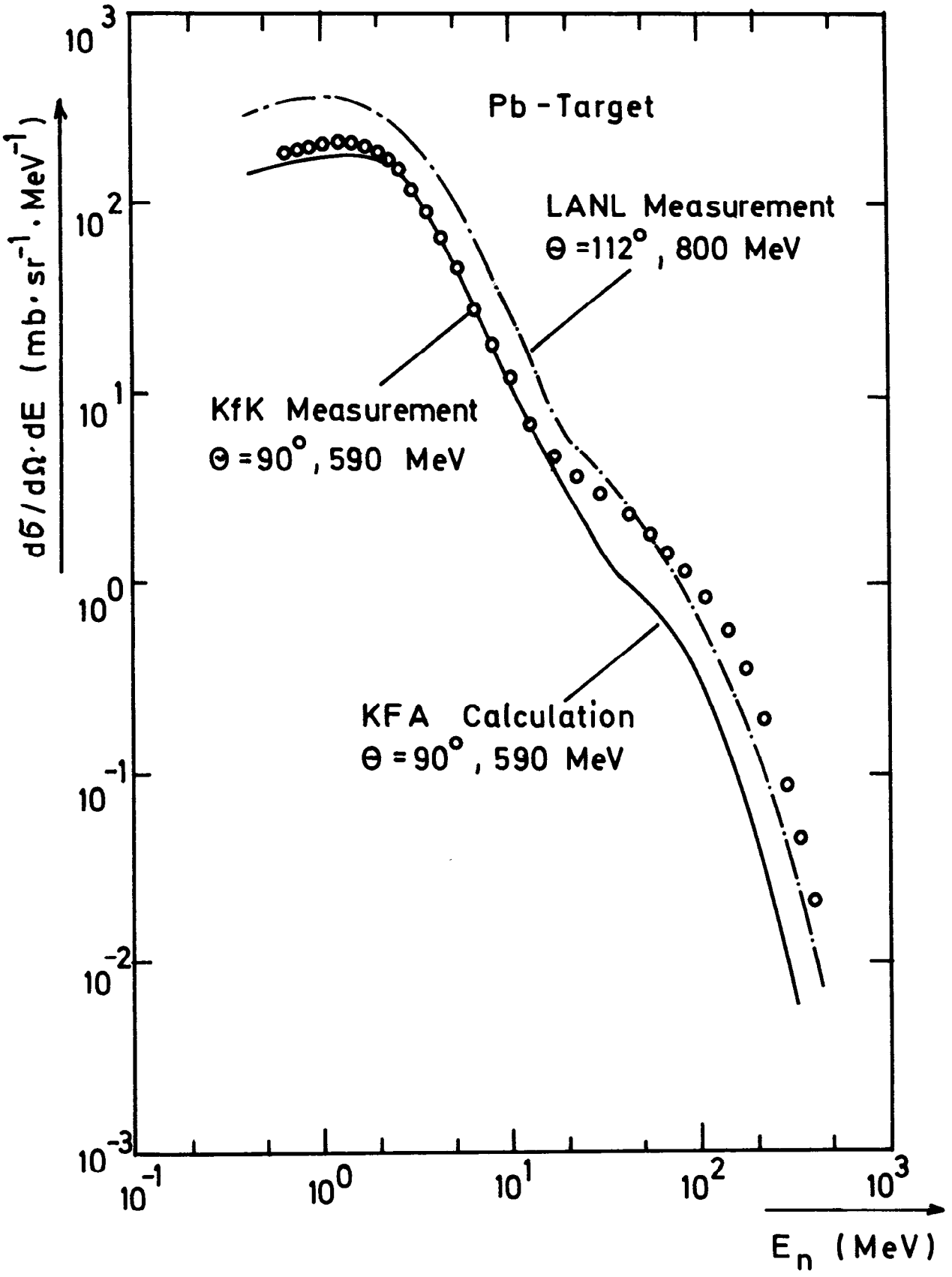

Figure 10 - Measured and calculated neutron production cross sections of lead for 590 and 800 MeV protons. The 800 MeV production cross section was taken from ref. 10

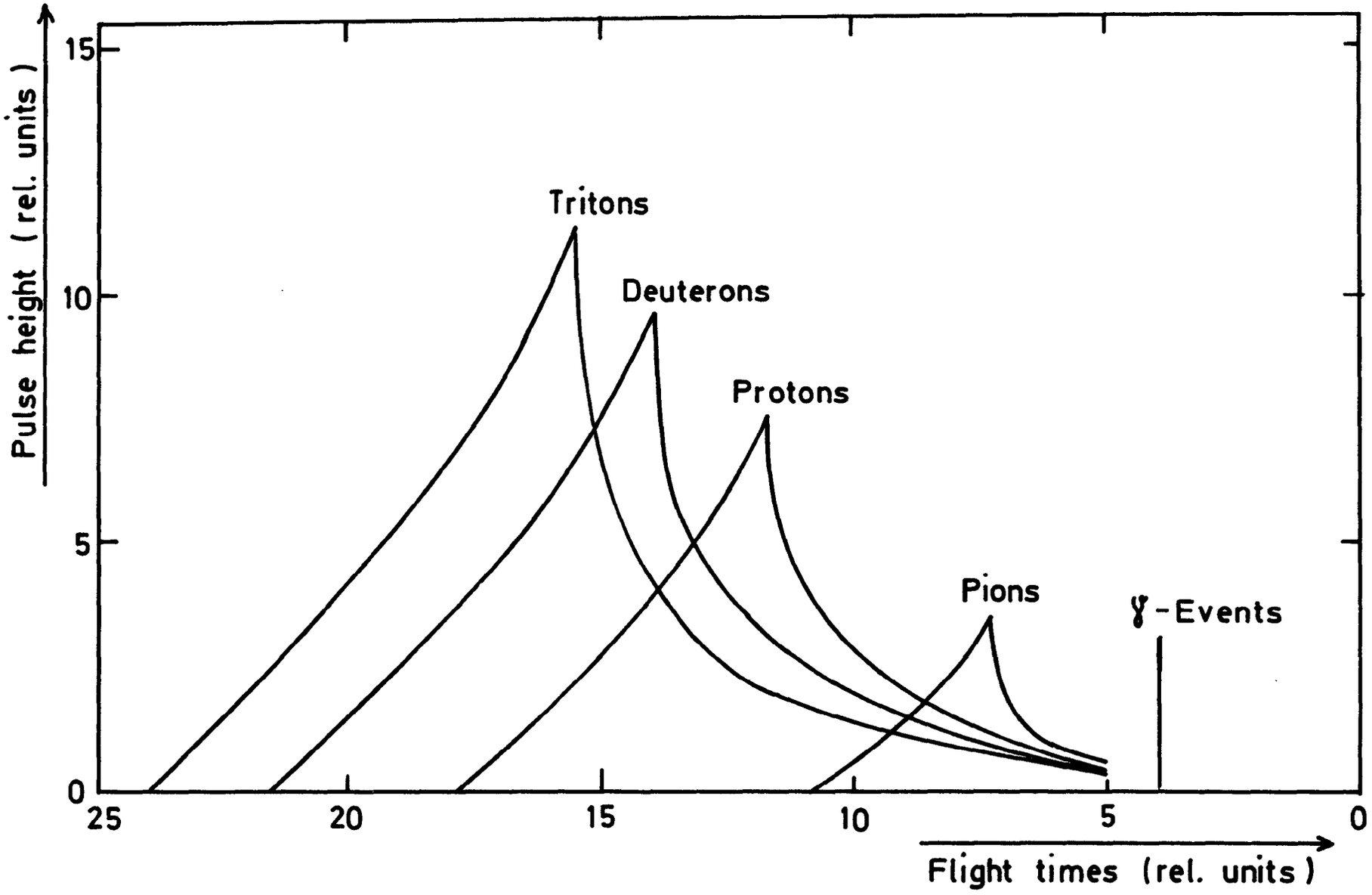

Figure 11 - Calculated relationship between energy deposition and time-of-flight for various light charged-particles. The given relationship applies for a thin detector (see text)

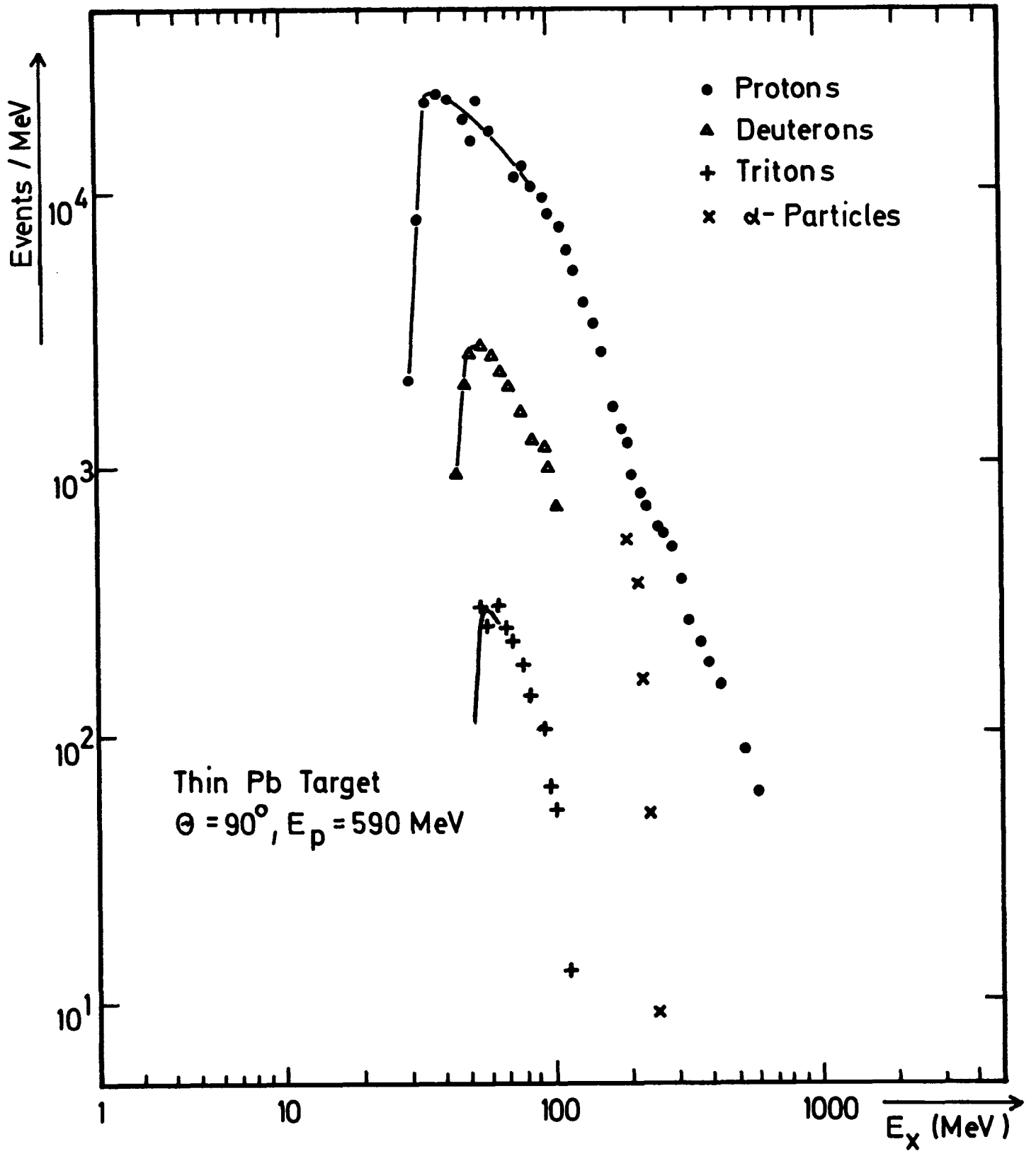

Figure 12 - Charged-particle spectra obtained at 90° from a 5.6 gr/cm^2 lead target bombarded by 590 MeV protons. Absolute spectra from thin targets are presented in a workshop contribution of this conference (11)

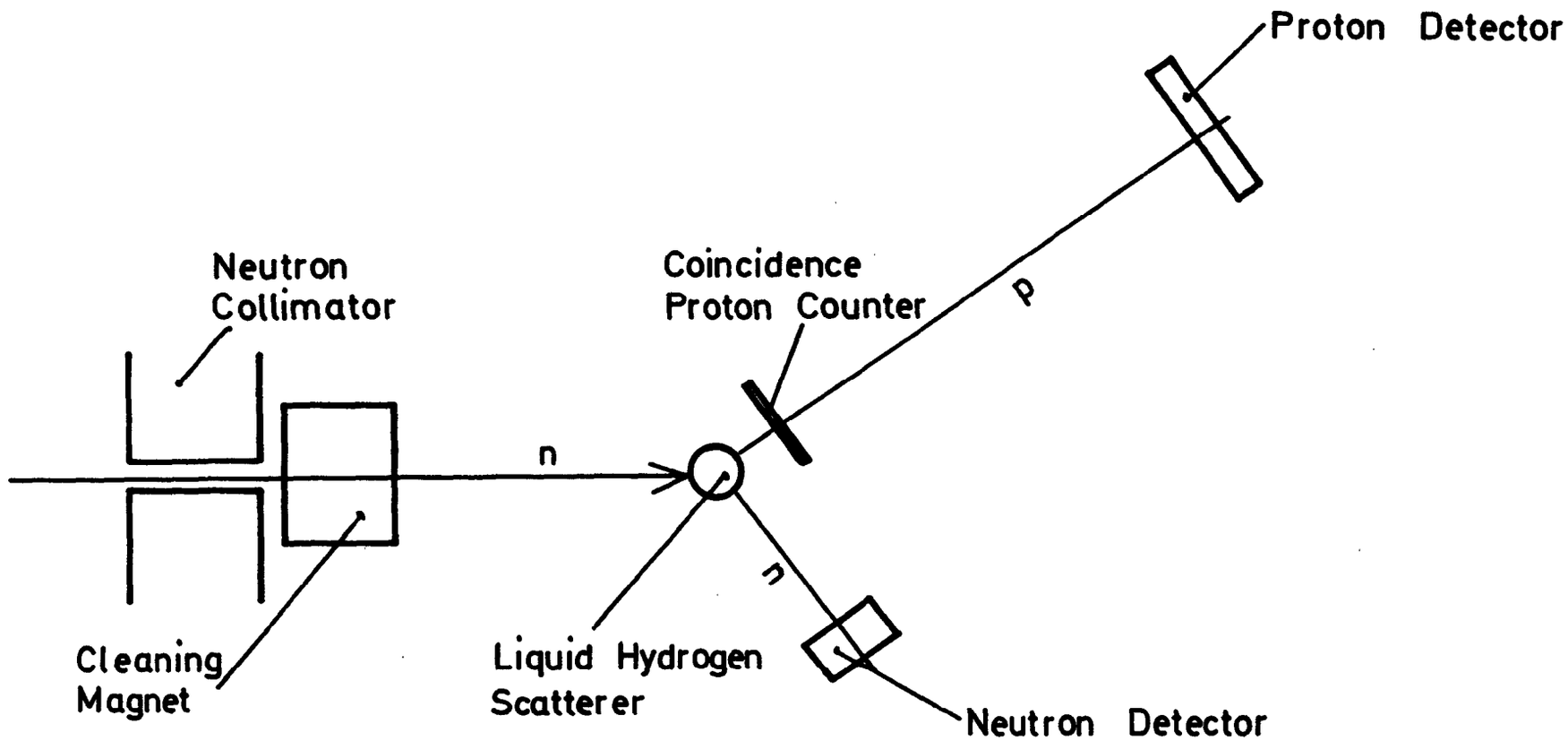

Figure 13 - Schematic drawing of the experimental arrangement used to measure neutron detection effiencies

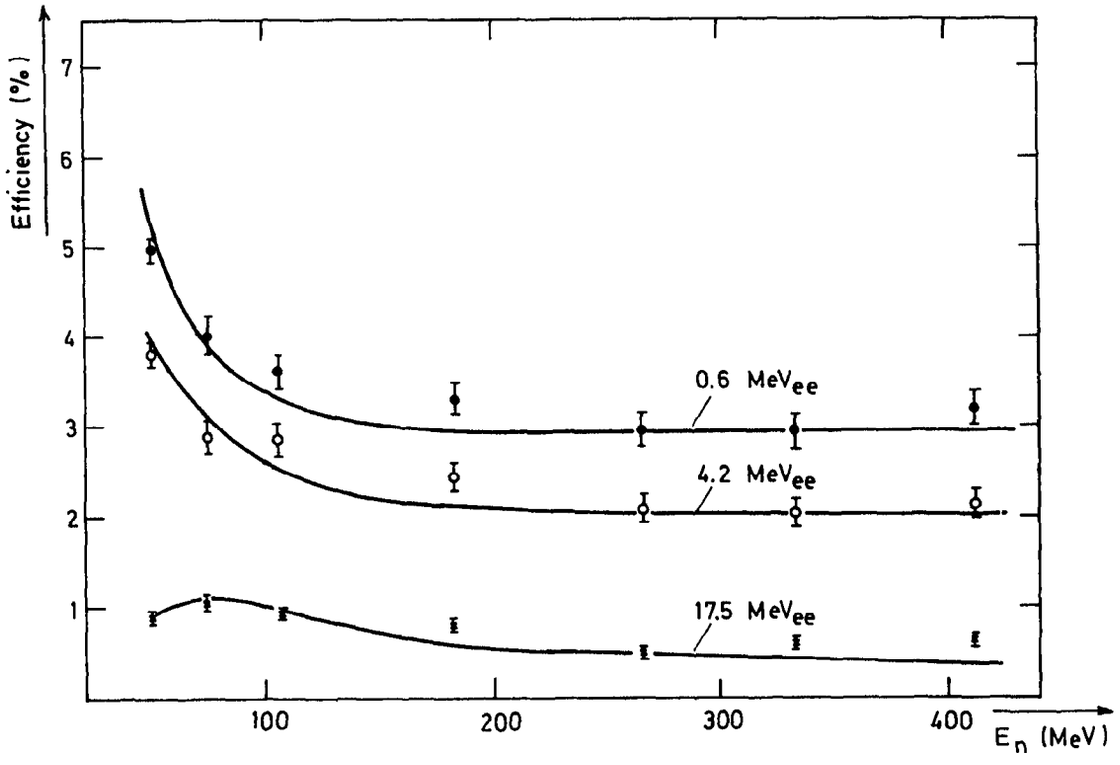

Figure 14 - Measured and calculated detection efficiencies for a 4.5 cm diameter, 3 cm thick, NE 213 liquid scintillator. Measurements and calculations were performed for detector thresholds of 0.6, 4.2 and 17.5 MeV electron energy (MeV_{ee})

Jül-Conf-45 B7

I C A N S - V

MEETING OF THE INTERNATIONAL COLLABORATION ON

ADVANCED NEUTRON SOURCES

June 22-26, 1981

Radiation Effects in Targets and Structural Components of a Spallation Neutron Source

P. Jung

Institut für Festkörperforschung, KFA Jülich, Germany

Assoziation Euratom-KFA

Abstract

The basic effects of radiation damage on mechanical properties of metals are reviewed with special consideration of the operation conditions of high power spallation neutron sources. The possibility to use data from fast reactor experiments is discussed. Guide lines to material selection for a spallation neutron source are given with emphasis on the implications from radiation damage.

I. Introduction

It is well known that irradiation by energetic particles changes the physical and mechanical properties of solids /1-3/. Unfortunately most of these changes have negative consequences on the behaviour of materials under the operation conditions for example of a nuclear reactor. At present, material problems must be considered to be the limiting factors of the life times of fast breeder and future fusion reactors, and are closely related to the question of safe and economic operation of these advanced reactors. High power advanced neutron sources will share some of these problems and will possibly encounter some now ones due to their special operation conditions. That means, to demonstrate the engineering and economic feasibility of a high power spallation neutron source (SNS) also the material problems must be solved.

As current designs predominantly consider metallic materials for components of a SNS, the present surview is confined to the behaviour of metals and alloys under irradiation.

No large-scale material testing program comparable to those for fast breeder or fusion reactors are envisaged for the SNS. Therefore material selection will be mostly based on existing data from the above programs. The major part of radiation damage in the SNS target area are caused by the proton beam (800 - 1100 MeV) and by the energetic part of the spallation neutron spectrum. Both types of irradiation cause atomic recoil spectra which are different from recoil spectra obtained in present reactors or in current simulation experiments employing charged particles. Therefore caution must be taken when presently available data are used to estimate the response of structural materials in a SNS environment

II. Basic effects of energetic particle irradiation in solids

II.1 Displacement damage

An energetic particle (energy E, mass m) which is absorbed in a target atom (mass M), transfers a kinetic energy

$$T_i = E \frac{mM}{(m+M)^2} \qquad (1)$$

to the atom. This energy must be modified by the distribution of the recoil energies of emitted secondary particles from nuclear reactions. Elastic recoils, which only predominate at small particle energies, cause a spectrum of recoil energies of the primary knocked-on atom up to a maximum energy of 4 T_i. The primary atom transfers its energy to surrounding lattice atoms, initiating a so-called displacement cascade. The number of defects $N_d(T)$ produced in a cascade of energy T can be calculated by a standard procedure /4/ if appropriate parameters are used (for Refs. compare Ref /5/). Integrating N_d over the distribution $d\sigma(T)$ of recoil energies which is derived from scattering experiments or calculated from nuclear models, yields the so-called displacement cross section σ_d:

$$\sigma_d(E) = \int N_d(T) d\sigma(T) \qquad (2)$$

The displacement dose K in units of displacements per atoms (dpa) for a certain particle fluence Φ is then given by:

$$K = \sigma_d \Phi \qquad (3)$$

Calculations for 800 MeV protons are published in Ref. /6/ and for spallation neutrons in Ref. /7/.

K describes only the total number of interstitials and vacancies produced, but does not reflect their spatial arrangement. Especially the size of a cascade may be important with respect to recombination and agglomeration processes. The size distribution of cascades produced by a certain particle is determined by the spectrum of recoil energies.

It is known that fast-fission neutrons produce a significant amount of damage only within a rather narrow range of recoil energies while spallation neutrons /7/ and probably also 800 MeV protons /6/ produce much broader recoil spectra. Broad recoil spectra are typical for light ion irradiations already in the 10 MeV range. The fact that for example the recoil spectrum of 800 MeV protons extends to much higher energies, presumably does not produce qualitatively new radiation damage effects. This may be deduced e.g. from the similarity of 14 MeV neutron damage and that of fast fission neutrons, /8/, and can be explained by the observation that displacement cascades above a certain energy split into smaller units (subcascades) /9/.

II.2 Transmutations

Nuclear reactions following inelastic collisions between the irradiation particle and a target nucleus have three consequences which are closely interrelated:

a) Production of light reaction products, preferentially H and He. Helium is supposed to be of special importance due to its very low solubility in metals. Therefore it tends to segregate to grain boundaries and eventually causes embrittlement.

b) Change of the chemical composition of the irradiated material. This may induce phase instabilies or precipitations with important effects on mechanical properties.

c) Radioactivity from instable daughter nuclei. Radioactivity is of great importance with regard to maintainance and final disposal of structural components.

These effects may vary strongly for different elements and even isotopes. Therefore they should be known for each isotope of a structural alloy.

In table I some of the basic radiation effect data of a conceptional high power SNS design are compared to values expected in fast fission and fusion power reactors. For the SNS-design Mo and Al were used as examples for stationary and rotating structures, respectively. The difference in damage parameters between these two columns are primarily not specific for these materials but

Reactor	Breeder [a]	Fusion [a]	SNS (Germany) [b]	
Material	Steel	Steel	Mo stationary	Al rotating
displacement rate [dpa/year]	50	20	700	4
appm He/year	10	400	$6 \cdot 10^4$	200
appm He/dpa	0.2	20	90	60
temperature [°C]	300-600	300-500	800	50
stress level [MPa]	60-120	60-200	100	80
cycles/year	10	10^4-10^8 [c]	$3 \cdot 10^9$	$1.6 \cdot 10^7$

a) Ref. /10/

b) Ref. /11/

c) The lower value is typical for a magnetic device (Tokamak) the upper value for intertial confinement (Laser fusion).

Table I Estimated irradiation parameters in different environments

are due to the fact that rotating parts in this design are only about 0.5% of the total time exposed to the proton beam. Table I shows that displacement rates and He-production in a stationary part would be orders of magnitude above the highest values expected in both fission and fusion reactors. On the other hand the data for the rotating parts are similar to those in a fusion reactor. Temperatures and stress levels of the SNS-design are inconspicuous but the high cycling frequences of the particle fluxes in the SNS are partly comparable only to inertial confinement fusion devices. The cyclic nature of damage production must be considered as an outstanding and widely unexplored peculiarity of the SNS.

III. Mechanical property changes under energetic particle irradiation

The basic irradiation effects described in the last section have implications on a variety of material properties. As mechanical property changes are assumed to have the most severe consequences on the operation of a SNS, they will be discussed now in more detail.

III.1 Dimensional changes

While sputtering is no longer considered a serious problem for structural materials with respect to surface erosion under high energy light ion or neutron irradiation, significant dimensional changes may be caused by void swelling, irradiation growth and irradiation creep /12/.

a) Void swelling
Voids are three dimensional aggregates of vacancies which nucleate preferentially under the action of gaseous impurities (helium) and grow due to vacancy supersaturation which is caused by the stronger attraction of self interstitials to dislocations. Void swelling shows a strong temperature dependence (Fig. 1): At low temperatures the low mobility of the vacancies causes high stationary vacancy concentrations and therefore enhanced recombination with the interstitials. Only at temperatures around half the melting temperature when vacancies become more mobile, recombination is reduced and maximum swelling occurs. At still higher temperatures thermal vacancy emission from the void surfaces competes with void growth, causing reduction of swelling.

The peak swelling temperature is shifted upward with increasing displacement rate, as high stationary vacancy concentration - on the low temperature side of the peak - and void growth - on the other side - persist to higher temperatures (Fig. 1).

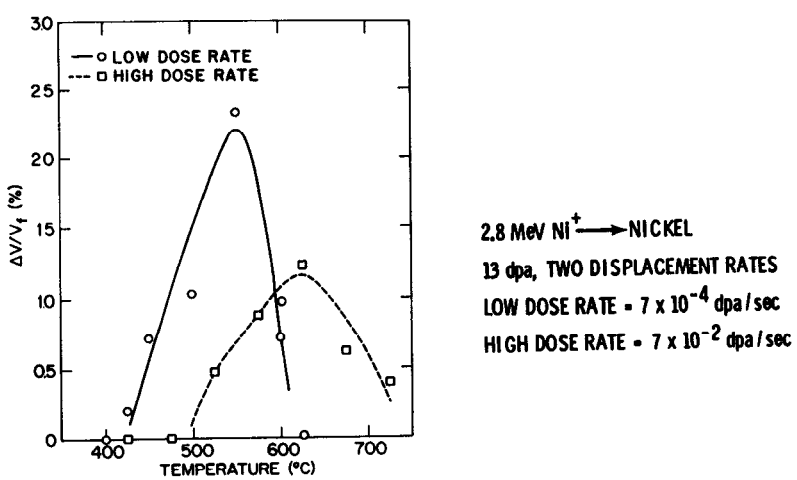

Fig. 1 Temperature dependence of swelling observed in Ni^+ ion irradiation of nickel at two displacement rates /13/.

Void swelling is also affected by the dislocation density. While at very low dislocation densities swelling is suppressed by enhanced recombination, a very high dislocation density also reduces void formation by capturing vacancies before they are able to agglomerate. But tailoring of the microstructure is only of limited use to reduce void swelling or other property changes under irradiation, as under irradiation a new microstructure evolves which is largely independent of the starting conditions.

These considerations also apply to the dependence of void swelling on composition. It is well established that for example in stainless steel void swelling is reduced by increasing the content of nickel, silicon, carbon or other "light impurities". But microchemical changes due to segregation or precipitation occur under energetic particle irradiation already at displacement doses of a few dpa /14/ even in thermally stable alloys. That means, compositional modifications of an alloy may become ineffective due to microchemical changes already at rather low doses, while changes in overall chemical composition by transmutations occur usually much later.

The microchemical alterations during irradiation may also be the reason that swelling resistant alloys shows an incubation period for void formation of about the same dose range in which segregation occurs /14/.

Tensile stresses reduce this incubation period but seem to have no pronounced effect on the subsequent void growth /15/.

Theoretical calculations predict a general but moderate reduction of void swelling under pulsed irradiation compared to an equal steady state dose /16/. This is mainly due to enhanced recombination during the pulse-on time. At higher temperatures void shrinkage by vacancy emission during the 'off'-times further lowers the swelling rate.

A recent study of void swelling of aluminium under 800 MeV proton irradiation /17/ shows reasonable agreement with results from neutron irradiation.

b) Irradiation growth

In non cubic metals like Zirkonium alloys and uranium, a further type of dimensional change is observed which is called irradiation growth. The underlying mechanism is distinct from void swelling as no density change occurs, and distinct from irradiation creep as no external stresses are necessary. At the moment no exhaustive theory is available. In agreement with experimental evidence, current theoretical models attribute microscopic straining to the climb of dislocations and loops on the prismatic planes by the absorption of interstitials while the excess vacancies go to grain boundaries or at lower temperatures are also trapped at substitutional atoms. The models differ in their assumptions whether this separation of interstitials and vacancies is achieved by a preferential attraction of vacancies to grain boundaries /18/ or by preferential attraction of interstitials to dislocations /19/.

Macroscopic straining resulting from strains in the individual grains, depends on texture and probably grain size of the polycristalline materials. Similar to the case of void swelling at least part of the strain is recoverable by annealing to temperatures where vacancy emission occurs.

Irradiation growth is essentially linear in dose with some intermediate leveling off, observed for example in Zircaloy. It decreases with increasing temperature probably due to a reduced strength of the vacancy sinks.

No information on the effect of cyclic irradiation is available. As current theories predict enhanced straining under pulsed irradiation only in those cases where glissile motion of dislocations is involved, no large effect of pulsing on irradiation growth should be expected.

c) Irradiation creep

Irradiation creep is an irradiation induced, volume concerving plastic deformation under external stress. Unlike swelling or growth, creep deformation also occurs without irradiation and is a well known phenomena at temperatures above about half the melting temperature. This thermal creep is driven by thermally activated vacancies which interact with dislocations or at very high temperatures with grain boundaries. As the concentration of thermal vacancies drops exponentially with decreasing temperature, thermal creep ceases at temperature below about half the melting temperature. On the other hand the concentration of irradiation defects is essentially temperature independent. Therefore irradiation creep prevails below $T_m/2$ (Fig. 2).

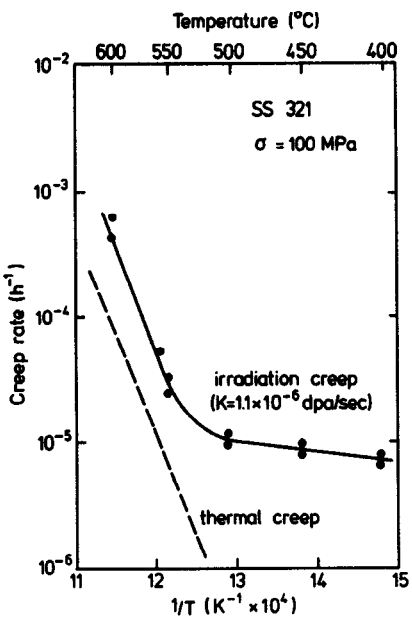

Fig. 2

Temperature dependence of thermal and irradiation creep in cold worked type 321 stainless steel /20/.

Several elaborate models for irradiation creep are proposed /18/. The most prominent are:

i) stress induced preferential nucleation of self-interstitial loops on those lattice plains which are oriented orthogonal to the external stress,

ii) stress induced preferential absorption of self-interstitials at such dislocations or loops, that the strain due to the incremental climb of the dislocation is parallel to the external stress,

iii) stress induced climb plus climb-enabled glide of dislocations. Irradiation defects enable the dislocation to climb across obstacles, while the major part of creep strain is achieved by glissile motion of dislocations.

At the time being, experimental results do not allow a safe decision for one of the above models. Some discrimination may be possible as the first two models predict a linear stress dependence of irradiation creep while the third model gives a higher stress exponent. As most metals investigated so far, show a transition from linear to quadratic stress dependence, a change of the prevailing creep mechanism seems to occur with increasing stress (Fig. 3).

In contrast to the incubation time observed for void swelling, irradiation creep is initially enhanced during some transient dose. Lateron irradiation creep strain is basically linear in dose as long as no significant alterations in microstructure and microchemistry occur. At high doses when void swelling is important an enhancement of irradiation creep is observed indicating a coupling of creep and swelling.

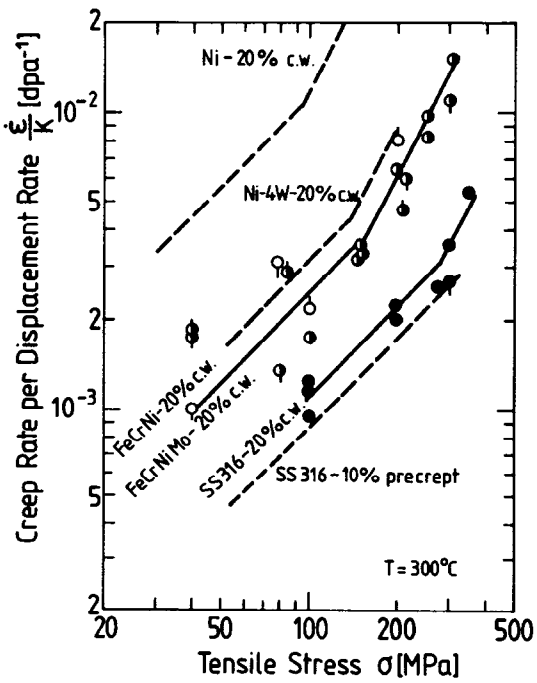

Fig. 3

Irradiation creep rates of 20% cold-worked Ni, Ni-4W, FeCrNi, FeCrNiMo, SS316, and of 10% precrept SS316 show linear stress dependence at low stresses and quadratic stress dependence at high stresses /21/.

The effect of cyclic irradiation on irradiation creep will strongly depend on the operative creep mechanism. For the first two mechanisms, the high defect concentration during pulse time will cause increased recombination. Therefore on the average a reduction in creep strain should be expected. For the third model a strong enhancement of irradiation creep under pulsed conditions is predicted /22/: The basic idea is that under pulsed irradiation interstitials and vacancies arrive at different times at the dislocations due to their widely different diffusion constants. The separate arrival of only one defect species at a time enables enhanced climb to free the dislocation from obstacles. The subsequent glide motion separates the dislocation far enough from the obstacle, such that the following inverse climb motion under the action of the other defect species does not bring the dislocation back to the obstacle. A similar separation of interstitials and vacancies as under pulsed irradiation could be imagined under the action of very large cascades /23/ when defect distribution is very inhomogeneous. The expected enhancement of irradiation creep rate under pulsed conditions ranges up to factors of about 30, but depends strongly on pulse rate, temperature and material properties.

In conclusion a rough estimate should be given what dimensional changes must be expected. For technical alloys uniaxial elongation rates due to void swelling or irradiation growth range up to maximum values around 10^{-3} per dpa and to values slightly below 10^{-3} per dpa for irradiation creep (at 100 MPa). By appropriate choice of temperature the effects of swelling and growth may be reduced, while irradiation creep is almost independent of temperature.

III.2 Strength changes

Structural components are subject to external and internal stresses. Internal stresses may be caused by temperature gradients or inhomogeneous dimensional changes. Some beneficial effects may arise from irradiation creep which enables stress relaxation.

Strength is probably the only basic mechanical property where irradiation has an advantageous effect. A significant increase in yield strength (YS) and a smaller increase in ultimate tensile strength (UTS) is observed (Fig. 4) in most metals already at fairly low doses. This irradiation hardening is ascribed to dislocation pinning by irradiation induced obstacles, which were identified as dislocation loops in the case of pure fcc metals.

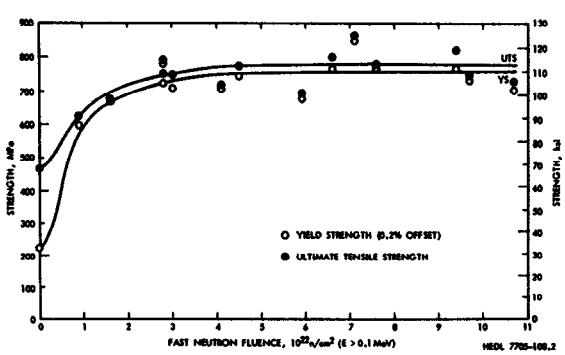

Fig. 4

Effect of neutron irradiation on the strength of annealed type 304 stainless steel at 370°C /24/.

In alloys with high interstitial impurity concentrations also radiation induced precipitation can contribute to obstacle formation. On the other hand in bcc metals occassionally the opposite effect of 'irradiation softening' is observed. This reduction of yield strength under irradiation is ascribed to a complex interaction of the dislocation structure with irradiation defects and alloying elements.

At elevated temperatures the strengthening effect disappears due to a reduced nucleation or even annealing of irradiation produced obstacles and due to an increased thermal mobility of dislocations (creep).

III.3 Ductility changes

Ductility is reduced under irradiation by different mechanisms mainly dependent on temperature and stress.

a) Low temperature embrittlement

The decreasing difference between UTS and YS (Fig. 4) with dose is accompanied by a decreasing elongation to fracture, that means with a loss in ductility (Fig. 5). Due to the close correlation of low temperature embrittlement with irradiation hardening, also the embrittlement disappears at

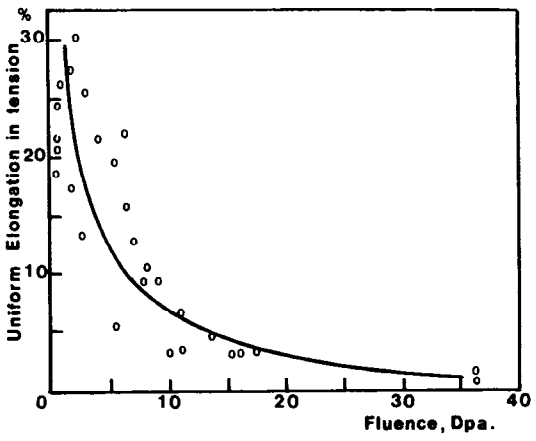

Fig. 5

Uniform elongation in tension of type 316 stainless steel at 400°C /25/.

elevated temperatures (above 450°C in stainless steels) by the reasons described above. Low temperature embrittlement is particular critical in alloys which undergo a ductile-to-brittle transition like most bcc metals and bcc alloys. In materials like ferritic steels the ductile-brittle transition temperature is raised by irradiation from below room temperature to a value within the operating range of e.g. reactor pressure vessels (Fig. 6). Spontaneous crack initiation and fracture is the possible consequence.

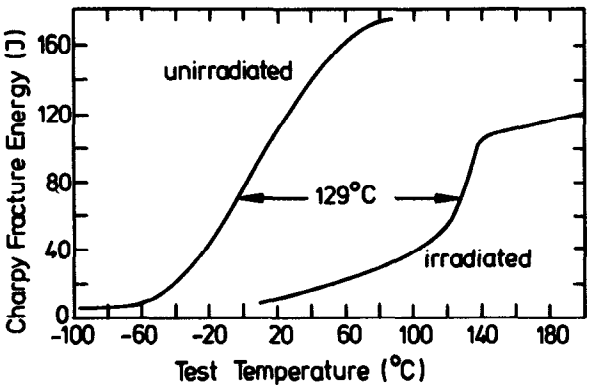

Fig. 6 Shift of ductile to brittle transition temperature of a Ni-Mo-Cr reactor pressure vessel steel irradiated to $1.25 \cdot 10^{20}$ fast neutrons per cm² (after Ref. /26/).

b) High temperature embrittlement

At elevated temperatures when low temperature embrittlement effects disappear new mechanisms of irradiation embrittlement become operative. Among these are irradiation-induced precipitation of new phases and void formation (see section III.1a). But it is now generally agreed that helium created by (n,α) processes (see section II.2) is the dominating factor.

'Helium-embrittlement' becomes noticeable already at concentrations of a few ppm (Fig. 7) and is accompagnied by intergranular fracture in contrast to transgranular fracture of helium free material. Elongation to fracture and rupture time are reduced and both depend strongly on temperature and stress. The application of a tensile stress drastically enhances the nucleation and growth of helium filled bubbles along grain boundaries. The grain boundaries eventually fail when a certain fraction of their areas is covered with bubbles.

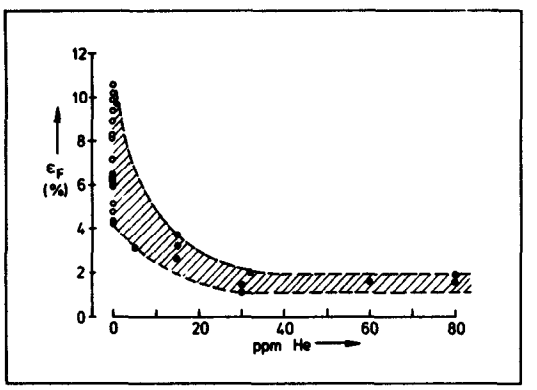

Fig. 7 Reduction of elongation to fracture under creep conditions of type 1.4970 stainless steel by implanted helium /27/.

It is not yet settled whether nucleation /28/ or growth /29/ of the bubbles is the time limiting factor for the embrittlement. So far, most information was obtained from post irradiation tests of neutron-irradiated or α-implanted specimens. Theory and recent experiments /30/ show shorter rupture times if the helium is produced in a specimen under tensile stress. On the other hand, simultaneous production of displacement damage may reduce embrittlement. This is documented by an investigation which is representative for SNS conditions: Irradiation of Al with 600 MeV-p /31/ indicates that under these irradiation conditions - high ratio of He to dpa production - more bubbles are formed near grain boundaries than for the lower He/dpa ratios obtained under fast neutron irradiation.

Only limited information on the effect of cyclic irradiation is available /32/, indicating enhanced coalescence of bubbles under pulsed conditions.

Helium-embrittlement is observed only at temperatures significantly above $T_m/2$. This fact and the strong dependence on temperature and stress may guide to reduce embrittlement by appropriate choice of parameters and materials /33/. Furtheron reduced grain sizes or finely dispersed precipitates - for example TiC in stainless steel /34/ - may be helpful.

c) Fatigue

Fatigue was soon recognized to be a serious problem in fast reactors. To reduce potential hazards, special consideration was given to unavoidable load ramps and shut down procedures. It is obvious that material response under this so-called low cycle fatigue condition which is characterized by low frequencies but high load changes may be entirely different from those in a SNS or an inertial confinement fusion system which both feature high frequencies but smaller stress changes.

Indeed opposite effects of irradiation on fatigue life are estimated in the low versus high cycle fatigue regimes (Fig. 8). In the low cycle fatigue regime strains are high and may even extend into the plastic regime. Therefore loss of ductility by the different mechanisms of irradiation embrittlement are supposed to reduce the fatigue life. On the other hand for high cycle fatigue, strains (must) remain well in the elastic regime. Therefore at not too high temperatures 'irradiation hardening' effects will increase fatigue life /35/.

Holding times under tensile stress during the cycles were found to reduce fatigue life by up to more than an order of magnitude /35/. This is explained in terms of creep-fatigue interaction, possibly with additional effects of the gaseous environment. Helium was also found to reduce fatigue life /36/. The largest effects occured under conditions which are typical for 'Helium-embrittlement' (see section III.3b).

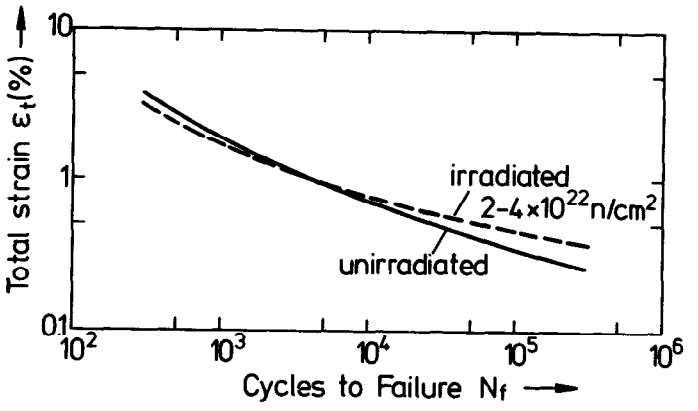

Fig. 8 Estimated fatigue properties of type 316 stainless steel after irradiation to a fast neutron dose of $2.4 \cdot 10^{22}/cm^2$. The results are based on tensile properties at 430°C /35/.

Inspite of the great importance which changes of fatigue properties may have on the economic and safe operation of advanced reactors (and SNSs), theoretical as well as experimental knowledge on this field is still very limited. Even without irradiation, fatigue is one of the least well understood mechanical properties. Furtheron experimental difficulties prevented in-pile tests up to now. Therefore the limited data which are so far available come from post-irradiation tests. From theoretical considerations /37/, simultaneous irradiation may have beneficial effects on crack growth, but only in a regime of temperature and dose rate, where appreciable irradiation hardening occurs during every load cycle.

IV. Guide line to SNS-material selection

The basic criteria for selecting materials for a high-powered SNS are similar to those for other large scala nuclear devices /38/. The following demands must be imposed on a candidate material:

1. Existence of a data base on mechanical and thermal properties and on irradiation effects.

2. Compatibility with coolants etc., corrosion resistance.

3. Fabricability and joining.

4. Adequate price and availability.

5. Low radioactivity (important for service and final disposal).

In the following those irradiation effects will be listed which probably impose the greatest problems to those SNS components which experience the most severe radiation damage:

1. Stationary windows (exposed to the pulsed, high energy proton beam): 'Helium-embrittlement' and probably 'high-cycle fatigue'.

2. Rotating windows, targets and cladding (exposed to the proton beam and to the spallation neutrons):
   'Fatigue' and 'irradiation creep'.
   For Al as cladding material also void swelling and He-embrittlement may be important.

3. Structure (exposed to spallation neutrons and moderated neutrons): 'Low temperature embrittlement'.

It is out of the scope of this paper to give a detailed recommendation for specific materials. Given the complex dependences of mechanical properties and irradiation effects on operation conditions, only for a well defined design the optimal materials can be selected (For a recent study compare Ref. /11/).

References

/1/ Radiation Effects in Breeder Reactor Structural Materials
(M.L. Bleiberg, J.W. Bennett, Eds.),
Scottsdale 1977

/2/ Comportement sous Irradiation des Materiaux Metalliques et des Composants des Coeurs des Reacteurs Rapides
(J. Poirier, J.M. Dupouy, Eds.),
Ajaccio 1979

/3/ Fusion Reactor Materials
(F.W. Wiffen, J.H. DeVan, J.O. Stiegler, Eds.),
Miami Beach, 1979, published in J. Nucl. Mater.Vol 85 & 86

/4/ M.J. Norgett, M.T. Robinson, I.M. Torrens
Nucl. Eng. Des. 33, 50 (1975)

/5/ P. Jung
Report KFA Jülich (1981)

/6/ C.A. Coulter, D.M. Parkin, W.V. Green
J. Nucl. Mater. 67, 140 (1977)

/7/ M.A. Kirk, R.C. Birtcher, T.H. Blewitt, L.R. Greenwood, R.J. Popek, R.R. Heinrich
J. Nucl. Mater. 96, 37 (1981)

/8/ J.B. Mitchell, C.M. Logan, C.J. Ecker
J. Nucl. Mater. 48, 139 (1973)

/9/ K.L. Merkle in Radiation Damage in Metals, ASM, Ohio 1976, p 58

/10/ R. Bullough, B.L. Eyre, G.L. Kulcinski,
Report UWFDM-184 (1976)

/11/ W. Lohmann in Realisierungsstudie zur Spallations-Neutronenquelle,
Kernforschungsanlage Jülich GmbH, Germany
Teil II, A-371 (1981)

/12/ H. Ullmaier, W. Schilling
'Radiation Damage in Metallic Reactor Materials' in Physics of Modern Materials,
Vol. 1, p 301, Vienna 1980

/13/ F.A. Garner, R.W. Powell, S. Diamond, T. Lauritzen, A.F. Rowcliffe, J.A. Sprague, D. Keefer in Ref. /1/ p 543

/14/ F.A. Garner, E.R. Gilbert, W.G. Wolfer, H. Gurol
in Second Topical Meeting on Fusion Reactor Materials,
Seattle 1981, to be publ. in J. Nucl. Mater.

/15/ S.K. Khera, C. Schwaiger, H. Ullmaier
J. Nucl. Mater. 92, 299 (1980)

/16/ N.M. Ghoniem, H. Gurol
Radiation Effects 55, 209 (1981)

/17/ H. Jang, J. Moteff, L. Levinson, R.D. Brown, W.V. Green
J. Nucl. Mater. 98, 98 (1981)

/18/ R. Bullough, M.H. Wood
J. Nucl. Mater. 90, 1 (1980)

/19/ E.J. Savino, C.E. Laciana
J. Nucl. Mater. 90, 89 (1980)

/20/ J.A. Hudson, R.S. Nelson, R.J. Mc.Elroy
J. Nucl. Mater. 65, 279 (1977)

/21/ P. Jung
to be published

/22/ H. Gurol, N.M. Ghoniem
Radiation Effects 52, 103 (1980)

/23/ L.K. Mansur, W.A. Coghlan, T.C. Reiley, W.G. Wolfer
in Second Topical Meeting on Fusion Reactor Materials,
Seattle 1981, to be publ. in J. Nucl. Mater.

/24/ J.J. Holmes, J.L. Straalsund
in Ref. /1/, p 53

/25/ J.M. Dupouy, J. Erler, R. Huillery
in Ref. /1/, p 83

/26/ A. Gerscha, E. Klausnitzer, C. Leitz
Atomwirtschaft 20, 567 (1975)

/27/ A.A. Sagués, H. Schroeder, W. Kesternich, H. Ullmaier
J. Nucl. Mater. 78, 289 (1978)

/28/ H. Trinkaus, H. Ullmaier
Philos. Mag. A39, 563 (1979)

/29/ S.S. Vagarli, G.R. Odette
in Second Topical Meeting on Fusion Reactor Materials
Seattle 1981, to be publ. in J. Nucl. Mater.

/30/ H. Schroeder, P. Batfalsky
in Second Topical Meeting on Fusion Reactor Materials
Seattle 1981, to be publ. in J. Nucl. Mater.

/31/ W.V. Green, S.L. Green, B.N. Singh, T. Leffers
in Second Topical Meeting on Fusion Reactor Materials,
Seattle 1981, to be publ. in J. Nucl. Mater.

/32/ D. Kaletta
J. Nucl. Mater. 85 & 86, 775 (1979)

/33/ K. Ehrlich, D. Kaletta
in Radiation Effects and Tritium Technology in Fusion Reactors
Gatlinburg 1975, CONF-750989, II-289

/34/ W. Kesternich, J. Rothaut
in Second Topical Meeting on Fusion Reactor Materials,
Seattle 1981, to be publ. in J. Nucl. Mater.

/35/ D.J. Michel, G.E. Korth in Ref. /1/ p. 117

/36/ K. Sonnenberg, G. Antesberger, B. Brown
J. Nucl. Mater 101 (1981)

/37/ J. Weertman, W.V. Green
J. Nucl. Mater. 97, 254 (1981)

/38/ R.W. Conn
J. Nucl. Mater. 85 & 86, 9 (1979)

ICANS V
MEETING OF THE INTERNATIONAL COLLABORATION ON

ADVANCED NEUTRON SOURCES

June 22-26, 1981

SUMMARY OF WORKSHOP SESSION ON SPALLATION AND FISSION IN COMPUTATIONAL MODELS

G. J. Russell

Los Alamos National Laboratory
Los Alamos, New Mexico 87545 U.S.A.

For spallation neutron source applications using medium-energy (500 MeV to 1 GeV) protons, it is necessary to calculate a variety of quantities including: a) thermal neutron beam fluxes, b) thermal neutron beam contamination by gamma-rays, charged particles, and high-energy neutrons, c) energy deposition in targets, moderators, reflectors, and shields, and d) shielding effectiveness of materials. The most widely used code to calculate spallation processes is the Oak Ridge National Laboratory (ORNL) High-Energy Nucleon-Meson Transport code (HETC). The predecessor to HETC is the ORNL Nucleon-Meson Transport Code (NMTC).

For high-mass target muclei and energies $\gtrsim$100 MeV, there is competition between evaporation and fission at each step of the nuclear de-excitation process. Recently, there have been two high-energy fission models developed for use in HETC (one by Alsmiller at ORNL and one by Atchison at the Rutherford and Appleton Laboratories (RAL)). Takahashi at the Brookhaven National Laboratory and Nakahara at the Japan Atomic Energy Research Institute have (independently) incorporated high-energy fission into NMTC. The inclusion of high-energy fission in spallation reactions is expected to alter predicted values of energy deposition, residual-nuclei mass distributions, neutron multiplicity in thick targets, and neutron spectrum.

Until recently, experimental data relevant to spallation neutron source applications have been relatively sparce (limited primarily to measurements by Fraser (Chalk River) of thick-target neutron yields and a few measurements of neutron production cross sections and neutron spectra from thick targets). Lately, Russell, Gilmore, et al. (Los Alamos) have measured neutron captures in a water bath for a variety of targets bombarded by 800-MeV protons; similar measurements have been done at lower proton energies by Thorson, et al. (TRIUMF). Howe, Russell, et al. (Los Alamos) have measured angle- and energy-dependent neutron production cross sections for a number of targets bombarded by 800-MeV protons. Differential production cross sections for charged particles (protons, deuterons, tritons, and pions) produced by 590-MeV proton bombardment of different materials have just been measured by Howe, Cierjacks, et al. (KFK Karlsruhe). Raupp, Cierjacks, et al. (KFK Karlsruhe) have measured neutron production yields and spectra from 590-MeV proton bombardment of thick uranium targets. Fertile-to-fissile and fission measurements for depleted uranium bombarded by 800-MeV protons have been done by Russell, Gilmore, et al. (Los Alamos). For the 19.7-cm-diam by 30.5-cm-long target used in this latter measurement, the

data indicate that when high-energy fission is neglected neutron production is underestimated by ~10%. All of the above experiments provide benchmark data for computer code validation; clearly, more experimental data are required. The experiments, however, need to be done very carefully if they are to be valuable for adjusting model parameters in the computer codes.

A detailed systematic intercomparision of model parameters used in the ORNL and RAL versions of HETC with high-energy fission is being done by Armstrong and Filges (KFA Jülich). They are also comparing these code packages with thin and thick target measurements and with thermal neutron production data. They want to establish a reliable computational capability to use in design calculations for the proposed German spallation neutron source. A quantity B_0 occurs in the analytic expression for the level density parameter used in the computer code models; from various analyses, B_0 ranges from 8-20 MeV. For thick targets, Armstrong and Filges conclude that theoretical predictions of neutron production ($\lesssim$20 MeV) agree with experimental data to within 20-30%, and that this general magnitude of agreement can be attained by neglecting high-energy fission. Armstrong and Filges also conclude: a) for standard B_0 values incorporated into models, the ORNL code predicts ~20% more neutrons than the RAL code, b) neutron production is sensitive to the value of B_0 assumed and varies by ~20% over the possible range of B_0, c) for the same B_0, the ORNL code predicts ~12% more neutrons than the RAL code, and d) the effect of including high-energy fission (compared to spallation without fission) is to increase neutron production by ~7% and to produce a slightly harder spectrum in the energy region from ~2 to ~15 MeV.

For energies $\gtrsim$ 20 MeV, calculated differential neutron production cross sections underpredict measured values by factors of 2-5. For energies $\gtrsim$50 MeV, calculations significantly underpredict measured differential proton production cross sections and overpredict measured differential pion production cross sections.

The possibility of having a hybrid neutron source by explicity combining fission and spallation was briefly discussed. Several laboratories have given cursory thought to booster-targets at spallation neutron sources; perhaps by ICANS-VI more consideration will have been given to this subject, including the effects of pulse broading and potential inter-pulse background.

Jül-Conf-45 C2

I C A N S - V

MEETING OF THE INTERNATIONAL COLLABORATION ON

ADVANCED NEUTRON SOURCES

June 22-26, 1981

Summary on the Workshop Session A-2 Spallation Products

N.F. Peek

There were two papers presented in this session covering the work which has been done by the group at KFA-Jülich. The first paper (Peek) described the radioactive measurements that were made and presented the results from a Pb target (3 cm diameter by 0.1 cm thick) 5 cm deep into a Pb target. A beam distribution experiment using Al plates was described and some results from U measurements were compared to the Pb target measurements. The second paper (Amian) described the computer programs which were used to analyze the data

State of Art:

Jülich	- Data has been (and is being) collected from Pb and U targets, but only about 10% has been analyzed
Los Alamos	- Data was collected from a series of U foils off the central beam axis and analyzed for fission products. More analyser will be performed. (Session A-1)
Future work	- Interest was expressed in having radioactive data from a W target (spallation products and possible fission)

Tasks:

Jülich	- Spallation products have been measured with H^+ at 600 and 1100 MeV on Pb and U targets
Los Alamos	- Spallation products (Mainly fission isotopes) have been measured with H^+ at 800 MeV.
TRIUMF	- It is possible that some measurements will be made with 480 MeV H^+

All three laboratories will compare the data obtained.

Needs:

More data should be analyzed in order to supply the HETC calculations with experimental parameters so that more realistic calculations can be made. It was suggested that results from isotope measurements from ICANS experimental groups be sent to:

N.F. Peek
Physics Dept.
Univ. of Calif.-Davis
Davis, California 95616
U.S.A.

Perhaps the data base can be set up and maintained.

Jül-Conf-45

ICANS-V

MEETING OF THE INTERNATIONAL COLLABORATION OF
ADVANCED NEUTRON SOURCES

June 22-26, 1981

Session A3: Beam Quality

A. D. Taylor
Rutherford and Appleton Laboratories
Chilton, Didcot OXON UK

Sessions A1 and A 2 covered problems in the production of fast neutrons in spallation targets. Session A3 is concerned with the conversion of that primary spectrum to a neutron distribution suitable for scattering experiments. Aspects of proposed target-moderator-reflector decoupler assemblies were discussed, together with the measurement of the fast spectrum from the moderator and its relation to background problems. Recent scattering data from the new KENS facility were also presented by Watanabe.

Conrad and Drüke presented data from the SNQ study, taken at SATURNE and SIN. Time-of-flight measurements by Conrad at SATURNE showed a lead reflector to be marginally superior to a beryllium reflector for both uranium and lead targets. The lead reflector aslo produced a better time structure. The gain from grooving the moderator surface was confirmed and a softening in the spectral distribution observed. Using the continuous source of SIN, Drüke measured neutron distributions in a D_2O moderator for a variety of quasicontinuous spallation source configurations.

Russell and Taylor presented data from moderator, moderator poison studies and reflector optimizations done at the WNR. Taylor showed how Monte Carlo codes have been used to chose likely reflector materials and to examine their optimum yield and time structure. Carpenter outlined the target-moderator reflector assembly installed in IPNS-I; the core of the beryllium reflector is cooled to 100 K and all four moderators are cryogenic (two liquid methane, two liquid hydrogen). Cooling the beryllium suppresses upscattering thus reducing the dwell time in the reflector. This allows a decoupling energy as low as 0.1 eV (eg. gadolinium) to be employed.

Hino presented fast neutron measurements from moderators obtained by the FERDOR unfolding method. This method shows a significant imporvement over previous techniques and he concludes that, particularly in slab

geometry, an intense high energy componet exists.

Golub gave a new analytic approach to pulsed moderator problems, based on the diffusion approximation but treating collisions with hydrogen exactly. Although only applicable to simplified problems, this approach provides much more insight than the Monte Carlo techniques.

There is now a wealth of experimental data from working spallation sources (KENS, WNR, ZING-P') as well as the SNQ mock ups at SIN, CERN, and SATURNE. From such practical experience, a better understanding of many aspects of 'beam quality' have emerged. As an example, figure 1 illustrates the relative intensities of the fast component of the spectrum for slab and wing geometries. The three orders of magnitude increase in fast neutron background from slab geometry therefore greatly outweigh the 2-3 gain in epithermal flux.

At ICANS-IV it was believed that no new target-moderator reflector-development designs would emerge; factors of 2 were no longer in dispute, only factors of 20 percent. In this session, new concepts, resulting mainly from the impetus given by the SNQ study, have been presented and 'factors of 2' are being discussed again.

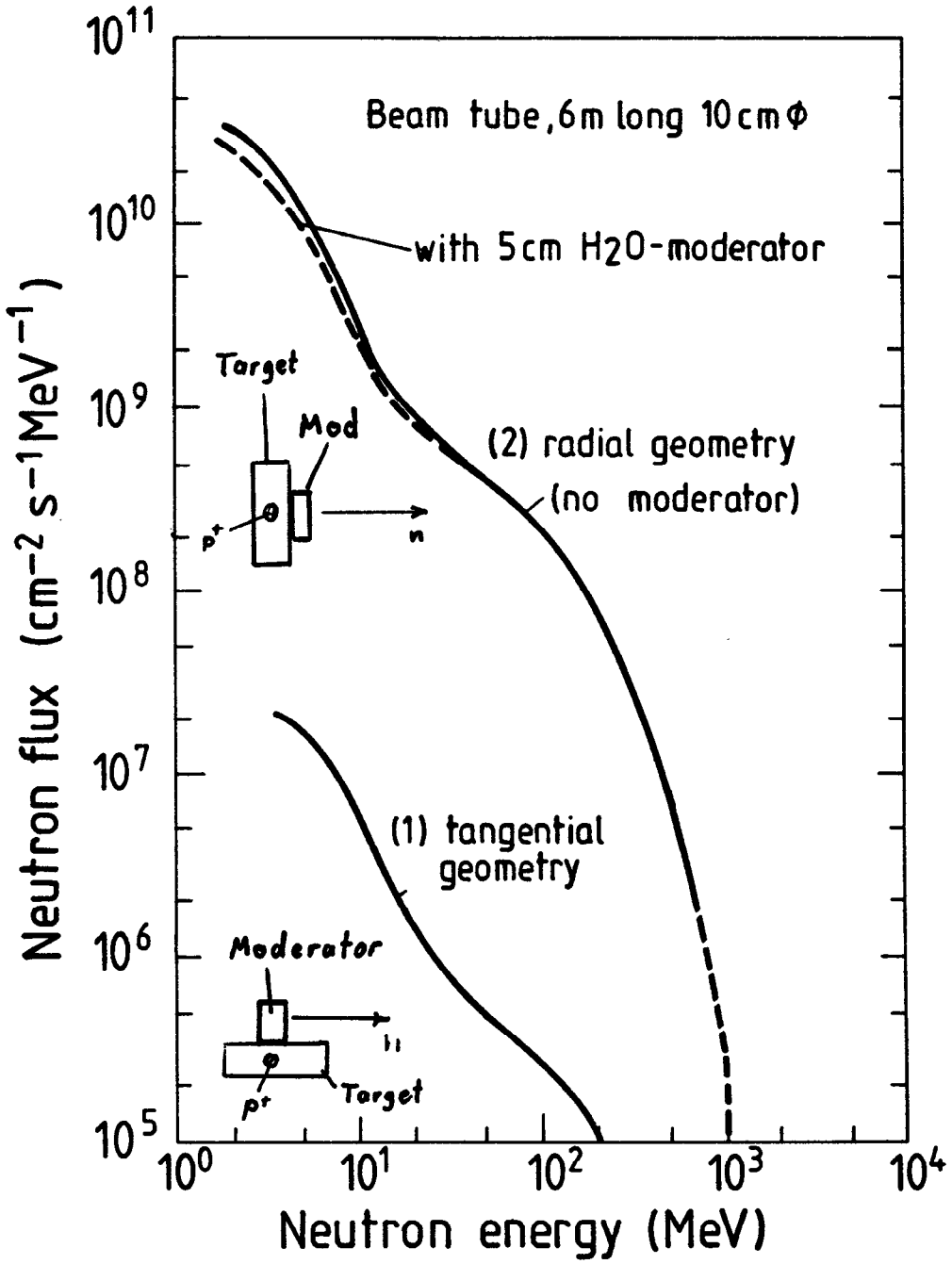

Figure 1 Fast Neutron flux from a slab (radial geometry) and wing (tangential geometry) moderators. (From the SNQ study)

Jül-Conf-45 C4

I C A N S - V

MEETING OF THE INTERNATIONAL COLLABORATION ON

ADVANCED NEUTRON SOURCES

June 22-26, 1981

A Carne

Summary of Session A4: "Radiation Effects in Targets and Structure Components"

There were two contributions under this direct heading: by W Lohmann of KFA (Jülich) on "Remarks on the Irradiation Effects on the Performance of a Rotating Tungsten Target for the SNQ" and C Tschalär (SIN) on "The SIN Liquid Metal Target". In addition the meeting heard an interesting paper by Prof M Heindler of the University of Graz on "Spallation in a Nuclear Energy System".

The present SNQ reference target is a rotating wheel, 2.5 m in diameter and containing some 9000 target elements of lead clad with aluminium. Total heat generation is about 5MW and cooling is obtained by flowing light water between the target elements. Wolfgang Lohmann presented a modificaiton to the basic wheel concept of replacing the lead target elements with unclad tungsten ones. The advantages of such a system were:

- Cooling need only be provided above and below the target elements, which simplifies the cooling channels; moreover the proton beam no longer passes through the coolant.

- Safe to operate, with low temperatures and stresses on the elements.

- Easy to make, with simple tungsten rods produced from powder metallurgy, possibly with Re alloying. This contrasts with the aluminium cladding required for the lead, with the need to prove integrity.

- No significant degradation of neutronic performance.

Radiation damage effects were discussed in detail and damage data were

presented for proton and neutron irradiations, for example, after 2 years' operation 7.3 dpa, 440 appm He and 4000 appm H. We note for comparison that for IPNS-1 dpa are 7.2/year and for SNS, dpa 440, 0.3 ℓ He, 1.6 ℓ H_2 (per year averaged over the whole target). The consequences of radiation gas production were discussed and the need to test He released from sintered tungsten was noted. No, or very little, void swelling was expected. The changes of mechanical properties were discussed, but there is a saturation of mechanical changes after 0.5 dpa and there should be no problems by strength increase. However under irradiation there may be a shift of DBTT to higher temperatures, so that DBTT should be kept as low as possible, perhaps by alloying. It was proposed to do tests on this under SNQ-type conditions.

The proposal to use tungsten target elements was well received by the participants: indeed it was felt at this, and at the special Heidelberg meeting to review SNQ, that it could well replace the "lead target" as the SNQ reference target design.

A discussion of radiation damage was also contained in the presentation by Chris Tschalär in session A7 on Liquid Metal Targets, and summarised by him in section C 6. Several examples of practical materials under proton irradiation in operating conditions were considered, notably

- reactor graphite (60 mA-h/cm^2, SIN, 600 MeV)
- pyrolytic graphite ($\gtrsim$ 800 mA-h/cm^2, LAMPF, 800 MeV)
- Inconel 718 (400 mA-h/cm^2, LAMPF, 800 MeV)
- Stainless Steel ($\sim$ 50 mA-h/cm^2, TRIUMF, 500 MeV)

where the numbers in brackets indicate the operation lifetime or experience. Fuller details are given in the paper by Dr Tschalär, but questions were raised of further materials, eg glassy carbons. The continued study and testing of possible structural materials for use in the various neutron sources, in building or being planned, is of vital interest.

The final paper of the Target Station session was by Professor Martin Heindler of the University of Graz on "Spallation in a Nuclear Energy System". The outstanding problems associated with fission are a) limited fuel resources, b) reprocessing and proliferation, c) radioactive waste

and d) public acceptance. This last problem is in many ways the most "difficult", however Professor Heindler felt that if a), b) and c) could be solved d) would become "easy"!

We are looking for a synergetic system which might utilise the spallation process or fusion. Spallation based systems could breed fuel, or incinerate radioactive waste or provide full cycle rejuvenation, whereas fusion systems could provide fast fission breeding. At best we are seeking an overall synergetic system in which there is an overall energy output. No solutions exist yet which include engineering and economic feasibility and practicability.

Professor Heindler discussed the case of ENB based on the symbiont system of a thermal reactor plus large linac (of typically 1.5 GeV, 300 mA). Support ratios were given for various kinds of reactors and, in general, about 1.5 t/a per GW of beam power was required; a figure of merit was also described as effectively Power available/Power produced. Domains of efficiency against several parameters including annual growth were shown.

There was much discussion related to the various types of thermal reactor that might be involved in such a system; there was also felt a need of hard economic values rather than parameterisation (eg how many kW-hrs per dollar?). Large linacs at such high currents are difficult and expensive machines to operate and require much further detailed study as does a target arrangement in such a system.

Overall the whole business of ENB is a very exciting one, with many problems to satisfy the accelerator and target station builders, with the ultimate goal of serving mankind with a safe, fuel efficient energy source.

Jül-Conf-45 C5

I C A N S - V

MEETING OF THE INTERNATIONAL COOPERATION ON
ADVANCED NEUTRON SOURCES

June 22 - 26, 1981

Summary of Target Workshop A5 on "Energy Deposition and Cryogenic Equipment"

Noboru Watanabe

National Laboratory for High Energy Physics
Oho-machi, Ibaraki, 305 Japan

Klaus Böning

Fakultät für physik, E21 der Technischen Universität München
James-Frank-Strasse, D-8046 Garching, West Germany

Abstract

This note is a summary of the contributions and discussions at the target workshop A5 session where the energy deposition and other topics concerning cold moderator at spallation neutron source, a low temperature irradiation facility at SNQ, and ultra cold neutron sources for spallation sources were discussed.

1. Cold Neutron Moderator

1.1 Energy Deposition of Cryogenic Moderator

This problem was one of the major topics discussed extensively at the last ICANS meeting. Measured value of the energy deposition of the KENS solid methane moderator was almost one order of magnitude larger than the values at other laboratories.[1] After the meeting, KENS group found that their earlier measurement was somewhat misleading, and they performed a new measurement.[2][3] The result was very much consistent with the measured values at ANL, when differences in proton energy, target material, moderator material, and distance from target to moderator are taken into accounted. The results are summarized in Table I. In the last column of the table, the equivalent values for a reference case of 500 MeV protons on a U-238 target are shown with the following assumptions.

i) Fast neutron slowing down is the predominant heat source in the moderator.[6] (A calculated estimate indicates the fraction of the neutron heat is more than 90 % for the reference case.)

ii) The ratio of the neutron yield per proton for the U-238 target bombarded by 500 MeV protons to that by 300 MeV protons is 2.38 which is determined from the measured results of the epithermal neutron beam at ZING-P'.[4]

iii) The gain factor of the neutron yield of the U-238 target to the tungsten is 2.

iv) Energy deposition of the solid methane is almost same to that of polyethylene.

Table I Comparison of Energy Deposition of Cryogenic Moderator

Facility	Ep (MeV)	Target Material	Moderator Material/ Temp. (K)	Mod. vol (cm^3)/ Size (cm x cm x cm)	Distance* (cm)	Nucl. Heat (mW/cm^3·μA)	
						Measured	Equivalent value for ref. case**
KENS	500	W	CH_4/20	900/12x5x15	12.1	1.28[2]	2.58
ZING-P'	300	U-238	$(CH_2)_n$/R.T.		11.5	1.2 [4]	2.86
ZING-P'	300	U-238	L-H_2	368		0.5 [5]	1.2
IPNS-I (calc.)	500	U-238	$(CH_2)_n$			1.54[6]	1.54
IPNS-I (calc.)	500	U-238	L-H_2			0.7 [6]	0.7

* Distance between center line of the target and that of the moderator
** 500 MeV protons on U-238 target

Except that the calculated estimates are somewhat smaller than the measured values, agreement between KENS and ZING-P' is excellent. Furthermore, if the value of 1.2 mW/cm^3-μA for liquid hydrogen moderator is multiplied by a factor of 2.2 which is the ratio of the calculated value of the nuclear heat for the polyethylene to that for the liquid hydrogen, we get a value of 2.64 mW/cm^3-μA which is very much close to the measured values of 2.58 or 2.86 for solid methane or polyethylene. We, therefore, believe that we have reached to agreement as far as the energy deposition of the cryogenic moderator is concerned.

1.2 Moderator Material

Choice of moderator material will be one of the most important problems for the design of the cryogenic moderator. As far as neutron beam intensity is concerned, solid methane moderator is superior to liquid hydrogen moderator. A calculated estimate indicates that the ratio of neutron beam intensity from a smaller liquid hydrogen moderator to that from the solid methane moderator of the same size is about 1/2 at 1 eV and about 1/5 at cold neutron region.[9] On the contrary, solid methane is susceptible to certain radiation damage induced by the spallation neutrons. It will, therefore, be interested to show an idea of the safty limit of the proton beam intensity for the solid methane moderator. Fraction of the hydrogen gas in the used methane gas will be an important measure of the radiation damage. A measured value at KENS was 0.14 % after 52 hours operation at full power which corresponds to 0.045 %/μA-day.[2] The concentration of hydrogen gas in the methane moderator after a long operation at Hokkaido University was 7 %.[2] This value will be considered to be still within a safty limit. Hydrogen gas concentration of 7 % corresponds to 155 μA-day operation in 500 MeV spallation neutron source. If we assume one or two weeks as a period of methane gas purging, 10 - 20 μA will be within a safty limit of the proton beam intensity for solid methane moderator. In Table II are summarized the moderator material at various facilities.

Table II Materials for Cryogenic Moderator at Various Laboratories

Moderator Material	Facility
Solid CH_4	KENS, SNS
Liq. CH_4	IPNS
Liq. H_2	IPNS, SNS
Liq. D_2	SNQ, SIN

1.3 Optimal Size and Shape

The grooved moderator was proposed by Bauer to increase the neutron leakage, and discussed extensively at the last ICANS.[7] A measurement on pulse characteristics of a grooved moderator was also reported by Carpenter.[4] In this meeting this topic was continued to discuss, and new measurements of the grooved moderator at room temperature were

presented by the German study group in connection with a proposal for a lead reflector.[8] This type of moderator will be very much useful also for the cryogenic moderator. An attempt for this was performed at IPNS where a grooved surface was realized by a lot of MgO rods installed inside the moderator chamber,[9] and the measured performance is being anticipated.

Optimization of the size of the cryogenic moderator will be another important problem. Most pulsed neutron laboratories have adopted the moderator size which is a little bit larger than 10 cm x 10 cm x 5 cm. KENS group is thinking the possibility of increasing the lateral size of the present solid methane moderator ($12\ cm^W \times 15\ cm^H \times 5\ cm^T$) in order to increase the cold neutron beam intensity.[10] It seems to me that the sizes of the cryogenic moderators for the pulsed cold neutron source which were already installed or designed are more or less smaller than the optimal size, especially in the case of liquid hydrogen moderator. There will be actual constraints to realize the optimal size, but further optimization studies for the cryogenic moderator size are anticipated.

1.4 Optimal Coupling

Optimal coupling or decoupling of cryogenic moderator with a reflector is also an important problem related to the neutron beam intensity as well as the pulse characteristics. Carpenter proposed a gadolinium decoupler with a cooled beryllium inner reflector which was adopted at IPNS.[11] The cooled reflector down to about 100 K lays the Maxwellian distribution of neutrons in the reflector below cut-off energy of gadolinium ($\sim$ 0.1 eV) which is lower than that of cadmium ($\sim$ 0.4 eV). This configuration will, therefore, improve the coupling efficiency without any sacrifice in the pulse characteristics.

Coupled moderators were tested at ZING-P' and at KENS (Hokkaido). The coupled hydrogen moderator at ZING-P' provided, by a factor of 2, higher beam intensity of time integrated cold neutrons than the decoupled one by cadmium, but the pulse width in the former was almost two times longer than in the latter.[5] The result may suggest that the moderator size was not sufficient. Anyhow, the result shows that the coupled moderator is useful for certain classes of experiments such as small angle scattering where the pulse characteristics are not so important. A bench mark test for KENS was also presented where the gain factor of a coupled solid methane moderator to the decoupled one was about 1.5 with 15 % increase in the pulse width.[12]

A coupled liquid hydrogen moderator with a beryllium reflector filter at the view surface was also tested at ZING-P' which provided further increase in time integrated cold neutron beam intensity.[5] KENS group has planned to test a solid methane moderator with a para-hydrogen reflector filter.[10]

1.5 Spectral Distortion

Some spectral distortions such as small peaks or steps appeared in the cold neutron spectrum from the cryogenic moderator were reported by ANL[5] and KENS[12] groups, and which were confired to be due to

wavelength-dependent attenuation effect in the aluminum wall of the cryostat.

Solid methane exhibits phase transition at about 20 K, but any appreciable spectral distortion was not recognized (KENS).[12]

2. Low Temperature Irradiation Facility

K. Böning reported on a feasibility study about the realization of a low-temperature irradiation facility (LTIF) at the SNQ. The irradiation temperature of the samples would be either 4.5 K in liquid Helium or 5 - 450 K in He gas. By means of two vertical irradiation tubes of about 8 m length two irradiation positions would be accessible: the position I deep in the D_2O tank with a high and clean thermal neutron flux ($\phi_{th} \approx 1 \cdot 10^{14}$ $cm^{-2}s^{-1}$) and the position II just below the D_2O tank for irradiations with fast neutrons ($\phi_f \approx 2 \cdot 10^{13}$ $cm^{-2}s^{-1}$). Measurements could be done in situ during irradiation as well as after irradiation in an on-line measuring cryostat or after cold transfer in any external lab. The heat production in the samples would always be dominated by the thermal neutrons. The problems of a LTI-facility at the SNQ consist not so much in the flux contamination by high energy neutrons and protons, but mainly in the 100 s^{-1} time structure and in some geometrical constraints. The advantage of the SNQ lies in its relatively weak background of direct γ-radiation (as compared to a reactor) and in its potential of spectrum tailoring. - See also paper in these proceedings.

3. Ultra Cold Neutrons

R. Golub reported on the possible features of a source of ultra cold neutrons (UCN) to be installed at the SNQ. There are two basic concepts for such a UCN source: the Doppler shifter source, where slow neutrons are decelerated by specular or Bragg reflections in a moving frame, and the superthermal source, where this deceleration is realized by excitation of phonons in superfluid liquid Helium. If both types of sources were placed at the ends of identical guide tubes so that the neutron solid angles were the same, the ratio of achievable densities ρ of UCN would be $\rho_{He}/\rho_{Doppler} = 64\ \eta$ since only the Doppler shifter source explicitely uses the time structure which enters through the duty cycle η (being 1/20 at the SNQ). However, the Helium source is able to accept much larger solid angles and so can be installed much closer to the target, profiting by the low γ-background of the spallation process. The result for the SNQ is $\rho_{He}/\rho_{Doppler} = 220$, then, and this considerable advantage of the Helium source should stimulate more effort to reduce the UCN extraction losses to below a factor of 10 and to solve the engineering problems. - See also paper in these proceedings.

M. Utsuro reported on an UCN experiment with a supermirror turbine at KUR and proposed a synchronized supermirror turbine for the UCN source at the pulsed spallation neutron facility which could utilize

the neutron flux at pulse peak.[13] As a third method for UCN source, an experiment on direct extraction of UCN from a pulsed cold source was presented. This experiment was performed using a small pulsed neutron source based on a small electron linac, but encouraging data were obtained.[13]

References

1) A. Carne, Proc. ICANS-IV (1981) p.426.
2) S. Ikeda, Y. Ishikawa, and K. Inoue, ibid. p.200.
3) N. Watanabe, ibid. p.433.
4) J. M. Carpenter and IPNS Program Staff. ibid. p.105.
5) J. M. Carpenter, et al., The Liquid Hydrogen Moderator on the ZING-P' Pulsed Spallation Neutron Source, to be published.
6) M. Kimura, J. M. Carpenter, and D. F. R. Mildner, ANL-81-22 (1981).
7) G. S. Bauer, Proc. ICANS-IV (1981) p.423.
8) G. S. Bauer, et al., Measurement of Time Structure and Thermal Neutron Spectra for Various Target-Moderator-Reflector configurations of an Intensity-Modulated Spallation Neutron Source, Proc. ICANS-V (1981).
9) J. M. Carpenter, private communication.
10) N. Watanabe, et al., Present Status and Future Program at KENS, Proc. ICANS-V (1981).
11) J. M. Carpenter, private communication.
12) K. Inoue, et al., Some Neutronic Aspects of Solid Methane Moderator System, ibid (1981).
13) M. Utsuro, K. Okumura, and Y. Kawabata, A Study on UCN Source for a Spallation Facility, ibid (1981).

Jül-Conf-45

I C A N S - V

MEETING OF THE INTERNATIONAL COOPERATION
ON ADVANCED NEUTRON SOURCES

June 22 - 26, 1981

at Kernforschungsanlage, Jülich

SUMMARY: LIQUID METAL TARGETS

C. Tschalär

Swiss Institute for Nuclear Research (SIN)
CH-5234 Villigen, Switzerland

Of the three liquid metal spallation target projects (SNQ, SIN, TRIUMF), the one at TRIUMF is the only one operating at present. New results or major changes, however, have not been reported of the TRIUMF target.

The other two projects, SNQ and SIN, are both in the conceptual stage. The variants primarily discussed at the liquid metal target meeting were both vertical cylindrical targets of a liquid eutectic mixture of lead and bismuth (LBE).

The SNQ project presented by Hoffmann, Piesche and Wild is designed for a proton beam of 1.1 GeV, 5 mA and an r.m.s. diameter of 5 cm. This high beam density, thought to be required by the pulsed neutron mode of the SNQ source, would make the use of a beam window rather hazardous. The window-less version presented on the last ICANS meeting, in which the beam enters the target vertically from the top through a free, conical LBE surface created by an appropriate nozzle, has been developed further. Flow calculations and measurements on a new LBE test circuit show that such a free surface can be generated and kept stable. An alternative version has been considered in which the LBE is pumped around a horizontal bend in such a way as to present a free surface to the proton beam near the centre of inside of the bend where a small section of the wall of the LBE channel is removed. This version would simulate the geometry of the wheel target which is the reference design for the SNQ.

For the SIN project (nominal beam characteristics: 0.6 GeV, 1.7 mA, 10 cm r.m.s. diameter), a new target concept has been developed in which the proton beam enters a vertical LBE target from the bottom through a beam window. The target is a vertical cylinder of 20 cm diameter and about 3.5 m height. The LBE is circulated by natural convection and is cooled by an internal heat exchanger thus eliminating the need for a complex external primary LBE circuit. Calculations for

stationary and start-up flow in the target have shown that proton beams of up to 2 MW, even if switched on instantanuously on to a stationary target, will not produce LBE temperatures above 500 °C. Preliminary studies indicate that it is possible to insert uranium fuel rods into the LBE target to boost neutron production. The feasibility of a beam window has been ascertained by several preliminary results of proton irradiation at LAMPF (800 mAh/cm2 on pyrolitic carbon, 400 mAh/cm2 on inconel), SIN (60 mAh/cm2 on reactor graphite) and TRIUMF (50 mAh/cm2 on stainless steel) which indicate, that a suitable beam entrance window would hold up for at least several thousand hours in the proposed beam density of 20 μA/cm2. Thermal strains and pressure stress in the window were shown to be well below limiting values.

An important aspect of liquid metal target operation is the emission of radioactive gases and vapors from the liquid metal surface. Preliminary data presented by Hellwig show that for an LBE temperature of 325 °C the activity released by mercury isotopes and their decay products is ten times higher than that of all other spallation and fission products in LBE exept possibly of Po. The exact amount of released Po activity is still under investigation but will still be dominated by the Hg activity. This is true to an even larger degree at lower LBE temperatures.

In general developments presented at this conference have shown that liquid metal LBE targets are thermodynamically stable and reliable in both the natural and forced convection versions. If the detailed problems of beam windows and handling of released radioactivity are solved successfully, which appears now to be possible, such targets would be inhearently safe due to their simplicity and large thermal capacities.

The examples presented show the wide choice of target geometries and source requirements that may be covered by liquid metal targets, ranging from powerful pumped versions for extremely high power densities above 10 kW/cm^3 to relatively cheap, simple natural convection concepts for moderate power densities of a few kW/cm^3.

In order to further substantiate the present promising predicitons for liquid metal target performance, the following studies seem to be particularly urgent for the immediate future:

- detailed, full scale radiation damage and associated corrosion tests on potentially suitable window materials with 500 - 1000 MeV proton beams in the dose range of 100 - 1000 mAh/cm^2

- LBE flow and corrosion tests including simulated beam heating

- determination of the release of radioactive spallation products and particularly of polonium from LBE, and concepts for handling this contamination

- concepts for the inclusion of uranium into liquid metal targets

The results of these studies would provide the basis on which to determine definite concepts and basic design parameters for future high power spallation targets.

Jül-Conf-45 D1-1

I C A N S - V

MEETING OF THE INTERNATIONAL COLLABORATION ON

ADVANCED NEUTRON SOURCES

June 22-26, 1981

A COMPARISON OF HIGH-ENERGY FISSION MODELS FOR THE HETC TRANSPORT CODE -- PART I: THIN TARGETS

T.W. Armstrong* and D. Filges

Kernforschungsanlage Jülich GmbH
Inst. f. Reaktorentwicklung
Postfach 1913
D-5170 Jülich
Federal Republic of Germany

*Consultant
P.O. Box 2807
La Jolla, California 92038, U.S.A.

Abstract:

Calculations have been made to compare results from high-energy fission models which have recently been developed by others for use in the high-energy transport code HETC. The cases considered are proton beam energies of 0.3, 1.0, and 2.9 GeV bombarding thin U-238 targets. Comparisons are given for fission cross sections, neutron production, and fission fragment energies.

1. INTRODUCTION

For high-energy hadrons incident on high-mass target materials (e.g., uranium), the target nucleus may undergo fission during de-excitation. Recently, there have been several high-energy fission models developed /1-4/ for the hadronic transport code HETC /5/, which is used for spallation neutron source studies. The objective here is to investigate the appropriate high-energy fission model for routine HETC calculations for spallation neutron source applications.

All of the calculations made here are for proton beams (0.3, 1.0, and 2.9 GeV) incident on thin U-238 targets, and were made using the Rutherford and Appleton Laboratory (RAL) high-energy fission model developed by Atchinson /1/.* Results for fission cross sections, neutron multiplicities and spectra, and fission fragment recoil energies are compared with available results for the same cases computed by the Oak Ridge National Laboratory (ORNL) model developed by Alsmiller, et al. /2/.

All of the comparisons in this paper are for thin targets -- i.e., for target thicknesses sufficiently small that the secondary particles created escape from the target without undergoing further collisions, so the results are for a single proton collision. Thus, such thin target comparisons are appropriate for identifying basic differences in model predictions. However, to determine the practical importance of such model differences for spallation source applications, thick targets must be considered, whose results represent an average of collisions initiated by primary beam protons and secondary particles (neutrons, protons, and pions) over a wide range of energies. A comparison of different high-energy fission models based on thick targets is given in a companion paper.

---

*We are very grateful to F. Atchison for his assistance in providing us the programming for this model.

2. HIGH-ENERGY FISSION PROCESS

Without fission, the spallation collisions can be treated as a two-step process: (a) an intranuclear cascade, described by a series of independent particle-particle collisions inside the nucleus, and (b) subsequent de-excitation by a series of particle emissions, which can be described by an evaporation model. For very heavy nuclei, there is competition between evaporation and fission at each step of the de-excitation sequence. The probability of fission at some step during de-excitation in high-energy ($\gtrsim$100 MeV) collisions is proportional to Z^2/A of the target nucleus. For example, $\sigma_f/\sigma_t \approx 0.05$ for lead and $\sigma_f/\sigma_t \approx 0.8$ for uranium.

The information which must be determined by the fission model is the probability of fission at each step and the parameters of the fission fragments immediately after fission, which are then used as input for a post-fission evaporation calculation for each fragment.

If fission occurs, the following quantities are expected to be different compared to spallation without fission: (a) energy deposition, (b) residual mass distributions, (c) neutron multiplicity and (d) neutron spectrum. There are clearly large differences in these first two items if fission takes place. The magnitude and spectral differences in neutron production is not well-determined, and this is the main emphasis of the calculations made here.

3. BASIC FEATURES OF FISSION MODELS

Recently, there have been two high-energy fission models developed for use in the thick-target nucleon-meson transport code HETC: one by Atchinson at Rutherford and Appleton Laboratories (RAL) /1/, and one by Alsmiller, et al. at the Oak Ridge National Laboratory (ORNL) /2/. Also, Takahashi at Brookhaven National Laboratory (BNL) /3/ and Nakahara at the Japan Atomic Energy Research Institute (JAERI) /4/ have developed high-energy fission models for

NMTC transport code /6/, which is an earlier version of HETC. (Barashenkov et al. have also developed a high-energy fission model for use in the Dubna transport code /7/.)

The fundamental basis of all of these models is the statistical model of fission developed by Fong /8/. Basically, the assumption is that the fission process is "slow" (i.e., the nucleus exists in an equilibrium state at any time), so the probability of a particular fission mode (state of the fission fragments) is proportional to the density of quantum states at the time of splitting. From the Fong theory, the fission mode probability is expressed as a function of eleven variables: $N(A_1, A_2, Z_1, Z_2, C, D, k, E, E_1, j_1, j_2)$, where the subscripts denote the fission fragments; A, Z, and j denote mass number, charge number, and angular momentum; and the remaining are energy variables (C, Coulomb; D, deformation; k, translational; E, total; and E_1, excitation).

The high-energy fission models developed differ in the apporoximations made in arriving at a practical implementation of the above general expression and in the physical data used. It is not the purpose here to evaluate these various approximations. Indeed, many of the approximations are interdependent, making judgement of the practical importance of particular assumptions difficult. Therefore, the model comparisons here are in terms of "output" rather than assessment of the intermediate physics. Simple characterizations of the different models are given in Figure 1.

Also given in Figure 1 are the values for the parameter B_0 assumed for the different models, which , as shown later, has an important influence on neutron production. This parameter is involved in the evaporation calculation in the following way. From evaporation theory (e.g., /9/), the probability of particle emission of type i with kinetic energy E is expressed as

$$p_i(E) \propto (2S_i+1)\ m_i E\ \sigma_{ci}(E)\ w(E^*),$$

with S_i = spin, m_i = mass, and σ_{ci} = cross section for

compound nucleus formation in the inverse reaction. The level density for excitation energy E^* is given by

$$w(E^*) = w_0 \exp\left[2(aE^*-\delta)^{\frac{1}{2}}\right],$$

where w_0 and a are constants for a given nucleus and δ is the pairing energy. The level density parameter , a, is given by

$$a = A/B_0(1 + Y\ (A-2Z)^2/A^2),$$

and $Y \approx 1.5$. From various analyses, B_0 is in the range from about 8 to 20 MeV (e.g./9/).

4. PREVIOUS VALIDATIONS

Several thick-target calculations, with and without high-enrgy fission taken into account, have been made for neutron production and compared with experimental data (Tables 1 and 2). We conclude from these, and other (e.g., /10,14/), comparisions that the theoretical predictions and measurements that have been made to date agree to within roughly 20 to 30%, and this general magnitude of agreement for neutron production can be obtained by neglecting high-energy fission. It is difficult to isolate the influence of the high-energy fission models in these thick targets comparisons where low-energy fission also contributes to the neutron production.

5. THIN TARGET COMPARISONS

In this section, calculations made here using the RAL fission model are compared with results from Alsmiller et al. /2/ obtained with the ORNL model. All of the comparisons are for protons incident on a thin U-238 target.

Figure 2 shows the fission cross sections calculated by the RAL and ORNL models compared with experimental data. The fission cross section predicted by thE RAL model is about 15-20% lower than for the ORNL model for beam energies below ≈1 GeV, and the energy dependence of the cross section predicted above ≈1 GeV appears to be

different for the two models. As is evident, the spread of the experimental data is too large to judge the correctness of either model. Also shown in Figure 2 are the nonelastic cross sections from the two calcualtions, which are in agreement, as expected, since both calculations use the same intranuclear cascade model.

Figures 3 and 4 show comparisons of neutron multiplicity from evaporation only (taken to be $\lesssim$12.5 MeV) and over all energies (evaporation plus intranuclear cascade), respectively. For the standard B_0 values used in the two models (B_0 = 14 for RAL, B_0 = 10 for ORNL), the RAL model predicts lower neutron emission by about 20-25%. These comparisions also show the sensitivity of neutron production to values assumed for B_0 . The variation in neutron production over the range of B_0 parameters suggested as reasonable from present experimental data are about the same as the model differences.

To consider further the influence of B_0, we have calculated the low-energy neutron production spectrum for 1-GeV protons using the RAL model (Figure 5). The integral neutron production below 12.5 MeV is 20% higher for B_0 = 8 than for B_0 = 14. Also, shown in Figure 5 is the neutron spectrum obtained when high-energy fissioning is neglected. With fission included, the neutron production is about 8% higher, and there is evidence of some "spectral hardening" for neutron energies above about 2 MeV. Neutron production above this energy is important because this corresponds approximately to the energy threshold for neutron induced fission for U-238. Thus, while the magnitude of spectral hardening introduced by high-energy fission appears to be small, its influence on total neutron production in thick U-238 targets can be amplified by providing a larger source of neutrons that can cause multiplication via low-energy fissioning.

There are large differences in energy deposition for spallation collisions with and without high-energy fissioning. If fission takes place, the "local" energy deposition at the collision site is mainly from the kinetic energy of the fission fragments which, as in low-energy fission, is expected to be about 170 MeV per fission. (From

non-fissioning spallation collisions, the deposition from heavy short-range secondary particles and residual nuclei is, nominally, only about 20-30 Mev per collision.) Thus, the fission fragment kinetic energies predicted by high-energy fission models is important in predicting the target heating for spallation neutron sources. A comparison of the (total) fission fragment energies calculated using the RAL and ORNL models is given in Figure 6, and the agreement is good. As also indicated in Figure 6, this energy is not sensitive to B_0. This is as expected since the fission fragment energy results mainly from the Coulomb repulsion between fragments. Thus, the fragment energies are not sensitive to few-neutron differences of the fragment masses.

6. SUMMARY AND CONCLUSIONS

A summary comparison of the RAL and ORNL high-energy fission models in terms of neutron multiplicities predicted is given in Table 3, from which we conclude: (1) for the standard B_0 values incorporated in the models, the ORNL model predicts about 20% more neutrons, (2) the neutron production is sensitive to the value of B_0 assumed, varying by about 20% over the range of B_0 values inferred from presently available experimental data, (3) for the same assumed B_0 in each model, the ORNL model still predicts more neutrons tham the RAL model, by about 12%, and (4) the effect of high-energy fissioning compared to spallation without fissioning is to increase the neutron production by about 7% (with a somewhat harder spectrum in the enegy region from ≈ 2 to ≈ 15 Mev).

Additional calculations are underway to investigate the isotope production distributions predicted by these spallation models.

REFRENCES

1. F. Atchison, "Spallation and Fission in Heavy Metal Nuclei Under Medium Energy Proton Bombardment", Meeting on Targets for Neutron Beam Spallation Sources, G. Bauer (Editor), KFA-Jülich, FRG, 11-12 June 1979, Jül-conf -34, January 1980.

2. F.S. Alsmiller, et al., "A Phenomenological Model for Particle Production from the Collision of Nucleons and Pions with Fissile Elements at Medium Energies", Oak Ridge National Laboratory, ORNL-TM-7528, March 1981.

3. H. Takahashi, "Fission Reaction in High-Energy Cascade", to be published in Proc. of Symp. on Neutron Cross Sections 10-50 MeV, Brookhaven National Laboratory, 12-14 May 1980.

4. Y. Nakahara, "Studies on High-Energy Spallation and Fission Reactions", Proc. of 4th Meeting of International Collaboration on Advanced Neutron Sources (ICANS-IV), KEK National Laboratory for High-Energy Physics, Tsukuba, Japan, 20-24 October 1980.

5. T.W. Armstrong and K.C. Chandler, "HETC - A High-Energy Transport Code", Nucl. Sci. and Engr. 49, 110 (1972).

6. W.A. Coleman and T.W. Armstrong, "NMTC - A Nucleon-Meson Transport Code", Nucl. Sci. and Engr. 43, 353 (1971).

7. V.S. Barashenkov, V.M. Mal'tsev, and V.D. Toneev, "Calculation of Fast Particle Induced Fission", Dubna Report JINR P-1970, 1965.

8. P. Fong, Statistical Theory of Nuclear Fission, Gordon and Beach Science Publishers, New York, 1969.

9. I. Dostrovsky, P. Rabinowitz, and R. Bivins, "Monte Carlo Calculations of High-Energy Nuclear Interactions. I Systematics of Nuclear Evaporation", Phys. Rev. 111, 1659 (1958).

10. R.G. Alsmiller, Jr., et al., "Neutron Production by Medium Energy ($\lesssim$1.5 GeV) Protons in Thick Uranium Targets", Oak Ridge National Laboratory, ORNL-TM-7527, January 1981.

11. J.S. Fraser, et al., "Neutron Production in Thick Targets of Lead, Thorium and Uranium Bombarded by 480 MeV Protons", to be published in Proc. of Symp. on Neutron Cross Section from 10-50 MeV, Brookhaven National Laboratory, 12-14 May 1980.

12. G.J. Russell, et al., "Measurements of Spallation Target-Moderator-Reflector Neutronics at the Weapons Neutron Research Facility", Proc. of 4th Meeting of International Collaboration on Advanced Neutron Sources (ICANS-IV), KEK Nationl Laboratory for High-Energy Physics, Tsukuba, Japan 20-24 October 1980.

13. R.G. Vasil'kov, et al., Atomnaya Energiya 44, 329 (1978).

14. V.S. Barashenkov, V.M. Mal'tsev, and V.D. Toneev, "Interaction of Fast Protons with Heavy Nuclei", JINR-R-1969, Dubna (1965).

15. V.S. Barashenkov and S. Ju. Shmakov, "Nuclear Fission Induced by High-Energy Protons," JINR, Dubna (1979).

16. R.L. Hahn and H.W. Bertini, "Calcualtions of Spallation-Fission Competition in the Reaction of Protons with Heavy Elements at Energies < 3 GeV", Phys. Rev. C6, 660 (1972).

Table 1. Comparison of ORNL Fission Model with FERFICON Data[a]

Target	Proton E (MeV)	Quantity Compared	Theory/Exp.
1. Depleted U (3.2Φ × 30.5 cm)	480	Neutron captures in water bath	11.8/9.6[b] = 1.23[d]
Depleted U (37 rod array)	480	" "	14.1/17.7[b] = 0.82[d]
2. Depleted U (10Φ × 40.6 cm)	800	" "	27.2/25.3[c] = 1.08
Depleted U (37 rod array)	800	" "	28.6/28.8[c] = 0.99

(a) Calculated results from Alsmiller, et al. /10/.

(b) Fraser, et al., FERFICON measurements at TRIUMF, reported at BNL Symposium /11/.

(c) Russell, et al., FERFICON measurements at LASL, reported at ICANS-IV /12/.

(d) Calculations of Fraser, et al. /11/, using NMTC without high-energy fission give theory/exp. ratios of 1.05 and 0.72 for cylindrical and array targets, respectively.

Table 2. Fission Model Comparisons with [a] Vasil'kov Experiments

Fission Model	Proton E (MeV)	Quantity Compared	Theory/Exp.
JAERI [e]	660	U-238 captures	$\frac{44.9 \pm 5.1}{46 \pm 4} = 0.98$ [b]
BNL [f]	660	" "	$\frac{38.3 \pm 5.2}{46 \pm 4} = 0.83$ [d]
JAERI [e]	400	" "	$\frac{15.96 \pm 4.65}{22.1 \pm 2.4} = 0.72$ [c]
BNL [f]	400	" "	$\frac{15.1 \pm 4.9}{22.1 \pm 2.4} = 0.70$

(a) Very large natural uranium assembly /13/.

(b) Without high-energy fission in model, theory/exp. = 0.72

(c) Without high-energy fission in model, theory/exp. = 0.61

(d) Assuming depleted uranium with 0.33% U-235 in calculations, theory/exp. = 0.88

(e) Ref. /4/.

(f) Ref. /3/.

Table 3. Summary comparison of neutron production predicted by RAL and ORNL high-energy fission models, for proton beams on thin U-238 target.

Case	Beam Energy (MeV)	Ratio: neutrons $\lesssim$12.5 MeV	Ratio: neutrons of all energies
1. ORNL*/RAL	300	1.23	1.19
	1000	1.28	1.22
	2900	1.26	1.19
2. ORNL (B_o = 8)/ORNL (B_o =15)	1000	1.22	1.17
3. ORNL (B_o = 8)/RAL (B_o = 8)	1000	1.14	1.12
4. RAL (with Fission)*/RAL (w/o Fission)	1000	1.08	1.07

---

*For Standard B_o Values incorporated in the models (B_o =10 for ORNL, B_o =14 for RAL).

Figure 1. Features of Different High-Energy Fission Models

1. Basic Approaches

- RAL
  - empirical formulas used far as possible
- ORNL
  - heavy reliance on empirically derived constants

    NOTE: Fissions neglected for subactinides ($Z < 91$)
- BNL
  - close simulation of Fong's statistical model formulas, minimum reliance on experimental data
- JAERI
  - similar to RAL approach, but different in detail

2. B_0 Values Used in Standard Versions

Model	B_0
RAL	14
ORNL	10
BNL	8
JAERI	8

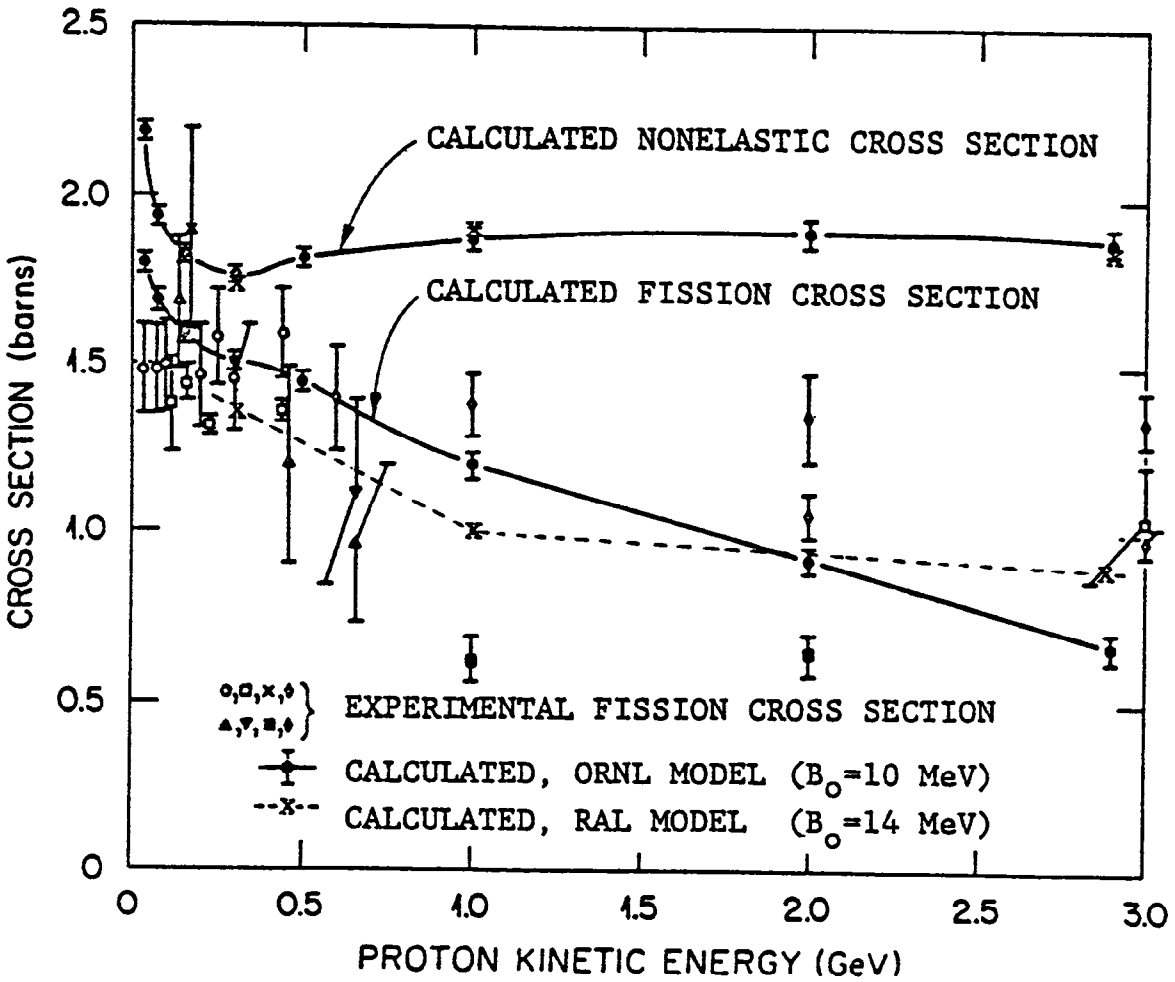

Figure 2. Comparison of calculated cross sections using the RAL and ORNL fission models for the case of protons incident on thin U-238 target. References for experimental data given in /2/.

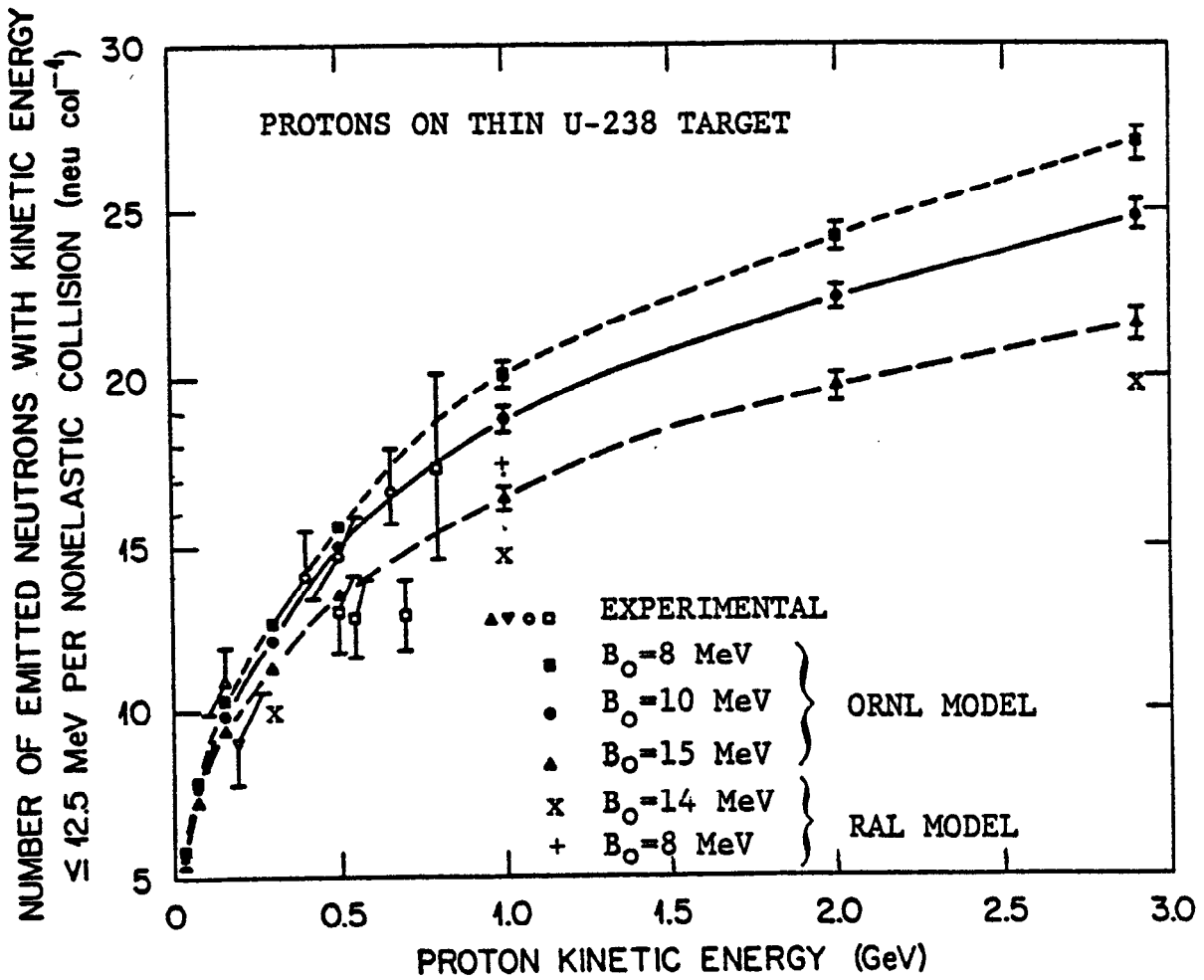

Figure 3. Comparison of RAL and ORNL fission model predictions for neutron production below 12.5 MeV. References for expermental data given in /2/.

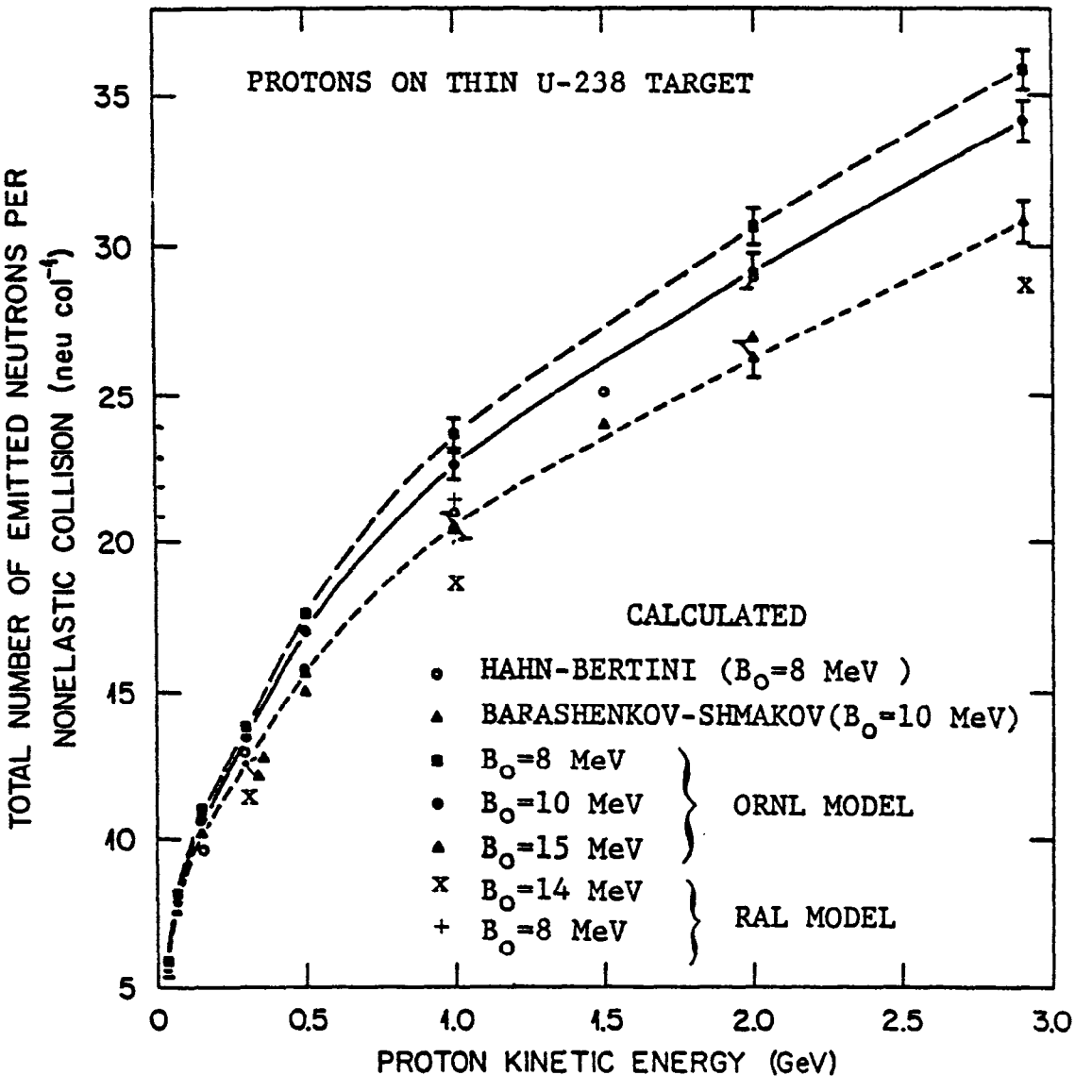

Figure 4. Comparison of total (evaporation plus cascade) neutron production predicted using RAL and ORNL high-energy fission models. Also shown are the results of Barashenkov and Shmakov using the Dubna fission model /15/. The calcualtions of Hahn and Bertini were made neglecting fission /16/.

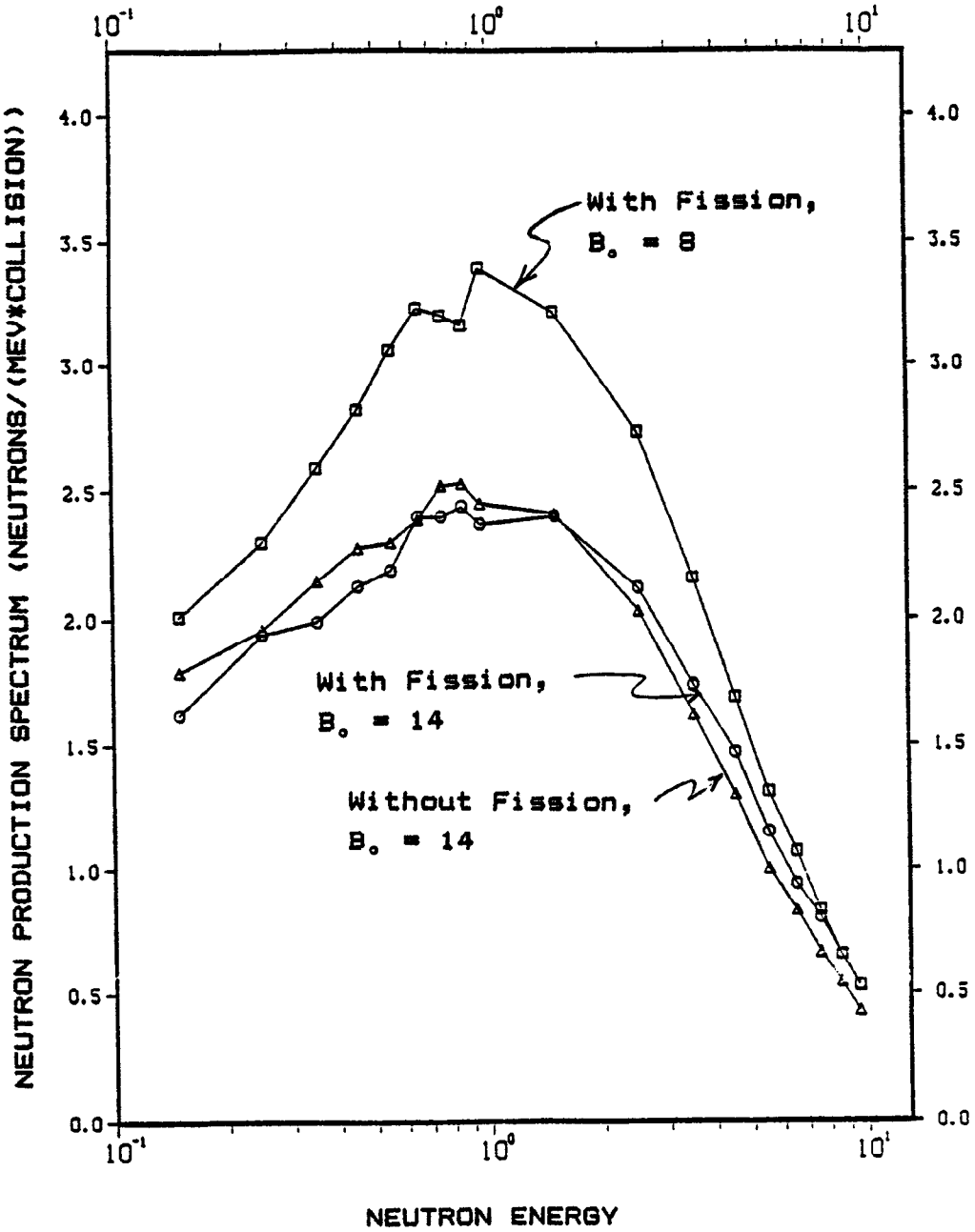

Figure 5. Low-energy neutron production spectrum calculated using RAL fission model, 1-GeV proton beam on thin U-238 target.

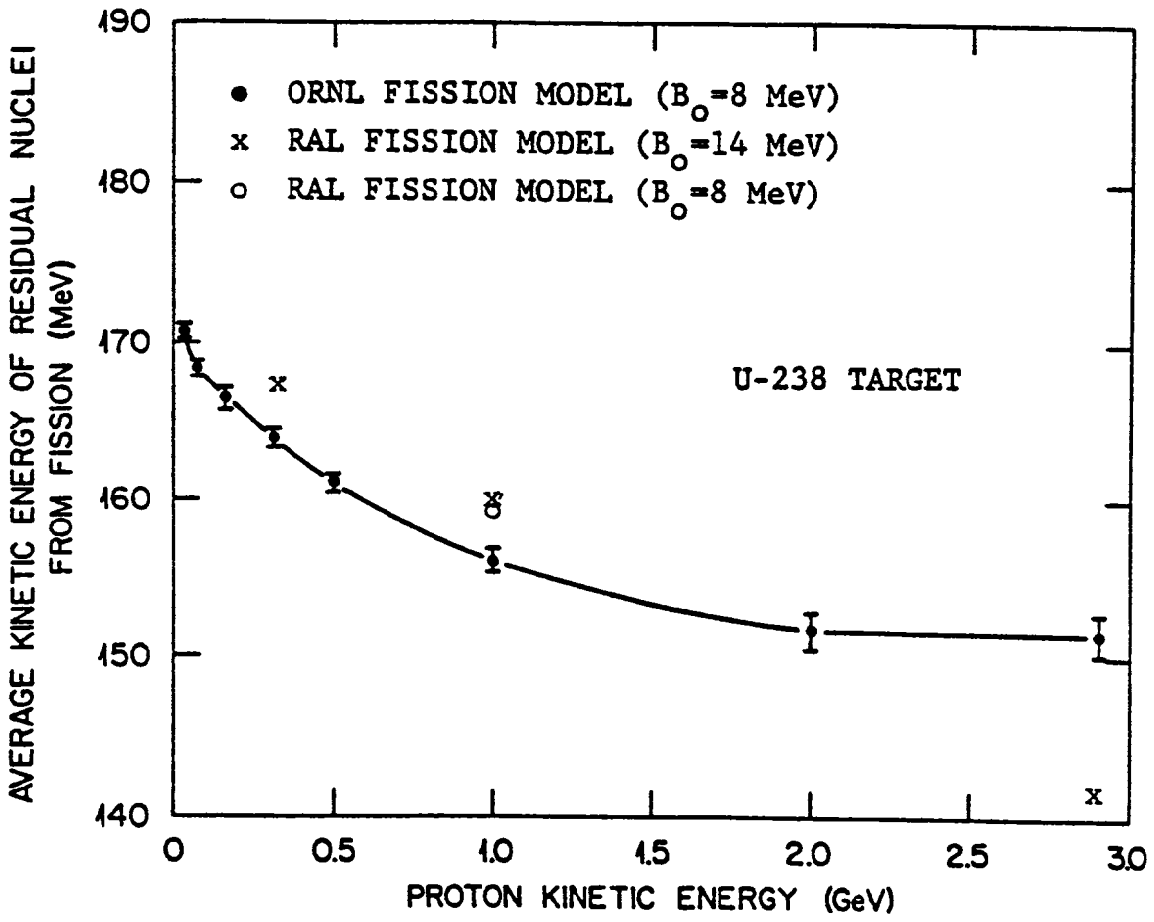

Figure 6. Comparison of fission fragment energies predicted by the RAL and ORNL fission models for protons incident on thin U-238 target.

I C A N S - V
MEETING OF THE INTERNATIONAL COLLABORATION ON
ADVANCED NEUTRON SOURCES
June 22-26, 1981

A COMPARISON OF HIGH-ENERGY FISSION MODELS FOR THE HETC-TRANSPORT CODE

PART II: THICK TARGETS

T.W. Armstrong*, P. Cloth, D. Filges, R.D. Neef
Institut für Reaktorentwicklung
Kernforschungsanlage Jülich GmbH
Postfach 1913
D-5170 Jülich, Germany

*Consultant, P.O. Box 2807
La Jolla, California 92038, USA

1 Introduction

To clarify the influence on practical calculational problems of the different "High-Energy Fission" (HEF) models and the relationship between the models, a series of calculations were performed and partly compared with existing experimental data taken from the BNL-Cosmotron experiment (see Refs. 1,2). This experiment consisted of a H_2O tank of 1.83 m diameter and 1.83 m height. Several targets of different sizes and materials, among them depleted uranium and lead were investigated in the center of the tank. The total capture rate in the H_2O tank was measured by foil-activation techniques. For the calculations we considered one depleted uranium target (0.22 wt % ^{235}U, length 609.6 mm and radius 50.8 mm) and a lead target of the same size. The calculations were done using HETC-, MORSE CG- and SIMPEL-spallation computer code system of KFA-IRE as described in Ref. 3. The fractional standard deviation in the Monte Carlo calculations is less than 1%, unless stated explicitely in the tables.

2 Neutron Production Using the HEF Model in the HET Code

For these calculations and in most of the following ones the BNL-Cosmotron setup with incident proton beam energy of 960 MeV was assumed. Calculations of the evaporation part of neutron production spectrum with and without the "Rutherford and Appleton Laboratories"- (RAL) HEF model /4/ incorporated in HETC were made. In Figure 1 the two spectra are given. Some spectral hardening in the case of HEF is clearly to be seen. The total neutron production (see Table 1) including low energy fission (< 15 MeV) is about 6-10 % higher using HEF model. Most of this effect is obviously due to low energy fission from spectral hardening.

3 Check of the HEF-RAL Model against the HEF-ORNL Model /5/

For comparison purposes of the two HEF models the calculations were performed first with their appropriate "standard" B_o values of the level-density formula (ORNL model, B_o=10 MeV /1/ and RAL model, B_o=14 MeV); and second the RAL model was run with two additional values of B_o namely 8 MeV and 10 MeV. The standards differ by 20 % in production and capture rates. If we assume an intermediate but equal value for B_o of 10 MeV, the difference is reduced to only 10 % (see Table 2). The neutron production spectra appear to be identical (Figure 2). The effect of different B_o values for the RAL-HEF model is shown in Table 3 and illustrated in Figure 3.

4 Neutron Captures in H_2O Compared with BNL-Cosmotron Experimental Results

According to the Cosmotron experiments /1,2/ calculations were made at incident proton beam energies 590, 960 and 1470 MeV. The measured and calculated quantity is the neutron capture rate in the H_2O tank. A variety of B_o values was applied to calculations with RAL- and ORNL-HEF models. As was found earlier, this parameter is an essential one. The last column of Table

4 shows the ratios of experimental and calculational results. With B_o=10 MeV RAL- and ORNL-HEF models give very similar results, which are in good agreement with experimental results (the "standard" RAL model B_o=14 MeV /6/ underestimates the experiment) for all incident proton energies upto 1 GeV, the energy of interest of SNQ. At energies above 1 GeV the deviation from experiment is higher and significant in case of the ORNL- HEF model (B_o=10 MeV,the "standard", /1/), the RAL model, however, meets the experiments even at B_o=14 MeV. Additional information of neutron production and neutron-reaction rates about the previous calculations is given in Table 5, and some spectral information is shown in Fig. 4.

5 Ratios of Thermal Peak Fluxes in H_2O Moderator Using Lead, Depleted Uranium and Natural Uranium Targets

The arrangement for the calculations is again the BNL-Cosmotron setup using an incident proton beam energy of 960 MeV. The thermal flux distribution in the H_2O tank was calculated around the lead and uranium targets. The peak values of the thermal flux (10^{-5}-0.41 eV) were intercompared to see the influences of the material and the B_o parameter on the maximum thermal flux that can be attained. The ratios are shown in Table 6. There is no significant influence of high-energy fission on the thermal peak flux with a uranium target. However, the ratio of the fluxes between depleted uranium target and lead target is about 1.3-2.5, depending on B_o and whether the HEF model is applied or not. The influence of B_o from 8-14 MeV is remarkable for lead, but this is not true for depleted uranium. Natural uranium as target material gains 20 % more thermal flux in the peak than depleted uranium. The neutron production numbers and neutron reaction rates are given in Table 7, together with evaporation spectra in Figure 5.

6 Conclusion

Spectrum hardening with high energy fission models incorporated in the HET code is evident. The neutron captures in water surrounding finite depleted uranium targets are found to be 5-10 % higher with HEF. Significant differences of RAL- and ORNL-HEF models are found at incident proton beam energies above 1 GeV. The RAL model gives lower values than the ORNL model. The B_o value seems to be model and somewhat energy dependend.

REFERENCES

/1/ R.G. Alsmiller Jr.,T.A. Gabriel, J. Barish, F.S. Alsmiller: "Neutron Production by Medium Energy ($\simeq$1.5 GeV) Protons in Thick Uranium Targets", ORNL/TM-7527 (1981)

/2/ J.S. Fraser et al.:"Neutron Production in Thick Targets Bombarded by High-Energy Protons", Phys. in Canada 21,17 (1965)

/3/ T.W. Armstrong, P. Cloth, D. Filges, R.D. Neef:"Theoretical Target Physics Studies for the SNQ Spallation Neutron Source", Jül-Spez-120 (July 1981)

/4/ F. Atchison:"The Inclusion of Fission in the High-Energy Particle Transport Code, HETC", Bulletin of the American Physical Society 24, 874 (1979)

/5/ F.S. Alsmiller, R.G. Alsmiller Jr., T.A. Gabriel, R.A. Lillie, J. Barish:"A Phenomenological Model for Particle Production from the Collisions of Nucleons and Pions with Fissile Elements at Medium Energies", ORNL/TM-7528 (1981)

/6/ F. Atchison:"A Theoretical Study of a Target Reflector and Moderator Assembly for SNS", RL-81-006 (1981)

TABLE 1

Calculations with and without High-Energy Fission Model (HEF)
(Proton Beam Energy 960 MeV, Target Material Depleted Uranium)

	neutron production per proton		number of fissions in target per proton from		number of captures in uranium target per proton	number of neutron captures in H_2O per proton
	≤ 15 MeV	> 15 MeV	(a) neutrons ≤ 15 MeV	(b) neutrons and charged particles > 15 MeV		
without HEF*	29.16	4.21	5.17	-	7.74	30.90
with HEF**	30.11	4.05	5.56	1.77	8.02	32.56
ratio of calculations with HEF vs. without HEF	-	-	1.08	-	1.04	1.06

* Rutherford high energy fission model (RAL model)

** B_o parameter 8 MeV

TABLE 2

Comparison of RAL- and ORNL-HEF Model for Different B_o Parameters
(Proton Beam Energy 960 MeV, Target Material Depleted Uranium)

HEF Model	B_o (MeV)	neutron production per proton		number of fissions in target per proton from		number of captures in uranium target per proton	number of neutron captures in H_2O per proton
		≤ 15 MeV	>15 MeV	(a) neutrons ≤ 15 MeV	(b) neutrons and charged particles >15 MeV		
RAL	8	30.11	4.05	5.56	1.77	8.02	32.56
RAL	10	28.48	4.26	5.39	1.73	7.87	30.88
ORNL	10	31.73	4.49	6.18	1.93	8.72	35.23
RAL	14	26.03	4.43	5.03	1.71	7.01	29.03
ratio of							
RAL(B_o=14) vs. ORNL(B_o=10) (Standard)		0.82		0.81		0.80	0.82
RAL(B_o=10) vs. ORNL(B_o=10)		0.89		0.87		0.90	0.88

TABLE 3

Effect of Different B_o Parameters (8,10 and 14 MeV)
Using RAL-HEF Model
(Proton Beam Energy 960 MeV, Target Material Depleted Uranium)

ratio of	neutron production per proton		number of fissions in target per proton from		number of captures in uranium target per proton	number of neutron captures in H_2O per proton
	≤ 15 MeV	>15 MeV	(a) neutrons ≤ 15 MeV	(b) neutrons and charged particles >15 MeV		
B_o=8 MeV vs. B_o=10 MeV	1.06	0.95	1.03	1.0	1.02	1.05
B_o=8 MeV vs. B_o=14 MeV	1.16	0.91	1.11	1.0	1.14	1.12

TABLE 4

Comparison with Cosmotron Data (Fraser et al./2/)
Depleted Uranium Target, H_2O Captures per Incident Proton

incident proton energy (MeV)	experiment	HEF	B_0 (MeV)	theory	theory vs. experiment
540	15.1±0.8	ORNL	10*	15.2±0.8	1.07
		RAL	14	13.5±1.1	0.81
960	32.3±1.6	ORNL	10*	33.7±1.0	1.04
		ORNL	10**	35.2±0.6	1.09
		RAL	10	30.9±0.3	0.96
		RAL	8	32.6±0.3	1.00
		RAL	14	29.0±0.3	0.89
1470	44.8±0.2	ORNL	10*	53.6±1.5	1.20
		RAL	14	46.0±0.4	1.03

* Calculations of Alsmiller et al.,ORNL-TM-7527

**KFA-IRE calculations using uranium cross sections with self-shielding corrections

TABLE 5

Neutron Production and Reaction Rates at Different Proton Beam Beam Energies with HEF Model* (B_o=14 MeV)

incident proton energy (MeV)	neutron production per proton		number of fissions in target per proton from		number of captures in uranium target per proton	number of neutron captures in H_2O per proton
	≤ 15 MeV	>15 MeV	(a) neutrons ≤15 MeV	(b) neutrons and charged particles >15 MeV		
540	12.46	1.73	2.25	-	3.14	13.48
960	26.03	4.43	5.03	1.71	7.01	29.03
1470	42.03	7.65	8.03	-	11.99	46.03

*"Rutherford" high energy fission model (RAL model)

TABLE 6

Ratios of Thermal Peak Fluxes* in the Cosmotron Experiments
Between Pb,Depleted U and Natural U Targets
(Proton Beam Energy 960 Mev)

B_o (MeV)	U_{dep} without HEF vs. Pb without HEF	U_{dep} with HEF vs. U_{dep} without HEF	U_{nat} with HEF vs. U_{dep} with HEF	U_{dep} with HEF vs. Pb with HEF
8	1.9	0.96	-	-
14	-	-	1.2	2.5
Ratio of Pb (B_o=8 MeV) vs. Pb (B_o=14 MeV) = 1.3 Ratio of U_{dep} with HEF (B_o=8 MeV) vs. U_{dep} with HEF (B_o=14 MeV) =1.05				

*fractional standard deviation 5-7%

TABLE 7

Comparison of Calculated Results for Lead, Depleted Uranium and Natural Uranium for the RAL-HEF Model (B_o=14 MeV at 960 MeV Proton Energy)

target material	neutron production per proton		number of fissions in target per proton from		number of captures in uranium target per proton	number of neutron captures in H_2O per proton
	≤15 MeV	>15 MeV	(a) neutrons ≤15 MeV	(b) neutrons and charged particles >15 MeV		
lead	19.46	4.30	-	-	0.502	18.75
depleted uranium	26.03	4.43	3.40 U238 1.63 U235	1.71	7.01	29.03
natural uranium	27.19	4.44	3.91 U238 4.07 U235	1.71	7.27	33.79
ratio of calculations						
natural U vs. depleted U	1.05		1.59	-	1.04	1.16
depleted U vs. lead	1.39	-	-	-	1.39	1.55

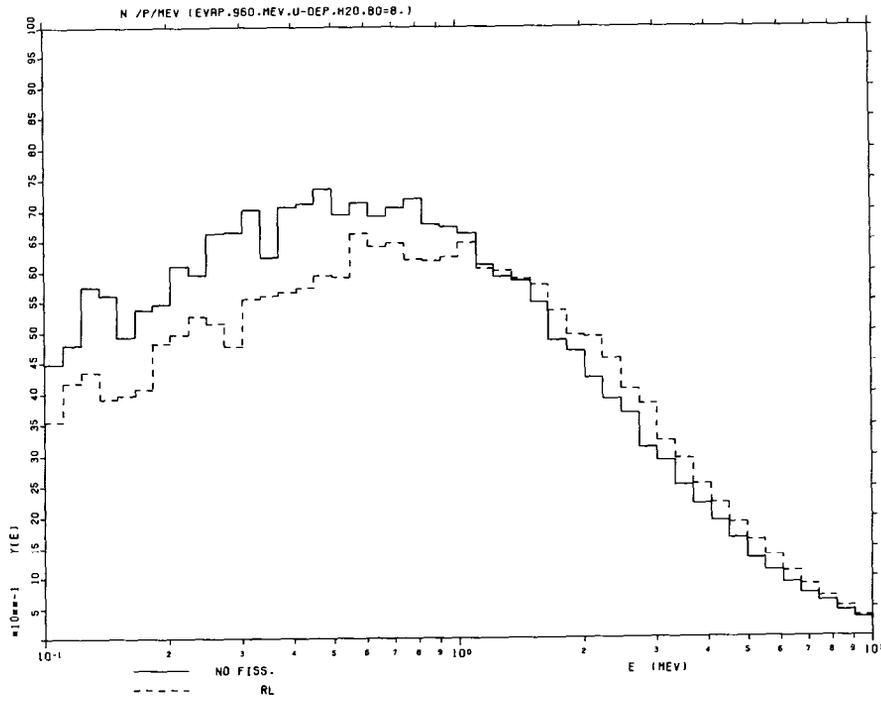

Fig. 1 Evaporatin neutrons with (solid curve) and without (dashed curve) RAL-HEF model (B_o=8 MeV, proton-beam energy 960 MeV, target material depleted uranium)

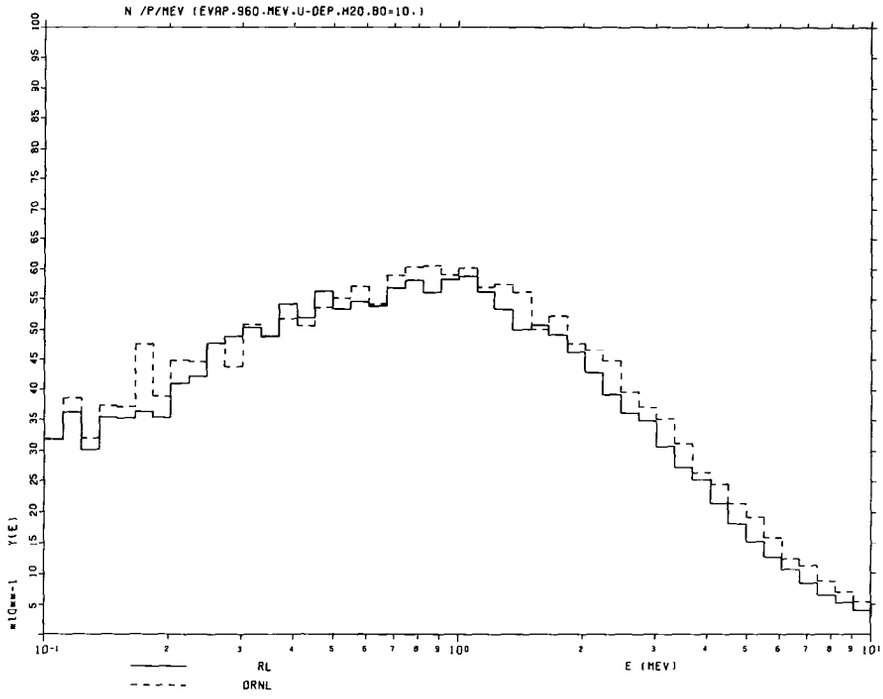

Fig. 2 Evaporation neutrons with RAL-HEF model (solid curve) and ORNL-HEF model (dashed curve) (B_o=10 MeV, proton beam energy 960 MeV, target material depleted uranium)

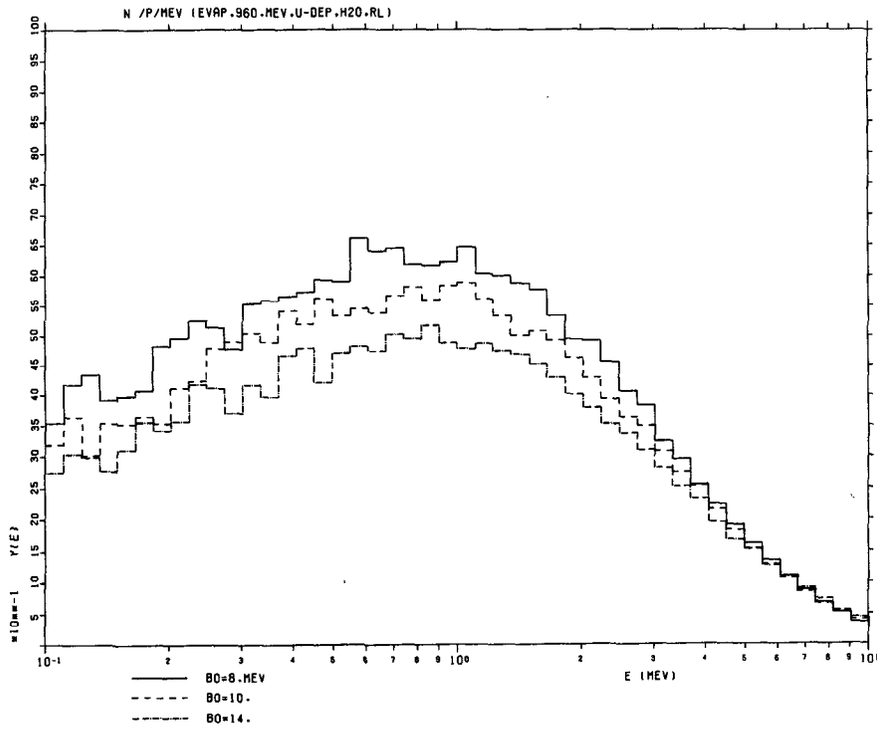

Fig. 3 Evaporation neutrons with RAL-HEF model at B_o=8 MeV (solid curve), B_o=10 MeV (dashed curve) and B_o=14 MeV (dashed-dotted curve) (proton beam energy 960 MeV, target material depleted uranium)

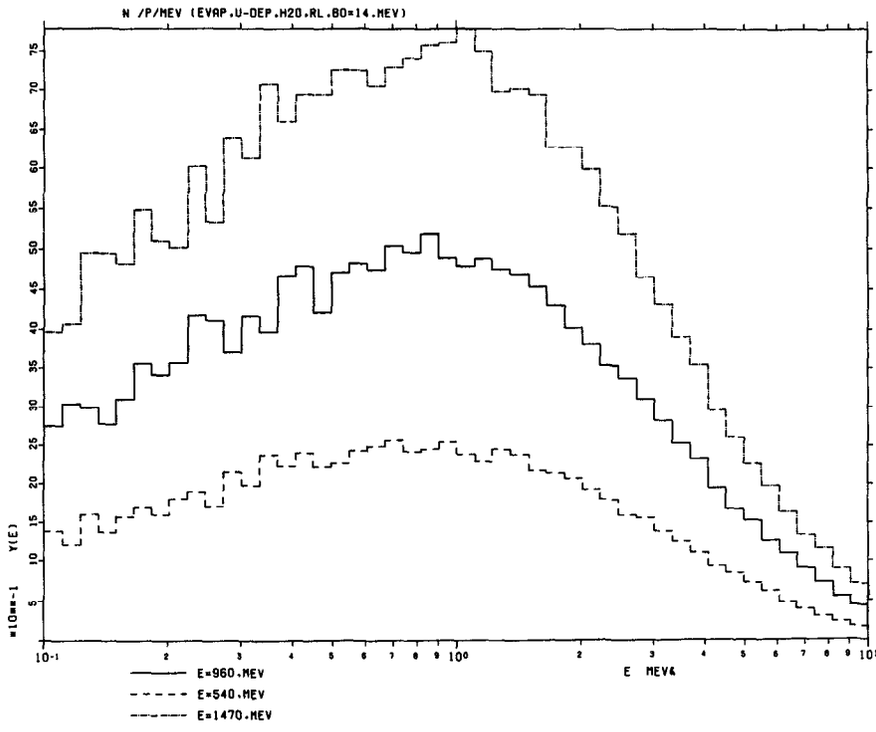

Fig. 4 Evaporation neutrons with RAL-HEF model at proton beam energy E=540 MeV (dashed curve), E=960 MeV (solid curve) and E=1470 MeV (dashed-dotted curve) with B_o=14 MeV

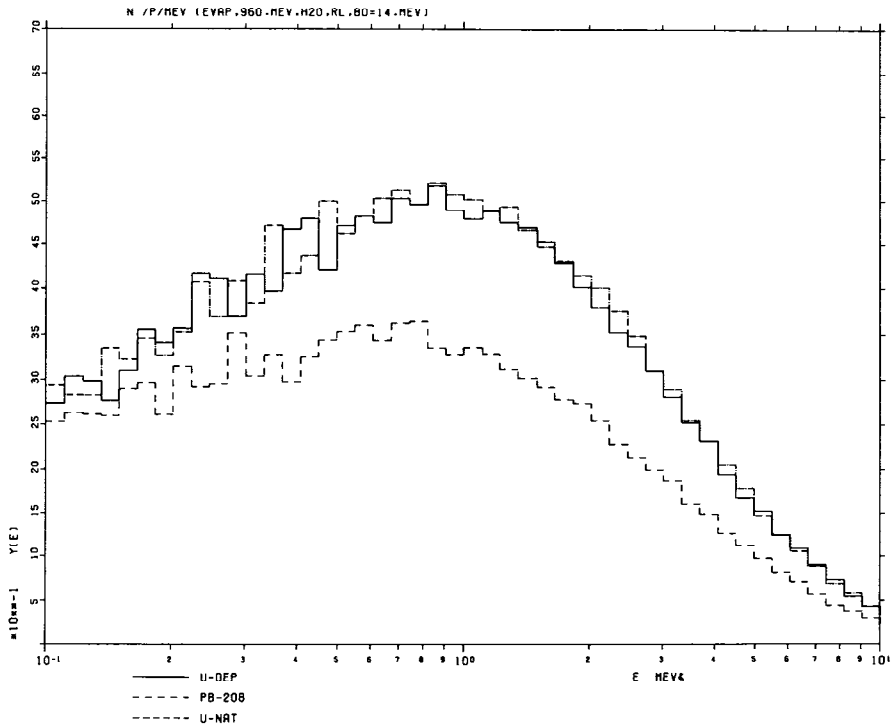

Fig. 5 Evaporation neutrons with RAL-HEF model for target material of depleted uranium (solid curve), natural uranium (dashed curve) at 960 MeV proton-beam energy and B_o=14 MeV

Jül-Conf-45

D1-3

I C A N S - V

MEETING OF THE INTERNATIONAL COLLABORATION ON

ADVANCED NEUTRON SOURCES

June 22-26, 1981

Differential Production Cross Sections for Charged Particles Produced by 590 MeV Proton Bombardment of Thin Metal Targets

S.D. HOWE, S. CIERJACKS, Y. HINO, F. RAUPP, M.T. RAINBOW, M.T. SWINHOE, AND L. BUTH.

KERNFORSCHUNGSZENTRUM KARLSRUHE
INSTITUT FÜR KERNPHYSIK
7500 KARLSRUHE, POSTFACH 3640
FEDERAL REPUBLIC OF GERMANY

Abstract

Differential production cross sections have been measured for the reactions (p,p), (p,d), (p,t) and (p,$\pi\pm$) using the 590 MeV proton beam at SIN. Here we report measurements made on thin targets of aluminium, niobium, lead, and uranium at laboratory angles of 90° and 157°. The data were taken over a proton energy range of about 50 MeV to 590 MeV. Differential cross sections are reported along with predictions by the intranuclear-cascade/evaporation model as computed by HETC.

1. INTRODUCTION

The use of high-current, medium-energy particle accelerators as spallation sources for nuclear research has gained widespread interest in recent years. Along with fundamental research, work performed at such facilities can provide valuable information in accessing the feasibility of using large scale spallation sources to breed nuclear fuel for conventional nuclear reactors. Design of such facilities, however , depends heavily on the characterisation of the particle spectra emitted by spallation targets.

Several researchers [1-6] have investigated the differential and integral neutron yields leaking out of large spallation targets. Comparisons between such measurements and predicted values calculated by the intranuclear-cascade/evaporation model have revealed a wide range of disagreement. Comparison of differential neutron spectra form thin targets have shown good agreement with calculated values for the evaporation, $E < 20$ MeV, region of the spectrum. For energies greater than 20 MeV, however, discrepencies exist between calculation and measurement.

Consequently, we have performed a series of measurements to determine the differential leakage spectra of protons, deuterons, tritons, and charged pions from thin targets bombarded by 590 MeV protons. Results at laboratory angles of 90° and 157° for targets of aluminium, niobium, lead, and uranium are reported.

2. EXPERIMENT

The measurements were performed using the 590 MeV proton beam of the SIN cyclotron in Switzerland. Proton pulses at a frequency of 16.84 MHz were impinged on thin metal targets of Al, Nb, Pb and U with thickness of 0.86, 3.43, 4.99, and 5.92gm/cm^2 respectively. The incident proton number was monitored using a small scatterer with a scintillator telescope which was calibrated periodically during the measurements.

The experimental set-up is shown in Fig.1. A more detailed description is presented elsewhere.[7] In brief, our assembly consisted of a 4.50 cm diameter by 3 cm deep NE213 liquid scintillator, D_2, positioned at 90° and then 157° with respect to the incident proton beam axis. The detector provided timing, pulse height, and pulse-shape-discrimination information which was recorded in an event-by-event mode. A thin plastic scintillator placed half-way between D_2 and the target was used in a single coincidence mode to denote charged particles. Total time-of-flight paths were through air and were 4.23 m and 1.87 m for 90° and 157° respectively.

In order to reduce the random coincidence rate due to neutron events in the NE213 detector, we placed an open ended lead cave around and extending 30-40 cm in front of the detector. About 1 m of lead shielding was also used to seclude the beam monitor scatter from the target-detector area.

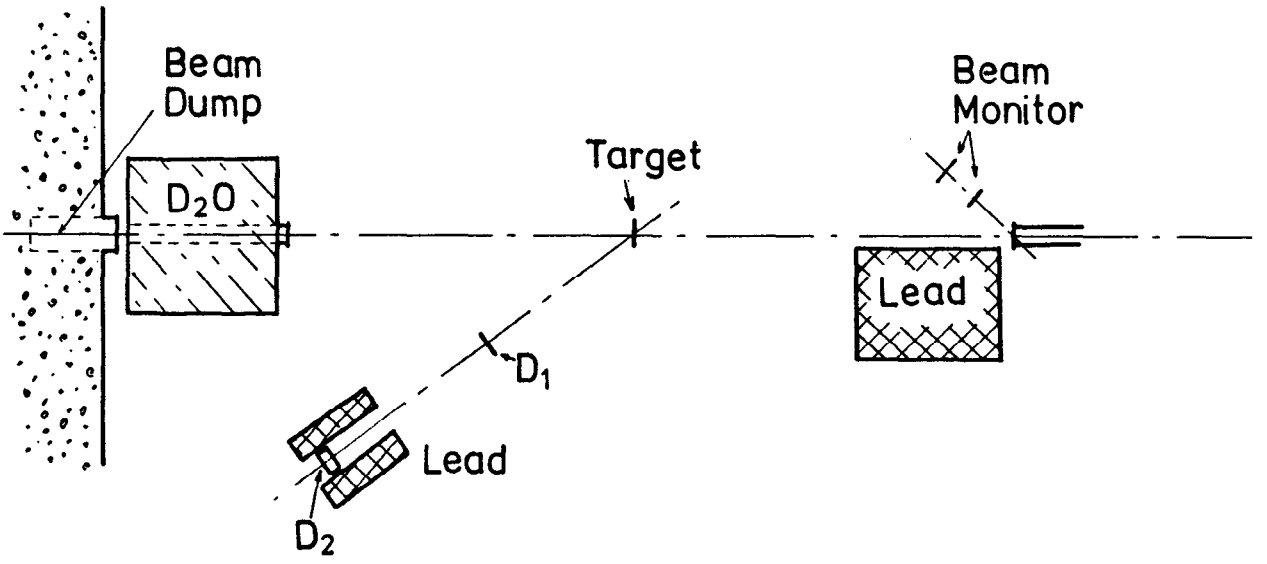

Figure 1: Experimental set-up for this measurement. D_1 and D_2 were a 0.2 cm thick plastic and a 3.0 cm thick Ne-213 scintillator respectively.

Results and Discussion

The results of these measurements are shown in Figs. 2 to 9 as differential cross sections as a funtion of the energy of the observed particle. In each case, the data have been corrected for energy losses of the secondary particle in the target material and intervening air path.

The results for secondary proton emission are shown in Figs. 2 and 3. The cross sections are seen to vary smoothly over the energy range considered up to maximum energies of about 360 MeV and 220 meV for 90° and 157° respectively. The data at 157° are also seen to decrease more rapidly with increasing energy than those at 90°. These effects and the reduction at 157° relative to 90° of the general magnitude of the cross sections are all indicative of the intranucleon cascade process which is strongly forward peaked.

Spectra for deuteron and triton production cross sections are shown in Figs. 4 to 7. The upper energy limit of the deuteron data is determined by the pulse-height resolution of our scintillation detector. For energies greater than those seen in Figs. 4 and 5, the separate proton-deuteron pulse-height peaks could no longer be resolved. Extrapolations of the deuteron data were subtracted from the proton results but are not reported with the deuteron values. Such corrections to the proton areas were typically $\leq$ 10%.

From the figures, we see that the deuteron values appear to follow an exponential behaviour as a function of particle energy. Performing least-square-fits to the data shows that the exponential coefficient is different for each angle but is relatively independent of the nucleon number in the target nucleus. Comparison of the fits at each angle shows that the slope of the data is much steeper for 157° than for 90° which is a result similar to the proton behaviour.

We can also observe an exponential behaviour for the triton emission results but the statistical errors of the data are greater and such behaviour is not entirely evident. Unlike the proton and deuteron results, though, the general trends of the cross sections appear to decrease at the same rate at both 90° an 157°. This may indicate that the heavier tritons are emitted later in the cascade process from a nuclens in a pre-equilibrium state.

The production cross sections of charged pions seen in Figs. 8 and 9 have a lower energy limit which is also determined by the inability to resolve separate proton and pion pulse height responses. The figures show that the cross sections are somewhat backward peaked and that the average energy in the backward direction is substantially smaller. The average energies were about 98 MeV and 63 MeV for 90° and 157° respectively and appear to be relatively independent of target nucleon number.

Integration of the differential spectra with respect to energy gives a good indication of the relative magnitudes of the cross sections for the different particles. In Table I, the integral values show that the production cross sections for protons, deuterons, and tritons are separated by about an order of magnitude. The results also show that the particle production at 157° relative to that at 90° is about a factor of 3.6, 5.3, 7.6, and 0.73 for protons, deuterons, tritons, and pions respectively.

TABLE I

Cross sections in mb/sr resulting from integration of the differential spectra over the observed energy range

	particle	Al	Nb	Pb	U
90°	p	18.2	53.4	88.3	97.6
	d	.840	2.68	4.50	5.17
	T	.051	.190	.399	.438
	π	2.61	4.98	6.62	7.36
157°	p	5.42	14.69	25.1	26.0
	d	.156	.462	.935	.988
	T	.0068	.0191	.0611	.0695
	π	3.16	6.60	10.4	10.5

Model Calculations

Calculations of charged particle production from thin targets of aluminum and lead have been performed using the HETC computer code[9]. Comparisons of the code's predictions for protons and pions at 90° and 157° are shown in Figs. 10 to 13. Comparisons of deuteron and triton results are not possible since the code only calculates deuteron and triton spectra emitted from the evaporation process. The calculations had an upper energy of about 30 MeV while the lower energy limit of our data was about 70 to 80 MeV.

In Figs. 10 and 11, we see that the calculations tend to underpredict our measured results for lead by about a factor of 2 throughout most of the energy range. At 90°, however, the code overpredicts the results at the upper energies and, in general, predicts a slightly different spectrum shape. For aluminum, the predictions are about a factor of 0.6 below the experimental values at 90° but are also a factor of 2 too low at 157°. The underpredictions by the code may indicate that nucleon clustering in the nucleus during the cascade, which HETC does not take into account, might be significant.

The HETC predictions and experimental results for charged pion production are compared in Figs. 12 and 13. Also shown in Fig. 12 are results of another experiment which measured differential production cross sections of π^+ and π^- separately. In these figures, we see that the calculations overestimate the measured values rather drastically. Although the agreement is better at 157° than at 90°, the spectra are still separated by a factor of 2 to 3. Consequently,

we feel that the angular distributions used in the code for the pion production processes should be carefully reexamined.

5. CONCLUSION

In conclusion, we have determined the differential production cross sections of protons, deuterons, tritons and pions for 590 MeV proton bombardement of thin metal targets at laboratory angles of 90° and 157°. The proton data are seen to decrease smoothly with increasing particle energy until an energy maximum, of about 360 MeV and 220 MeV for protons at 90° and 157° respectively, is reached. At both angles, the deuterium cross sections appear to follow an exponential behaviour and are about an order of magnitude smaller than the proton values. Similar behaviour is seen in the triton spectra with still another factor of 10 reduction in magnitude. The triton spectra also appear to be produced by a nucleus in a pre-equilibrium state.

Comparison between our results and calculations by the HETC computer code show a significant underprediction of the proton values by the code and an overprediction of the pion results. The comparisons indicate that 1) the effect of nucleon clustering in the nucleus may be important during the cascade process, and 2) the angular distribution used in the code for the pion production mechanisms needs review. In the near future, we intend to supplement these results with data taken at 23°, 45°, and 135° in order to develop a more complete understanding of behaviour of the spallation process.

The authors would like to acknowledge the help of the SIN staff, especially Dr. W. Fischer and Dr. C. Tschalär. We are also indebted to Dr. C. Weddigen and Dr. J. Hoftiezer for their advice and the loan of miscellaneous equipment.

REFERENCES

1. J.S. FRASER, et al., Physics in Canada 21, No. 2, 17018 (1965).
2. R. Madey and F.M. Waterman, Phys. Rev. C8, 2412 (1973).
3. C.G. Cassapakis, et al., Phys. Lett. 63B, 35 (1976).
4. G.J. Russell, et al., Intl. Conf. on Neutron Physics and Nucl. Data for Reactors and Other Appl. Purposes, Harwell, England (1978).
5. H. Takahashi and Y. Nakahara, Int. Conf. of Neut. Cross Sections for Technology, (1979).
6. P.M. Garvey, Proc. of Meeting on Targets for Neutron Beam Spallation Neutron Sources, Jül-Conf-34, ISSN 0344-5798, Jülich (1980).
7. S. Cierjacks, Proc. of ICANS-V Conf., Jülich (1981). (to be published)
8. J.F. Crawford, et. al., Phys. Rev. C, 22 , No. 3, 1184 (1980).
9. Filgess and T. Armstrong, Proc. of ICANS-V Conf, Jülich (1981)

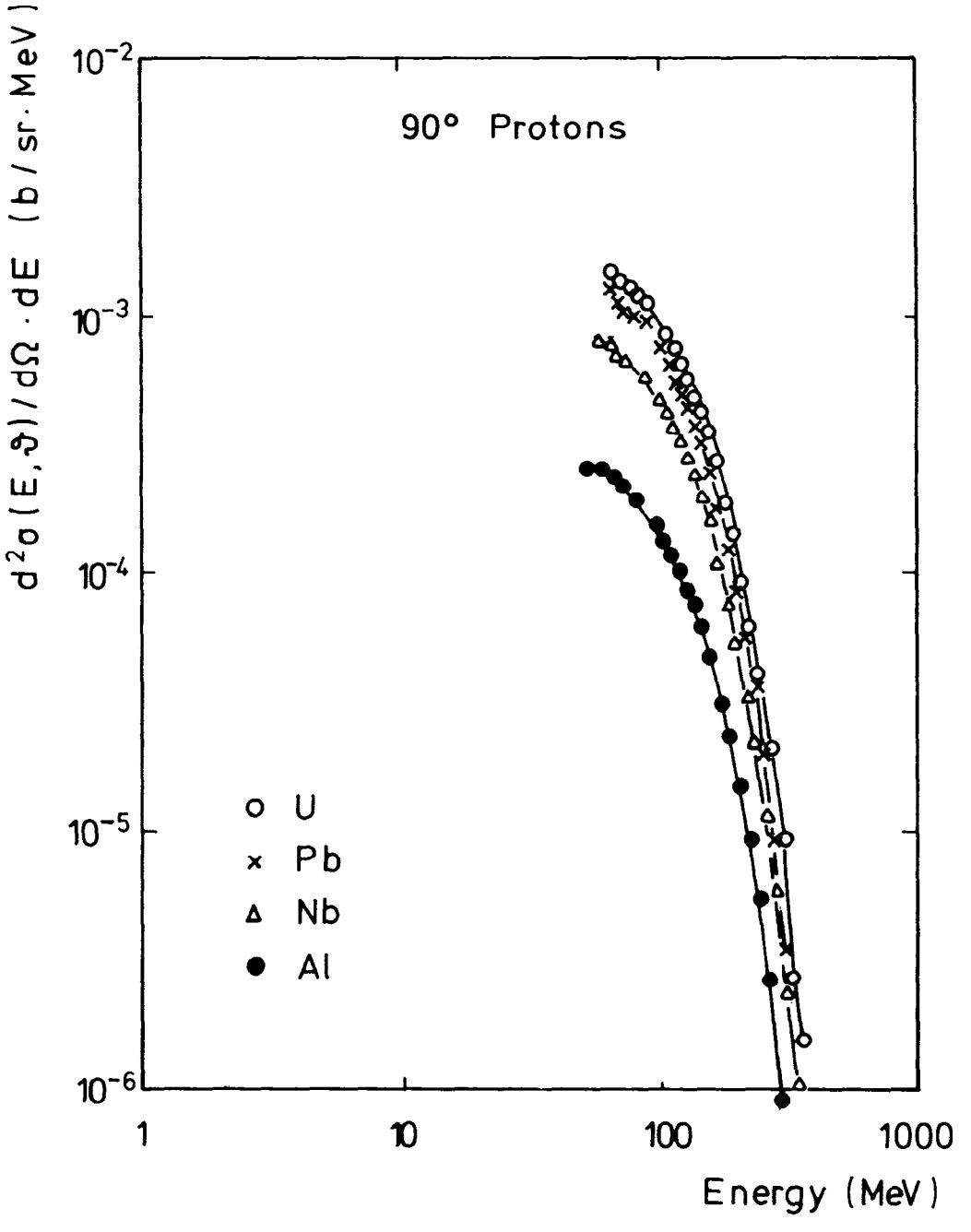

Figure 2 - Differential cross sections for secondary protons emitted from aluminum, niobium, lead, and uranium at a laboratory angle of 90°. The character size indicates the statistical uncertainty.

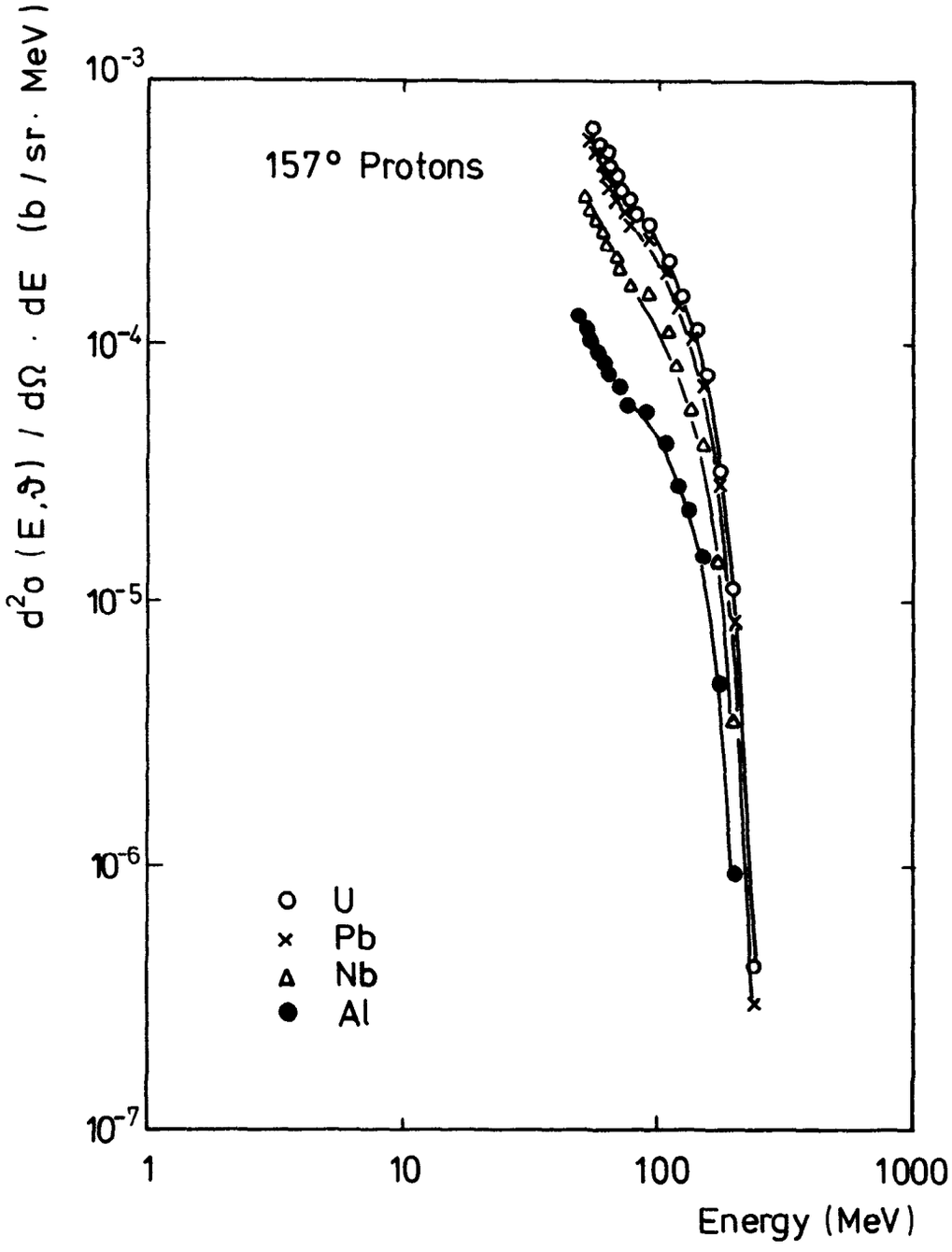

Figure 3 - Same as Fig. 2 except for a laboratory angle of 157°.

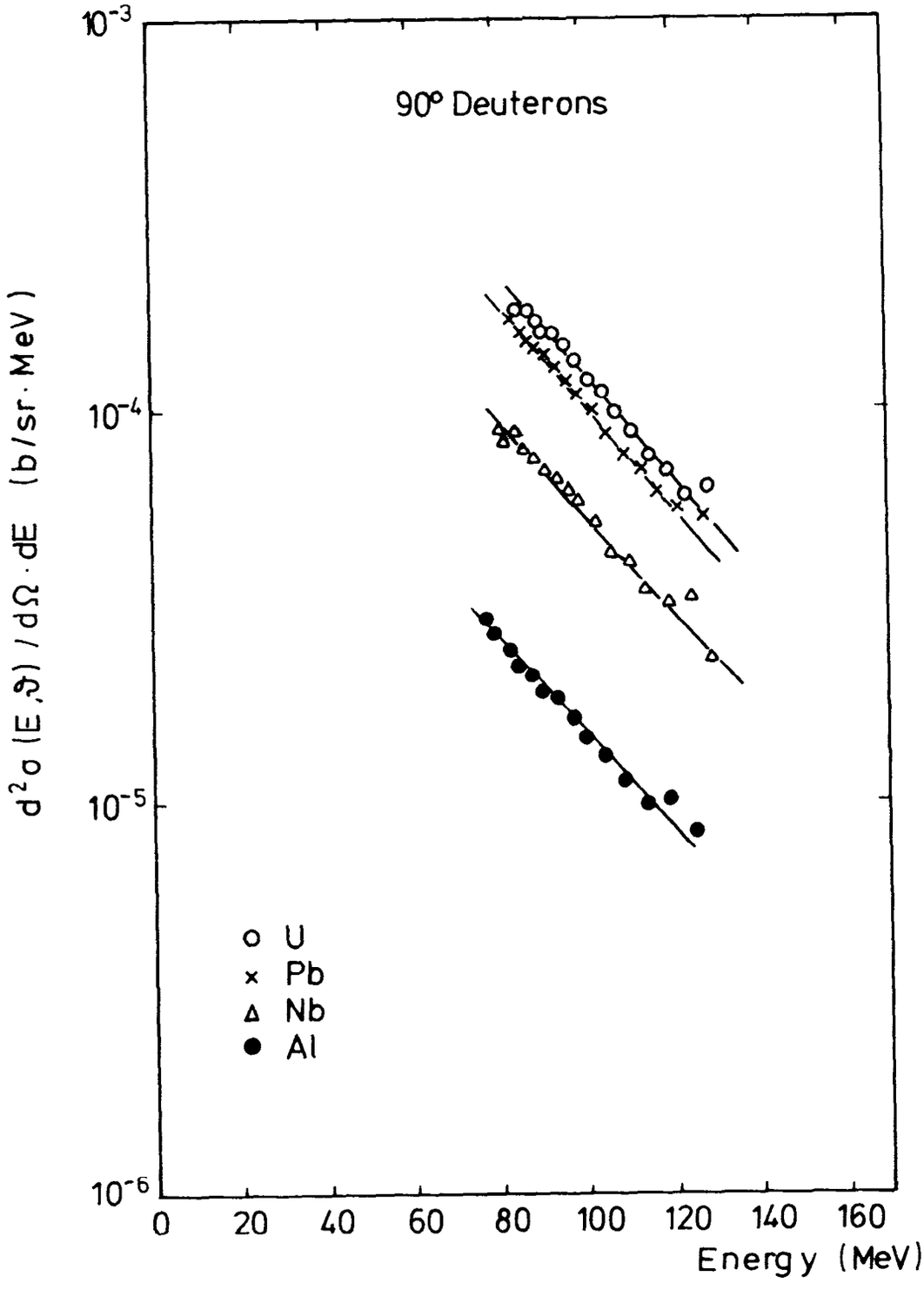

Figure 4 - Differential cross sections for deuterons emitted from aluminum, niobium, lead, and uranium at a laboratory angle of 90°. The character size indicates the statistical uncertainty.

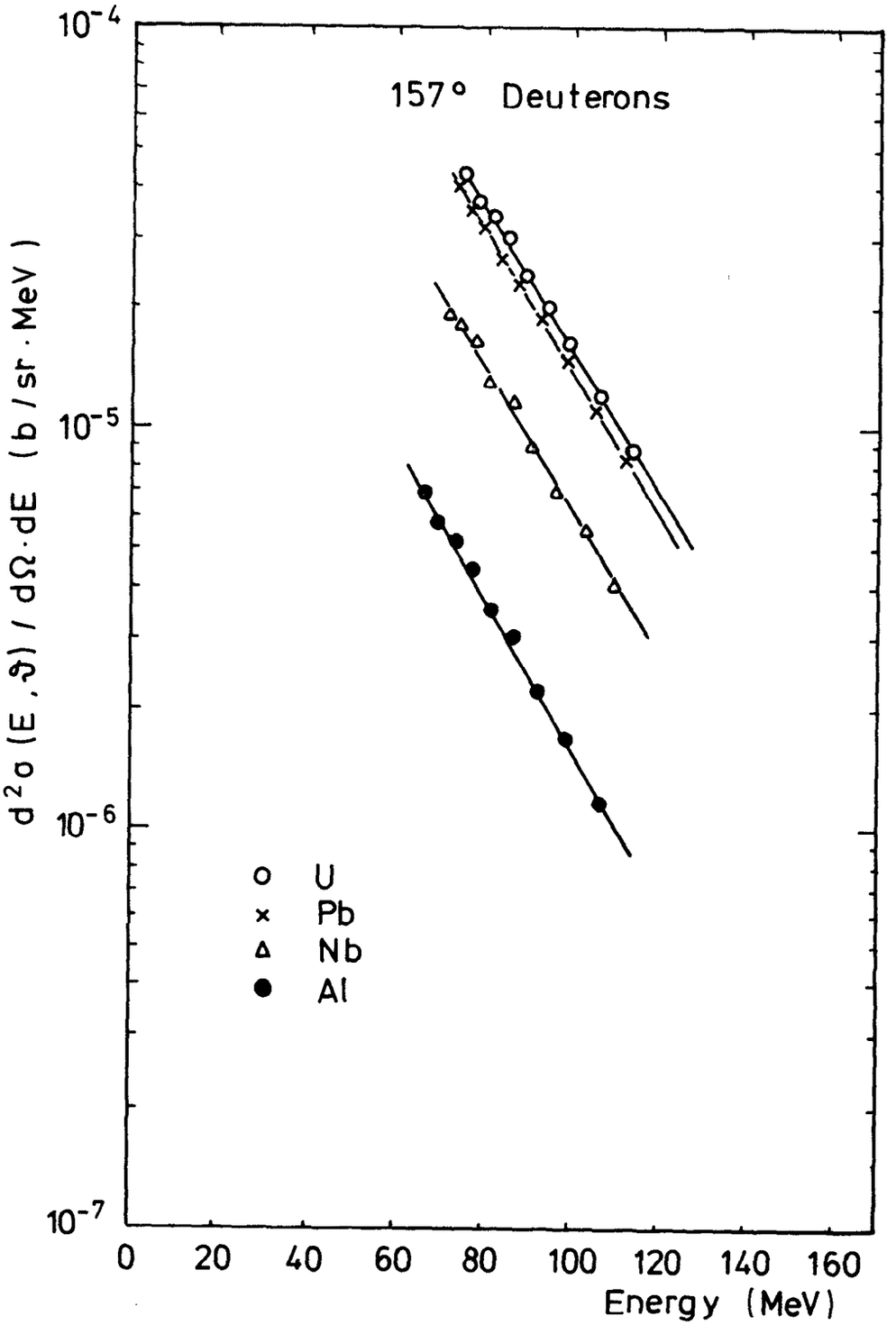

Figure 5 - Same as Fig. 4 except for a laboratory angle of 157°.

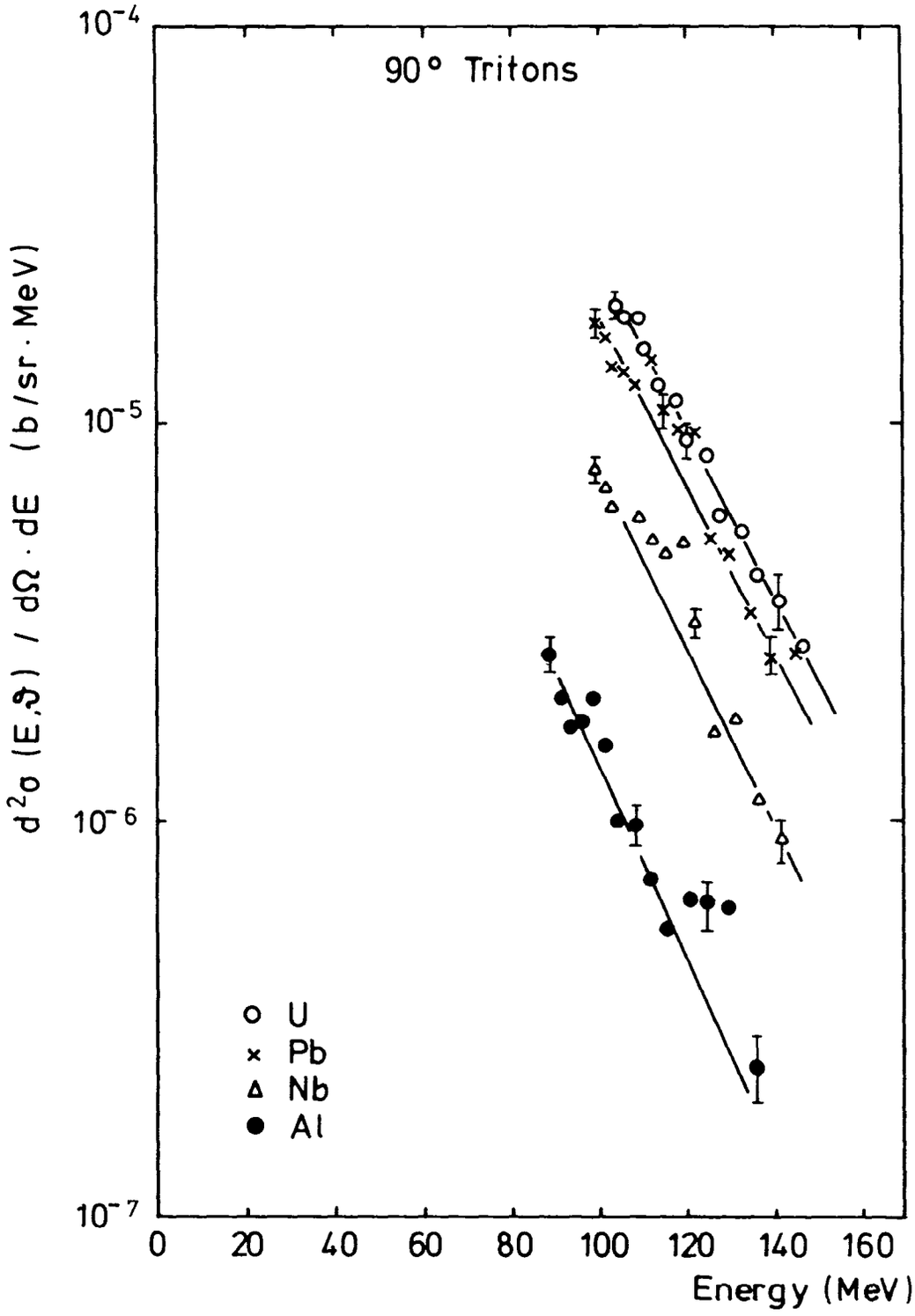

Figure 6 - Differential cross sections for tritons emitted from aluminum, niobium, lead, and uranium at a laboratory angle of 90°.

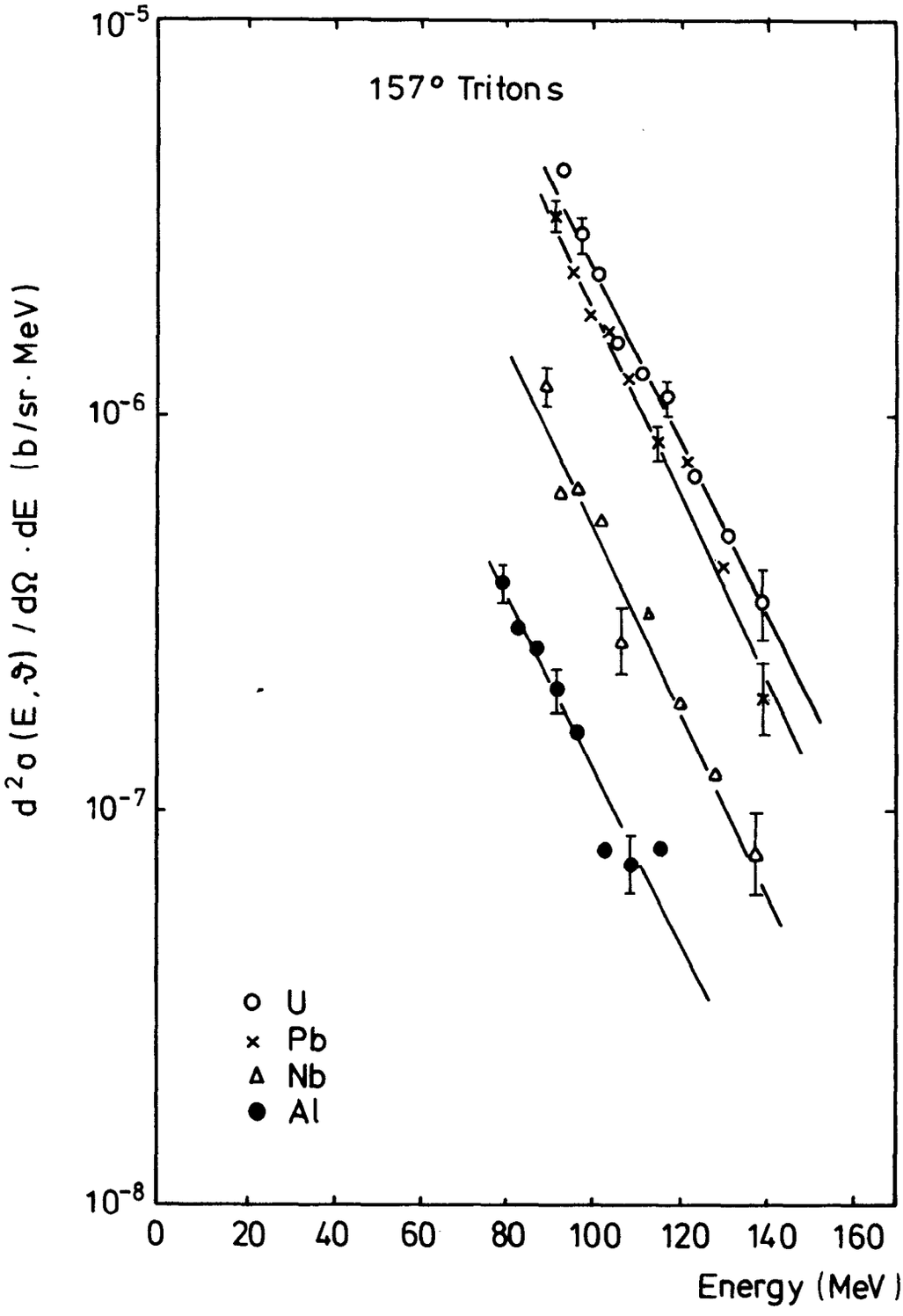

Figure 7 - Same as Fig. 6 except for a laboratory angle of 157°.

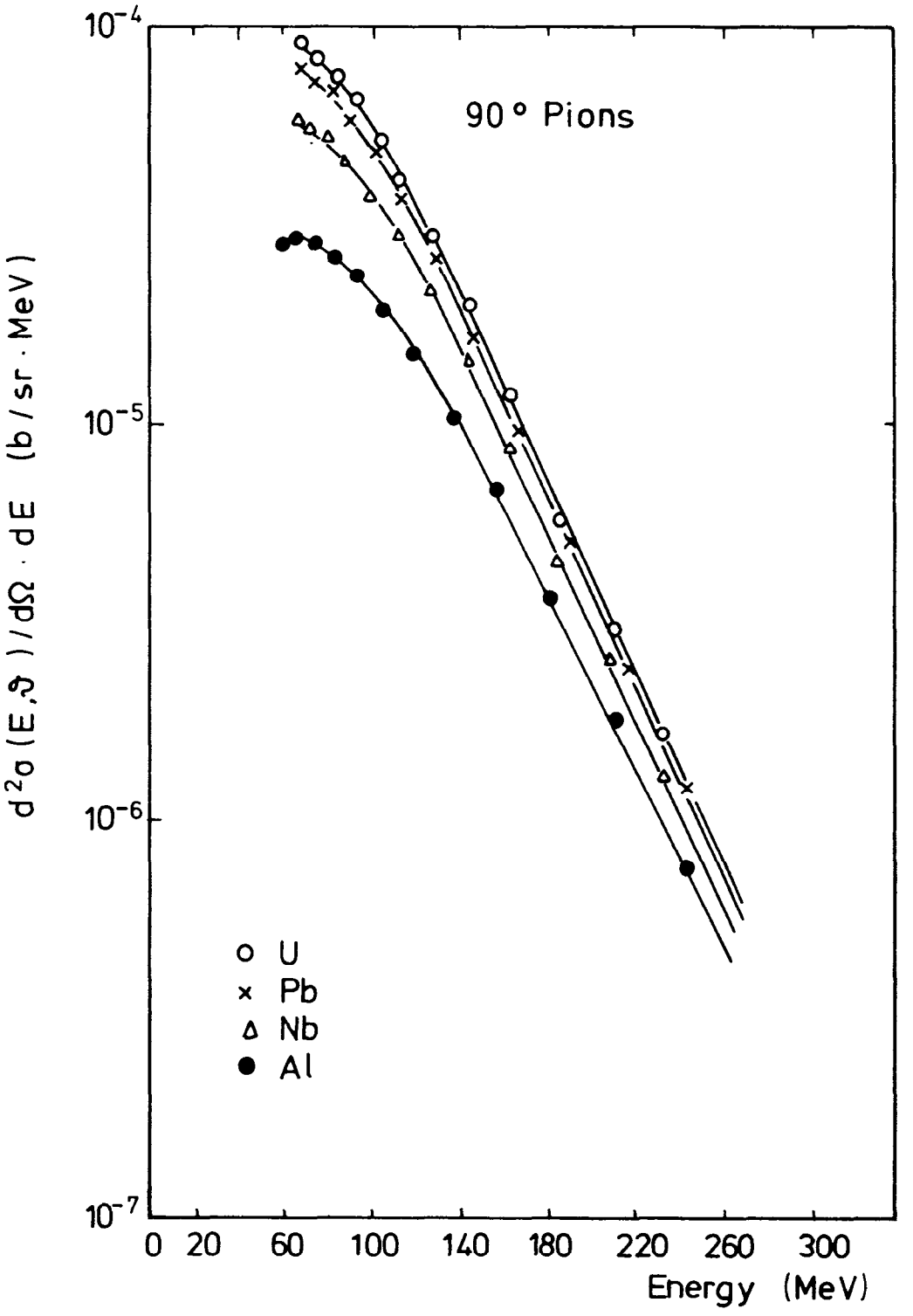

Figure 8 - Differential cross sections for pions (π^+ and π^-) emitted from aluminum, niobium, lead, and uranium at a laboratory angle of 90°. The character size indicates the statistical uncertainty.

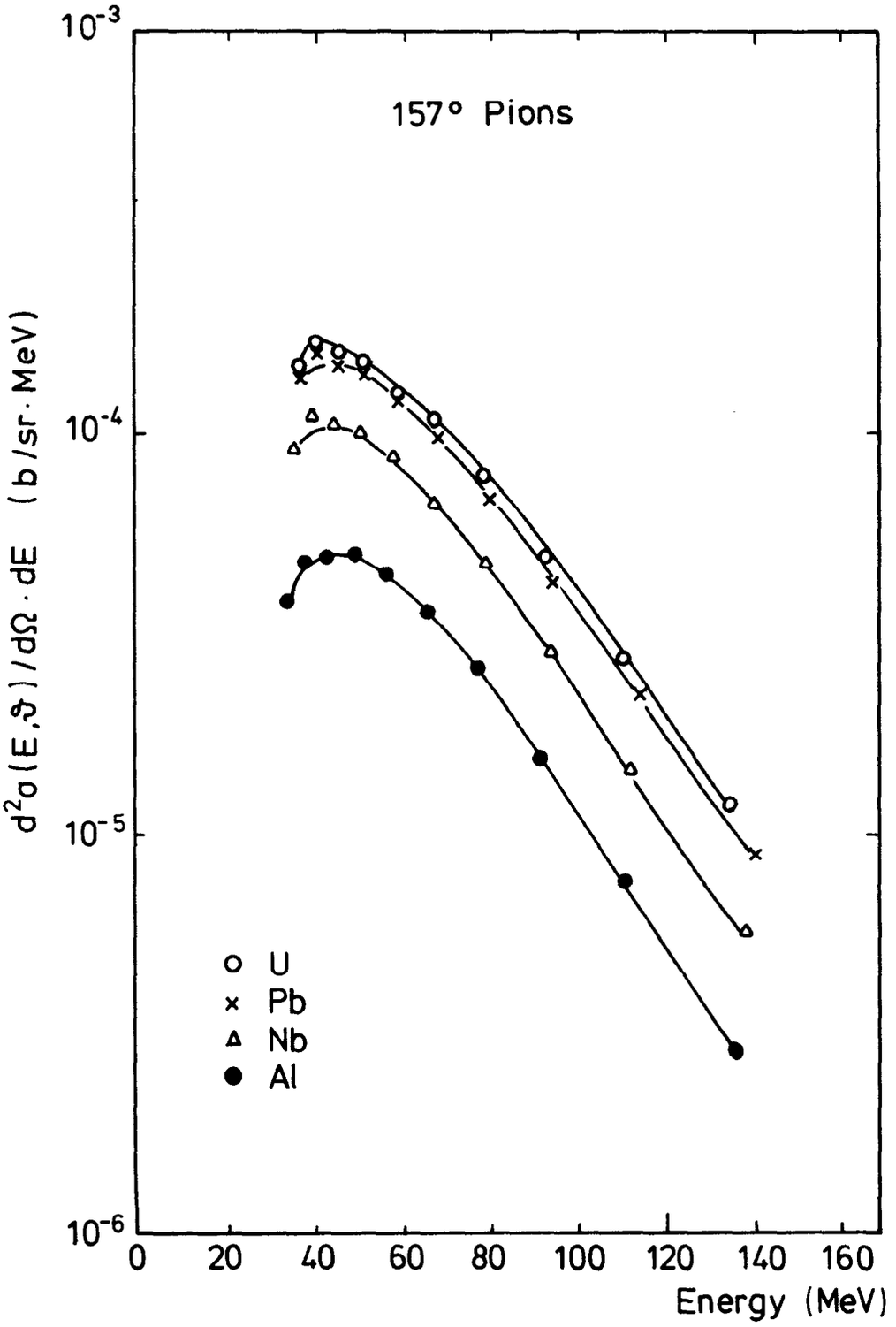

Figure 9 - Same as Fig. 8 except for a laboratory angle of 157°.

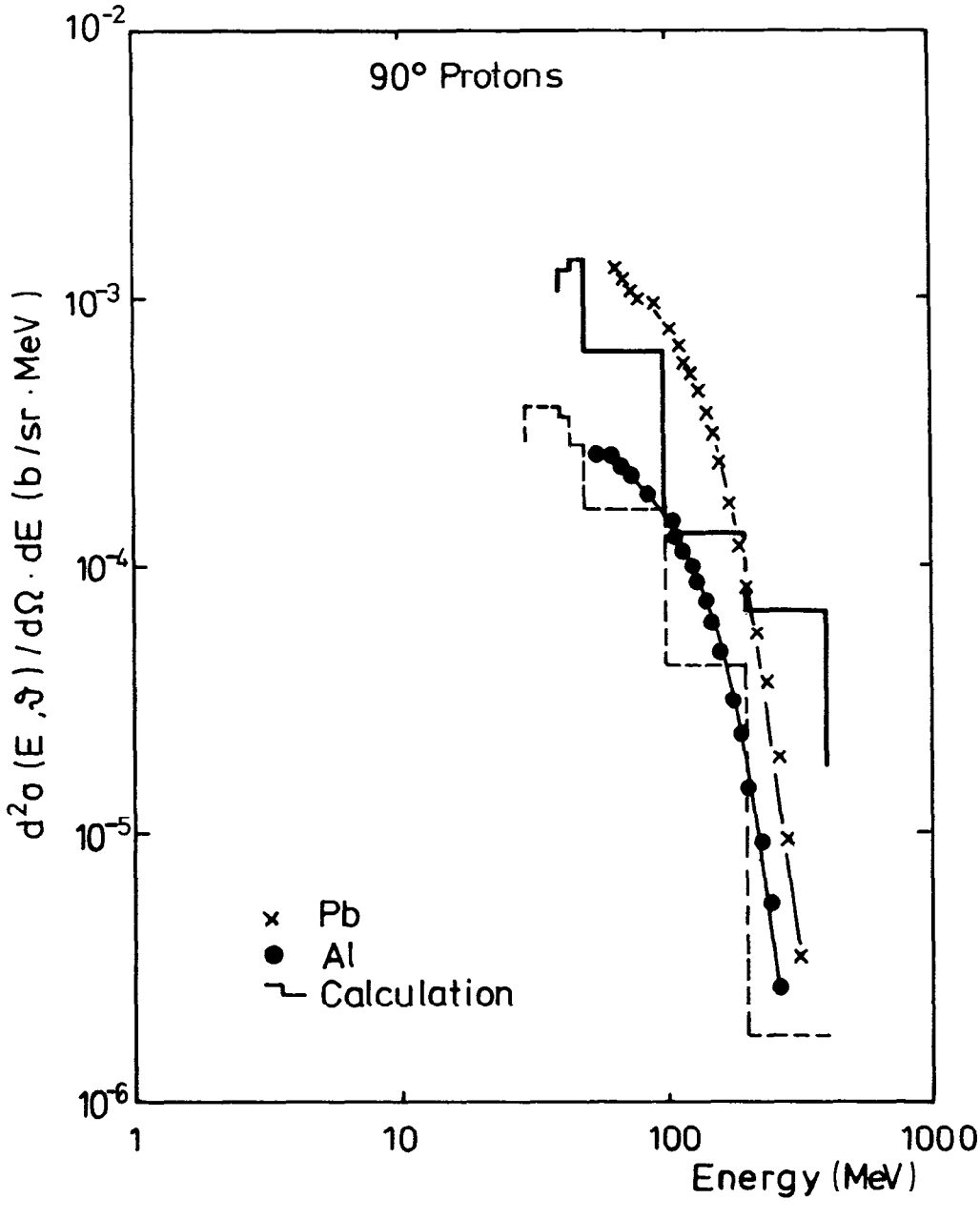

Figure 10 - Comparison of measured and calculated differential cross sections for secondary protons emitted from aluminum and lead at a laboratory angle of 90°.

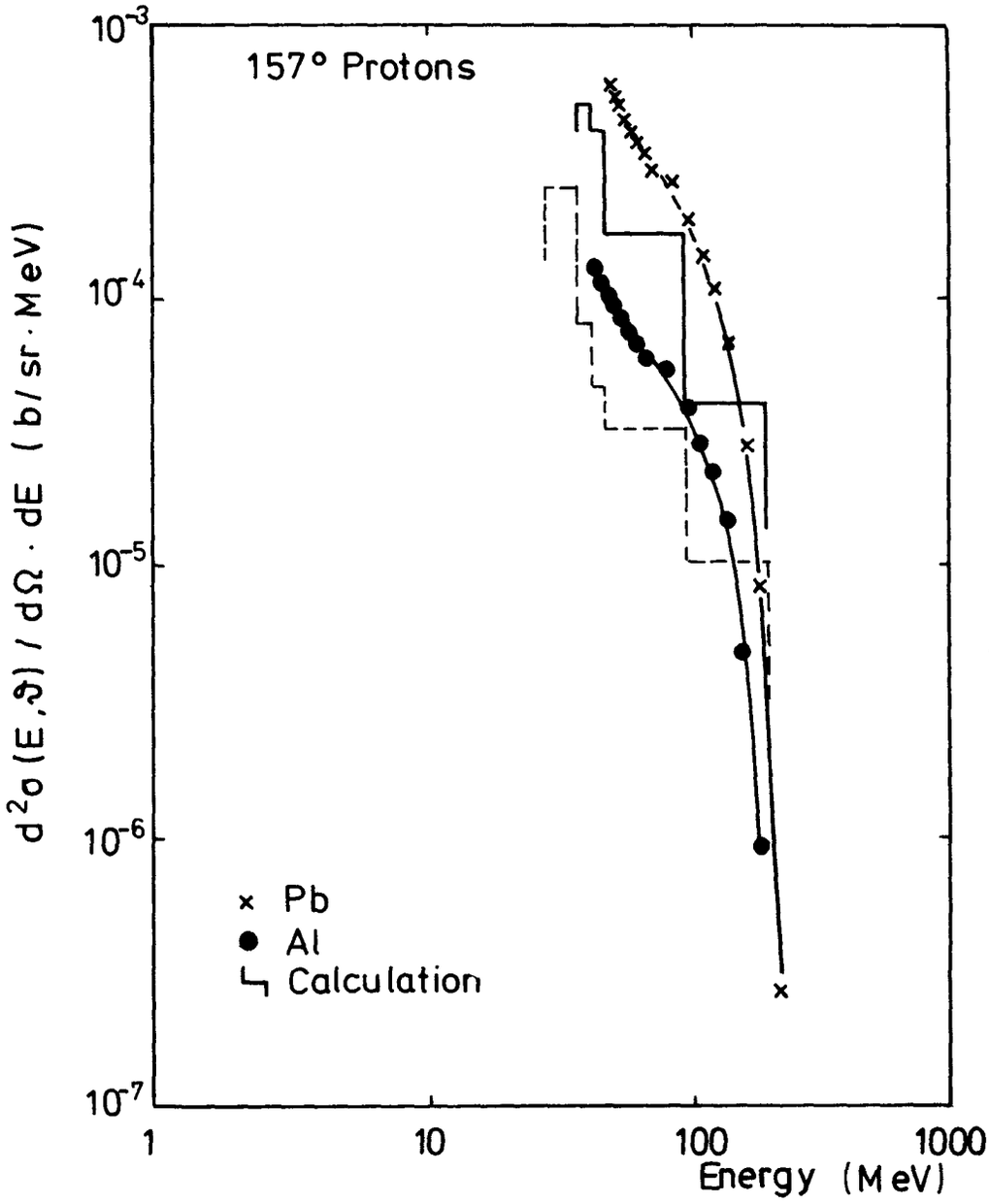

Figure 11 - Same as Fig. 10 except for a laboratory angle of 157°.

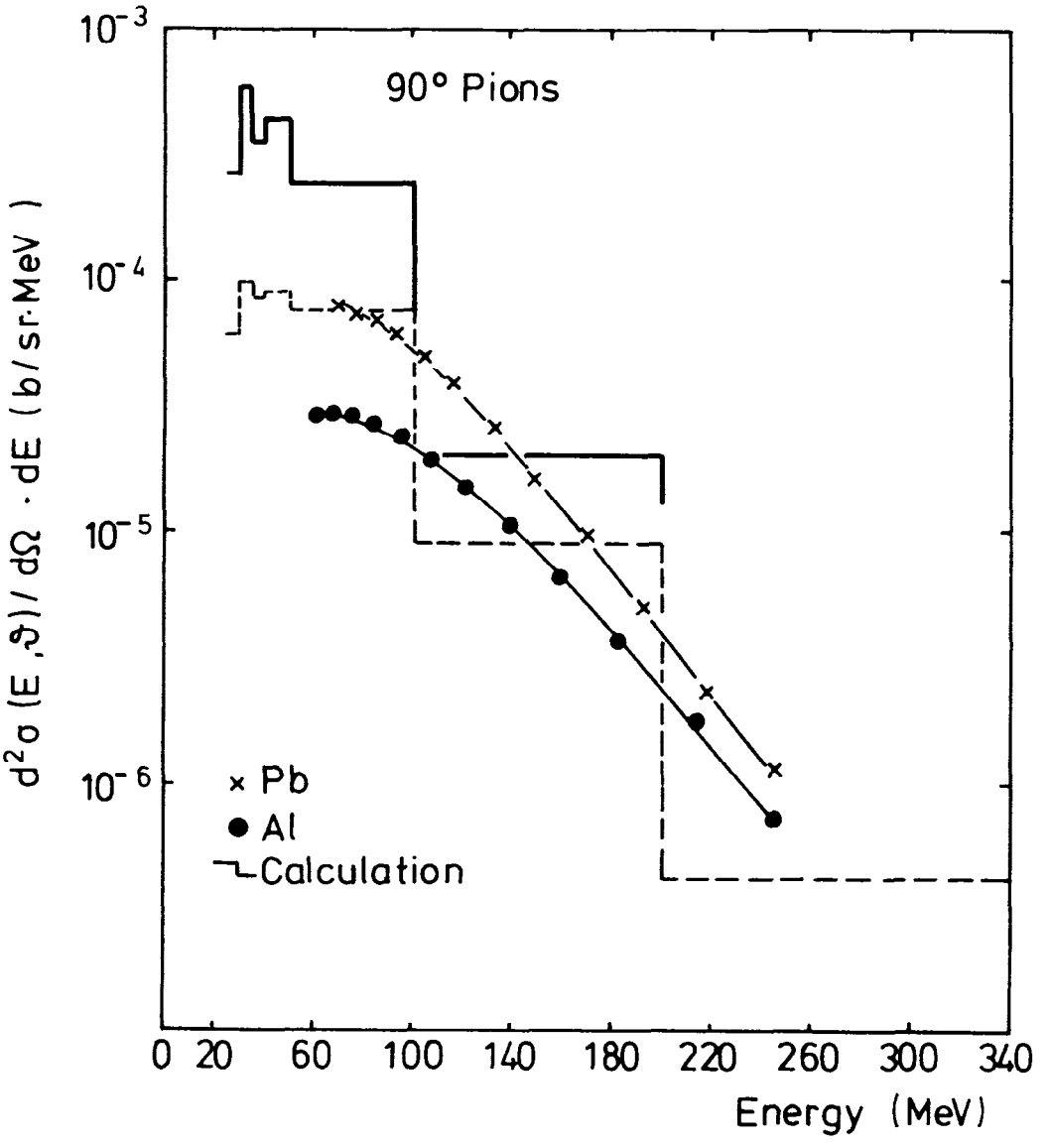

Figure 12 - Comparison of measured and calculated differential cross sections for pions (π^+ and π^-) emitted from aluminum and lead at a laboratory angle of 90°.

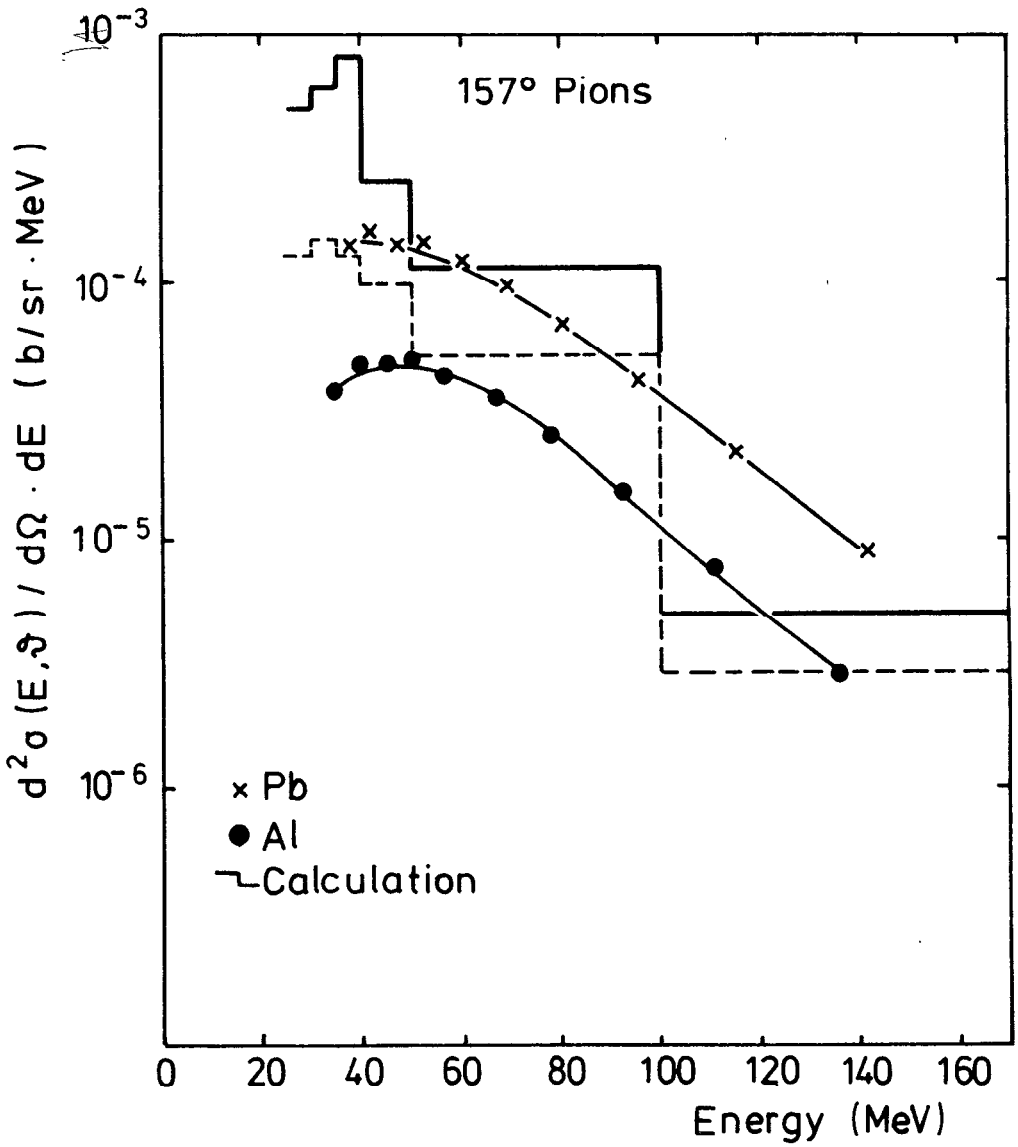

Figure 13 - Same as Fig. 12 except for a laboratory angle of 157°.

Jül-Conf-45

D1-4

I C A N S - V
MEETING OF THE INTERNATIONAL COLLABORATION ON
ADVANCED NEUTRON SOURCES
June 22-26, 1981

Neutron Production Yields and Spectra from 590 MeV Proton Bombardment of Thick Uranium Targets

F.Raupp, S.Cierjacks, Y.Hino, S.D.Howe,
M.T.Rainbow, M.T.Swinhoe and L.Buth

Kernforschungszentrum Karlsruhe
Institut für Kernphysik
D-7500 Karlsruhe, Postfach 3640
Federal Republic of Germany

Abstract

Time-of-flight measurements of neutrons produced by bombardment of a thick uranium target with 590 MeV protons have been performed at SIN cyclotron. Measurements were made at angles of 30°, 90° and 150° relative to the incident proton beam for different penetration depths of protons in a 10 cm x 10 cm x 40 cm long target. The detector was a liquid scintillator. Differential and integral neutron data are presented and discussed.

1. INTRODUCTION

In addition to the measurements of neutrons and protons produced by bombardment of a thick lead target[1], measurements with a thick target of depleted uranium have also been carried out using 590 MeV protons obtained from the cyclotron of the Swiss Institute for Nuclear Research (SIN). In the following sections the results of the measured yields and spectra of the thick uranium target will be shown and discussed.

2. EXPERIMENTAL DETAILS

The experimental arrangement and the method of data analysis were similiar to that described previously[2]. Therefore only a brief summary is given below. The measurements of neutron yields and spectra were performed at angles of 30°, 90° and 150°. The NE213 liquid scintillator was placed at the exit of a 1 m long iron collimator. At 30° and 90° flightpaths of 120 cm and at 150° of 168 cm were employed. Measurements were made for 6 penetration depths into the target, staggered at 5 cm intervals.

In contrast to our previous lead target measurements with a 10 cm diameter and 60 cm long cylindrical target, a rectangular parallelepiped uranium target of 10 cm x 10 cm x 40 cm was used. This target was composed of individual blocks of 5 cm x 5 cm x 10 cm arranged as shown in Figure 1.

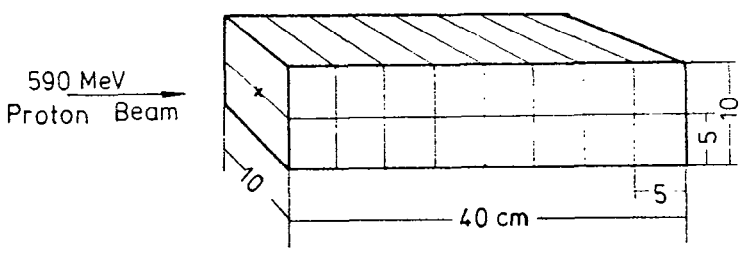

Figure 1 - Uranium target configuration used for the foreground measurements.

For background measurements in the 90° position the respective blocks opposite the collimator entrance were removed. In the 30° and 150° positions a target arrangement as shown in Figure 2 was used. Blocks of 5 cm x 5 cm x 2.5 cm were used to produce the wedge-shaped volumes.

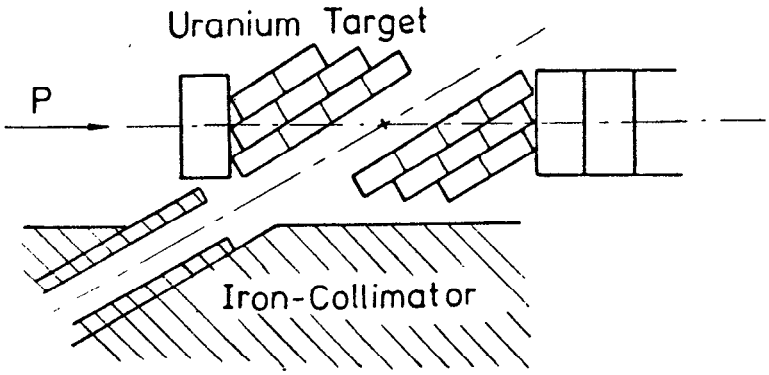

Figure 2 - Target arrangement for background measurements at 30° and 150° positions.

Data acquisition was accomplished by the same method as for lead[2]. Pulse height, pulse-shape-discrimination and time-of-flight information was stored event by event on magnetic tape.

3. RESULTS

3.1 DIFFERENTIAL NEUTRON SPECTRA

In Figures 3-5, the spectra of neutrons emitted from the first 3 blocks of the target are shown as a function of the energy of the emitted neutrons. The spectra show the typical two component shape also seen in previous measurements for lead targets[1]. The most obvious difference between lead and uranium is the considerably lower energy of the maximum yield which is below 1 MeV for uranium and about 1.5 MeV for lead. This can be seen best in the top curve in Figure 3 where we measured the spectra down to 0.7 MeV.

The spectra shown have different lower energy cutoffs because different detector thresholds were used in the measurements. The 150° measurements performed this year at SIN used the 16.9 Mhz beam pulse frequency and a detector threshold of 0.6 MeV. The 90° and 30° measurements were carried out last year with a beam pulse frequency of 50.7 Mhz and a detector threshold of 1.2 MeV. The first block of the 90° angle was also measured

3.2 INTEGRATED NEUTRON YIELDS

In Figure 6, the neutron flux at 90° integrated over all energies higher than 1.5 MeV has been plotted versus the penetration of protons into the target. It can be seen that the flux decreases rapidly with distance into the target. The measured distribution is in close accordance with the calculated 16.1 cm range of 590 MeV protons in uranium.

The yields of angular dependent spectra integrated over the whole target length (0 - 30 cm distance into the target) have also been calculated. The resulting spectra are plotted in Figure 7. In the lower energy region the 150° spectrum shows the higher yields compared to the 90° data and especially to the 30° spectrum. Although neutrons emitted in this energy range are expected to have an isotropic angular distribution the observed yields are greatly effected by self-shielding of the target at the different angles. Since the average mean-free-path of neutrons in uranium is about 2 cm for low energies the neutron yield at 30° should be more attenuated than at 90° or 150°. The same effect is true for the 150° measurement, but becomes important only at greater depths into the target where the neutron production is much less. Also seen in Figure 7, the high energy component of the spectra decreases rapidly with increasing emission angle as expected.

The total number of neutrons per proton was calculated by integrating over energy and over the target surface area, averaging the yields obtained from the 3 measured angles, and integrating the result over the leakage angle. In this way a value of 15.8 n/p was obtained for neutrons emitted from the target with energies higher than 1.5 MeV. An estimate of the fraction of neutrons emitted with energies below 1.5 MeV can be made by calculating the yield as a function of lethargy and extrapolating the spectrum below the experimental energy threshold. This estimation showed that the fraction of leakage neutrons below 1.5 MeV is 35 % of the total number of neutrons. This gave a total yield of 24.3 n/p.

REFERENCES

1. S. Cierjacks, M. T. Rainbow, M. T. Swinhoe and L. Buth, Contr. ICANS-IV, Tsukuba (1980).
   S. Cierjacks, M. T. Rainbow, M. T. Swinhoe and L. Buth, Report, KfK-3097B (1980)
2. S. Cierjacks, Proc. of ICANS-V Conf., Jülich (1981). (to be published)

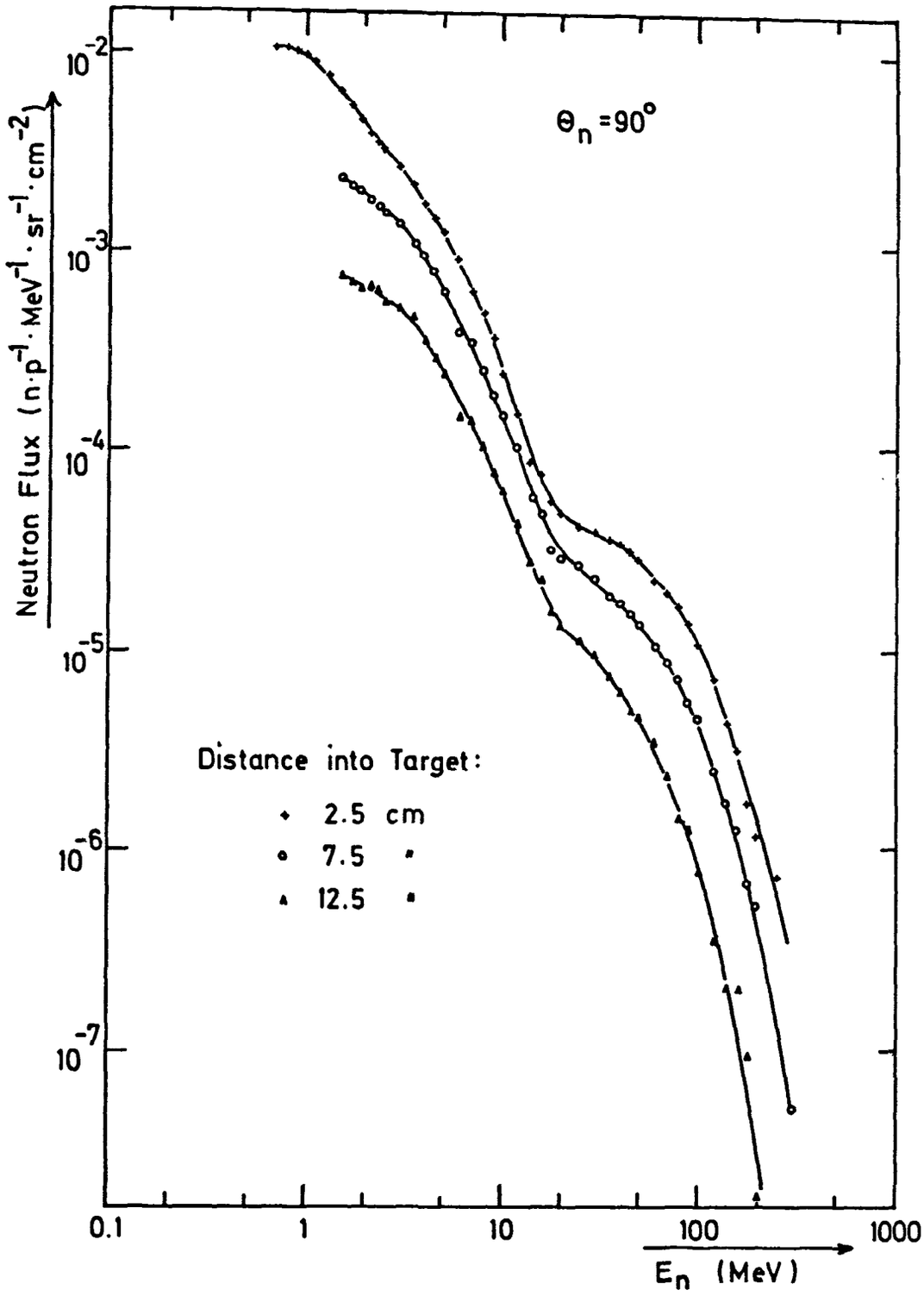

Figure 3 - Differential spectra of neutrons emitted at 90° from 590 MeV protons on a 10x10x40 cm uranium target measured at depths into the target of 2.5 cm, 7.5 cm and 12.5 cm.

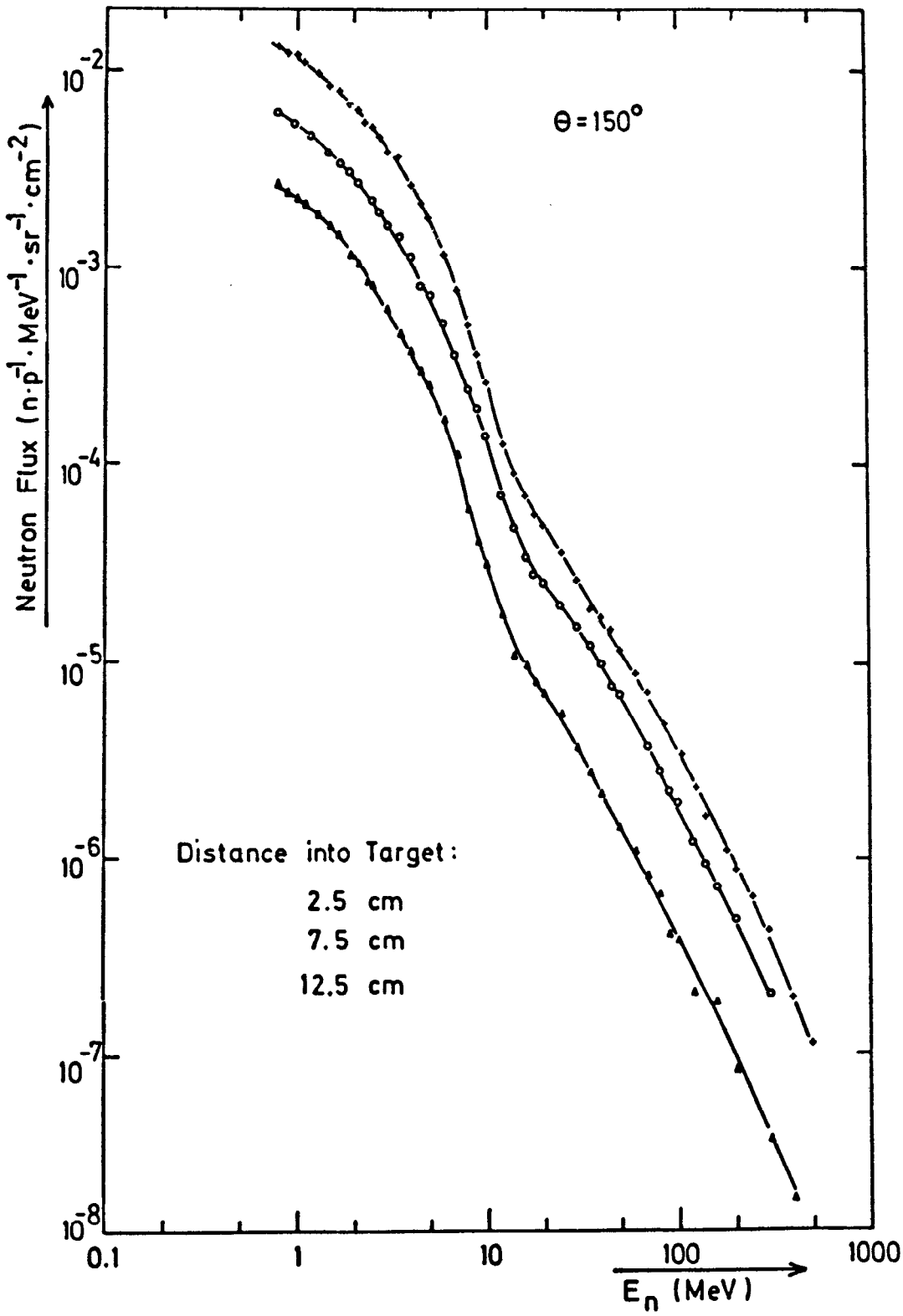

Figure 4 - Differential spectra of neutrons emitted at 150° from 590 MeV protons on a 10x10x40 cm uranium target measured at depths into the target of 2.5 cm, 7.5 cm and 12.5 cm.

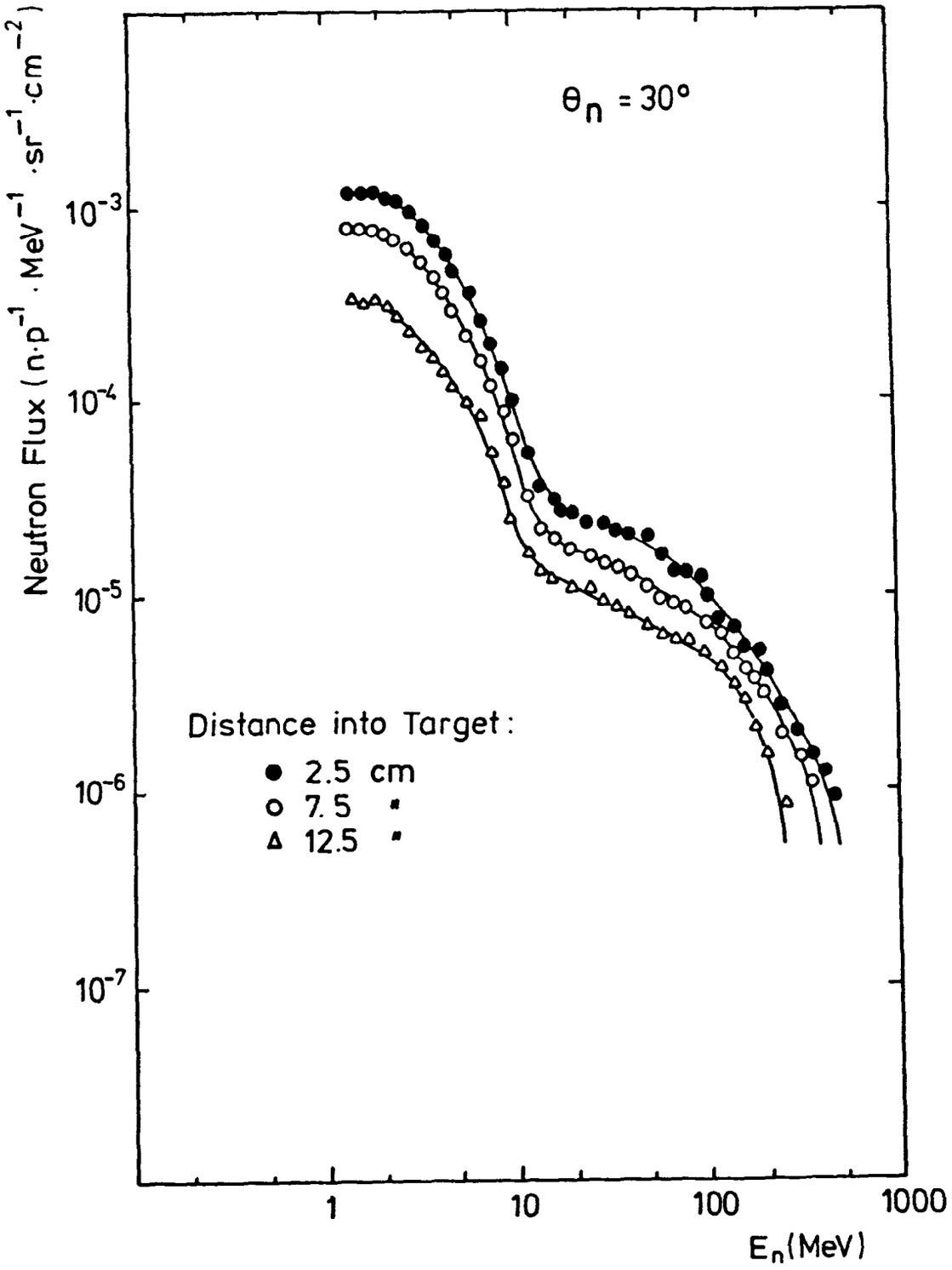

Figure 5 - Differential spectra of neutrons emitted at 30° from 590 MeV protons on a 10x10x40 cm uranium target measured at depths into the target of 2.5 cm, 7.5 cm and 12.5 cm.

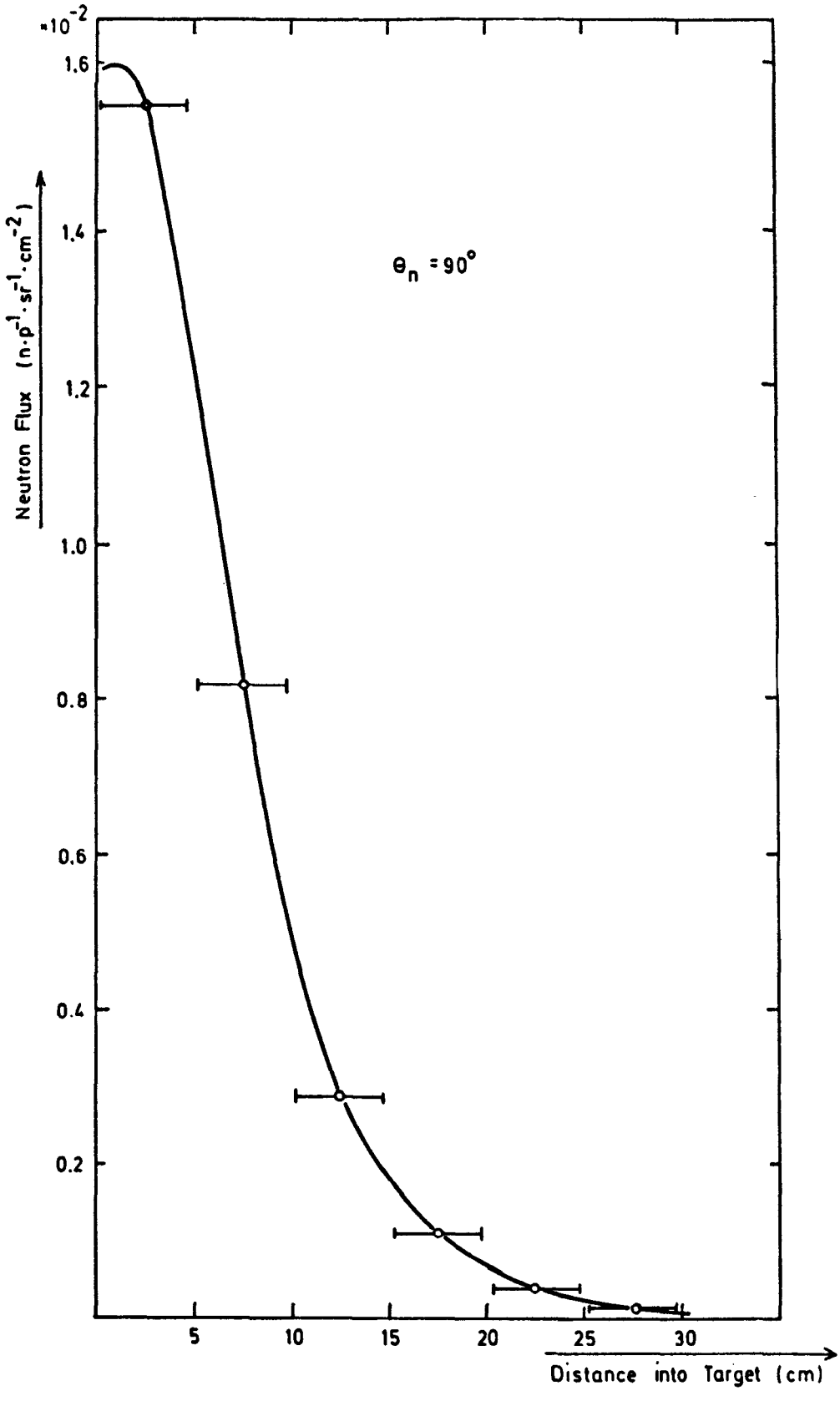

Figure 6 - Total neutron flux at 90° (E_n > 1.5 MeV) as a function of proton penetration into the uranium target.

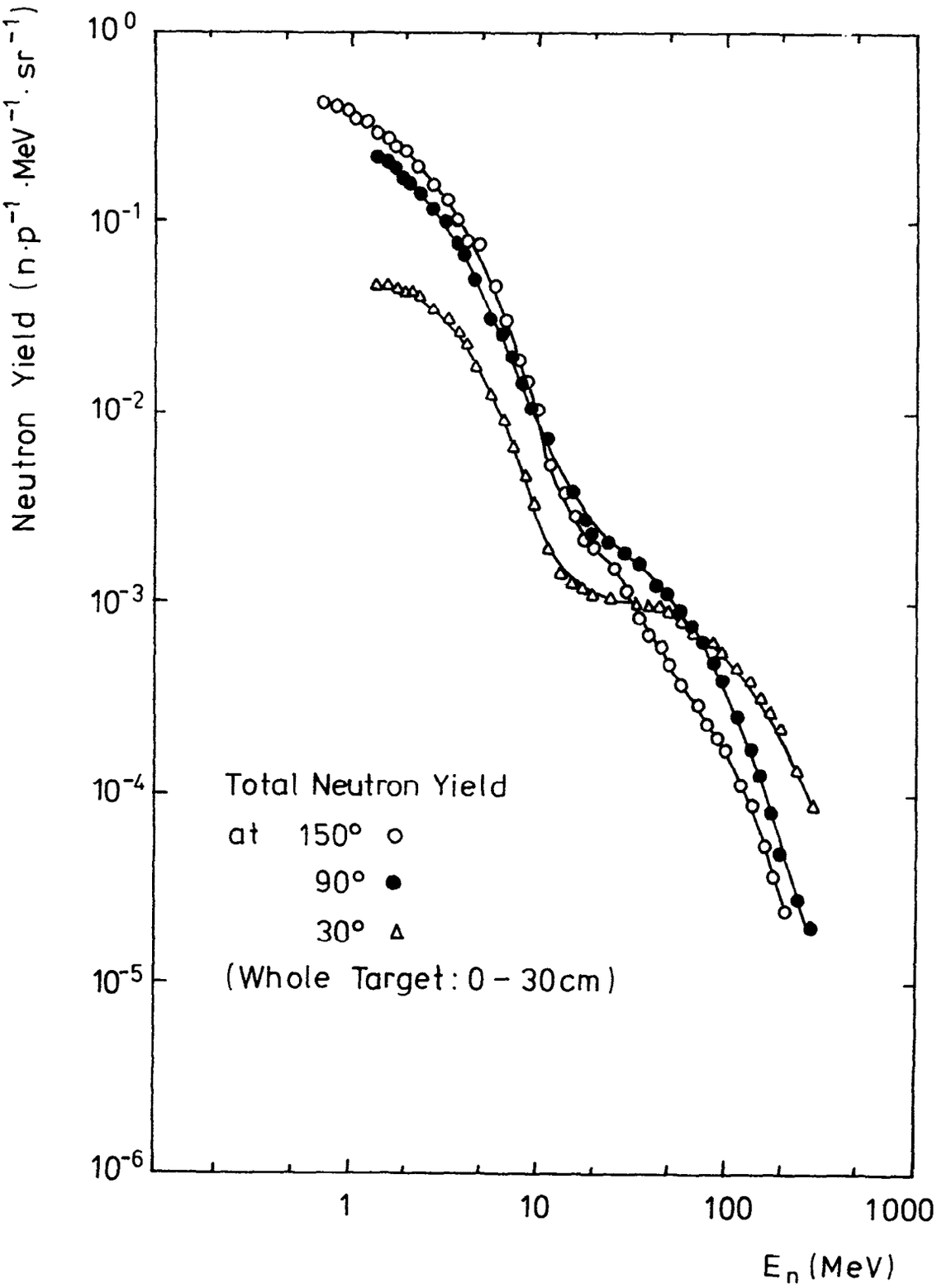

Figure 7 - Spectra of neutrons emitted at 30°,90° and 150° integrated over the first 30 cm of the uranium target. Given yield values correspond only to the fraction of neutrons which are emitted through a 4 cm high centre region of the target surface.

Jül-Conf-45 D1-5

I C A N S - V

MEETING OF THE INTERNATIONAL COLLABORATION ON

ADVANCED NEUTRON SOURCES

June 22-26, 1981

GAMMA-RAY SPECTROMETRIC PRODUCT IDENTIFICATION AND HALFLIFE ANALYSIS FROM PROTON INDUCED SPALLATION AND FISSION REACTIONS OF LEAD AND URANIUM

W. AMIAN[1]
N.F.PEEK[2]
D.J.SHADOAN[2]

KERNFORSCHUNGSANLAGE JÜLICH GMBH

POSTFACH 1913, D-5170 JÜLICH 1

1) INSTITUT FÜR REAKTORENTWICKLUNG,

2) INSTITUT FÜR FESTKÖRPERFORSCHUNG,

permanent address: The University of California at Davies

Abstract

A computer aided analysis system has been developed for measuring the product yield distribution from proton induced spallation reactions. This system is based on gamma-ray spectrometric identification of product radioactivities in the irradiated target materials lead and uranium. Gamma-ray spectra are collected as a function of time. All peaks and peak areas are identified and measured with the computer code AGAMEMNON.

Decay curves for all gamma-rays observed in the measured spectra are constructed and analyzed by the computer code YELLOW. The essential features of YELLOW are: any number of nuclides may be fitted to the experimental data, parent-daughter decays are included, the complete Erdmann-Soyka library is used, the program prepares a collection of plots containing all neccessary information to decide on the correctness of the program's assignment.

INTRODUCTION

Development of a high flux neutron source utilizing the spallation reaction necessarily involves extensive study of residual activity produced in the target material. To accomodate this task, gamma-ray spectrometric methods have been developed to deduce mass yield distributions for proton-induced spallation at incident particle energies of 600 MeV and 1100 MeV. This nuclear reaction produces radioactive nuclides, most of them emitting γ-rays, that cover almost the entire chart of the nuclides. Figure 1 shows a typical γ-ray spectrum for a lead-target. The complexity of this spectrum is easily seen.

SCHEME OF THE ANALYSIS

The object of the analysis of these types of spectra is to translate the complicated gamma-ray spectra into a data set consisting of the partial cummulative and independent yield production cross sections. From these data isobaric mass yield distributions can be deduced.
In the development of a computer aided partially interactive analysis system, attention was payed to making all routine data handling and processing completely automatic and simple to use. This includes photo-peak search and analysis, preparation for decay halflife analysis and the halflife analysis itself. At all points sufficient output information is given to the user to be able to recognize readily any systematic errors that the previous automatic part of the analysis may have introduced. The user is able to make all corrections necessary and rerun that part.
The flow diagram of the analysis is given in figure 2. The recorded spectral information on magnetic tape is translated and transferred to easily accessible disc data sets. At this point it is possible to screen for energy calibration drift, incorrectly recorded start and stop times and other necessary information.
In the second step the peak find and peak fit procedure AGAMEMNON /1/ is run. The code outputs all information on a disc for the halflife analysis as well as a printer output of the fit obtained for each peak. The last step is the code YELLOW, which sorts the outputs of AGAMEMNON by energy and time, plots the calculated activity for each peak-energy as a function of time and identifies the reaction products based on their halflives and known gamma-ray transitions. Besides the activity-time plot the present system prints a list of all candidates which fit the experimental points best. The resulting decay curves of the best candidates are drawn in the

graph. If the decay is of parent-daughter nature, this is taken into considuation. Any number of overlapping nuclides may be taken into account, but at present we only use two for simplicity (for parent-daughter decay, four).
A substantial help in analyzing these plots is the cross reference to the other peak energies of a candidate. The list of candidate isotopes is derived from the compilation of Erdtmann and Soyka /2/.
All programs are written in Pl/1 and are run on an IBM-370/168 TSS computer. This enables the user to work with the conversational or nonconversational mode. All plots may be displayed on a Tectronix- or HP-screen, but in our opinion, it is much more comfortable to prepare a collection of plots. This allows us to observe the computer analysis and make necessary corrections or additional calculations if needed.

THE ANALYSIS PROGRAMS

Peakfit: All peak area fitting is done with an automatically operating computer code AGAMEMNON /1/. This computer code takes the prepared spectral input from the disc and processes each spectrum individually to determine the energy that corresponds to the centroid as well as the area of all peaks above a controlable significance level. The code outputs this information on disc for the halflife analysis, and prepares a printer output of the fit obtained for each peak.
AGAMEMNON offers a variety of options: internal or external lineshape calibration, only gaussion on a smoothly varying background or gaussian with exponential tail and optional step function under strong peaks.
In this way the problem of high count rate distortions of the peak shape associated with a very radioactive target that is continuously decaying is attacked. Goodness-of-fit criteria are χ_r^2 and RMS for the fitted region and FOM for the peak and the background regions individually.
The resolution of multiplets is performed by the peakfind algorithm which is by the method of convolution with a zero-area gaussian. The peakfind is applied to the original spectrum and (in cases where the goodness-of-fit criteria are not reached) with the updated peakshape parameters to the region under consideration and to the residual spectrum to decide if an additional peak has to be considered.

All these features of the program make it possible to detect reliably and automatically over 100 photopeaks in a single 4K-spectrum, and to calculate

their associated decay rates in the target.
Halflife analysis: It is a well-known fact that difficulties occur when one tries to fit experimental data with a sum of exponentials $f(t) = \sum_{i=1}^{n} A_i e^{-\lambda_i t}$, especially if all the parameters are unknown. As shown by Lanczos /3/, the classical methods (least-squares,...) generally fail to provide a meaningful solution. Even the Golub-Pereyra /4/ algorithm is inadequate.
A method in which the analytical behaviour of the exponential functions is taken into account has been proposed by Gardner /5/. The method makes use of Fourier transform and decomposes so to say the experimental data in Fourier space into the leading components of the decay constants λ_i.
The success of Gardner analysis is strongly related to the success of the numerical Fourier transformation (the Fast Fourier Transformation) which calls for sufficient data points to integrate the fast oscillating functions with enough precision. From a practical point of view at least some hundred data points are necessary to fit the problem. Our experiments had some ten data points in time only, hower with additional spectral information. This is why we decided to use a more hand-taylored method consisting of sorting for peak-energy first and then computing decay-curves with the known halflifes of the candidates, thereby reducing the number of free parameters by a factor of two.

The complete analysis is as follows:
All outputs of the peakfit program AGAMEMNON for one foil are sorted into energy-groups with a maximum allowable width of 2 keV. To each group of spectral peaks possible candidates are assigned by comparing the peak energies with energies stated in the Erdtman-Soyka Compilation of gamma lines. At this point some criteria enter to reject assignments. These are: at least one out of the three most intense gamma-lines of the nuclide must be present in the spectra, the cut, what is meant by most intense, is set to 1% of absolute intensity, the halflife of the nuclide must be longer than, say, one half hour. In this way about half of the chart of nuclides is rejected. The information gained is stored in memory nuclide by nuclide with pointers serving as connectors between spectral-peaks and the nuclide entry in memory (just as a catalogue entry points to a special drawer).
The advantage of this procedure is that all gamma lines of a nuclide are accessible to the program and the associated spectral peaks can be used for further analysis.

We are thinking about rejecting nuclides if the activities calculated from the individual peaks differ by a given value. But because of the strong overlapping of peaks this criterion is very delicate.

For the final halflife analysis the candidates for a given energy group are combined and the decay curve is fitted to the experimental lines with the now known halflives. At present we either use only one nuclide to fit the data points or a combination of any two. It is up to the user to decide of the number of nuclides to be combined. For simplicity and mainly by experience we decided to use two at maximum, which is augmented to four if the decay of both nuclides is of parent daughter nature.
The fitting procedure is a simple analytical ohne. For a decay curve of the type

$$f(t) = \sum_{i=1}^{n} A_i^o \, e^{-\lambda_i t}$$

the minimization of χ^2 is performed

$$\chi^2 = \sum_i \frac{1}{\sigma_i^2} \{ R_i - \sum_{j=1}^{n} A_j^o \, e^{-\lambda_j t_i} \}^2$$

where

σ_i^2	:	experimental variance of the measured activity
R_i	:	measured activity at time t_i
t_i	:	time
A_j^o	:	initial activity of the jth isotope
λ_j	:	decay constant of the jth isotope

The minimization with respect to the parameters A_j^o gives a set of n independent linear equations which are easily solved by a Gauss-Pivot algorithm /6/.

The situation is not as simple for a parent-daughter decay because constraints are imposed on the fit.
For a parent-daughter decay of the type

$$N_1 \xrightarrow{\lambda_1} N_2 \xrightarrow{\lambda_2} N_3$$

one finds for the activity of the nuclide N_2

$$A_2(t) = \frac{\lambda_2}{\lambda_2-\lambda_1} A_1^o \left(e^{-\lambda_1 t} - e^{-\lambda_2 t}\right) + A_2^o e^{-\lambda_2 t}$$

where A_1^o, A_2^o are the activities at time t = 0 for the nuclides N_1, N_2 respectively. This may be written as

$$A_2(t) = C_1 e^{-\lambda_1 t} + C_2 e^{-\lambda_2 t}$$

Now C_1 and C_2 are not necessarily positive but only the time-zero activities A_1^o and A_2^o are. Thus we have inequality constraints imposed on the parameters of the type

$$A_1^o = \frac{1}{\lambda_2} C_1(\lambda_2-\lambda_1) \equiv h_1(C_1,C_2) \geq 0$$

$$A_2^o = C_1 + C_2 \qquad \equiv h_2(C_1,C_2) \geq 0$$

We now minimize χ^2 with respect to the parameters C_1 and C_2. If the minimum occurs at a point (C_1^+, C_2^+) which is in the interior of the feasible region, that is $A_{1,2}^o > 0$, then the constraints are irrelevant and the fit is like an unconstrained one. If the minimum found is within the infeasible region or on the boundary, the procedure has to be repeated in a modified version. The modification is to change χ^2 in such a way that it remains almost unchanged in the interior of the feasible region, but increases drastically as one approches the constraints. To accomplish this, we assign a function to each inequality constraint, which is nearly zero when the constraint function is strongly positive, but increases sharply as the constraint function aproaches zero from above. To the constraints above we assign the functions

$$B_i(C_1,C_2) \equiv \alpha_i/h_i(C_1,C_2), \qquad i = 1,2$$

Where α_i are small positive constants. We now modify χ^2 by adding to it the functions assigned to the constraints:

$$\tilde{\chi}^2(C_1,C_2) \equiv \chi^2(C_1,C_2) + \sum_i \alpha_i/h_i(C_1,C_2)$$

The numerical procedure to find the minimum in the feasible region is now as follows /6/:
select the α_i and a feasible initial guess of C_i, find (C_1^*, C_2^*) using the Marquard algorithm for minimzing the now unconstrained problem $\tilde{\chi}^2$, reduce the values of the α_i and repeat the minimization using the values C_1^* , C_2^* as initial guesses.

The process is continued until C_1^*, C_2^* do not change significantly upon reducing the α_i. Then we accept C_1^*, C_2^* as our best estimates of the parameters. It has been proven by Fiacco and Mc Cormick /7/ that under suitable conditions this type of procedure is convergent.

Having performed all fits of the candidate nuclides to the experimental points, we are in the situation to select the best fits by their values of the reduced χ_r^2 . Fits with reduced χ_r^2 less than 2.5 are presented besides the plot of experimental data. At least three of single-nuclide type and three of double-nuclide type are printed even if the reduced χ_r^2 is greater than 2.5. The best fits are drawn in the plot for visual aid.

OUTPUT INFORMATION OF YELLOW

The ourput of YELLOW contains all information necessary to identify the nuclides. Figure 3 presents an example of such an output.
Besides the plot of the calculated peak count rate versus time for the peak energy indicated in the right corner a list of data is printed in the left part. This list includes the identification of the sample ("51 Pb 2"), the tagward (5214), the time since end of bombardment for the midpoint of the counting interval in hours, the counting live time, the FOM value computed in AGAMEMNON, the error of the peak count rate and the peak count rate itself, the energy of the peak centroid, the full width at half maximum of the peak, the counting efficiency and the dead time correction. All of this information serves as control output.
The next lines present estimated halflives and time-zero-activities assuming one or two nuclides fitting the experimental points. These numbers are not used by the program later. They only help the user orienting in the order of magnitude of halflives encountered.
The next lines represent the essential output of YELLOW. This list of candidates is ordered by the candidates atomic numbers and masses. A hint is given to the user showing which candidates fit the experimental data

best. These are the entries E1, E2, for single-nuclide fits and Z1, Z2,.... for double nuclide fits.
Double nuclide fits and parent-daughter decays are indicated below the plot of experimental data. The name of the respective nuclide, its halflife, the time-zero-activities and the reduced χ^2 are given. The complete description of the nuclide is presented in the left part. This includes: the halflife, the time-zero-activity assuming one nuclide fitting the data, the mean difference between spectral peak energy and listed peak energy for all γ-transmissions of the nuclide, the factor $e^{-\lambda t}$, the ratio of the total line intensities of the nuclide found by the peak search to the one listed in the Erdtmann-Soyka-Compilation.

The next entries give the spectral peak energies which are assigned to the lines of the nuclide listed. A zero in this column means that this line of the nuclide is missing in the spectra. The number is the number of the plot (the page-number) where the respective peak energy and the type of analysis described here can be found. The last column is the nuclides gamma-line intensity. All time-zero-activities have to be divided by this number to get the activity of the nuclide identified.
In this way the user gets a complete set of information helping him to decide on the proper assignments of nuclides to each peak.

CONCLUSION

The analyzing scheme described here has been developed to translate the extremely complicated gamma-ray spectra resulting from gamma-ray spectrometry of irradiated foils into a data set of spallation and fission products present in these irradiated foils. The complexity of this task makes it impossible to the experimenter to do so by hand. Only with the help of the programs described it was possible to extract information from the gamma spectra resulting from the many nuclides produced from spallation in lead.

REFERENCES

/1/ W. Amian, "AGAMEMNON" - a Computer Code to Analyse Complex Gamma Ray Spectra"
in preparation

/2/ G. Erdtmann, W. Soyka, "The Gamma Rays of the Radionuclides", Verlag Chemie, Weinheim and New York 1979

/3/ C. Lanczos, "Applied Analysis", Prentice Hall, New York 1961

/4/ G.H. Golub, V.Pereyra, "The Differentiation of Pseudo-Inverses and Nonlinear Least Squares Problems whose Variables Separate", SIAM. J. Numer.Anal. 10(1973)413

/5/ D.G. Gardner et al., "Method for the Analysis of Multicomponent Exponential Decay Curves", Journal of Che.Phys. 31(1959)978

/6/ The reader not familiar with Numerical Mathematics and Statistics is referred to standard textbooks, especially to
Y. Bard, "Nonlinear Parameter Estimation", Academic Press, New York and London 1974

/7/ A.V. Fiacco, "Second Order Sufficient Conditions for Weak and Strict Constrained Minima", SIAM J. Appl. Math. 16(1968)105
A.V.Fiacco, G.P. Mc Cormick, "Nonlinear Programming: Sequential Unconstrained Minimization Techniques". Wiley, New York 1968

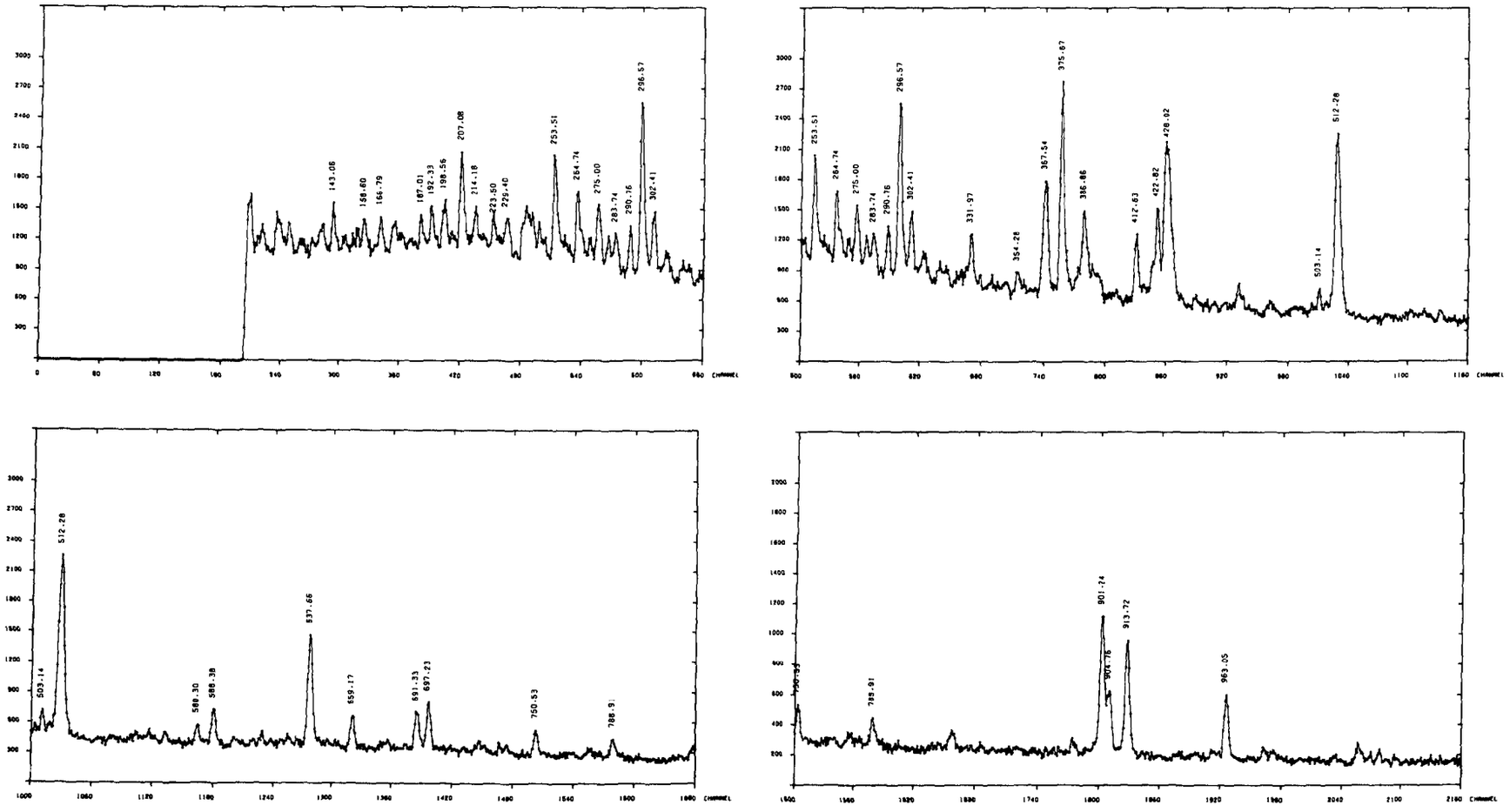

Fig. 1: Typical spectrum from Pb target 5 cm deep in the over-all target taken one houer after the proton irradiation (numbers on peaks are the energies)

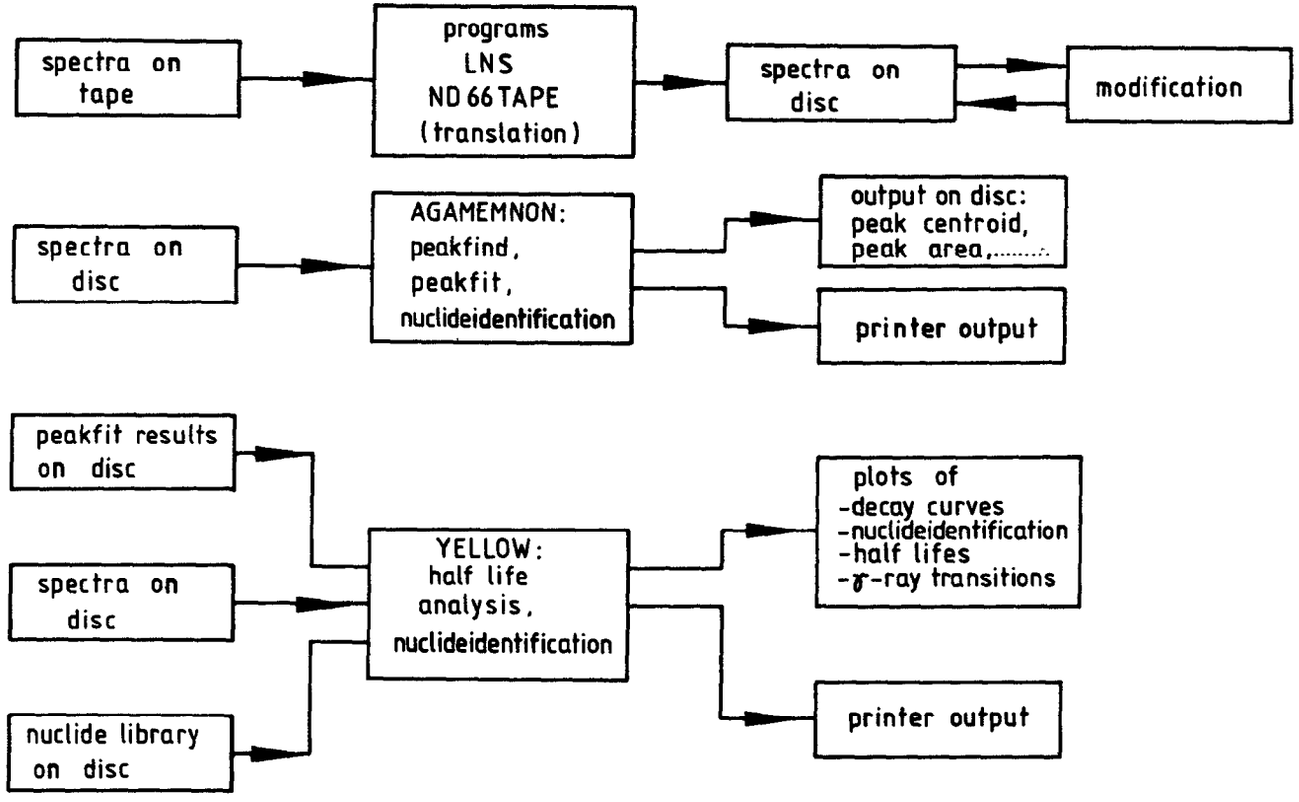

Fig. 2: Flow diagram of the analysis. Refer to text for further details

```
ENERGY       ERROR     CORR
  621.118     0.583   1.060E+00
  ID          S-EOB      LIVETIME    % RESIDUE  CPS ERROR    CTS/S      ENERGY     FWHM     EFFICIENCY    DTCORR
51PB2         6.002E+00  3.370E+02  3.181E+00  1.611E+04  1.289E+05  621.12  2.862E+00  1.022E-04  1.105E+00
51PB2         1.274E+01  6.270E+02  6.773E-01  9.026E+03  7.851E+04  621.76  2.706E+00  3.149E-04  1.151E+00
51PB2         2.067E+01  1.186E+03  1.383E+00  1.201E+03  6.133E+04  621.23  2.328E+00  3.149E-04  1.085E+00
51PB2         3.085E+01  1.329E+03  1.544E+00  8.348E-02  4.841E+04  621.20  2.290E+00  3.149E-04  1.046E+00
51PB2         5.486E+01  3.295E+03  2.280E+00  4.562E+02  1.703E+04  620.95  2.297E+00  3.149E-04  1.020E+00
51PB2         1.614E+02  1.030E+04  1.414E+00  5.892E+01  1.278E+03  620.38  2.351E+00  9.941E-04  1.009E+00
51PB2         1.735E+02  1.035E+04  1.540E+00  5.347E+01  1.125E+03  620.43  2.403E+00  9.941E-04  1.009E+00
51PB2         2.126E+02  2.094E+04  2.789E+00  3.355E+01  7.948E+02  619.93  2.507E+00  9.941E-04  1.006E+00
51PB2         2.742E+02  2.114E+04  5.869E+00  2.446E+01  4.344E+02  620.21  2.281E+00  9.941E-04  1.004E+00
51PB2         3.355E+02  2.126E+04  3.867E+00  2.085E+01  3.322E+02  620.09  2.305E+00  9.941E-04  1.002E+00
51PB2         3.596E+02  2.129E+04  3.914E+00  1.957E+01  2.595E+02  620.03  2.232E+00  9.941E-04  1.002E+00
51PB2 5403    6.451E+02  4.289E+04  2.144E+00  8.129E+00  9.293E+01  620.42  2.209E+00  9.931E-04  1.000E+00
51PB2 5407    7.042E+02  4.222E+04  1.725E+00  8.361E+00  4.834E+01  620.37  2.178E+00  9.931E-04  1.000E+00
HLF=  4.55E+01 HRS   AO =  5.81E+04 1/SEC   LOG10(AO*SEC) =  4.76E+00
AO-LONG-   =( 2.08E+03 +- 4.16E+01) 1/SEC HLF-LONG-  =( 1.33E+02 +- 1.68E+00) HRS
AO-SHORT-  =( 1.36E+05 +- 1.45E+03) 1/SEC HLF-SHORT- =( 1.85E+01 +- 1.45E-01) HRS
CHISQR     = 8.90E-00
 621.12  119          HALFLIFE      HLF/H        AO  (E-EO)/N     DECAY      1/IO   PEAK  NR   LINE    INTENS

    Z3  65 TB 152   1.75E+01 H  1.75E+01  4.73E+05  9.97E-01  7.70E-13  8.35E-01  344.43  61  344.28  8.60E+01A
                                                                                   511.38  94  511.00  1.74E+01A
                                                                                   585.36 110  586.29  1.25E+01A
                                                                                   621.12 119  622.80  1.25E+00A
+ E1    67 HO 160M  5.10E+00 H  2.86E+01  1.26E+05  1.04E+00  3.78E-08  4.91E-01 1272.46 234 1271.50  2.90E+00A
  CHISQR= 9.32E+01                                                                 621.12 119  620.80  0.00E+00
  E4    71 LU 170   2.00E+00 D  4.80E+01  5.43E+04  9.87E-01  3.83E-05  7.79E-01 1280.96 236 1280.25  7.93E+00A
  CHISQR= 4.45E+02                                                                 985.52 188  985.10  5.38E+00A
                                                                                   621.12 119  621.40  4.35E-02A
                                                                                   621.12 119  622.75  2.46E-02A
+ E4    71 LU 170   2.00E+00 D  4.80E+01  5.43E+04  9.87E-01  3.83E-05  7.79E-01 1280.96 236 1280.25  7.93E+00A
  CHISQR= 4.45E+02                                                                 985.52 188  985.10  5.38E+00A
                                                                                   621.12 119  621.40  4.35E-02A
                                                                                   621.12 119  622.75  2.46E-02A
    Z2  72 HF 170   1.60E+01 H  1.60E+01  6.51E+05  9.41E-01  5.64E-14  9.89E-01  165.19  12  164.71  3.35E+01A
                                                                                   621.12 119  620.70  2.29E+01A
                                                                                   573.60 108  572.90  1.85E+01A
    Z1  77 IR 186   1.58E+01 H  1.58E+01  6.82E+05  1.04E+00  3.83E-14  8.76E-01  296.18  48  295.75  4.62E+01A
                                                                                   137.28   4  137.15  2.80E+01A
                                                                                   434.96  82  434.78  2.38E+01A
                                                                                   621.12 119  622.20  2.31E+00A
Y E3Z1  77 IR 188   1.73E+00 D  2.45E+02  2.00E+04  1.03E+00  1.36E-01  8.73E-01  154.94   9  155.03  3.34E+01A
  CHISQR= 2.75E+02                                                                 633.80 123  633.10  2.16E+01A
                                                                                   479.44  89  478.10  1.60E+01A
                                                                                   621.12 119  620.60  1.00E+00A
  E2    77 IR 194   1.91E+01 H  5.26E+04  1.57E+04  1.04E+00  9.91E-01  8.19E-01  326.81  56  328.54  1.30E+01A
  CHISQR= 1.01E+02                                                                 645.80 127  645.32  1.16E+00A
                                                                                   621.12 119  622.30  3.10E-01A
  E6    79 AU 194   1.65E+00 D  3.95E+01  7.09E+04  8.63E-01  4.30E-06  7.38E-01  326.81  56  328.50  6.09E+01A
  CHISQR= 4.98E+02                                                                   0.00   0  293.60  1.07E+01A
                                                                                   621.12 119  622.00  1.70E+00A
                                                                                   621.12 119  621.20  6.09E-01A
  E6    79 AU 194   1.65E+00 D  3.95E+01  7.09E+04  8.63E-01  4.30E-06  7.38E-01  326.81  56  328.50  6.09E+01A
  CHISQR= 4.98E+02                                                                   0.00   0  293.60  1.07E+01A
                                                                                   621.12 119  622.00  1.70E+00A
                                                                                   621.12 119  621.20  6.09E-01A
```

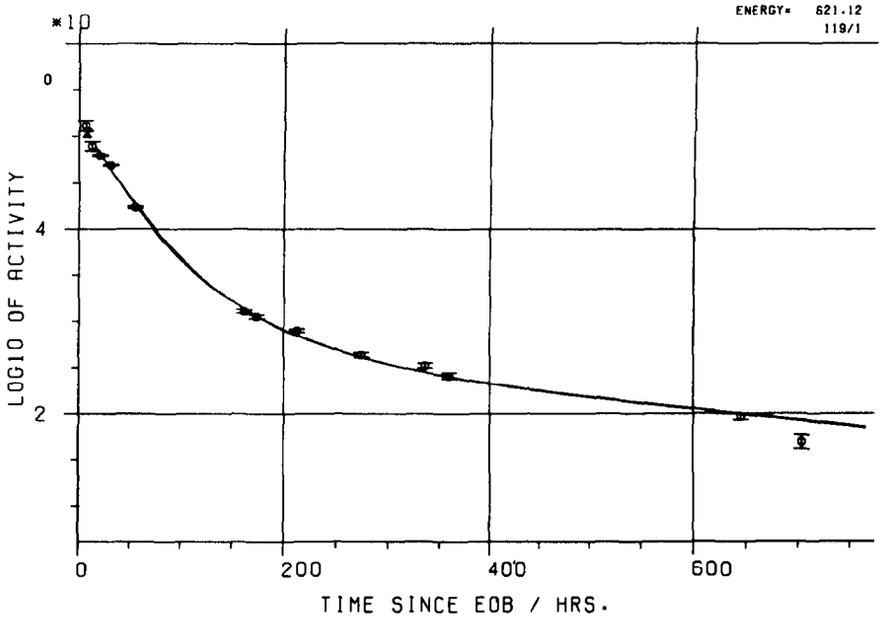


```
▲ PT 188  -->   10.20 D -->  77 IR 188  -->    1.73 D AI= 5.21E+02 1.19E+04  CHI= 9.47E+00
  65 TB 152   1.75E+01 HRS  AO= 1.24E+05
X ER 160  -->    1.19 D AO= 6.52E+04 -->  67 HO 160M -->    5.10 H AO= 3.12E+05 CHI= 9.32E+01
X PT 188  -->   10.20 D -->  77 IR 188  -->    1.73 D AI= 5.08E+02 1.34E+04  CHI= 8.11E+00
  72 HF 170   1.60E+01 HRS  AO= 1.36E+05
Z PT 188  -->   10.20 D -->  77 IR 188  -->    1.73 D AI= 5.04E+02 1.38E+04  CHI= 8.08E+00
  77 IR 186   1.58E+01 HRS  AO= 1.38E+05
X PT 188  -->   10.20 D AO= 1.06E+02 -->  77 IR 188  -->    1.73 D AO= 3.58E+04 CHI= 2.75E+02
X OS 194  -->    6.00 A AO= 1.47E+02 -->  77 IR 194  -->   19.15 H AO= 1.38E+05 CHI= 1.01E+02
```

Fig. 3: Typical output information of YELLOW. Refer to text for further details

I C A N S - V

MEETING OF THE INTERNATIONAL COLLABORATION ON

ADVANCED NEUTRON SOURCES

June 22-26, 1981

Gamma-ray measurements of isotopes produced by 1.1 GeV protons on lead and uranium targets

N.F. Peek, D.J. Shadoan and W. Amian*

University of California at Davis, California 95616, U.S.A.

* Institut für Reaktorentwicklung der KFA Jülich GmbH, Germany

Abstract

In order to simulate the spallation neutron source target, 3 cm diameter by 1 mm thick disks of Pb and U with Al monitoring foils and plates were irradiated at the Saturne National Laboratory at Saclay, France. The targets were embedded between 5 cm thick bricks (either natural Pb or depleted U). The overall target was 45 cm thick. In the case of the Pb experiment, 10 targets were included and for U, eight or nine. The study is progressing and has provided, so far, information on some 65 isotopes found in the 5 cm deep Pb target. Results are shown in the form of activities and atoms produced per incident proton. It will be possible to integrate the activities over all of the targets and estimate the isotope production, radioactive heat developed and, perhaps, the ensuing damage to the target materials.

Introduction

Development of a high flux neutron source utilizing the spallation reaction necessarily involves extensive study of residual activity produced in the target material. The majority of this activity arises via two mechanisms: a) high energy proton spallation reactions and the accompanying nuclear reactions from lower energy secondary particles produced during the spallation process and b) nuclear fission, i.e. fissioning of the high Z target material induced with particles from a high energy, high intensity proton irradiation. Equally important in spallation target design and optimization is isotope identification, isotope production rates and their spatial distribution throughout the target. Of interest are the possible target degrading elements which may, either from direct production or later via chemical reactions, be involved in excess gas production, corrosion or amalgamation in the target material.

Briefly, the experimental procedures involved irradiation of relatively thin, 1.0 mm thick, target foils embedded at equally spaced intervals in a larger target whose physical dimensions were similar to those of the proposed "infinitely thick" spallation target wheel. Two target materials were chosen for investigation, natural Pb and depleted U. An 1100 MeV proton beam with an average intensity of up to 80 nA was used for irradiations. Once irradiated the target foils were removed and counted using high resolution gamma-ray spectroscopy. The resulting data were recorded on magnetic tape for subsequent computer analysis and isotope identification. The inherent complexity of the data presented difficulties for complete analysis by computer and in most cases final values were confirmed before inclusion in this report. Many of the data have been compared to theoretical calculations from Monte Carlo transport codes and, in general, agree favorably /1/.

Experimental Procedures

a) High energy proton source

All irradiations for this experiment were conducted at Saturne National Laboratory within the Centre d'Etudes Nucléaires de Saclay located 25 km southwest of

Paris, France. The Saturne synchrotron provided proton beams of 600 MeV and 1100 MeV with average intensities of from 20 to 80 nA. Two quadrupole doublet magnets, upstream of the target area, provided strong focusing with resultant beam diameters at the target entrance between 1.0 and 1.5 cm FWHM. Small crossed-wire proportional chambers enabled the measurement of the horizontal and vertical profiles of the beam upstream and downstream from the target area before the insertion of the remotely controllable target blocked the beam from the downstream wire chamber. Figures 1 and 2 show, in general, a Gaussian intensity distribution for both vertical and horizontal beam profiles. The beam spot was nearly circular. The beam position was monitored continuously throughout each irradiation with the upstream wire chamber.

b) Target configuration

Two target materials were investigated during this research, natural Pb and depleted U. For both materials the gross features of the total target, target foil assembly were kept as nearly identical as possible. Figure 3 shows the configuration of the Pb target in detail. The first target foil shown was an aluminum foil (3.0 cm diameter by 1.0 mm thick) positioned 5.0 cm in front of the main target assembly. In this position it was utilized to monitor the incoming proton intensity by a method discussed later in this section. The next target foil (the first Pb foil) was positioned directly in front of the main assembly to receive full beam energy. Immediately behind the first Pb foil followed a 1.0 mm thick aluminum plate scribed with lines forming a grid with 1.0 cm divisions used to monitor the beam distribution (Figs. 1 and 2) (i.e. vertical and horizontal intensity profiles), in the same manner as the first aluminum target foil. The three target elements described above, Al foil, Pb foil, and Al plate, constituted a repetitive unit and appeared a total of 10 times; each unit separated by a 5.0 cm thick Pb brick. Individual target foils consisted of 3.0 cm diameter by 1.0 mm thick natural Pb disks. These dimensions were chosen as a compromise between adequate counting intensity and corrections due to self-absorption and non point-source geometry. Due to space limitations in the target area the total length, 45 cm, of the complete Pb target assembly was short of the "infinite thickness", 65 cm, required to completely absorb 1100 MeV protons. Stopping-power calculations indicated an energy loss of 700 MeV in 45 cm of Pb.

The uranium target, target foil assembly was identical except for two instances. First, the entire target assembly was infinitely thick at an overall length of only 35 cm and therefore the number of uranium target foils irradiated was eight in one run and nine in the next. Secondly, the uranium foils were vacuum encapsulated in aluminum cases to prevent the escaping of radioactive gases.

c) Beam intensity monitoring

Aluminum activation provided an excellent method for determining beam particle intensity via the reactions listed in Table 1. This table shows the possible modes of production of three isotopes from an Al target namely ^{24}Na, ^{22}Na and ^{7}Be. Also included are the calculated Q-values for each reaction and the production cross-sections at spallation energies as well as at lower energies where compound nuclear reactions dominate. The large differences in Q-values between the sodium isotopes and beryllium-7 provided some information on the secondary particle energy distribution throughout the target. The lower energy secondary particles produced less ^{7}Be due to the 190 MeV Q-value. As previously described, each Pb and U target foil was preceeded by an aluminum beam-monitoring foil of the same diameter and thickness. Data from these foils provided incident intensity normalizations for activity calculations for both Pb and U target foils. After the initial target, beam particles were no longer distinguishable as primary beam protons but contained, in addition, scattered protons and neutrons from spallation. Following each target foil an aluminum plate, 10 x 20 x 0.1 cm, was used to establish the beam particle distribution as a function of depth into the target. The beam profile plates were analyzed for Na isotopes and ^{7}Be by scanning an area of 1 cm^2 in 1 cm steps over the rectangular coordinate system scribed on the plates. The data points were plotted and fitted mathematically with a Gaussian distribution and the results are shown in figures 1 and 2. The position of the beam with respect to the monitor foil was determined by this technique and integration over the target area produced the percentage and intensity of the beam that struck the target. (Note that the beam in this run was about 0.1 cm to the right and about 1.1 cm low). The shape of the beam became broader and less intense, with depth into the target (see figure 4). The parameters for the construction of figure 4 are found in table 2.

d) Data collection

The data collection system included, besides normal high resolution gamma-ray counting electronics, a multichannel analyzer controlled automatic sample changer (Fig. 5). The 80 cm^3 Ge(Li) detector, pulse amplifier and shaping electronics and 100 MHz ADC, all Canberra products, had an energy resolution of 2.0 KeV at 1.0 MeV and 5000 c/sec. The microprocessor controlled multichannel analyzer, also from Canberra, was keyboard programmable to collect, record and partially analyze gamma-ray data from two simultaneously operating detector systems. After data from each target foil was collected the analyzer sequenced the automatic sample changer and the next target foil was counted. The capacity of the sample changer was 16 foils. Although the analyzer contained "dead time" accounting electronics a 50 MHz precision pulser was used to calculate any dead time not compensated for by the analyzer. The counting system showed negligible gain shift and line broadening up to 30,000 c/sec. IAEA and PTB standard reference sources with ± 2% accuracy were used for absolute calibration. The automatic sample changer with a capacity of 16 samples was mounted on rails and could be easily positioned at different distances from the detector to maximize data acquisition rates to the Ge(Li) system. Both the detector and target wheel assembly were enclosed in Pb shielding 10 cm thick. Target foil and detector geometries were defined by 5.0 cm diameter openings in each enclosure. Counting of irradiated target foils began at Saturne in Saclay 30 minutes after end of irradiation and continued after 6 days at KFA in Jülich on a similar detector system. (In order to count at close distances at Jülich, the target wheel was not shielded and contained only four sources). The counting time interval was calculated by dividing the elapsed time since end of irradiation by 5 (this would be an isotope half-life whose activity had decreased by a factor of 32) and counting for 10% of that time. In this manner, the error made by assuming a linear decay over the counting interval is less than 1%.

Data Reduction

Computer analysis and reduction was performed primarily in two main stages. Initially, all data were translated and transferred to an IBM 370 from the

analyzer created magnetic tapes and a gamma-ray fitting procedure, AGAMEMNON, provided all gamma-ray intensities as a function of energy. Finally, a sorting and isotope identification procedure produced output as a function of energy and time-since-end of irradiation for each target foil. During both stages of analyses software modifications were required in order to accomodate the enormous number of gamma-rays emitted by each target foil (see Fig 6 and 7). Each spectrum contained no less than 150 identifiable gamma-rays (maximums of over 300 were common). At short times after irradiation gamma-rays were so numerous that a high background was generated, making it difficult to identify isotopes.

During the initial translation and transfer of data, all additional relevant parameters required for analysis were included in the data set. These parameters included elapsed time since the end-of-irradiation, target foil counting geometry and target foil identifiers. The resulting data became input to AGAMEMNON which processed an average of 30 spectra per hour of CPU time. This computer code takes the prepared spectral input from disc and processes each spectrum individually to determine the energy that corresponds to the centroid and the area of all peaks above a controllable significance level. The code outputs this information as a disc file for the half-life analysis, and as paper output of the fit obtained for each peak.

AGAMEMNON offers a variety of fitting options: Internal or external lineshape calibration, Gaussian on a smoothly varying background or Gaussian with exponential tail and optional stepfunction under strong peaks /2, 3/. Goodness-of-fit criteria are χ_r^2 and RMS /4/ for the fitted region and FOM /5/ for the peak region and the background region individually.

The resolution of multiplets is performed by the peak locating algorithm a method of convolution with a zero-area Gaussian /6/. This algorithm is applied to the original spectrum and, in cases where the goodness-of-fit criteria are not reached, updated peakshape parameters for the region under consideration and the residual spectrum are allowed to vary to decide if an additional peak has to be considered. The output from AGAMEMNON, line energies and intensities, was collected for each individual target foil and the subsequent data array

was ordered with increasing time since end of irradiation. From these data all gamma-rays with energies from 120 KeV to 2000 KeV were sorted into energy groups with a maximum allowable deviation of 2.0 KeV. In this manner, all gamma-ray intensities from each target foil were cataloged by increasing time since end of irradiation thereby allowing decay curves to be plotted for each energy.

Initial isotope identification was made from a search of gamma-ray energies from Erdtmann and Soyka /7/ and the Table of Isotopes /8/ and choosing only those which match with isotopes having gamma-rays within ± 2.0 KeV of the energy of the line plotted on the decay curves. The best combination of isotopes which fitted the decay curve was selected as the constituent isotopes for a particular target foil and energy. Once preliminary identification was made parent daughter relationships for these isotopes were investigated and total activity reported as cummulative i.e.

$$A_c = A_d + A_{pd}$$

where A_d = Activity directly made

A_{pd} = Activity from parent-daughter decay

In the case of Bi isotopes and most metastable (high ground state spin) isotopes, direct made activities were calculated (table 3).

Discussion

The nature of isotope counting dictates that counting continue over a period of several months. This is especially true if the number of isotopes is very large such as in the case of spallation reactions. For isotope production with 100 MeV protons, it is expected that one gamma line in 10 will be a doublet. However, with isotopes produced by 1100 MeV protons approximately 7 out of 10 gamma lines are multiplets (Figs. 6, 7). Therefore, counting must continue for an extended period in order to unfold the half-lives and identify each isotope. Considering these facts it is reasonable that the data presented are preliminary.

Table 3 presents the isotopes found thus far in the target foil Pb 2. The distinction has been made between direct and cumulative production for these isotopes. The cumulative isotopes represent a parent-daughter cascade in the direction of the stability curve and the activities are given at a time when the daughter growth was a maximum, (t_{max}). In all cases, the cumulative isotopes column includes the direct made portion. Table 3 includes possible induced fission products. They are listed in the "direct made" column. With these data it is possible to calculate the number of atoms of a particular isotope produced per incoming proton per g/cm^2 thickness of the target foil. By gathering similar information from the other 9 targets (in the case of the Pb target) it will be possible to calculate the amount of each isotope produced in the total target assembly by integrating over the pathlength of the beam.

Figure 8 shows a comparison between the radiation power generated by the gamma-rays in the decay of the U and Pb targets. These data are from the second target foil at a depth of 5.0 cm into the target assembly. The data points were calculated by integrating the gamma radiation from 100 KeV to 2000 KeV in 100 KeV steps, and folding in the efficiency of the detector. The power is given as Watts per incoming proton per g/cm^2 thickness and, as shown, approximately 5 times more power was generated from the U target foil than from the Pb target foil. It is interesting to note from the figure that the two curves cross at about 1700 KeV. This behavior is explained by the fact that the activities produced by U have many more low energy gamma-rays than Pb and comparatively less at high energy.

Figures 1 and 2 are calculated from the production of ^{24}Na by the beam at two locations in the Pb target. Sodium-24 with its higher cross-section for lower energy protons and neutrons is more likely to indicate the presence of lower energy secondary particles, along with the primary high energy beam (Table 1). Sodium-22 and particularly ^{7}Be would show the distribution of the higher energy beam particles in the target assembly. The combination of these data help provide information on the energy distribution of the beam particles throughout the total target. It is interesting to note that the peak flux from the second plate at 5 cm depth into the main target is about 25 times higher than the peak flux at 40 cm. When comparing total intensity only one order of magnitude

difference appeared, due to beam spreading (Fig. 4). When the same comparisons are made between ^{7}Be and ^{22}Na the results should indicate that the ^{7}Be has a much narrower distribution more representative of the high energy proton beam.

At this writing a phenominally large amount of data has been collected and partially analyzed. The outlook for accurate and repeatable results is very good. There have been two successful accelerator irradiations, of both the Pb and U targets, with adequate beam intensity to provide sufficient activation of the target foils. Data collection and analysis will continue over the next year and final results will be more complete at that time.

References

/1/ T.W. Armstrong,
Realisierungstudie zur Spallations-Neutronenquelle
Vol. 2, A 2.6 (1981)

/2/ J.W. Phillips, et al.
Nucl. Inst. + Meth. 153 (1978) 449

/3/ L.A. McNelles et al.
Nucl. Inst. + Meth. 127 (1975) 73

/4/ T. Sehine et al.
Nucl. Inst. + Meth. 133 (1976) 171

/5/ H.I. Balian et al.
Nucl. Inst. + Meth. 145 (1977) 389

/6/ I. De Lotto et al.
Nucl. Inst. + Meth. 143 (1977) 617

/7/ G. Erdtmann, W. Soyka
The Gamma Rays of the Radionuclides, Vol. 7
Verlag Chemie, Weinheim-New York, 1979

/8/ C.M. Lederer, V.S. Shirley
Table of Isotopes, 7th Edition, John Wiley + Sons Inc. New York 1978

/9/ N.F. Peek, F. Hegedüs
The Production of Xenon Isotopes with Protons of Energies from 320 to 590 MeV
Int. J. of Applied Rad. + Isotopes, 30 (1979) 661-635

Reaction	Q(MeV)	Spallation σ(mb) at 1.1 GeV	Nuclear σ_{max}(mb)	at E(MeV)
^{27}Al (p,x) ^{24}Na		11	11	80
x = 3 p,n	-31			
x = p,d	-20			
^{27}Al (n,α) ^{24}Na	- 3	-	129	13
^{27}Al (p,x) ^{22}Na		15	40	45
x = 3p,3n	-50			
x = α,d	-20			
^{27}Al (n,x) ^{22}Na				
x = 2p,4n	-51			
x = α,2n	-23			
^{27}Al (p,x) ^{7}Be		8	1	80
x = 10p,11n	-190			
x = 5α,n	- 46			
^{27}Al (n,x) ^{7}Be				
x = 9p,12n	-190			
x = 4α,d,3n	- 72			

Table 1 Aluminum Monitor Foil Reactions /9/

target	depth (cm)	μ_{vert} (cm)	FWHM (Γ cm)	Intensity (c/sec)	% on target
1	0	-1.24	1.3	255	81
2	5	-1.13	1.8	230	80
3	10	-1.06	2.4	172	76
4	15	- .97	3.2	100	67
5	20	- .89	4.3	58	56
6	25	- .80	5.8	33	45
7	30	- .73	7.9	19	34
8	35	- .62	10.6	11	28
9	40	- .54	14.4	6.2	19
10	45	- .46	19.4	4.6	15

(μ_{horiz} = + .095 cm)

Table 2 Beam Parameters from ^{24}Na Measurements for the Series Pb 51 Targets

Isotope	T1/2	Direct made Activity (d/sec; $\Delta t_{EOB} = 0$) $\cdot 10^5$	Cumulative Activity (d/sec; $\Delta t_{EOB} = t_{max}$) $\cdot 10^5$	(Atoms/g/cm²/H⁺) $\cdot 10^{-5}$
^{202}Bi	1.67 h	22.		1.3
^{203}Bi	11.8 h	4.8		2.0
^{204}Bi	11.3 h	6.9		2.8
^{205}Bi	15.3 d	0.25		3.3
^{206}Bi	6.2 d	0.42		2.2
^{197M}Pb	42. m	370.		9.2
^{198}Pb	2.4 h		60. at 0.8 h	5.1
^{199}Pb	1.5 h		30. at 1.1 h	1.6
^{200}Pb	21.5 h		15. at 3.1 h	11.4
^{201}Pb	9.4 h		50. at 5.0 h	16.7
^{202M}Pb	3.6 h	30.		3.8
^{203}Pb	52.1 h		6.3 at 32.7 h	11.6
^{204M}Pb	1.15 h	110.		4.5
^{194M}Tl	33. m	48.		0.94
^{196}Tl	5.3 h		35, at 5.0 h	6.6
^{198M}Tl	1.87 h	97.		6.4
^{199}Tl	7.4 h		23. at 4.3 h	6.0
^{200}Tl	26.1 h		6.6 at 34.1 h	6.1
^{201}Tl	73.5 h		3.8 at 31.9 h	9.9
^{202M}Tl	12.2 d		.48 at 23.2 h	5.0
^{192}Hg	4.9 h		25.9 at 0.84 h	4.5
^{193M}Hg	11.1 h	5.8		2.3
^{195M}Hg	1.7 d	2.2		3.2
^{197M}Hg	23.8 h	0.28		0.24
^{199M}Hg	42.6 m	31.		0.78
^{190}Au	42.8 m		120. at 40.8 min	3.0
^{192}Au	5.0 h		8.7 at 7.1 h	1.5
^{193}Au	17.6 h		11. at 10.2 h	6.9
^{194}Au	39.5 h	0.96		1.3
^{196}Au	6.17 d	0.15		0.79
^{196M}Au	9.7 h	16		5.5

Isotope	T1/2	Direct made Activity (d/sec; $\Delta t_{EOB} = 0$) $\cdot 10^5$	Cumulative Activity (d/sec; $\Delta t_{EOB} = t_{max}$) $\cdot 10^5$	Production (Atoms/g/cm²/H⁺) $\cdot 10^{-5}$
^{198}Au	2.7 d	0.30		0.69
^{198M}Au	2.3 d	0.21		0.41
^{200M}Au	18.7	0.46		0.31
^{188}Pt	10.3 d		0.67 at 1.6 h	5.9
^{189}Pt	10.9 h		37. at 2.3 h	14.3
^{191}Pt	2.8 d		2.6 at 14.8 h	6.2
^{195M}Pt	4.1 d	1.3		4.5
^{184}Ir	3.0 h		23. at 1.1 h	2.4
^{186}Ir	15.8 h		3.4 at 6.8 h	1.9
^{187}Ir	10.5 h		23. at 6.5 h	8.6
^{188}Ir	41.4 h		0.7 at 128. h	1.0
^{190}Ir	12.2 d	0.03		
^{182}Os	21.8 h		7.8 at 1.6 h	6.0
^{185}Os	94. d		0.076 at 104. h	6.1
^{182M}Os	2.7 d	0.66		1.5
^{178M}Ta	2.2 h	77.		6.0
^{173}Hf	23.6 h		30. at 11.5 h	25.1
^{169}Lu	1.4 d		2.4 at 0.5 h	2.9
^{171}Lu	8.2 d		0.47 at 52.3 h	3.3
^{169}Yb	32.0 d		0.15 at 1.3 h	4.1
^{160}Er	28.6 h		0.95 at 1.2 h	0.96
^{147}Gd*	38.0 h	17.		22.9
^{149}Gd*	9.3 d	.07		0.55
^{146}Eu*	48.3 d	0.5		20.5
^{148}Eu*	54.5 d	0.65		30.2
^{128}Ba*	2.42 d	0.97		2.0
^{89M}Zr*	78.5 h	0.14		0.39
^{87}Y*	80.3 h	0.20		0.57
^{83}Rb*	68.2 d	0.008		0.59
^{74}As*	17.8 d	.02		0.30

* Possible Fission Fragments

Table 3 Isotope Production of the Second Pb Target (5 cm deep)

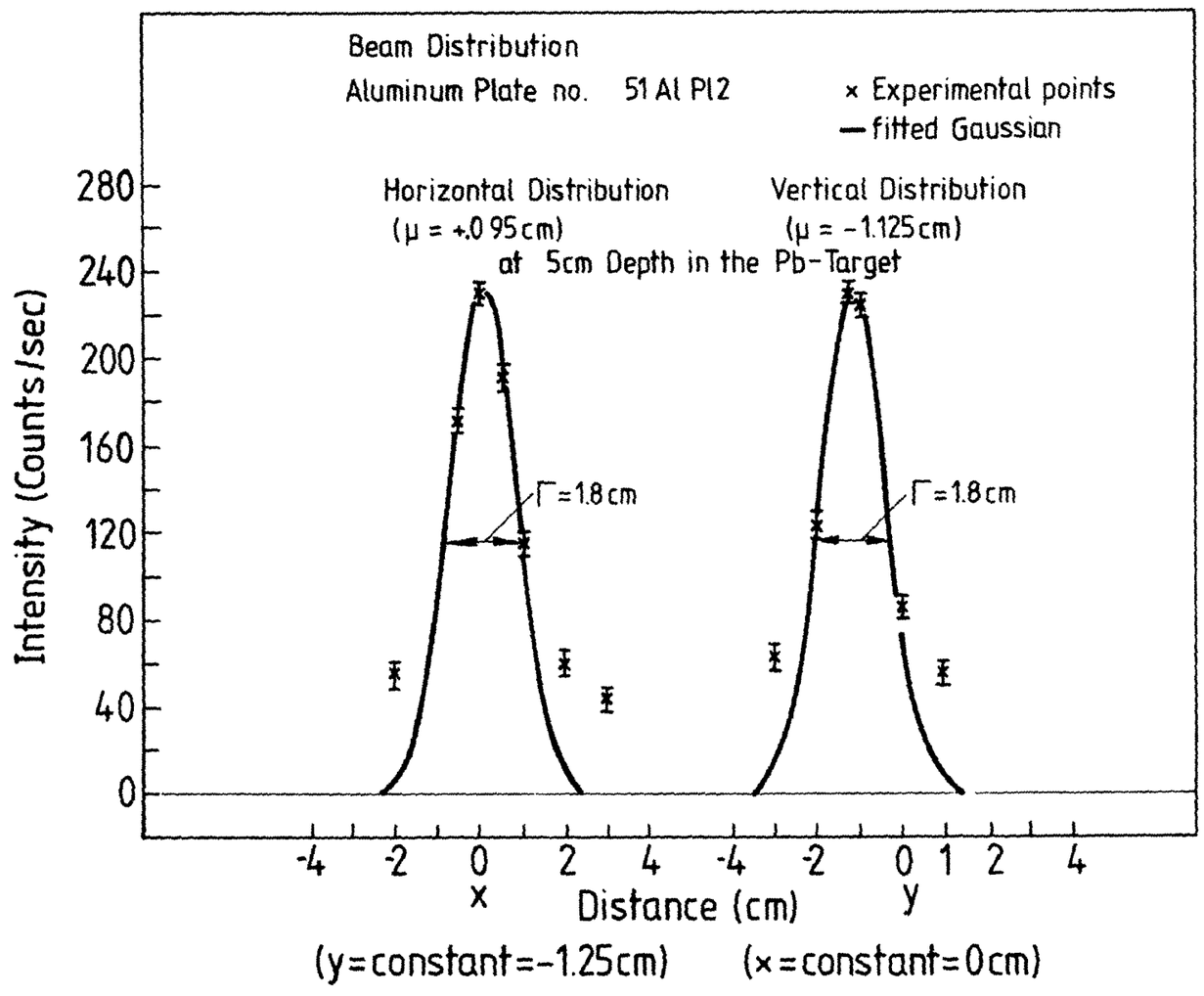

Fig. 1 Beam distribution 5 cm deep in the Pb target produced from induced ^{24}Na activity measurements in an aluminum plate (10 x 20 x 0.1 cm)

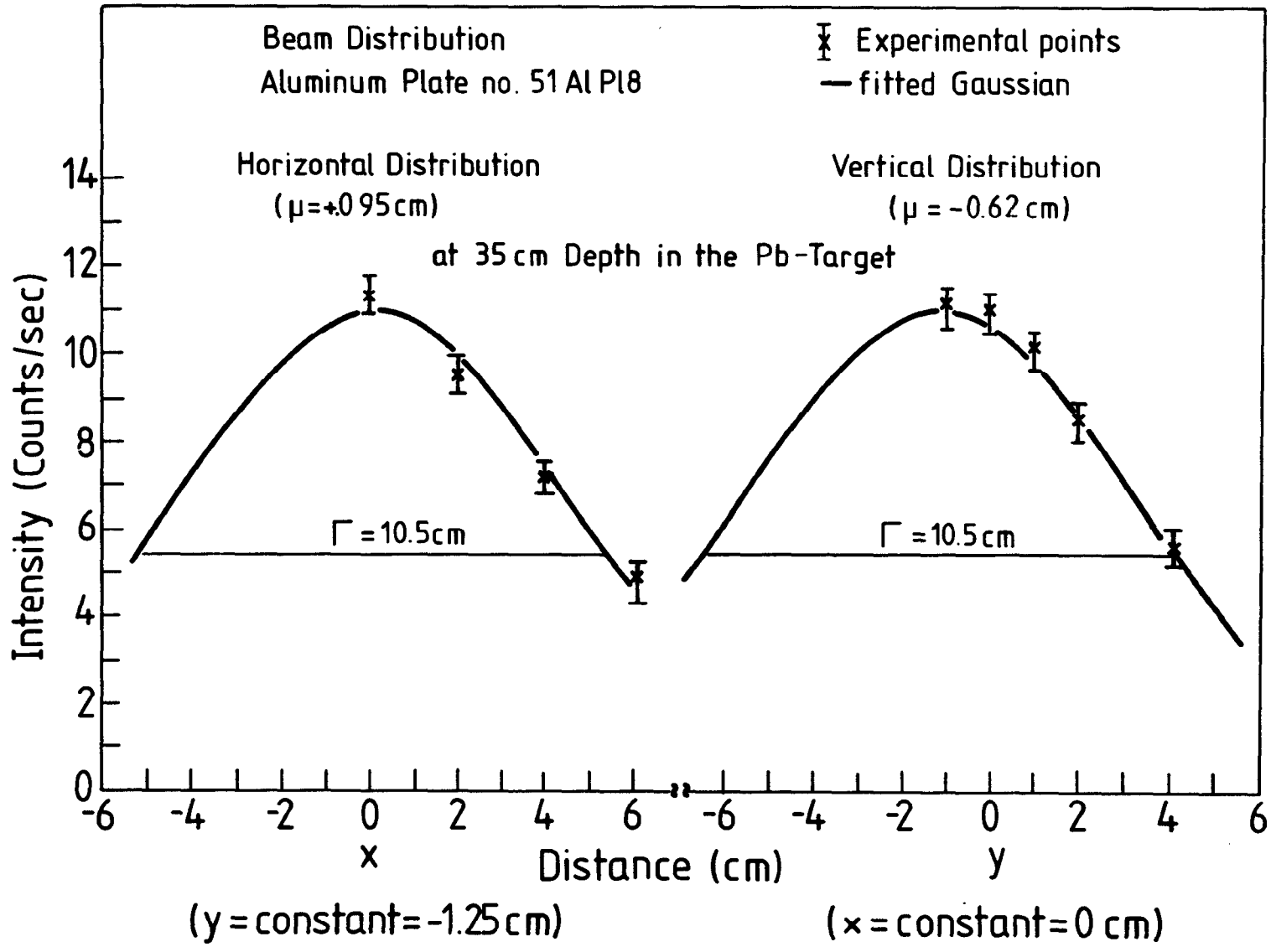

Fig. 2 Beam distribution 35 cm deep in the Pb target produced from induced ^{24}Na activity measurements in an aluminum plate (10 x 20 x 0.1 cm)

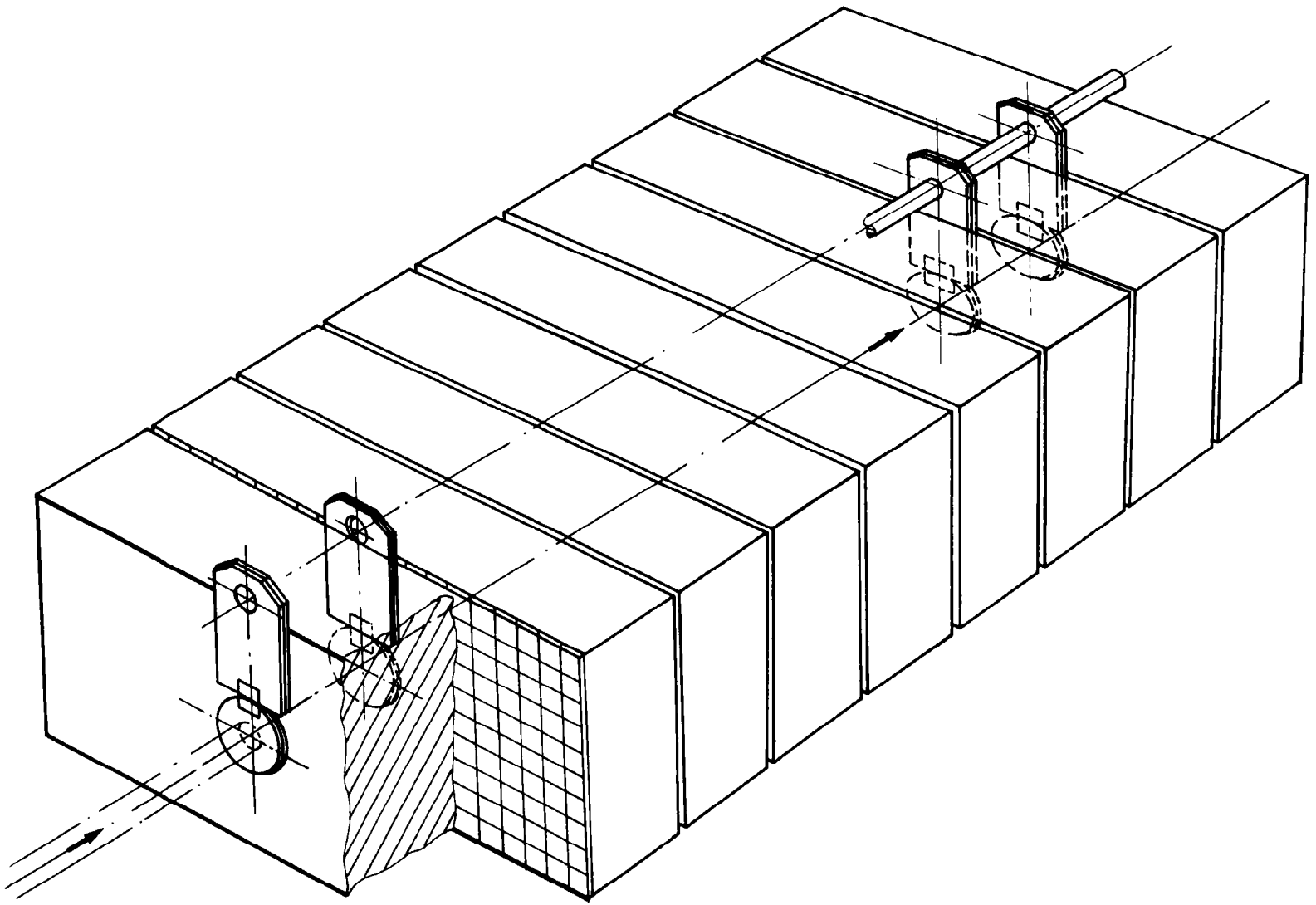

Fig. 3 Target configuration showing the small target disk followed by an aluminum disk and an aluminum plate along with the 5 cm thick Pb brick.

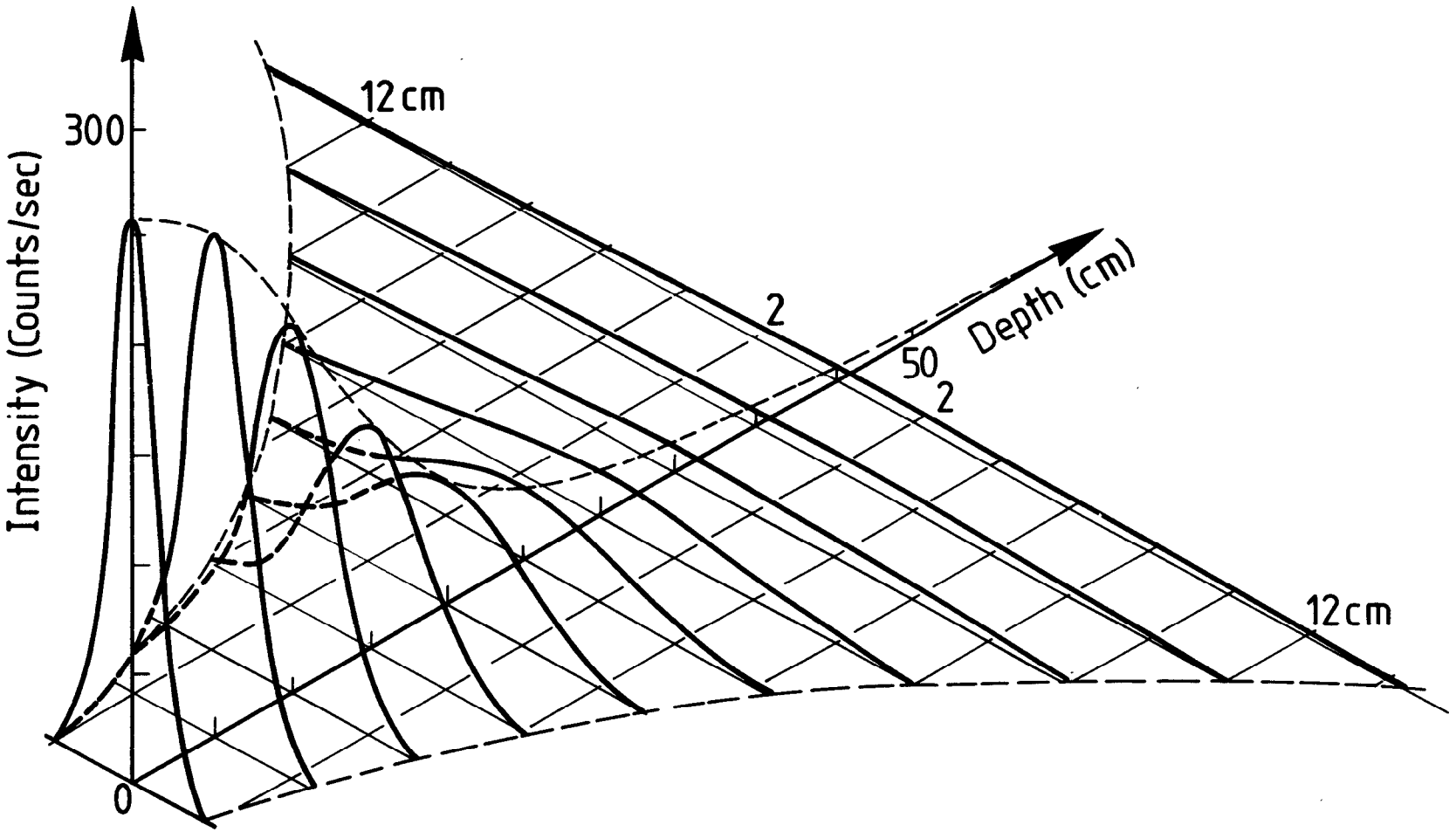

Fig. 4 Overall beam distribution on a function of depth constructed from ^{24}Na measurements of the 10 Al plates from the Pb target

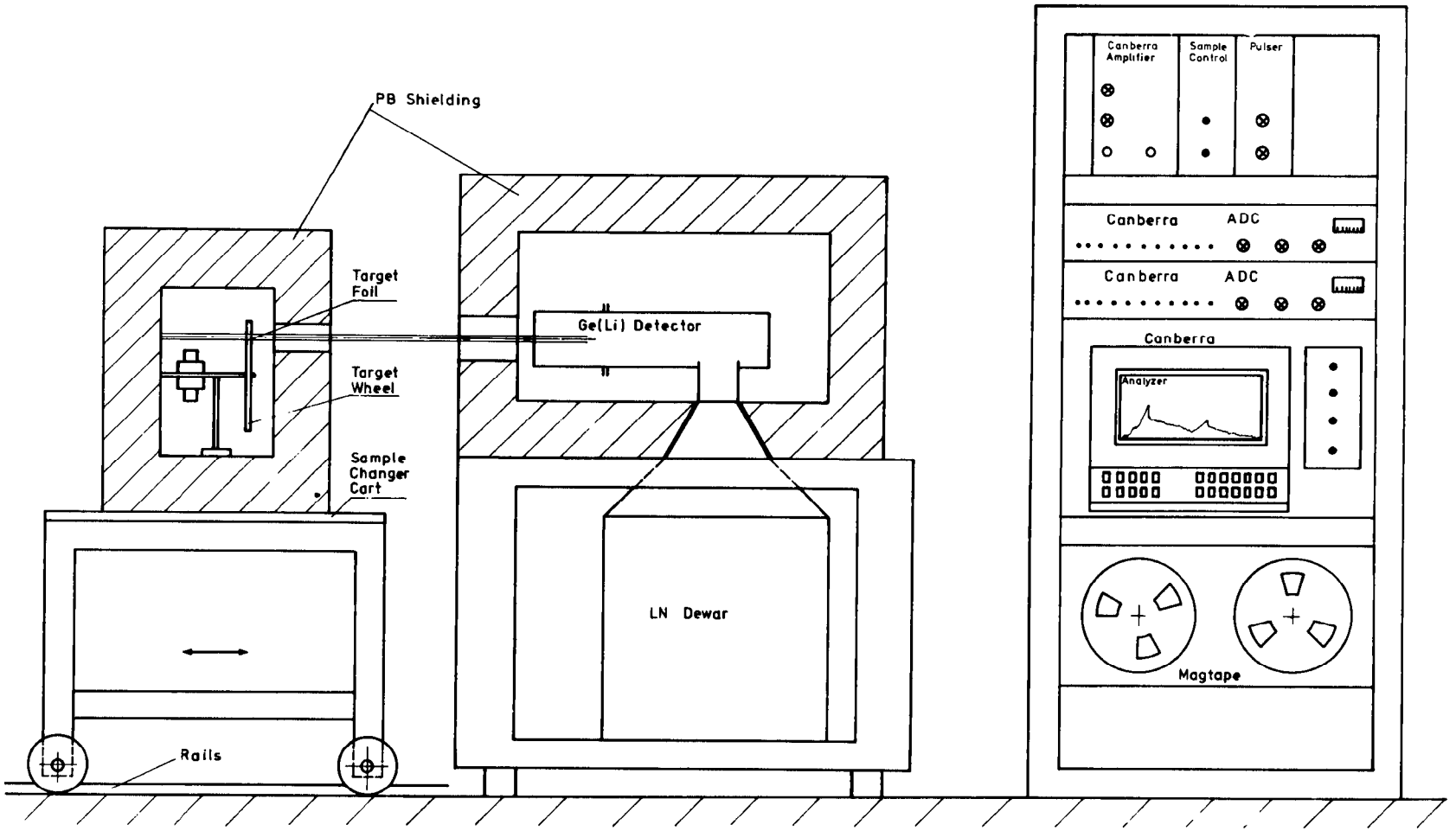

Fig. 5 Schematic of the radioactive counting equipment

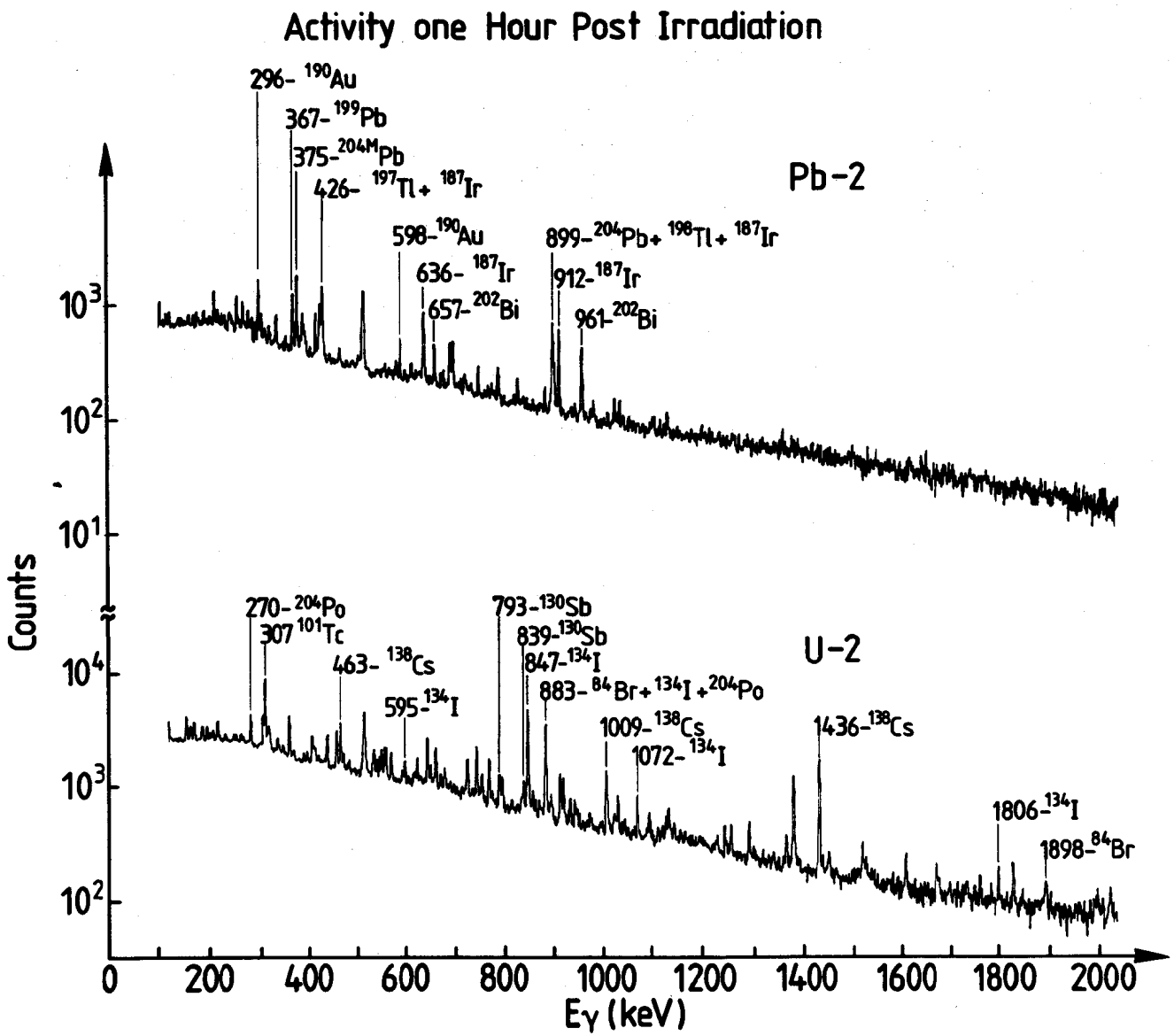

Fig. 6 Spectra from both Pb and U targets which were 5 cm deep in the over-all target taken on hour after the bombardment

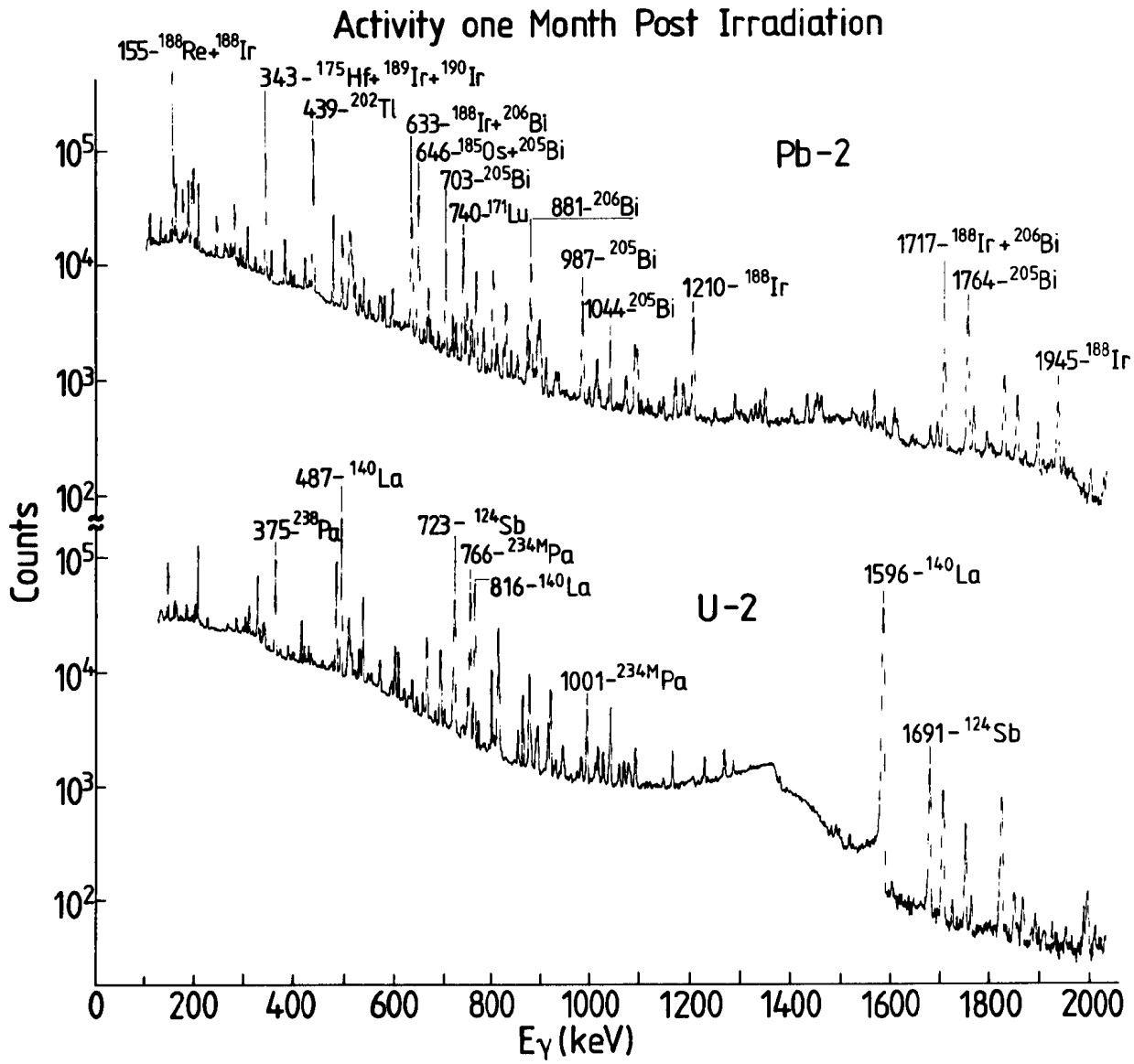

Fig. 7 Spectra from both Pb and U targets which were 5 cm deep in the over-all target taken one month after the bombardment

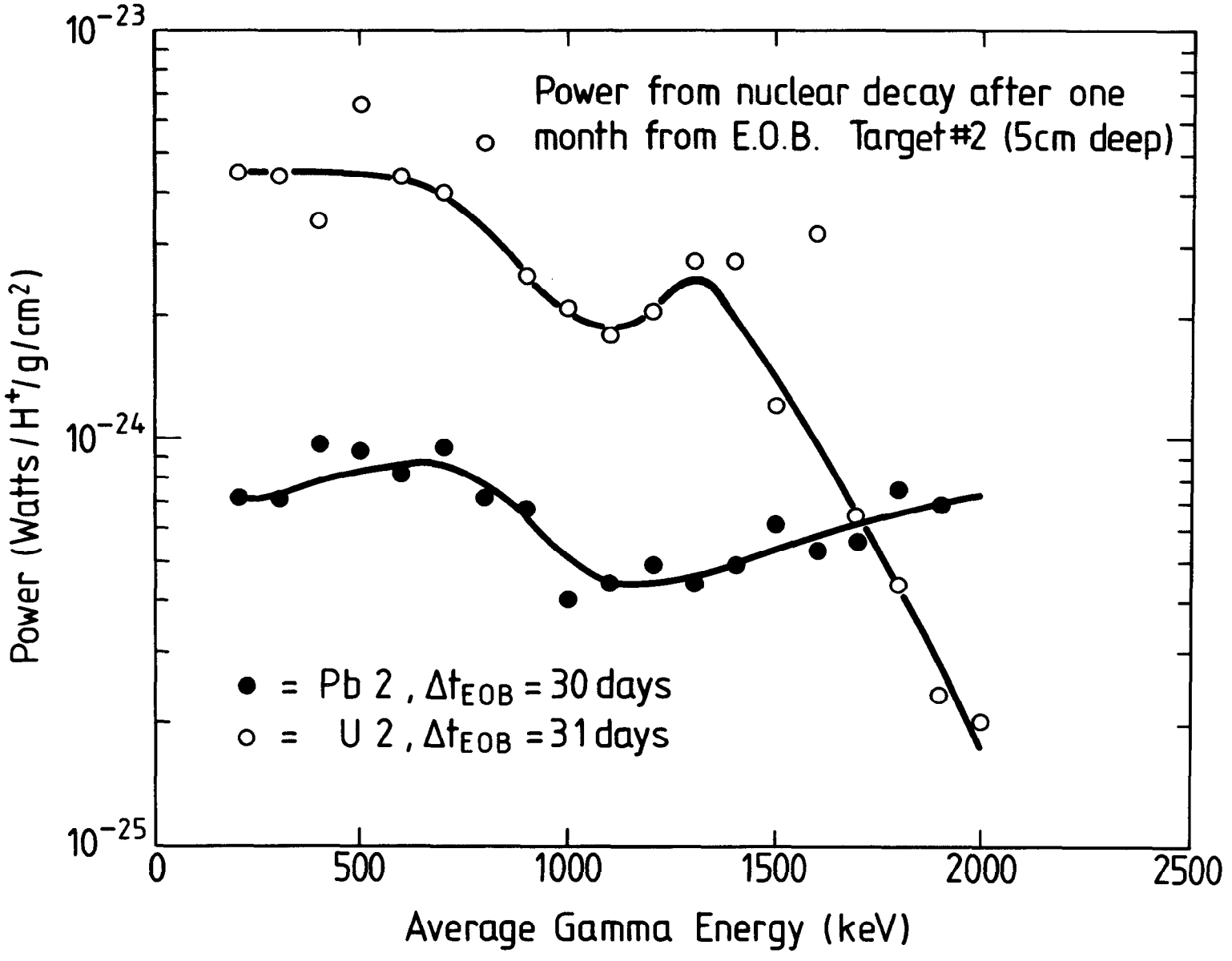

Fig. 8 Radiation power generated by the gamma rays from the decay of the U and Pb targets 5 cm deep into the over-all targets

ICANS-V
MEETING OF THE INTERNATIONAL COLLABORATION ON

ADVANCED NEUTRON SOURCES

June 22-26, 1981

Monte Carlo Reflector Studies for a Pulsed Neutron Source

A. D. Taylor
Rutherford and Appleton Laboratories

Chilton, Didcot, OXON UK

Pulsed neutron sources use hydrogeneous moderators to slow down and thermalize the fast spectrum of neutrons produced in a target. In order to maintain the pulse structure required for time of flight techniques, these moderators must be small in at least one of their dimensions and are typically (for a water moderator) 10X10x5 cm^3. The resulting coupling between target and moderator is inefficient, but may be improved by embedding the target-moderator assembly in a material which acts as a neutron reflector [1]. The reflector increases the effective solid angle between target and moderator and returns partially moderated neutrons which leak from the moderator. A decoupler [1,2] is employed to prevent neutrons which have spent a long time in the reflector from degrading the tightness of the time structure of the pulse.

A neutron reflector must have a high macroscopic cross-section and a low absorption. As discussed below, it may also be advantageous for it to have a high (but not too high) lograrithmic energy decrement. Further requirements for high intensity sources are that the material be easy to fabricate, be resistant to radiation damage and have suitable thermal properties to facilitate heat removal. Table I summarizes the neutronic properties of some candidate reflector materials. A is the atomic weight of the principal neutronic component, ρ_A is its atomic density and σ its atomic cross-section. Mean values of σ in the neighborhood of 10^6 eV (corresponding to primary reflection from the target) and 10^3 eV (leakage from the moderator) are given, together with the resulting macroscopic cross-sections, Σ . Reflectors may be divided into several groups according to ξ, the logarithmic energy decrement and n, the mean number of collisions between 10^6 ev and 1 eV: strongly moderating reflectors (CH_2); moderating reflectors (D_2O, Be, C) and non moderating reflectors (Fe, Ni, Cu, Pb, etc.). The choice of decoupler depends critically on the time-energy relationship of neutrons in these three classes of reflector: in a strongly moderating reflector, little time degradation will result from even low energy ($\sim$1 eV) neutrons returning to the moderator; in a moderating reflector ,$\sim$1 eV neutrons will spoil the time structure and so must be prevented by the decoupler from reaching the moderator; in a non moderating reflector escape from the system or capture by the moderator will occur before significant degradation in energy (and hence lengthening of dwell time) has occurred. Thus in the two extreme cases of excessive moderation and negligible moderation, only a very weak decoupler is required.

The neutronic properties of target-moderator-reflector-decoupler systems have been studied experimentally by many groups [3, 4, 5, 6] and bench mark comparisons have been made with Monte Carlo codes. These codes, using extensive cross-section libraries such as ENDF/B are a powerful tool complementing the experimental approach. They are particularly useful for parametric studies of small systems and lend themselves to the study of the slowing down region and questions of energy deposition. Such studies are difficult to perform experimentally. Conversely, highly differential parameters such as the time structure of a small energy group in the thermal region require a large amount of computation, but may be obtained experimentally, for example by Bragg diffraction.

The code used in this study was TIMOC [7] as implemented at the Rutherford Laboratory and the main aim was an optimisation of the target-moderator-reflector-decoupler system for that laboratory's SNS project. Figure 1 shows a test SNS geometry using one 'wing' moderator. The moderator is surrounded by a 2 cm 'cryogenic' gap and the entire assembly enclosed by a 1 cm decoupling layer of B_4C. The density of boron-10 in that layer may be varied. The target region is filled with a composition corresponding to a zircalloy-2 plated depleted uranium target with D_2O coolant and structural material. The regions on either side of the target contain D_2O coolant and structural material. This assembly is embedded in a reflector cube of side 70 cm.

Table IIa gives the bulk flux in the moderator, ϕ_B, and the surface flux escaping from the moderator, ϕ_S, in the direction of the beam tube for polyethylene, heavy water, beryllium, iron, nickel, and lead reflectors. The decoupling density was $\rho_B^{10} = 0.01$ corresponding to a decoupling energy (1/e) of 36 eV. Table IIb gives these data for polyethylene, beryllium, and lead reflectors when no decoupler is employed. In both cases N is the number of primary neutron histories started. Polyethylene is seen to be considerably poorer than beryllium, whereas non moderating reflectors such as nickel and lead have a comparable performance at both decoupling energies. It is known that reflector size effects have saturated by 70 cm cube size for beryllium [2], but it is thought that this size of lead reflector may be less than optimum.

A comparison of a strongly moderating reflector such as polyethylene with beryllium at the same decoupling energy may be less than fair in view of the disscussion above. Figure 2 gives the performance of a polyethylene and a beryllium reflector as a function of decoupler energy. Such a clear separation of their relative performance shows that polyethylene is less optimal than beryllium, without the need to study time structure.

The comparability in yield of beryllium and lead (lead is a more practical material than nickel and provides excellent additional shielding of the target) requires that the time structure resulting from both reflectors be studied. Such a calculation is difficult for the

thermal region (neutron transport through nine decades in energy followed by time binning of a single energy group results in low statistics). In the slowing down region, however the pulse shape takes the form

$$\phi(v,t) = (\Sigma vt)^2 \exp(-\Sigma vt)$$

where v is the neutron velocity and Σ the macroscopic cross-section of the moderator. Since this function is a universal function of vt, data from say 1 eV to 100 eV may be summed in bins of vt, thus greatly improving the statistical accurracy. Such an analysis is given in figure 3 for an unreflected SNS target-moderator geometry. The solid line is the infinite medium value and the discrepancy between this and the data at small values of vt (note the logarithmic scale) reflects the time delay due to transport through the target into the moderator. Figure 4 represents data taken with a beryllium reflector present. The width at half height is not increased greatly, but a long vt tail appears from neutrons reflected back by the beryllium. Figure 5 shows a similar analysis of data from a lead reflector. Again the width at half height hardly changes and, when compared with the beryllium data, the long vt tail has marginally improved.

Conclusion

The role of beryllium as the traditional neutron reflector is not challenged by other moderating reflectors. However neutronic equivalence (both in yield and time structure) may be achieved by using a high Z material eg. lead. Such a choice of reflector may well be favoured because of its engineering benefits.

References

[1] J. M. Carpenter, "Pulsed Spallation Neutron Sources for Slow Neutron Scattering", Nucl. Instr. and Meth. 145 (1977) 91-113.

[2] A. D. Taylor, "Neutron Transport from Targets to Moderators", Rutherford and Appleton Laboratories Report, RL-81-057 (1981).

[3] B. C. Boland, A. Carne, G. C. Stirling, and A. D. Taylor, "Spallation Target-Moderator-Reflector Studies on NIMROD", Rutherford Laboratory Report, RL-78-070 (1978).

[4] G. J. Russell, M. M. Meier, H. Robinson, and A. D. Taylor, "Preliminary Neutronics of a Reflected 'T'-Shape Moderator for the Weapons Neutron Research Facility", these proceedings.

[5] G. S. Bauer et al. "Realisierungsstudie zur Spallations--Neutronquelle", Teil II. Julich-Karlsruhe (1981).

[6] Y. Ishikawa et al. "KENS Report I", KEK-80-1 (1980).

[7] H. Kschwendt and H. Reif, "TIMOC--A General Purpose Monte Carlo Code for Stationary and Time Dependent Neutron Transport", Euratom Report EUR 4915e (1970).

Table I

Neutronic Properties of Possible Reflector Materials

Reflector	H (in CH_2)	D (in D_2O)	Be	C	Fe	Ni	Cu	Pb
A	1	2	9	12	55.9	58.7	63.5	207.2
ρ_A atoms A^{-3}	0.079	0.066	0.124	0.080	0.085	0.091	0.085	0.033
σ (10^3eV) barns	21	5.1	6.1	4.6	9.0	15	6.0	11
σ (10^6eV) barns	4	3.0	3.5	2.5	2.5	3.2	3.5	5.5
Σ (10^3ev) cm^{-1}	1.58	0.33	0.76	0.37	0.77	1.37	0.51	0.36
Σ (10^6ev) cm^{-1}	0.32	0.19	0.43	0.20	0.21	0.29	0.31	1.60
ξ	0.913	0.504	0.209	0.158	0.035	0.034	0.031	0.0096
n 10^6 ev $\downarrow$ 1 ev	15	27	66	87	391	409	446	1440

Table IIa

Reflector	CH_2	D_2O	Be	Fe	Ni	Pb
ϕ_B	8.6	12	15	16	17	17
ϕ_S	2.5	4.1	4.6	3.5	4.1	3.6
N(k)	18	160	13	120	75	189

Decoupler density $\rho_{B^{10}} = 0.01$ (36 eV)

Table IIb

Reflector	CH_2	Be	Pb
ϕ_B	14	33	31
ϕ_S	2.7	6.3	7.2
N(k)	14	30	132

Decoupler density $\rho_{B^{10}} = 0.0$

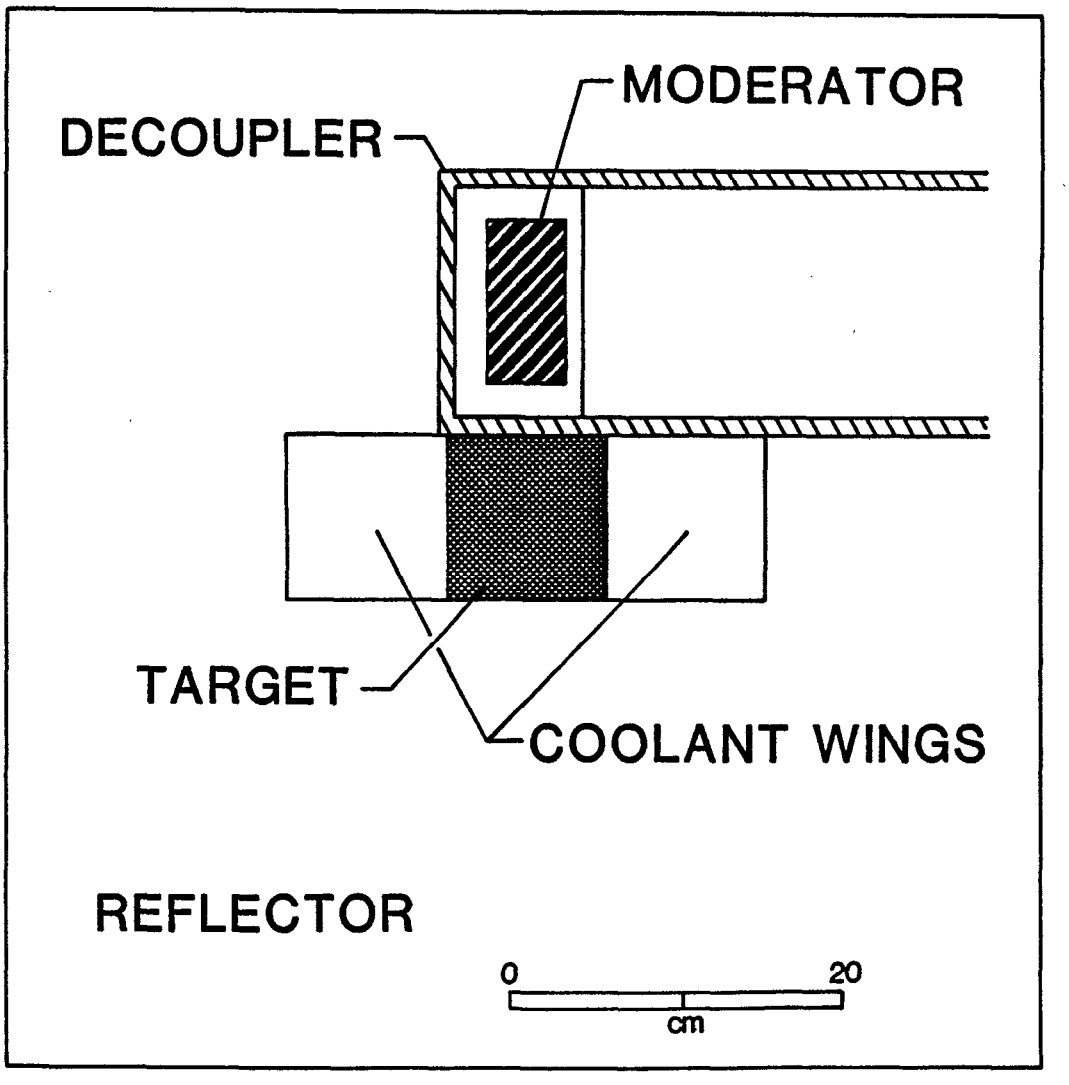

Figure 1. Vertical section through the centre of a TIMOC geometry. The reflector cube is 70 cm on side, and the target is 30 cm long.

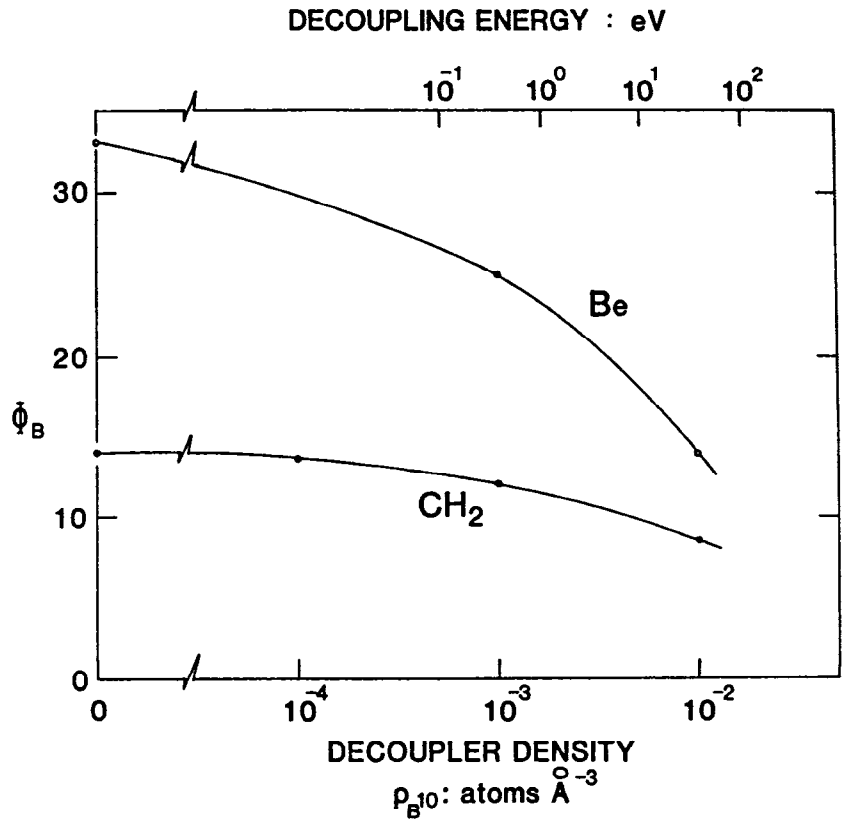

Figure 2a Comparison of the bulk flux in the moderator for a polyethylene and a beryllium reflector as a function of decoupler density. A 1/e decoupling energy scale is given at the top.

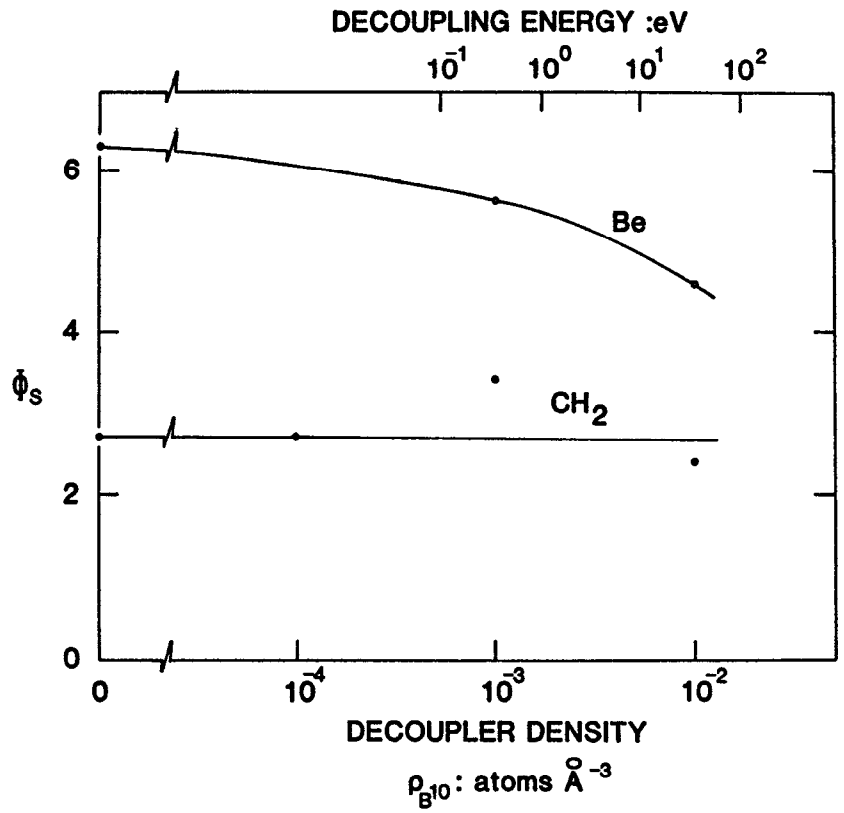

Figure 2b Comparison of the surface flux in the moderator for a polyethylene and a beryllium reflector as a function of decoupler density. A 1/e decoupling energy scale is given at the top.

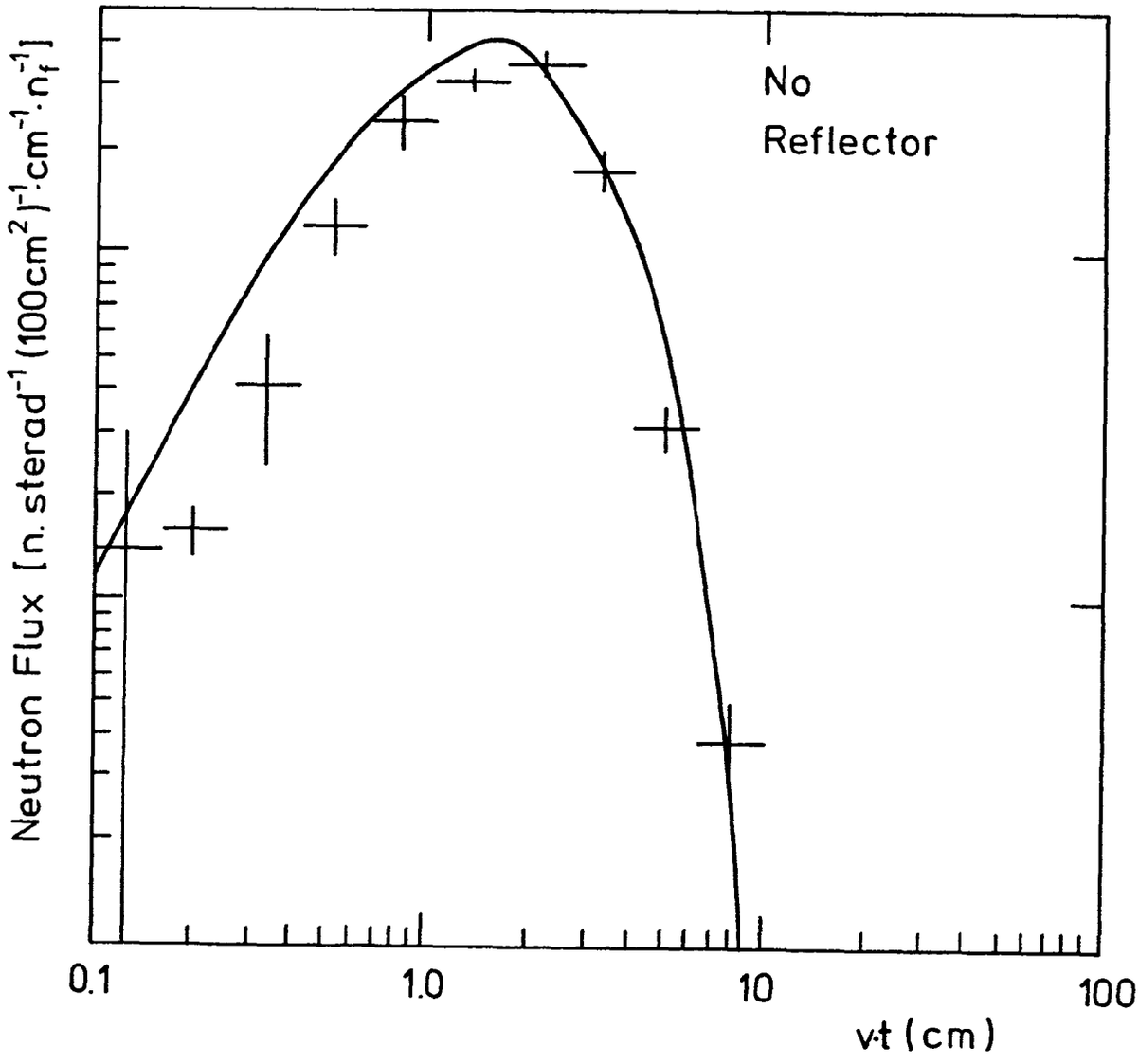

Figure 3. Time structure of the neutron pulse in the slowing down region presented as a vt diagram. The solid line is the infinite medium case. Data points refer to a calculation with no reflector present.

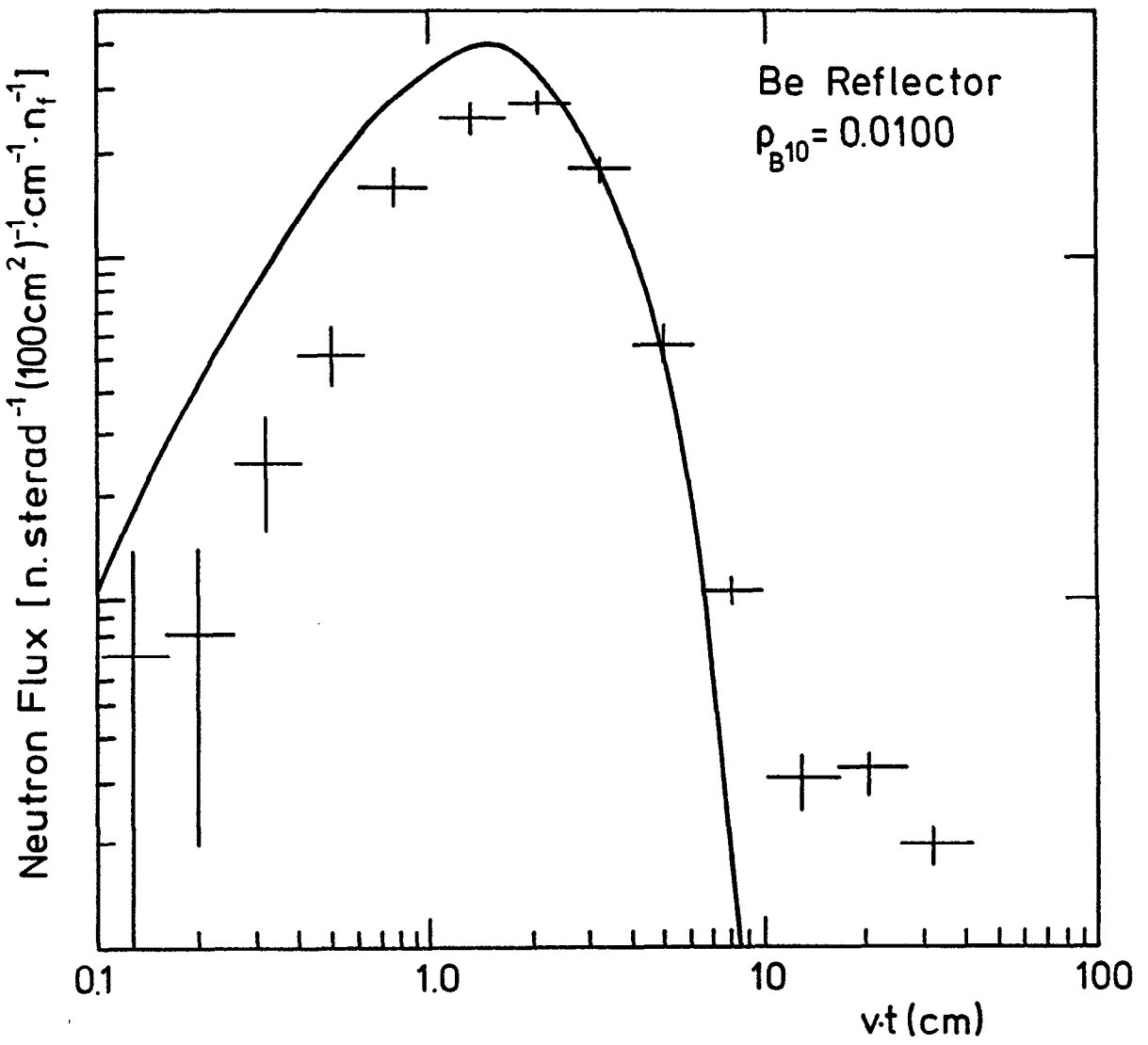

Figure 4. As figure 3 but with data points from a beryllium reflector

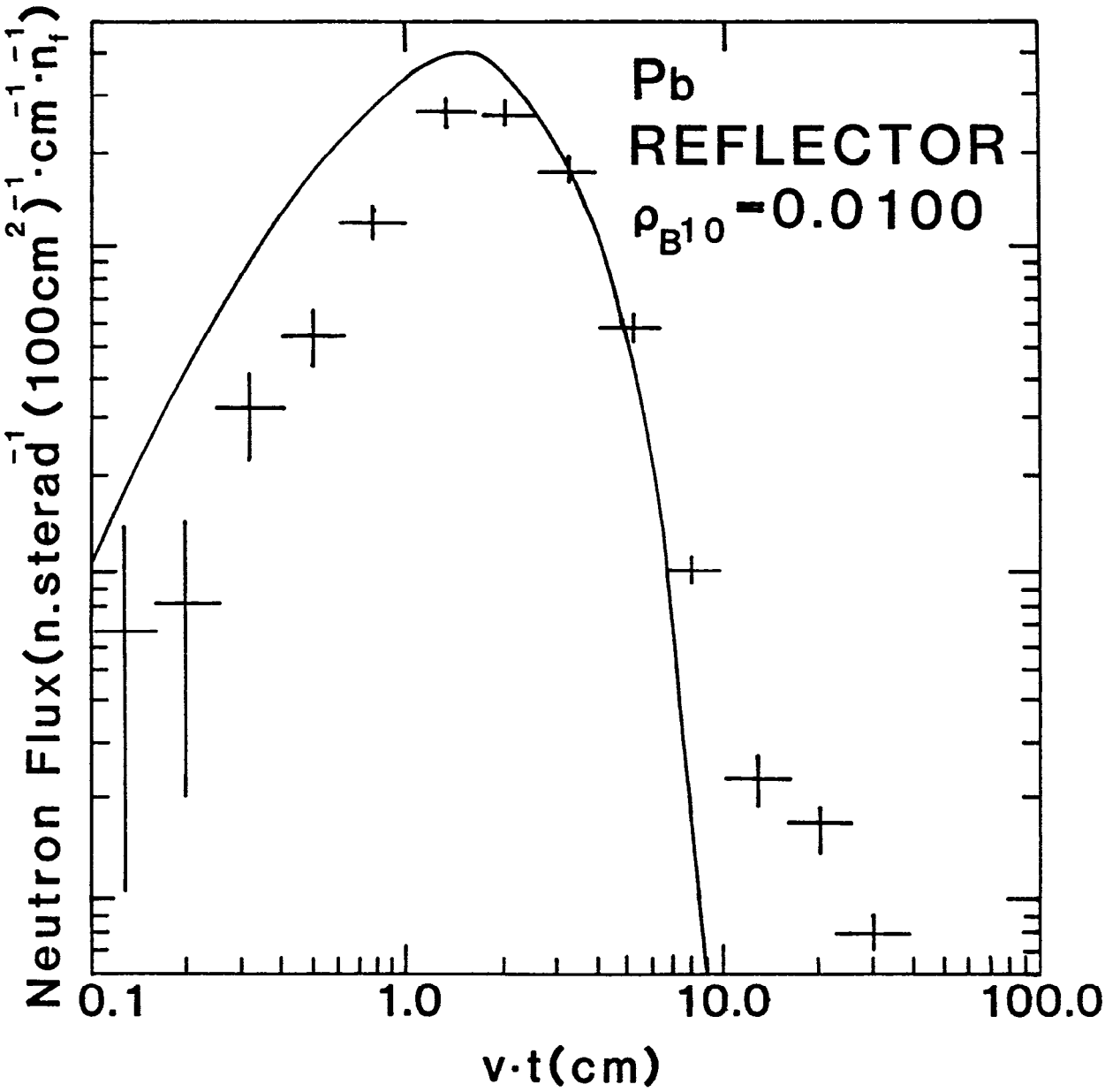

Figure 5. As figure 3 but with data points from a lead reflector.

Jül-Conf-45

D2-2

ICANS V

MEETING OF THE INTERNATIONAL COLLABORATION ON
ADVANCED NEUTRON SOURCES

June 22-26, 1981

Preliminary Neutronics of a Reflected 'T'-Shape Premoderator/Moderator for the Weapons Neutron Research Facility

G. J. Russell, M. M. Meier, and H. Robinson
Los Alamos National Laboratory
Los Alamos, New Mexico 87545, U.S.A.

A. D. Taylor
Rutherford and Appleton Laboratories
Chilton, Didcot, OXON OX11 OQX, U.K.

ABSTRACT

At the Los Alamos pulsed spallation neutron source, we are developing the capability of measuring absolute neutron spectra and beam fluxes $\lesssim 10$ eV and neutron pulse widths $\lesssim 0.2$ eV. We utilize this capability in a development program directed toward characterizing and optimizing our source and providing basic neutronics data relevant to spallation neutron sources. We describe here the facilities being developed and show some preliminary results.

INTRODUCTION

The Weapons Neutron Research facility (WNR) is an operational pulsed spallation neutron source[1] at the Los Alamos National Laboratory. The layout of the WNR is illustrated in Fig. 1. The 800-MeV proton source for the WNR is the Clinton P. Anderson Meson Physics Facility (LAMPF).[2] Note in Fig. 1 that the WNR has two target areas: a) a high-current target area shielded to accept 20 μA, and b) a low-current target area shielded to accept 0.1 μA. The high-current target is equipped with a flexible target-moderator-reflector handling system which allows us to relatively easily interchange targets and moderators for various experimental programs. We use the high-current target area to provide neutrons for nuclear physics applications ($\sim$1 eV to $\sim$300 MeV) and for materials science research ($\lesssim$1 eV). We use the low-current target area to study (and optimize) the neutronics of moderated neutrons.

The characteristics of the WNR proton beam, and the capabilities built into the low-current target area are unique in the world; they include:

- continuously variable proton pulse widths from $\sim$35 ns to $\sim$8.5 μs,
- variable proton pulse repetition rates from 1 Hz to 120 Hz,
- a shielded (vertical) flight path for measuring absolute neutron beam fluxes and spectra $\lesssim$10 eV, and
- a time-analyzer arm (attached to the vertical flight path) for measuring neutron pulse widths from moderators.

Also, the low-current target area is readily accessible for moderator, collimator, and detector alignment, and for changing target-moderator-reflector configurations.

Once we have studied, optimized, and characterized the neutronic performance of a particular target-moderator-reflector geometry, we can incorporate the changes into the high-current target to take advantage of the neutron enhancement. We recently demonstrated this capability by measuring (in the low-current target area) an increase in neutron beam fluxes ($\lesssim$0.5 eV) of $\sim$1.7 when changing the poison between our premoderator and moderator from 0.076-cm of Cd to 0.0025-cm of Gd. We made the poison change in the high-current target during the next LAMPF cycle break. Subsequent neutron scattering measurements in the high-current target area confirmed our predicted neutronic enhancement.

The combination of the WNR low- and high-current target areas, the facilities built into each area, continuously variable proton pulse widths, and variable proton repetition rates provide us with an unequaled

capability to characterize the neutronics of spallation neutron sources using 800-MeV protons. Our spallation target-moderator-reflector development program has been described in Refs. 3 and 4, and is summarized in Table I.

We describe here the capabilities built into the WNR low-current target area for neutronics measurements $\lesssim 10$ eV, and show some preliminary results. We use calculated predictions from Monte Carlo codes to help guide our experimental program. Our measurement program also provides a check on the validity of the computer codes (model evaluation). The computer codes used are: a) the Oak Ridge National Laboratory code HETC for particle transport $\gtrsim 20$ MeV,[5] b) the Los Alamos code MCNP for neutron and gamma-ray transport $\lesssim 20$ MeV,[6] and c) the Ispera code TIMOC implemented at the Rutherford Laboratory.[7,8]

WNR LOW-CURRENT TARGET FACILITIES

The WNR low-current target area is built of reinforced concrete (0.2-m thick) and shielded with ~ 4.9-m dirt. The center portion of the floor (~ 30 m^2) is aluminum; the walls are ~ 6.2 m from the center of the room to minimize neutron return from the walls to configurations located at room-center. In Fig. 2, we show the location of the vertical flight path in the low-current target area. The details of this flight path are illustrated in Figs. 3-5. The nominal distance from the proton beam line to the center of the BF_3 neutron detector is ~ 5.61 m; the nominal distance from the diffraction crystal to the ^{3}He detector is ~ 1.02 m.

The shielding in the vertical flight path and that around the time-analyzer arm is sufficient to make background corrections to the data small. Specifically, the shielding in the vertical flight path consists of the following materials: a) 0.89-m iron, b) ~ 3.3-m iron shot, c) ~ 0.90-m lead shot, d) 7.6-cm borated (5 wt%) polyethylene, and e) 2.5-cm borated (32 wt%) polyethylene. The detector/crystal chamber (at the bottom of the flight path) is lined with 0.051-cm-thick cadmium. On the side opposite the time-analyzer arm, the detector/crystal chamber is shielded by ~ 10-cm paraffin and ~ 14-cm iron shot. The neutron shield around the time-analyzer arm consists of the following materials: a) 36-cm iron, b) ~ 50-cm paraffin, c) 5.1-cm borated (both 5 wt% and 32 wt%) polyethylene, d) 0.79-cm boral, and e) 0.076-cm cadmium. In the vertical flight path, we initially shape the neutron beam with two 5.1-cm-thick borated (32 wt%) polyethylene collimators. These two collimators are located at 3.96 m and 0.24 m from the center of the BF_3 detector. A final collimator (located 2.5 cm from the center of the BF_3 detector) is a 1.8-cm-thick piece of sintered natural boron carbide; the 2.0 cm by 2.0-cm hole through the boron carbide collimator is lined with 0.0025-cm gadolinium. There are additional baffles (to reduce the penumbra in the moderator field-of-view) located between the aluminum floor and the target-moderator-reflector configuration; these baffles are made from 2.5-cm-thick borated (32 wt%) polyethylene. The need for additional baffles and selected shielding is being evaluated.

A Pyrolitic Graphite (PG) crystal with a 0.4° mosaic (FWHM) was used in our initial neutron pulse width measurements. The crystal was set in as backscattering a geometry as practical (a 2ϑ of 137°) to minimize the $\cot\vartheta\,\Delta\vartheta$ contribution to the resolution. We plan to use crystals with smaller d-spacings in the time-analyzer arm which will enable us to measure neutron pulse widths at higher energies than available with the PG crystal.

THE 'T'-SHAPE PREMODERATOR/MODERATOR

An unreflected 'T'-shape premoderator/moderator is illustrated in Fig. 6. Such a target-moderator configuration has good neutronic coupling (useful-neutrons/protons•sr). Note in Fig. 6, that both center and offset moderator geometries can be accommodated with the larger leg of the 'T'; offset geometry is indicated. We are using a premoderator/moderator approach where the premoderator and moderator may be different materials. The choice of materials will be based on neutronic performance (intensity and pulse width), beam quality (contamination of the useful neutron beam by charged particles, gamma-rays, and high-energy neutrons), and radiation damage considerations.

For pulsed spallation neutron sources, a neutron reflector can enhance the thermal neutron production by factors of 2-4. [3,9] A reflected 'T'-shape premoderator/moderator is illustrated in Figs. 7 and 8. We are presently concentrating our efforts on studying the neutronics of 'T'-shape premoderator/moderators, and have installed a prototype reflected 'T'-shape premoderator/moderator in the high-current target area. An optimized version of this configuration (using ambient temperature moderators) will be installed in the high-current target area early in 1982.

Our interest in the 'T'-shape configuration is best illustrated using Fig. 9. In this figure, we depict the layout of the neutron flight paths in the high-current target area. The flight paths occur in clusters of three at right angles to each other. Our goal is to provide optimized neutron beams to as many flight paths as possible so that concurrent experiments can be performed. One orientation of the 'T'-shape moderator relative to these flight paths is shown in Fig. 10. The premoderator/moderator approach allows individual moderators to be optimized for a particular class of instruments using the neutron beams (see Fig. 11).

DETECTORS AND ELECTRONICS

In the vertical flight path, we use a 2.54-cm-diam BF_3 proportional counter to detect moderated neutrons ($\lesssim$10 eV). The counter is oriented with its axis perpendicular to the neutron beam; its sensitive area is

defined by a slot (2.5-cm long and exposing half the detector diameter) cut into the 0.076-cm-thick Cd sheath surrounding the detector. The BF_3 pressure is 40-cm Hg and the boron is enriched to 96% ^{10}B. For 0.025-eV neutrons, the detector efficiency, averaged over the effective area of the neutron beam, is 0.101. Commercial bias supplies, preamplifiers, amplifiers, and integral discriminators are used in a conventional manner to generate timing pulses for events occuring in the counter. We set the discriminator bias at 42% of the $^{10}B(n,\alpha)^7Li^*$(0.478 MeV) peak pulse level, a level at which 10.0% of the total (n,α) events are rejected. Following a 50 μs delay after the proton burst strikes the target, the data are electronically gated 'on' during an 8 or 12 ms period depending on the effective LAMPF repetition rate. The former is done to reject the extremely high counting rates at early times, and the latter to eliminate frame overlap.

A capacitive pickup located in the WNR beam line senses the proton pulse 80 ns before it strikes the spallation target. This pulse starts a clock which can accept multiple stops from the neutron detector. The conversion cycle (70 ns), detector resolution, cable delay differences and time slewing in the discriminators are negligible relative to the 3.2 μs channel width of the clock. The digitized times are internally stored in a 16-word buffer which derandomizes the acquisition rate. The clock/buffer is interfaced to the computer through CAMAC. Data are transferred via a direct memory access (DMA) channel to a set of three 256 word buffers in main memory. When one of these buffers fills, a histogramming task is activated which increments the buffer relative addresses in a data area. Simultaneously, DMA storage into the computer is switched to a new buffer. The system was tested with random stops at a continuous rate of 55 kHz at which the clock buffer began to completely fill. At a 50 kHz rate, deadtime measurements were made and found to be less than 0.01%. In general, maximum instantaneous rates from the BF_3 counter were less than 8 kHz and electronic dead times were ignored.

At high instantaneous rates, the BF_3 detector incompletely collects the charge generated by each event. This effectively reduces the detector gain and efficiency. One can study this effect by obtaining neutron time-of-flight data at short proton bursts (where the rates are low enough that the effect is negligible) and with longer proton pulses. The spectrum of the ratio of these spectra should be flat where the effect is negligible; however, as the pulse width is increased, the relative efficiency in the high-rate portion of the Maxwellian region of the neutron spectrum decreases. Such a study was performed and the data are shown in Fig. 12. These effects are negligible for our rates and were ignored.

The BF_3 detector must also recover from the very high counting rates occuring shortly after the protons strike the target. One can follow a procedure similar to that described in the preceeding paragraph, that is, taking the ratio of the counting rate near the fast-burst to that in the Maxwellian as a function of proton pulse width. By observing the behavior of a time region as a function of pulse width, one can extrapolate to zero pulse-width to estimate the necessary correction for that region. For the neutron spectra reported here, we estimate $< 2\%$

losses for neutron energies < 4 eV. We have not made this correction to the data.

In the time-analyzer arm, a single 1.27-cm-diam ^{3}He counter (at 10 atm) is used to detect neutrons. The diameter of this detector closely matches the neutron beam spread from the moderator surface and the mosaic of the PG crystal.

PROTON MONITORING

As part of the WNR target-moderator-reflector development program, absolute measurements of neutron beam fluxes and spectra are planned. Aluminum foils are presently used to obtain the number of protons striking a target, and an 'on-line' proton monitoring system based on secondary emission monitors (SEM's) is being implemented.[10] Two SEM's (one with an Au-plated emitter and one with an Al emitter) have been installed in the low-current target beam line; these SEM's are ~ 1 m upstream of the neutron producing target. Although a failure in our charge integration electronics precluded our use of the system as an absolute proton monitor, the following conclusions are valid: a) the SEM's are stable (relative to neutron production) to ± 0.9% over a ten-day interval, and b) the linearity of the SEM's (again referenced to neutron production) was better than ± 0.9% (1 σ) over the proton pulse width range 35 ns to 2.0 μs. With a reconfiguration of electronics, we expect to use SEM's (in conjunction with periodic Al foil activations) as an absolute monitor of proton charge striking a target.

DATA REDUCTION AND ANALYSIS

We want to measure 'useful' neutrons, that is, neutrons of a given energy which originate in the moderator and reach the detector by a direct route through the collimated flight path. All other neutrons arriving at the detector are classed as 'background'. We estimate this background component by measuring the detector response when the useful neutron beam is attenuated by a 1.8-cm-thick sintered B_4C filter. We placed this filter as close to the moderator surface as practical (~1.2 m). At ~600 eV, this filter has an attenuation of 1/e; at 10 eV, the attenuation is ~0.04%. With the filter in place, neutrons detected below ~10 eV arise from the moderation of fast neutrons in the collimators and from neutrons reaching the detector by non-direct paths. To get the sub-cadmium neutron spectrum from a moderator, we estimate the neutron background component by measuring the detector response when the useful neutron beam is attenuated by a 0.076-cm-thick Cd sheet.

Raw spectral distributions are measured by time-of-flight (TOF) techniques over the 5.61 -m vertical flight path, and are binned into 3.2-μs time channels. Using SEM values for the number of incident protons, signal and background data sets are normalized to each other prior to a point-by-point subtraction. A TOF spectrum, n(t) is

transformed to an energy spectrum, n(E), by the following relationship:

$$n(E) = n(t)\,\frac{dt}{dE} \qquad (1)$$

Corrections are made to the data for detector efficiency, η_d, for transmission losses through the detector wall, t_w, and for transmission losses through air, t_a, due to absorption and scattering in the 1.56 m of unevacuated flight path at the mean for Los Alamos pressure of 580-mm Hg. These corrections are as follows:

$$\eta_d = 1 - \exp(-0.0169/\sqrt{E}\,), \qquad (2)$$

$$t_w = 0.97, \text{ and} \qquad (3)$$

$$t_a = \exp -\ell(3.51 \times 10^{-4} + 1.76 \times 10^{-5}/\sqrt{E}\,) \qquad (4)$$

where E is in eV and ℓ is the air flight path in cm.

The corrected neutron spectrum with no filters, with a Cd filter, and difference between the two spectra are shown in Fig. 13. This latter (sub-cadmium) spectrum will be used to obtain an average cross section for converting foil activation measurements into an absolute average sub-cadmium neutron beam flux. Note that there is a larger fraction of neutrons in the 0.1 - 2.0 eV energy interval compared to Maxwellian and 1/E distributions as found in reactors.[11] The corrected neutron spectra with no filter and with a B_4C filter are compared in Fig. 14.

The spectral distribution of neutrons emitted from a finite hydrogenous moderator may be characterized by an epithermal component given by

$$\varphi(E) = \frac{\varphi_{epi}}{E^{\gamma}} \qquad (5)$$

where $\varphi(E)$ is the differential neutron flux (n/p·eV·sr), φ_{epi} is a constant, and the departure of γ from unity is indicative of neutron leakage. The thermal neutron differential flux can be represented by a Maxwellian-type distribution given by

$$\varphi(E) = \varphi_m \frac{E}{T^2} \exp(-E/T) \qquad (6)$$

where φ_m is the integrated Maxwellian intensity, and T is the neutron temperature in energy units. The characterization of the neutron

spectrum (in between the epithermal and thermal regions) can be completed by introducing a joining function $\Delta(E)$ given by [12]

$$\varphi(E) = \varphi_m \frac{E}{T^2} \exp(E/T) + \Delta(E) \frac{\varphi_{epi}}{E^{\gamma}}. \qquad (7)$$

An example of such a function is

$$\Delta(E) = \left[1 + \exp\left(\frac{W_1}{\sqrt{E}} - W_2\right)\right]^{-1}, \qquad (8)$$

which switches on at an energy-

$$E' = \left[\frac{W_1}{W_2}\right]^2, \qquad (9)$$

and W_2 is a measure of the spread of the switch function.

We analyze our data in the following manner:

- The slowing down neutron spectrum is characterized by fitting the data to Eq. (5) using φ_{epi} and γ as parameters.
- The Maxwellian is characterized by fitting the data to Eq. (6) using φ_m and T as parameters.
- With φ_{epi}, γ, φ_m, and T fixed, the parameters W_1 and W_2 are used to fit Eq. (7).

Both the individual fits (dashed lines) and the overall fit (solid lines) are illustrated in Fig. 15. The open circles indicate the limits of the fitting regions for the Maxwellian and slowing down portions of the spectra.

RESULTS AND DISCUSSION

We have used the spectral characterization just described to evaluate the performance of the WNR reflected 'T'-shape premoderator/moderator. We present here preliminary experimental results which are relevant to all pulsed spallation neutron sources. Our studies include the effects on moderator neutronics of varying the following: a) reflector size, b) reflector material, c) thickness and type of poison between the premoderator and moderator, and d) moderator thickness.

The neutronic performance of an unreflected 'T'-shape premoderator/moderator (see Fig. 6.) was also measured. We observed an increase of 3.9 in thermal neutron production and an enhancement of 3.5

in the slowing down region when the 'T' was surrounded by a beryllium reflector (an 'effective' cube with a side of ~45 cm). These data are shown in Fig. 16. The reflector was decoupled from the moderator by a 0.076-cm-thick Cd poison (see Fig. 8).

For a moderating reflector like beryllium and a decoupled moderator, Monte Carlo studies show that thermal neutron beam intensities quickly saturate with increasing reflector size. Neutrons scattered deep in the reflector are thermalized by the beryllium and absorbed in the decoupler; they cannot contribute to an increase in neutronic performance. For neutrons decoupled at 0.5 eV, saturation is expected to occur for a reflector radius of ~30 cm.[9] For a reflector dimensions of ~45 cm on a side comapred to ~61 cm, our data show an increase in thermal neutron beam intensity of ~15% (see Fig. 16); this is consistent with the Monte Carlo predictions.

Beryllium is the traditional candidate for a spallation neutron source reflector; we will investigate the neutronic performance of other reflector materials. We will refer to moderating reflectors like beryllium, water, etc. as 'slow' reflectors; we will call non-moderating reflectors such as copper, lead, etc., 'fast' reflectors. In future studies, we will investigate the necessary decoupling energy for 'slow' reflectors and the need for decoupling 'fast' reflectors; we will also compare the neutronic performance of different reflector materials.

In Fig. 17, we show neutron spectral comparisons from a standard moderator configuration surrounded by (decoupled) beryllium, (undecoupled) polyethylene, and (decoupled) lead/beryllium reflectors. The beryllium reflector produces a slowing-down flux ~2.3 times that for a polyethylene reflector; in the thermal region, the beryllium reflector outperforms the hydrogenous reflector by at least a factor of 2. These results are consistent with Monte Carlo studies.[13,14] The computations also show that for all decoupler energies of interest ($\lesssim$50 eV), a beryllium reflector outperforms a polyethylene reflector. The data in Fig. 17 for the lead/beryllium reflector compared to the beryllium reflector show a performance drop of ~12%. The improvised lead/beryllium reflector consisted of lead bricks crudely surrounding the premoderator (see Fig. 8) placed on a beryllium base. Computations and experiments not only indicate comparable neutronic performance between lead and beryllium reflectors, but the time-structure of neutron pulses with the lead reflector may be marginally superior.[14,15]

Data sets comparing cadmium and gadolinium poisons are shown in Fig. 18. Above ~1 eV, the effects of both poisons are similar; below ~0.2 eV, an enhancement of ~1.7 in the performance of the gadolinium poison is evident.

In Figs. 19 and 20, we show the observed thermal neutron production as a function of poison thickness and moderator thickness. These data, used in conjunction with measured neutron pulse width measurements, will be used to match moderators to the requirements of the instruments for the WNR materials science program.

TIME-ANALYZER ARM

The reduction and analysis of neutron time distribution data taken with the time-analyser arm are in a preliminary stage. We note:

- Excellent signal-to-background ratios (~100:1) have been achieved allowing orders up to (0 0 24) from PG to be clearly seen (see Fig. 21).
- Subtle differences in line shape between moderator configurations are clearly seen (see Fig. 22 and 23).

Exploitation of the capability to measure neutron pulse widths (in conjunction with neutron beam fluxes and spectra) will form a major part of our future efforts.

FUTURE PLANS

Combined neutron spectral and pulse width measurements will be used for continued optimization of the WNR spallation neutron sources. Our experimental and computational program will include:

- premoderator optimization,
- moderator-reflector and target-reflector decoupling studies,
- target material and size optimization,
- target-moderator-reflector coupling studies,
- reflector material investigations,
- cold moderator studies, and
- implementation of capability to study neutron beam quality.

ACKNOWLEDGEMENTS

This work was performed under the auspices of the U. S. Department of Energy. We acknowledge the support and encouragement of R. Woods, and useful discussions with J. M. Carpenter. We appreciate the help of J. R. Baldonado and K. J. Hughes in setting up the experiments, and E. R. Whitaker in the experiment design. We acknowledge the cooperation of the WNR operations crew of R. D. Ryder (head), H. M. Howard, R. A. Johnson, and M. R. Lopez.

REFERENCES

1. G. J. Russell, et al., "The WNR Facility--A Pulsed Spallation Neutron Source at the Los Alamos Scientific Laboratory," Intl. Conf. on Neutron Physics and Nucl. Data for Reactors and Other Applied Purposes, Harwell, England (1978).

2. M. S. Livingston, "LAMPF a Nuclear Research Facility," Los Alamos Scientific Laboratory report LA-6878-MS, UC-28 and UC-34 (September 1977).

3. G. J. Russell, et al., "Spallation Target-Moderator-Reflector Studies at the Weapons Neutron Research Facility," Symp. on Neutron Cross Sections from 10-50 MeV, Brookhaven National Laboratory, Upton, NY, May 12-14, 1980, BNL-NCS-51245, Vol. I, pp. 169-192.

4. G. J. Russell, et al., "Measurements of Spallation Target-Moderator Reflector Neutronics at the Weapons Neutron Research Facility," Proc. of the 4th Meeting of the International Collaboration on Advanced Neutron Sources (ICANS-IV), National Laboratory for High Energy Physics (KEK), Tsukuba, Japan, October 20-24, 1980, KENS report II (March 1981).

5. T. W. Armstrong and K. C. Chandler, "Operating Instructions for the High Energy Nucleon Meson Transport Code HETC," Oak Ridge National Laboratory report ORNL-4744 (January 1972).

6. Los Alamos Monte Carlo Group, "MCNP--A General Monte Carlo Code for Neutron and Photon Transport, Version 2B," Los Alamos National Laboratory report LA-7396-M, Revised (April 1981).

7. H. Kschwendt and H. Rief, "TIMOC--A General Purpose Monte Carlo Code for Stationary and Time Dependent Neutron Transport," Euration report EUR 4915e (1970).

8. D. Picton, Ph. D. Thesis, University of Birmingham, U. K. (1981).

9. A. D. Taylor, "Neutron Transport from Targets to Moderators," Proc. of Meeting on Targets for Neutron Beam Spallation Sources, Jül-Conf-34 ISSN 0344-5798 Jülich (1980).

10. V. Agoritsas and R. L. Witkover, "Tests of SEC Stability in High Flux Proton Beams," IEEE Trans. on Nucl. Science, Vol. NS-26. No. 3, pp. 3355-3356 (1979).

11. J. M. Carpenter, et al., "IPNS--A National Facility for Condensed Matter Research," Argonne National Laboratory report ANL-78-88 (November 1978).

12. K. H. Beckurts and K. Wirtz, Neutron Physics, (Springer-Verlag, New York Inc., 1964) Ch. 10.

13. G. J. Russell, Los Alamos Scientific Laboratory, unpublished data, December 1973.

14. A. D. Taylor, "Monte Carlo Reflector Studies for a Pulsed Spallation Source," these proceedings.

15. G. S. Bauer, et al., "Measurement of Time Structure and Thermal Neutron Spectra for Various Target-Moderator-Reflector Configurations of an Intensity-Modulated Spallation Neutron Source," Realisierungsstudie zur Spallations-Neutronenquelle, Teil II (to be published.)

TABLE I
PROGRAM FOR MEASURING SPALLATION TARGET-MODERATOR-REFLECTOR NEUTRONICS AT THE WEAPONS NEUTRON RESEARCH FACILITY

GENERAL GOALS

- Obtain basic data relevant to spallation neutron source development, accelerator breeder technology, and computer code validation
- 'Optimize' a target-moderator-reflector configuration for materials science research at the present WNR and any upgraded WNR
- Characterize WNR targets and moderators for nuclear physics applications

SPECIFIC OBJECTIVES

- Measure the effects of different targets, moderators, reflectors, and decouplers on thermal and epithermal neutron beam fluxes and thermal neutron pulse widths
- Ascertain the 'practical' gain of a uranium spallation target (versus lead, tantalum, tungsten, etc.) by measuring thermal neutron beam fluxes and pulse widths
- Measure the high-energy neutron and particle contamination in thermal neutron beams for offset and center-looking geometry
- Study neutron yields and pulse widths from cold moderators
- Measure neutron production and spectra from thin and thick targets
- Measure the fertile-to-fissile conversion yields inside thick targets of thorium and depleted uranium
- Measure energy deposition in spallation targets and cold moderators
- Compare all measurements with calculated predictions

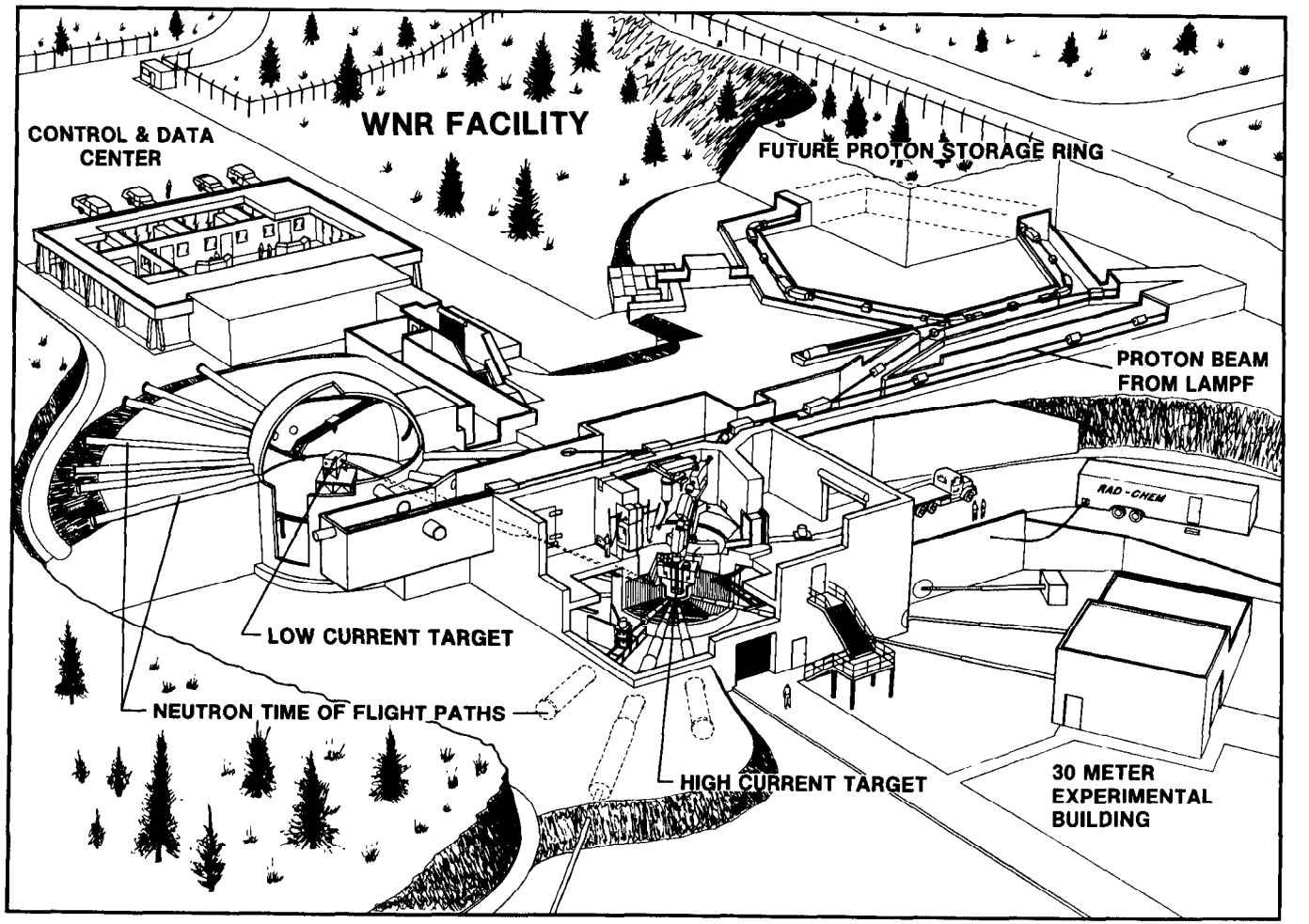

Fig. 1. General layout of the WNR showing the two target areas. The high-current target is located in a vertical proton beam and is viewed by 11 horizontal flight paths. The low-current target is located in a horizontal proton beam and viewed by 11 horizontal flight paths and one vertical flight path.

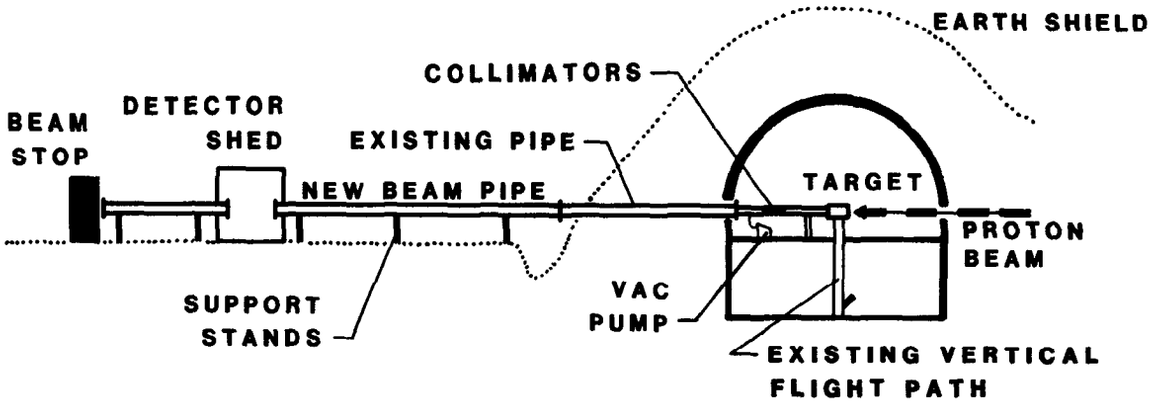

Fig. 2. Section through the low-current target area showing the location of the vertical flight path.

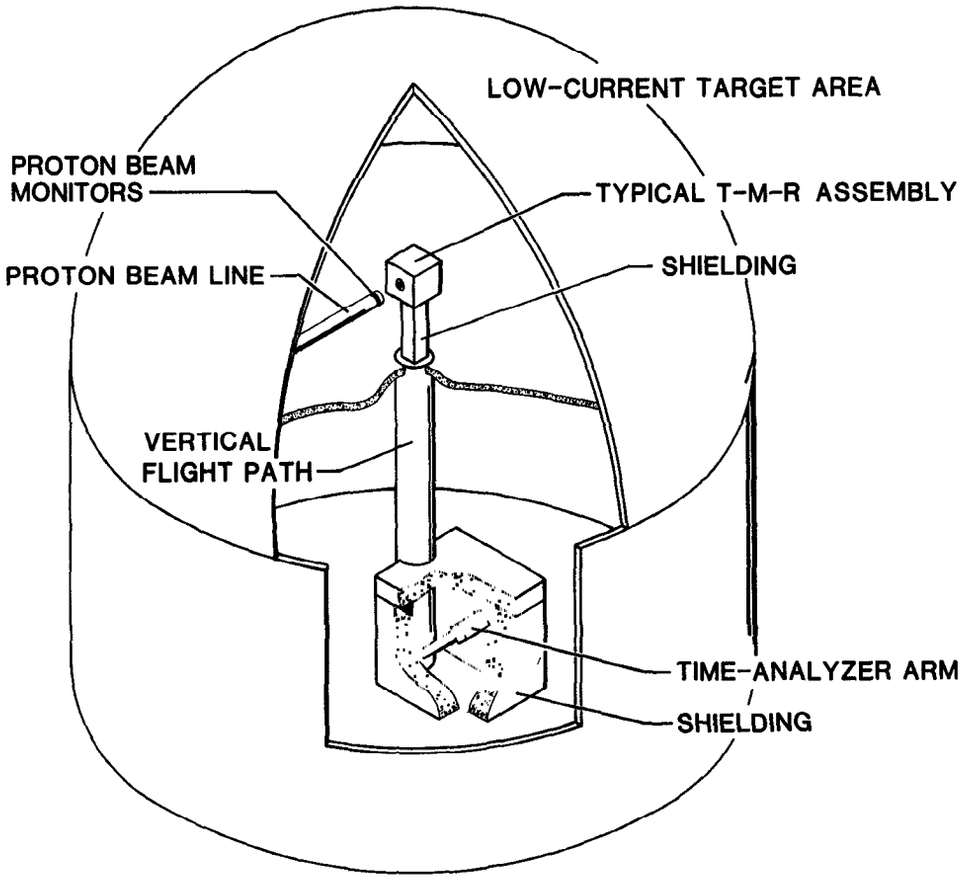

Fig. 3. Location of a target-moderator-reflector assembly, the vertical flight path, and the time analyzer arm in the low-current target area.

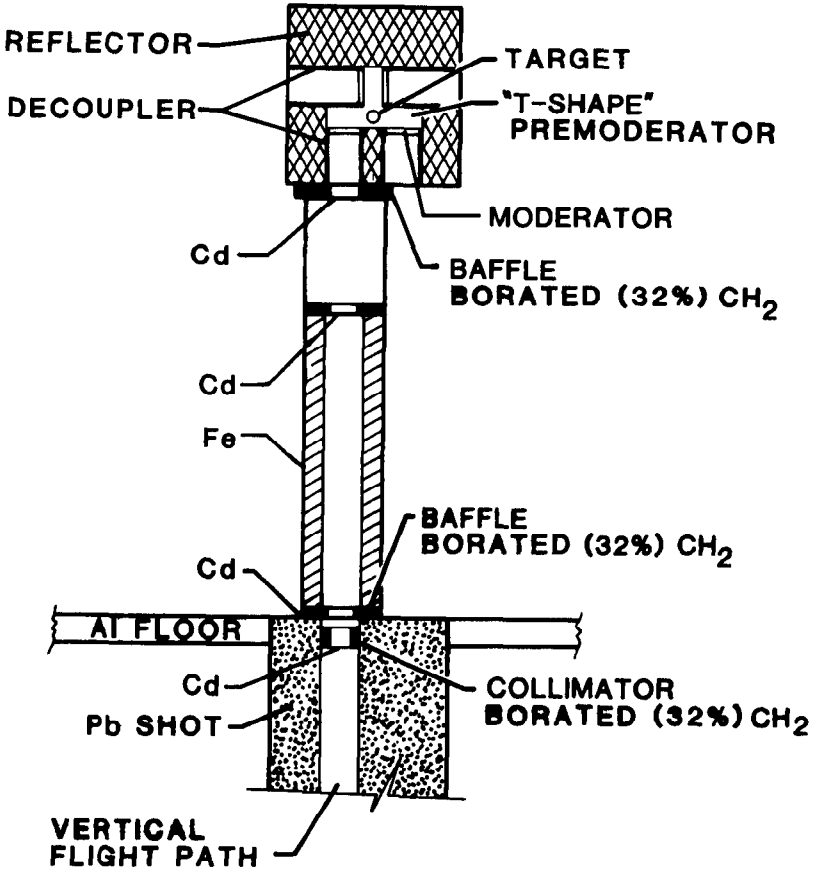

Fig. 4. Detail of the upper portion of the vertical flight path.

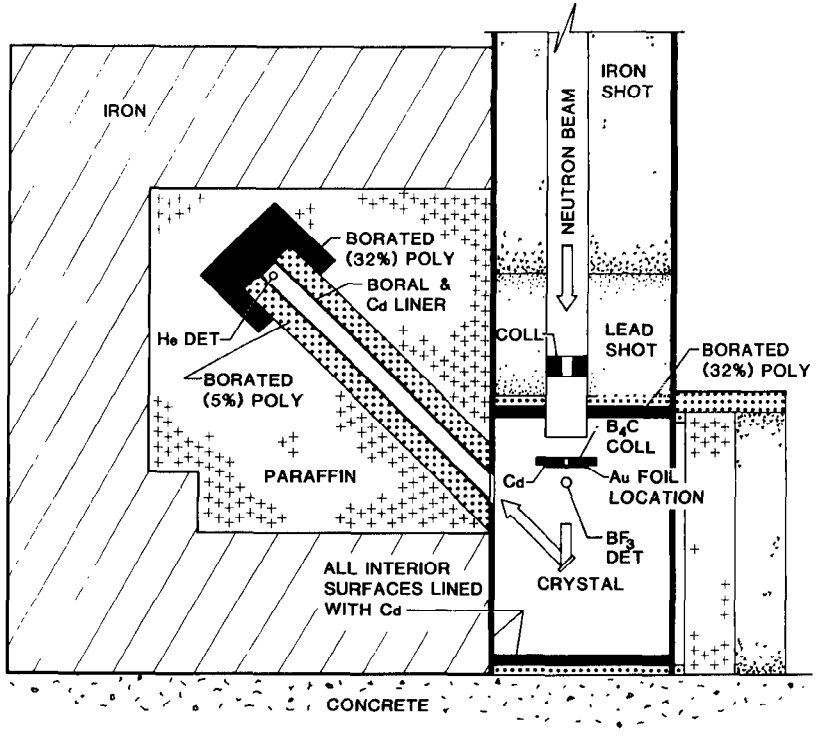

Fig. 5. Detail of the time analyzer arm and location of the BF_3 detector at the bottom of the vertical flight path.

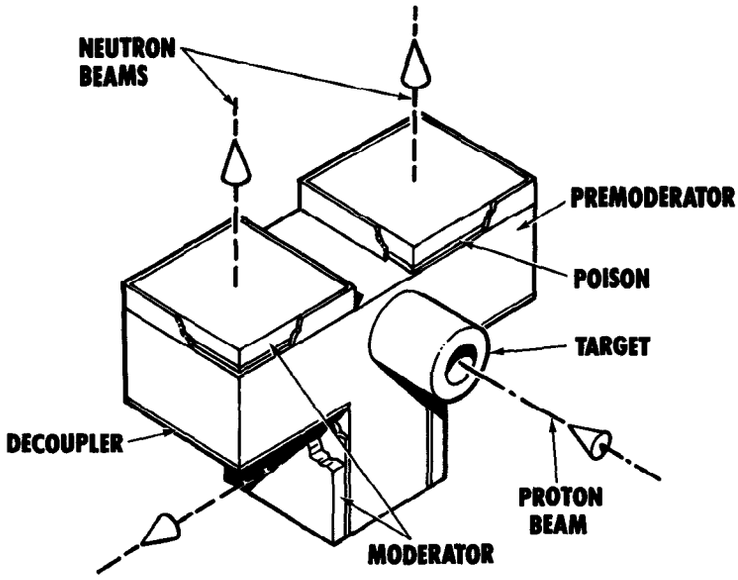

Fig. 6. Unreflected 'T'-shape premoderator/moderator.

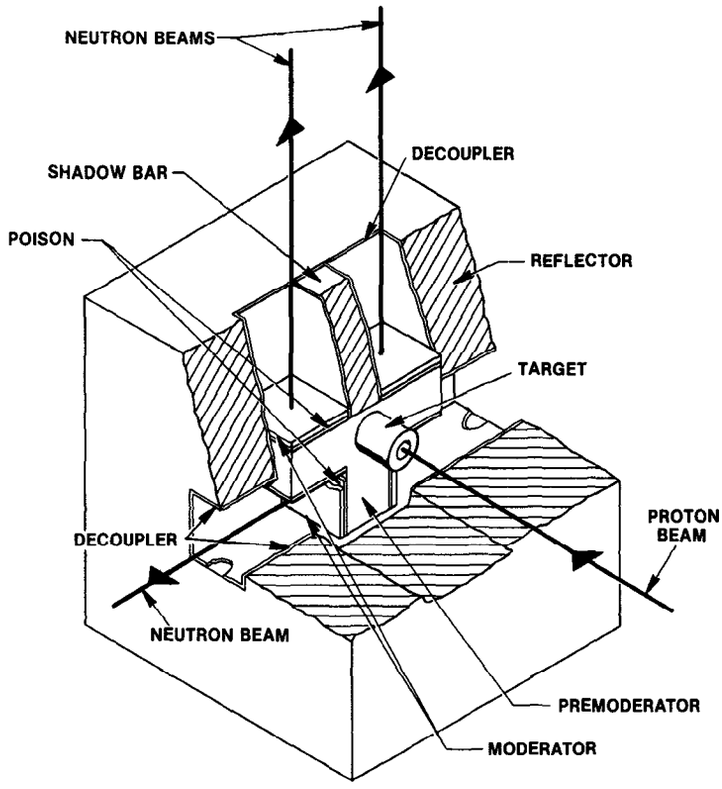

Fig. 7. Reflected 'T'-shape premoderator/moderator.

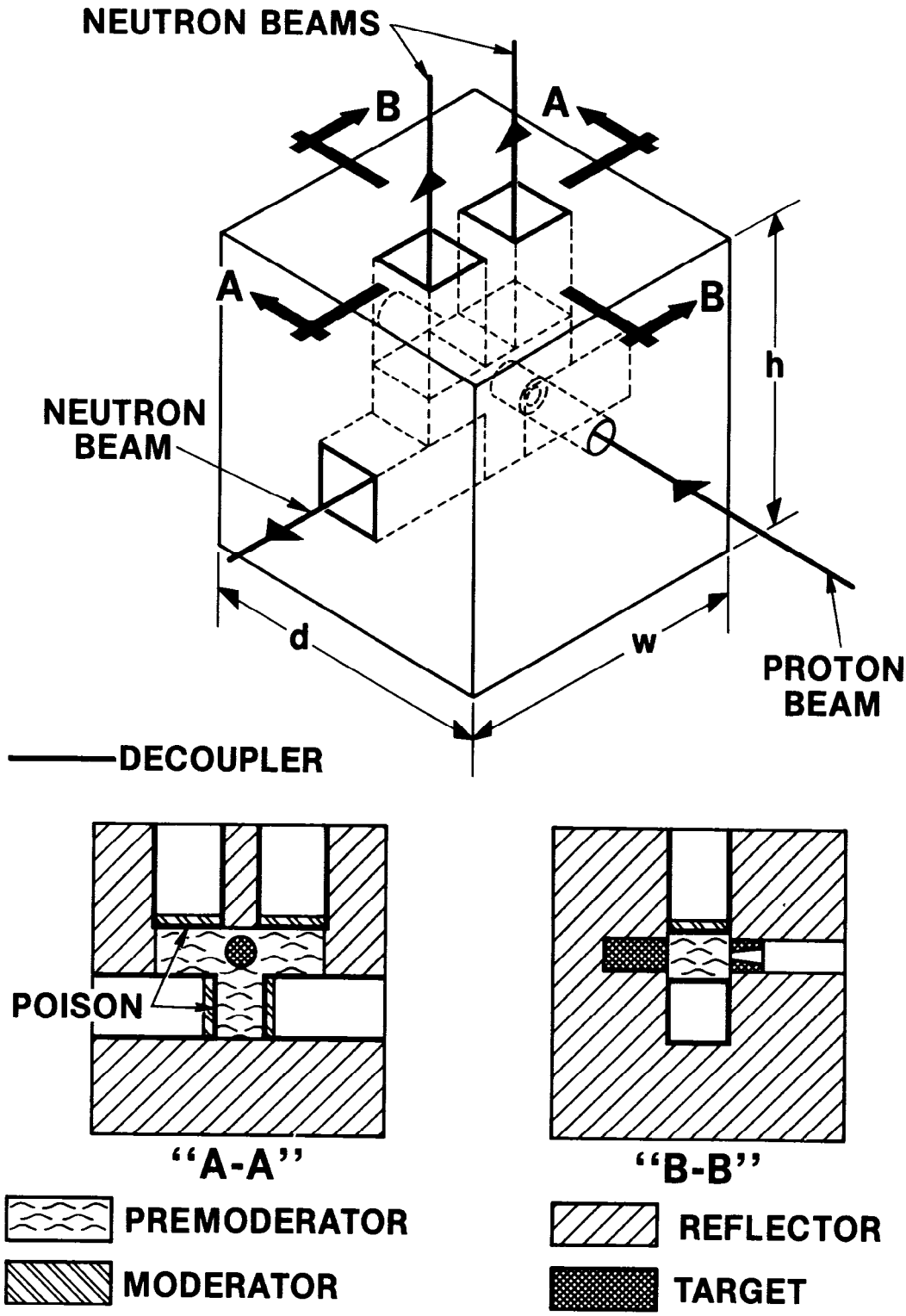

Fig. 8. Section thru a reflected 'T'-shape premoderator/moderator.

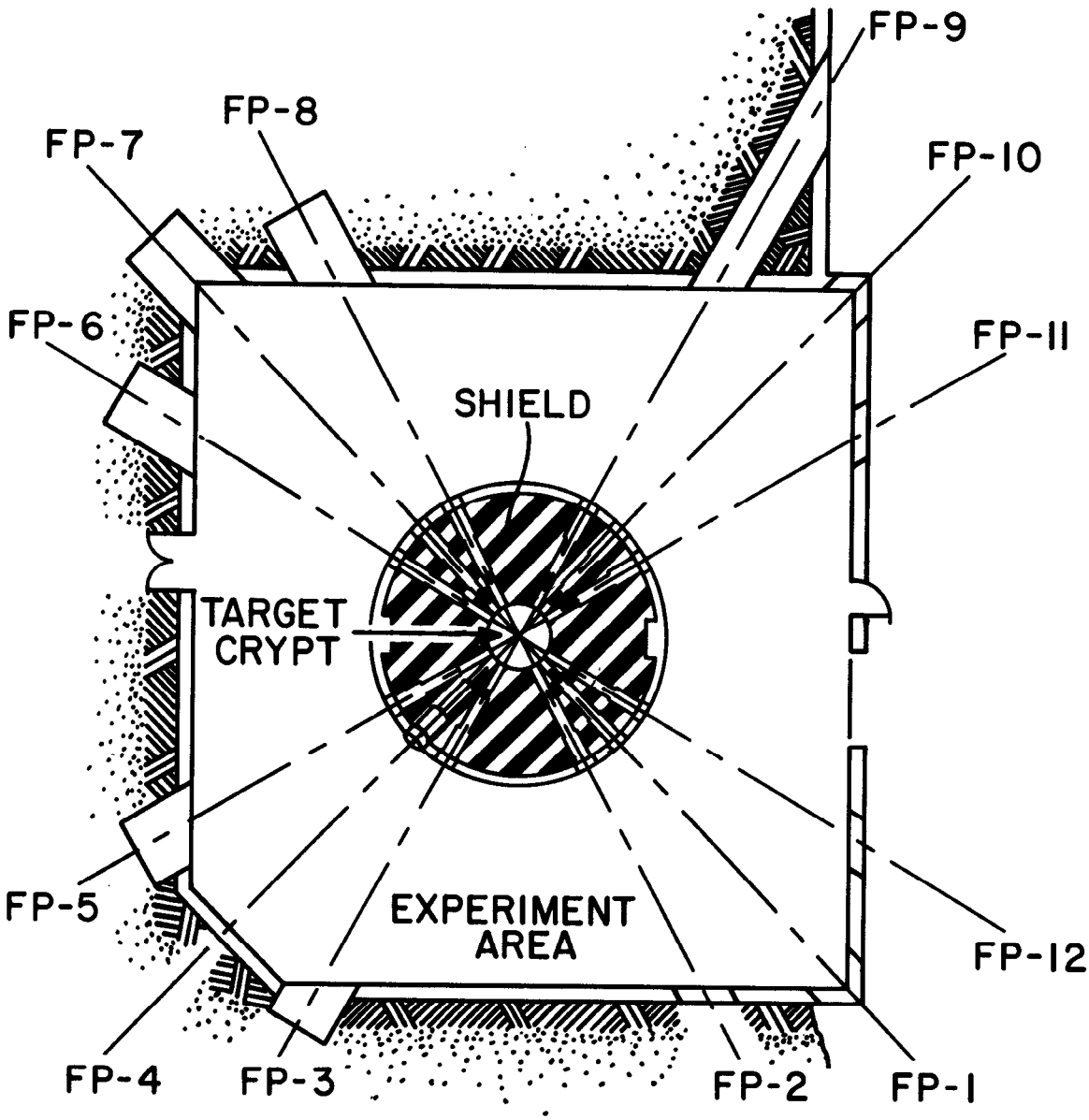

Fig. 9. Layout of the neutron flight paths in the WNR high-current target area.

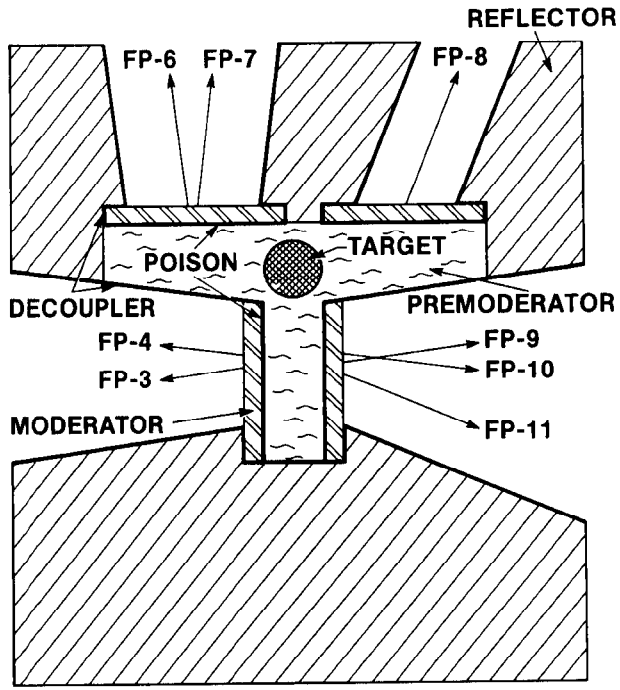

Fig. 10. Section through a reflected 'T'-shape premoderator/moderator configuration showing the location of various neutron flight paths (in the WNR high-current target area) relative to moderator surfaces.

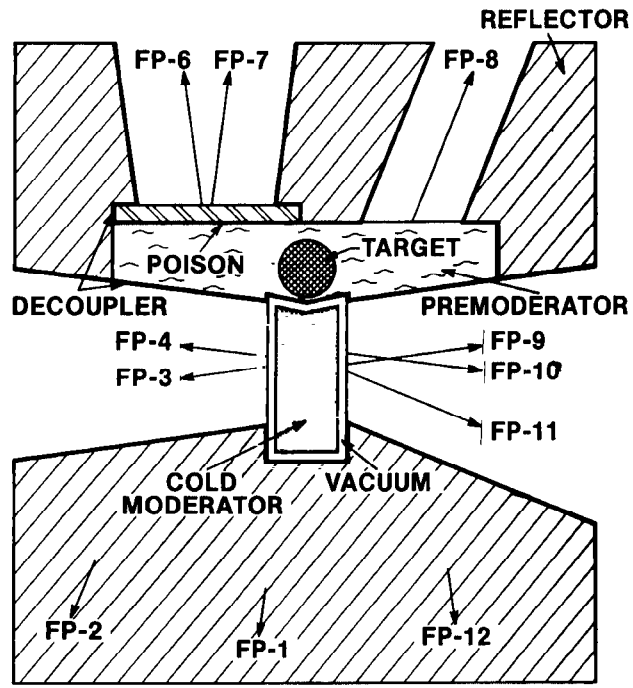

Fig. 11. A possible reflected 'T'-shape premoderator/moderator configuration in which the various moderators are 'optimized' for each cluster of flight paths in the WNR high-current target area.

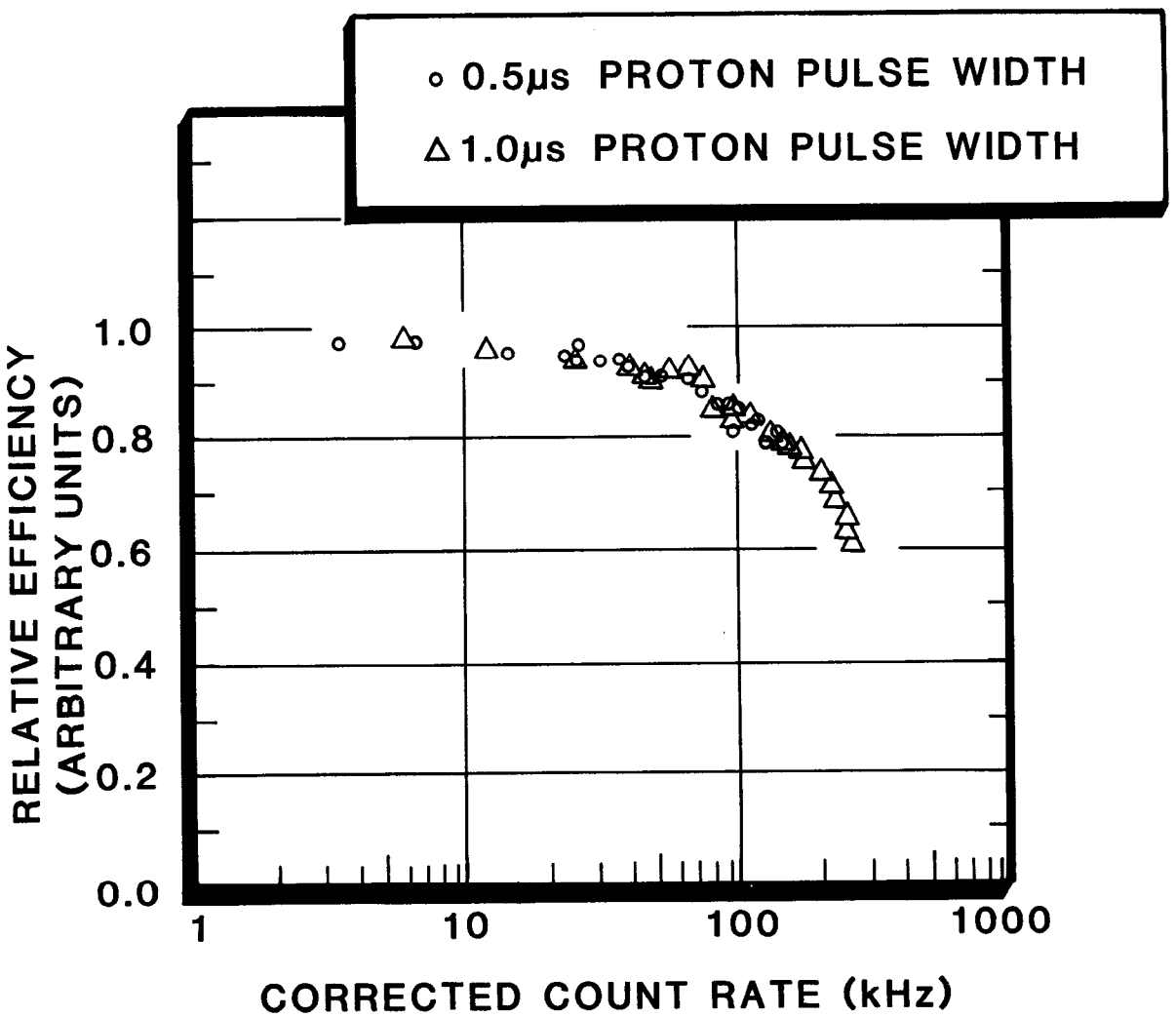

Fig. 12. Count rate dependence of BF_3 detector response.

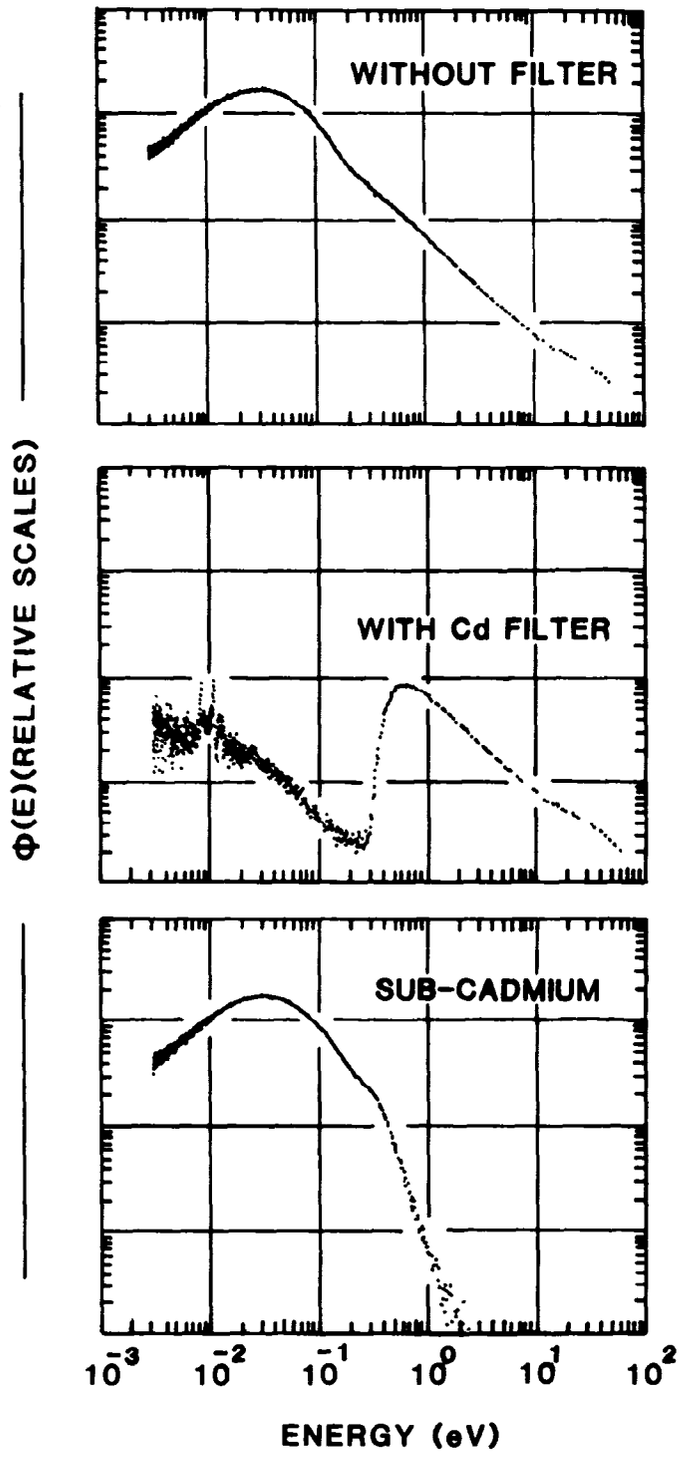

Fig. 13. Measured neutron spectra with and without a cadmium filter. The difference between these two spectra gives the sub-cadmium neutron spectrum.

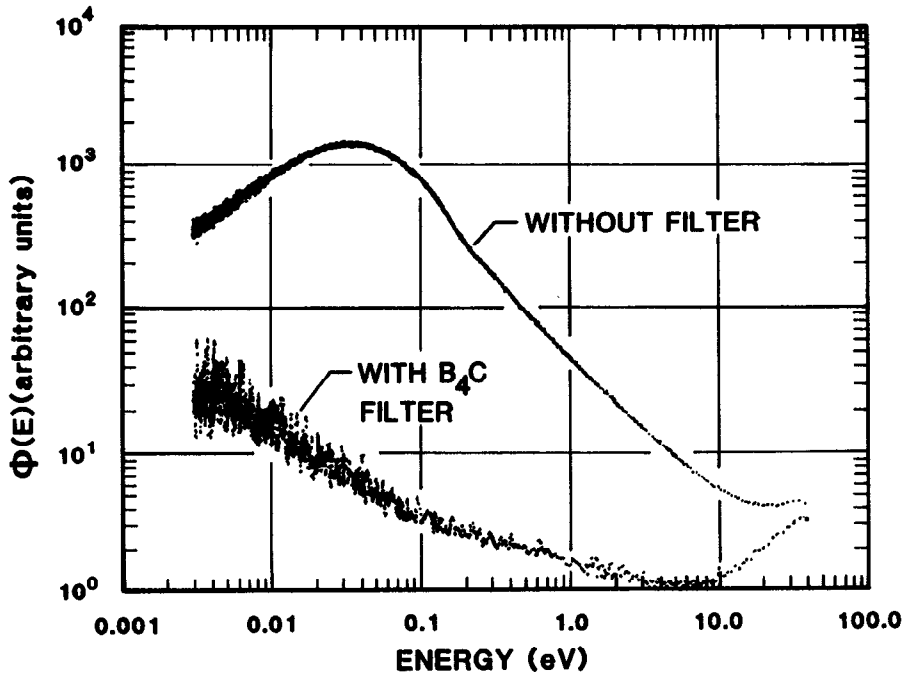

Fig. 14. Measured neutron spectra with and without a B_4C filter.

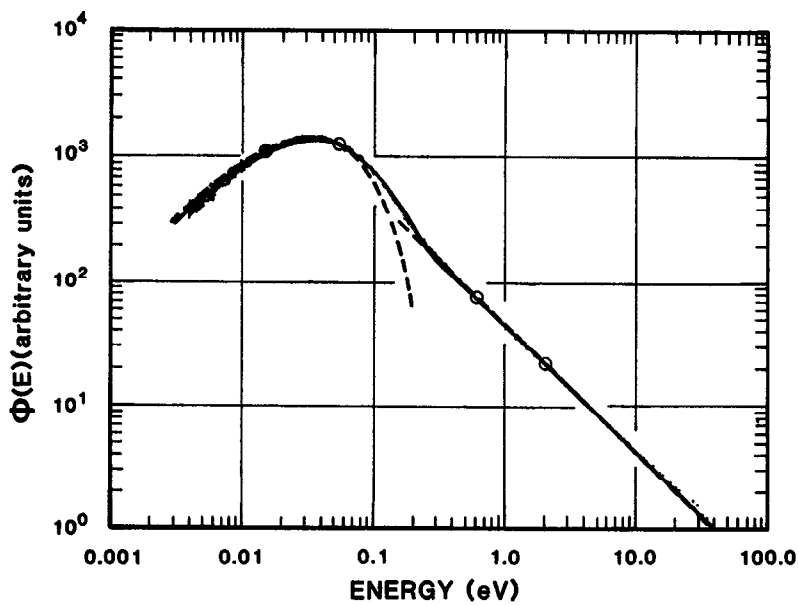

Fig. 15. A fit of Eq. 7 in the text to a representative data set. The dashed lines are independent fits to the Maxwellian and slowing down portions of the spectrum. The solid curve is the overall six parameter fit using a joining function.

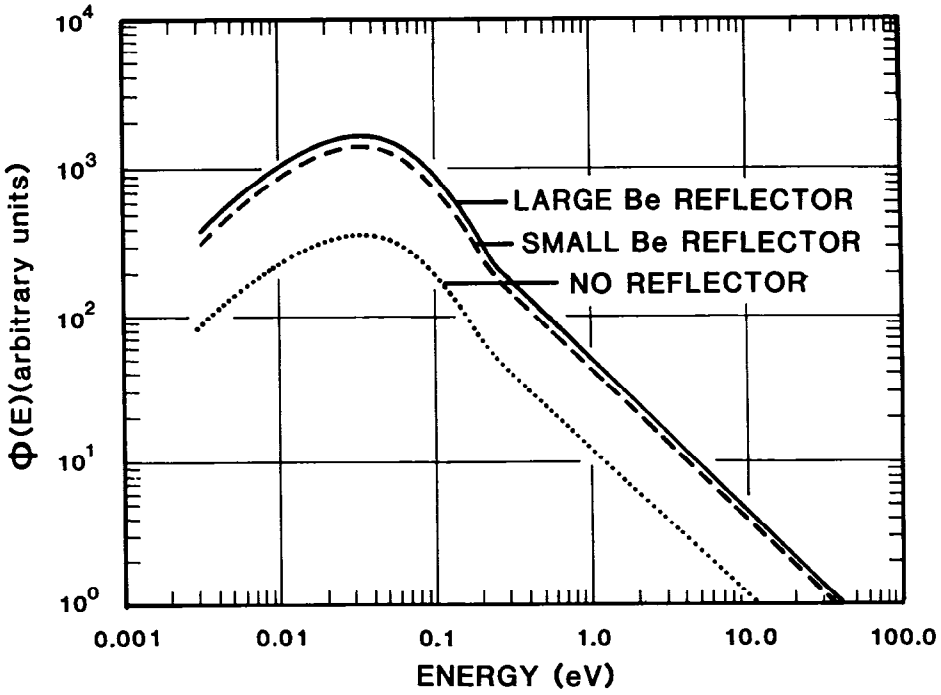

Fig. 16. Measured neutron spectra using a large and small beryllium reflector. The measured neutron spectrum from a unreflected system is also shown.

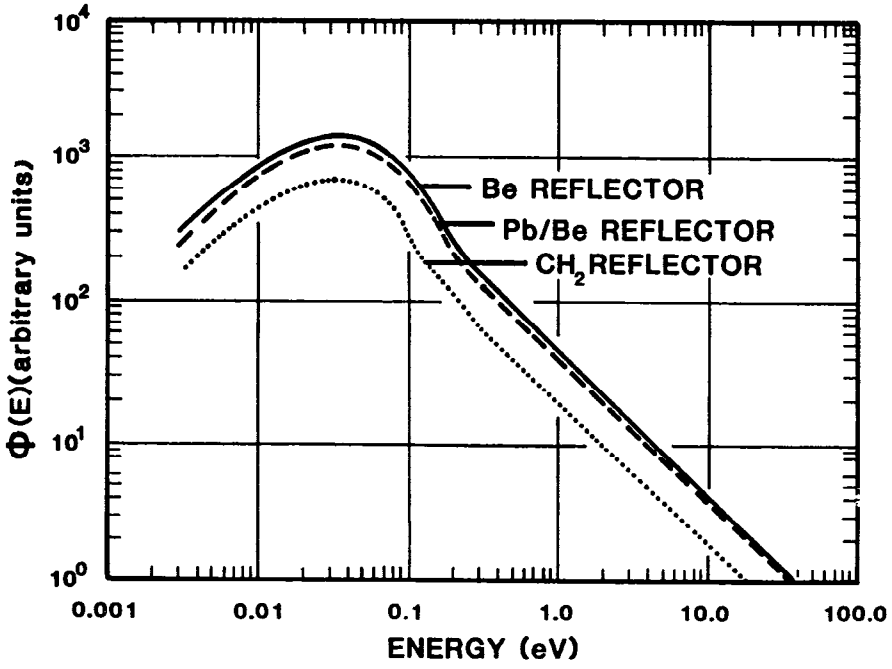

Fig. 17. Measured neutron spectra using beryllium, polyethylene, and beryllium-lead reflectors.

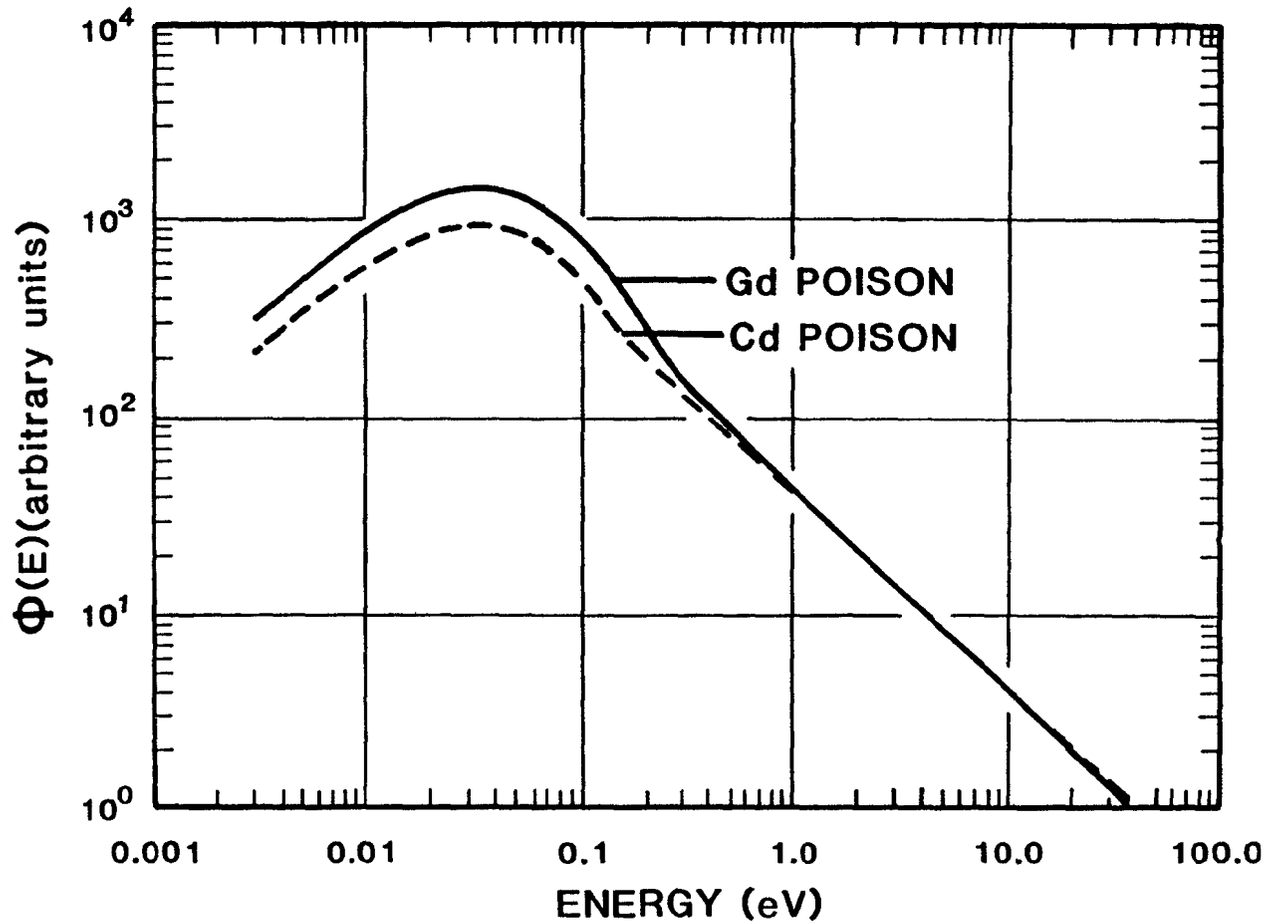

Fig. 18. Measured neutron spectra from a moderator poisoned at a depth of 1.27 cm by gadolinium and cadmium. The gadolinium was 0.0025-cm thick, and the cadmium was 0.076-cm thick.

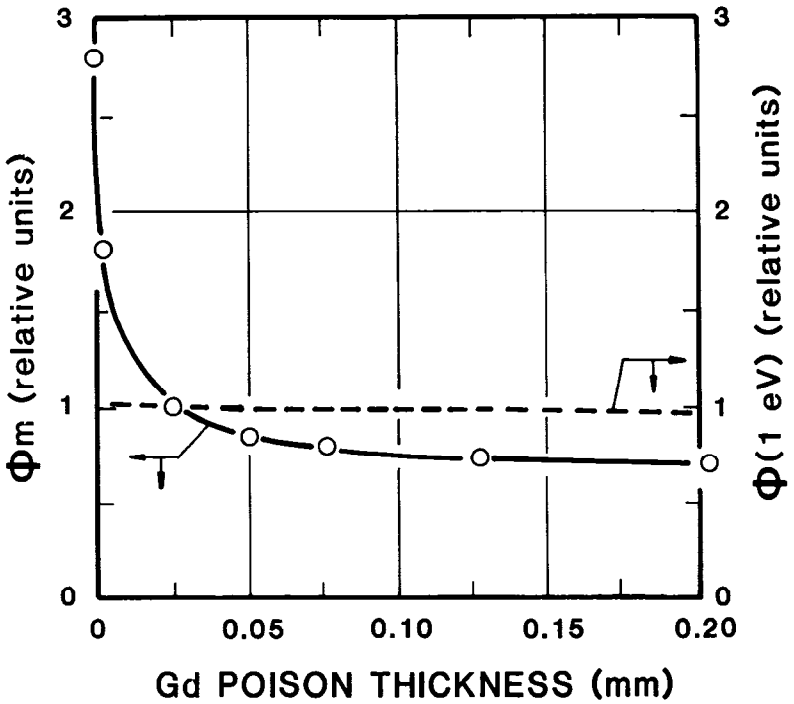

Fig. 19. Variation of measured thermal and 1-eV neutron fluxes from a moderator as a function of gadolinium poison thickness.

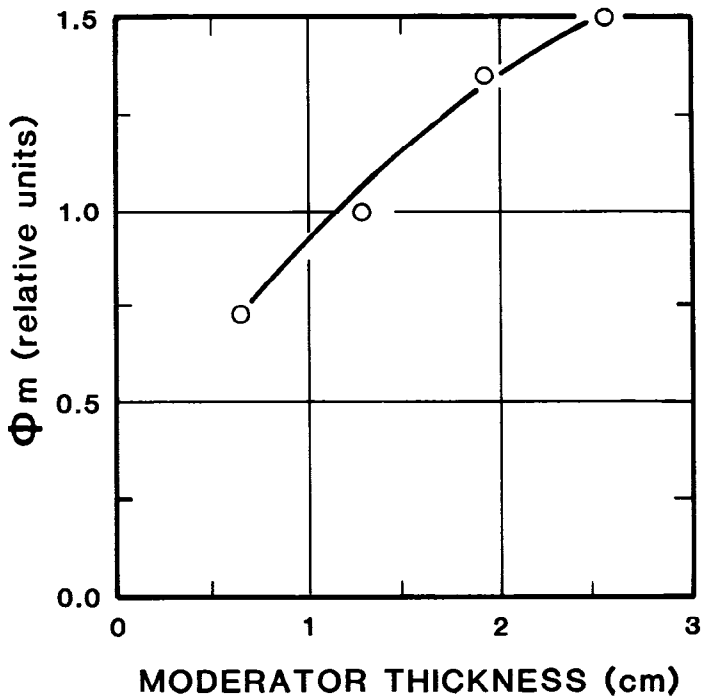

Fig. 20. Variation of measured thermal neutron flux from a moderator as a function of moderator thickness.

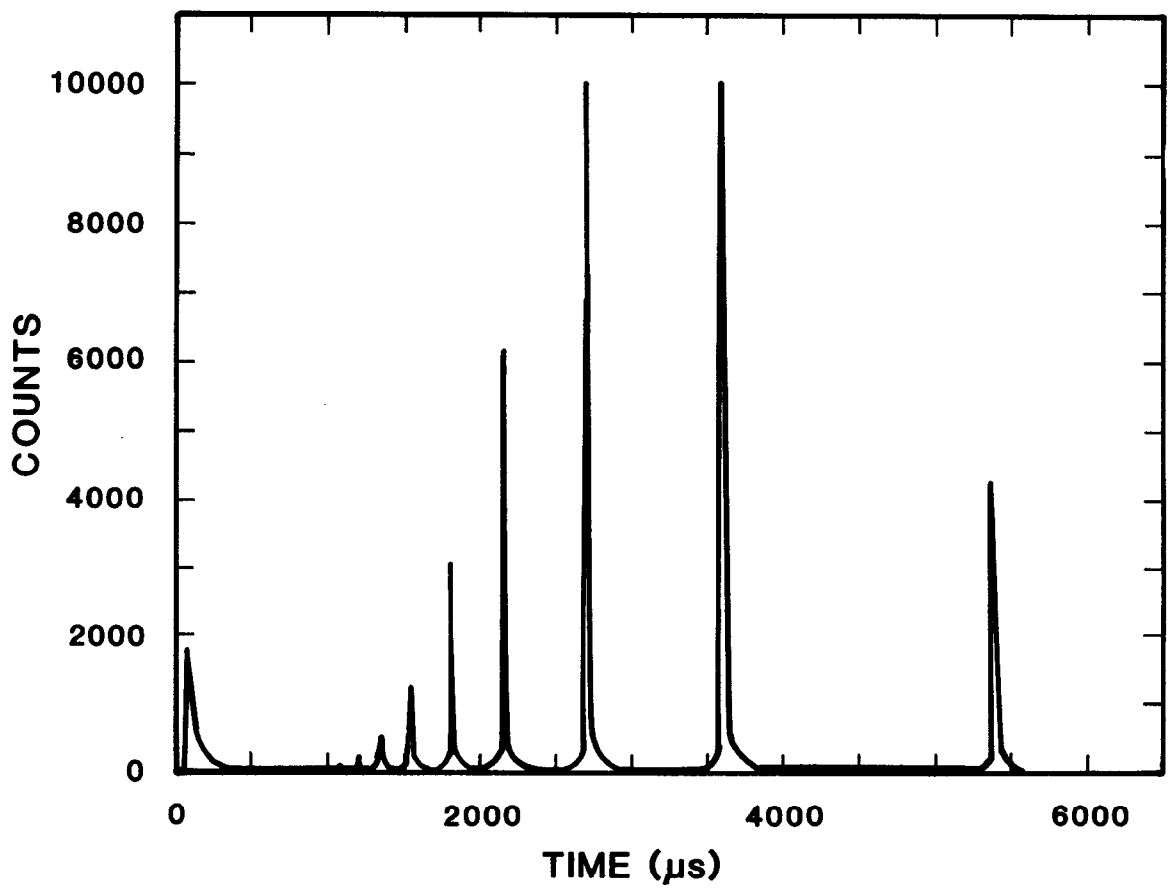

Fig. 21. Time distribution of neutrons diffracted by the (0 0 2ℓ) planes of pyrolitic graphite, starting with the (0 0 4) reflection.

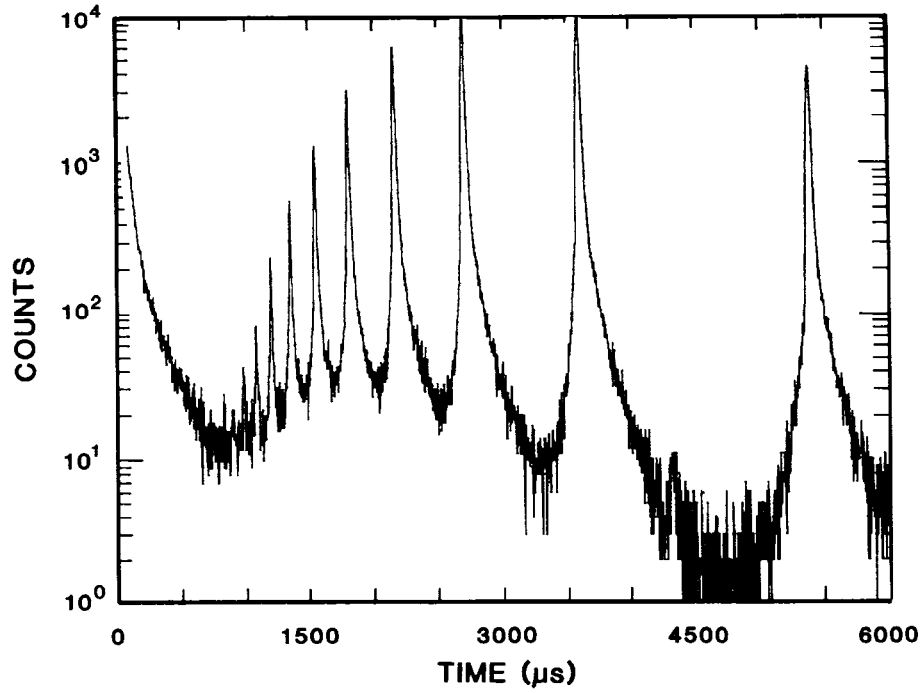

Fig. 22. Semi-log plot of measured neutron time distributions from a gadolinium poisoned moderator.

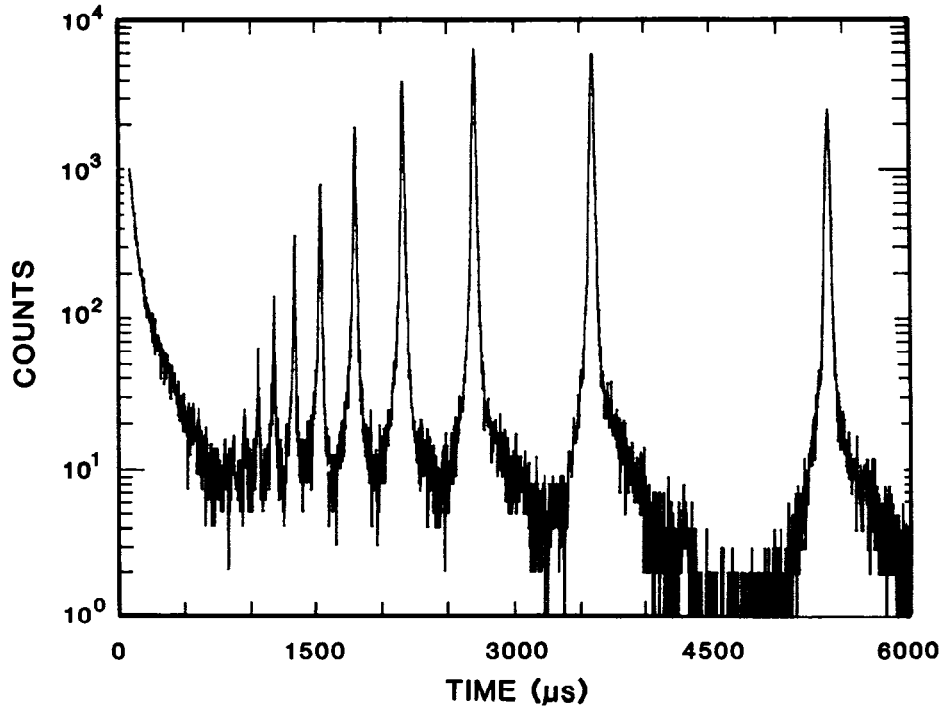

Fig. 23. Semi-log plot of measured neutron time distributions from a cadmium poisoned moderator.

Jül-Conf-45 D2-3

I C A N S - V

MEETING OF THE INTERNATIONAL COLLABORATION ON

ADVANCED NEUTRON SOURCES

June 22-26, 1981

Relative Intensities and Time Structure of Thermal Neutron Leakage from Various Moderator-Decoupler Systems for a Spallation Neutron Source

G.S. Bauer, J.P. Delahaye**, H. Spitzer*, A.D. Taylor+ and K.Werner**

* Institut für Festkörperforschung, Kernforschungsanlage Jülich
D-5170 Jülich, West Germany

** Division PS, CERN, CH-1200 Geneva

+ Rutherford and Appleton Laboratories, Chilton, Didcot, OX11 OQX, UK

Abstract

Measurements were performed using the short bursts of 800 MeV protons at the CERN booster synchrotron to study the effect of surface structure, decoupling and poisoning of moderators on the intensity and time structure of a spallation neutron source. It was found that grooves in the moderator surface can enhance the neutron leakage by almost a factor 2 for poisoned and decoupled moderators as well as for non-decoupled ones, with only a minor effect on the time structure. Also, it could be shown that Cd with a decoupling energy of only 0.4 eV can replace B_4C with a decoupling energy of 3 eV with almost no effect on the time structure. This makes it much easier to provide decoupler cooling in a real design.

1. Introduction

In recent years there has been a growing interest in pulsed neutron sources based on the spallation reaction as induced by energetic particles impinging on heavy nuclei (see e.g. J.M. Carpenter, 1977). These sources are accelerator driven and can therefore be designed with a high degree of flexibility with respect to time structure and neutron spectral distribution. Similar to the case of a fission reactor, the neutrons are originally generated with a kinetic energy around 1 MeV and have to be slowed down to energies below 1 eV to be used in the condensed matter research for which such sources are designed. In these sources moderators are placed close to the target, and to increase their efficiency, they are surrounded by a fast neutron reflector. The task in designing such a system is threefold:

(1) Provide as intense a neutron beam as is possible

(2) Provide neutron bursts of very short duration

(3) Find a design which is technically feasible with respect to space requirements and heat removal.

Generally the figure of merit for a pulsed neutron source is taken as

$$M = \frac{I(E)}{(\Delta t(E))^2}, \qquad (1)$$

where I is the neutron current emerging from the moderator surface and Δt is the width of the pulse of neutrons of energy E.

To achieve short pulses, the moderator is surrounded by a layer of material called decoupler (see Fig. 1), which ideally is transparent for fast neutrons but opaque for thermal and slow neutrons. If a 1/v-absorber, such as boron-10 is used, one has a high degree of flexibility in choosing the effective decoupling energy by adjusting the thickness of the boron layer (Taylor, 1979). 2.3 MeV of energy is, however, released by the absorption process and appears as kinetic energy of the recoil fragments (Li-7 and He-4). This energy is deposited locally, making such a decoupler difficult to cool. It is therefore desireable to use an (n,γ) absorber such as cadmium or gadolinium so that the reaction energy may be dissipated over an extended volume. Similar considerations hold for the heterogeneous poison (Fig. 1) embedded in the moderator to avoid too long a time spread due to neutrons emerging from deep inside the moderator.

On the other hand, it had been found (Bauer et al, 1980) that the integrated leakage of neutrons from a hydrogeneous moderator can be considerably increased by not using a flat surface moderator but working a series of grooves into the surface. These have the effect of extracting neutrons from the higher flux inside the moderator.

It was the purpose of the present experiments, to study the effect of using low energy decouplers (like Cd, with a decoupling energy of 450 meV) and grooved surface moderators on the intensity and time structure of the extracted thermal neutron beam.

2. Experimental setup and -procedure

The measurements were performed at the end of the measurement line of the 800 MeV CERN booster synchrotron (PSB). This synchrotron is part of the CERN ring system (Fig. 2). It takes protons from the 50 MeV linac and, after acceleration to 800 MeV delivers them to the 28 GeV PS-ring (PSR) which in turn can serve the Super Proton Synchrotron (SPS), Intersecting Storage Rings (ISR) or the 28 GeV experimental areas. The cycle time of these systems being an integral multiple of the cycle time of the booster (0.8 sec), there are spare cycles available at the booster where parasitic use of accelerated particles is possible. Depending on the mode of operation of the other facilities, the separation between these parasitic pulses may be up to 2.4 sec. The maximum number of protons that can be accelerated in the four rings of the PSB is 2×10^{13}. In each ring the pulse train of 5 pulses is 0.6 μs long and the four pulse trains can be combined to give one pulse train of 20 pulses and 2.4 μs long (Fig. 3). If pulses from less than four rings are used, there results an even shorter proton burst. In most of our measurements only ring 3 was used with 5×10^{11} protons accelerated. This was to minimize dead time effects in the detector.

The spallation target was located in front of the PSB beam dump. It consisted of solid lead, 400 mm long, 100 mm high and 600 mm wide. It was designed to simulate the geometry of the rotating target conceived for the high power spallation source presently under study in West Germany. The moderators used were 20 cm long blocks of polyethylene placed above the front end of the target. They were surrounded on three sides by 20 cm of beryllium to act as a fast neutron reflector. Only the moderators were changed in the course of the experiment. The target-moderator-reflector arrangement was mounted on a cart which could be remotely moved out of the path of the proton beam to make the PSB-beam dump available for normal use (Fig. 4). A stationary shield of 0.5 to 1 m thickness of iron and lead was put in place to avoid excessive radiation levels in the adjacent PSR-tunnel and to reduce the fast neutron return from the walls around the experimental setup.

A pyrolytic graphite crystal (mosaic 0.4° FWHM) was used to select neutrons of well-defined energies from the thermal spectrum emerging from the moderator and to diffract them onto a well shielded detector located at 5.19 m from the moderator (Fig. 5). A Soller type collimator, 5 cm high and with an aperture of 0.75° was placed between the moderator and the analyser crystal. The scattered beam was limited by a B_4C-slit 2 mm wide and 40 mm high (6 mm wide and 90 mm high for measurement N* of Table 1) at 342 cm from the detector which was an 8 atm He-3 detector of 12 mm diameter and 30 cm active length. As imposed by the spatial constraints, the analyzer was set at $2\,\theta_A = 90°$. It was mounted on a turntable which could be controlled remotely to move the analyser out of the beam for background measurements. A second motor provided a rocking adjustment about the $2\,\theta_A = 90°$ position.

The protons were monitored by an intensity transformer which delivered a signal between 0 and 5 volts whose height was proportional to the number of protons in a pulse train. This signal was digitized by an ADC and a pulse height analysis performed in the multichannel analyser. In this way the proton burst intensity distribution was measured and the total number of protons on the target was proportional to the first moment of this distribution. Examples of measured proton distributions are shown in Fig. 6. Each time a proton pulse train hit the target, a time circuit was triggered and the number of neutrons arriving

at the detector were analyzed as a function of time. With the energy defined by the scattering angle of the analyser crystal ($2\theta_A = 90°$), this yielded the time distributions of the neutrons of energies corresponding to the various orders of the crystal reflections.

3. Measurements and Data Evaluation

The moderators used are shown in Fig. 7. They were made of polyethylene and in general were 20 cm long and 10 cm high (18 cm long and 8 cm high for the case of the B_4C-decoupler). The "flat" moderators were 75 mm thick with the possibility of placing a heterogeneous poison (a 0.025 mm thick sheet of Gd) at 25 mm under the viewed surface. In the case of the "grooved" moderators, the front part was machined as shown in Fig. 7a to contain 15 mm deep grooves with 50 % of the material removed. They could be heterogeneously poisoned like the flat ones. Decouplers consisted either of 0.5 mm cadmium sheet surrounding the moderator and leaving a 100 x 100 mm^2 channel towards the analyser open or of 10 mm thick boron-loaded plastic (decoupling energy $\sim$ 3 eV) of the same shape (see Fig. 8). The combinations examined are given in Table 1 and are labelled according to the following notation: grooved moderators are marked by an asterix, the poison used is set in paranthesis and the decoupler is used for the characterization with N standing for no decoupler.

For each combination a run with the crystal analyser in place and one without analyser was taken. An example of the raw data is shown in Fig. 9 for run B_4C. The various orders of reflexions are superimposed on a strongly time-dependent continuum. This is caused by fast neutrons penetrating the shielding and getting slowed down somewhere near the detector. The minimum visible at about 400 μs corresponds to the Cd-resonance. (The shield of the detector had an inner layer of cadmium). For the first 200 μs the detector was saturated.

It was found that this continuous background was not only caused by fast neutrons emerging from the target but there seems to have been a strong contribution from beam spills at other positions along the beam line. This was confirmed by removing the target from the beam and measuring the background with the beam going into the beam dump. For this reason it was not possible to correct for the background by normalizing to the number of protons recorded.

However, it was found that, except in the region of the Bragg peaks, the ratio between signal and background was completely flat. This is examplified in Fig. 10, where this ratio is given in a logarithmic representation for the B_4C-run. The same is true, if the background measurements for the various runs are compared. It was therefore concluded that the continuum part of the data is independent of the moderator configuration used. Since the proton energy, target and shielding remained the same for all runs, the continuum in the region of the Cd-resonance (644 μs ÷ 720 μs), was used to normalize the spectral and background measurements.

Examples of spectra corrected for background in this way are shown in Figs. 11 through 15. From Figs. 11a, b and c the effect of decoupling and poisoning on the line width is clearly visible. Note that the plots are not normalized. A comparison between Figs. 12a and 12b shows that the grooves have no significant effect on the time structure. However, the relative intensities between the

reflections corresponding to different energies indicate that the grooved moderator produces a considerably softer neutron spectrum than does the flat one.

From Fig. 13, which is the same as Fig. 9 but in logarithmic representation, it is obvious that the background cannot be described by one single exponential function, so the following procedure was adopted to examine the individual peaks of the spectra more closely:

- For the time window corresponding to the peak under consideration, an exponential function is fitted to the background run.
- The intensity of this exponential is then scaled at the Cd-resonance region (see above) and this fitted function is removed from the data. (Fig. 14 shows these data for the B_4C-run)
- From the net intensities thus obtained the following parameters were derived:

  normalized peak height, P

  normalized peak intensity, I

  "width" of peak, $W = \frac{I}{P}$

  standard deviation σ in μs (second moment of the intensity distribution)

Normalization of P and I was done with respect to the number of protons recorded. For the standard deviation only 99 % of the peak intensity was included to avoid domination of the integral by statistical errors in the long time tail of the peak. The results are given in Table 2 through 5.

The intensity data for the N^* case have not been included in all listings because these measurements were taken with a strongly detuned analyser crystal which resulted in low count rates and relatively poor statistical accuracy. The experimental setup has been changed after measuring the N^* case (different slits, fully aligned analyser crystal). More extensive studies on undecoupled and unpoisoned moderators will be reported separately (Bauer et al, 1981).

In order to evaluate the N and N^* measurements, which is not as straightforward as for the decoupled moderators due to overlap between pulses, the procedure followed was:

- The background was determined as before
- Starting with the 00 12 reflection, an exponential decay with two decay constants was fitted to the difference (signal minus background).
- This contribution was extrapolated to longer times and subtracted from the following peak.
- The result was used for fitting an exponential decay to the following peak etc.

In this way, the net intensities of the various peaks were obtained, which were then used to derive the same quantities as for decoupled moderators. An example of the peaks obtained after correction for overlap and the corresponding fit data is shown in Fig. 15. While there was an obvious need for two decay constants, it was necessary for the 006-reflection to keep the amplitude (A_1) of

one of the decay modes fixed in order to obtain results which are consistent with the neighbouring peaks. This amplitude was derived from a smooth curve drawn through the amplitude obtained for the other peaks as shown in Fig. 16, where the open circles indicate the amplitudes that resulted from the first fit and the full symbols give the data obtained with A_1 selected to lie on the curve. Also shown in Fig. 16 are the decay contants associated with the various amplitudes.

A comparison of the integrated intensities relative to those obtained for the B_4C(Gd) case is given in Fig. 17. It can be seen that the Cd(Gd) case is very similar to the B_4C(Gd) case. The effect of the grooves in the surface on the intensity in the Cd(Gd) case is a gain by a factor of 1.8 above 10 meV and even more below 10 meV (indicating, as noted before, that the grooved moderator gives a much softer spectrum than the flat one). Similarly, in the unpoisoned case the grooves lead to a considerable intensity gain (see also Bauer et al, 1981).

The "width" as determined by the ratio of the integrated intensity to peak height is affected by the spectrometer resolution (see below) only through the reduction of the peak height, whereas the second moments, in addition to being sensitive to peak broadening, are also affected by the somewhat arbitrary choice of the integration limits.

On the other hand, the shape of the peaks, which is not well represented by either one of the two quantities may become very important if a weak reflection has to be separated from an intense one by time-of-flight in an actual neutron spectrometer. For this reason we give in Table 7 a summary of the contours of the various peaks measured. For each peak the measured width at 50 %, 30 %, 10 %, 3 % and 1 % of the peak intensity are given (excluding the N and N^* cases).

From these data it can be seen that some pulse shape degradation takes place with the grooved moderator surface, especially at longer neutron wavelengths, but around 1 Å the pulse shape is not significantly affected.

From the semi-logarithmic plots of Fig. 14 it can be seen that the trailing edge of most of the peaks can be described fairly well by one or two exponential decay modes. Since, if measured not too close to the peak, the decay constants are fairly independent of the time resolution of the arrangement, we give a list of decay constants obtained for the various moderators in Table 6. If two decay constants are given, the first one is the dominant one at long times whereas the second one is measured in the region close to the peak and hence may be somewhat less certain. For the N and N^* cases, two decay constants are given for all reflections. Their respective amplitudes in the N-case can be found in Fig. 15, from which it is obvious that the two contributions are of similar magnitude.

4. Discussion

4.1 Time resolution of the experimental arrangement

Owing to the space and equipment available to perform the present measurements, it was not possible to set up a backscattering time focussed arrangement which would have minimized resolution effects on the measured data. The resolution of the configuration used can be estimated as follows: Due to the fact that a 2 mm wide slit and a 12 mm Ø detector, 3.42 m apart determined the angular resolution of the detector leg, this contribution to the total resolution is

negligible. The wavelength (and time-) resolution of the arrangement is therefore determined by the collimator in front of the analyser crystal ($\Delta\theta_1 = 0.75°$ FWHM) and the mosaic width of this crystal ($\Delta\theta_2 = 0.4°$ FWHM).With the direction of the outgoing beam strictly fixed, the crystal acts as a mirror, i.e. each orientation of its mosaic blocks will only reflect neutrons of a well defined wavelength and incident angle onto the detector. In this case the transmission of the system is given by the product of the transmissions of the components.

$$T(\theta) = T_1(\theta) \times T_2(\theta)$$

Approximating both, T_1 and T_2 by Gaussians whose standard deviations are equal to the standard deviation of the true resolution functions, we have

$$\text{for the crystal} \quad T_2 = \exp\left\{-\frac{\theta^2}{2\sigma_2{}^2}\right\}$$

$$\text{with} \quad \sigma_2 = \frac{\Delta\theta_2}{2\sqrt{2\ln 2}} = 2.96 \cdot 10^{-3}\text{rad}$$

$$\text{for the collimator} \quad T_1 = \exp\left\{-\frac{\theta^2}{2\sigma_1{}^2}\right\}$$

$$\text{with} \quad \sigma_1 = \sqrt{\frac{\Delta\theta_1{}^2}{6}} = 5.34 \cdot 10^{-3}\text{rad}$$

(the transmission function of the collimator is actually a triangle)

This yields

$$\frac{1}{\sigma^2} = \frac{1}{\sigma_1{}^2} + \frac{1}{\sigma_2{}^2} = 1.49 \cdot 10^5 \text{ rad}^{-2}$$

$$\sigma = 2.59 \cdot 10^{-3} \text{ rad} \qquad (2)$$

From the Bragg condition it follows

$$\frac{\Delta\lambda}{\lambda} = (\text{ctg } \theta_A) \cdot \sigma = 2.59 \cdot 10^{-3} \text{ (standard deviation)} \qquad (3)$$

with $\theta_A = 45°$.

In order to apply a correction for time resolution to quantities other than the standard deviation, such as the FWHM, the shape of the measured curve has to be known. In some cases (such as the higher order reflections in the unpoisoned moderator cases as shown in Fig. 14) a steep rise followed by an exponential decay is a fairly good description. In this case (exponentially decaying function with decay time τ) we have

for the full width at half maximum

$$(\text{FWHM})_{\text{exp}} = \tau \cdot \ln 2 \qquad (4)$$

and for the standard deviation

$$\sigma_{exp} = \tau \cdot \sqrt{2} \tag{5}$$

The resolution at FWHM then is

$$\left(\frac{\Delta t}{t}\right)^{exp}_{1/2} = \sigma \frac{\ln 2}{\sqrt{2}} = 1.27 \cdot 10^{-3} \tag{6}$$

For the case of a poisoned moderator and especially for lower order reflections where the rise time and the decay time are of the same order of magnitude, such a description is not sufficient. In these cases the curves become more symmetrical. If, for the purpose of determining the FWHM, a triangular shape can be assumed, we have

$$(FWHM)_{tri} = \sigma \cdot \sqrt{2} \tag{7}$$

or

$$\left(\frac{\Delta t}{t}\right)^{tri}_{1/2} = 3.66 \cdot 10^{-3} \tag{8}$$

Finally, if a Gaussian shape of the peak would have to be assumed, one would get

$$(FWHM)_{gauss} = \sigma \cdot 2\sqrt{2 \ln 2} \tag{9}$$

or

$$\left(\frac{\Delta t}{t}\right)^{Gauss}_{1/2} = 6.10 \cdot 10^{-3} \tag{10}$$

The FWHM's given in Table 7 have been calculated, using equ (8) throughout.

4.2 Comparison of configurations

4.2.1 Effect of grooves in the surface

As noted before, a grooved moderator surface results in an increase of thermal neutron leakage (for the case without decoupler, this has been shown indenpendently, (Bauer et al, 1980 and 1981). However, it also affects the pulse shape. From Fig. 18, where we show the 004-reflections for the various configurations as an example, it can be seen by comparing plots c to e and d to f respectively, that both the rise and the fall times are affected by the grooves. The rise occurs at an earlier time for the grooved moderators in both cases. This effect is more pronounced in the unpoisoned than in the poisoned case. This cannot be explained by actual flight path difference since, for the case of the unpoisoned moderator, the shift corresponds to 1 % of the total flight time which would mean a flight path difference of almost 6 cm. It appears therefore that in the grooved moderator the neutrons start leaking out of the surface earlier than without the grooves. Also, a small feature seems to appear before the actual rise in the case of the grooved moderators. On the other hand, somewhat surprisingly, the decay times for the grooved moderators seem to be shorter in the undecoupled and Cd-decoupled cases than for a moderator without grooves, at least in the low energy range (cf. Table 6).

4.2.2 Effect of Gd-poison

The addition of the Gd-poison has a significant effect on the pulse width through the decay time but - within the experimental resolution - not on the rise time. The overall effect on the integrated intensity being quite dramatic (Fig. 17), the peak intensity (Table 3) is only reduced by a factor between 0.75 (002-reflection) and 0.93 (006-reflection) for the Cd-decoupled moderator and seems to be virtually unaffected for the higher decoupling energy of the B_4C (the apparent slight increase is probably within the limits of the experimental accuracy).

4.2.3 Effect of Cd-decoupler vs. B_4C-decoupler

Using a Cd-decoupler which has a relatively low decoupling energy of only 0.4 eV rather than a B_4C-decoupler (the effective decoupling energy of the B_4C used was $\sim$ 3 eV), results only in marginal pulse broadening, especially for the poisoned moderator. Since, in a practical design, B_4C would be hard to use because of the high energy deposition density of the α-particles produced, Cd seems to be a viable alternative as a decoupler. Here the energy of the γ-ray produced is carried much further away from the decoupler.

5. Conclusions

The present measurements, which were mainly aiming at giving an idea as to what the penalty in intensity (peak height and integrated intensity) would be by going from an undecoupled moderator system as proposed for the German spallation neutron source project with 500 μs duration of the proton pulses to a decoupled one with short pulses show, that the reduction of the peak intensity caused by the decoupler and poison is a modest one, the effect on integrated intensity of course being quite dramatic.

Using an improved time resolution spectrometer, a study of moderator optimisation and target-moderator geometry is necessary to assess the possible benefits of working grooves into the moderator surface for a pulsed spallation source. Such a program is presetly in progress at Los Alamos (Russell et al 1981)

Acknowledgement

We are very much indepted to Dr. G.L. Munday, leader of the CERN PS-Division, for granting the permission to do these experiments on very short terms and in an unburocratic way. The personal engagement and continuing support by Dr. K.H. Reich, leader of the PS-Booster-group, and his staff and their readiness in fulfilling our needs and demands in every possible way, were of invaluable help to our crew. The help of Mr. B. Boland with part of the measurements and of Dr. H. Conrad with part of the data evaluation is greatly appreciated. Also, we would like to thank Mr. E. Hanning, Mr. H. Crämer and Mr. H. Möller for their technical assistance.

References

Bauer G.S., Conrad H.M., Friedrich K., Milleret G. and Spitzer H. (1981)
"Measurement of Time Structure and Thermal Neutron Spectra for Various Target-Moderator-Reflector Configurations of an Intensity-Modulated Spallation Neutron Source", this volume

Bauer G.S., Grünhagen K. und Spitzer H. (1980)
"Einige Voruntersuchungen zu wasserstoffhaltigen Moderatoren für eine Spallations-Neutronenquelle", SNQ-report, part III A2, unpublished

Carpenter J.M. (1977)
"Pulsed Spallation Neutron Sources for Slow Neutron Scattering"
Nucl. int. Math., 145 91-113

Russell G.J., Meier M.M., Gilmore J.S., Prael R.E., Robinson H. and Taylor A.D. (1981)
"Measurement of Spallation Target-Moderator Neutronies at the Weapons Neutron Research Facility"
in Proc. ICANS IV meeting, report KENS-2 pp. 210-241

Taylor A.D. (1980)
"Neutron Transport from Targets to Moderators"
in Proc. Meeting on Targets for Neutron Beam Spallation Sources (G.S. Bauer et al), Jül-Conf. 34, p. 47-76, ISSN 0344-5798

Decoupler	Flat Moderator		Grooved Moderator	
	Poison		Poison	
	none	Gd	none	Gd
B_4C	B_4C	$B_4C(Gd)$		
Cd	Cd	Cd(Gd)	Cd*	Cd(Gd)*
none	N		N*	

Table 1 Combinations of moderators, decouplers and poison investigated and corresponding abbreviated notations.

Configuration	Reflection					
	00.2	00.4	00.6	00.8	00.10	00.12
B_4C	27.6	145.0	156.1	95.9	33.7	9.7
$B_4C(Gd)$	17.4	85.5	86.2	53.1	20.0	5.3
Cd	47.8	228.7	242.7	150.8	49.8	9.8
Cd(Gd)	19.1	87.1	88.7	56.9	21.6	6.2
Cd*	96.4	340.3	334.0	207.8	71.4	16.4
Cd(Gd)*	47.8	160.9	150.6	95.0	36.2	10.1
N	180	838	854	405	154	42
N*	-	-	-	-	-	-

Table 2 Normalized integrated intensities of reflection peaks from graphite analyser. Data not corrected for crystal reflectivities and detector efficiency.

Configuration	Reflection					
	00.2	00.4	00.6	00.8	00.10	00.12
B_4C	1.0	5.3	6.0	4.8	2.4	1.1
B_4C(Gd)	0.9	5.7	6.5	5.2	2.7	1.1
Cd	1.6	7.2	7.7	6.3	3.6	1.4
Cd(Gd)	1.0	5.3	5.8	4.9	2.6	1.0
Cd*	3.1	8.9	8.9	7.6	4.4	1.9
Cd(Gd)*	2.3	8.1	8.3	7.0	3.9	1.6
N	2.38	8.5	9.4	7.52	4.02	1.8
N*	-	-	-	-	-	-

Table 3 Normalized heigths of reflection peaks from graphite analyser. Data not corrected for crystal reflectivities and detector efficiency.

Configuration	Reflection					
	00.2	00.4	00.6	00.8	00.10	00.12
B_4C	107	109	104	80	55	34
B_4C(Gd)	75	59	53	41	29	19
Cd	121	127	126	95	54	28
Cd(Gd)	78	66	60	46	34	25
Cd*	126	153	150	110	65	34
Cd(Gd)*	83	79	72	54	37	25
N	313	394	363	218	147	93
N*	235	309	218	(266)	(227)	(191)

Table 4 "Width" of reflection peaks in μs from graphite analyser as obtained from the ratio of integrated intensity to peak height. Values in parentheses for the N* 008, 0010 and 0012 reflections are uncertain due to convergency problems of the fit.

Configuration	Reflection					
	00.2	00.4	00.6	00.8	00.10	00.12
B_4C	65.1	69.1	76.5	66.0	57.7	40.2
B_4C(Gd)	33.1	29.7	27.5	25.8	47.2	38.6
Cd	70.8	77.5	82.0	69.2	52.5	25.2
Cd (Gd)	37.7	32.2	30.6	29.5	38.7	22.6
Cd*	71.0	80.9	86.1	71.2	55.6	35.8
Cd (Gd*)	38.7	38.1	50.0	40.0	38.2	23.5
N	330.8	380.5	378.8	243.4	305.1	245.1
N*	300.0	356.5	185.1	551.9	471.4	258.8
σ^*_{res}	16.6	8.4	5.6	4.2	3.4	2.7

Table 5 Second moments of intensity distribution (μs) in the analyser reflections.

Configuration	Reflection					
	00.2	00.4	00.6	00.8	00.10	00.12
B_4C	70	75	77	75/55	75/25	
B_4C(Gd)	30	30	25	25	15	
Cd	75	85	88	84/60	80/30	
Cd(Gd)	30	30	30	27	20	
Cd*	75	80	80	85	85/30	
Cd(Gd)*	35	35	32	30	20	
N	468/113	577/232	547/155	352/83	455/46	350/20
N*	414/ 51	557/161	258/120	(900/120)	(700/70)	(350/22)

Table 6 Decay times (μs) for the various reflection peaks from the graphite analyser. Data are not corrected for time resolution. Data in parentheses indicate difficulties with the fits.

Configuration	% of Peak Int.	Reflection 00.2	00.4	00.6	00.8	00.10	00.12
B_4C	50	85	85	79	49	25	17
	30	128	135	128	98	59	27
	10	227	220	216	190	174	(120)
	3	326	319	319	302		
	1	418	426	433	(390)		
B_4C(Gd)	50	65	50	45	33	20	15
	30	92	71	63	49	30	21
	10	131	106	99	80	56	46
	3	176	145	128	119	83	
	1	220	200	177	149		
Cd	50	94	103	99	65	29	
	30	147	156	156	115	58	
	10	248	255	255	210	147	
	3	348	358	358	314		
	1	440	468	472			
Cd(Gd)	50	69	57	52	39	25	18
	30	96	79	72	55	38	26
	10	135	117	110	88	61	42
	3	191	150	152	136	90	
	1		213	206	176		
Cd*	50	101	133	128	84	35	18
	30	156	184	177	136	70	27
	10	252	284	284	234	180	112
	3	355	390	(383)	(325)		
	1	454	532				
Cd(Gd)*	50	77	71	64	43	26	18
	30	99	98	85	61	39	27
	10	149	138	121	98	72	49
	3	199	181	167	153	122	
	1	262	248	248			
Wavelength (Å)		4.7	2.4	1.6	1.2	0.95	0.79
time μs		6582	3306	2212	1659	1331	1065
Resolution (μs)		23.5	11.6	7.8	5.8	4.7	3.9

Table 7 Intensity contours (μs) for the various reflections, not corrected for resolution. The resolution at FWHM is given in the bottom line.

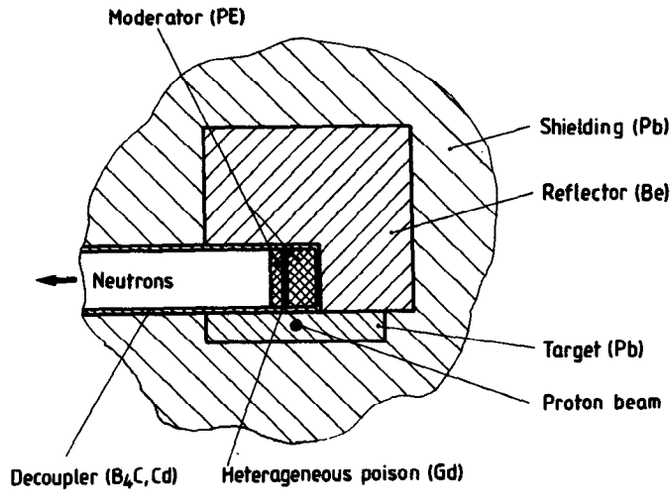

Fig.1
General arrangement of a target-moderator-reflector setup for a pulsed spallation neutron source. The moderator is decoupled from the surrounding materials (target and reflector) by an absorber for thermal neutrons. To improve pulse quality, a heterogeneous poison (absorber) can be used at a certain depth below the surface, from which the neutrons are extracted.

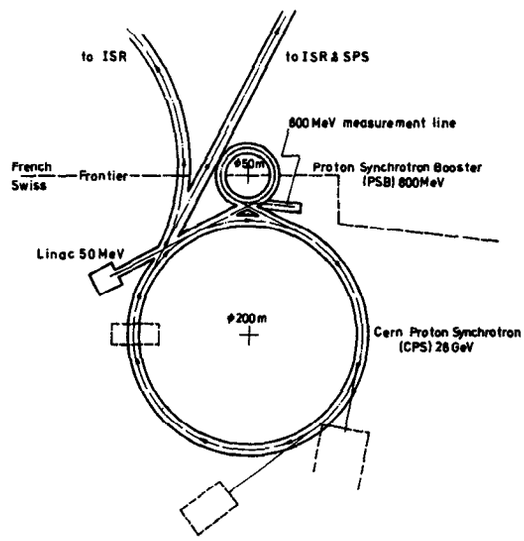

Fig.2
The CERN-PS ring system. The experiments described in this report were performed at the end of the 800 MeV measurement line.

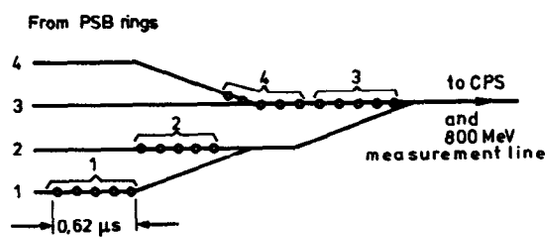

Fig.3
Combination of proton bunches accelerated in the four rings of the PSB to form one 2,6 µs pulse. If only one ring is used, as in the present experiments, the pulse is 0,62 µs long.

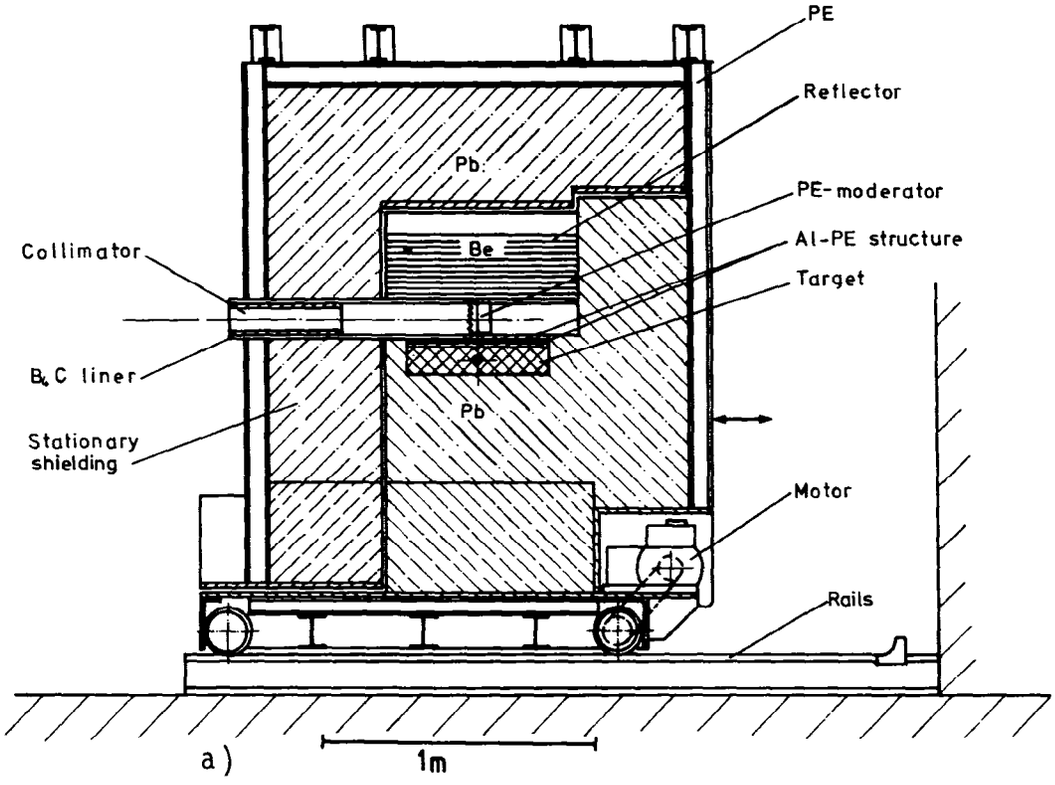

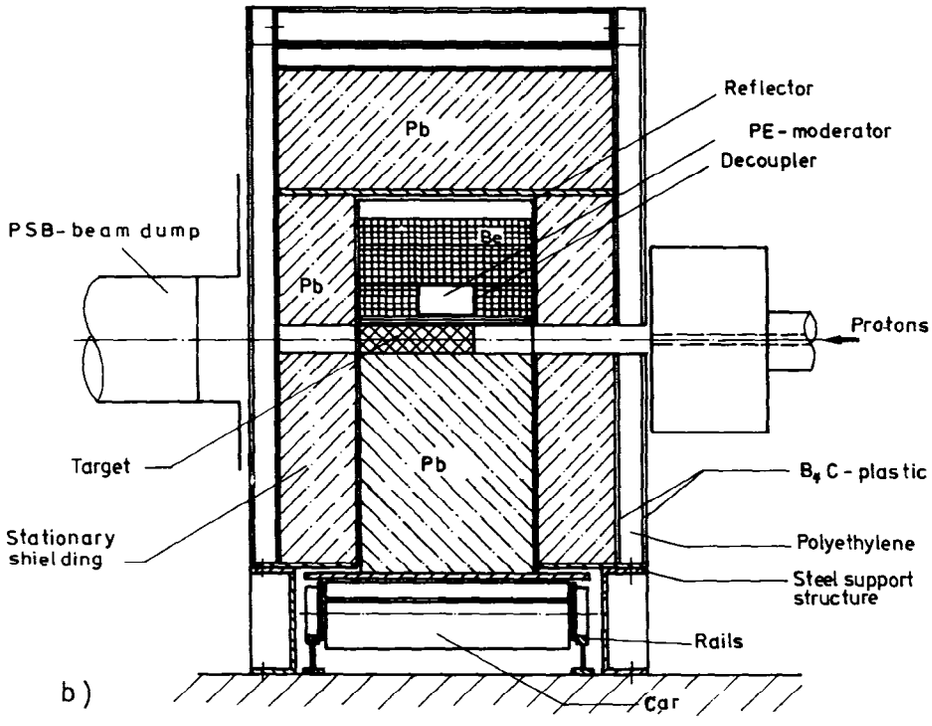

Fig. 4

Mockup of spallation neutron source arrangement used in the experiments.
For easier replacement of target, moderator and reflector part of the arrangement could be moved on a trolley.

a) Elevation perpendicular to the direction of the proton beam.
b) Elevation parallel to the direction of the proton beam.

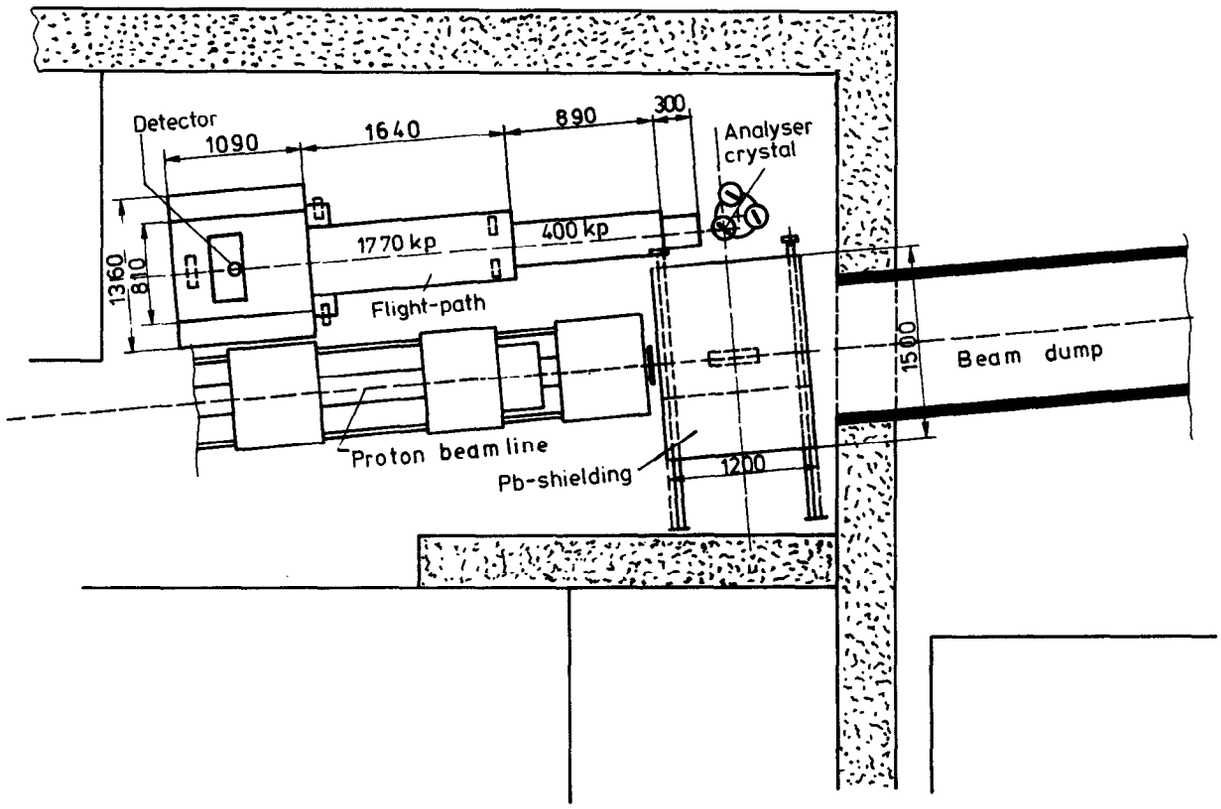

Fig. 5 Plan view of the experimental setup showing the proton beamline, the spallation source mockup, the crystal analyser table and the neutron flight path at the end of the 800 MeV measurement line.

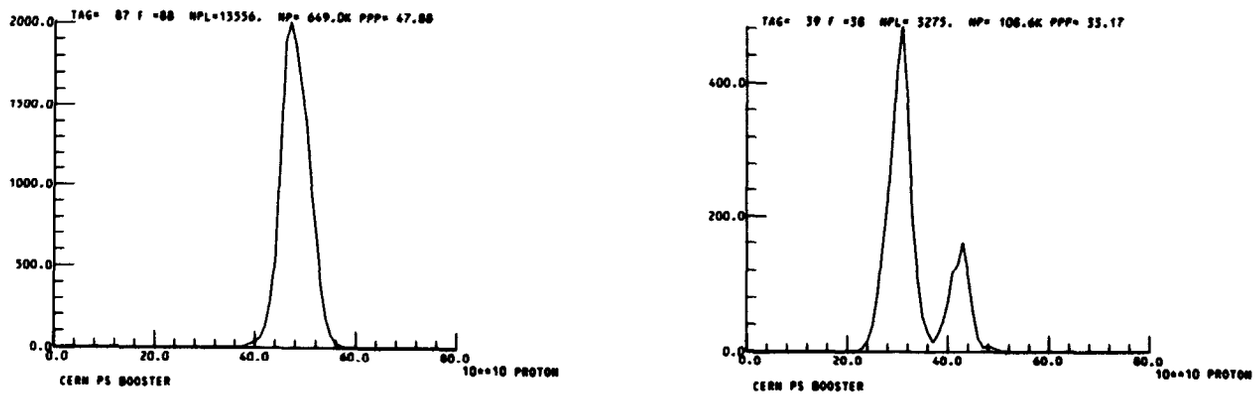

a) b)

Fig. 6 Examples of proton pulse-height spectra, showing one case of fairly constant proton intensity and one case where the number of protons per pulse changed during the experiment as visible from the two distinct peaks in the spectrum.

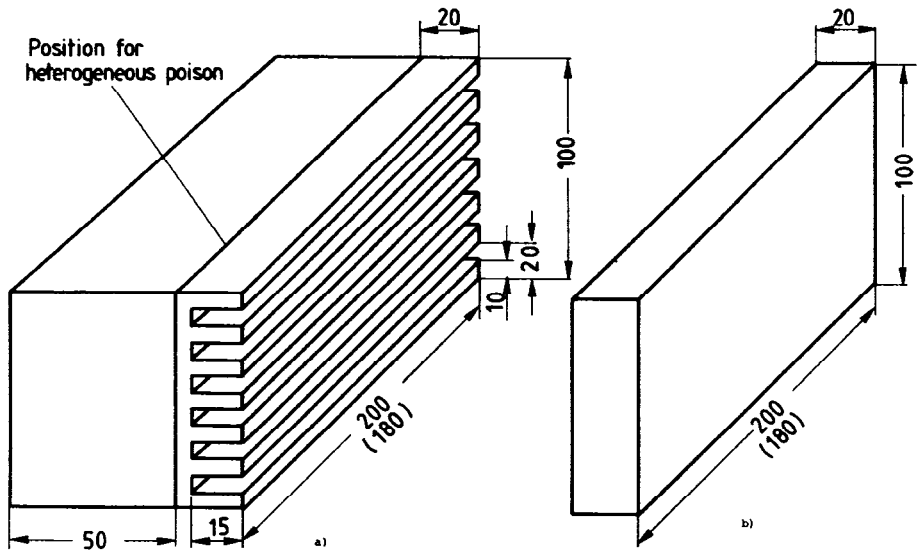

Fig. 7 The moderators (polyethylene). The flat slab of 20 mm thickness could be exchanged for the grooved part of the moderator. Neutrons were extracted at right angles to the grooved surface. If a heterogeneous poison was used, it was placed between the two parts of the moderator.

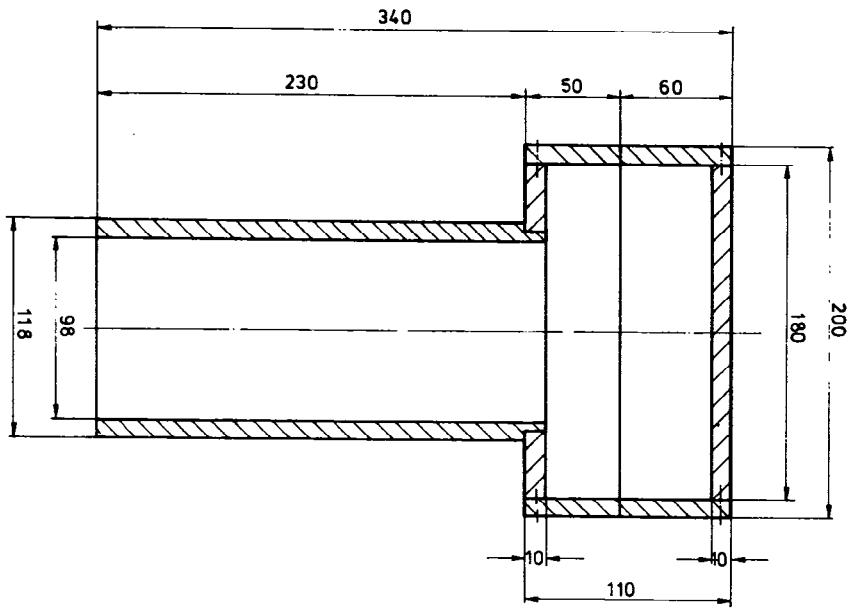

Fig. 8 The B_4C-plastic decoupler used. The B_4C-content was 50% natural B_4C in the material.

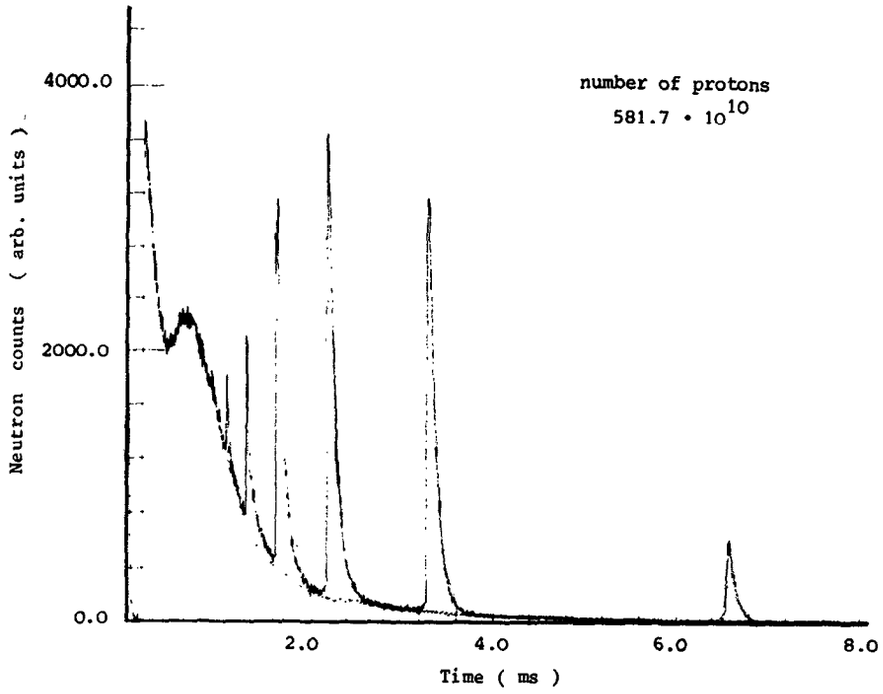

Fig. 9 Neutron spectrum as measured for the flat moderator with B_4C-decoupler. The peaks corresponding to the various orders of reflections from the graphite crystal are superimposed on a strongly time-dependent background. The minimum at about 500 µs corresponds to the Cd-resonance.

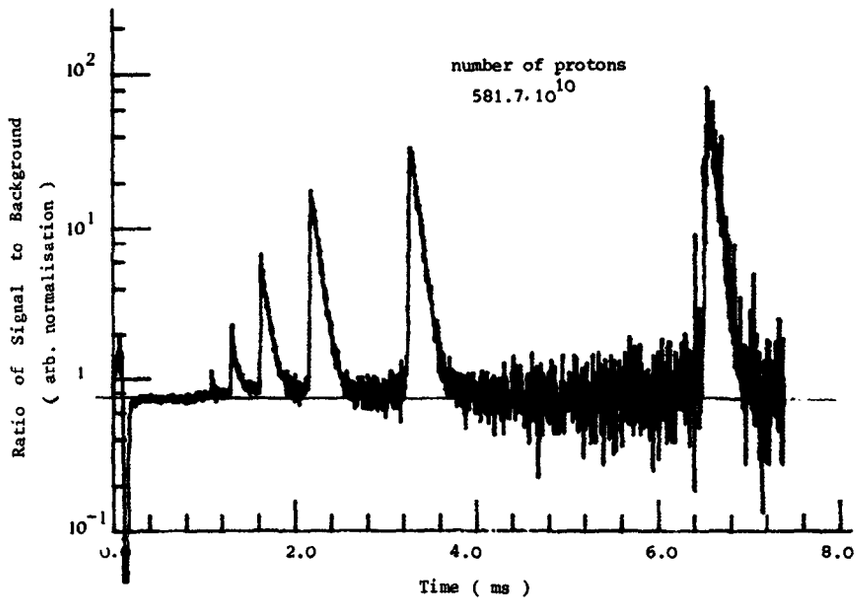

Fig. 10 Logarithmic representation of the ratio between measured data and background measured without analyser for the same measurement as Fig. 9. Apart from the reflection peaks, the ratio is seen to be completely flat.

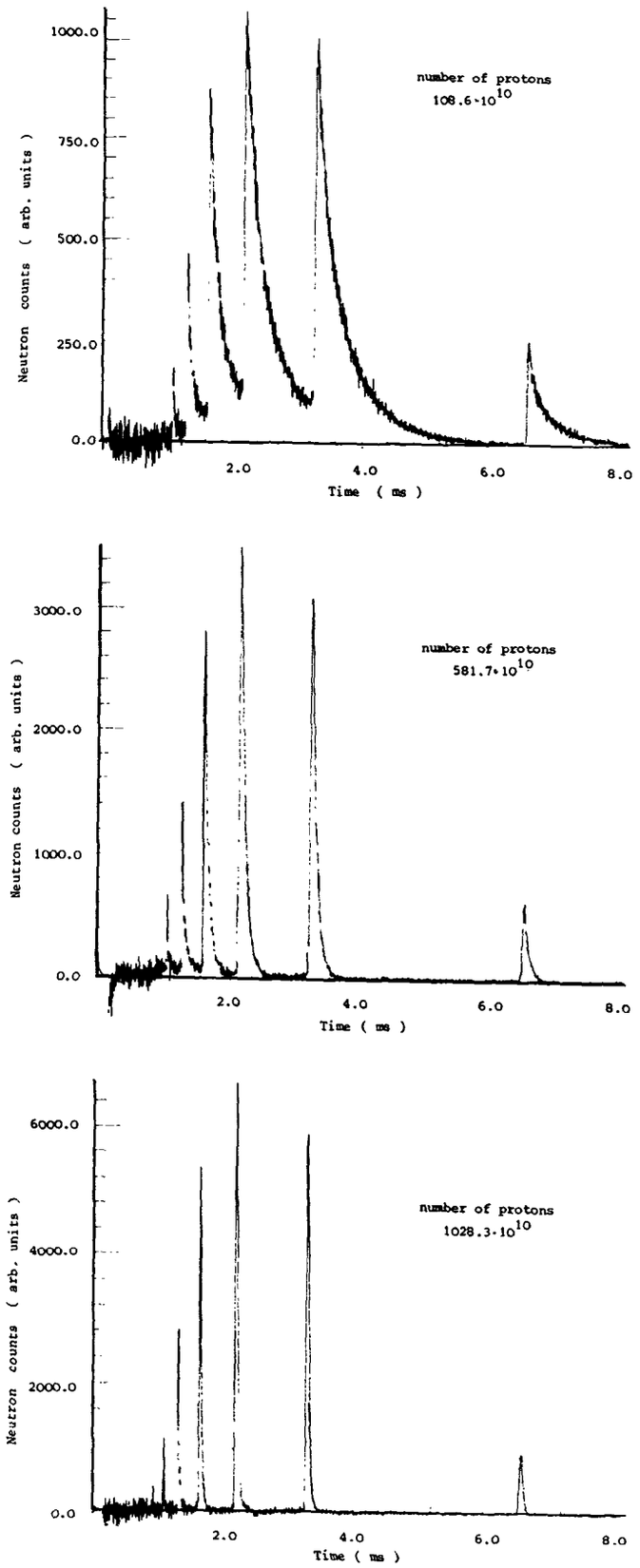

Fig. 11 Effect of decoupler and poison on pulse shape of the crystal reflections (flat moderator surface)

a) no poison, no decoupler

b) no poison, B_4C decoupler

c) Gd-poison, B_4C decoupler

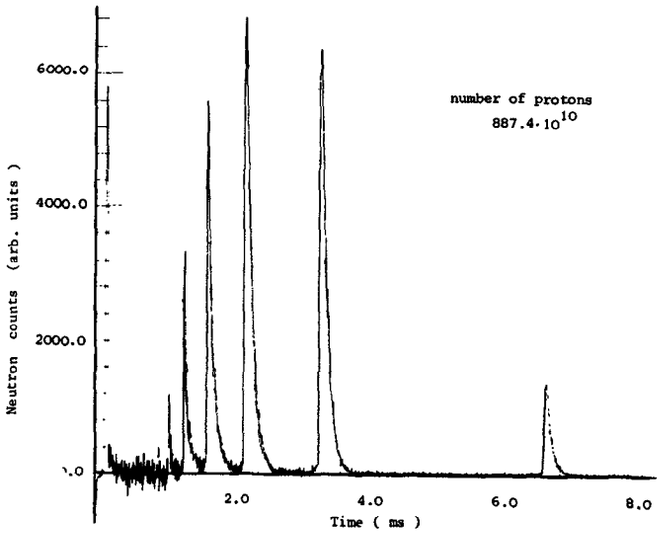

a)

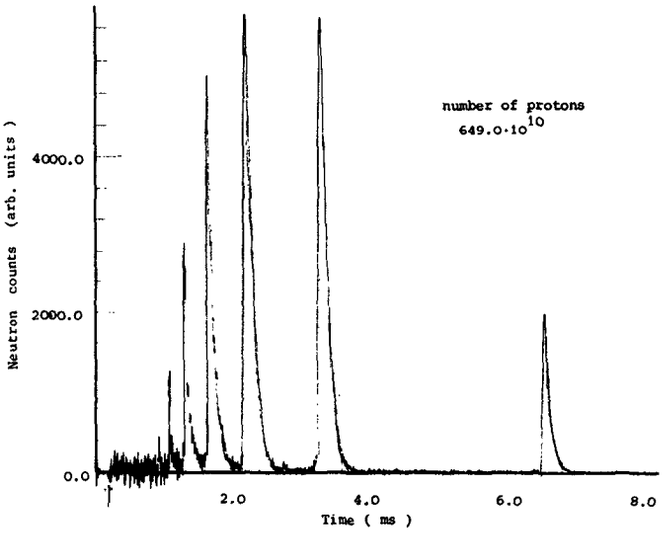

b)

Fig. 12
Comparison of pulse shapes from flat and grooved moderator surface with Cd-decoupler, no poison.
a) flat surface
b) grooved surface

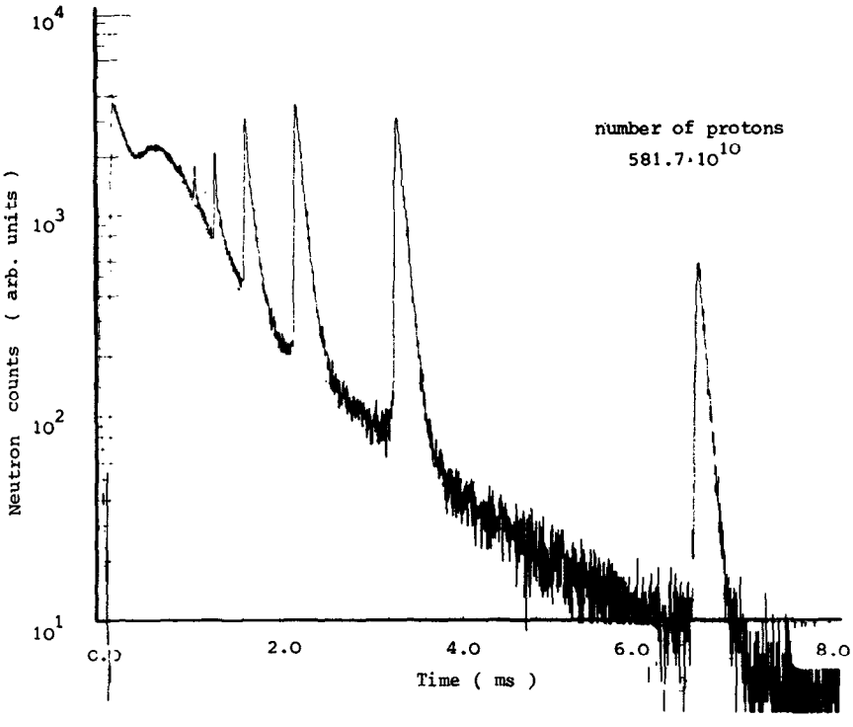

Fig. 13

Logarithmic representation of measured raw data (same as Fig. 9) showing, that the background cannot be described by a single exponential decay function.

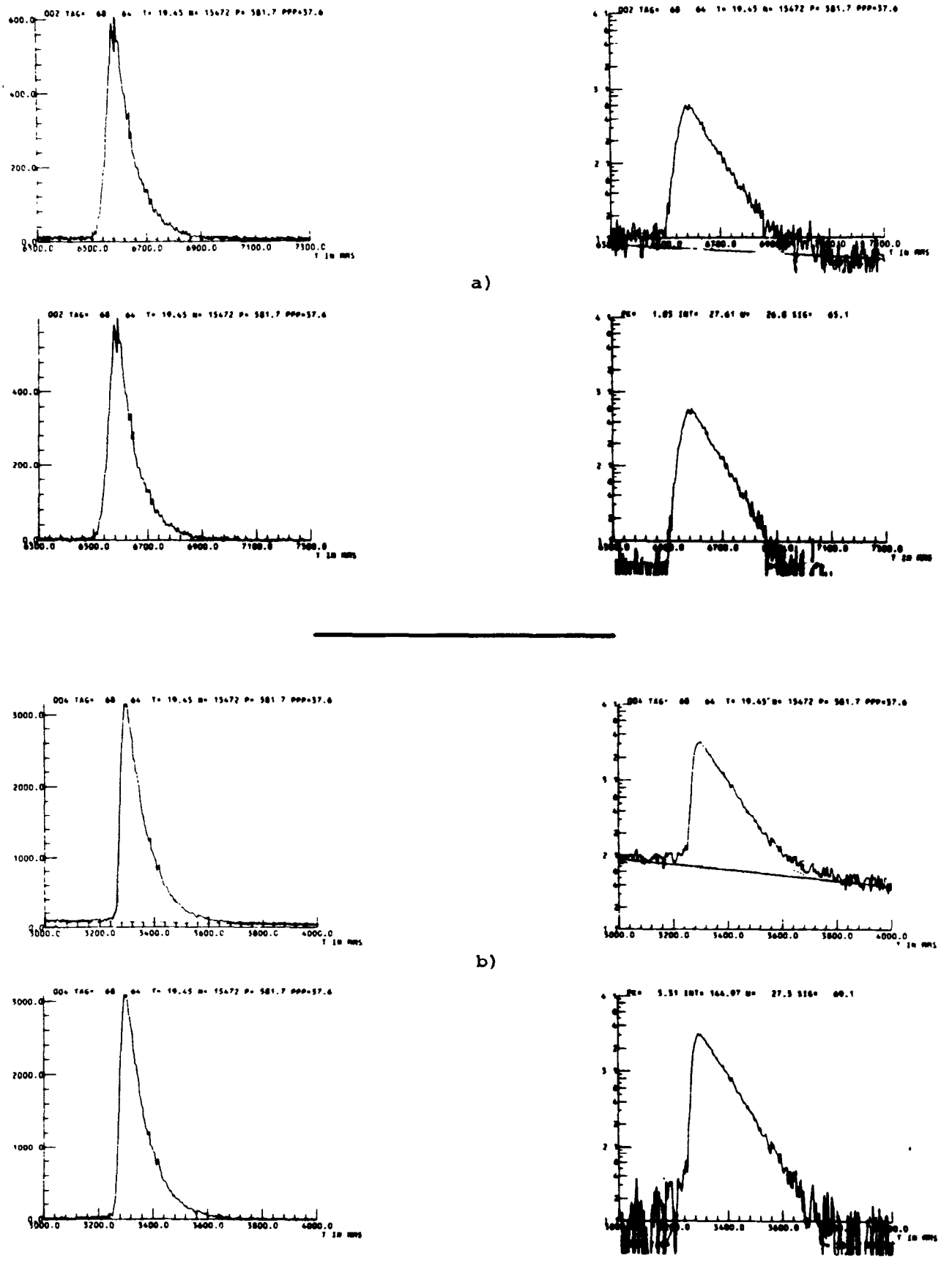

Fig. 14 a - f

Examples of background subtraction from the individual peaks in the spectrum of Fig. 13.

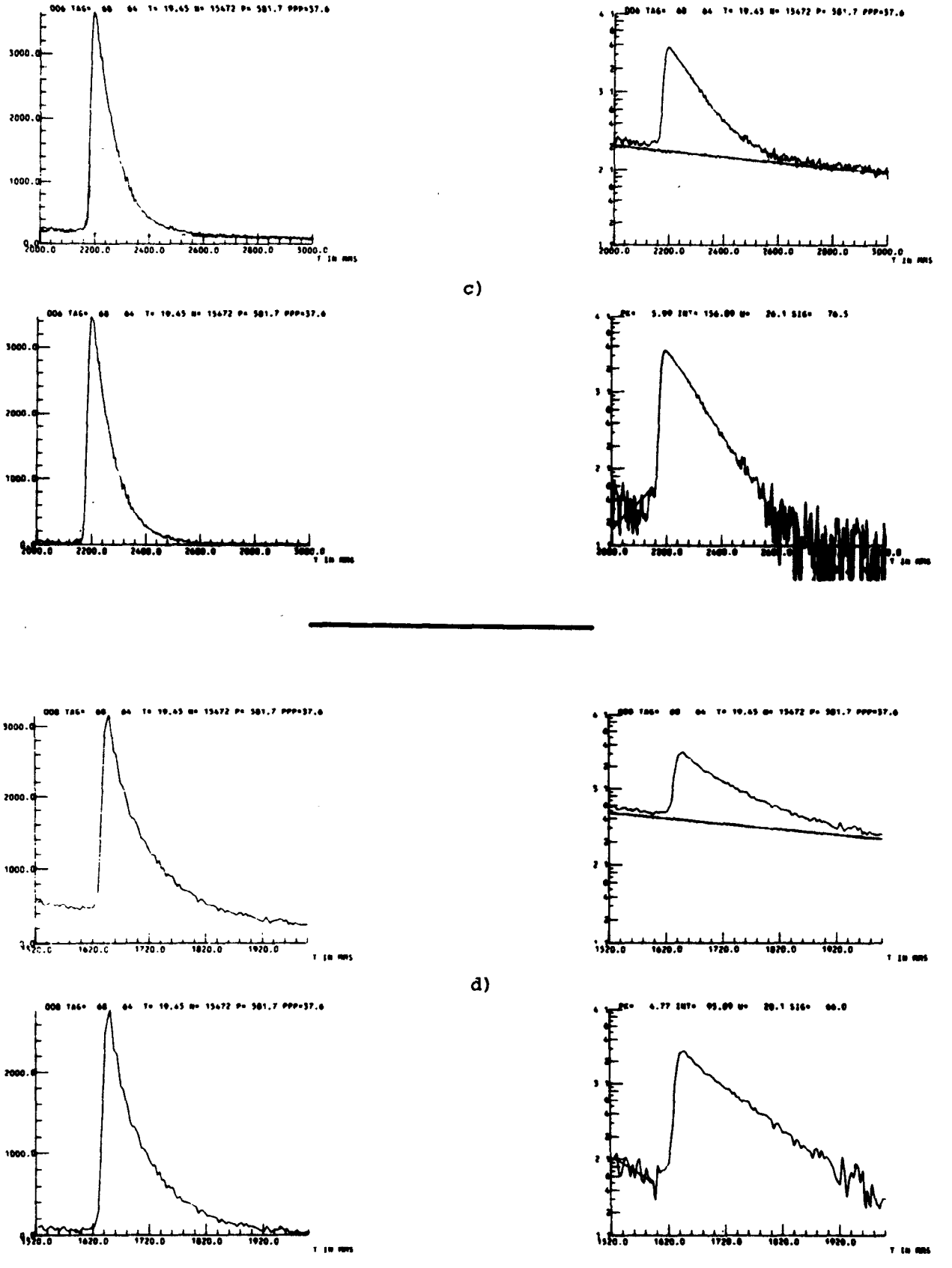

Fig. 14 a - f

Shown are the raw data in linear (upper left) and semilograrithmic representation (upper right) with the background level indicated and the same data with the background subtracted (lower right and left). Since the level of the background subtracted is scaled at the Cd-resonance region (see Fig. 13), there may remain some which is not part of the peak at the higher order reflections, which could be an overlap from the preceding peak.

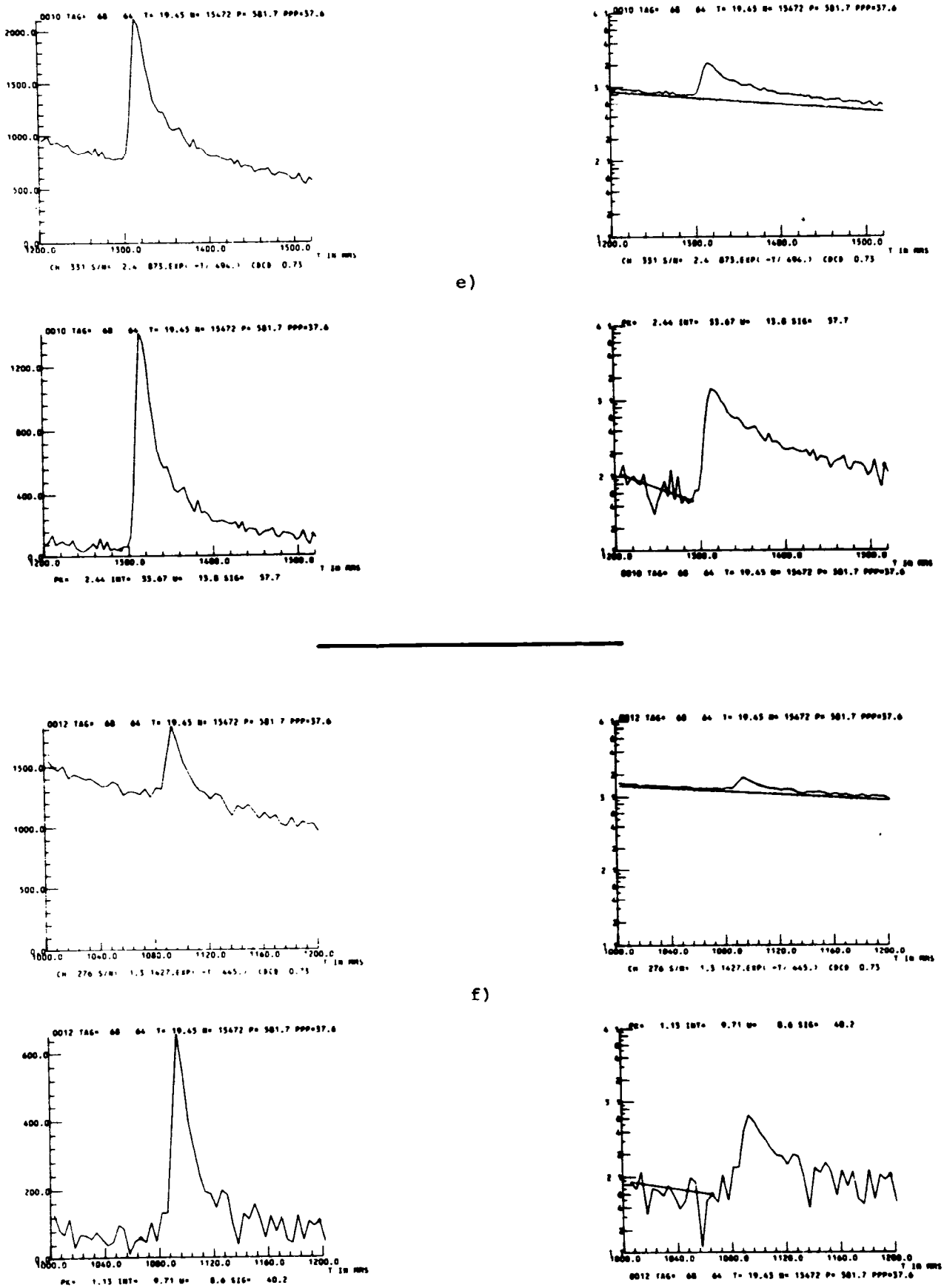

Fig. 14 a - f

One exponential decay function is sufficient to describe the 002, 004, 006 and also the 008 reflex. For the 0010 and 0012 reflex two decay constants are needed, but, at the same time, the statistical accuracy is getting poor.

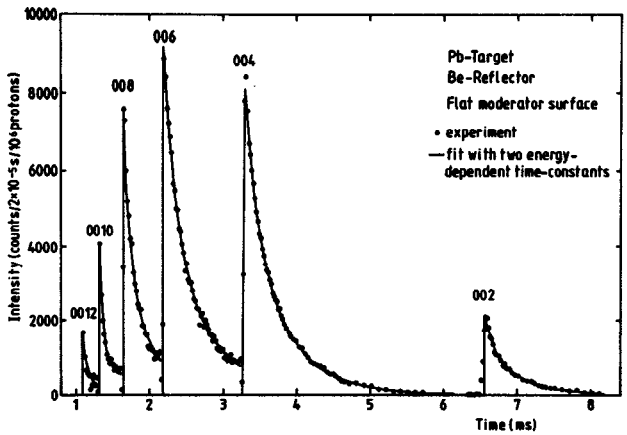

Fig.15 Reflection peaks of the graphite analyser for the flat surface moderator without decoupler and poison. The dates give the experimental data after the extrapolated overlap form the preceding peak has been substracted. The solid line is the result of a fit with two decay constants for each individual peak.

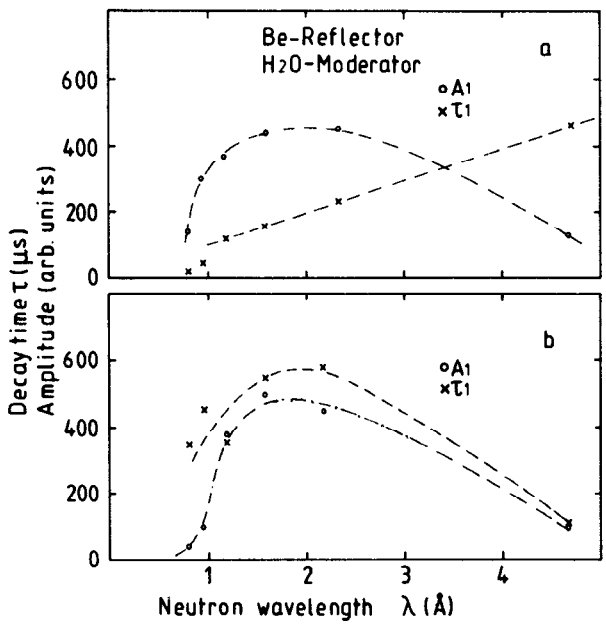

A_2, τ_2 ?

Fig. 16 Decay constants and corresponding amplitudes obtained from the fits of Fig. 15 as a function of neutron velocity.

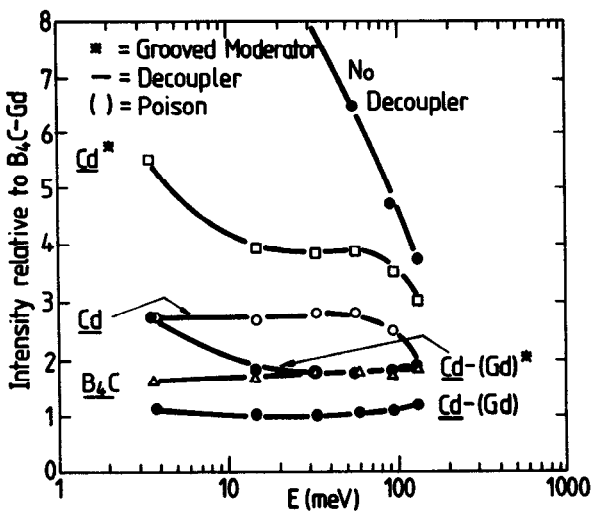

Fig. 17 Integrated intensities of the reflections for various combinations of decoupler and poison relative to the B_4C-decoupled-Gd poisoned case as a function of neutron energy.

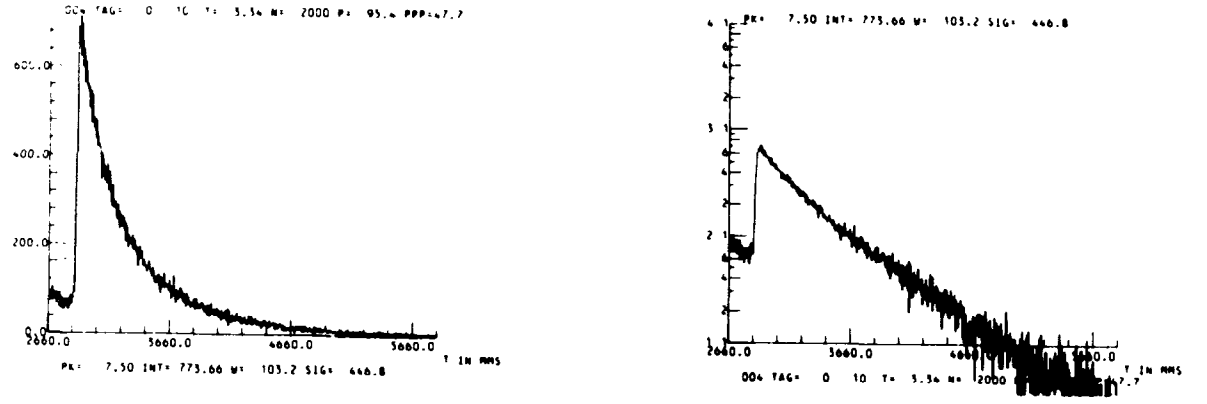

a)

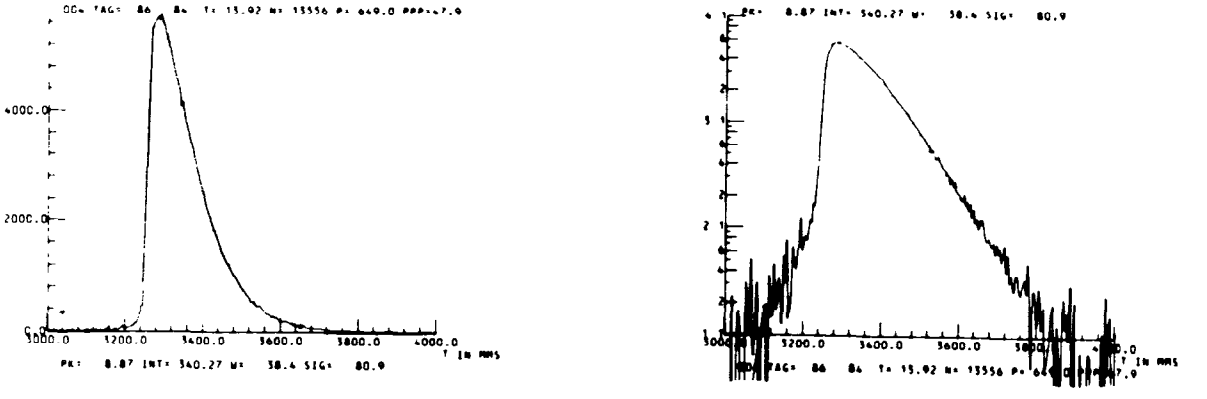

b)

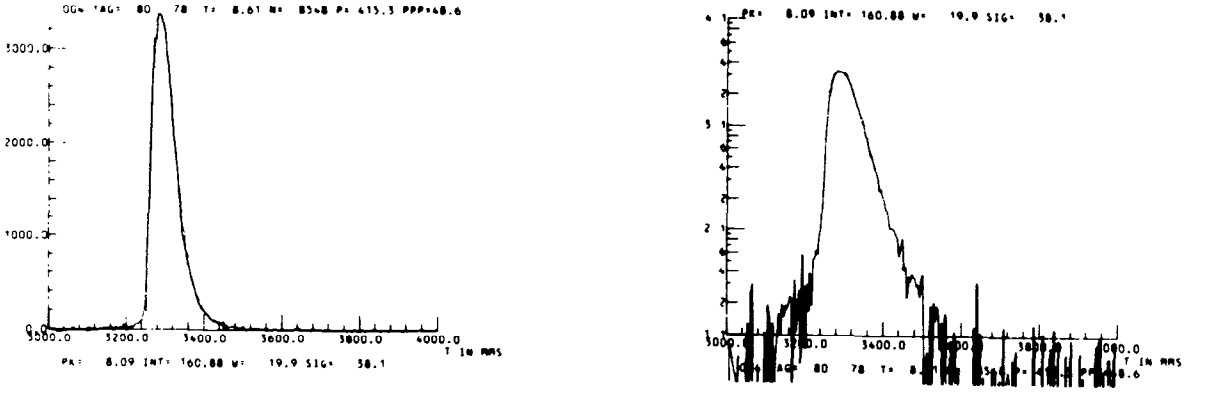

c)

Fig. 18 Comparison of the shapes of the 004-reflection (λ = 2.4 Å) for various combinations of moderator, decoupler and poison used

a) Grooved moderator, without decoupler and poison

b) Grooved moderator, Cd-decoupler

c) Grooved moderator, Cd-decoupler, Gd-poison.

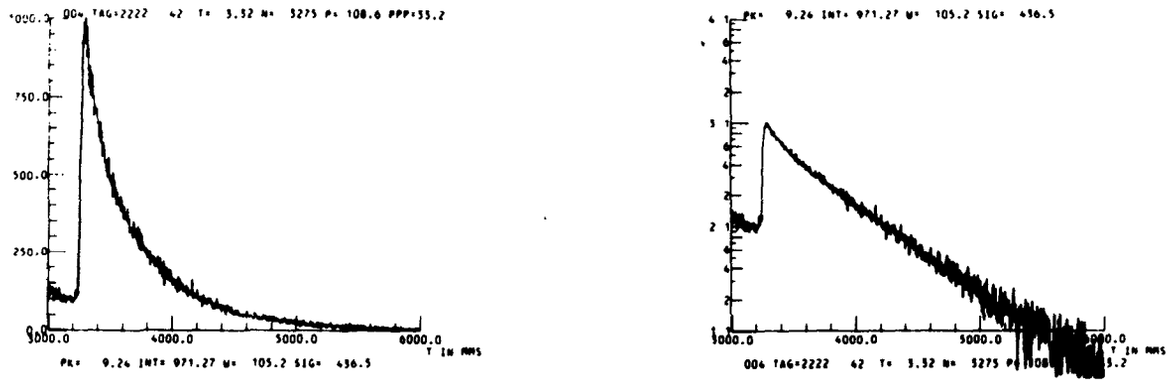

d)

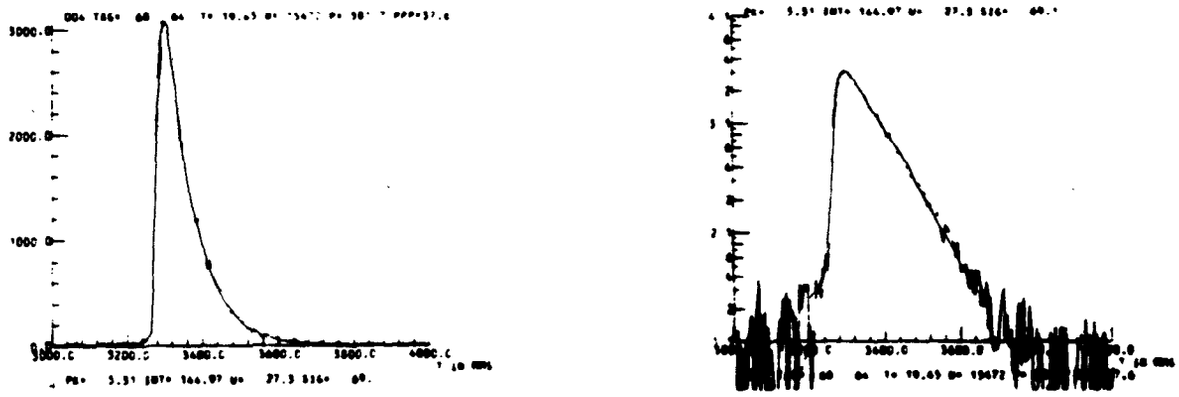

e)

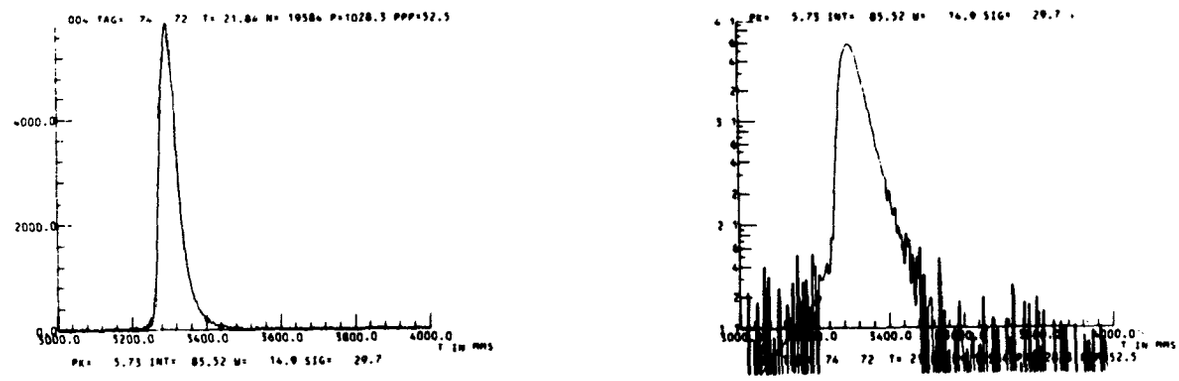

f)

Fig. 18 d) Flat moderator, without decoupler and poison

e) Flat moderator, B_4C-decoupler

f) Flat moderator, B_4C-decoupler, Gd-poison.

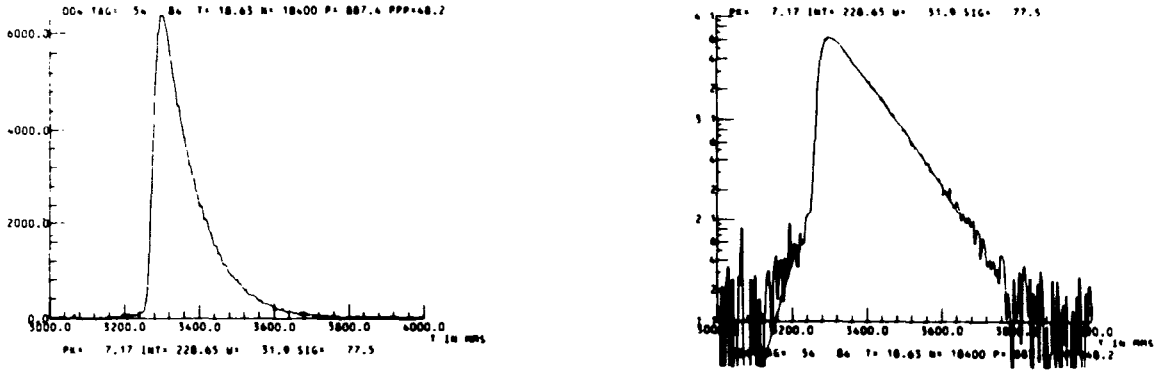

g)

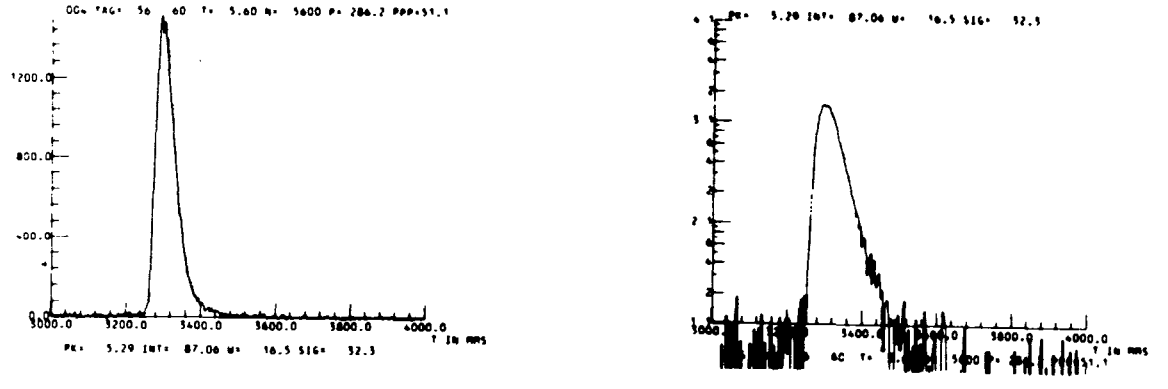

h)

Fig. 18 g) Flat moderator, Cd-decoupler

h) Flat moderator, Cd-decoupler, Gd-poison.

Jül-Conf-45 D2-4

I C A N S - V

MEETING OF THE INTERNATIONAL COLLABORATION ON

ADVANCED NEUTRON SOURCES

June 22-26, 1981

Thermal Neutron Leakage and Time Structure Measured for Various Target-Moderator-Reflector Configurations for a Spallation Neutron Source

G.S. Bauer, W.E. Fischer**, F. Gompf[+], M. Küchle[++], W. Reichardt[+] and H. Spitzer**

* Institut für Festkörperforschung, Kernforschungsanlage Jülich
D-5170 Jülich, West Germany

** Schweizerisches Institut für Nuklearforschung
CH-5234 Villigen, Switzerland

\+ Institut für Angewandte Kernphysik I, Kernforschungszentrum Karlsruhe
D-7500 Karlsruhe, West Germany

++ Institut für Neutronen- und Reaktorphysik, Kernforschungszentrum Karlsruhe
D-7500 Karlsruhe, West Germany

Abstract

Measurements were performed at the Swiss Institute of Nuclear Research of the integrated thermal neutron leakage, the thermal neutron flux distribution and the time structure of the thermal neutron field for various configurations of target, moderator and reflector for a spallation neutron source. Among them were a cylindrical Pb-Bi-target in a D_2O-tank and a slab target with a hybrid moderator configuration consisting of a D_2O half tank below and a reflected H_2O moderator above the target. The results are used to predict performance data for a spallation neutron source with 500 μs long proton pulses. Although there remains some ambiguity due to non-perfect simulation of the real situation, correction factors derived from independent measurements could be used. The effect of beam tubes in the D_2O on the thermal neutron flux was measured directly.

1. Introduction

The present measurements are part of two studies carried out in the Federal Republic of Germany and in Switzerland to assess the feasibility and expected performance of a neutron source for beamhole research, based on the spallation reaction. The design goal of the German source being a thermal neutron leakage out of the beamholes equivalent to that of a reactor with a flux of $6 \cdot 10^{14}$ cm^{-2} sec^{-1}, the heat removal from the target becomes a major problem. To achieve this, two possibilities are considered, namely a flowing-liquid metal /1/ and a rotating solid target /2/. The first concept is also considered for the Swiss project, where a continuous proton beam will be utilized. In the German project a Linac is foreseen which delivers proton pulses of 100 mA peak current and 0.5 msec duration once every 10 msec. In this case the neutron flux will also have a time-structure which is an advantage for many neutron scattering experiments. The degree to which the time structure of the proton beam can be preserved in the neutron flux depends on the type of moderator and reflector chosen. Generally there will be a tradeoff between pulse width and average neutron flux. It was the purpose of the present measurements to provide a basis for the comparison of the various arrangements shown in Fig. 1, namely

- a flat target plate in a D_2O-tank representing a rotating solid target in a large moderator tank (slab target),

  a slab target with the D_2O-tank only half filled and with a polyethylene moderator and reflector above the target representing a hybrid arrangement where one part of the moderator is trimmed for maximum peak flux whereas the other part should provide as high an average flux as possible.

- a cylindrical Pb-Bi-target in a D_2O-tank representing the liquid metal target concept.

In the case of the rotating target both, Pb and U-238 were investigated as possible target materials.

2. Experimental Arrangement

The measurements were performed in the PM1 experimental area of the SIN where a scattered 590 MeV proton beam from the production target E can be used. This beam is deflected and shaped by a series of deflection magnets, variable collimators and focussing elements. It was directed onto a graphite scatterer viewed by a telescope of scintillator counters operated in coincidence to allow quantitative proton beam monitoring. The graphite scatterer was originally placed at a distance of $\sim$ 4 m from the target. The telescope was calibrated by reducing the beam current to a level where direct counting was possible and by comparing the number of coincidences recorded to the number of protons counted in the direct beam. The ratio at the initial setup was

$$G_1 = 312{,}8 \cdot 10^3 \text{ protons per coincidence recorded.}$$

The profile of the proton beam was monitored by wire-chambers placed in front of (and, for the purpose of alignment, also behind) the target position (Fig. 2). The proton beam profiles obtained in the horizontal and vertical directions

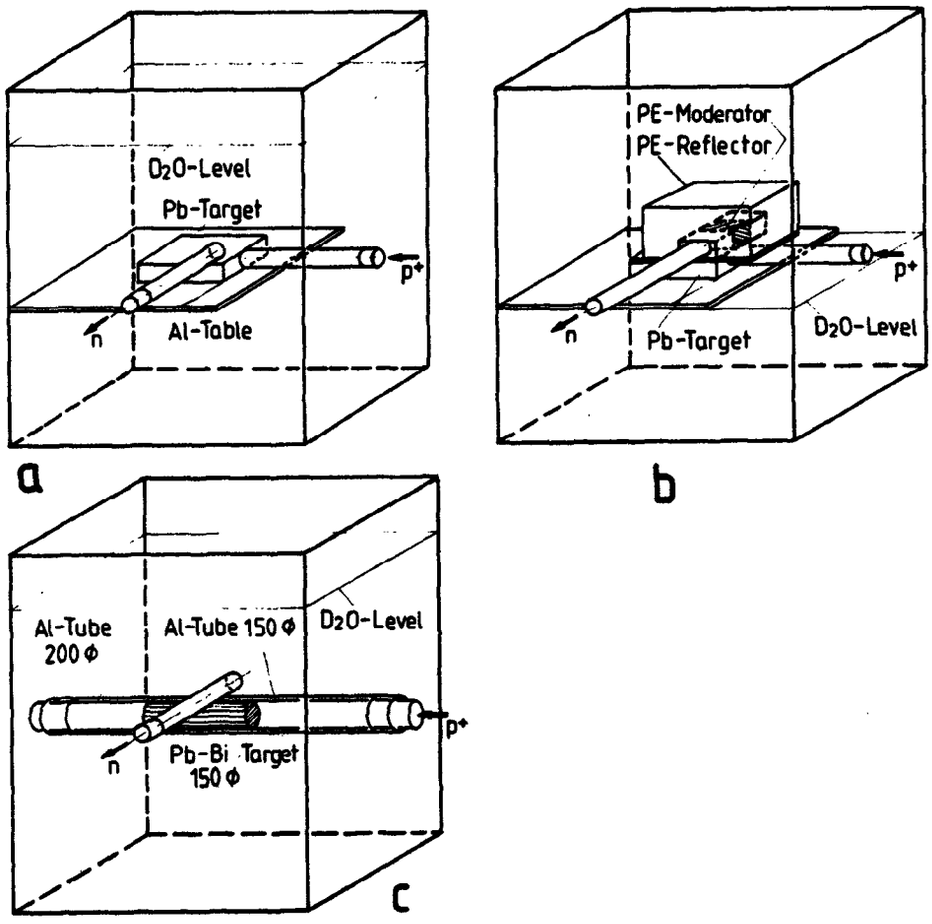

Fig. 1: Schematic representation of target-moderator-reflector arrangements used.

a) Slab target in D_2O-tank
b) Slab target with hybrid moderator configuration (D_2O below target and "H_2O" moderator with reflector above target)
c) Cylindrical target in D_2O-tank

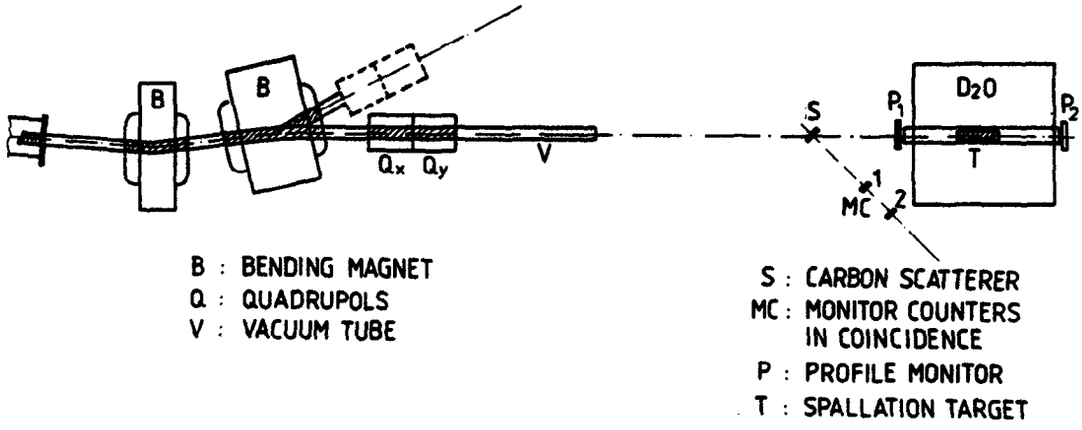

Fig. 2: End of proton beam line in the PM1 experimental area at SIN as used for the neutron source mock-up studies.

before and after the target are shown in Fig. 3. Although the beam could be properly aligned relative to the target, it was not possible to obtain as narrow a beam profile as desired. During a subsequent attempt to improve the situation (after measurement # 18), it was found that this beam blurring was due to beam scattering in the graphite. With the graphite placed at 2 m from the target, the situation was considerably improved. The calibration factor for the relocated scintillator counter telescope was determined as

$$G_2 = 336.6 \cdot 10^3 \text{ protons per coincidence.}$$

Redoing the same experiment with the now much better focussed beam showed a gain of a factor of $F_1 = 1.15$ (Measurement # 19 relative to # 18). This gain was initially considered as due in part to protons missing the target in the older arrangement and in part to an increased probability for an internuclear cascade with the better focussed beam. Later on it was found, however, that other measurements yielded almost identical results before and after the change. (# 30 relative to # 12 and # 63 relative to # 8 + # 9). Hence it is concluded, that measurement # 18 must have been slightly in error.

The targets used were placed inside a tank of stainless steel 170 x 170 cm² wide and 250 cm high which could be filled with heavy water up to a level of 170 cm. For the measurements with the cylindrical target (Pb-Bi, 150 mm diameter 600 mm long) the proton beam port was a 150 mm Al-tube coaxially placed inside a 200 mm diameter Al-tube to allow for space needed in a real design (Fig. 4). A total of 10 mm Al was present between the Pb-Bi and the D_2O.

For the simulation of the rotating target, an Al-table of an effective thickness of 30 mm was placed 5 cm below the mid-plane of the tank. The target was built up of Pb bricks or U-238 bricks of 10 cm height and 5 cm thickness interlaced with 6 mm thick polyethylene sheets to simulate the coolant inside the structure (Fig. 5). Similarly, 6 mm of polyethylene were placed above and below the target

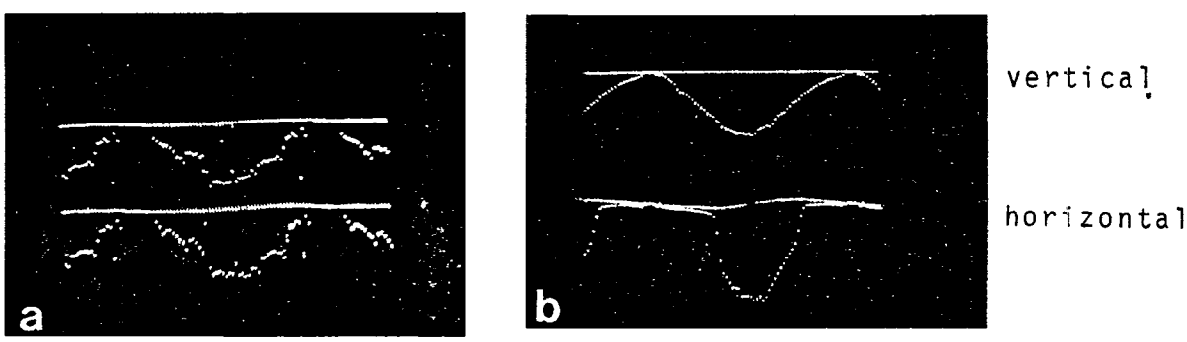

Fig. 3: Proton beam profiles as measured by wire chambers in the initial setup

a) in front of target (1 m from head of target). The separation between wires is 1 mm giving a FWHM of about 35 mm for both, the horizontal and the vertical direction.

b) behind target (2 m from first chamber). The separation between wires is 2 mm, giving a FWHM of 66 mm in the vertical direction. In the horizontal direction the profile is cut off by the target whose central 5 cm of material had been removed to show correct positioning.

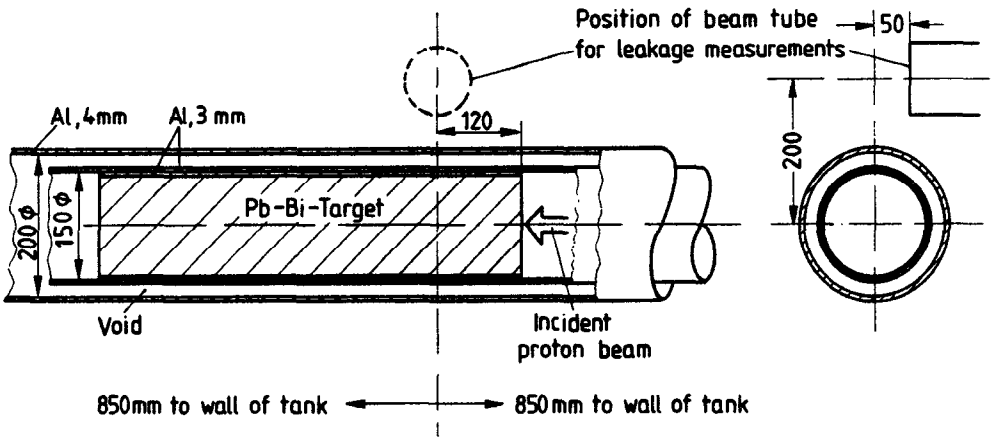

Fig. 4: The cylindrical target used as a mock-up for a liquid Pb-Bi target system. Dimensions are given in mm.

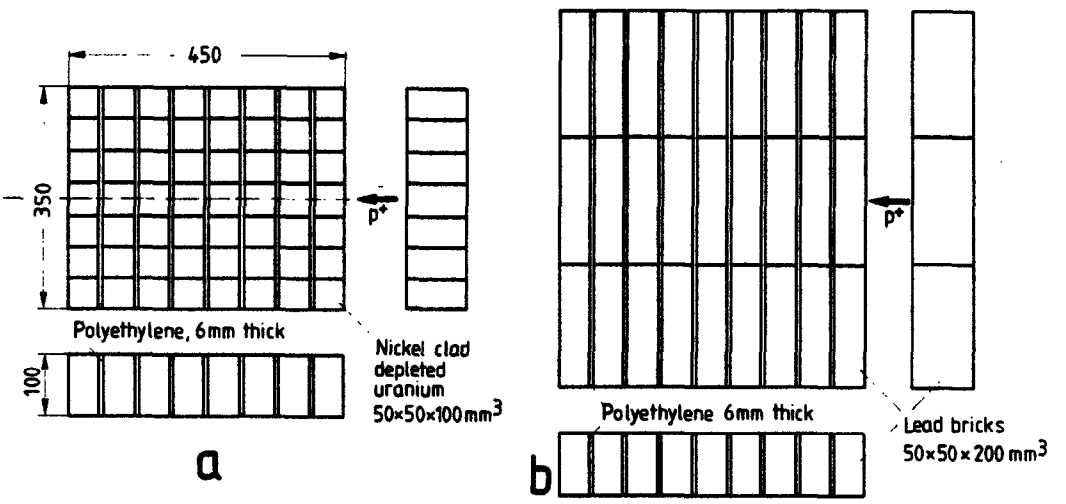

Fig. 5: The slab targets used as mock-up for the rotating target concept.

a) Depleted uranium target
b) Lead target

The positions of proton incidence are marked by arrows.

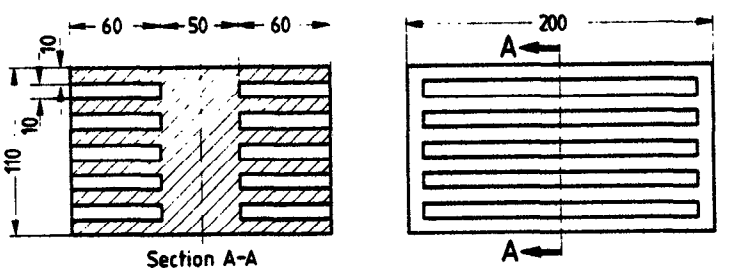

Fig. 6: The polyethylene moderator: a 50 mm thick polyethylene slab at the centre with 60 mm long and 10 mm thick fins on both sides.

with 20 mm of Al on the top. The slab targets were not extended all the way through the tank but only in the central part (35 cm wide for U-238 and 60 cm wide for Pb), but this can be considered as a sufficiently good representation regarding fast neutron yield as well as thermal neutron flux depression. The proton beam was entering through a 100 mm diameter Al-tube. Another 100 mm Al-tube was placed above the target at 12 cm (10 cm for uranium) downstream of the face of proton entry to serve as a thermal neutron beam hole for leakage measurements. For the hybrid moderator version only the lower half of the tank was filled with D_2O. A polyethylene (PE) moderator composed of a massive central part of 50 mm thickness, 120 mm high and 200 mm long and of two parts with 10 mm thick and 60 mm deep fins on either side was placed on top of the target (Fig.6). It was surrounded by a polyethylene reflector 600 mm long, 500 mm wide and 270 mm high. To measure the thermal neutron flux and time distribution, small BF_3-detectors were placed in a thimble below the target in the D_2O and between the fins of the polyethylene moderator.

The following configurations were investigated

A U-238 slab target in D_2O-tank

B U-238 slab target with hybrid moderator-reflector configuration

C U-238 slab target with no D_2O in tank; PE moderator and reflector

D U-238 slab target with no D_2O in tank; PE moderator, no reflector

E Pb slab target in D_2O-tank

F Pb slab target with hybrid moderator-reflector configuration

G Pb slab target with hybrid moderator configuration; no PE-reflector

H Pb slab target with no D_2O in tank; PE moderator and reflector

I Pb slab target with no D_2O; PE moderator, no reflector

K cylindrical target; tank filled with D_2O

L Pb slab target in D_2O-tank with PE moderator immersed in D_2O

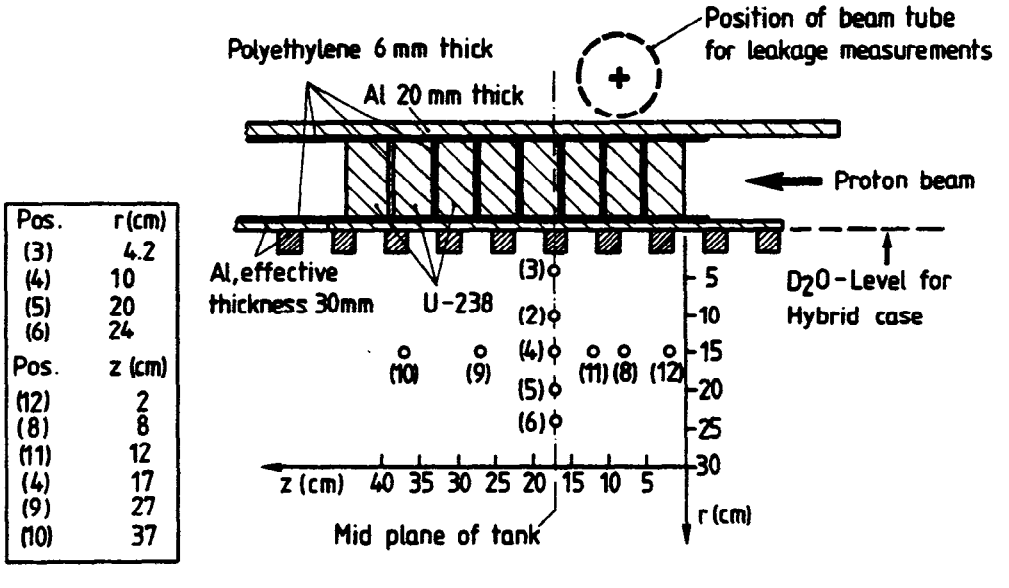

Fig. 7: Positions in the D_2O below the target, where flux measurements with the BF_3-detector were taken.

The individual measurements have been labelled by consecutive numbers which are underlined in this report. Some of them being runs for testing and checking purposes, not all will be reported here.

3. Thermal neutron flux distribution

Although a more detailed investigation of the thermal neutron flux distribution using Dy-foil activation has been carried out /3/, we did a crude survey of the flux distribution in the D_2O by moving the small BF_3-detector to different positions in order to be able to assess the flux at the position of our leakage measurement relative to the maximum flux and to compare by direct counting the flux in the full D_2O-tank to that in the semi-tank of the hybrid version. The

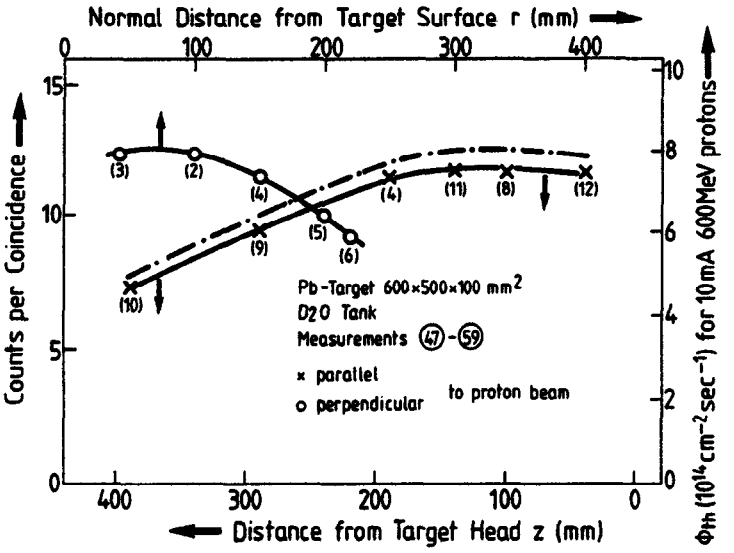

Fig. 8. Thermal neutron flux distribution measured for the case of a slab target of lead in a D_2O-tank. The dash-dotted curve gives the values corrected for the radial position of maximum flux.

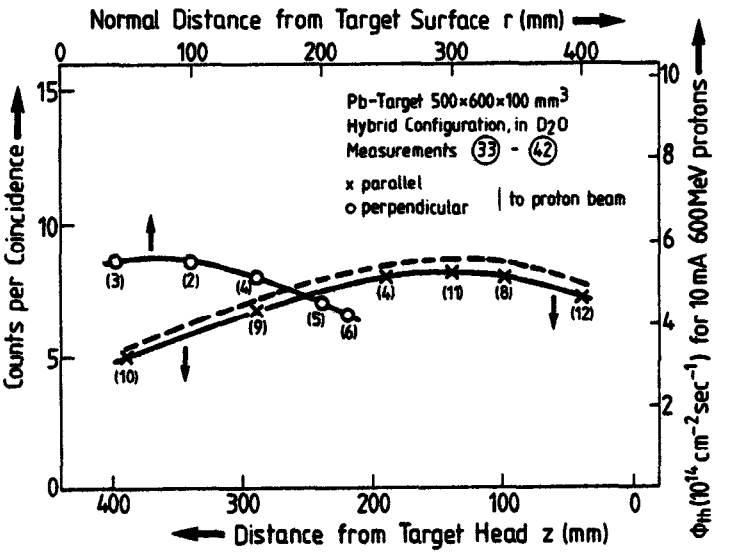

Fig. 9: Thermal neutron flux distribution measured for the case of a slab target of lead in the D_2O part of a hybrid moderator configuration. The dashed curve gives the axial distribution corrected for the maximum radial flux value.

positions, where flux measurements were taken for the slab target are shown in Fig. 7. The flux distributions measured in the directions parallel and perpendicular to the proton beam are shown in Figs. 8 through 11. There was only a limited region of accessibility with the Al-thimble holding the detector. The flux values given at the right hand scales have been derived from the neutron leakage measurements as described below.

For the case of the lead target the measurements parallel to the proton beam were not in the maximum flux region. A curve corrected by the ratio of the intensities at the respective maxima of the parallel and perpendicular distributions

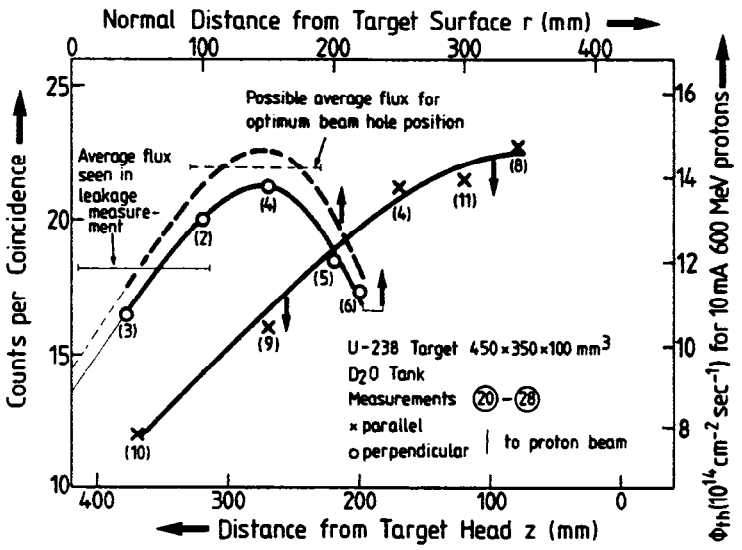

Fig. 10: Thermal neutron flux distribution measured for the case of a slab target of depleted uranium in a D_2O-tank. The dashed curve gives the normal distribution as corrected for the maximum value along the target. The horizontal lines give the range actually averaged over by the beam tube (solid) and the possible best position (dashed).

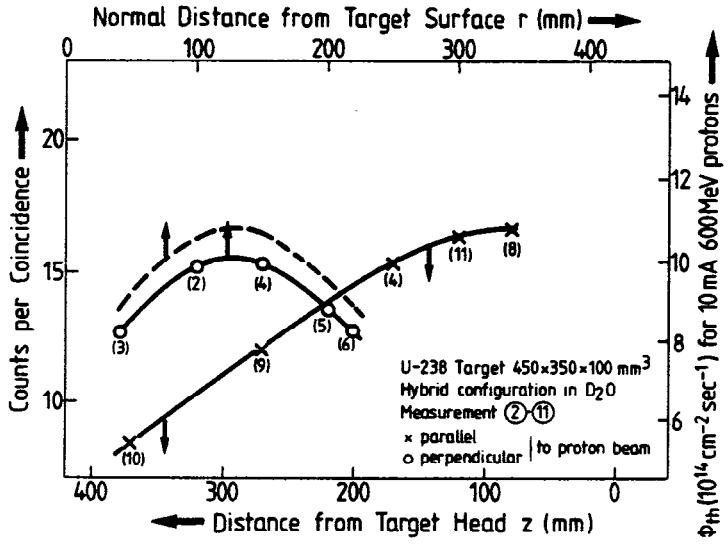

Fig. 11: Thermal neutron flux distribution measured for the case of a slab target of depleted uranium in the D_2O part of a hybrid moderator configuration. The dashed curve gives the normal flux distribution corrected for the maximum value along the target.

is given by the broken lines in Figs. 8 and 9. For the lead target the thermal neutron flux in the D_2O of the hybrid arrangement is by a factor of $F_2 = 0.72$ lower than in the full tank. Here the measured hybrid configuration has to be considered as a worst case limit because in a real arrangement some neutron back scattering would occur from the then present lead shield above the D_2O-tank.

In the case of the uranium target the flux distribution perpendicular to the proton beam was not taken at the position of the maximum of the parallel distribution. Therefore a dashed curve scaled with the ratio of the maximum fluxes measured in both directions is also given in the plots. Since the measurements in the U-target hybrid version (Fig. 11) were done before the repositioning of the carbon scatterer mentioned above, there is some uncertainty about the magnitude of the flux relative to the subsequent measurements. However no correction was attempted according to what was said in the previous chapter. Similar to the case of the lead target, the flux in the hybrid version is down by a factor of 0.74 relative to the full tank. Some, but relatively less improvement may also be expected in this case, if a complete target and lead shielding is present in the real situation. Also marked in Fig. 10 is the distance from the target surface which was viewed by the beam hole for the leakage measurements. Obviously, in order to obtain maximum leakage, the position should have been as indicated by the dashed horizontal line. The gain that would have been obtained is the ratio of the average fluxes at these positions which is

$$F_3 = 1.2 .$$

This factor will be used for the comparison of maximum leakage. (This factor depends slightly on the extrapolation used towards the target surface but the possible uncertainty is small.)

From Fig. 8 to 11 it is obvious that the uranium target causes a severe flux depression in the surrounding D_2O with the peak flux shifted some 15 cm away from the target surface, whereas in the case of lead the flux stays high up to the target surface. This has some effect on the optimum distance of the beam holes from the target surface, in particular since the fast neutron and γ-flux will decrease much more rapidly with distance than the thermal neutron flux.

Table 1 gives a listing of corrected count rates for the peak fluxes and the peak flux positions. Also included is the ratio of the flux 25 cm further downstream from the target head to the peak flux (measuring position (8)). This

Target	Configuration	Peak Flux			$\frac{I_{25}}{I_{max}}$
		z(mm)	r(mm)	I_{max}	
Pb	D_2O-Tank	120	70	12.6	0.65
Pb	Hybrid	140	70	8.8	0.60
U-238	D_2O-Tank	80	150	22.5	0.61
U-238	Hybrid	80	130	16.7	0.59
Pb-Bi	Cylinder in D_2O-Tank	120	75	13.8	0.80

Table 1: Comparison of thermal neutron count rates for various target moderator configurations. For I_{max} the corrected peak values have been taken (in units of counts per proton coincidence). I_{25} is the value 25 cm downstream from the position of maximum flux at the same radial distance.

ratio is only slightly lower for the uranium target. The more concentrated source of primary neutrons in the uranium is largely smeared out by the D_2O. More detailed investigations of the thermal neutron flux distributions in the moderators will be reported separately. The flux distribution for the cylindrical target had been measured earlier /3/. The result is shown in Fig. 12. No direct comparison of the flux level to the present measurement is possible but from the thermal neutron leakage results reported in the following chapter, a relative value for I_{max} can be deduced which is I_{max} = 13.9 . This has been included in Table 1.

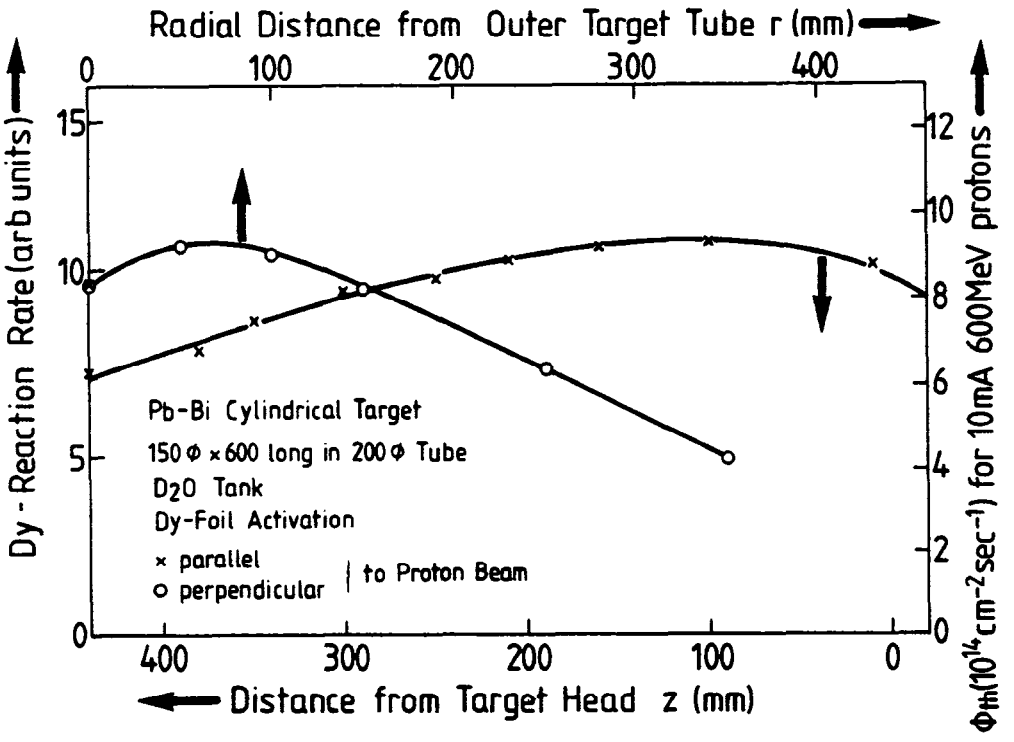

Fig. 12: Thermal neutron flux distribution in a D_2O-tank surrounding a Pb-Bi target of 150 mm Ø and 600 mm length placed concentrically in a 200 mm diameter Al-tube (Fig. 4) as measured by Dy-foil activation. The figure shows the Dy-reaction rate as a function of position.

4. Thermal neutron leakage from the moderators

4.1 Comparison of target-moderator-reflector configurations

In order to be able to compare the thermal neutron leakage from the various moderators, measurements were made on an extracted neutron beam with a fixed

geometry for all moderators. The setup is shown in Fig. 13. The detector used was a BF_3-proportional counter with 23 mm diameter and an average detection efficiency over the cross section of

$$\varepsilon = 0.056$$

for a thermal neutron spectrum. The active height was limited to 50 mm by a Cd slit and the effective solid angle was determined by a Cd diaphragm of 50 mm diameter placed at 2330 mm from the detector. The detector was looking at the bottom of a 100 mm diameter beam tube inserted in the D_2O-tank, which, for all measurements using the flat targets, ended at 10 cm from the central plane of the tank. For the measurements using the cylindrical target, the beam hole ended at a radius of 20.5 cm from the centre line of the target.

Data were taken for a preset number of coincidences of the proton monitor with and without a 2 mm cadmium sheet inserted at the position marked Ⓐ in Fig. 13. The difference of the two recordings gives the thermal neutron counts, Z_o. A list of results is given in Table 2.

From these data it can be seen that the D_2O in the hybrid configuration has some effect on the leakage from the PE-moderator (12 % gain for the U-target and 30 % gain for the Pb-target). It is therefore of interest to look whether the D_2O is merely acting as a fast neutron reflector or whether there is a noticeable effect on the thermal neutron time structure. We will come back to this in chapter 5.

The efficiency of the polyethylene moderator is also different for the various configurations. With no D_2O present it is smaller than with D_2O present under the target. This indicates that D_2O acts more as a reflector for fast neutrons than for thermal ones, since the mean freee path of thermal neutrons in polyethylene is small. Also the lower efficiency in the case of the U-238 target relative to the Pb-target can be qualitatively understood, because for the U-target the primary source of fast neutrons is more concentrated under the moderator itself.

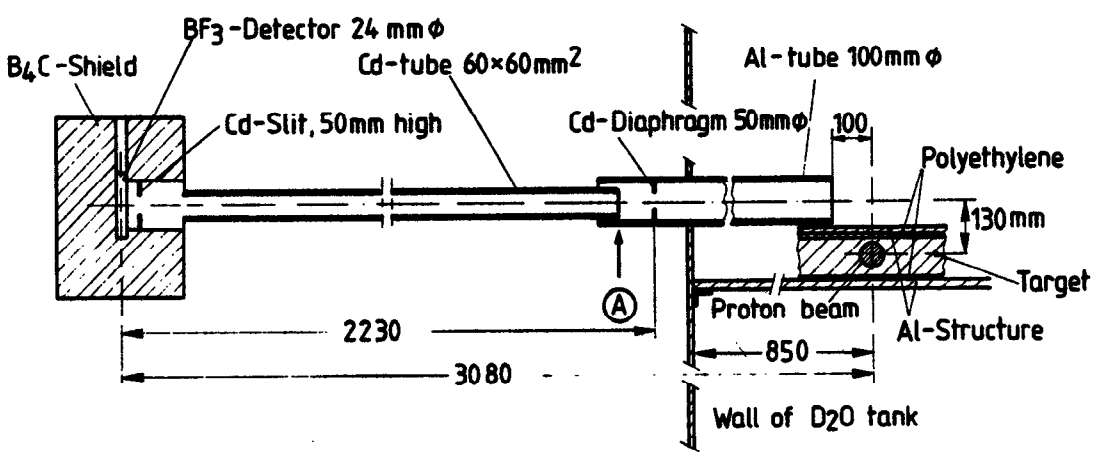

Fig. 13: Schematic representation of the setup used for the thermal neutron leakage measurements.

Measurement	Configuration	Target	upper moderator	upper reflector	lower moderator + reflector	Z_0 (2×10^5 coinc.)	G 10^3 p/coinc.	Z_0^* (10^{-7} n/p)
(18	A	U-slab	D_2O	D_2O	D_2O	10925	312.8	1.75)
19		"	"	"	"	13770	336.6	2.05
64		"	"	"	"	13217	336.6	1.96
8 + 9	B	U-slab	PE	PE	D_2O	8572	312.8	1.37
63		"	PE	PE	"	8857	336.6	1.32
12 + 16	C	U-slab	PE	PE	-	7465	312.8	1.19
17	D	U-slab	PE	-	-	5673	312.8	0.91
30		"	PE	-	-	6132	336.6	0.91
46	E	Pb-slab	D_2O	D_2O	D_2O	8700	336.6	1.29
66		"	"	"	"	8818	336.6	1.31
32	F	Pb-slab	PE	PE	D_2O	4295	336.6	0.64
65		"	PE	PE	"	4340	336.6	0.65
62	G	Pb-slab	PE	-	D_2O	2494	336.6	0.37
31	H	Pb-slab	PE	PE	-	3359	336.6	0.50
60	I	Pb-slab	PE	-	-	2375	336.6	0.35
61		"	PE	-	-	2410	336.6	0.36
72 + 7	K	Pb-Bi cyl.	D_2O	D_2O	D_2O	9661	336.6	1.44 1.58
57	L	Pb-slab	PE	D_2O	D_2O	8365	336.6	1.24

Table 2: Thermal neutron counts per proton for the various target-moderator-reflector configurations investigated. All leakage measurements were taken at the upper moderator. (+Measurement 7 was done in an earlier period, see footnote on page 11)

The Z^*-values, which give the number of thermal neutrons recorded per 600 MeV-proton incident on the target, are not directly relevant for the expected performance the neutron source because the actual configuration has not been simulated properly in these experiments. Corrections to be applied will be discussed in chapter 6.

For the D_2O-moderators, some flux depression will occur due to further beam holes placed in the moderator. This effect has also been investigated and will be reported in the following section.

4.2 Effect of additional beam holes in the D_2O

4.2.1 Cylindrical Pb-Bi target[1]

The effect of beam holes in the D_2O on the thermal neutron leakage from a given tube has been investigated by inserting 10 empty Al tubes of 10 cm diameter in the tank, in addition to the one used for the measurement. The extra tubes were arranged in two planes with 5 tubes in each plane and placed at distances of 15 cm upstream and downstream of the reference tube. They were suspended on a mechanism which allowed to change the positions of the noses of the 5 tubes in one plane simultaneously relative to the target centre line. The noses were placed at r = 20 and r = 40 cm. The results obtained without the extra tubes and with the tubes in place are given in Table 3. It can be seen that the overall flux depression by having as many as 11 beam tubes in the tank is relatively small (18 % for r = 20 cm). It should be noted, that one of the extra tubes was very close to the standard tube. A radial position of 20 cm corresponds to r' = 100 cm in Fig. 12. The axial positions of the tubes would be z = 250 and z = - 50 mm. It can be seen that the flux at these positions is still very close to the maximum value.

Measurement	Number of tubes in place	Radial position of extra tubes	$Z_0^*(10^{-7}n/p)$
1	1	-	1.58
2	11	20 cm	1.26
3	11	40 cm	1.34

Table 3: Effect of additional beam holes in the D_2O-tank for a Pb-Bi cylindrical target

4.2.2 Pb-slab target

In order to estimate the effect of additional beam holes placed in the D_2O in the case of a slab target, a set of runs was performed, where beam holes were consecutively removed from the D_2O, starting with a configuration as shown in Fig. 14. In the region above the target there were effectively 6 beam tubes with four of them arranged as two twin tubes. This means that the two tubes shared

1) These measurements were done in a different measuring period where the calibration yielded an absolute neutron to proton ratio which is 10 % higher than obtained in the period where most of the measurements were done. The numbers for the beam tube effect have not been corrected for this fact.

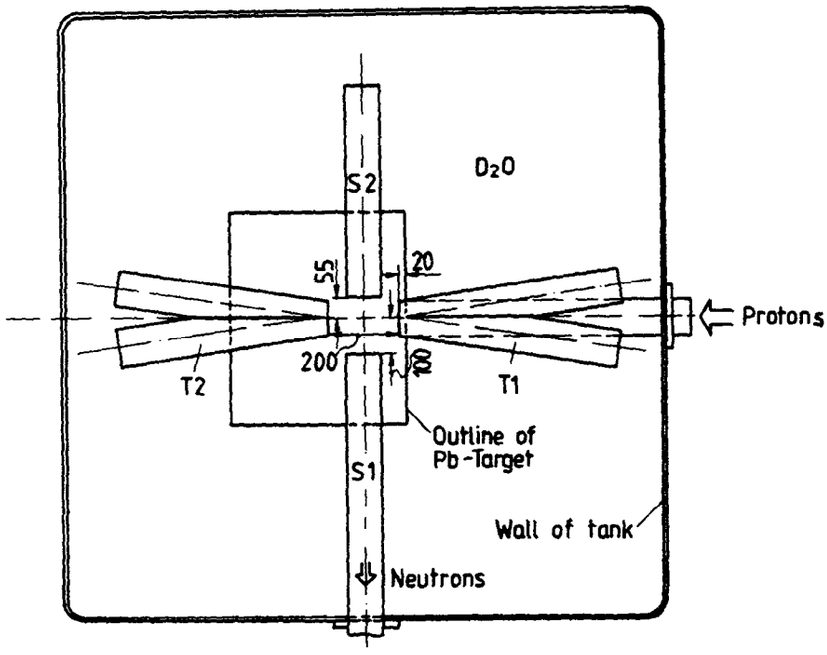

Fig. 14:

Arrangement of beam-tubes used for the measurement of the resulting flux depression for the case of a lead slab target. Beam tubes are in the plane above the target. T1 and T2 are twin tubes and S1 and S2 are standard tubes of 10 cm diameter. The neutrons leaking out of S1 were measured.

one common bottom from which two tubes of 100 mm diameter emerged with an angular separation of 15°. In this way the amount of D_2O displaced can be reduced relative to two single beam tubes. Two of the tubes (including the one on which the measurements were made) were single beam tubes. Table 4 lists the measured leakage values with different numbers of tubes in place. The tubes T1 und T2 had slightly different positions relative to S1 but in general it can be said, that the effect of both, twin tubes and single tubes is small with an overall flux depression of 13 % occuring in response to five additional holes in the same half of the moderator. From the little crosstalk observed before, it can be expected that beam holes in the lower half of the tank would hardly affect the upper half at all.

Measurement	Tubes in place	$Z_0^*(10^{-7}n/p)$	ΔZ^*
67 / 68	S1, S2, T1, T2	1.12	
69	S1, S2, T2	1.19	0.07
70	S1, S2	1.25	0.06
71 / 46	S1	1.29	0.04
			0.17

Table 4: Measured neutron leakage for the Pb-slab target in D_2O with different beam tubes in place.

5. Time structure of the neutron field in the moderators

Since it is foreseen in the German project that the proton beam shall hit the target in pulses of 0.5 ms duration once every 10 ms, it is of interest to predict the time structure of the resultant thermal neutron field in the different concepts considered. To this end measurements were made with the secondary beam of the cyclotron pulsed by means of a mechanical chopper placed near the entrance of the PM1 beam line. The chopper consisted of a spinning hollow Al-cylinder of 1 cm wall thickness and 9 cm outer diameter with 2 slits of 1 cm width at its circumference. When the 2 cm of Al were in the beam, its energy was sufficiently degraded that the following bending magnet system did not transport it through the downstream collimator. The idea was that intensity should be transmitted only, when the two slits allowed the proton beam to pass through unperturbed. The chopper was spun at 100 rps which resulted in a proton pulse every 5 ms. The time structure of the proton intensity hitting the target is shown in Figs. 15a and 15b. The pulse of Fig. 15a was obtained with the original setup, the one of Fig. 15b after the realignment mentioned above which took place after measurement number 18. In both cases, the pulse is well des-

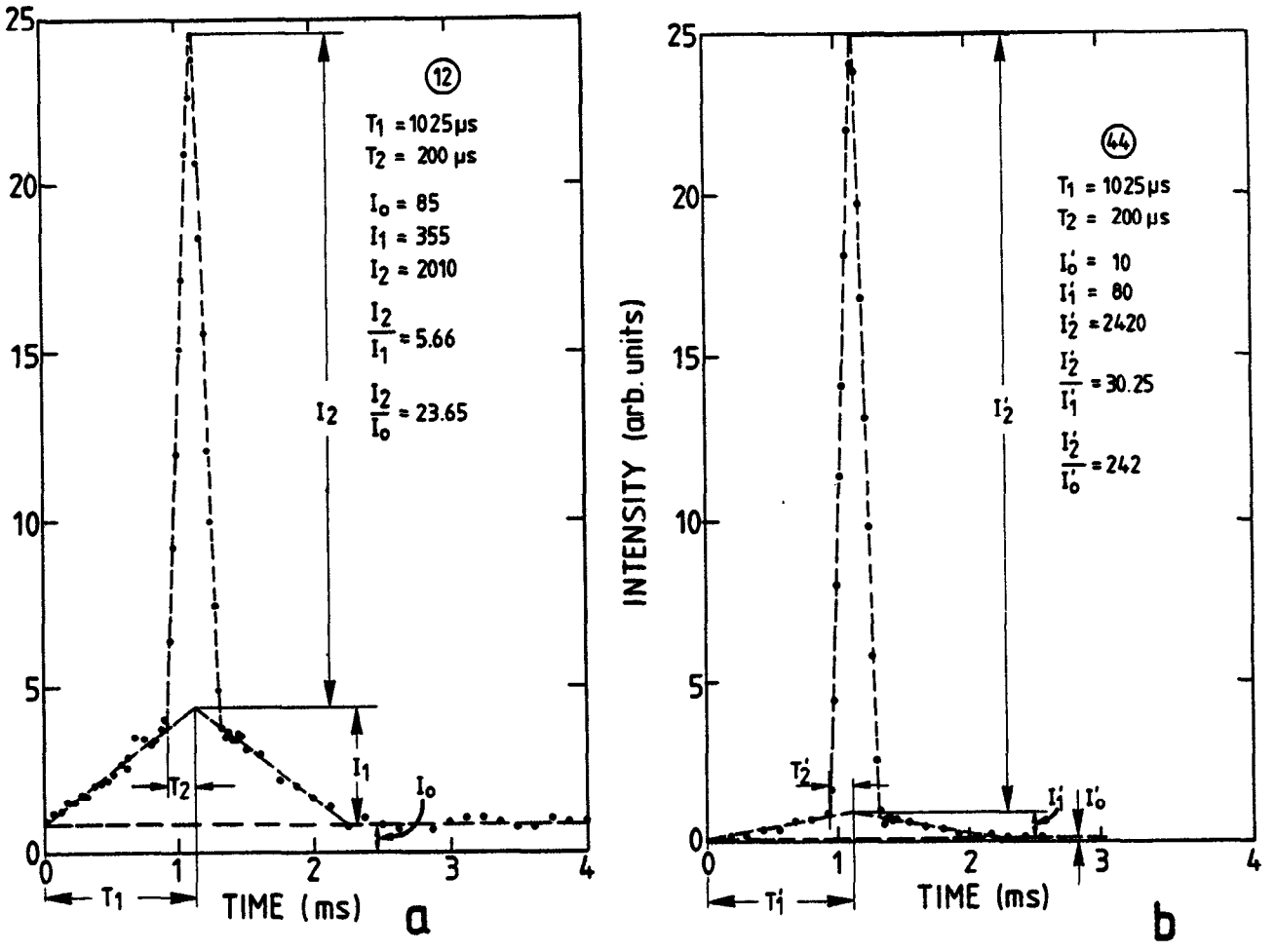

Fig. 15: Time structure of proton pulses as measured by the scintillator telescope for the chopped PM1-beam.

a) Graphite scatterer at 4 m from target (i.e. before realignment of beam.

b) Graphite scatterer at 2 m from target (i.e. after realignment of beam).

cribed by two triangles superimposed upon one another plus a constant background. The base widths of the triangles were very near to constant. Only a slight variation was observed for the various measurements, as can be seen from Table 5. The ratio between the intensities of background and the two triangles, also contained in Table 5, showed somewhat stronger variations. With such a proton pulse, the resulting time structure of the neutron pulse is easily predictable, if the time needed for thermalisation is neglected and a decay constant α is assumed.

Measurement	T_1 (μs)	T_2 (μs)	$\frac{I_2}{I_o}$	$\frac{I_2}{I_1}$	$\frac{I_2^*}{I_o}$	$\frac{I_2^*}{I_1}$	F
1	1125	200	22.6	6.58	94.9	9.9	0.908
12	1125	200	23.6	5.66	99.1	8.5	0.895
29	1000	200	173	22.8	-	-	0.956
44	925	200	160	30.2	-	-	0.966
45	1050	187.5	235	36.1	-	-	0.973
74	1050	200	165.5	37.8	-	-	0.974

Table 5: Characteristics of the proton beam time distributions as determined in the various measurements. The values marked by an asterix are obtained by correcting I_o and I_1 by factors of 4.2 and 1.5 respectively, as described in the text.
F is given by $F = (1-I_1/I_2)^{-1}$.

With the notation given in Fig. 15 and using E as a coupling constant which relates the neutron flux to the proton beam intensity[1] we obtain for

$$0 \leq t \leq T_1 - T_2 \qquad \Phi' = \Phi_0 + \Phi_1^1$$

$$T_1 - T_2 \leq t \leq T_1 \qquad \Phi' = \Phi_0 + \Phi_1^1 + \Phi_1^2$$

$$T_1 \leq t \leq T_1 \pm T_2 \qquad \Phi' = \Phi_0 + \Phi_2^1 + \Phi_2^2$$

$$T_1 + T_2 \leq t \leq 2T_1 \qquad \Phi' = \Phi_0 + \Phi_2^1 + \Phi_3^2$$

$$2T_1 \leq t \qquad \Phi' = \Phi_0 + \Phi_3^1 + \Phi_3^2$$

---

1) E is, of course, a function of geometry and the materials used and is considered, for the time being, as an adjustable parameter.

with

$$\Phi_0 = E \cdot I_o \cdot \lim_{t\to\infty} \int_0^t e^{-\alpha(t-t')} dt = \frac{E \cdot I_o}{\alpha}$$

$$\Phi_1^1(t) = E \cdot \frac{I_1}{T_1} \cdot \frac{1}{\alpha^2} \left\{ e^{-\alpha \cdot t} + \alpha \cdot t - 1 \right\}$$

$$\Phi_2^1(t) = E \cdot \frac{I_1}{T_1} \cdot \frac{1}{\alpha^2} \left\{ e^{-\alpha(t-T_1)} \left(e^{-\alpha T_1} - 2\right) - \alpha(t-2T_1) + 1 \right\}$$

$$\Phi_3^1(t) = E \cdot \frac{I_1}{T_1} \cdot \frac{1}{\alpha^2} \left\{ e^{-\alpha(t-T_1)} \; 2[\cosh(\alpha \cdot T_1) - 1] \right\}$$

$$\Phi_1^2(t) = E \cdot \frac{I_2}{T_2} \cdot \frac{1}{\alpha^2} \left\{ e^{-\alpha(t-T_1+T_2)} + \alpha(t-T_1+T_2) - 1 \right\}$$

$$\Phi_2^2(t) = E \cdot \frac{I_2}{T_2} \cdot \frac{1}{\alpha^2} \left\{ e^{-\alpha(t-T_1)} \left(e^{-\alpha T_2} - 2\right) - \alpha(t-T_1-T_2) + 1 \right\}$$

$$\Phi_3^2(t) = E \cdot \frac{I_2}{T_2} \cdot \frac{1}{\alpha^2} \left\{ e^{-\alpha(t-T_1)} \; 2[\cosh(\alpha \cdot T_2) - 1] \right\} \qquad (1a)$$

Frame overlap of z pulses due to a separation T_3 between proton pulses can be taken into account by putting

$$\Phi(t,\alpha) = \Phi_0(\alpha) + \sum_{n=1}^{n=3} \sum_{m=1}^{m=2} \sum_{l=0}^{z-1} \Phi_n^m\left((t + l \cdot T_3), \alpha\right) \qquad (1)$$

5.1 The polyethylene moderator

It is likely that, in a small hydrogeneous moderator, one decay constant α is sufficient to describe the time dependence of the neutron field. This view is supported by the slope of the trailing edge of the neutron pulses measured for the polyethylene moderator as shown in Fig. 16 b and 17 b. The decay constants derived from these slopes are not the true decay constants due to the contribution of the proton pulse to the pulse width. An approximate correction can be obtained by using the second moment as time resolution. With the resolution function given by a sum of two triangles with base widths $2T_1$ and $2T_2$ and fractional heights (1-F) and F, the second moment is

$$\int_{-\infty}^{\infty} t^2 R(t) dt = \frac{(1-F) \cdot T_1^3 + F \cdot T_2^3}{6[(1-F) \cdot T_1 + F \cdot T_2]} = \sigma^2 \qquad (2)$$

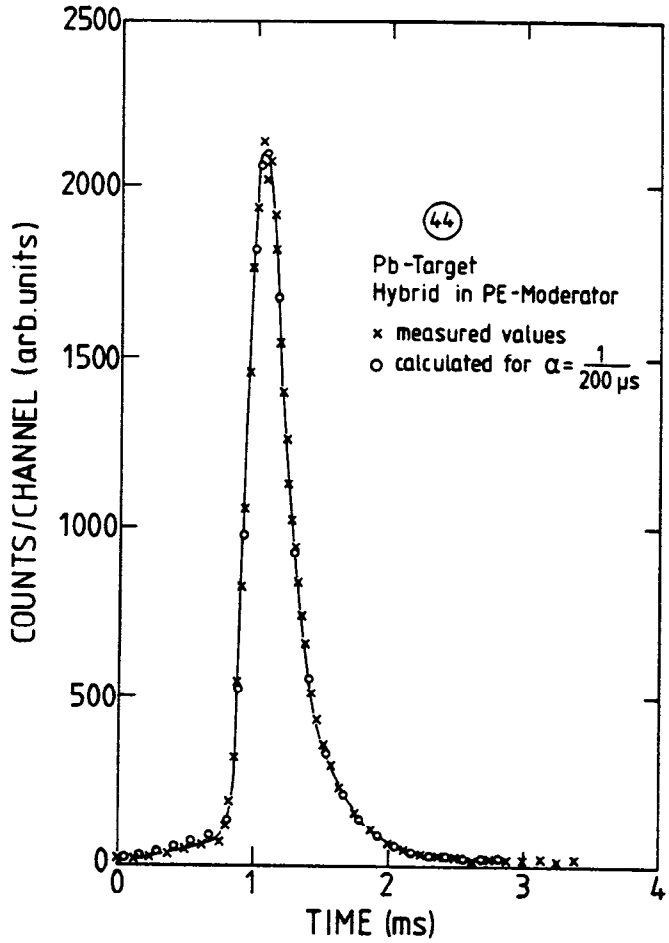

16a

Fig. 16:

Time structure of the neutron field in the polyethylene moderator of the hybrid configuration with a Pb-target. (measurement 44)

a) linear plot, solid curve is a guide to the eye through the measured data (crosses) open circles are values calculated with equ. (1) and $\alpha = \frac{1}{200\ \mu s}$ and the proton pulse of Fig. 15b.

b) logarithmic plot showing that decay is dominated by one single life time.

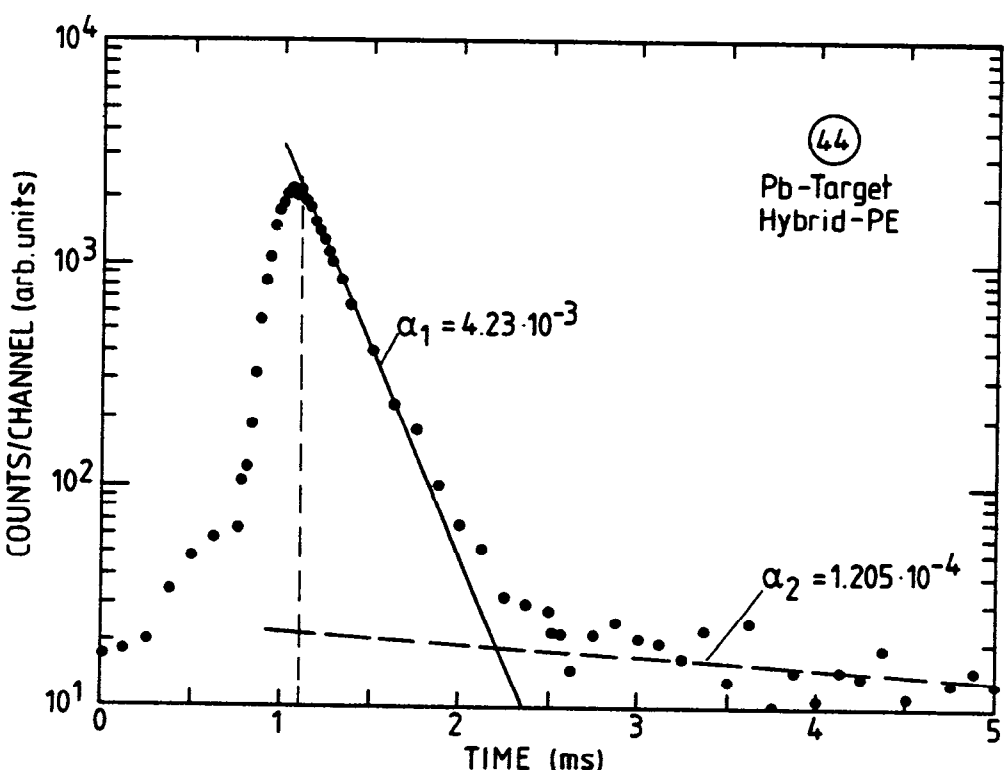

16 b

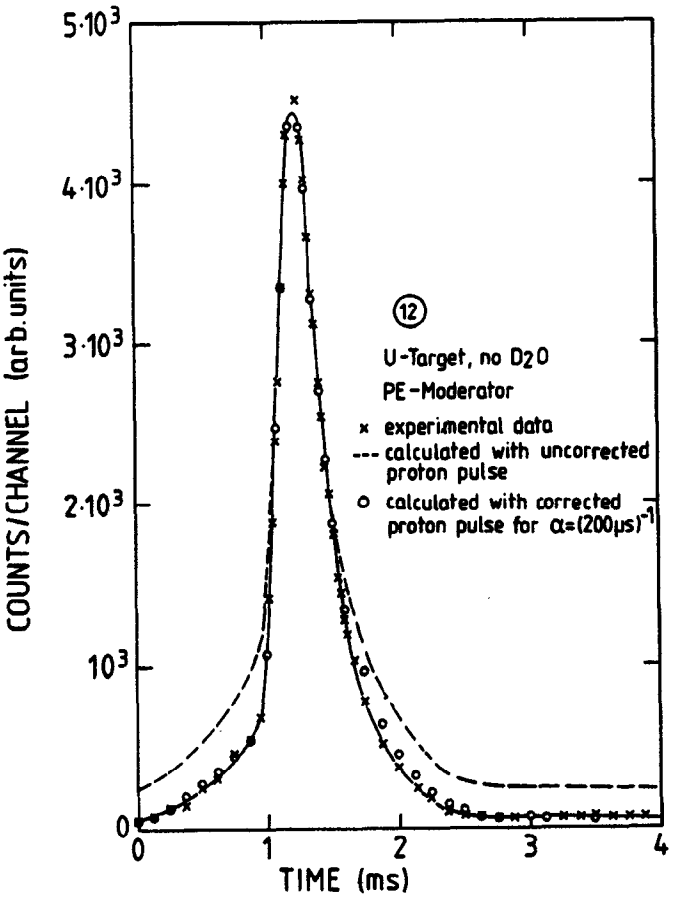

17a

Fig. 17:

Time structure of the neutron field in the polyethylene moderator with a target of depleted uranium and no D_2O present in tank (measurement # 12)

a) linear plot, solid curve is a guide to the eye through the measured data (crosses).

The dashed curve was obtained, using equ. (1) and $\alpha = (180\ \mu s)^{-1}$ with the proton pulse as shown in fig. 15a.

Open circles are values calcuculated with equ. (1) and $\alpha = (200\ \mu s)^{-1}$ and with the proton pulse corrected as described in the text.

b) Logarithmic plot showing one decay constant.

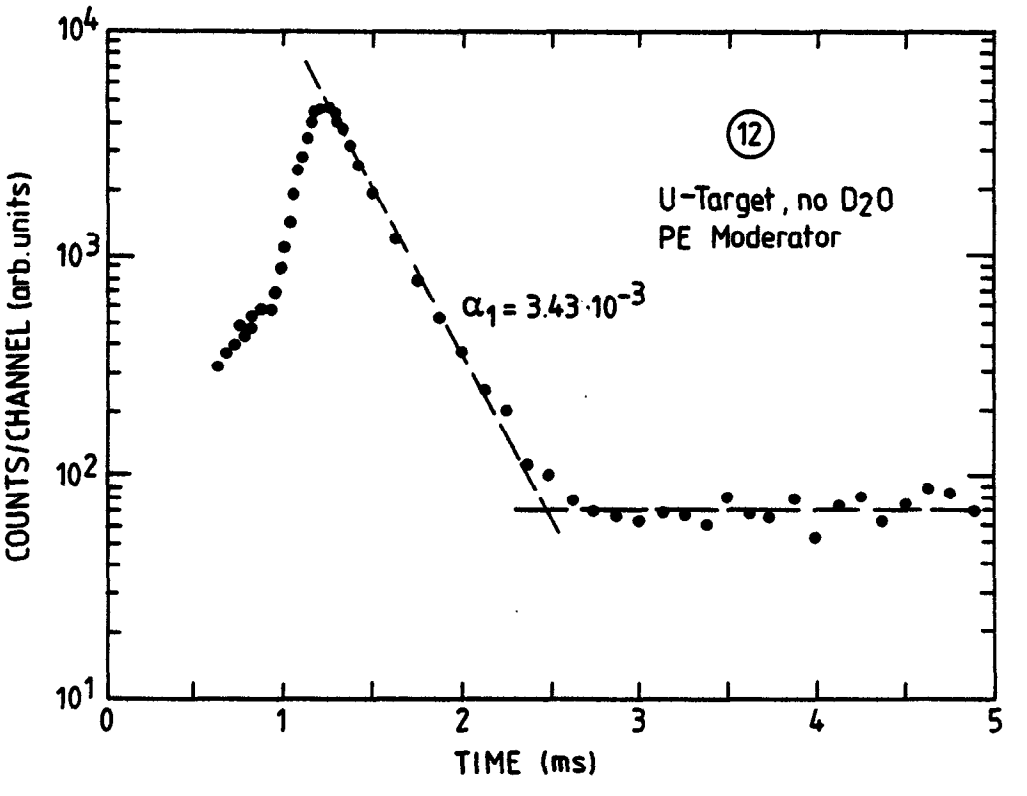

17b

For the proton distribution of Fig. 15b, using the values of Table 5, this yields

$$\sigma_p = 160.3\ \mu s$$

Since the second moment of an exponential decay is given by $\sigma_{exp}^2 = 2\tau^2$, we obtain for the "true" decay time

$$\tau^* = \sqrt{\tau^2 - \frac{\sigma_p^2}{2}} \qquad (3)$$

which leads to $\tau^* = 207\ \mu s$ for the case of Fig. 16.

In Fig. 16a the open circles represent a calculation with equ. (1) and a decay time of 200 μs using the proton pulse of Fig. 15b. The result can be seen to agree reasonably well with the measured data. Attempting a similar fit for the case of a curve measured with the proton pulse shown in Fig. 15a yielded curve b (dashed) in Fig. 17a, which has been adjusted to the measured data at the peak value. Obviously the calculated background is much higher than the measured one and also the rise in the part where $t < T_1 - T_2$ is significantly faster than measured. This indicates that not all of the background proton current and of the proton intensity in the wide triangle seen by the monitor at 4 m from the target actually hit the target. This can be qualitatively understood by the way the chopper worked, since it is assumed that the background in caused by insufficient energy degradation when the proton beam was blocked by one wall of the hollow chopper only. If the background contribution and the intensity in the wider triangle are scaled down by factors of 4.2 and 1.5 respectively, the values given in Fig. 17a by open circles are obtained from equ. (1) with $\alpha = (200\ \mu s)^{-1}$.

In Fig. 18, the curves measured for the case of a slab target of depleted uranium with and without D_2O present under the target are shown, normalized to the same number of measured proton coincidences. There is a 10 % increase in peak intensity due to the D_2O but practically no long time effect on the intensity. This shows that the D_2O acts mainly as a reflector for fast neutrons and that the uranium target is a sufficiently good decoupler for thermal neutrons to prevent any significant cross talk.

This is even true to a large extent for a lead target as can be seen from Fig. 16. Only a very small tail with a long decay constant is noticeable in Fig. 16b, corresponding to less than 1 % of the peak intensity.

Due to the different shapes of the proton pulses in the various measurements, the peak intensities obtained for a fixed number of proton coincidences are not directly comparable among one another. Under the condition that the total number of protons remain constant for the pulses characterized by primed and unprimed quantities one has:

$$I_1 \cdot T_1 + I_2 \cdot T_2 = I_1' \cdot T_1' + I_2' \cdot T_2'$$

In our case we have $T_1 \approx T_1$ and $T_2' \approx T_2'$.

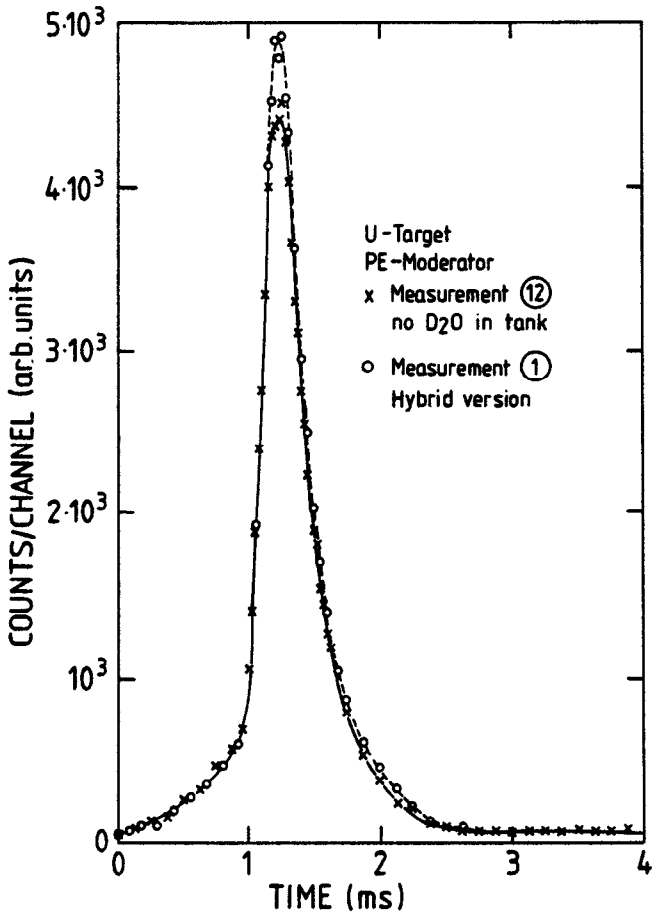

Fig. 18:

a) Comparison of neutron time distributions measured for equal numbers of protons for a polyethylene moderator and a unranium target without (solid curve) and with D_2O under the target (dashed curve).

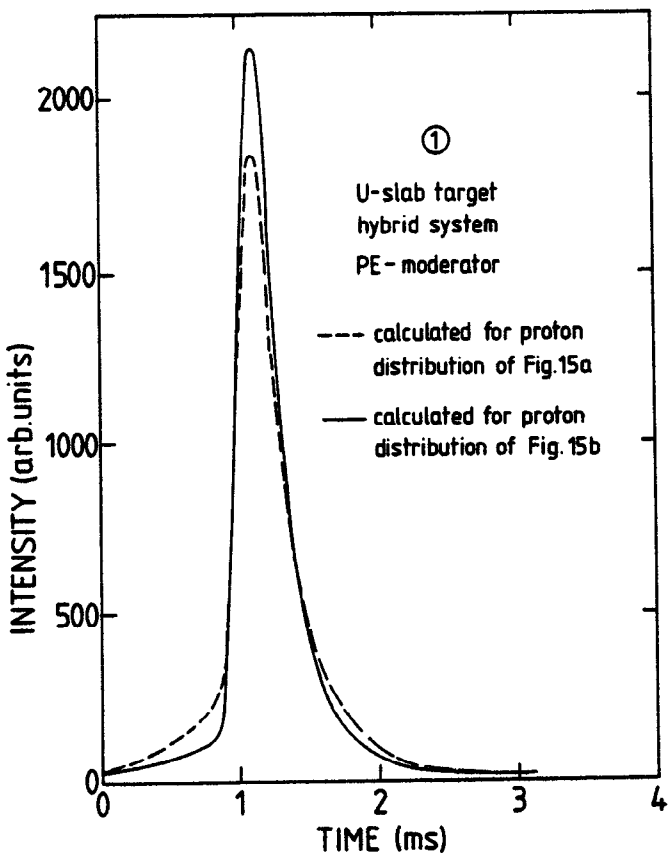

Fig. 19:

Computed curve of neutron time distribution for the polyethylene moderator of the hybrid configuration with a proton distribution as shown in Figs. 15a and 15b.

This yields

$$I_1' = \frac{I_1 + I_2 \frac{T_2}{T_1}}{1 + \frac{I_2'}{I_1'} \cdot \frac{T_2}{T_1}} \qquad (4)$$

where the ratio I_2'/I_1' is known.

Inserting numbers for measurements 1 and 44 (primed) from Table 5 we have

I_1^* = 80 p/channel, I_2 = 790 p/channel, I_2'/I_1' = 30.2,

T_1 = 1025 μs, T_2 = 200 μs which leads to

I_1' = 34 p/channel, I_2' = 1025 p/channel.

I_o is not affected.

The actual correction factor depends also on the decay constant α and can be determined relatively easily if one time constant is clearly dominating as for the case of the polyethylene moderator. The curve that would have been obtained in the case of the U-target for a proton distribution as in Fig. 15b can thus be computed for comparison to the Pb-target. It is shown in Fig. 19.

The resulting increase in peak intensity is by a factor of 1.18. A direct comparison between peak intensities on a per proton basis is difficult from the time structure measurements because the various measurement were done in different positions. However, the leakage measurements can be used to get ratios of mean intensities which can be converted to peak intensities if the shape of the proton pulse is known. An example will be given later.

5.2 The D_2O moderator

For the case of the heavy water tank the analysis of the measured time distributions is less simple due to the fact that

- more than one time constant is contributing to the decay behaviour
- frame overlap is important in the measured data.

Although a more sophisticated analysis is in progress, the following simple approach, that was used for the time being, is believed to give reasonably accurate results already:

It was assumed that only two time constants α_1 and α_2 are important with the respective fractions D•E•I and (1-D)•E•I decaying in these modes. Hence

$$\Phi(t,\alpha_1,\alpha_2) = D \cdot \Phi(t,\alpha_1) + (1-D) \cdot \Phi(t,\alpha_2) \qquad (5)$$

with $\Phi(t,\alpha_1)$ calculated according to equ. (1). The effect of the background between proton pulses was negelcted[1]. In order to obtain a first set of input

---

[1] For large contributions from slowly decaying modes this is probaly the major source of error.

parameters for a calculation, the measured data were plotted on a semilogarithmic plot and straight line was drawn through the long-time part of the curve. These values were subtracted from the measured data to yield another straight line whose slope was taken as the measured value of the fast decay constant α_1. This was corrected for resolution according to equ. (3) to yield α_1^*. Frame overlap was taken into account in a global manner by drawing a third straight line parallel to the first one such that its value for T = 0 was the same as that of the first one for T = 5 ms. This line was used as a base-line to read the slope of the first one (α_2) and the relative intensites of the fractions decaying with the two time constants. This latter reading was taken near the position of the apparent maximum of the curve. The procedure is examplified in Fig. 20 for measurement 29.

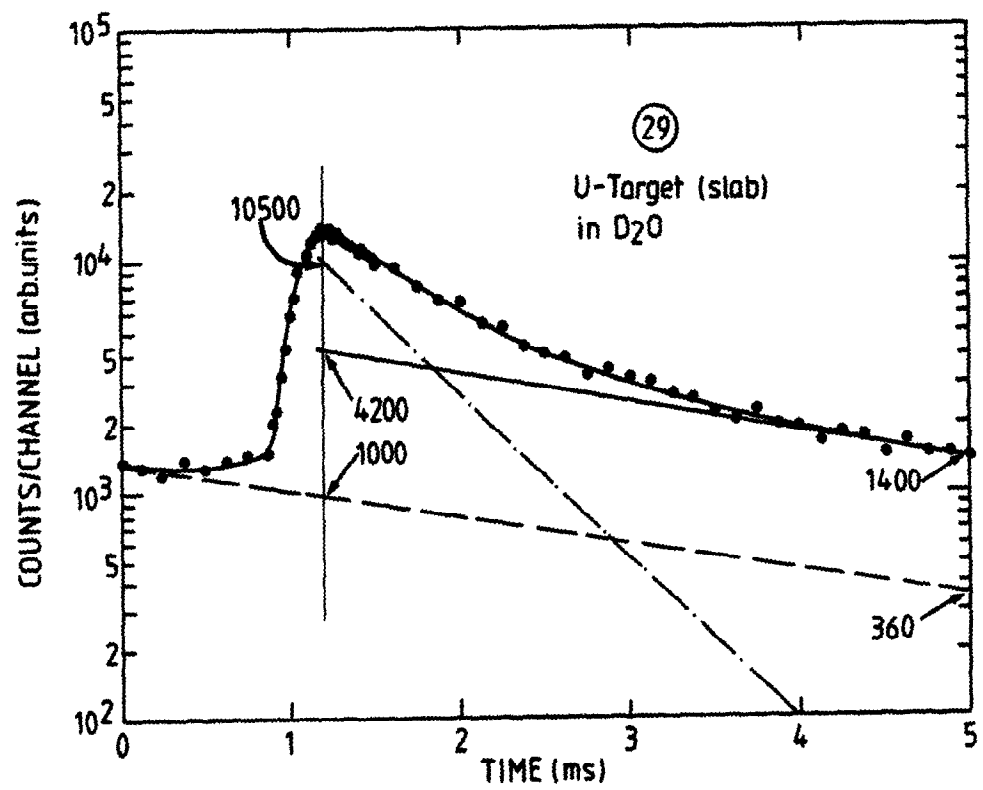

Fig. 20: Semilogarithmic plot of the thermal neutron time structure measured for a U-238 slab target in a D_2O tank. The solid straight line has been adjusted to the slope of the data at large t. The difference between the measured data (curve through data) and the solid line is given by the dash-dotted line. The dashed line represents the frame overlap from previous pulses.

For this case we have

$$\alpha_1 = \frac{\ln 1050 - \ln 100}{2800\ \mu s} = 1.66 \cdot 10^{-3}\ \mu s^{-1}$$

$$\alpha_2 = \frac{\ln (4200 - 1000) - \ln (1400 - 360)}{(5000 - 1200\ \mu s)} = 0.296 \cdot 10^{-3}\ \mu s^{-1}$$

$$\frac{\Phi_o(\alpha_1)}{\Phi_o(\alpha_2)} = \frac{10500}{4200 - 1000} = 2.97 = \frac{D \cdot \Phi_o}{(1-D) \cdot \Phi_o}$$

or D = 0.766

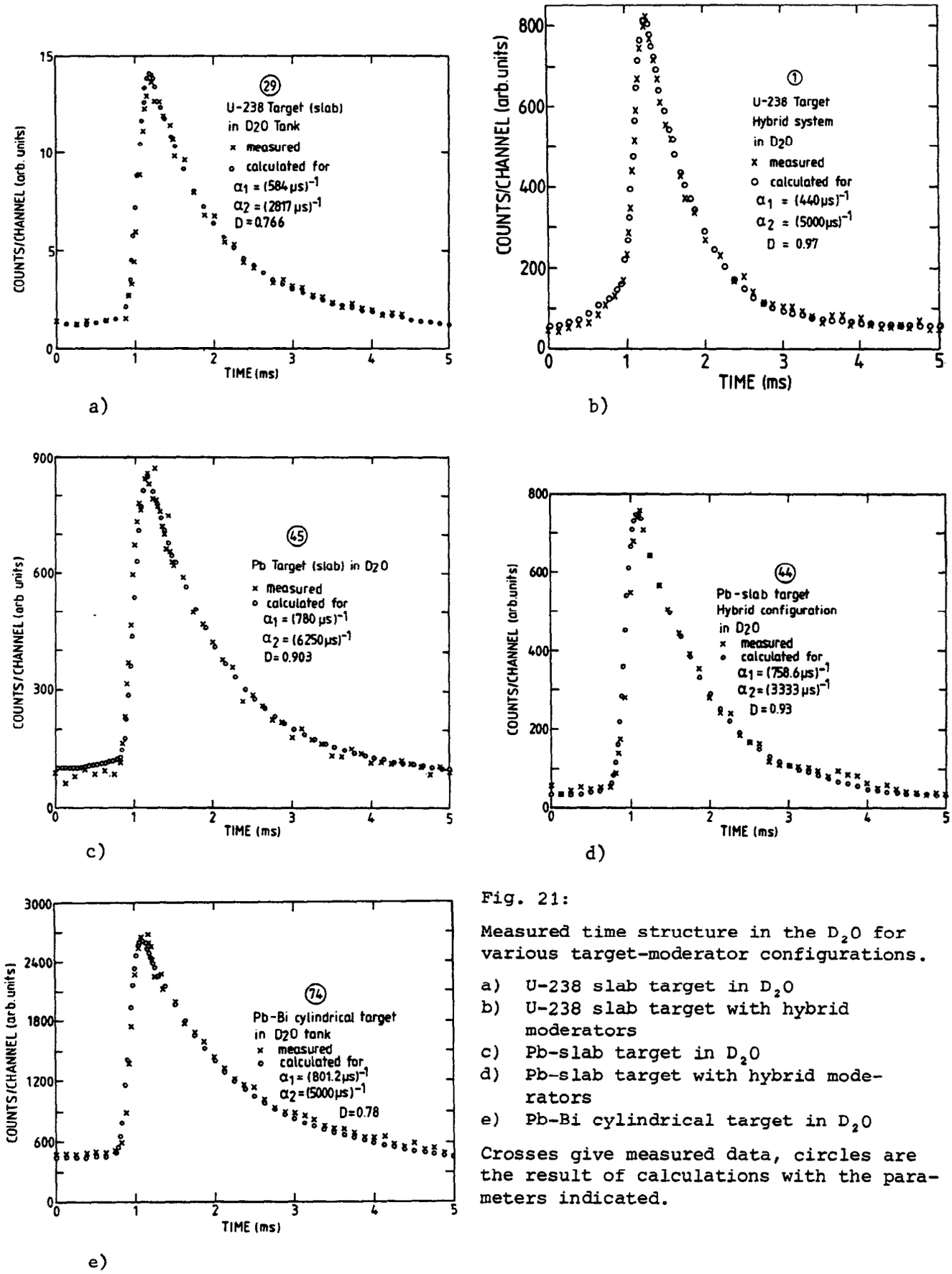

Fig. 21:

Measured time structure in the D_2O for various target-moderator configurations.

a) U-238 slab target in D_2O
b) U-238 slab target with hybrid moderators
c) Pb-slab target in D_2O
d) Pb-slab target with hybrid moderators
e) Pb-Bi cylindrical target in D_2O

Crosses give measured data, circles are the result of calculations with the parameters indicated.

Measurement	Configuration		α_1 10^{-3} μs^{-1}	τ_1 (μs)	α_2 10^{-3} μs^{-1}	τ_2 (μs)	D	σ (μs)	τ_1^* (μs)	α_1^* 10^{-3} μs^{-1}	τ_2^* (μs)	α_2^* 10^{-3} μs^{-1}	D*
1	U-Hyb	PE	3.384	295.5	-	-	1	296.44	208.4	4.80	-	-	1
		D_2O	1.89	529.6	0.230	4348	0.890	296.44	440.0	2.27	5000	0.200	0.97
12	U	PE	3.43	291.0	-	-	1	308.0	193.0	5.18	-	-	1
29	U	D_2O	1.66	600.0	0.296	3381	0.766	191.3	584.5	1.71	2817	0.355	0.766
44	Pb-Hyb	PE	4.227	226.3	0.121	8290	0.996	160.3	195.9	5.1	8290	0.121	1
		D_2O	1.304	767	0.300	3330	0.80	160.3	758.6	1.32	3333	0.300	0.930
45	Pb	D_2O	1.286	790	0.137	7300	0.903	172.6	780.5	1.28	6250	0.160	0.903
74	Pb-Bi	D_2O	1.233	810	0.195	5128	0.670	168.6	801.2	1.25	5000	0.200	0.780

Table 6: Decay parameters for the various target-moderator configurations. The unmarked values have been derived from semilogarithmic plots of the measured data. Values marked by an asterix are those used to calculate the values given by circles in Fig. 21.

The values thus obtained are summarized in Table 6. Using these values to calculate the curves according to equ. (5) did not result in a satisfatory agreement with measured data. Therefore α_2 and, if necessary also D was varied to improve the agreement. In this way the values α_2^* and D^* given in Table 2 were obtained[1]. Figs. 21a through 21e show the curves calculated with these data and the (corrected) proton pulse parameters of Table 5. In view of the assumptions made (see above) it did not seem reasonable to try and further improve the fits. The decay parameters thus obtained are considered sufficient to estimate the time structure expected for a different shape of the proton pulse.

6. Discussion

6.1 Thermal neutron flux

As mentioned in chapter 4.1, the Z^*-values obtained in the present measurements are not in all cases representative for the expected performance of a real spallation source because:

- in the case of the uranium slab target the flux at the measuring position was by a factor of 1.2 down from the flux at the "best" position,

- the polyethylene reflector used in these measurements is much less efficient than the combination of Be-reflector and Pb-shield foreseen for the projected German source. From earlier experiments /4/ it is known that a factor of 3 can be gained relative to an unreflected moderator. The gain by the polyethylene reflector used here was roughly 1.4. The fact, that PE rather than H_2O was used as a moderator in these measurements does not affect the thermal neutron leakage in a reflected geometry as has been shown earlier /4/.

A set of "best" Z_o^{**}-values obtained by taking these corrections into account, is given in Table 7 for the various target-moderator-reflector combinations. The values given for the D_2O moderators in the hybrid systems have been deduced from the full tank values using the ratio of measured thermal neutron fluxes. They have to be considered as lower limit values because the albedo of the air above the D_2O is much less than that of the aluminium and lead which will be present in a real design. From the effect the D_2O has on the PE-moderator a gain of roughly a factor of 1.3 seems to be likely.

It is of interest to note that, despite the fact that a considerable flux depression occurs near the uranium target, the thermal neutron leakage from the D_2O moderator is almost twice that for a Pb-target (ratio 1.85 in good agreement with the value of 1.8 obtained in the flux measurements).

Also given in Table 7 is a figure which represents the isotropic thermal neutron flux in D_2O delivering the same neutron current as a spallation source operated at 600 MeV, 10 mA (roughly equivalent to 1100 MeV, 5 mA) with the given configuration. This value is obtained from the geometry of the setup used for the measurement and the efficiency of the detector, ε. Allowing for the fact that the current at a moderator surface, j, is given by /5/.

$$j = \frac{\Phi}{2}$$

---

1) For the case of the D_2O in the U-target hybrid version it was necessary to vary also α_1 and take a constant background into account.

Configuration	Moderator	Correction factor	Z_o** (10^{-7} n/p)	$\bar{\Phi}_{equ}$ ($10^{14}cm^{-2}sec^{-1}$)	$\frac{\hat{\Phi}}{\bar{\Phi}}$
U-238 rotating target in D_2O tank	D_2O	1.2	2.54	14.7	
U-238 rotating target hybrid version	D_2O H_2O	(1.3) 3	1.9 2.7	11.0 (14.4) 16.7	10.5 18.2
Pb-rotating target in D_2O tank	D_2O	1	1.3	8.0	
Pb-rotating target hybrid version	D_2O H_2O	(1.3) 3	0.9 1.1	5.6 (7.2) 6.8	7.9 18.4
Pb-Bi flowing liquid target in D_2O	D_2O	1	1.5	9.3	4.6

Table 7: List of "best" neutron leakage values and corresponding equivalent thermal neutron flux (at 600 MeV, 10 mA) for the various configurations considered. Values of $\bar{\Phi}_{equ}$ in parenthesis are guesses taking into account the albedo of the materials present in a real design.

one obtains:

$$\bar{\Phi}_{equ} = \frac{8\pi \cdot R^2}{F_1 \cdot F_2} \cdot \frac{Z_o^{**}}{\varepsilon}\left(\frac{n}{p^+}\right) \cdot I(mA) \cdot 6.25 \cdot 10^{15}\left(\frac{p^+}{mAs}\right)$$

with $F_1 = 2.3 \cdot 5\ cm^2$, $F_2 = 2.5^2\pi\ cm^2$, $R = 223$ cm, $\varepsilon = 0.056$ and $I = 10$ mA this yields

$$\bar{\Phi}_{equ} = 6.18 \cdot 10^{21} \cdot Z_o^{**}\ cm^{-2}\ sec^{-1}.$$

The same value of ε has been used throughout, because the spectrum in a well reflected H_2O-moderator with grooves should be very similar to that in a D_2O-tank.

6.2 Expected time structure for a rectangular proton pulse

For a rectangular proton pulse of duration t_p and intensity I the time-dependent thermal flux is

$$\Phi(t) = \sum_i \Phi_i^{as} \cdot (1-e^{-\alpha_i t}) \qquad \text{for } t < t_p$$

$$\text{and} \quad \Phi(t) = \sum_i \Phi_i^{as} \cdot (1-e^{-\alpha_i t_p})\ (e^{-\alpha_i (t-t_p)}) \qquad \text{for } t \geq t_p \qquad (6)$$

where Φ_i^{as} is the contribution of the fraction of neutrons decaying with time constant α_i to the asymptotic value of the flux that would be reached at long times if the proton pulse were on continuously (equ. 1a). For two contributions with time constants α_1 and α_2 and weights D and (1-D) respectively the total asymptotic flux is

$$\Phi^{as} = \Phi_1^{as} + \Phi_2^{as} = \frac{D \cdot E \cdot I}{\alpha_1} + \frac{(1-D) \cdot E \cdot I}{\alpha_2}, \tag{7a}$$

or, conversely

$$E \cdot I = \frac{\Phi_{as}}{\frac{D}{\alpha_1} + \frac{1-D}{\alpha_2}} \tag{7b}$$

Φ_i^{as} is related to the average flux Φ_i^{av} in a pulsed mode with duty cycle $\Delta = (t_p \cdot \nu)^{-1}$ (ν = repetition rate)

$$\Phi_i^{av} = \Phi_i^{as} \cdot t_p \cdot \nu. \tag{8}$$

Representative values for Φ^{av} can be obtained from the data of Table 7, if allowance is being made for effects like flux depression due to beamholes and further structural materials where necessary (which will of course also affect the α's). Examples of the expected time dependent flux are shown for the measured cases 44 (PE-moderator of hybrid configuration with Pb slab target) and 74 (Pb-Bi cylindrical target in D_2O with one beam hole present) in Fig. 22.

For the peak-to-average ratio one finds

$$\frac{\hat{\Phi}}{\bar{\Phi}} = \frac{1}{t_p \cdot \nu} \frac{\frac{D}{\alpha_1}(1-e^{-\alpha_1 t_p}) + \frac{1-D}{\alpha_2}(1-e^{-\alpha_2 t_p})}{\frac{D}{\alpha_1} + \frac{1-D}{\alpha_2}} \tag{9}$$

For the two above cases this yields with the data of Table 6:

$\frac{\hat{\Phi}}{\bar{\Phi}}$ = 18.4 for the PE-moderator in the hybrid version

$\frac{\hat{\Phi}}{\bar{\Phi}}$ = 4.6 for the Pb-Bi target in the D_2O-tank

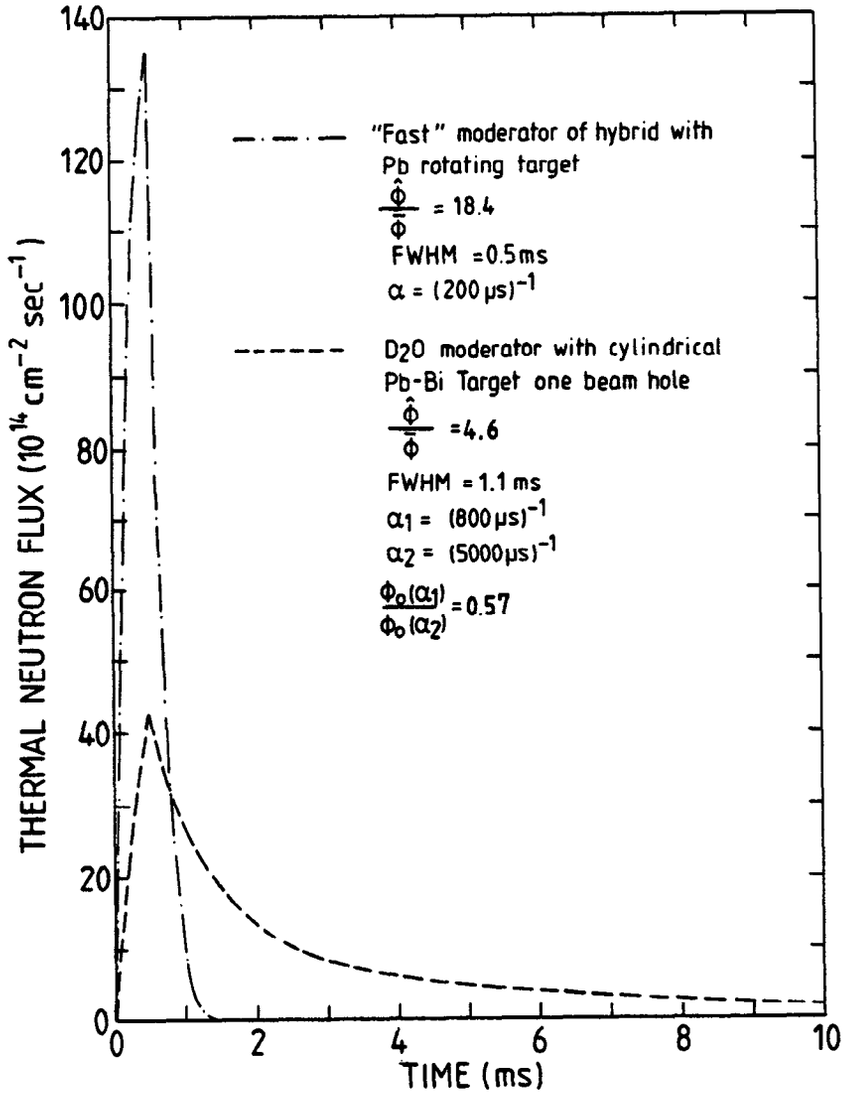

Fig. 22:

Expected time structure of thermal neutron fluxes for the case of a rotating Pb-target with a fast moderaotr (curve a) and a cylindrical Pb-Bi target in a D_2O tank for a 0.5 ms proton pulse of 1100 MeV once every 10 ms.

References

/1/ Hoffmann H., "Prospects for a Liquid Metal Target System for a Spallation Neutron Source", (1979), Jül-Conf. 35 pp 127-153

/2/ Bauer G.S., "Design Studies for a Rotating Target Arrangement for a Spallation Neutron Source" (1979), Jül-Conf. 35 pp 155-183

/3/ Drüke V., Paul N., Bauer G.S. and Spitzer H., "Measurement of thermal neutron flux distributions for various target-moderator configurations for a spallation neutron source by activation of Dy-foils", this volume

/4/ Bauer G.S., Gompf F., Mannhardt W., Reichardt W., Scherm R. and Spitzer H., "Thermal Neutron Leakage from Hydrogeneous Moderators for a Spallation Neutron Source" (1981), SNQ-report, part III A2, unpublished

/5/ Beckurtz K.H. and Wirtz K., "Neutron Physics", Springer, Berlin (1964)

Jül-Conf-45 D2-5

I C A N S - V

MEETING OF THE INTERNATIONAL COLLABORATION ON

ADVANCED NEUTRON SOURCES

June 22-26, 1981

Measurement of Time Structure and Thermal Neutron Spectra for Various Target-Moderator-Reflector Configurations of an Intensity-Modulated Spallation Neutron Source

G.S. Bauer*, H.M. Conrad*, H. Spitzer*, K. Friedrich** and G. Milleret***

* Inst. f. Festkörperforschung der KFA Jülich GmbH

** Physikalisch-Technische Bundesanstalt, Braunschweig

*** Laboratoire National SATURNE, Saclay, France

Abstract

Lead and uranium spallation targets have been bombarded with proton pulses of about 0.14×10^{-3} s duration at a repetition rate of 100 s^{-1} and an energy of 1.1 GeV. The spectra of neutrons thermalized in compact or grooved polyethylene moderators with lead or beryllium reflectors have been investigated. Also, the dwell-times of the neutrons in the moderator were measured. The grooved moderator gives a softer spectrum than the compact one. The same holds for the use of a beryllium reflector as compared to the lead reflector. The dwell-times of the neutrons in the polyethylene moderator depend on both the neutron energy and the target-moderator-reflector arrangement. Lead was found superior to beryllium as reflector material for an intensity modulated spallation neutron source, because it results in a better time structure without loss in peak intensity of the neutron pulses.

1. Introduction

Mainly three questions were to be investigated by measuring the thermal neutron leakage from moderators in different target-reflector configurations. From the thermal spectrum we wanted to determine the effective moderator temperature (Maxwell temperature) in order to deduce a relation of moderator geometry as well as target/reflector combinations to the hardness of the spectrum. Next we wanted to study the energy dependence of the decay times of the thermal neutron field in the moderator and finally the influence of different target/reflector combinations on these decay times. These latter questions are important in the optimization of the configurations with respect to physical and technical parameters. Physically one wants to obtain a short residence time of thermalized neutrons in the moderator to avoid long tails of the monochromatic neutron pulses extracted from the designed spallation source. Technically one is interested in an easy-to-build and inexpensive target-moderator-reflector combination.

The measurements were performed at the French proton synchrotron SATURNE which could deliver the desired 1.1 GeV protons and were a time structure of the proton pulses similar to the one proposed for the German SNQ-project could be obtained.

2. Experimental details

2.1 The experimental set-up

To simulate the conditions of the projected spallation source the beam was extracted from the ring accelerator with 100 s^{-1}. The pulse duration was about 140 µs (FWHM). The target and detector set-up was very similar to that used in previous experiments at CERN /1/ and therefore will be described only briefly (see also Fig. 1).

The pulsed proton beam with an average of 2.9×10^9 p/s hit the lead or uranium targets surrounded by moderators and reflectors as described in section 2.2.

The neutrons slowed down in the polyethylene moderator (used instead of water for experimental reasons) were extracted at 90° relative to the proton beam. For the spectra measurements the detector was placed in a straight-through position to perform an energy selection of the neutrons by time-of-flight. The measurement of the pulse structure was accomplished by placing a graphite crystal into the beam path, which deflected certain well-defined neutron energies through an angle of 90° and thus enabled the measurement of their intensity as a function of time (see Fig. 1).

An [002]-oriented pyrolytic graphite crystal was placed in reflection configuration in the thermal neutron beam, thus forming a selective velocity filter. If stored according to their time-of-arrival at the detector, neutrons of different velocities are thereby distinguished by assignment to different orders of the crystal reflections, except for an overlap caused by the "tails" of the time distribution due to an insufficiently long flight path.

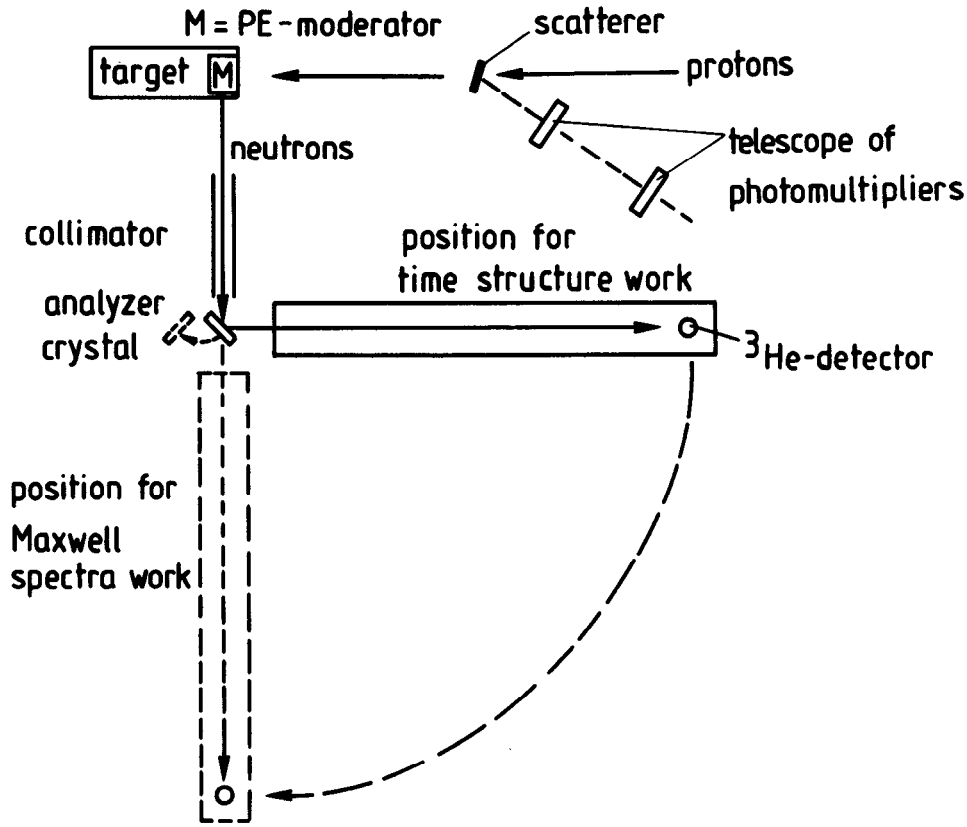

Fig. 1: Schematic (top) view of the experimental set-up

A CANBERRA multichannel analyzer MODEL 8603, into which the data from a time-of-flight interface were fed, was used for data acquisition. The neutron detector (^3He and BF_3) counts and the photomultiplier counts representing the primary proton distribution were stored in 2048 time channels of 4 μs width simultaneously. In some cases the counts recorded with a low-efficiency fission chamber placed in the grooves of the moderator were also stored. These latter data represent the average dwell-time of neutrons in the moderator and were necessary for defining the time-zero and the time-resolution for the Maxwell- spectra work. The time correlation between proton pulse, fast neutron background in the detector and neutron flux in the moderator is shown in Fig. 2.

The multi-channel analyzer was triggered by the 100-Hz-machine-signal from the accelerator. For the time structure work (crystal reflection data) the experimental resolution function is represented by the shape of the primary proton pulse (photomultiplier data). Fig. 3 compares its shape to the shape of the pulse for neutrons of 14.4 meV of energy (004-reflection).

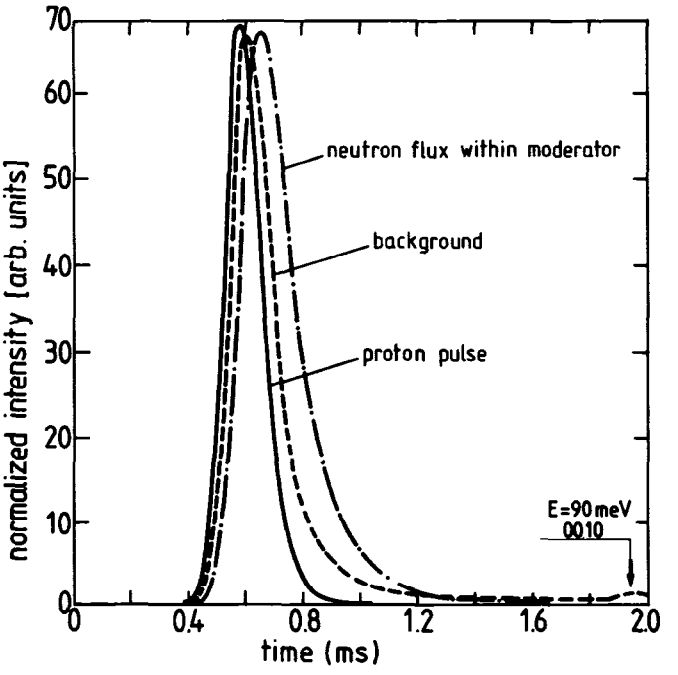

Fig. 2: Sequence and shape (on the actual time scale) of proton pulse, fast neutron background in the counter and neutron flux measured in the moderator grooves

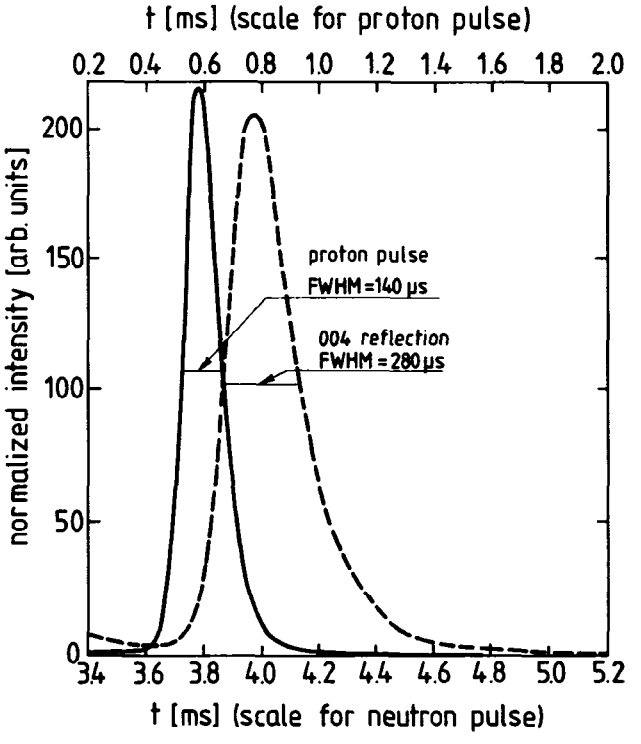

Fig. 3. Comparison of the shapes of the proton signal (employed as the resolution function) and one of the crystal analyzer reflections. (Note the shift of time scales!)

2.2 The various target-moderator-reflector configurations

The standard set-up of target-moderator-reflector combinations is shown in Fig. 4. The graphite below the target was used to simulate to some extent the D_2O-tank of a hybrid moderator configuration. It remained unchanged in the course of the experiments, whereas different combinations of the fast moderator, (simulated by compact or grooved polyethylene), and target as well as reflector materials were used (see Table 1).

	target	reflector
fast moderator (grooved)	Pb Pb U U	Pb Be Be Pb
fast moderator (compact, "flat")	Pb	Pb

Table 1: Target-moderator-reflector configurations investigated

Only one configuration with a compact fast moderator was tested for comparison, as it was known from earlier experiments that the grooved moderator gives an intensity gain of about a factor of 2 /4/. (The grooves have been worked into the moderator face pointing towards the neutron extraction channel.)

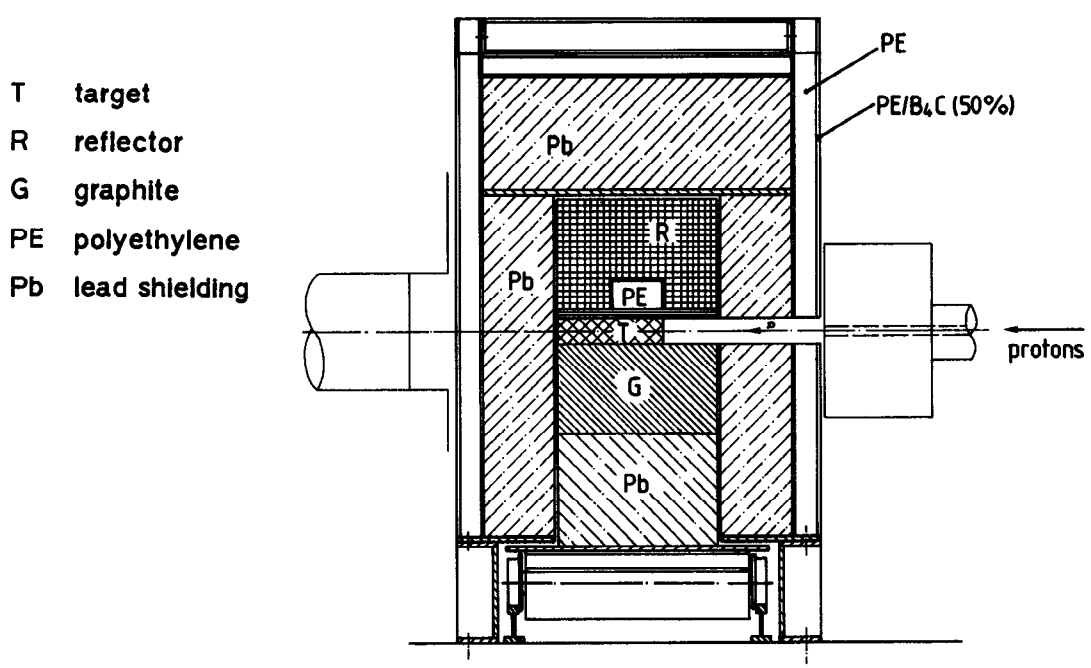

Fig. 4: Target-moderator-reflector arrangement

3. Experimental results and data evalution

3.1 Thermal neutron spectra

In Fig. 5 a typical example of the distribution of flight-times of the neutrons emerging from the fast moderator is shown, as measured in a distance of about 5.5 metres from the moderator. (This is little less than the distance of the moderator from the outer surface of the shielding of the projected spallation source.) In addition to the Maxwellian spectrum, a contribution of fast and epithermal neutrons is present at short flight times.

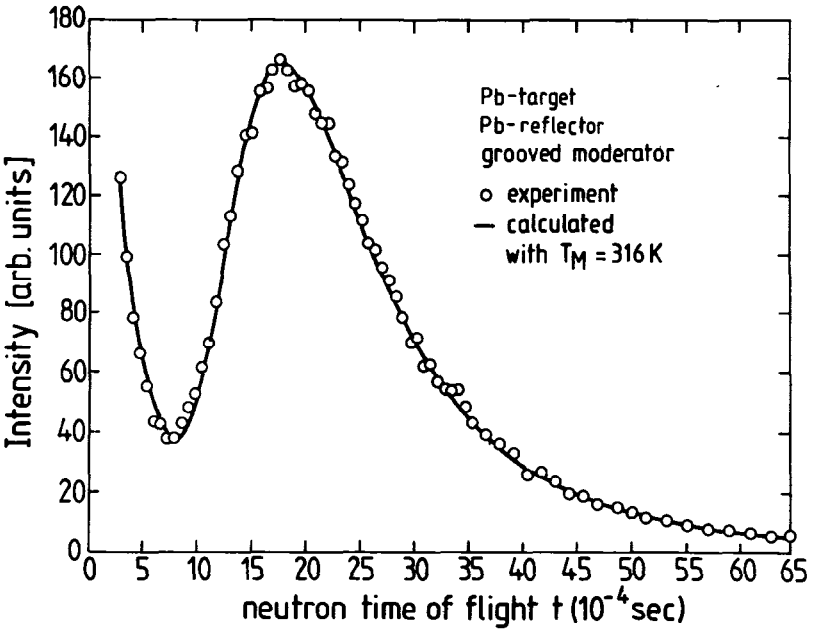

Fig. 5: Time-of-flight spectrum of neutrons emerging from the grooved polyethylene moderator (Pb target and Pb reflector). Open circles are the experimental data points (summed up over 16 4-μs-time-channels) and the solid line is a fit as described in the text.

As can be seen from Fig. 5 , the measured data could be fairly well described by a Maxwell distribution superimposed on a power-law for the fast background ($E^{-1+\alpha}$). In order to obtain the characteristic parameter of the Maxwell spectrum, i.e. the Maxwell temperature, the assumed functional expression was transformed into the time scale of the experimental data and fitted to these data using a least-squares-procedure /2/.

Two corrections have been applied to the mathematical expression to adequately describe the experimental situation. These corrections were:

a) accounting for the energy dependence of the counter efficiency, and

b) accounting for the finite width of the thermal neutron peak in the moderator (resolution correction).

The second correction was applied by convoluting the measured thermal neutron distribution in the moderator (determined experimentally with a small fission chamber placed in the moderator grooves) with the following expression (t = time of flight, with t = 0 defined at the maximum of the neutron flux pulse in the moderator; compare also Fig. 2):

$$I(t) = P_1 \cdot \left[\left(\frac{t_M}{t}\right)^4 \cdot \exp\left(-\frac{t_M^2}{t^2}\right) + \frac{P_2 \cdot t^{-2\alpha}}{1 + \left(\frac{\sqrt{5}t}{t_M}\right)^{14}} \right]$$

The convolution was then fitted to the experimental data by varying the parameters P_1, P_2, α and t_M, t_M being the "Maxwell-time", which can be easily transformed to give the Maxwell temperature T_M. (The denomimator in the second term of the above equation acts as a step function truncating the $E^{-(1-\alpha)}$-dependence at about $E = 5 \cdot k_B T_M$.) The velocity dependence of the counter efficiency (1/v) is already contained in the above expression. A list of the results for the Maxwell temperatures obtained by this evaluation procedure is given in Table 2. (The more or less unimportant scale factors P_1 and P_2 were omitted.)

	target	reflector	T_M[K]	α
grooved PE-moderator	Pb	Pb	316 ± 4	o.68 ± 0.10
	Pb	Be	284 ± 5	0.36 ± 0.14
	U	Be	293 ± 5	0.24 ± 0.12
	U	Pb	322 ± 3	0.48 ± 0.10
"flat" PE-moderator	Pb	Pb	355 ± 6	0.54 ± 0.07

Table 2: Maxwell temperatures of different target-moderator-reflector configurations. Little relevance should be attributed to the values of α (see discussion).

One remark should be added concerning the resolution function. In fact, the dwell time of the thermal neutron field in the moderator is a function of neutron energy. This is physically obvious, since faster neutrons leave the moderator volume faster and has also been found in the time structure measurements performed at CERN /1/ and in this work (see next section). For this reason, strictly speaking, an energy-dependent resolution function should be used. In our case, due to the long proton pulses the resolution is dominated by the width of the "prompt" thermal neutron pulse in the moderator, which is of the order of the dwell times found in the following section. Therefore we used one single resolution function for all energies (flight times).

3.2 Time structure of crystal reflections

In order to obtain the dwell times of the neutrons of different energies in a fairly wide energy range it is necessary to evaluate as many orders of reflections as possible. Unfortunately the higher orders are difficult to measure for mainly three reasons. Firstly, they decrease in intensity at high energies due to the shape of the Maxwell spectrum, secondly, they become less and less separable because of the t^{-3}-dependence of time-of-flight spectra and thirdly, the highest orders are superimposed on a steep background of fast neutrons because of the poor shielding in these experiments (see Fig. 6).

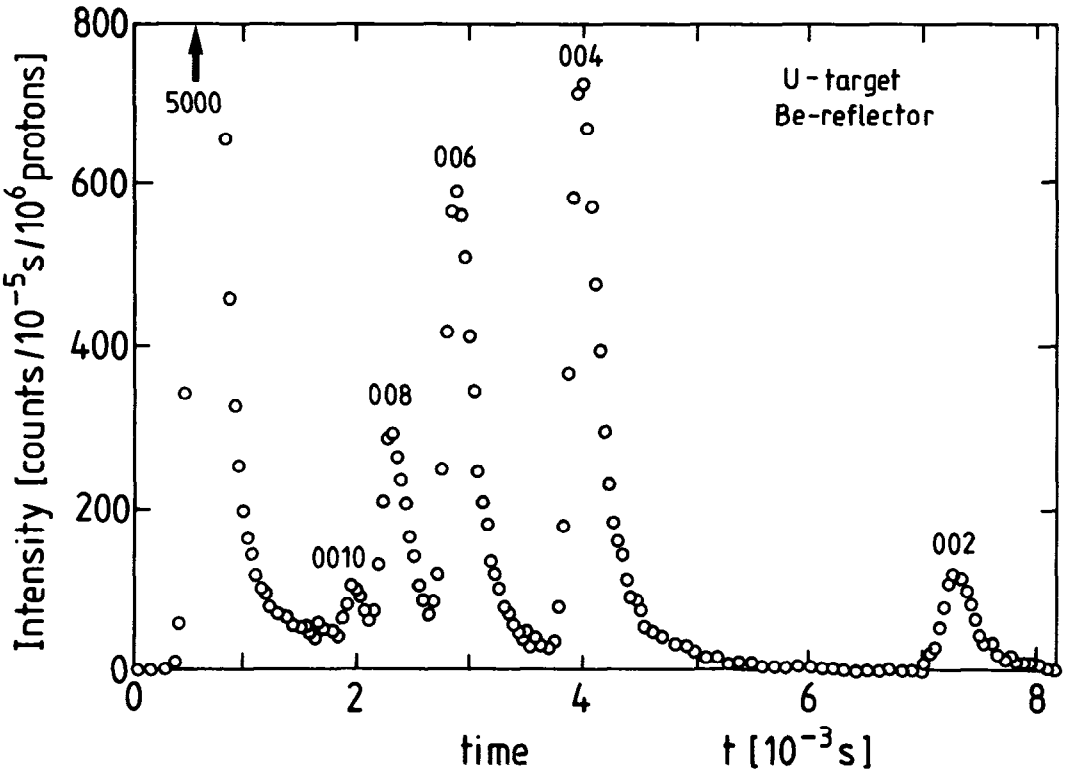

Fig. 6: Graphite analyzer crystal reflections and fast neutron background (peak intensity of background: 5000.)

This background was, of course, subtracted in our evaluation procedure (see Fig. 7), but the statistical errors quickly become considerable for higher order reflections due to the difference of nearly equal numbers. The background was measured with the crystal analyzer rotated out of reflection position and subtracted from the crystal data normalized to the number of protons recorded.

For the analysis of the dwell times the complete scan was partitioned into five sections containing one observable reflection each, by chosing six channel numbers to define five evaluation intervals. For reasons of computation time each reflection was treated separately after subtraction of

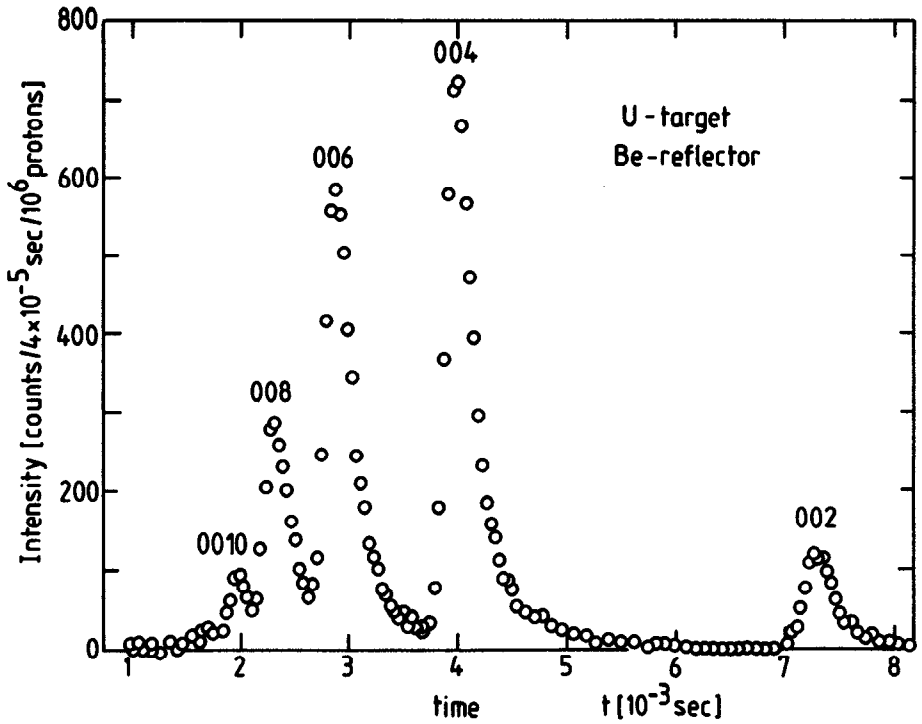

Fig. 7: Normalized crystal analyzer scan (background subtracted) revealing the finite neutron dwell time in the moderator (saw-tooth characteristic of the crystal reflections).

the overlap from higher order reflections obtained by extrapolation of the exponential decay. The detailed procedure was as follows. Starting with the highest observable reflection order ([0010] in this experiment) an exponential decay law of the form

$$f(t) = P \cdot \exp[-(t-t_o)/\tau] \qquad \text{for } t \geq t_o$$
$$f(t) = 0 \qquad \text{for } t < t_o \tag{1}$$

was assumed and weighted according to the normalized distribution p(t) of the primary proton intensity. This resulted in the expression

$$I(t) = P \cdot \int_{t_a}^{t} p(t')\exp[-(t-t'+t_a)/\tau]dt' \tag{2}$$

which was fitted to the experimental data by varying the parameters P, t_a and the dwell-time τ /3/. (The parameter t_a defines the zero-point within the different selected reflection intervals, i.e. the lower limit of the proton distribution function p(t). The boundary condition of equ. 1 was applied to equ. 2 accordingly.)

It should be mentioned that in the case of the lead reflector we found it sufficient to use only one time-constant to fit the data within the resolution of this experiment (see also section 4.2). On the other hand the

peaks obtained with the beryllium reflector exhibited more pronounced tails for longer times than with the lead reflector, as can be seen in Fig. 8. Therefore we applied eq. (2) with two exponentials and two decay constants τ_1^{-1} and τ_2^{-1} respectively. Some representative fits are shown in Fig. 9.

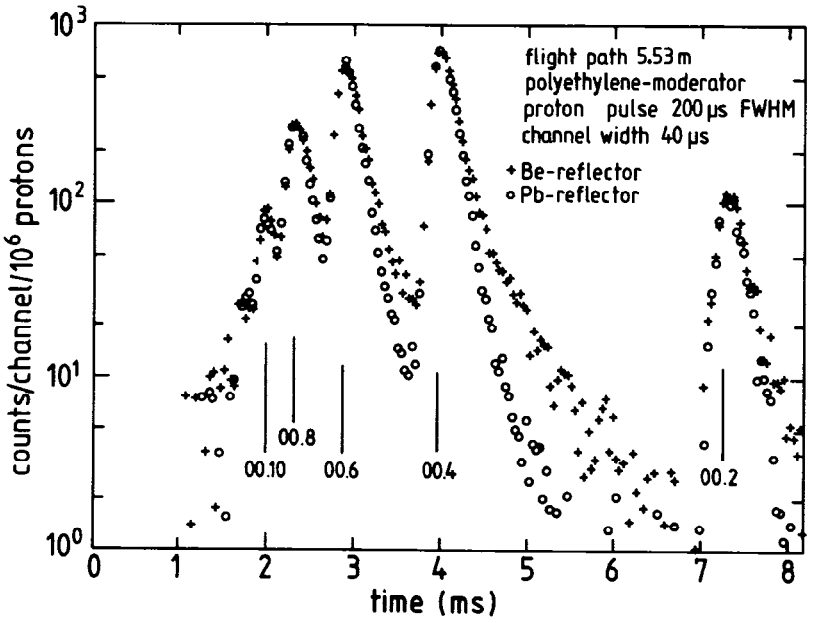

Fig. 8: Comparison of analyzer crystal reflections for two different reflector materials. Clearly, the Be-reflector exhibits wider tails.

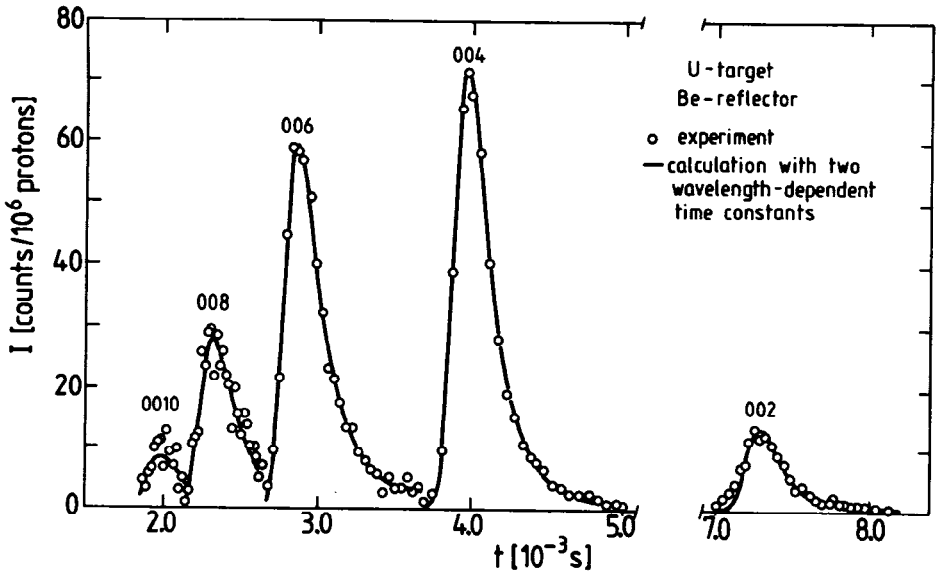

Fig. 9: Example of the numerical fits for a set of analyzer crystal reflections. The solid line is the convolution of the thermal neutron distribution (measured in the moderator) with two exponentials as described in the text.

A compilation of numerical results for the different target - moderator - reflector configurations is given in Table 3.

configuration		dwell times τ [10^{-6}s] and scale factors P [relative units]				
		order of crystal reflection				
(target -reflector -moderator)		002 (3.64 meV)	004 (14.4 meV)	006 (32.8 meV)	008 (57.8 meV)	0010 (90.3 meV)
Pb-Pb-"flat"	τ	184 ± 10	188 ± 4	169 ± 4	125 ± 5	(300)
	P	4.3 ± 0.3	29.6 ± 0.7	28.5 ± 0.7	16.1 ± 0.6	(4.2)
Pb-Pb -grooved	τ	152 ± 5	168 ± 3	178 ± 3	167 ± 8	278 ± 58
	P	15.2 ± 0.6	76.7 ± 1.5	56.1 ± 0.9	24.6 ± 0.9	8.4 ± 0.7
Pb-Be -grooved	τ_1	118 ± 28	140 ± 15	134 ± 55	(165 ± 383)	22 ± 17
	P_1	10.5 ± 1.3	55.1 ± 3.7	44.1 ± 3.8	(21. ± 100.)	(3.9 ± 11.4)
	τ_2	469 ± 258	482 ± 125	505 ± 64	(437 ± 10^4)	(249 ± 316)
	P_2	1.7 ± 1.6	9. ± 4.5	7.1 ± 4.7	(0.5 ± 96.)	(5.6 ± 5.9)
U-Pb -grooved	τ	132 ± 5	128 ± 3	139 ± 3	115 ± 4	198 ± 35
	P	26.6 ± 1.2	168. ± 5.	125. ± 3.	63.6 ± 2.1	13.4 ± 1.
U-Be -grooved	τ_1	102 ± 35	151 ± 9	153 ± 10	(151 ± 600)	(115 ± 600)
	P_1	25.7 ± 2.7	141. ± 5.	115. ± 3.	(55.8 ± 10^3)	(19. ± 120)
	τ_2	397 ± 240	577 ± 400	(9771 ± 10^5)	(239 ± 10^3)	($3 \cdot 10^4$ ± 10^6)
	P_2	4.4 ± 3.3	3.7 ± 6.6	2.6 ± 2.	(0.4 ± 10^3)	(0.4 ± 132)

Table 3: Dwell-times of neutrons of different energies for different target-moderator-reflector-configurations. Values with low confidence level are put in parentheses.

4. Discussion

4.1 Thermal neutron spectra

Although two of the deduced Maxwell temperatures appear to be somewhat low (see Table 2), the following conclusion can be drawn. The grooved moderator exhibits a softer spectrum than the flat one. This was expected and can be understood, at least qualitatively, as from a grooved moderator slower neutrons from the interior can escape. Without the grooves these neutrons could not have reached the moderator surface due to their short mean free path in a hydrogeneous substance. Besides this spectral softening a gain in intensity of roughly a factor of 2 was observed /4/. The beryllium reflector also gave a softer spectrum, as compared to the lead reflector.

As to the exponent α (see section 3.1 and Table 2), it does not seem to constitute only a small correction (0.1 ... o.2) to an 1/E-law as expected. An obvious reason could be that there were too few data points for the fit in the relevant energy range. More likely were an experimental explanation, as the background was not subtracted for technical reasons. The background clearly does not obey an 1/E law and therefore may falsify the α-values. An interference of these most likely unphysical α's with the result for the Maxwell temperatures can be excluded because of the small overlap of these contributions (see Fig. 5).

4.2 Time structure of crystal reflections

The energy, respectively velocity dependence of the thermal neutron field in a finite moderator can certainly not be described mathematically by a few parameters only. The spatial flux distribution ought to be represented properly by a Fourier series, each of its components revealing a different dwell time. Although one or two time-constants will normally be dominating it might appear fairly arbitrary to describe the situation with only one or two time constants for each velocity band, i.e. order of reflection of the analyzer crystal. On the other hand, in view of the resolution of this experiment, it seemed not reasonable to use more parameters.

For an easier interpretation of the results some additional figures have been calcualted from the fit parameters. These were:

a) the integrated intensity $I = P \cdot \tau$, resp. $I = P_1\tau_1 + P_2\tau_2$ in the cases of the Be reflectors,

b) the ratio of integrated intensity to peak maximum, i.e. $I/P = P\tau/P$, which is the "unfolded width" τ of the reflection. In the case of a superposition of exponentials this value is an "effective" width τ_{eff} $\tau_{eff} = (P_1\tau_1 + P_2\tau_2)/(P_1 + P_2)$, and

c) the standard deviation S (= square root of the normalized second moment) $S = \sqrt{\sigma^2}$, with $\sigma^2 = 2P\tau^3/I = 2\tau^2$ and $\sigma^2 = 2(P_1\tau_1^3 + P_2\tau_2^3)/(P_1\tau_1 + P_2\tau_2)$ respectively.

A compilation of these results is given in Table 4.

configuration (target-reflector -moderator)	integr. intensity I I_{max} (= P, resp. P_1+P_2) $I/I_{max} = \tau_{eff}$ standard deviation S	order of crystal reflection 002 3.64 meV	004 14.4 meV	006 32.8 meV	008 57.8 meV	0010 90.3 meV
Pb-Pb-"flat"	I [relative units]	0.78	5.6	4.8	2.0	1.3
	I_{max} [relative units]	4.3	29.6	28.5	16.1	4.2
	τ_{eff} [10^{-3}s]	0.184	0.188	0.169	0.125	(0.300)
	S [10^{-3}s]	0.260	0.266	0.239	0.177	(0.424)
Pb-Pb-grooved	I	2.3	13.	10.	4.1	2.3
	I_{max}	15.2	76.7	56.1	24.6	8.4
	τ_{eff}	0.152	0.168	0.178	0.167	(0.278)
	S	0.215	0.236	0.252	0.236	(0.393)
Pb-Be-grooved	I	2.	12.	9.5	3.7	1.5
	I_{max}	12.2	64.1	51.2	21.5	9.5
	τ_{eff}	0.166	0.188	0.185	0.171	0.156
	S	0.433	0.439	0.463	0.271	(0.343)
U-Pb-grooved	I	3.5	22.	17.	7.3	2.7
	I_{max}	26.6	168.	125.	63.6	13.4
	τ_{eff}	0.132	0.128	0.139	0.115	(0.198)
	S	0.187	0.181	0.197	0.162	(0.281)
U-Be-grooved	I	4.4	23.	(43.)	8.5	(14.)
	I_{max}	30.1	145.	118.	56.2	19.3
	τ_{eff}	0.145	0.162	(0.366)	0.152	(0.750)
	S	0.373	0.320	(10.6)	0.216	(42.3)

Table 4: Integrated intensities, effective widths and standard deviations of the crystal reflections for different target-reflector-moderator configurations. Numbers of small confidence levels are put in parentheses.

In the cases of the lead reflector the effective dwell-times τ_{eff} are identical to the τ-values of Table 3. For the Be reflector configurations an effective broadening is observed, which was already apparent from the raw data (see Fig. 8).

A more sensitive indicator of the "broadening" is the standard deviation S of the intensity distribution within the reflections since it weighs the "tails" more heavily. The S-values for the beryllium reflector are significantly larger than those of the lead reflector.

As all results have been normalized to 10^6 primary protons, a quantitative comparison with respect to intensities can be made for the different configurations. The gain of roughly a factor of two found for the grooved moderator as compared to a compact ("flat") one by measuring the neutron leakage flux /4/ was established (compare line 1 and 5 of Table 4). Using uranium instead of lead as target material yields an additional gain of a factor of two.

For the efficient application of mechanical choppers as "tail-cutters" it is important to obtain pulse structures with large peak intensities. From the values of I_{max} in Table 4 one can see that the lead reflector fulfills this condition better than the beryllium one.

Summarizing we can conclude:

1) For an intensity modulated neutron source, no decoupler is used and the time structure is to be taken advantage of for the separation of higher order reflections from the monochromator, Pb is to be preferred as a reflector material as compared to Be because of its better time structure and comparable peak flux.

2) The dwell time of 200 μs, which has been used to estimate the peak-to-average flux ratio /5/ for the intensity modulated source is too long. This means, that it underestimates the peak flux of the source.

References

/1/ G.S. Bauer, J.P. Delahaye, H. Spitzer, A.D. Taylor and K. Werner
Relative Intensities and Time Structure of Thermal Neutron Leakage from Various Moderator-Decoupler Systems for a Spallation Neutron Source; this volume

/2/ H.M. Conrad, computer program "submit.maxwell", KFA-time-sharing-system (user identification IFF 022) unpublished

/3/ H.M. Conrad, computer program "submit.zeitstrk", KFA-time-sharing-system (user identification IFF 022) unpublished

/4/ G.S. Bauer, K. Grünhagen and H. Spitzer (1980)
Einige Voruntersuchungen zu wasserstoffhaltigen Moderatoren für eine Spallations-Neutronenquelle; SNQ-study report, part III A2, unpublished

/5/ G.S. Bauer, W.E. Fischer, F. Gompf, M. Küchle, W. Reichardt and H. Spitzer (1981),
Thermal Neutron Leakage and Time Structure Measured for Various Target-Moderator-Reflector Configurations for a Spallation Neutron Source; this volume

Jül-Conf-45 D2-6

I C A N S - V
MEETING OF THE INTERNATIONAL COLLABORATION ON
ADVANCED NEUTRON SOURCES
June 22-26, 1981

Measurement of the High Energy Component of the Neutron Spectrum from a Moderated Source

Y. Hino, S. Cierjacks, S.D. Howe, M.T. Rainbow, F. Raupp, M.T. Swinhoe and L. Buth

Kernforschungszentrum Karlsruhe
Institut für Kernphysik
D-7500 Karlsruhe, Postfach 3640
Federal Republic of Germany

Abstract

The high energy component of the neutron spectrum from a moderated source has been measured by an improved method at the LNS synchrotron. The detector size of 7 cm diam. by 30 cm long NE-213 liquid scintillator was used and a FERDOR unfolding code was adopted for the spectrum data analysis. This result is compared with a previous measurement employing a smaller detector and a rectangular unfolding technique. The accuracy of the new method was tested by measuring the same high energy neutron spectrum which was measured and analyzed both by time-of-flight and by the FERDOR unfolding method.

1. INTRODUCTION

The neutron yield and spectra from spallation reactions have been measured as a part of a feasibility study for the German spallation source project. Measurement of the high energy component of the neutron spectrum from a moderated source has been carried out since these fast neutrons may cause shielding problems as well as unwanted background for some experiments with

thermal and epithermal neutrons. In our previous work, neutron spectra measurements of this type were carried out at SIN with a commercially available 10 cm diam. by 8.9 cm long NE-213 liquid scintillator. The use of an unfolding method of analog spectra appeared to be necessary because the time-of-flight method was not applicable for spectrum measurment from a moderated source. In order to receive quick results, the pulse height spectra were analyzed with a rectangular unfolding method[1]. These measurements revealed that a large number of high energy neutrons leaked out of the moderator. Results of this type obtained for light-water-moderated target assembly and 590 MeV proton beam were presented at the last ICANS-IV meeting[1]. Since the reference concept was changed from the original energy of 600 MeV to 1.1 GeV, additional measurements were carried out at this energy at LNS, Saclay. For this measurement, a 30 cm long NE-213 detector was constructed which allowed spectrum measurements over an extended neutron energy range up to 250 MeV. In addition, The FERDOR code was employed for spectrum unfolding instead of the previous rectangular unfolding method. A comparison of the results from these two methods will be discussed in this paper. In order to check the accuracy of the new unfolding method, the same high energy neutron spectrum from a thick bare uranium target was measured and analyzed both by the time-of-flight and by the FERDOR unfolding method. The results and comparison are also presented.

2. EXPERIMENTAL DETAILS

The experimental details of the measurements are the same as those described in ref. 1. The target configuration used in the SATURNE experiment is shown in Fig. 1. In order to simulate a realistic spallation neutron target design, the primary target was composed of alternately arranged plates of lead, polyethylene, and aluminum. The polyethylene and aluminum represented the coolant and structural materials.

3. SPECTRUM UNFOLDING AND RESULTS

The rectangular unfolding method simply employs response functions of a rectangular form in a given energy bin while the FERDOR analysis employs realistic response functions. In the present work, the ORNL version of the FERDOR code[2] was used. The necessary response functions have been generated by the Monte-Carlo program of Stanton[3] as modified by Cecil et al[4]. In order to avoid problems using wide energy bins and also a wide smoothing window width, a special kick-back routine has been added to the FERDOR code. In particular, this means the first result from FERDOR is smoothed with the same window function and the differences of the first and the second results are kicked-back to the first result to correct the wide energy bin effect.

The results of spectrum measurements for moderated target configurations are shown in Fig. 2. The absolute values were determined for a 6 m distance from the source and a 5.5 mA incident beam current. The discrepancy between the FERDOR and the rectangular unfolding methods is seen at energies above about 70 MeV, while agreement below this energy is still reasonable. Above 70 MeV, the rectangular unfolding distorts the spectrum shape significantly. Integration over energy of both spectra, however, yields comparable values.

The results for the SIN spectrum measurements are shown in Fig. 3. As can be seen, the agreement between the FERDOR and the time-of-flight method is fairly good. The sharp decrease above 200 MeV in the FERDOR result is caused by a range effect in the 30 cm detector. The present results also display the typically large uncertainties associated with the FERDOR unfolding. These uncertainties can possibly be reduced by using more improved unfolding routines which have recently become available.

4. SUMMARY

The fast neutron flux from the moderated spallation source has been successfully determined using unfolding methods. The FERDOR unfolding

method has shown a significant improvement over the small detector measurement and over the rectangular unfolding technique at energies above 70 MeV. It becomes clear that a large number of high energy neutrons leak out of the moderator and such a result is an important piece of information with respect to the design of spallation neutron sources.

The authors are indebted to the SIN staff, especially Dr. W. Fischer and Dr. C. Tschalär, and to the LNS staff, in particular Dr. F. Faure, Dr. J. Ciret, and Dr. G. Milleret for the invaluable support during the measurements.

REFERENCES

1. S. Cierjacks, M. T. Rainbow, M. T. Swinhoe, and L. Buth, Contr. ICANS-IV, Tsukuba (1980).
   S. Cierjacks, M. T. Rainbow, M. T. Swinhoe, and L. Buth, Report, KfK-3097B (1980).
2. W. R. Burrus, Report, ORNL-3743 (1965).
3. N. R. Stanton, Report, COO-1545-92 (1971).
4. R. A. Cecil, B. D. Anderson, and R. Madey, Nucl. Inst. and Meth. 161, 439 (1979).

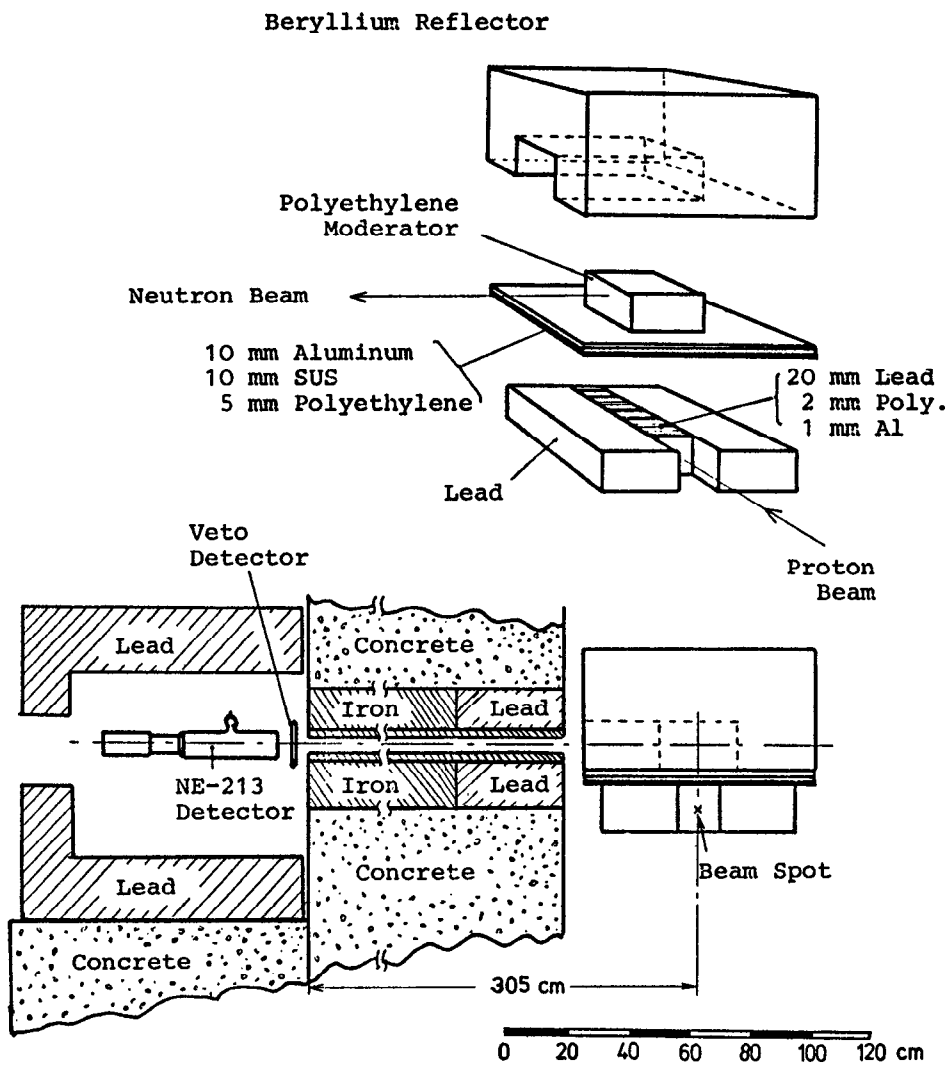

Fig. 1 Experimental arrangement for moderated neutron source.

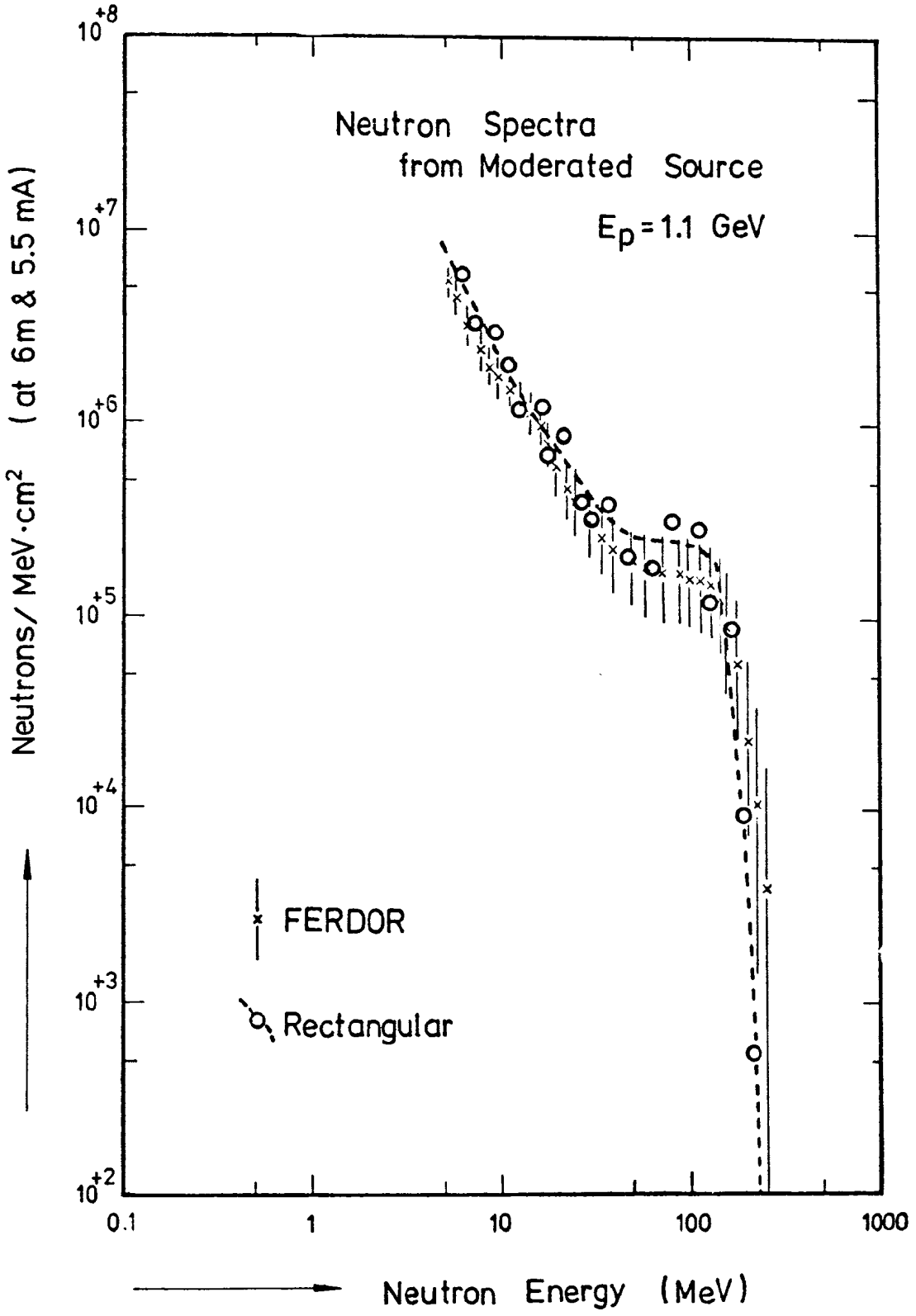

Fig. 2 Neutron spectra from moderated source. The absolute values are normalized to give the neutron flux at 6 m distance and 5.5 mA beam current.

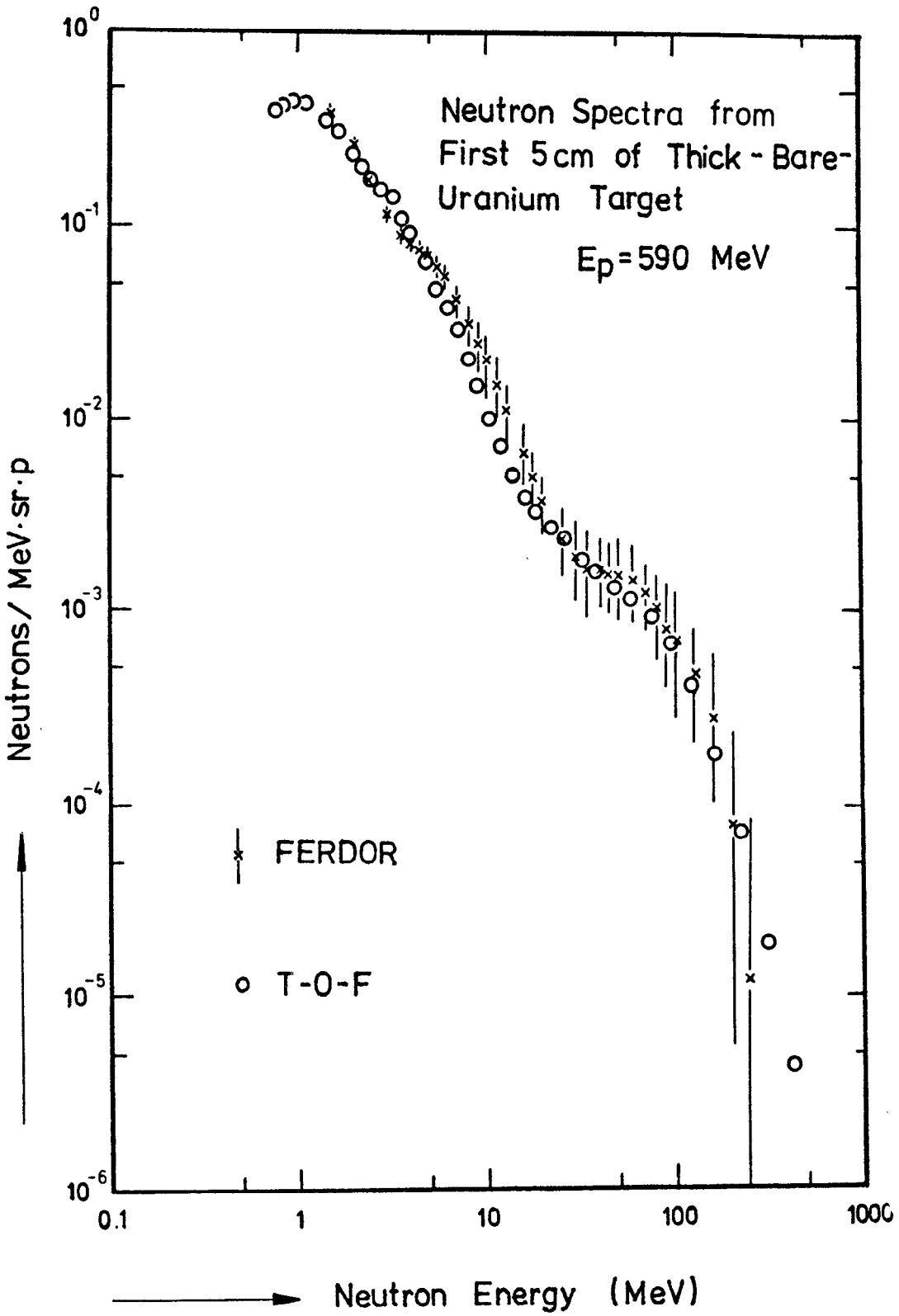

Fig. 3 Neutron spectra from thick-bare-uranium target. The absolute values are normalized to give the number of neutrons from the first block (10 x 10 x 5 cm) of the uranium target.

Jül-Conf-45 D2-7

I C A N S - V
MEETING OF THE INTERNATIONAL COLLABORATION ON
ADVANCED NEUTRON SOURCES
June 22-26, 1981

An Effective Inbeam Screening of Background by Choppers at a Pulsed Spallation Neutron Source

Nikolaus Nücker
Kernforschungszentrum Karlsruhe, Institut für Angewandte Kernphysik I
7500 Karlsruhe, Postfach 3640, Federal Republic of Germany

Abstract

The energy spectrum of background neutrons at a spallation neutron source extends to rather high energies. Shielding against these fast neutrons is difficult . It is proposed to fill the beam holes with a series of choppers to reduce effectively the pulsed background of fast neutrons. The effective shielding length during the proton pulse may extend up to about 4 m in a time-of-flight-spectrometer.

The spectrum of fast neutrons at a spallation neutron source extends to higher energies than at a conventional fission reactor neutron source. Therefore a more effective shielding is needed at a spallation neutron source. The main biological shield of the source will be thicker compared to that of a reactor and may consist of higher density materials such as steel. The shielding of the experiments must be more effective and will be in most cases different from that used on conventional neutron scattering instruments at reactors. Care should be taken that the improvement of the shielding does not cause losses in intensity due to an increased moderator to sample distance.

At a pulsed source the background is time dependent and may be separated in time from the useful neutrons by the choice of an adequate length of the flight path. Using non-moderating or highly absorbing shielding at the instruments reduces the background to low counting rates. Due to the high intensity of fast neutrons during the spallation process there will be no access to such an instrument during operation.

A better solution for background screening will be an effective shielding inside the biological shield with choppers synchronized to the pulsed source. The best we can do is to close the beam tubes with as much as possible of an effective shielding material during the time the proton pulse hits the target and open them for the time the neutrons of interest should pass through.

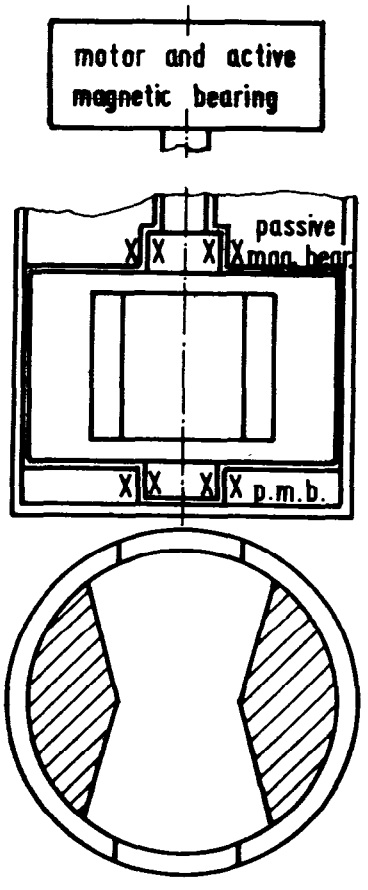

Fig. 1 Chopper for background shielding

If we could do it mechanically a big (of about the same size as the biological shield) rotating wheel beam shutter with a curved beam hole would be perfect to select one neutron energy. For several reasons the size of the chopper wheels inside the biological shield will be limited to somewhat between 20 cm and 40 cm in diameter. Therefore a series of choppers will be necessary for a good screening of fast neutron background.

The features of such a chopper is shown in fig.1. The chopper will be housed in a tube which fits into the shielding of the source. It will consist of a vertical cylindrical rotor centered by passive magnetic bearings and an active magnetic suspension at the far end outside the biological shield. The shape of the beam hole through the rotor allows a 100% transmission of neutrons within the energy band and the pulse length of interest. The speed of the choppers will be about 12000 rpm for the choppers nearest to the moderator and 3000 rpm at the end of the beam hole in front of the sample. The total shielding length obtainable is related to the diameter and speed of rotation of the choppers. With the size of the rotors the stored energy, which is proportional to the forth power of the rotor's diameter, raises rapidly. Limiting the stored energy to values below 50 Wh restricts the rotor diameter to about 20 cm for choppers

spinning at 18000 rpm and about 40 cm at 3000 rpm.

The efficiency of this shielding may be demonstrated for three typical instruments: a time of flight (TOF) spectrometer, an inverse TOF instrument and a triple axis spectrometer when installed at a source as the German SNQ (Spallationsneutronenquelle) project. Contrary to most existing or planned sources the SNQ is planned to give 0,5 msec of pulse length at a rate of 100 pulses a second. This pulse structure makes these types of instruments rather attractive at the SNQ.

Time of flight spectrometer at the SNQ.

The optimum in flexibility may be achieved using two fermichoppers for the selection of energy and the energy and time resolution combined with a series of background choppers in between (fig. 2). The same considerations are valid for a spallation source with short pulses as the SNQ-option with compressor ring. Then of course no fermichopper close to the moderator is needed.

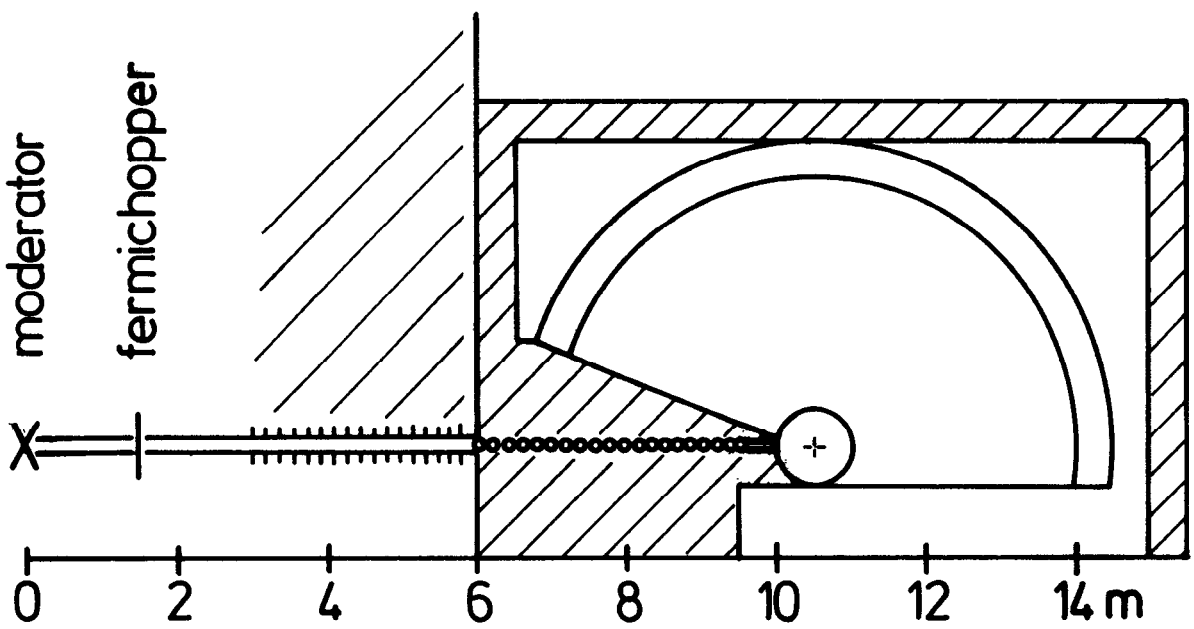

Fig. 2 Time of flight spectrometer with background choppers

This TOF-spectrometer may be compared to the IN4 at the HFR at Grenoble. The length of the total flight path in both spectrometers will be about the same. Admitting aproximately the same losses in intensity for the two fermichoppers compared to the losses in reflectivity of the two monochromator crystals at the IN4 the flux at the sample position will be higher by a factor of about 20 (which is the peak to avarage flux ratio of the SNQ) times the repetition times ratio of SNQ and IN4 (for same energy and resolution). If we admit a rather high repetition rate at the IN4 of 2.5 msec between pulses this factor will be about 5. To be able to use this gain factor and the higher flexibility of such an instrument, the background should be of the same order of magnitude or less compared to the IN4. This will be achieved by the phased chopper system combined with the pulse structure of the SNQ. The fast neutron background will be reduced by the total shielding length ac-

complished by the background choppers during the linac pulse.

An optimal shielding (fig. 2) will consist of a densely packed series of choppers with vertical axes starting at about 3 m from the moderator and ending at the outer edge of the biological shield. Outside the biological shield all the remaining space in front of the sample may be used for shielding by large choppers with horizontal axes. Since TOF-instruments with an analyser flight path of 3 m to 4 m to the detectors need large, flat flight boxes they should be arranged vertically (as IN4) to enable a maximum of instruments at the SNQ. Under the assumtion of a moderator surface of 10 cm x 10 cm and a sample sized 5 cm horizontal and 2.5 cm vertical the dimensions of choppers in the beamline and their speed of rotation, phases with respect to the proton pulse and shielding lengths were calculated for neutron energies of 20 meV and 100 meV (see table 1).

d (m)	Chopper dimensions (cm)				E_o = 20 meV			E_o = 100 meV		
	diam.	slit ↔	slit ↕	axis	speed sec^{-1}	phase degrees	l_s %	speed sec^{-1}	phase degrees	l_s %
1.5-3	13	9	9	↕	fermi chopper					
3	20	8.6	7.9	↕	150	83.2	48	200	48.6	36
4	20	8.1	7.1	↕	100	73.8	49	200	64.8	48
5	20	7.6	6.4	↕	100	92.5	54	200	82.8	54
6	23	7.1	5.7	-	100	110.5	66	150	74.0	67
7	23	6.7	5.0	-	50	64.3	69	150	81.5	71
8	30	6.2	4.3	-	50	73.8	79	100	65.9	78
9	30	5.7	3.6	-	50	82.8	82	100	74.2	82
9.5	5	5.5	3.2	-	fermi chopper					

Table 1 Dimensions and speed of supressor choppers in a TOF instrument (d = distance of chopper from moderator, phase = phase between end of proton pulse and open position of the chopper, l_s = shielding length of the chopper during the proton pulse relative to the length of the device)

A total shielding length of all the choppers during the proton pulse of about 4.2 cm can be obtained when the phases of the choppers are synchronized for thermal neutrons. At higher neutron velocities the time between the proton pulse and the time the neutrons should pass through the first background choppers becomes shorter and reduces the effective shielding length which can be obtained (to about 3,5 m at E_n = 200 meV).

While in a TOF spectrometer with two choppers for energy selection at the SNQ with rather long pulses only the distance between the fermi choppers is relevant, the maximum distance of the pulse generating fermi chopper from the moderator in an inverse TOF instrument is limited due to the energy selection by the finite length of the pulse from the moderator. A distance of 1,5 m from the moderator seems to be a good choice: on one hand good intensities within a wide range of neutron energies are available, on the other the distance is far enough to reduce the problems which may arise from the immediate vicinity of the target (nuclear heating, activation).

For higher flexibility we propose to use a fermi chopper (fig. 3) with a series of collimators on top of each other. The collimation and thereby the resolution may be changed by simply changing the level of the entire chopper.

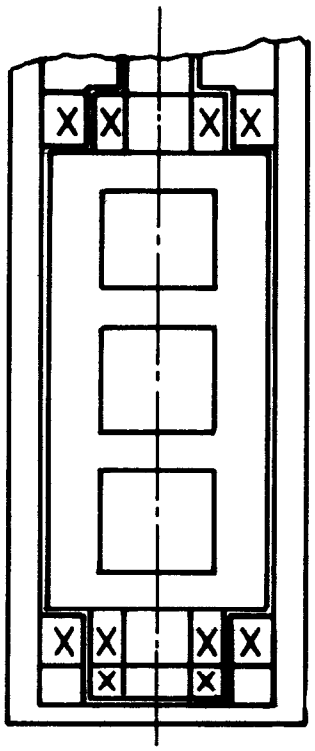

Fig. 3 Fermi chopper with three interchangeable collimators

Further adaption of time resolution can be achieved by spinning the chopper at multiples of 50/sec.

The background screening at an inverse time of flight spectrometer.

The best conditions for an inverse TOF spectrometer would be a narrow, symmetric neutron pulse emerging from the moderator. This may be achieved at a spallation neutron source with short proton pulses and with a poisoned and decoupled moderator. The option of the SNQ project with a storage ring certainly will give optimal conditions. While the gain in the peak flux by such a compressor ring will be enormous for epithermal neutrons it will be only a factor between two and three in the thermal region. Without storage ring a chopper is needed to provide short symmetric pulses. The pulse width and hence the intensity may be optimized to the problem of interest.

The proposed screening of an inverse TOF spectrometer by choppers is similar for both types of sources. As demonstrated in fig. 4 the transmission time of background choppers will rise with the distance from the fermi chopper (or moderator). The distance from the moderator of the time zero defining fermi chopper limits the energy band to be transmitted. A limitation at the low energy side is needed to avoid time overlap at the detectors. The energy band of interest and thereby the energy with optimal transmission may be adapted by the choice of the chopper's phases. The example in fig. 4 gives optimal transmission at 60 meV and is designed for an energy band ranging from 20 meV to 200 meV.

Choppers for a triple axis spectrometer.

The pulse structure of the German SNQ allows an application of choppers for background screening without losses in intensity for all types of instruments using a monochromatic neutron beam. The choppers will have the same shape as those of an inverse TOF spectrometer with an angle of transmission corresponding to the length of the neutron pulse. The phases of the choppers will be adapted to the energy of the neutrons of interest and thereby an energy band will be preselected. In combination with a crystal monochromator there will be no higher order contaminations. The inbeam screening with choppers at a triple axis spectrometer will reduce essentially the shielding problems at such an instrument. Access to the sample enviroment will be allowed which would be impossible without such a shielding. A facility of high flexibility may be installed at the quasi-continuous SNQ.

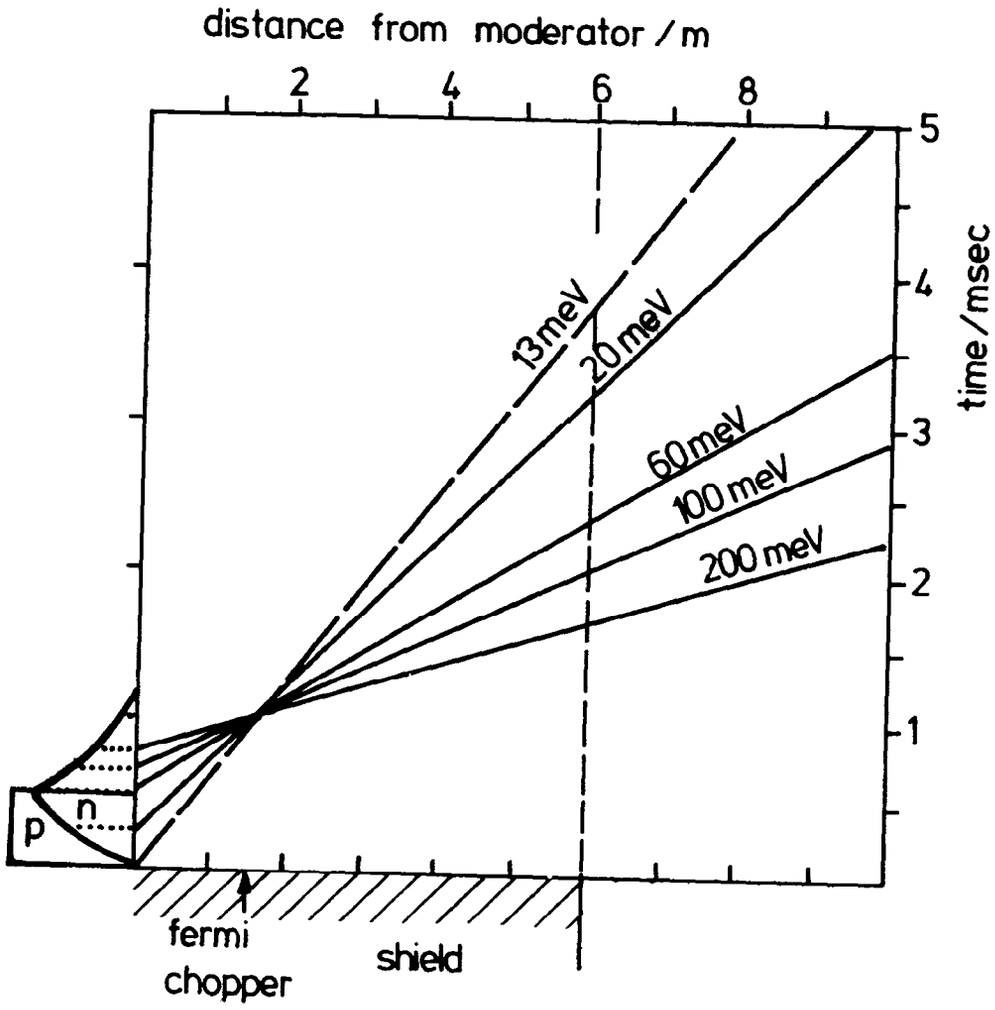

Fig. 4 The neutron time to flight path distribution at an inverse TOF-spectrometer

Jül-Conf-45 D2-8

ICANS-V

MEETING OF THE INTERNATIONAL COLLABORATION ON

ADVANCED NEUTRON SOURCES

June 22-26, 1981

Measurements of Neutron Fluxes at Spallation Source Models and Bare Targets

V. Drüke, N. Paul and W. Litzow

Institut für Reaktorentwicklung der KFA Jülich GmbH

Postfach 1913, D-5170 Jülich, Germany

ABSTRACT

Thermal and fast neutron fluxes have been measured at spallation source models and bare target configurations. Different moderators and target materials have been used. The peak values of thermal fluxes were calculated from reaction rates to 9.6 10^{-3} n/cm^2 s p for H_2O, 1.4 10^{-2} n/cm^2 s p for D_2O and for the hybrid system 9.0 10^{-3} n/cm^2 s p in the case of slow moderator and 1.5 10^{-2} n/cm^2 s p in that of fast moderator. Tungsten targets gave a 20 % reduced flux, uranium targets produced by factor of 1.8 increased flux in the moderator. Fast fluxes have been measured on the surface of bare Pb and U-targets using the Rh103 (n,n') reaction. All measurements will be compared with calculations in future.

INTRODUCTION

As a part of the German study of a spallation neutron source (SNQ) /1/ neutron fluxes in the thermal and fast energy region have been measured recently. Targets consisting of lead, lead-bismuth, uranium and tungsten/lead have been bombarded by 590-MeV protons at the Schweizerisches Institut für Nuklearforschung (SIN). The produced neutrons were moderated in H_2O, PE and D_2O and the distribution of the thermal neutron flux have been measured. Using the proton beam of the SATURNE-accelerator (CEA Saclay) fast neutron distributions have been determined at surface of bare lead or uranium targets with an incident proton energy of 600 and 1100 MeV. The experimental results may give indications of the layout of a spallation source and can be compared with calculations.

EXPERIMENTAL SETUP AND PROCEDURES

Measurements of the thermal neutron fluxes were done with different moderators and target configurations. As moderators were used light water, heavy water and polyethylene and as target compositions lead, lead-bismuth, uranium and tungsten/lead in slab and cylindrical geometries (see table I).
The experimental setup of each experiment is shown in the corresponding figure.
The thermal neutron flux was determined by the measurement of reaction rate of dysprosium- and uranium detectors. Small aluminum-dysprosium wires (ϕ 0.7 x 10 mm^3) containing 10.4 % Dy were used to measure the flux distribution in the moderators. Due to the relative short half-live period of 141 min only 150 detectors could be used in one experiment at the same time. To determine the absolute flux value several uranium detectors were irradiated together with the Dy-wires. Counting the 1.6 MeV-γ-line of La 140 (fission product of U-235) the absolute reaction rate of the uranium samples was

Table I: Target Configurations and Compositions
Sizes of Moderators and Dimensions of Targets
are given in the Figures

Moderator	Target Material	Target Geometry
H_2O	Pb-Bi	cylindrical
H_2O	Uranium (depl. 0.4%)	"
D_2O	Pb	"
"	Pb-Bi	"
"	Pb	slab
"	Uranium (depl. 0.4%)	"
D_2O/PE	Pb	slab
"	"	"
"	W-Pb	"

determined. The comparison of the uranium and the Dy detectors gave the absolute reaction rate in the moderator. The conversion from reaction rate to flux has been calculated with the fission cross section of U-235. In these calculations a Maxwellian energy distribution of the thermal flux was assumed in all moderators with a corresponding fission cross section of 515 barn. The validity of this assumption has to be proved by other experiments or calculations. The counting errors from the Dy-wires can be indicated with 0.4 up to 2 % due to the time dependent γ-background in the accelerator areas. The uncertainty of the uranium detectors was about 3 % including that of the calibration standard. The uncertainty of the resulting thermal neutron flux can be given with 3.5 % not included the exact value of the fission cross section of U-235. The relative flux distribution however has a possible error of 2 % maximum.

Another uncertainty has to be remarked of the beam calibration. The proton beam was directed onto a graphite scatterer viewed by a telescope of scintillator counters operated in coincidence. The telescope was calibrated

by reducing the beam current to a level where direct counting was possible and comparing the number of coincidences recorded to the number of protons counted in the direct beam. The uncertainties of this method were estimated to be 5 up to 10 % from reproducibility obtained in different runs.
The measurements of the fast neutron flux were done by activation of rhodium foils placed on the surface of bare targets configurations. The neutron scattering cross section of rhodium 103 is shown in figure 14, the conversion from reaction rate to flux is considerably dependent on the neutron spectrum. Therefore in the corresponding figures the measured reaction rate is indicated, rather than neutron fluxes. The reaction rate has been measured with an uncertainty of 3.5 %.

EXPERIMENTAL RESULTS AND CONCLUSIONS

In figure 1 the cross section of the target configuration is shown for the H_2O and several of D_2O experiments. The cylindrical targets were surrounded by an inner aluminum tube, an air gap and an outer aluminum tube. In the case of H_2O moderators the outer tube and air gap are not present. All targets were mounted in a stainless steel tank with the dimensions of 1.7 m x 1.7 m x 1.7 m. Fig. 2 shows the response of the flux measurements in general. In the following figures only a few sections of this flux distributions parallel and perpendicular to the incident proton beam is given. Fig. 3-5 show the neutron flux space dependent as indicated on the figures in the H_2O case.
The peak flux in the case of Pb/Bi-target is given in Fig. 3 in dashed line with 3 10^7 n/cm^2 s 0.5 nA. A three times higher peak flux is obtained at a distance of 5 cm from the target surface. For the uranium target Fig. 5 shows a flux measurement with and within a beam tube.
Fig. 6 and 7 give some typical results to the D_2O measurements. Fig. 6 shows the unpertubated case with peak flux of 4.3 10^7 n/cm^2 s 0.5 nA and a FWHM of 85 cm. Fig. 7 gives an impression of the flux pertubation in the D_2O system due to beam tube arrays.

Fig. 8-13 show some results and views related to the hybrid systems with a slow and a fast moderator. Fig. 8-10 give the results of a benchmark experiment with a simple geometry: target, fast moderator PE, slow moderator D_2O. The peak flux of the Pb target in D_2O has a FWHM of 50 cm and a value of 0.94 10^7 n/cm^2 s 0.5 nA. For U-target the flux increases by a factor of 1.72. In the fast moderator the maximum of thermal flux is four times higher than in D_2O. Fig. 10 shows the flux perpendicular to the proton beam. The ratio of the flux in case of U- and Pb-target is strongly space dependent due to the properties of the target materials.

In Fig. 11 the mock up assembly of the SNQ design is illustrated. The target is diluted with sheets of PE to simulate the water cooling.

The fast moderator with grooves on the surface is reflected by PE or Pb. Fig. 12 and 13 show some results measured in this assembly. Fig. 12 shows the flux values in D_2O with a peak flux of 2.75 10^7 n/cm^2 s 0.5 nA and with a FWHM of 60 cm. The thermal flux increases by a factor of three compared to the results of measurement without "PE-coolant". This effect can be explained by reason of premoderation of neutrons in the target. In the fast moderator the premoderation causes only a flux gain of 30 %.

Other target materials than Pb were used, uranium and tungsten. Uranium increases the thermal flux by a factor of 1.8 and tungsten (without "coolant") decreases the flux within 20 % in the slow moderator. If we compare the W-target with the compact Pb-target we would get roughly a factor of 2.3 in the thermal flux in D_2O.

Figs. 15-17 show the results of fast reaction rates measured with rhodium foils on the surface of bare targets. Fig. 14 gives the inelastic scattering cross section of rhodium with a threshold energy of 0.1 MeV. A conversion from reaction rates to flux is strongly dependent of the neutron spectrum and has to be calculated.

Fig. 15 and 16 show the results of the activation at two different proton energies (600 and 1100 MeV). The different behaviour of the 100 x 300 mm^3 targets is due to the scattering from neutrons from the target sides.

Fig. 17 gives the result of different target materials for a proton energy of 1100 MeV. The measurement shows a factor of 1.7 in the peaks of U- and Pb-target. As expected the range of the protons is shorter in the uranium target than in the lead target. The integrated reaction rate over the target length gives a factor of about 2.2 between the proton energies of 1100 and 600 MeV for both target materials, lead and uranium.

ACKNOWLEDGEMENTS

The authors acknowledge the help provided during the measurements by the SIN people, especially Dr. W. Fischer and Dr. C. Tschalär, and by the LNS staff, particularly Dr. F. Faure, Dr. G. Milleret and Dr. J. Ciret.

REFERENCES

/1/ SNQ - Realisierungsstudie JüL-Spez-113 / KfK 3175

/2/ Annual Progress Report on Nuclear Data 1980 NEANDC (E) 222 "U" VOL. III EURATOM March 1981

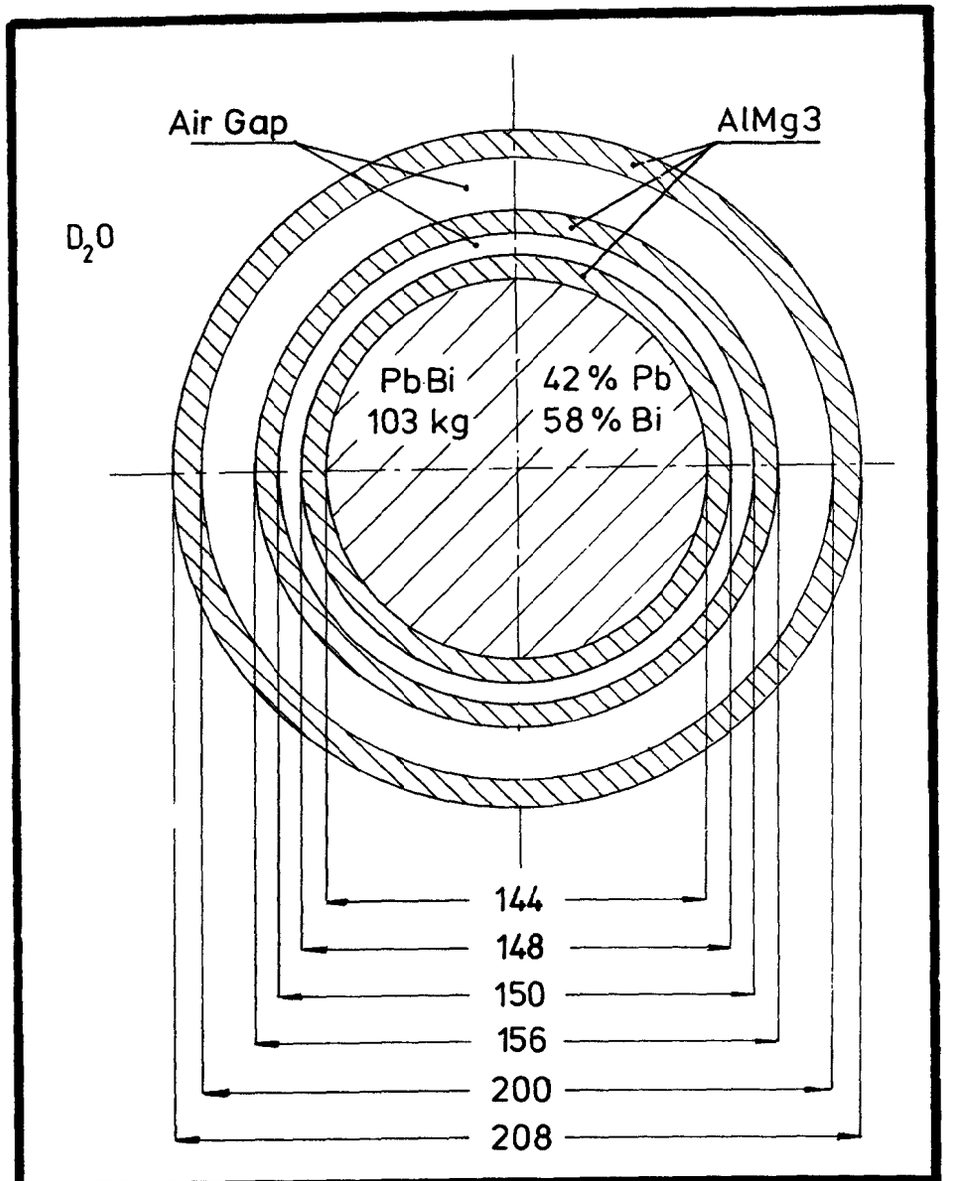

KFA

Section of the Pb Bi-Target Configuration in D_2O-Tank

Fig.: 1

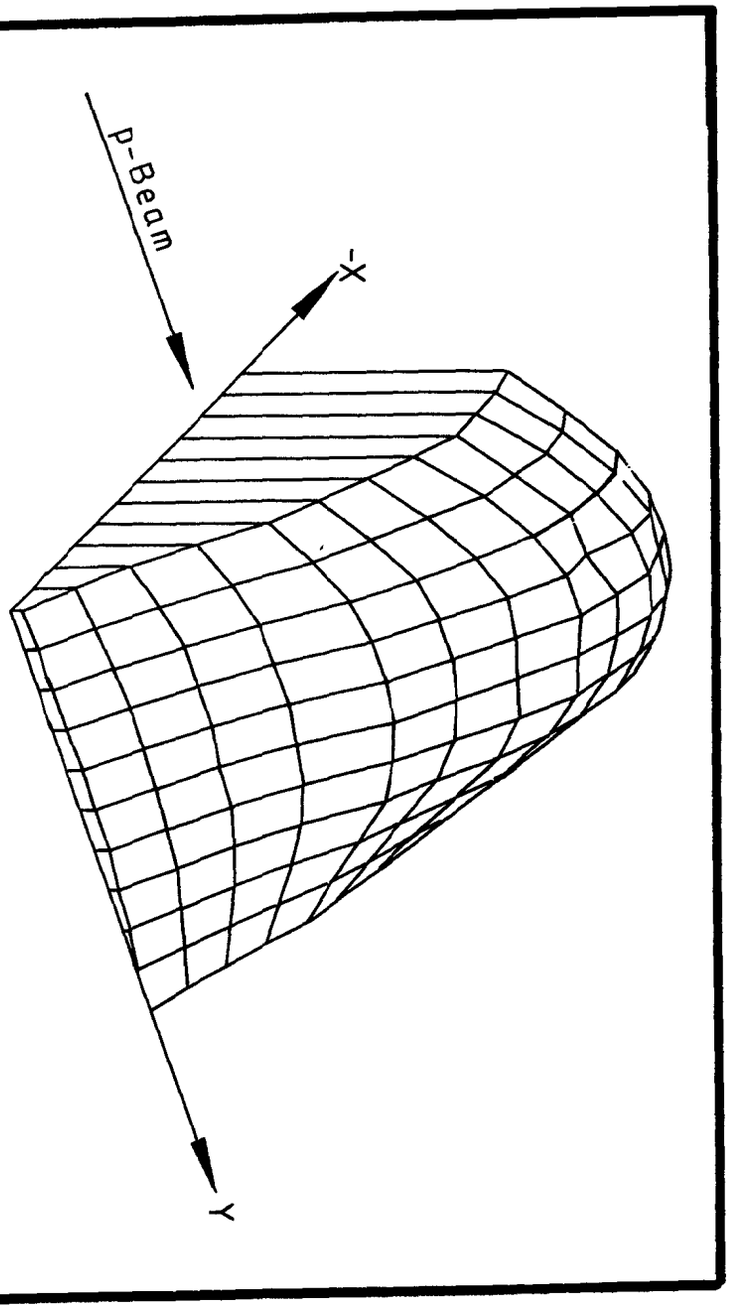

KFA

Thermal Flux in X-Y Direction

Fig.: 2

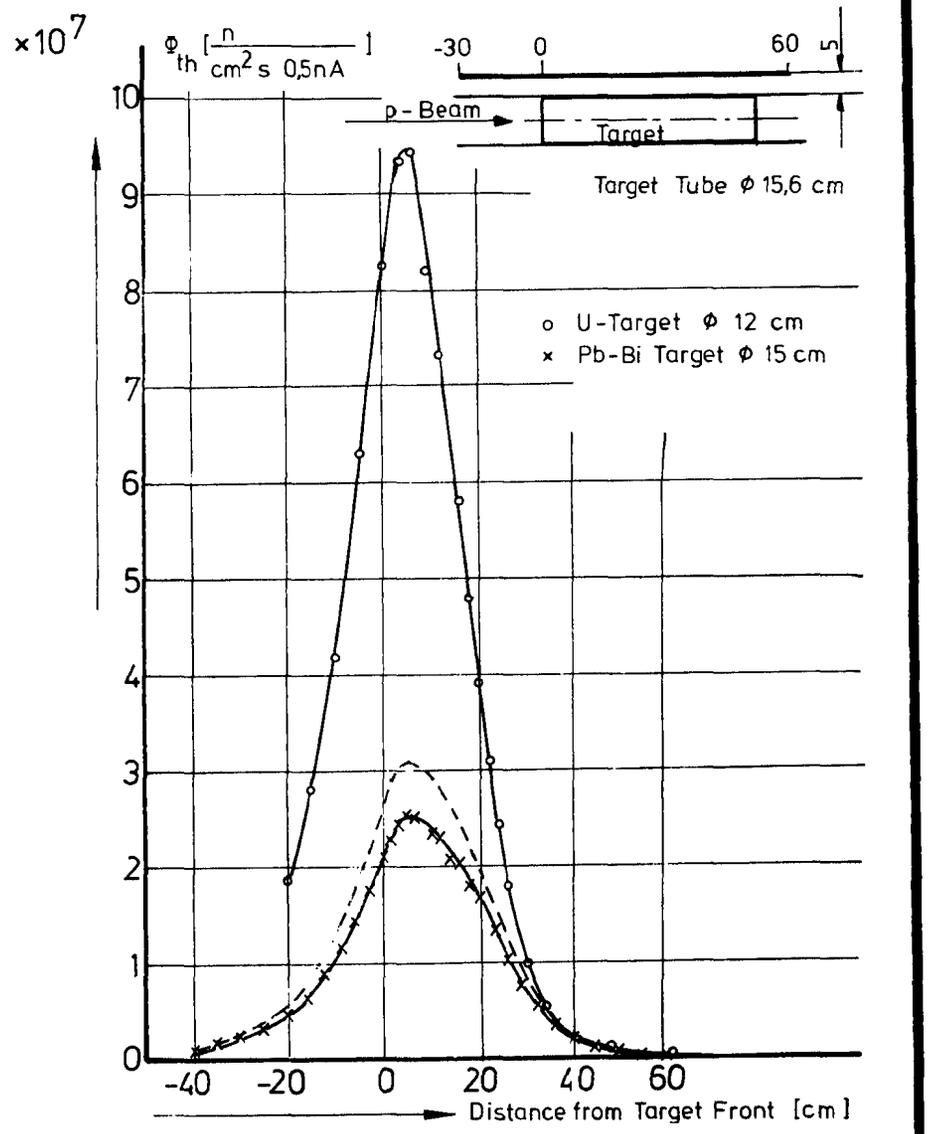

KFA	Thermal Flux, U-and Pb-Bi Target in H_2O	Fig.: 3

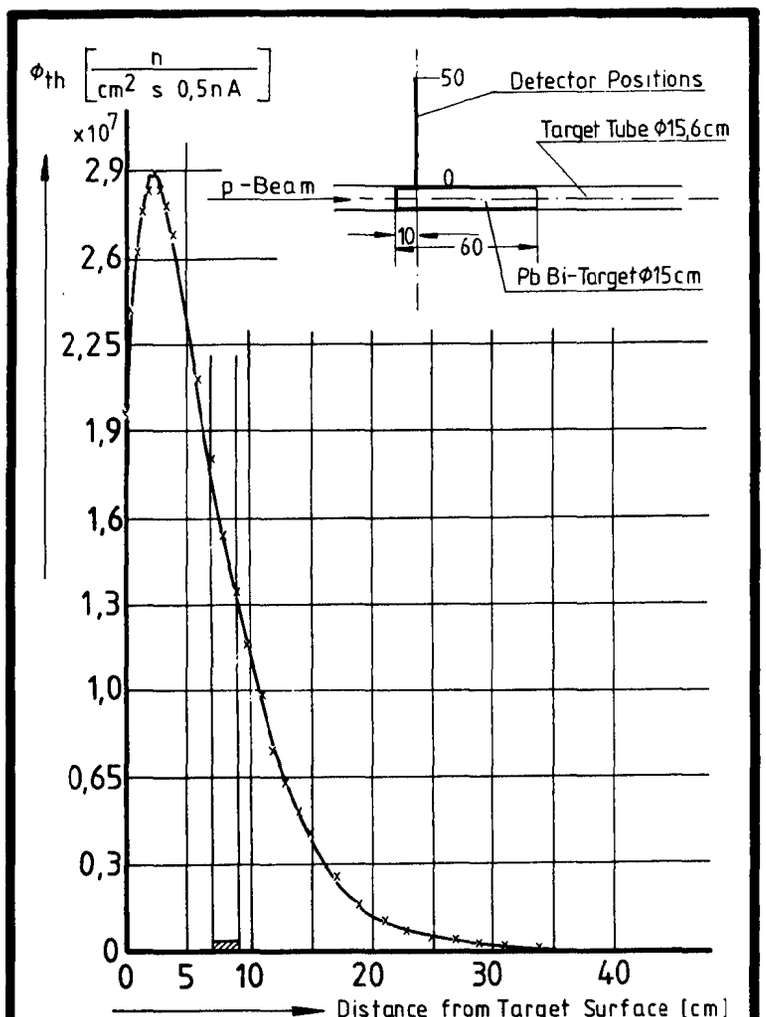

KFA	Thermal Flux PbBi-Target in H_2O	Fig.: 4

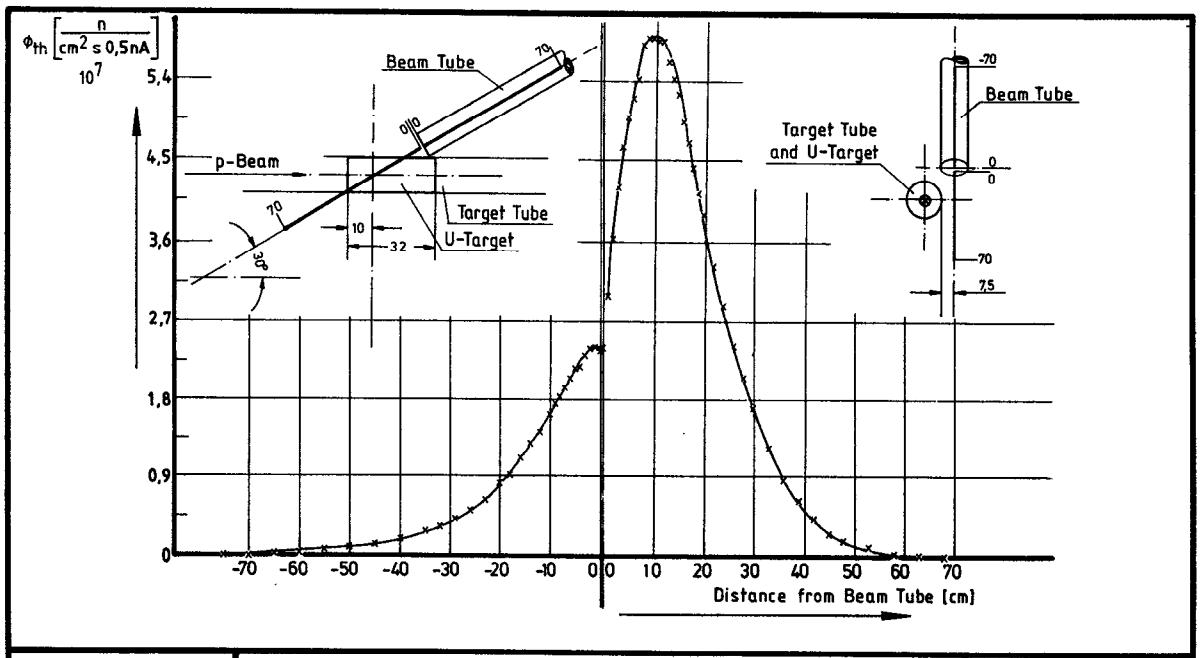

KFA	Thermal Flux U-Target in H_2O	Fig.: 5

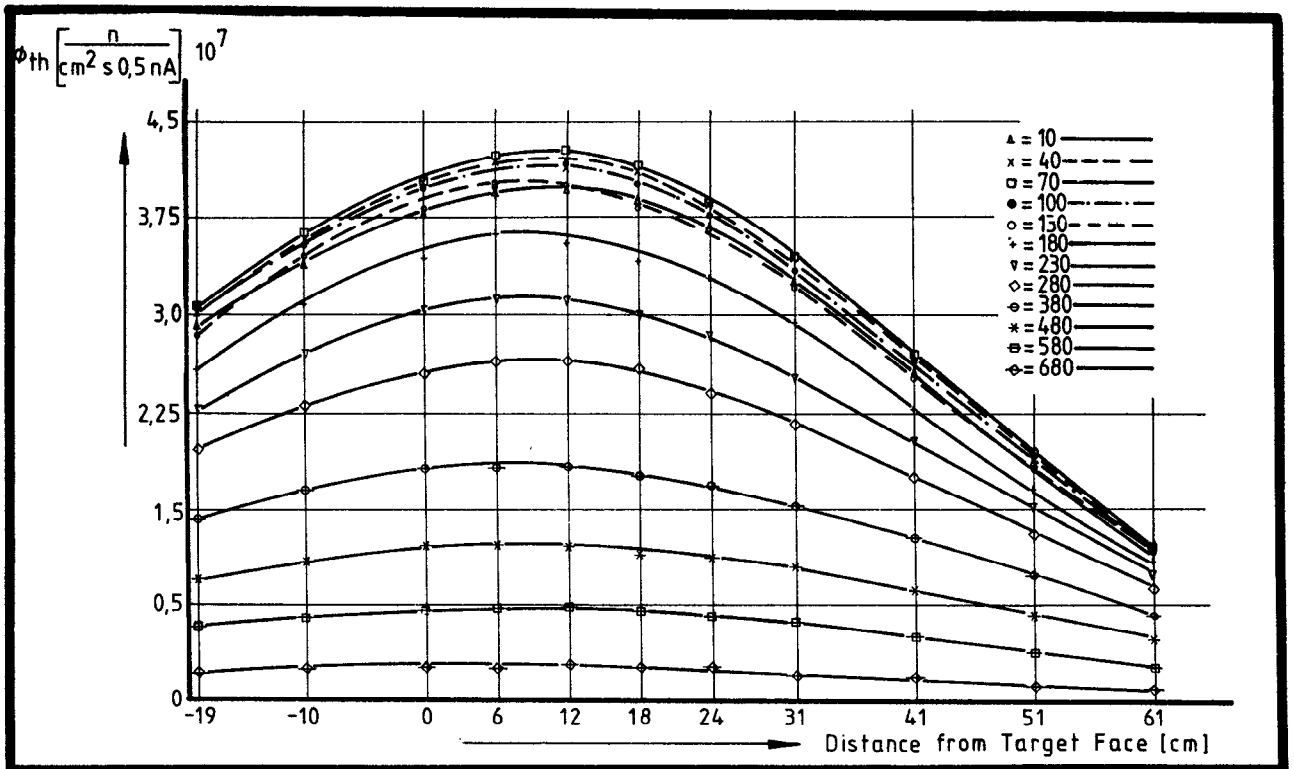

KFA	Thermal Flux in D_2O Pb-Target ; Pb Bi-Target	Fig.: 6

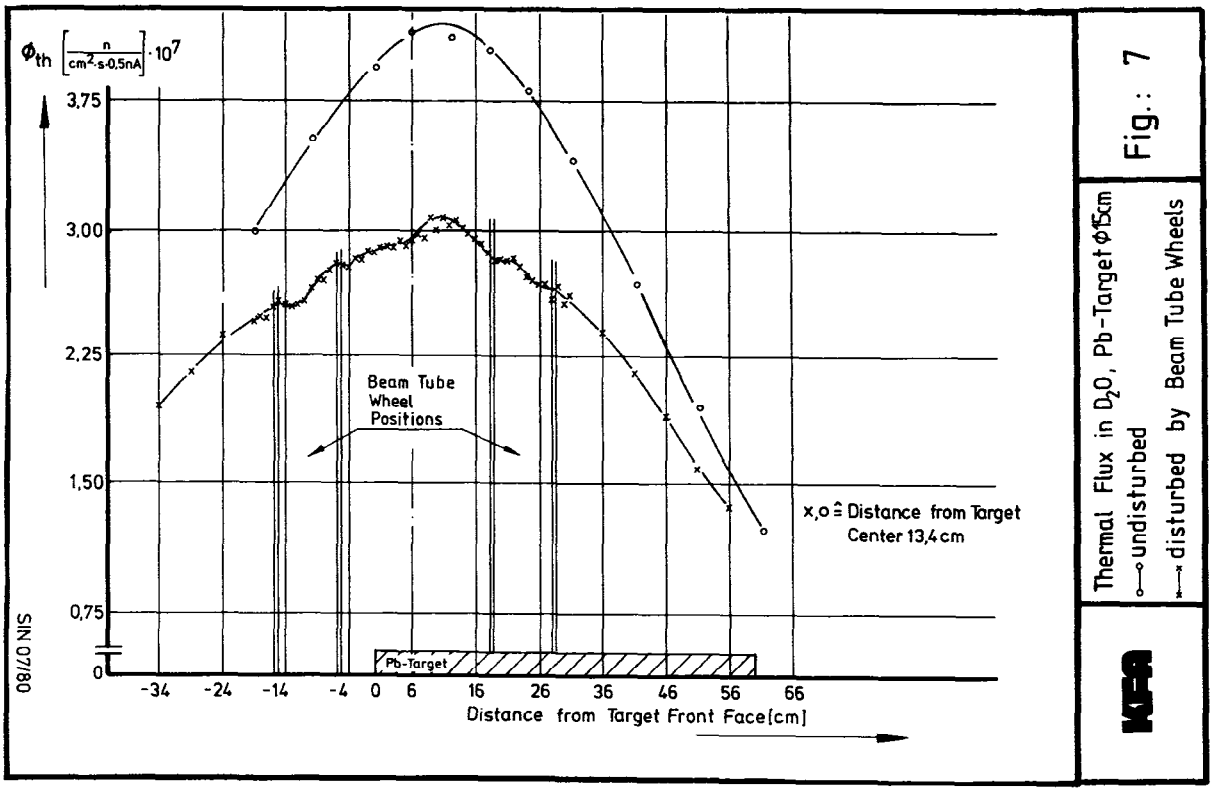
Φ_{th} $\left[\frac{n}{cm^2 \cdot s \cdot 0{,}5nA}\right] \cdot 10^7$
3,75
3,00
2,25
1,50
0,75
0
Beam Tube Wheel Positions
x,o ≙ Distance from Target Center 13,4 cm
Pb-Target
-34 -24 -14 -4 0 6 16 26 36 46 56 66
Distance from Target Front Face [cm]
SIN 07/80
Thermal Flux in D_2O, Pb-Target Φ15cm
o—o undisturbed
x—x disturbed by Beam Tube Wheels
Fig.: 7

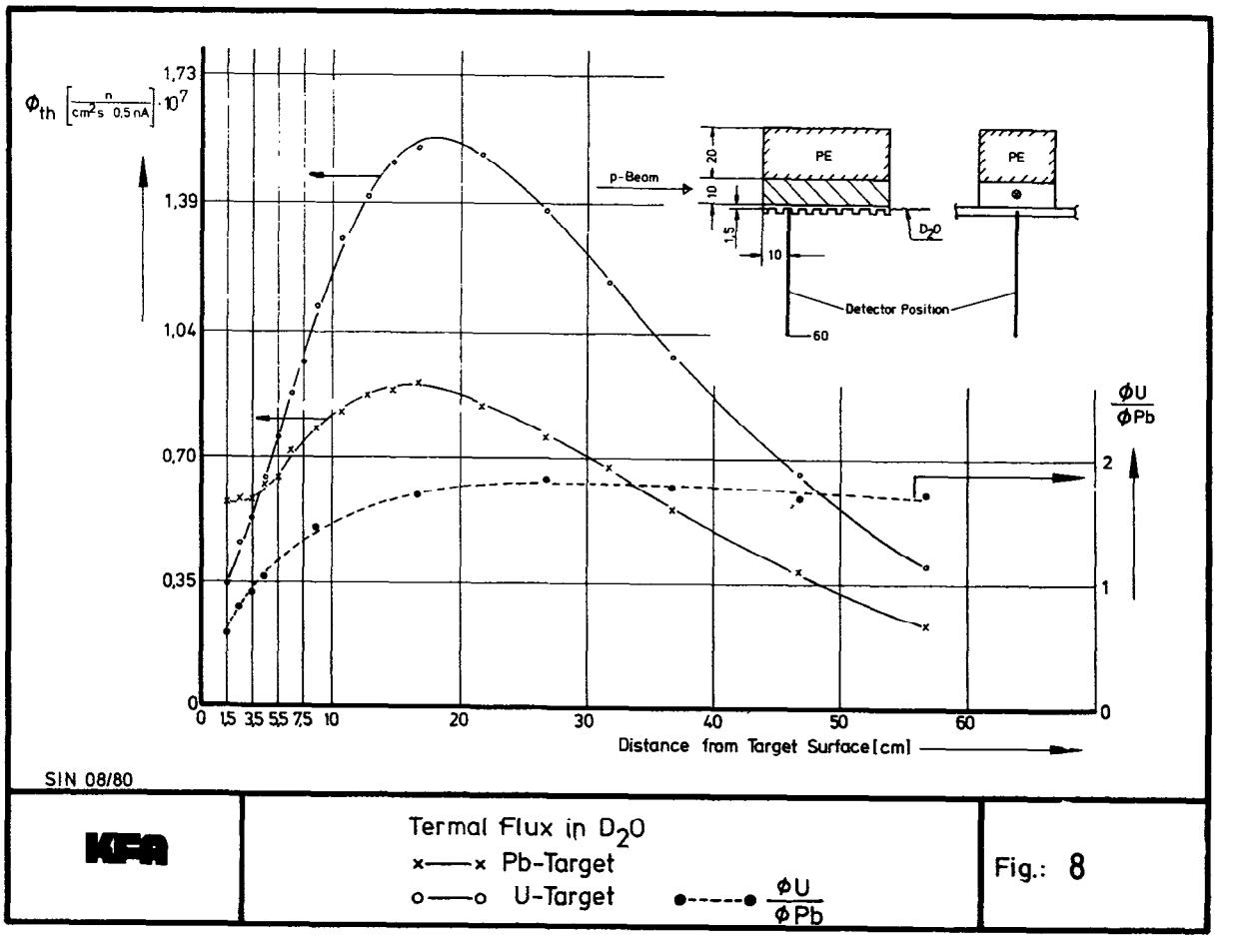
Φ_{th} $\left[\frac{n}{cm^2 s\ 0.5nA}\right] \cdot 10^7$
1,73
1,39
1,04
0,70
0,35
0
p-Beam
PE
PE
20
10
1,5
10
D_2O
Detector Position
60
$\frac{\Phi U}{\Phi Pb}$
2
1
0
0 1,5 3,5 5,5 7,5 10 20 30 40 50 60
Distance from Target Surface [cm]
SIN 08/80
Termal Flux in D_2O
x——x Pb-Target
o——o U-Target
●------● $\frac{\Phi U}{\Phi Pb}$
Fig.: 8

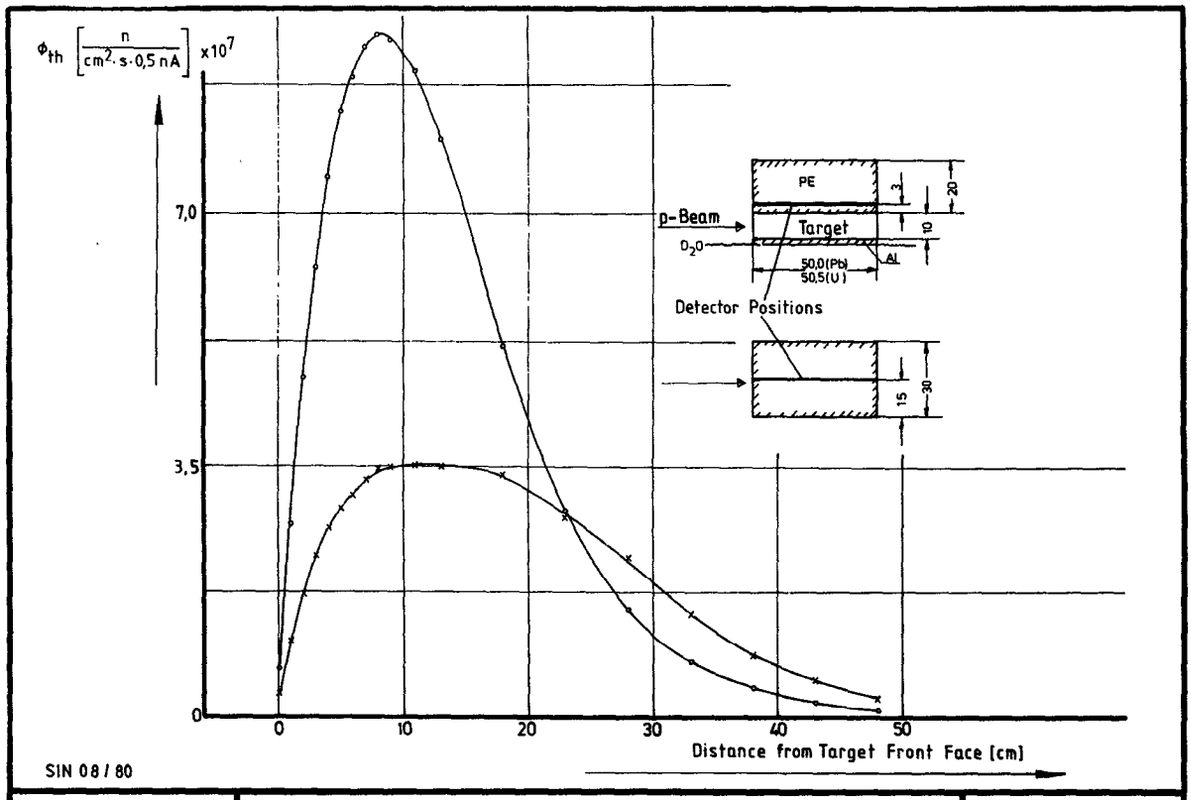

Thermal Flux in PE

×——× Pb - Target

○——○ U - Target

Fig.: 9

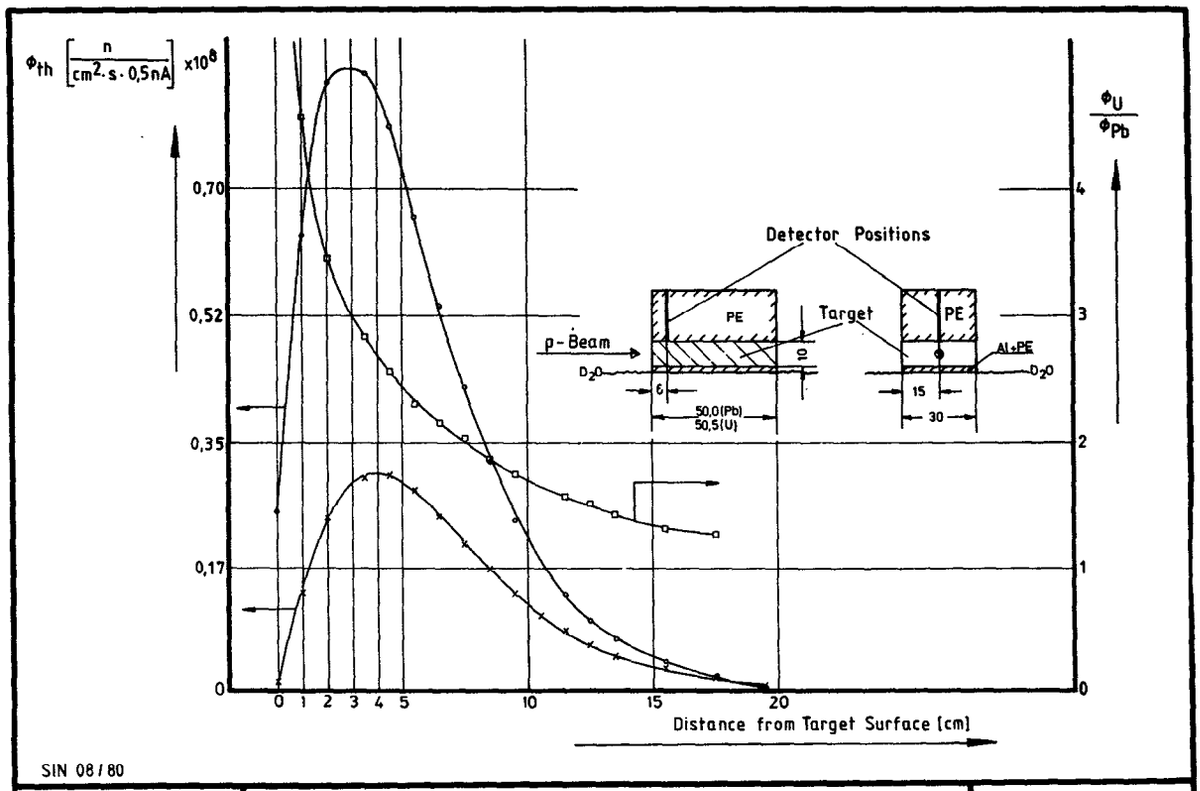

Thermal Flux in PE

×——× Pb - Target

○——○ U - Target

□——□ $\frac{\Phi_U}{\Phi_{Pb}}$

Fig.: 10

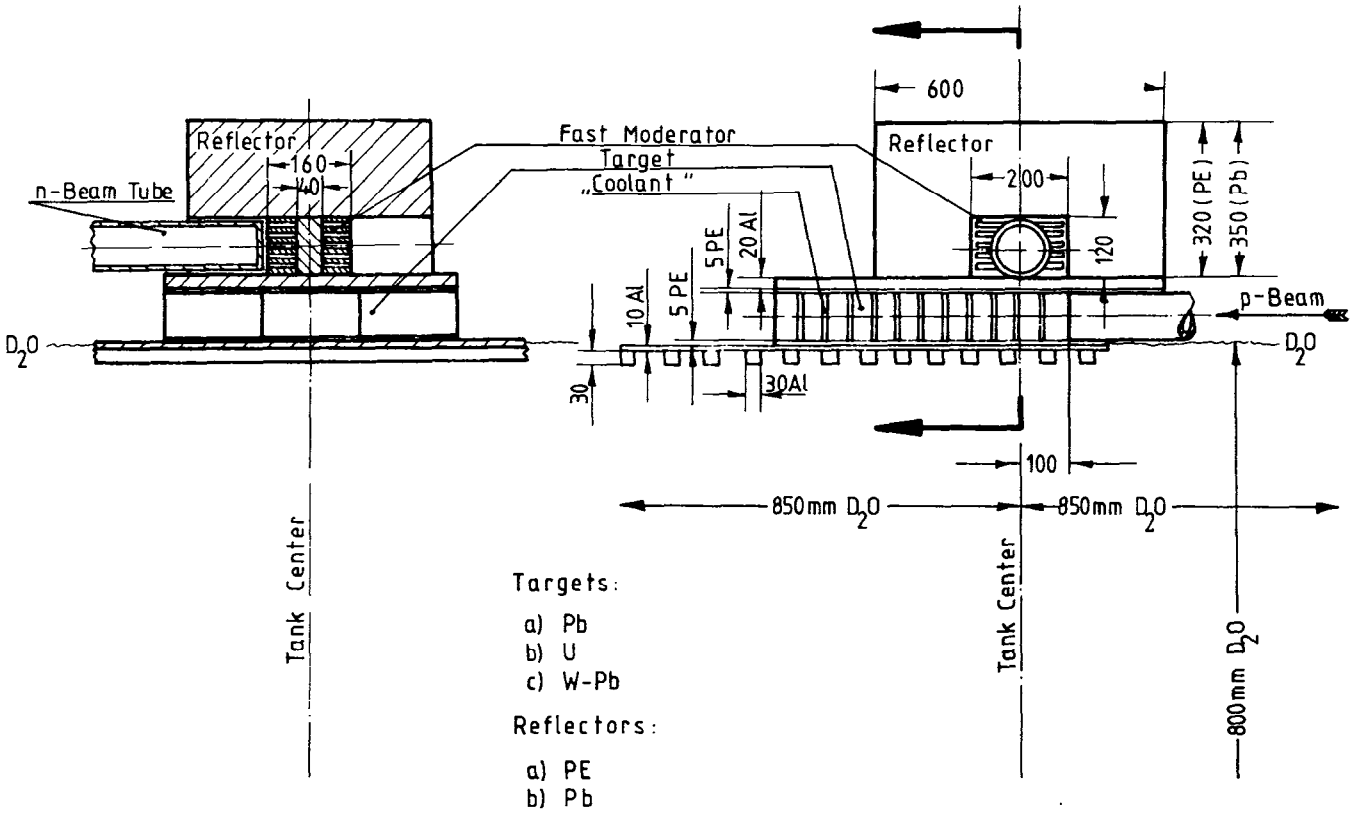

Mock up Assembly of the SNQ Design Fig.:11

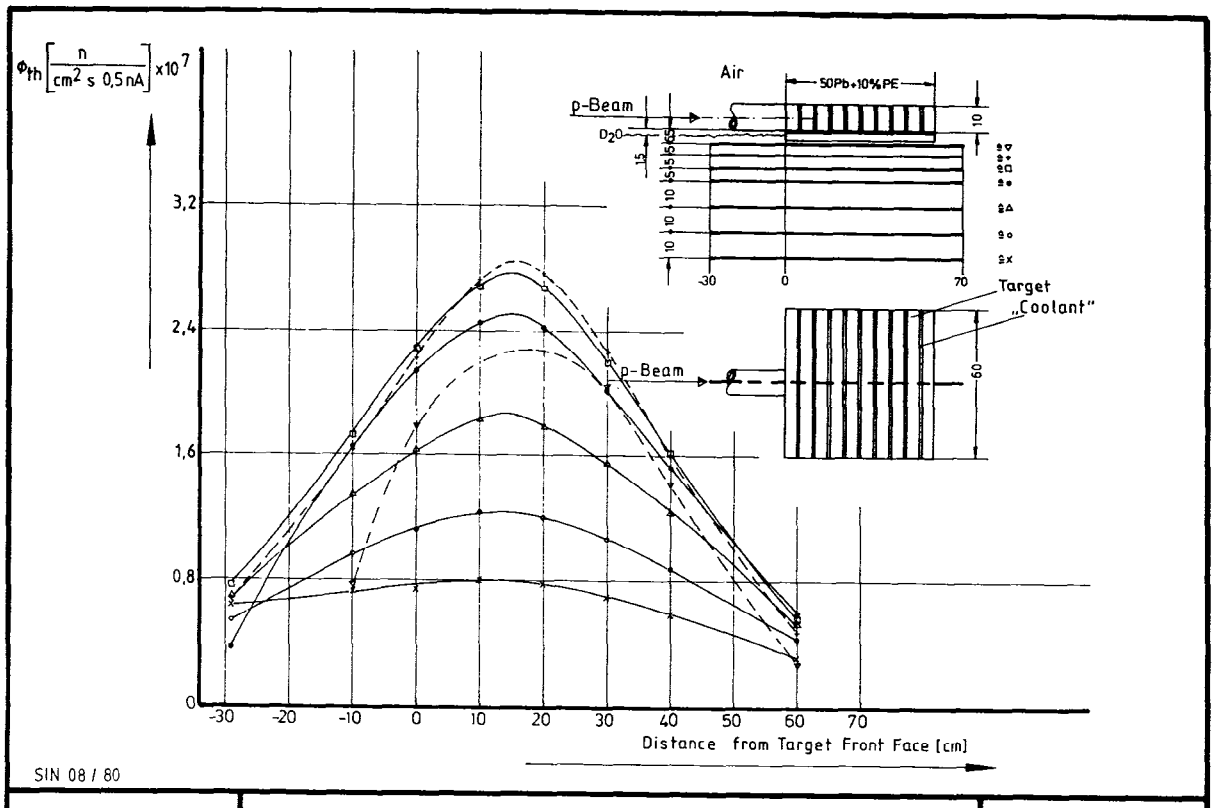

KFA

Thermal Flux in D_2O, Hybridsystem, Pb-Target, Slab with „Coolant"

Fig.: 12

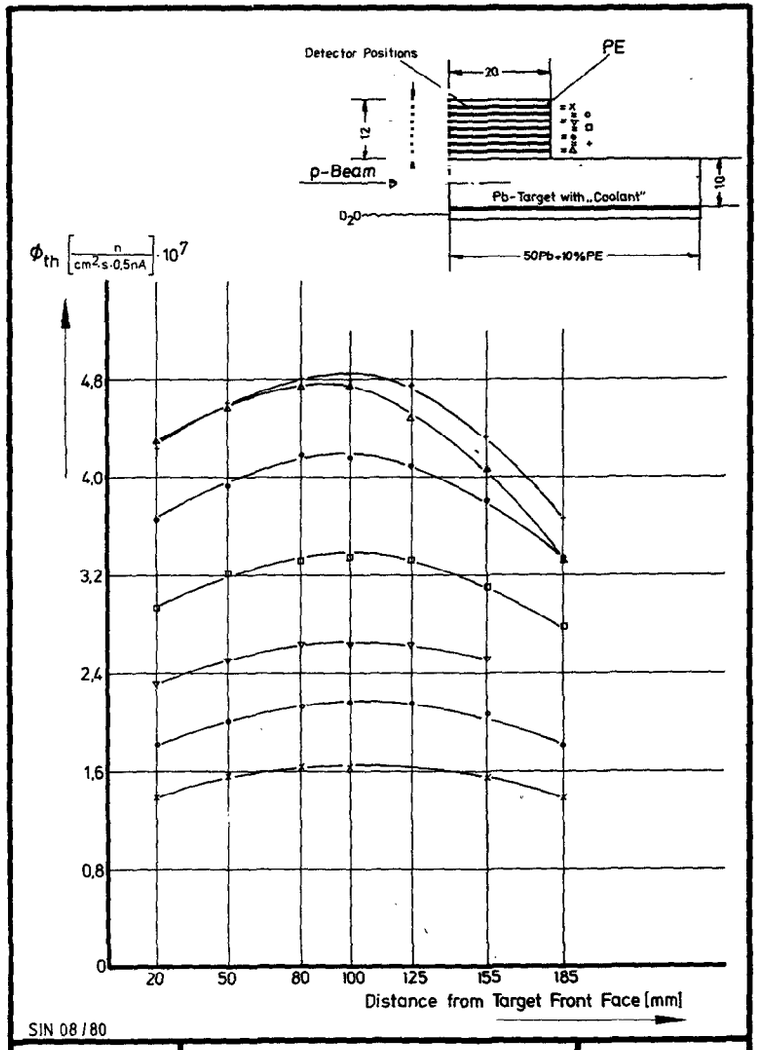

KFA	Thermal Flux in PE, Hybridsystem, Pb-Target, Slab with „Coolant"	Fig.: 13

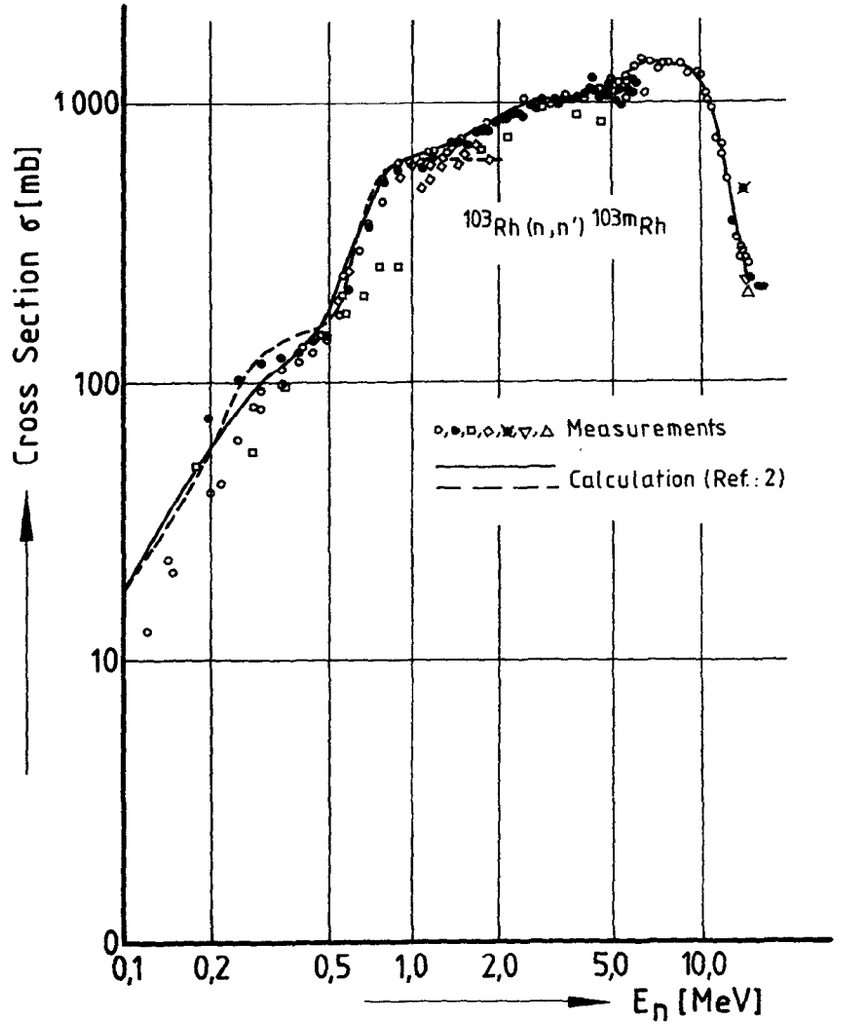

Inelastic neutron scattering cross section of ^{103}Rh Fig.: 14

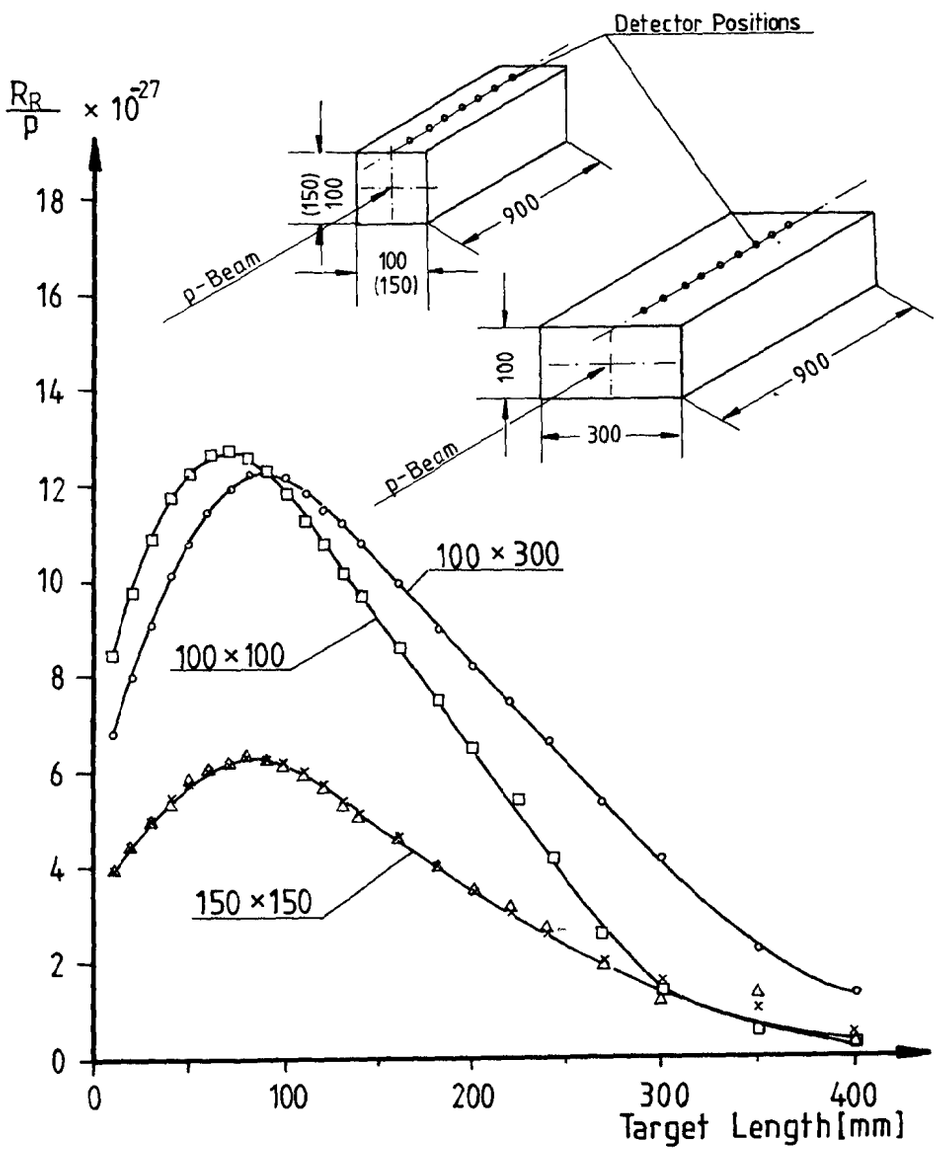

Absolut Rh-Reaction Rate Pb-Target, 600 MeV-Proton Energy, Different Target Dimensions

Fig.: 15

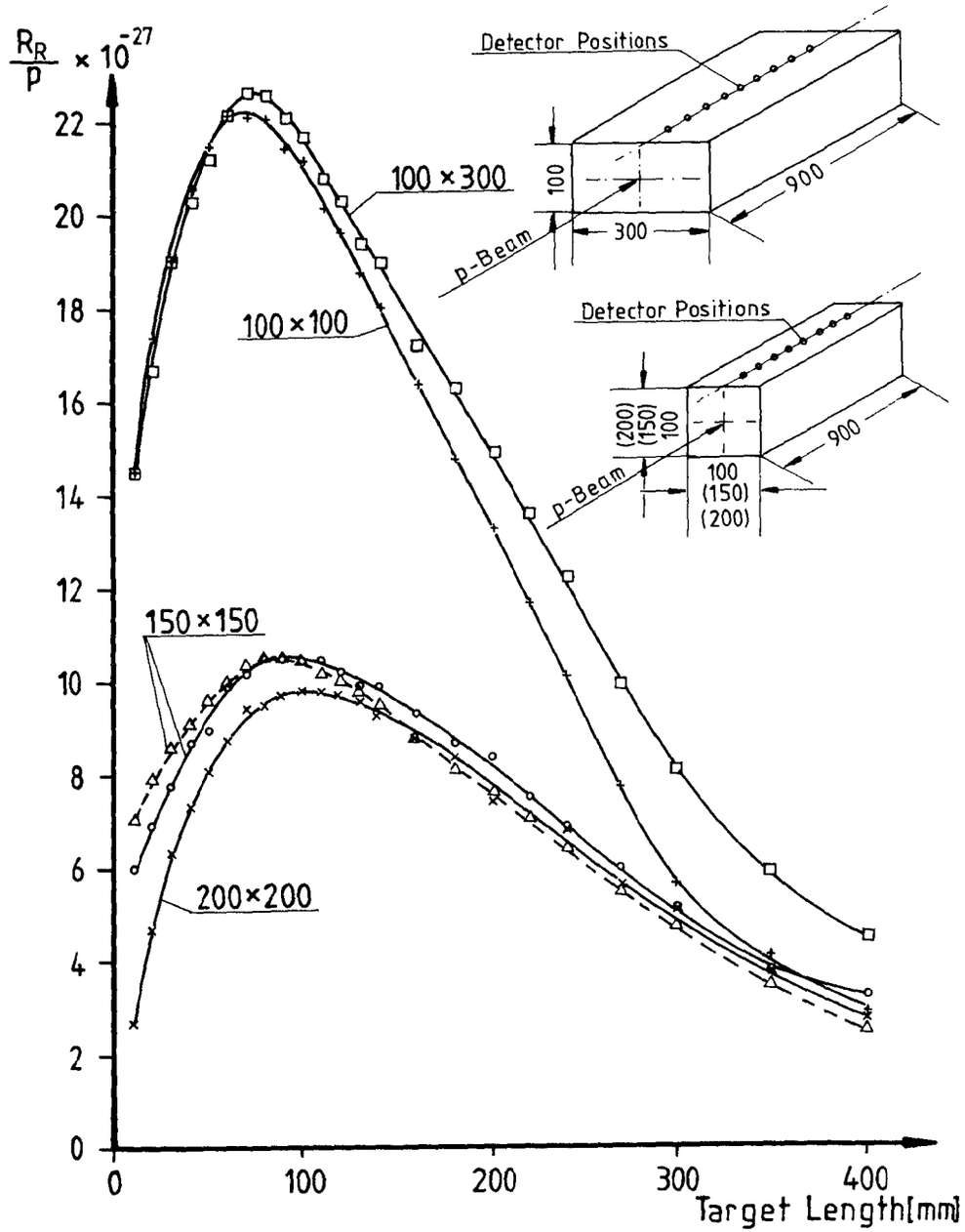

Absolut Rh-Reaction Rate Pb-Target, 1100 MeV-Proton Energy, Different Target Dimensions Fig.: 16

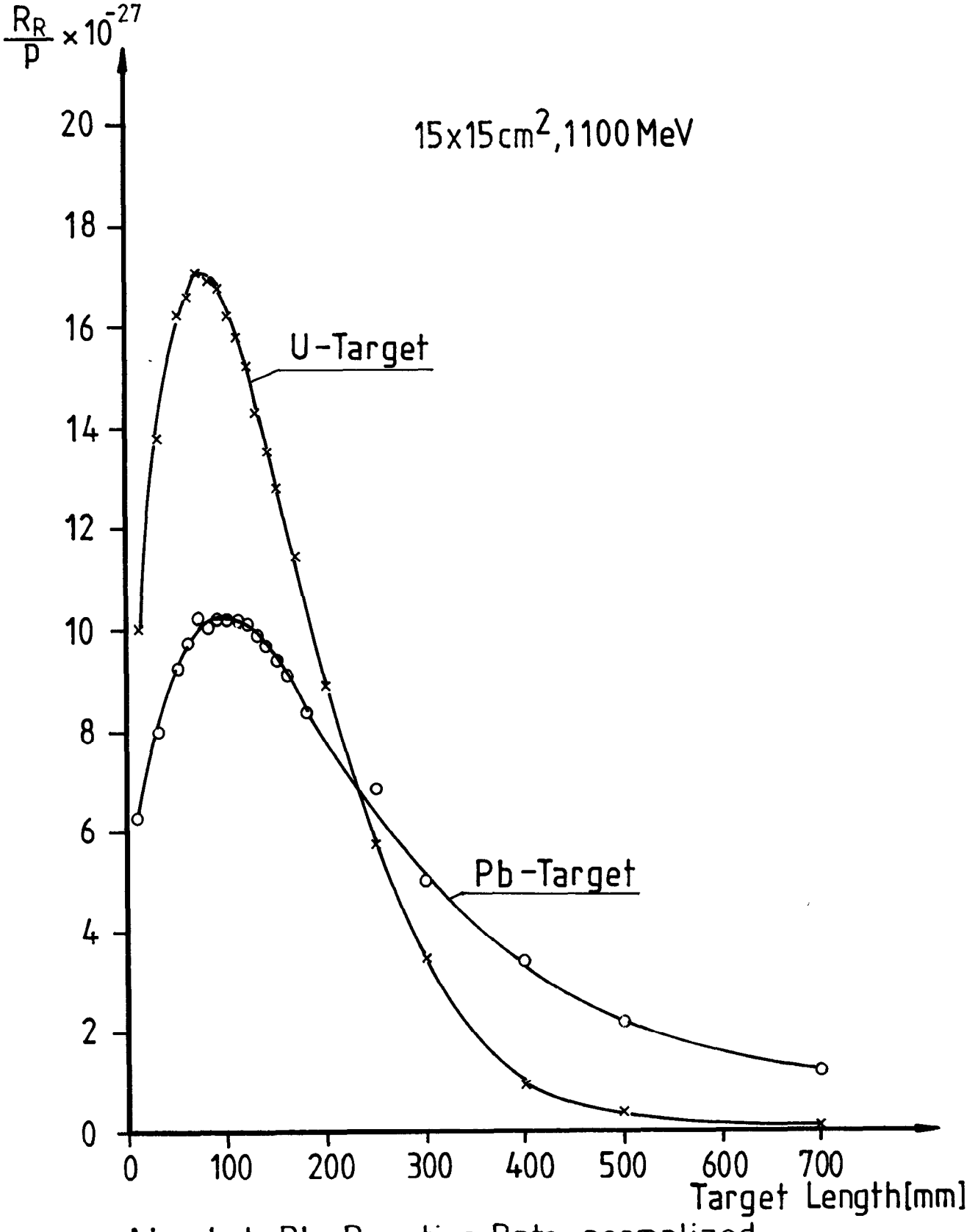

Absolut Rh-Reaction Rate normalized to one incident Proton

Fig.:17

Jül-Conf-45 D3-1

I C A N S - V

MEETING OF THE INTERNATIONAL COLLABORATION ON

ADVANCED NEUTRON SOURCES

June 22-26, 1981

Some Neutronic Aspects of Solid Methane Moderator System

Kazuhiko Inoue, Yoshiaki Kiyanagi

Hirokatsu Iwasa and Kiyoshi Jinguji

Department of Nuclear Engineering, Hokkaido University

Sapporo, 060 Japan

Noboru Watanabe, Susumu Ikeda and Yoshikazu Ishikawa

National Laboratory for High Energy Physics

Oho-machi, Ibaraki, 305 Japan

Abstract

Beam intensities and pulse characteristics of the cold neutrons emanating from a coupled and a decoupled solid methane moderators were measured. The result suggets the possibility of adopting a coupled solid methane moderator as a KENS cold source. The effects of the cryostat wall and the phase transition of the solid methane on the neutron spectrum are also discussed.

1. Cold Neutron Characteristics for a Coupled and a Decoupled Systems

Based on the program to improve the performance of the KENS target-moderator-reflector assembly[1], some optimization studies on the solid methane moderator have been performed since the last ICANS meeting. As a first step of the measurements, the beam intensity of cold neutrons as well as the pulse characteristics from a coupled and a decoupled solid methane moderators with a graphite reflector were measured using the cold moderator system at Hokkaido linac[2]. Solid methane moderator with a dimension of 25 x 25 x 5 cm^3 was placed in slab geometry to the Pb target and was embeded into a graphite reflector (about 60 x 60 x 60 cm^3) under the condition of with and without Cd decoupler of 0.5 mm thickness. Moderator temperature was kept to 20 K throughout the measurements. The neutron spectra measured by Vanadium scattering for the both coupled and decoupled moderators are plotted in Fig. 1 normalized at the neutron energy above Cd cut-off. Neutron beam intensity obtained from the coupled moderator turned out to be about 35 % higher than that from the decoupled one around λ = 4A.

Pulse shapes of cold neutrons at various energies from the coupled moderator have also been measured by means of the back scattering from a mica crystal. The measured results are summarized in Fig. 2 with previous results obtained for the decoupled one[3]. The results of both cases for E = 5.26 meV are also compared in a linear scale in Fig. 3. In Fig. 4 are demonstrated three time constants; the rise time, the half width and the decay time. Note that the elongations in the time constants for the coupled system are fairly small.

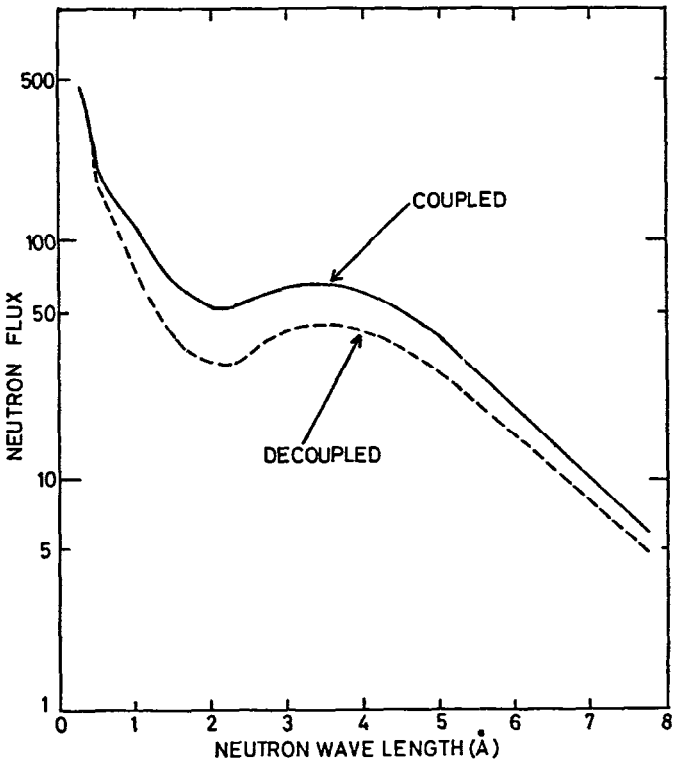

Fig. 1 Time of flight spectra for the coupled and the decoupled moderators

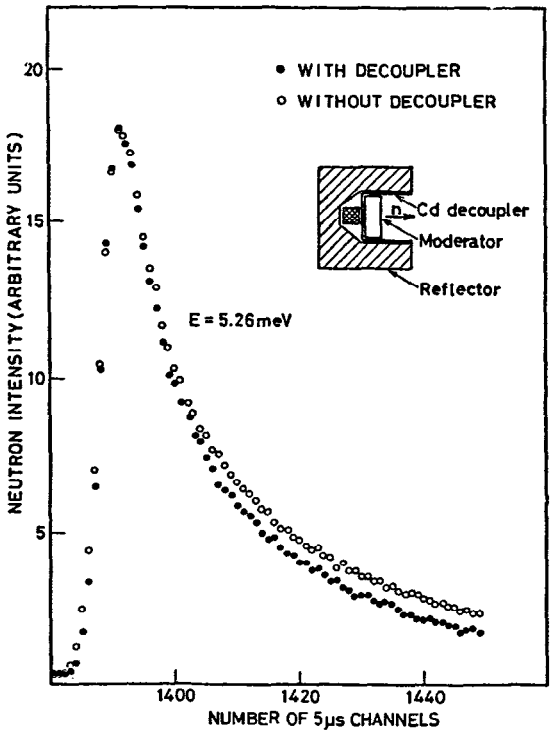

Fig. 3 Time shapes for the coupled and the decoupled moderators at 5.26 meV

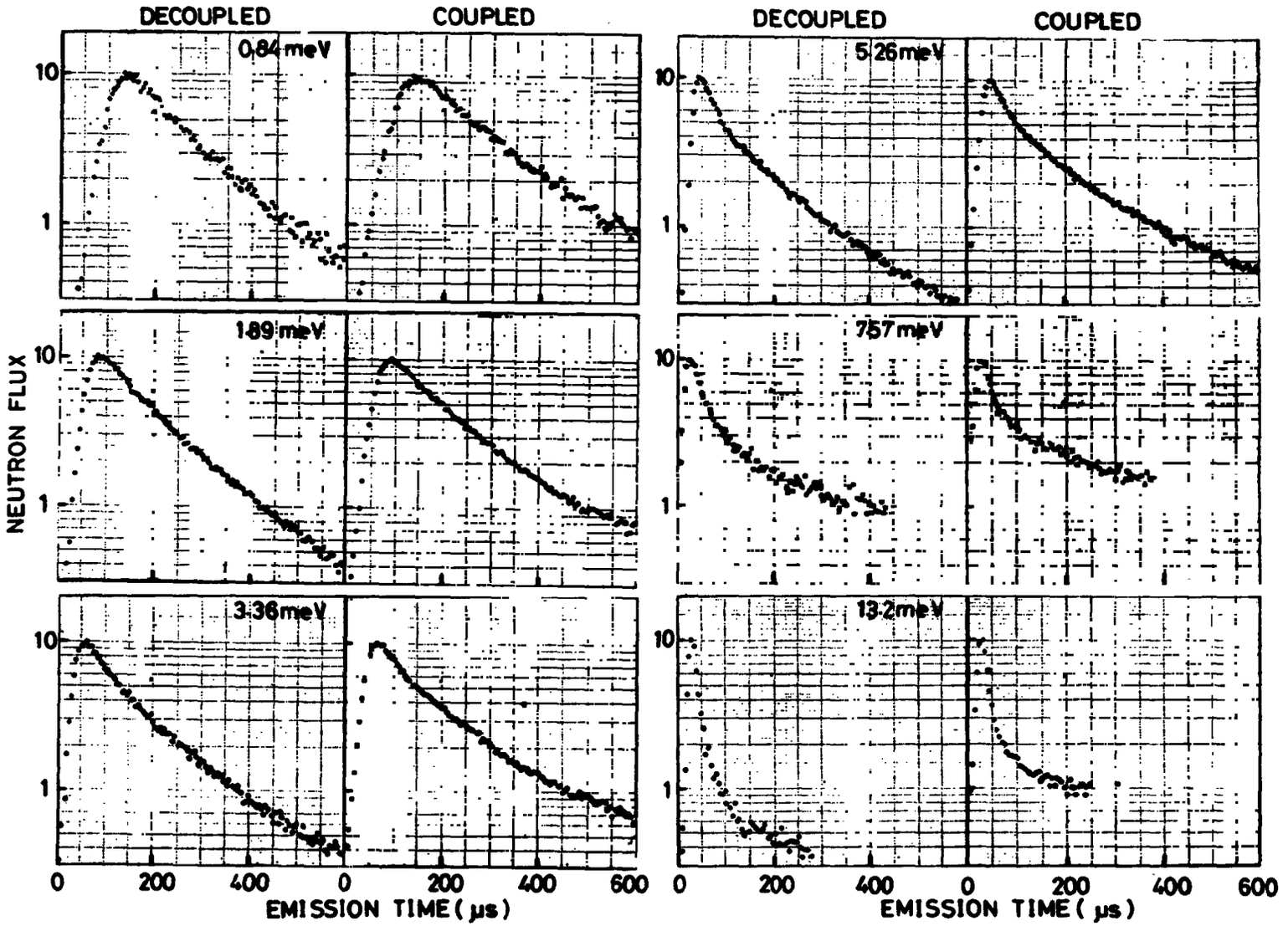

Fig. 2 Pulse shapes of cold neutrons from the coupled and the decoupled moderators

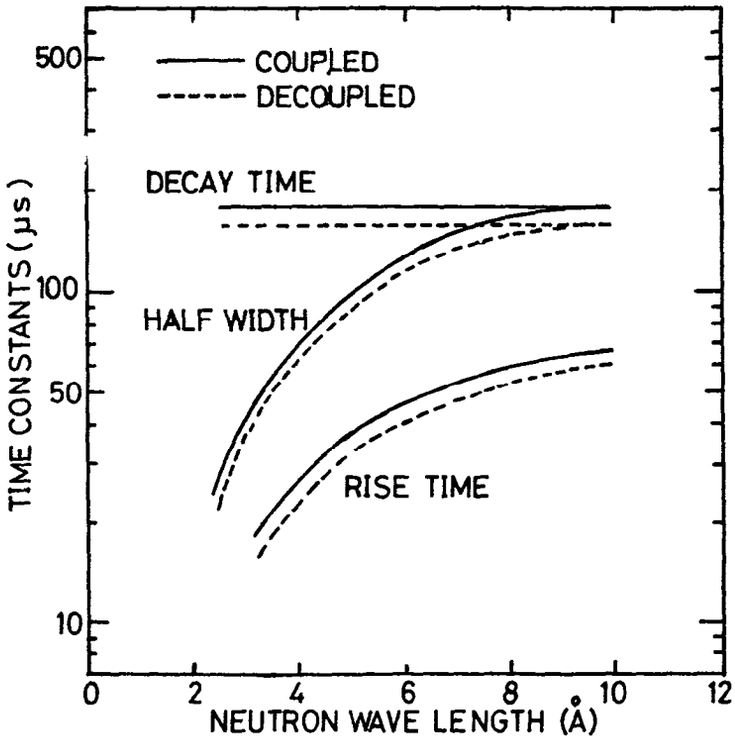

Fig. 4 Three time constants

2. Fine Structure of Cold Neutron Spectra

Fine structure of the neutron spectrum from the cryogenic moderator has been noticed in some laboratories[4)5)]. It has been argued that, in case of solid methane moderator, the fine structure may be related with the phase transition which exists at about 20 K. We have found, however, the measured spectra from the solid methane moderator at various temperatures below and above the transition temperature exhibit quasi-equilibrium spectra as shown in Fig. 5[3)]. The result is consistent with the calculated spectra based on the hindered rotation model which show that the anomalous fine structure becomes appreciable only below about 10 K as shown in Fig. 6.

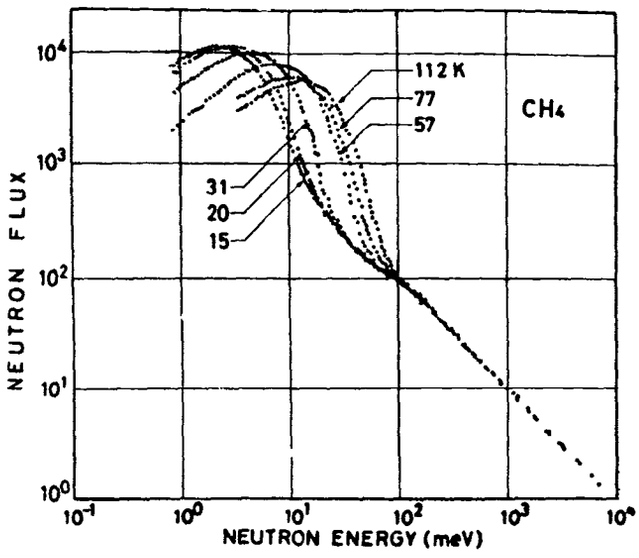

Fig. 5 Energy spectra from the solid methane moderator at various temperatures

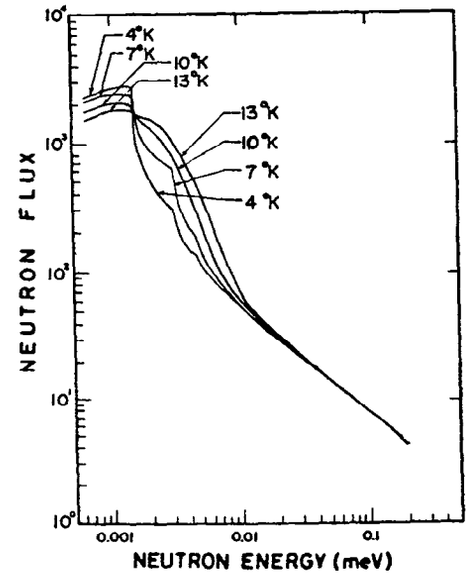

Fig. 6 Calculated energy spectra for solid methane moderator at lower temperatures

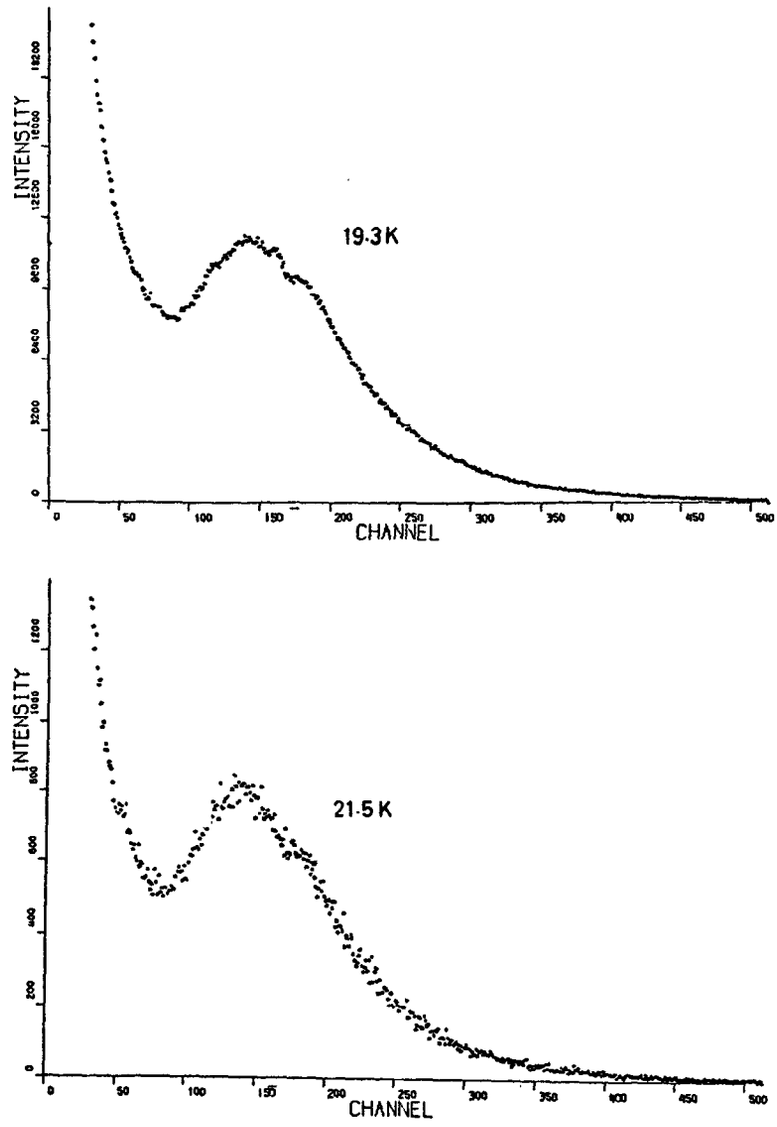

As for the cryostat wall effect, some deformations of the neutron spectra have also been reported[4]. A careful measurement of the cold neutron spectrum from the KENS cold moderator demonstrated that the spectrum was contaminated by a fine structure as displayed in Fig. 7. By changing the moderator temperature, from 19.3 K to 21.5 K, no appreciable change of the fine structure was recognized. The fine structure was found to be explained by the total cross section of aluminum; the total thickness of alminum of the moderator cryostat is 11 mm in the view surface. Since we found that the cooling power of our cryostat system is sufficient compared with the energy deposition the fine structure can be reduced to some extent.

Fig. 7 Time of flight spectra for KENS methane moderator

References

1) N. Watanabe, H. Sasaki, Y. Ishikawa, Y. Endoh and K. Inoue; Status Report of KENS, presented to this meeting (1981).

2) K. Inoue, Y. Kiyanagi, H. Iwasa and Y. Sakamoto; Nucl. Instrum. Methods, 178(1980)459.

3) K. Inoue, Y. Kiyanagi and H. Iwasa; to be published.

4) J. M. Carpenter, R. Kleb, T. A. Postol, R. H. Stefiuk and D. F. R. Mildner; The Liquid Hydrogen Moderator on the ZING-P' Pulsed Spallation Neutron Source, to be published.

5) C. G. Windsor; "Pulsed Neutron Scattering", AERE Harwell, to be published.

6) K. Inoue; Bulletin of the Faculty of Engineering, Hokkaido University, 63(1971)99 (in Japanese).

Jül-Conf-45 D3-2

I C A N S - V

MEETING OF THE INTERNATIONAL COLLABORATION ON

ADVANCED NEUTRON SOURCES

June 22-26, 1981

A Study on UCN Source for a Spallation Facility

M. Utsuro, K. Okumura and Y. Kawabata
Research Reactor Institute, Kyoto University
Kumatori-cho, Sennan-gun, Osaka, JAPAN

Abstract

Results of pulsed UCN experiments with a supermirror turbine in KUR and some Monte Carlo calculations are reported. A turbine efficiency and the UCN output intensity satisfying designed values are obtained. Similar UCN experiments with a cold source at an electron linac are also carried out and compared. UCN gains by a cooled polyethylene converter are derived from the experiments. From these studies, a concept of a synchronized supermirror turbine is proposed for a spallation UCN source which can serve multi-loads uses of UCN experiments.

I. Possible Types of UCN Sources

There are several possibilities of approach to an efficient UCN source for a spallation facility. A superthermal liquid helium converter is expected to give the highest gain factor of UCN conversion, and such a device is proposed to be used for a pulsed spallation source in KENS.[1] However, the technical problem of the heat removal remains to be solved in a cryostat put near to a cold moderator to see the moderator in a large solid angle. Further, the pulsed UCN flux produced inside of a thick converter will be time-averaged when extracted because of the low velocity of UCN.

Next approach will be to use a mechanical velocity shifter, and experimental results using a Doppler shifter of a moving crystal were appeared in the previous meeting.[2] Another type of machine, a supermirror neutron turbine, was also constructed and reported in the meeting.[3] The former part of the present paper will describe the experimental results from the operation of this supermirror turbine.

Third method of UCN source is to extract UCN directly from the surface of a cold source or from a thin converter attached on the cold source. This kind of experiment by using an electron linac is also reported here for a comparison with the turbine results.

The method of a supermirror turbine presented here has advantages of giving a largely widened output of UCN beam which makes several experiments simultaneously possible, and further the use of supermirror blades makes it easy to fit for a higher velocity of incident neutrons than in the case of an ordinary mirror turbine.[4] As a result, it gives the possibility of utilizing the phase space density at the peak neutron flux from a pulsed spallation source with less broadening of the neutron density. From these studies, a concept of a synchronized supermirror turbine will be proposed as an efficient UCN source for a pulsed spallation facility.

II. Experimental Results of a Supermirror Turbine

The principle, design and construction of the present supermirror turbine was already reported in the previous meeting,[3] including the VCN feeding device for the turbine. For the measurements of UCN production in the turbine, as shown in Fig.1, a couple of reflecting supermirror blades (5) were attached at two symmetrical positions in 180° directions around the wheel(4), and the remaining part around the wheel was shielded by cadmium plates(6). Thus, for a continuous feeding of VCN from a reactor (a phase space density being about 0.6×10^{-4} $n/cm^{2}sec(m/s)^{4}$ at the outlet of VCN-GT.), pulsed productions of UCN were performed and their distributions were analysed by a time-of-flight method through a short guide tube system(7 and 8), in which the distance from the output edge of the blades to a UCN detector(9) was about 13 cm.

The starting time of the time-analyser for detected neutrons was adjusted to the center of neutron bursts at the blade edge by using a pick-up system(11 and 12). Figure 2 shows one of the measured results with a gate opened during 10∿35 msec after the burst center. The "Ni-Al filtered" in Fig. 2 means the results of measurements with a filter of Ni-coated Al thin foil inserted in front of the detector window (i.e. between 7 and 8 in Fig. 1), which should consist of background and faster neutron countings. These non-UCN countings were essentially constant for the change of turbine speed, while the differences between two curves to be considered as UCN contribution becomes maximum at about 6 rps, i.e. the blade velocity of about 21 m/s.

Since the present measurements were performed for a continuous feeding of VCN, the non-UCN contribution in an actual condition of a pulsed source will be greatly decreased, and will be furthermore diminished by shielding the turbine vessel which was not done at all in the present study.

Further, Fig.3 gives the time-of-flight distribution of the UCN component for the optimum turbine speed of 6 rps. In this Figure, results of Monte Carlo calculations of UCN flights through the guide tube system were also shown for comparison.

From these measurements and analyses, the turbine efficiency of about 35 % expected in the present design is assured to be well attained in the present device of a simple and easy construction.

III. Direct Extraction of UCN from Pulsed Cold Source

Another time-of-flight experiment of UCN was carried out by using an electron linac and a cold source of solid mesitylene.[5] The experimental arrangement is shown in Fig. 4, where a bent guide tube of Ni-coated glass was used for the time-of-flight analyses. The effect of a polyethylene converter of 3 mm^t attached to the cold source was also studied, since the 3 mm^t Al wall of the cold pile (2) causes severe attenuation of UCN produced inside.

Figure 5 shows the result of the case with the polyethylene converter where the linac electrons were injected during a burst time of about 60 msec with the highest frequency of about 180 pps. The peak flux of cold neutrons at the cold moderator surface is estimated to be about 1×10^{10} $n/cm^2 sec$.

As seen in Fig. 5, the present arrangement gives a larger contribution of non-UCN component comparing to the case of the turbine. In Fig. 6, a large gain factor of the cooled polyethylene converter for UCN intensity is illustrated as a result of these experiments.

IV. A Proposal of a Synchronized Supermirror Turbine

From these studies, it is proven that the neutron

turbine gives a good elimination of non-UCN components and a high efficiency of UCN conversion. These advantages will be further multiplied by a possible utilization of the peak density of incident neutrons from a pulsed source by preparing appropriate UCN reflecting plates at remaining parts around the wheel, and also by a multi-loads uses of the wide UCN output from the turbine. Such a concept is illustrated in Fig. 7 as a possible combination of a synchronized supermirror turbine to a pulsed spallation source. The use of supermirror blades makes it easy to prepare the machine for faster incident neutrons, and this improves undesirable effect of neutron density broadening at the turbine inlet.

An example of the specifications resulted from these considerations is listed in Table 1. The construction of such a machine is a quite easy task within the present techniques.

Acknowledgements

The authors express their thank to Prof. A. Steyerl of Technical University of Munich for his encouragement to the present study.

References

1) H.Yoshiki: Proc. 4th Meeting of ICANS (KENS Report II), March 1981, p.715.
2) T.Dombeck: ibid.,p. 723 and p.732.
3) M.Utsuro et al.: ibid., p.743.
4) A.Steyerl: Nucl. Instr. Methods, 125, 461 (1975).
5) M.Utsuro et al.: J. Nucl. Sci. Technol. 14,390 (1977). Ann. Rep. Res. Reactor Inst., Kyoto Univ., 12, 12 (1979).

Table 1.
SPECIFICATIONS OF
A SYNCHRONIZED SUPERMIRROR TURBINE PROPOSED

Velocity Range of Incident Neutrons Used:	100 m/s ± 7 m/s,
Cross Section of VCN Feeding Guide Tube:	10 cm^H x 1.5 cm^W,
Length of VCN-GT:	∿2.5 m from Cold Source,
Turbine:	
Diameter of turbine wheel;	300 cm,
Blade velocity;	50 m/s,
Blade shape;	Polygon of 5 flat supermirrors with 15cm^H,
Blade arrangement;	
a) For High Repetition Source (∿ 100 pps);	Alternative arrangements of 2 blades(pitch $W_b \cong 7.5$cm) and a reflector($W_r \cong 35$ cm).
b) For Low Repetition Source (∿ 10 pps);	Symmetrical 2 blade-groups in 180° directions around the wheel. Two blades in each group, and a wide reflector between the groups.
Cross Section of UCN Output:	∿ 8 cm^H x ∿25 cm^W ≅ 8 cm square x 3 loads

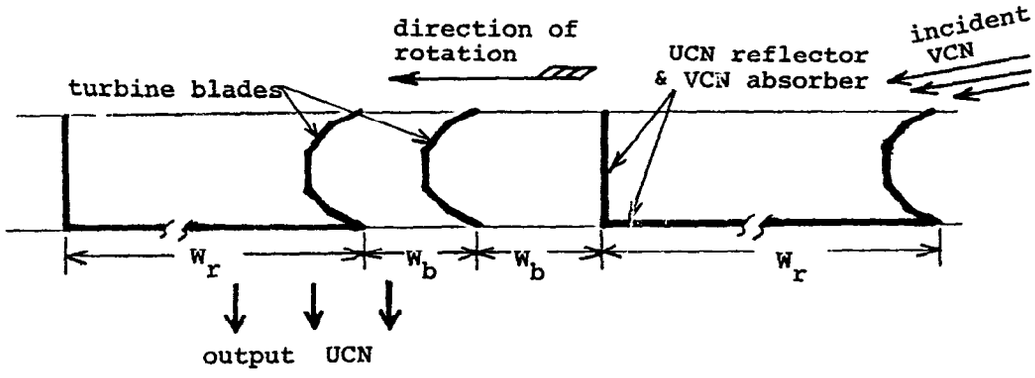

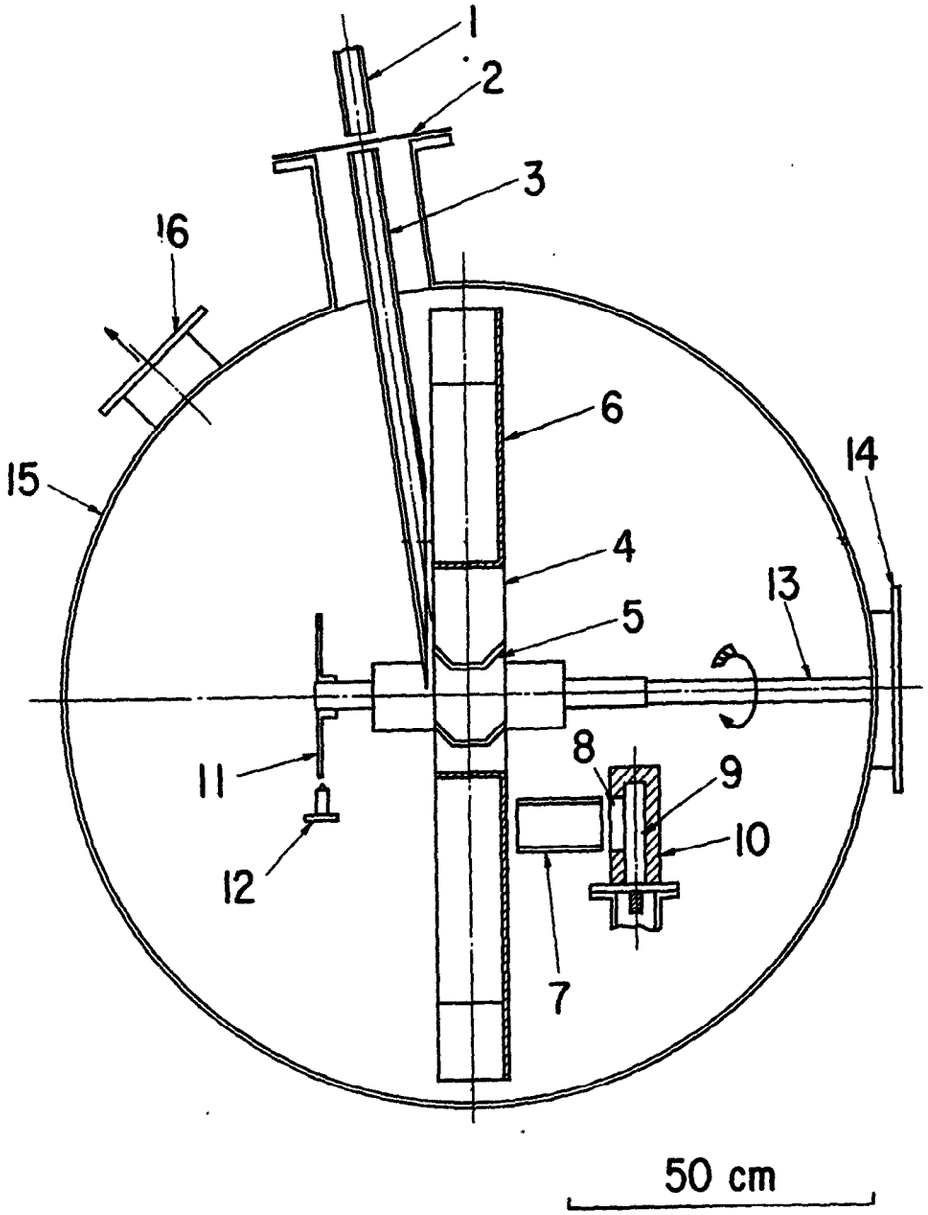

1:Double-curved VCN-GT from a Reactor, 2:Al window, 3:VCN feeding GT, 4:Turbine wheel, 5:Supermirror blades,6:Cd plates, 7:Ni-coated glass GT, 8:Guided window of Ni mirror, 9:UCN detector of He^3, 10:B_4C shielding, 11:Rotating disc with iron chips, 12:Magnetic pick-up, 13:Driving shaft, 14:Magnetic coupling, 15:Vacuum vessel, 16:Evacuation port.

Fig. 1 Experimental arrangement of UCN production with a supermirror turbine.

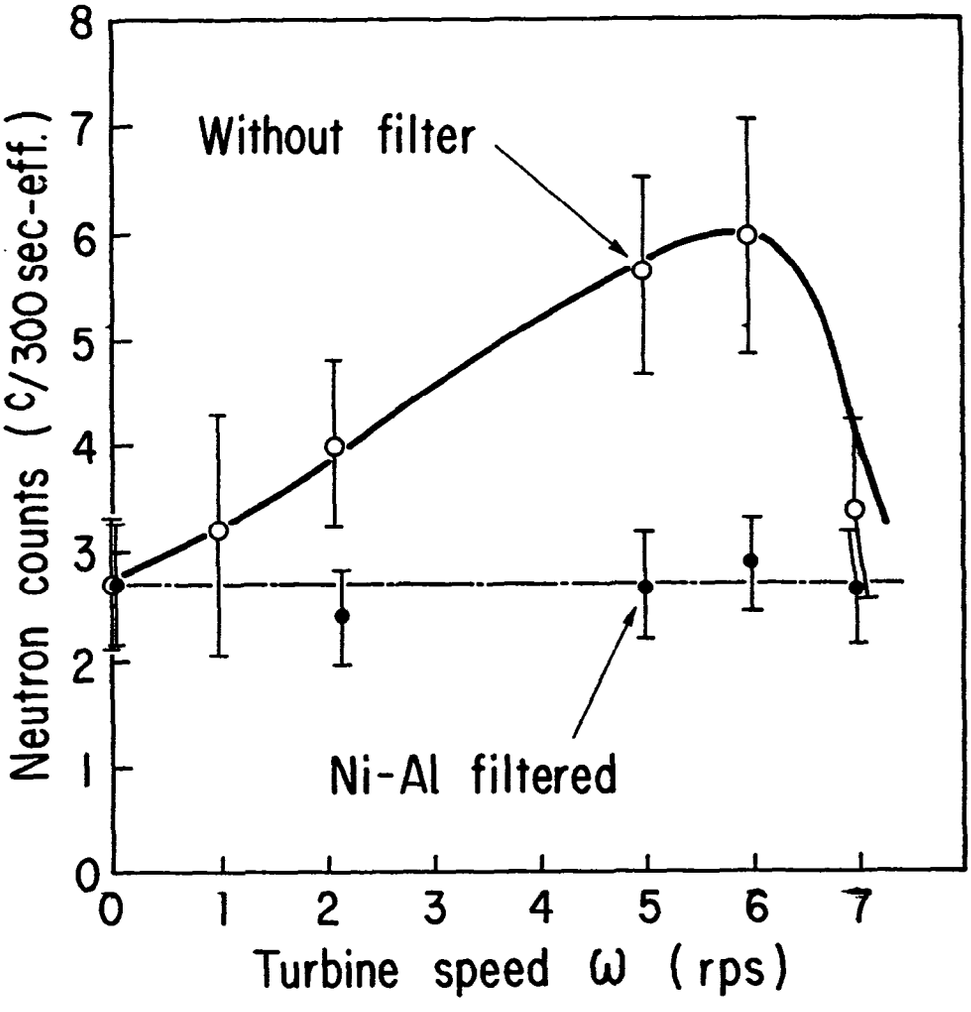

Fig. 2 Measured results of the turbine output for various rotation speed with a gate time of detected signals at 10∿35 msec. (Detector background subtracted.)

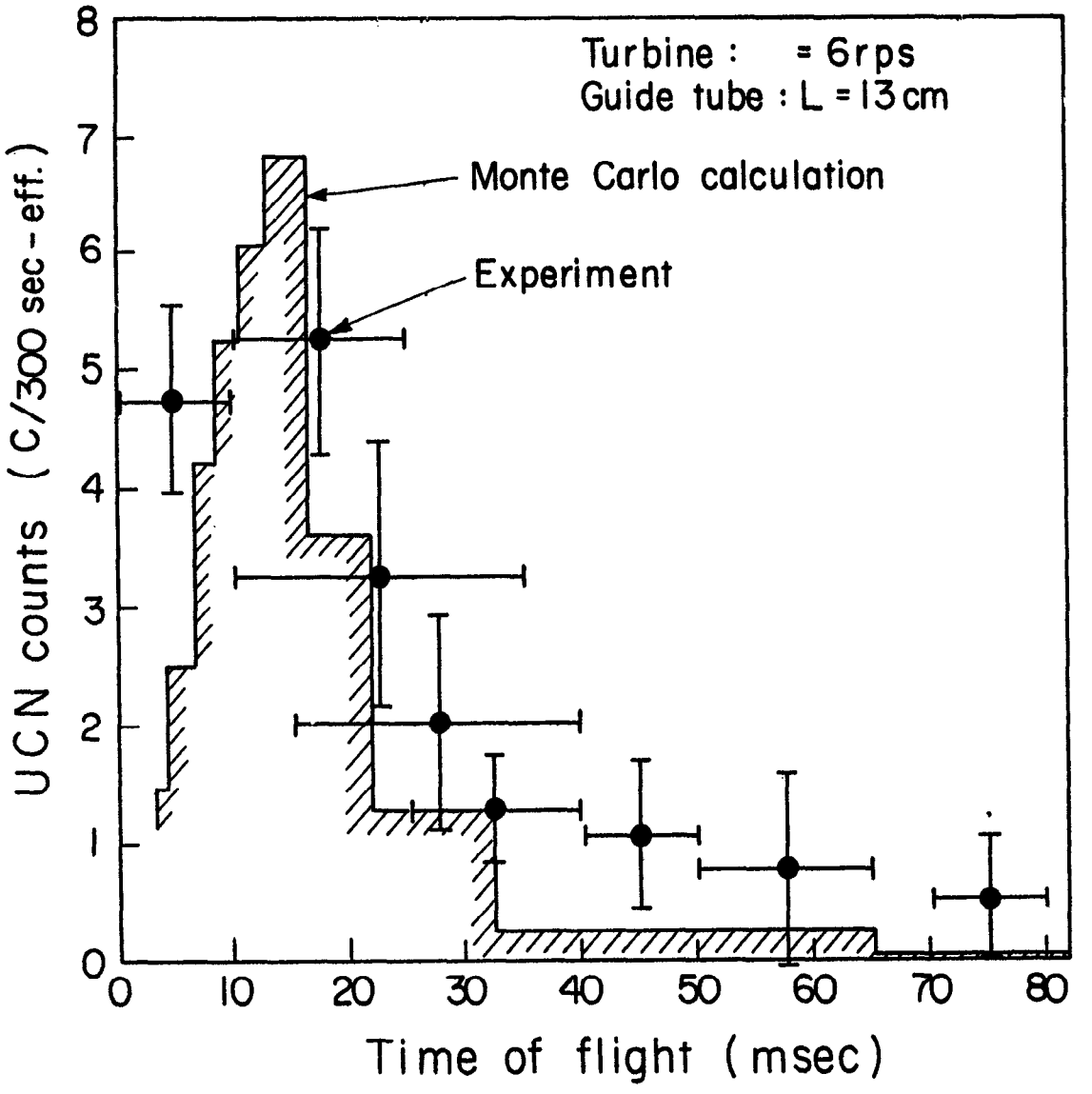

Fig. 3 Time-of-flight distribution of the difference between no-filter and filtered counting rates. Monte Carlo calculation was also shown for comparison.

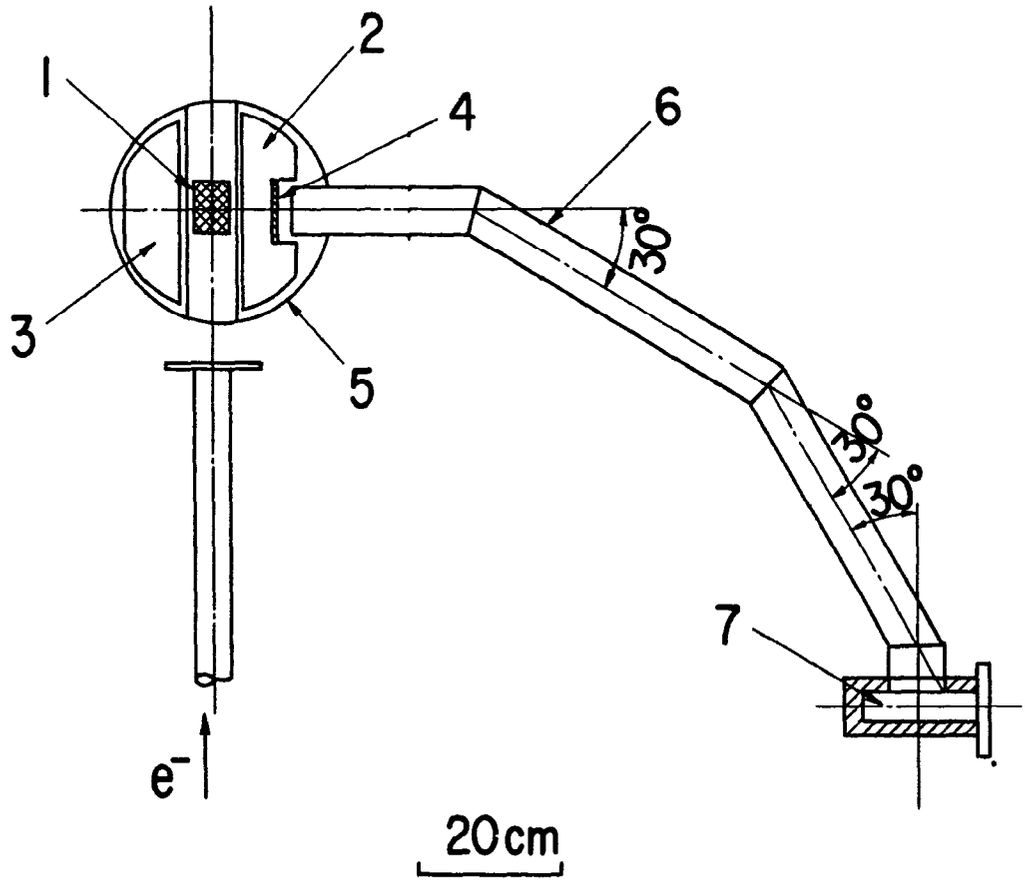

1:Target, 2:Cold source, 3:Reflector, 4:UCN converter, 5:Vacuum vessel, 6:Evacuated guide tube, 7:UCN detector.

Fig. 4 Experimental arrangement of UCN production with a linac-cold source system.

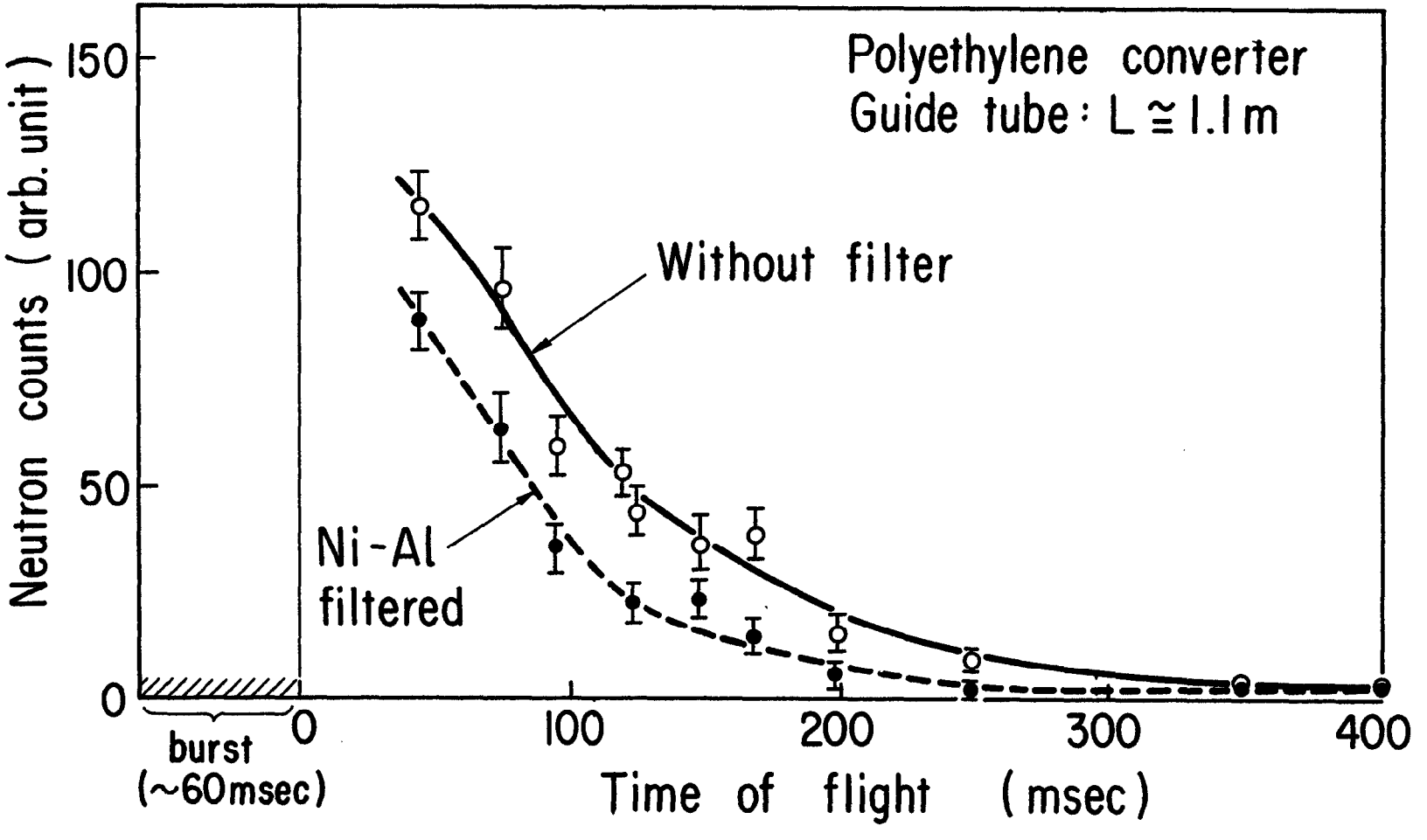

Fig. 5 Measured results with a polyethylene converter on the cold source.

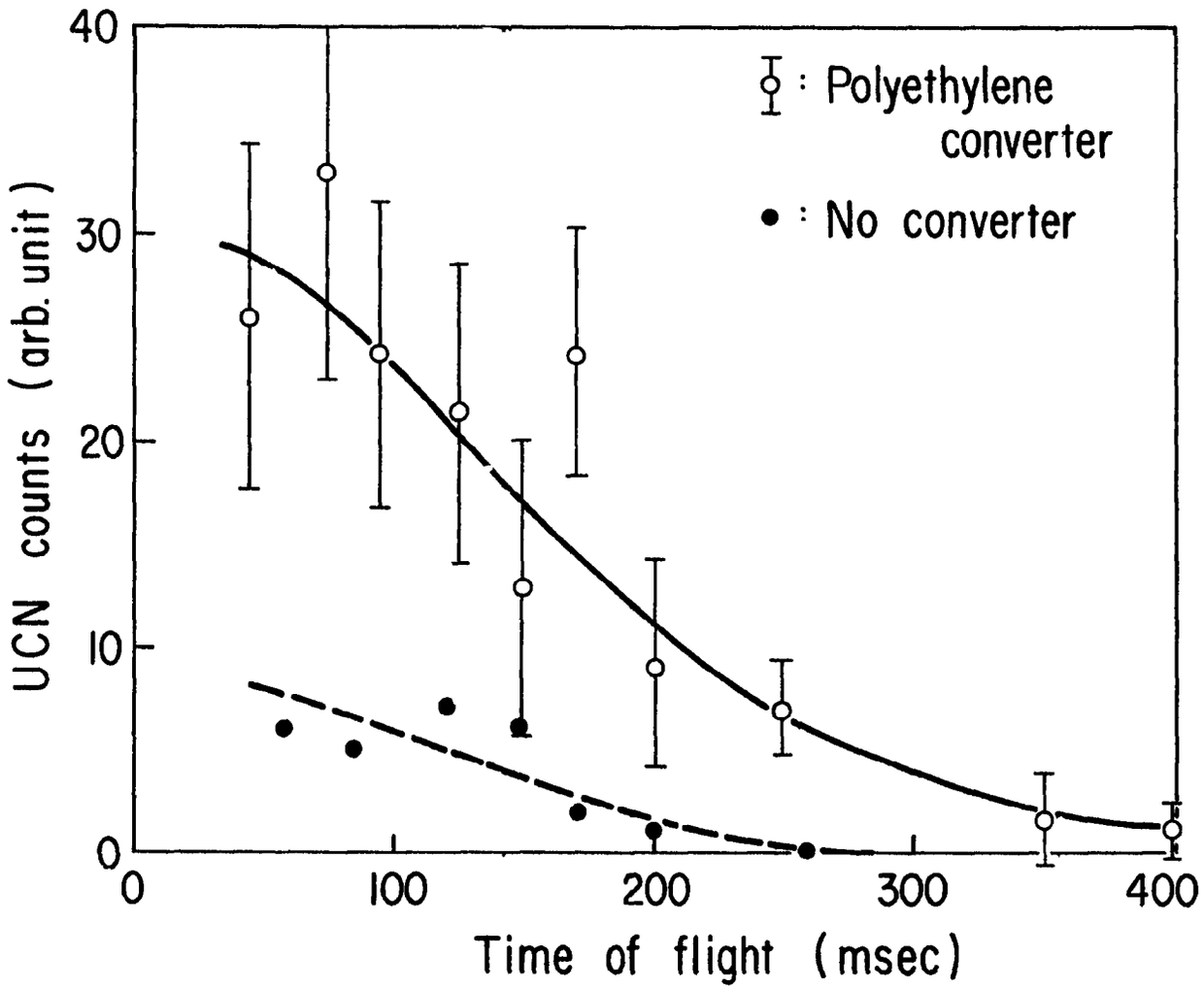

Fig. 6 Measured effects of the polyethylene converter to increase the difference between no-filter and filtered counting rates.

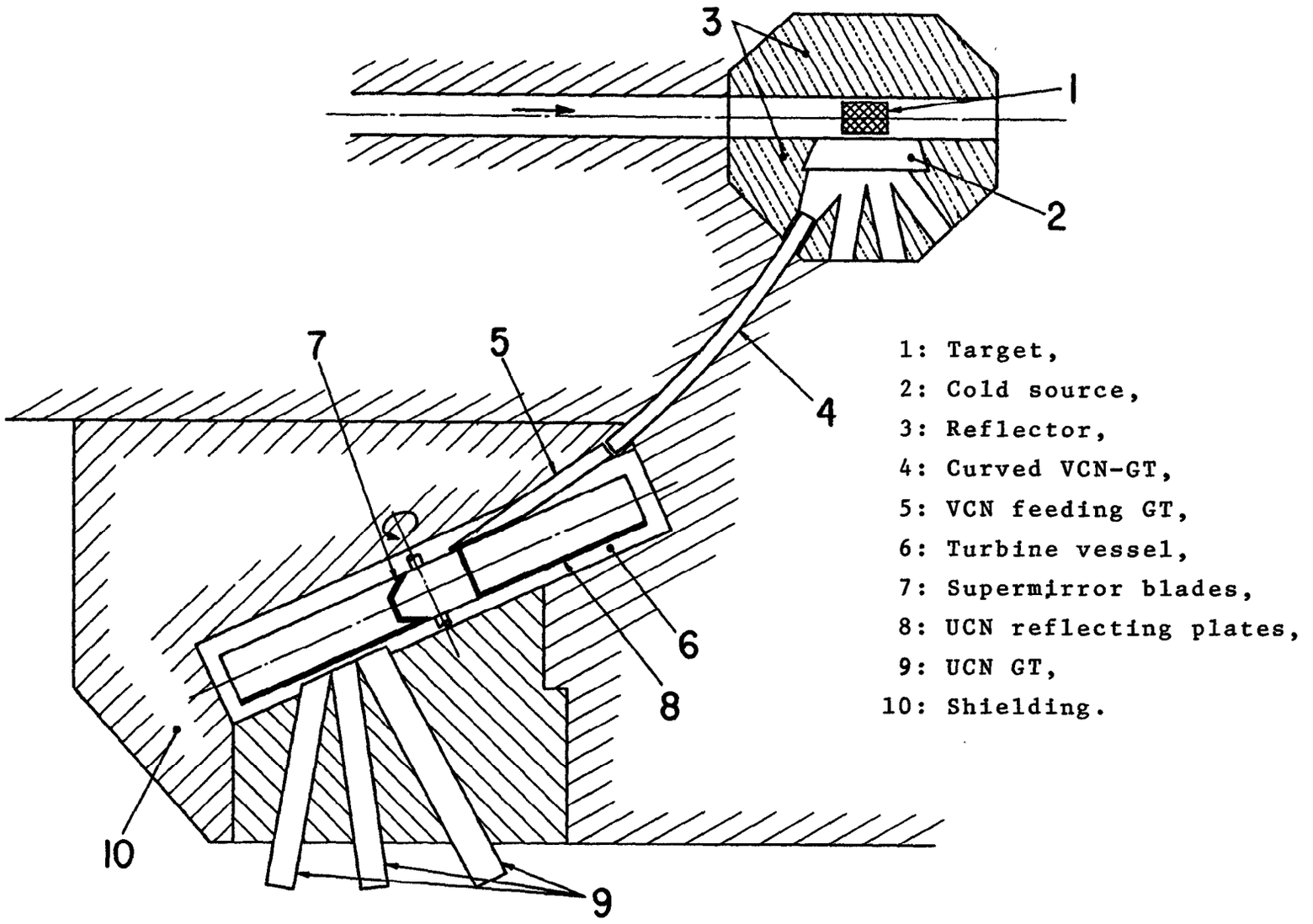

Fig. 7 A conceptual drawing of a synchronized supermirror turbine combined to a pulsed spallation source.

Jül-Conf-45

D3-3

I C A N S - V

MEETING OF THE INTERNATIONAL COLLABORATION ON

ADVANCED NEUTRON SOURCES

June 22-26, 1981

Feasibility Study of a Low-Temperature Irradiation Facility at the German Spallation Neutron Source SNQ

K.Böning and R.Golub

Physik Department, Technische Universität München,

8046 Garching, Germany

Abstract

A feasibility study was performed on the possible installation of a low-temperature irradiation (LTI) facility at the projected German spallation neutron source SNQ. The LTI facility should allow the irradiation of samples at temperatures between 4.5K and about 450K with either thermal or fast neutrons. We first outline the scientific motivation and then describe the design features and the performance of the facility, which essentially consists of an on-line He refrigerator and two vertical irradiation tubes providing two irradiation positions I and II. In position I a very clean thermal neutron flux $\phi_{th} \approx 1 \cdot 10^{14}\ cm^{-2}\ s^{-1}$ can be realized, the γ-background being dominated by the contribution from the LTIF structural material. In position II the fast neutron flux is $\phi_f \approx 2 \cdot 10^{13}\ cm^{-2}\ s^{-1}$ (for E > 0.1MeV) or even more. In both cases the dominant heat production comes from the thermal neutrons. The $100 s^{-1}$ time structure of the SNQ represents a major problem for irradiations at the lowest temperatures. Other minor problems for a LTI facility at the SNQ as compared to a new reactor are the high energy neutrons, the secondary protons and some geometrical constraints. The great advantage of the SNQ lies in the very low γ-background and also in its potential of flux tailoring.

1. Introduction

The present concept of the planned German Spallation Neutron Source (abbreviated SNQ from "Spallationsneutronenquelle") assumes a platelike rotating lead target with a vertical axis. The horizontal proton beam of energy 1100MeV, average current 5 mA and repetition rate 100 s^{-1} (pulse length 500 μs) hits the target wheel radially /1/. A large D_2O moderator tank will be placed directly above the target plane (compare fig. 1) and will lead to high time-averaged thermal neutron fluxes ϕ_{th}.

The Low-Temperature Irradiation (LTI) Facility should allow irradiations in the region of this D_2O tank. The samples could have a maximum size of 25 mm diameter and 100 mm length and the irradiation temperature would be either 4.5K in liquid Helium or 5 ÷ 450K in gaseous Helium. Two extreme irradiation positions I and II are considered: in position I the thermal neutron flux should be high and as clean as possible ($\phi_{th} \approx 1 \cdot 10^{14}$ cm^{-2} s^{-1}) and in position II the fast neutron flux should be as high as possible ($\phi_f \approx 2 \cdot 10^{13}$ cm^{-2} s^{-1} for neutron energies above 0.1MeV). By changing the irradiation position continuously in between these two extremes mixed neutron spectra can be realized, and smaller values of ϕ_{th} with reduced background radiation are possible beyond position I if necessary.

In what follows we first give an overview of the scientific applications planned for the LTI facility (Chapter 2). The design features of the facility and its estimated performance are described in Chapter 3. Finally, Chapter 4 summarizes the particular aspects which are relevant for a LTI facility at the SNQ as compared to a similar facility on a new middle-flux research reactor /2/. In this context the advantage of a strongly reduced background of γ-radiation and the disadvantage of the time structure of the SNQ are of major concern.- A somewhat more detailed description of the various aspects of a LTI facility at the SNQ can be found in ref. /3/.

2. Scientific Motivation

2.1 Irradiation of Metals with Thermal Neutrons

The emission of prompt γ-rays after thermal neutron capture corresponds to the transfer of small effective recoil energies to the irradiated nuclei and so leads to the production of single vacancies and self-interstitials in metals, i.e. of Frenkel defects. The radionuclides which are simultaneously produced in most cases give rise to some doping and can often be used as radioactive probes for investigating the samples. In contrast to electron irradiation a statistical distribution of isolated Frenkel defects can be produced also in bulk samples. The fast neutron flux must be sufficiently low (see Chapter 3.2) to avoid the production of defect agglomerates in high-energetic cascade processes. A low irradiation temperature is necessary to immobilize the defects produced.

The technique of low-temperature irradiation in a high thermal neutron flux practically opens a new field of research applications, the

investigation of isolated Frenkel defects with neutron scattering methods, since bulk samples can be provided. Inelastic measurements should enable the search for low-frequency resonant vibration modes of isolated dumbbell interstitials under significantly better conditions than before and so help to answer a fundamental open question. Elastic diffuse neutron scattering measurements allow the investigation of the size and symmetry of the displacement fields of the point defects and, after stepwise annealing, of defect agglomerates; they complement analogous measurements using X-ray scattering techniques, where the experimental parameters are different.

The radioactive probes can be used for measurements of the Mößbauer effect and of the perturbed angular correlation. Since the probe nucleus as well as the radiation damage have been produced in the same (n,γ) elementary process they are correlated in space. Investigations of this type can be compared with "uncorrelated" experiments, where the probe atoms have been brought into the samples already before irradiation. In all these cases the trapping of interstitials or vacancies at the probe nuclei becomes detectable via hyperfine interactions.

In addition the following types of measurements are planned: elastic constants, mechanical and magnetic properties, precise defect production rates and ideal isochrones, and positron annihilation and myon spin rotation.

2.2 Irradiation of Nonmetals with Thermal Neutrons

During low-temperature irradiation of semiconductors, insulators, organic and biological substances with thermal neutrons not only is one interested in the structural defects, which have been discussed in Chapter 2.1 and which now occur in different charge states,but also in the subsequent chemical reactions. Because of the radiolysis problem in nonconducting materials a very pure thermal neutron flux is now particularly essential, i.e. above all the γ dose rate must be sufficiently low (see Chapter 3.2).

There are many important research applications which are specific for nonmetals and which will be realized in addition to those already discussed for metals. We begin with neutron transmutation doping of solids at low temperature. In nonmetals the simultaneously produced correlated point defects and their annealing behaviour can be studied very efficiently with optical methods, ESR and NMR. The spectroscopic properties of the isolated foreign atoms are interesting in many cases, too (matrix isolation technique, e.g. K in the solid rare gas Ar). Positron annihilation in nonmetals often goes along with the formation of a positronium atom which can chemically react with the radiation transmuted foreign atoms (positronium chemistry). The diffusion behaviour of the statistically distributed and radioactive foreign atoms can also be investigated (e.g. Ar in the ionic crystal KCl).

The field of hot atom chemistry in solids deals with the study of the chemical reactions of the recoil atoms. These "hot" atoms are characterized by both high kinetic and electronic energies. A low irradiation temperature is important to suppress competitive thermal reactions. Hot atom reactions can also be used e.g. for the preparation of rare

chemical compounds, and in many cases they allow the production of starting material for a rapid labelling of radiopharmaceuticals.

In a similar way one can also investigate and optimize the production and high enrichment of radioisotopes. During the irradiation of an appropriate complex compound the hot isotopes produced are knocked out ot their chemical bonds and can be easily separated after the irradiation. Again unfavourable interfering reactions can be suppressed by a low temperature and a very low γ dose rate.

Activation analysis experiments must be performed at low temperature if the irradiated substances are sensitive to thermal or radiolytical decomposition, or if the radioisotopes produced are volatile.

2.3 Irradiation with Fast Neutrons

The high recoil energies transferred during the collisions of MeV neutrons with sample nuclei lead to the formation of displacement cascades. It is possible again to use bulk samples. The thermal flux ϕ_{th} should be sufficiently low to reduce unfavourable activation and heat production effects (see Chapter 3.2).

Most of the research applications of thermal neutron irradiation as considered in the previous chapters for metals and, to some lesser degree, for nonmetals will also be realized with fast neutrons under otherwise identical experimental conditions. This is on the one side for comparison purposes, since because of the cascade nature of defect production the degree of agglomeration of the Frenkel defects is relatively high already at liquid helium irradiation temperature, and on the other side due to the fact, that the defect production rate is much larger and hence saturation effects can be investigated now.

In addition there are experiments which shall be mainly performed with fast neutrons. A major field of interest will be the investigation of decomposition and segregation phenomena in concentrated alloys. Since up to now fundamental research has concentrated mainly on the irradiation of pure metals and dilute alloys, this will represent an important trend in the future. Small angle scattering measurements will certainly be useful.

The study of the radiation stability of insulators and technical superconductors is a more technological application. In future fusion reactor magnets these materials will be irradiated during regular operation in very much the same way as in the LTI facility, i.e. with fast neutrons at liquid helium temperature; however, the intensity in the fusion reactors will be smaller by some orders of magnitude so that the time scale will be speeded up in these experiments.

A somewhat different application is the immobilization of dislocations in cold worked material under external stress by irradiating the bulk samples with fast neutrons. In this way the dislocations get pinned by the large defect cascades whereas creep is suppressed by the low temperature. After irradiation and warm up the external stress can be relieved and the samples can be cut and thinned into the extremly thin foil samples which are necessary for observation in the transmission

electron microscope, where the unperturbed dislocation pattern can be investigated.

3. Design and Performance of the Facility

3.1 Design Features

The concept of a low-temperature irradiation (LTI) facility as presented in this chapter is based on that of the existing LTI facility at the Munich research reactor FRM which has been used now for over 20 years with outstanding success /4/.

The LTI facility at the SNQ would have its own liquid He refrigerator with a cooling capacity of about 400 W at 4.5K, which would be installed in the hall directly above the target. From there the whole LTI facility would be operated and the irradiation experiments would be performed. The He refrigerator would be connected, probably by flexible tubing, to two vertical irradiation tubes B and A for irradiations with either thermal (position I) or fast (position II) neutrons, respectively; see also fig. 1. On top of each irradiation tube a transfer or measuring cryostat could be plugged in and connected to the He system of the facility. In this way cold sample transfers into or out of the facility could be achieved, e.g. for external measurements, but in many cases the measurements could be performed in the measuring cryostat on the LTIF before or after the irradiation or, in simpler cases, even in situ during the irradiation.

A sample can have a maximum size of about 25 mm $\emptyset \cdot 100$ mm and will be fastened to the end of a metal capillary being about 10 m long and usually containing electrical measuring leads. By means of this capillary the sample can be moved through an irradiation tube down into the irradiation position, being always cooled in a direct flow of either liquid Helium (4.5K) or gaseous Helium having the desired temperature ($5 \div 450$K). Both irradiation tubes are about 8 m long and are vacuum shielded from cryogenic reasons and doubly bent (about 16° each) for radioprotection purposes. They are installed along with shielding material in vertical channels in the biological shield of the SNQ, so that some limited vertical movement remains possible.

As shown in fig. 1, the lower end of the irradiation tube A is located in a vertical channel through the D_2O moderator tank in the SNQ vacuum. It extends about 30 cm below the bottom of the D_2O tank and there is located by the side of the proton beam and in front of the target wheel. At this point a very good irradiation position II for fast neutrons is provided. However, it will be very much necessary that the high thermal flux $\emptyset_{th}$ in the bottom region of the tank can effectively be shielded with respect to position I and even then the large tube length in the tank being exposed to high values of $\emptyset_{th}$ remains a major problem (activation of the sample capillary, heat production). Mixed irradiation spectra can be realized by leaving the sample in some distance above position II whereas the irradiation tube A itself has to be lifted by about 30 cm only in case of a necessary dismounting of the target wheel.

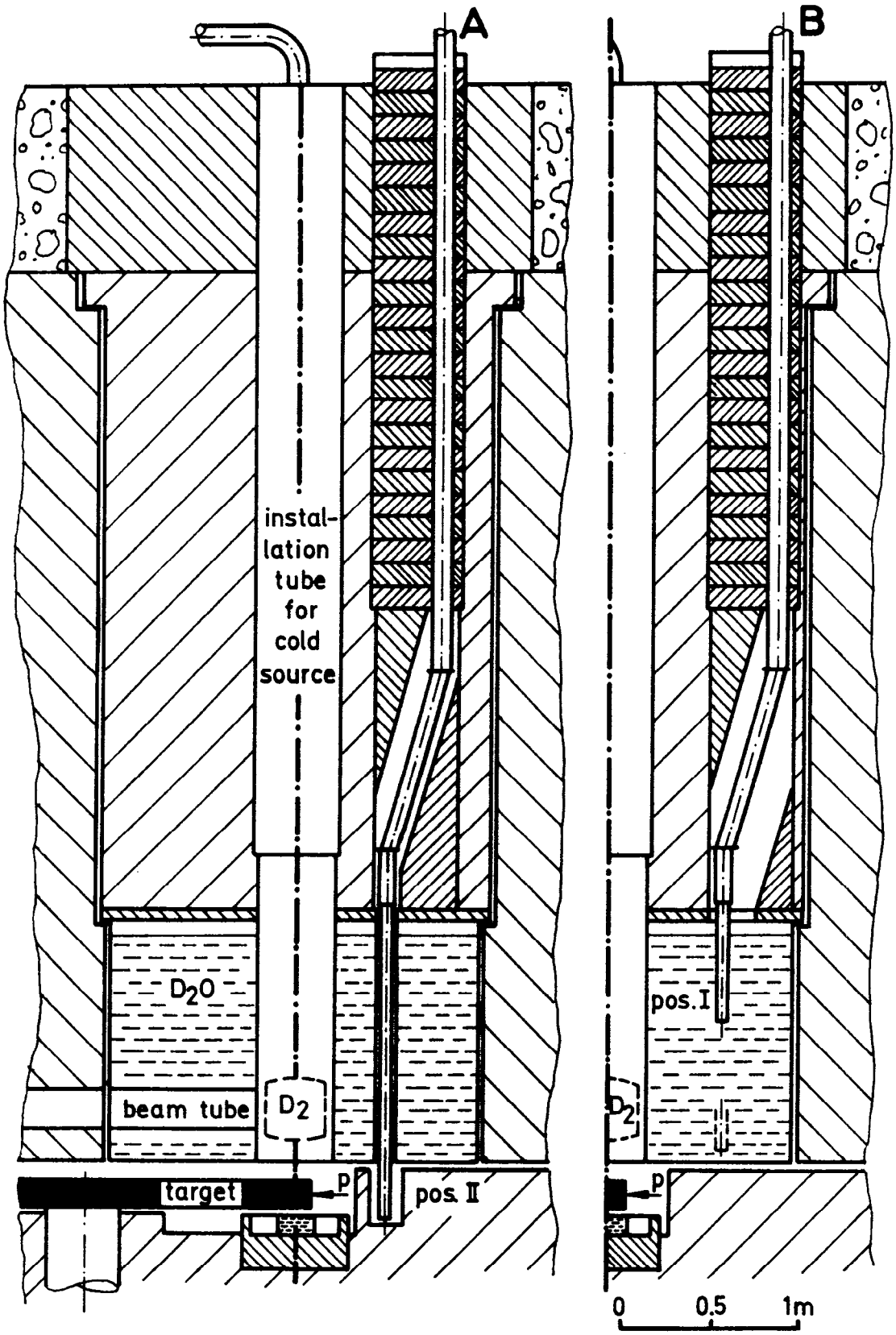

Fig. 1: Low temperature irradiation facility at the SNQ with vertical irradiation tubes A (fast neutrons position II) and B (thermal neutrons position I)

The irradiation tube B is immersed directly in the liquid D_2O of the moderator tank and can be vertically moved by about 100 cm. In the position I shown in Fig. 1 the lower tube end finds itself in a practically unperturbed D_2O environment as desired for irradiations in a very pure spectrum of thermal neutrons. Irradiations in a smaller thermal flux ϕ_{th} with correspondingly reduced background radiation are possible by further lifting the irradiation tube above position I, whereas mixed spectra can again be realized below position I.

3.2 Flux Values and Heat Production

For a LTI facility at an intense neutron source the problem is not only to realize very high thermal or fast neutron fluxes in the irradiation positions, but also (or even more) to achieve sufficiently pure neutron spectra with low background radiation and, for irradiations at the lowest temperatures, to keep the nuclear heat production small enough so that the samples can still be effectively cooled. Taking up this latter argument, we can obtain a conservative estimate by assuming a maximum stable heat flow density of 0.5 W/cm^2 from the sample surface to boiling liquid helium ($T \approx 4.5K$) /3,5/. It follows that for long cylindrical bulk samples of radius r the maximum tolerable rate of nuclear heat production $\dot{q}$ is of the order of 10 W/cm^3 for r = 1 mm and of 1 W/cm^3 for r = 1 cm. The sample surface temperature would be about 5.0K, then, and there would be an additional temperature gradient within the sample as determined by its bulk thermal conductivity. At values of $\dot{q}$ higher than just mentioned an instable transition from bubble to film evaporation sets in and so an irradiation of samples can only be guaranteed at temperatures well above that of liquid helium. Further significant problems arise from the SNQ time structure which is not considered here (compare Chapter 4) since in this chapter we assume a steady state situation /3/.

In the irradiation position I (fig. 1, tube B) the thermal neutron flux ϕ_{th} should be high and as clean as possible. A value of $\phi_{th} \approx 1 \cdot 10^{14}\ cm^{-2}\ s^{-1}$, which is very attractive for the irradiation of metals (Chapter 2.1), can be realized in the D_2O moderator tank in about 1 m distance from the target wheel /1/. Examples of the nuclear heating rate $\dot{q}_{th}$ corresponding to this value of ϕ_{th} are 0.48 W/cm^3 for an Al-sample and 10.6 W/cm^3 for Cu /3/. All other contributions to nuclear heating as produced by other types of radiation are comparatively small (see also below). For the fast neutron flux ϕ_f which counts all neutrons with energies above 0.1MeV a ratio of $\phi_{th}/\phi_f \gtrsim 5 \cdot 10^3$ can well be achieved, which is also very favourable since cascade effects in the samples are very effectively suppressed, then. The applications in the field of nuclear chemistry (Chapter 2.2) desire a value of the γ dose rate D_γ as low as about 10^6 rad/h. Although the direct γ radiation from the SNQ target is smaller by a factor of about 10 as compared to that from an equivalent reactor core, whence this direct contribution is $D_\gamma < 10^6$ rad/h, indeed, the secondary γ (and β) radiation from the structural material of the LTIF irradiation tube is proportional to ϕ_{th} and yields a contribution of about $D_\gamma \gtrsim 6 \cdot 10^6$ rad/h. In critical experiments the distance of the irradiation position from the target could be further increased in order to reduce ϕ_{th} and correspondingly $\dot{q}$ and

D_γ . The flux of secondary protons in position I is $\phi_p \lesssim 2 \cdot 10^9$ cm^{-2} s^{-1} which is negligible for both $\dot{q}$ and D_γ .

In the irradiation position II (fig. 1, tube A) the fast neutron flux ϕ_f should be high. A value of $\phi_f \approx 2 \cdot 10^{13}$ cm^{-2} s^{-1} is attractive again for the scientific applications mentioned in Chapter 2.3 and can be realized in about 40 cm horizontal distance from the target wheel /3/. This value of ϕ_f gives rise to a nuclear heating rate $\dot{q}_f$ of 0.12 W/cm^3 for Al and 0.14 W/cm^3 for Cu. The main heat input, however, is due to the thermal neutron flux ϕ_{th} which is expected to be pretty large due to the nearby D_2O tank and which has to be effectively shielded. Assuming $\phi_{th} \approx 5 \cdot 10^{13}$ cm^{-2} s^{-1} in position II we obtain values $\dot{q}_{th}$ of 0.24 W/cm^3 for Al and 5.3 W/cm^3 for Cu. The contribution $\dot{q}_\gamma$ of the direct γ radiation from the target is again relatively small as compared to a reactor and is estimated to be 0.15 W/cm^3 for Al and 0.4 W/cm^3 for Cu. Finally, the flux of secondary protons is effectively reduced by some additional lead shielding; assuming about 10 cm of Pb as in fig. 1 we estimate $\phi_p \approx 3 \cdot 10^{10}$ cm^{-2} s^{-1} and $\dot{q}_p \approx 0.07$ W/cm^3 for Al and 0.2 W/cm^3 for Cu. Summing up the individual contributions to $\dot{q}$ we obtain 0.6 W/cm^3 for Al and 6.1 W/cm^3 for Cu /3/.

4. Special Considerations

We will now mention some specific aspects /3/ which are important for a low-temperature irradiation (LTI) facility installed at a spallation neutron source, and in particular at the German SNQ /1/,in comparison with a similar LTI facility say at a new D_2O reflected middle flux reactor /2/.

The 100 s^{-1} time structure of the SNQ implies that all direct radiation from the target (unmoderated neutrons, secondary protons, γ ,...) will be emitted in pulses of 500 μs length and with a peak to average ratio of 20, whereas this ratio is still about 10 for the broadened pulse of thermal neutrons in the D_2O tank /1/. It follows that the time-averaged rates of nuclear heat production $\bar{q}$ as discussed in Chapter 3.2 (with $\dot{q} \equiv \bar{q}$) have to be multiplied by these factors to obtain the maximum rate of heat production $\hat{q}$ in the pulse. To illustrate the problem we will assume for a moment that we have a Cu sample with $\bar{q}$ = 5 W/cm^3 and that sample cooling during the pulse can be neglected compared to cooling between the pulses (or equivalent: δ-pulses); then the energy deposition of $\bar{q}/(100s^{-1})$ induces a jump of the sample temperature from 4.5K to about 12K during the pulse. Higher values of the sample specific heat or of the irradiation temperature or lower values of $\bar{q}$ reduce this effect. Although in the real case there will be some sample cooling also during the pulse, the possibility of instabilities in the heat transfer to the flowing liquid helium at too high values of $\hat{q}$ (which definitely exist in a static helium bath /5/) make the problem difficult and experimental investigations necessary. The problem does not exist at all on a reactor and also not on a quasi-continuous spallation neutron source (e.g. with a proton-cyclotron) since the time separation of the micropulses is much shorter than the time constants of the heat transfer problem /3/.

The presence of high-energy neutrons with energies between about 10MeV and that of the proton beam (1100MeV at the SNQ) is a unique feature of spallation neutron sources. For a Pb target they represent about 5% of all neutrons, which also means about 5% of the fast neutrons in irradiation position II. The heat which they produce in the samples is negligible. Their contribution to the production of Frenkel defects in metals (Chapter 2.3) is larger by about a factor of three than their contribution to the total fast neutron flux ϕ_f since the recoil energies are much higher. However, due to the formation of subcascades a relatively similar structure of the defects (agglomeration etc) is expected as in the case of reactor neutrons, although the amount of gas production from (n, p) and (n, α) reactions will be larger by one to three orders depending on the sample material.

The spectrum of high-energy secondary protons also extends up to the energy of 1100MeV of the SNQ primary proton beam. In irradiation position II the fast proton flux ϕ_p corresponds to about $1.5 \cdot 10^{-3}$ of the total flux ϕ_f of fast neutrons (Chapter 3.2). First, these protons undergo relatively low energy transfer Rutherford scattering processes and so produce Frenkel defects in metals at a rate which is typically some 10^{-3} of that of the fast neutrons. Second, due to the high proton energies nuclear processes are possible, too, which are roughly equivalent to those of the high-energy neutrons but which contribute only with a few percent of those because of the smaller flux. Third, the proton interaction with the electrons accounts for the main part of the proton heat production in metals, whereas in addition defects are produced in nonmetals.

The heavy biological shielding which is necessary at spallation neutron sources to attenuate the high-energy radiation components (see fig. 1) makes the design and operation of a LTI facility relatively inconvenient. This becomes obvious by comparison with a swimming-pool type research reactor as in ref. /2/ where the LTI facility could easily be moved around or taken out for repair and modification purposes. In particular, in the present design of the German SNQ /1/ the D_2O moderator tank is most favourable of course for providing an excellent irradiation position I for thermal neutrons, see fig. 1, but the problems of the D_2O tank for the fast neutron position II have already been mentioned in Chapter 3.

The main and essential advantage of a spallation neutron source as the SNQ for a LTI facility is its strongly reduced level of direct γ radiation. Although it is difficult to obtain reliable numbers for this behaviour, there seems to be general agreement that the direct γ radiation from a nonfissionable SNQ target is about one order of magnitude smaller than that from the core of an equivalent reactor. In contrast, it is obvious from Chapter 3.2 that in the case of an irradiation position II being realized at an equivalent reactor the direct γ dose rate would produce an essential and often the dominant contribution to the heat production in the samples.

Finally, also a general but perhaps practically not so important advantage is the SNQ potential of flux tailoring. We have emphasized in Chapter 3.2 how essential it is for a LTI facility to provide proper neutron spectra and fluxes as well as acceptable levels of background

radiation for the irradiation positions I and II. At a spallation neutron source such an optimization procedure can be generally performed more rigorously than at a reactor since no criticality criteria have to be satisfied.

Acknowledgement

We are greatful to H. Weber for considerable help with the heat production calculations.

References

/1/ Realisierungsstudie zur Spallationsneutronenquelle; AG Kernforschungsanlage Jülich und Kernforschungszentrum Karlsruhe, Teil I (1981)

/2/ Bericht des ad-hoc-Ausschusses "Mittelflußreaktor" des BMFT, Teil I "Strahlrohrreaktor" (1978); Anlagen 2.1-2.5

/3/ K. Böning, R. Golub, H. Weber; in Ref. /1/, Teil III (Experimentiereinrichtungen)

/4/ R. Doll, H. Meissner, N. Riehl, W. Schilling. F. Schmeissner; Z. für angewandte Physik 17, 321 (1964)

/5/ D.N. Lyon; Adv. Cryogenic Engin. 10, 371 (1965)

Jül-Conf-45

D4-1

I C A N S - V

MEETING OF THE INTERNATIONAL COLLABORATION ON

ADVANCED NEUTRON SOURCES

June 22-26, 1981

THE LIQUID METAL TARGET FOR THE GERMAN NEUTRON SOURCE (SNQ) - STATUS OF THE THEORETICAL AND EXPERIMENTAL INVESTIGATIONS OF THE TARGET THERMO- AND FLUIDDYNAMICS -

H. Hoffmann, M. Piesche*, E. Wild, K. Marten, E. Baumgärtner

Kernforschungszentrum Karlsruhe
Institut für Reaktorbauelemente
Postfach 3640, 7500 Karlsruhe 1
Federal Republic of Germany

* Technische Universität Karlsruhe
Institut für Strömungslehre und
Strömungsmaschinen
Postfach 26, 7500 Karlsruhe, FRG

ABSTRACT

The heat released in the target of the SNQ amounts to several MW and must be transfered continuously to a heat sink. Flowing liquid metals (PbBi, Pb) can be used as target material as well as for heat transport. The liquid metal target can be realized as standing vertical cylinder or as lying horizontal plate type design:

- A funnel shaped hollow jet coalesces to a free falling cylinder jet forming the target. At the location of coalescence the proton beam injects vertical the free liquid target surface.
- In a curved channel of rectangular cross section a plate type target with a nearly vertical free surface is formed by centrifugal forces acting on the flowing liquid metal. The proton beam hits horizontal the free liquid target surface.

Theoretical and experimental investigations of the global flow behavior, the velocity and temperature distributions show that a standing cylinder target can be realized. A stable free jet with only small local flow reductions near the point of coalescence could be demonstrated in H_2O- and PbBi-flow supporting a developed hollow jet theory. Two PbBi circuits are operable to study the handling of PbBi and for investigations of model and true scale test section geometries. For the horizontal curved rectangular channel target up to now only theoretical calculations have been performed. Results already proved heat removal being possible in temperature levels clearly lower than limiting values. Experiments were prepared to demonstrate the operability of this target design and to proof the flow behavior.

THE LIQUID METAL TARGET FOR THE GERMAN NEUTRON SOURCE (SNQ) - STATUS OF THE THEORETICAL AND EXPERIMENTAL INVESTIGATIONS OF THE TARGET THERMO- AND FLUIDDYNAMICS -

1. INTRODUCTION

A liquid metal target for the spallation neutron source (SNQ) is being investigated as an alternative to the rotating wheel /1/. The flowing liquid metal is so routed that optionally a vertical cylindrical or a horizontal plate shaped target geometry is obtained. The cylindrical target geometry calls for a vertical, the plate type geometry for a horizontal entrance of the proton beam. Whilst the cylindrical target version requires a specific station, the plate shaped target can be mounted on the support to be provided for the wheel target design. Both versions could then be installed and interchanged at option.

The objective of the investigations was to prove that a liquid metal target with free surface of the flowing target material (Pb, PbBi) seems to be feasible in the desired geometries. The target is to fulfil the following requirements:

- Stable flow passage with free surface, implying that at the point where the proton beam hits the target, a fixed window as a flow guidance can be dispensed with.
- Safe heat removal. At the point of maximum load the lowest possible temperature shall prevail. Any excessive temperatures occurring shall appear within the fluid and not at the confining walls so as to minimize the influence on material properties undergoing variations due to corrosion and neutrons.
- Confinement of the volatile radioactive spallation products. Since the release of radioactive products into the evacuated space of the accelerator becomes the smaller the lower the temperature of the releasing surface is, the free surface should have the inlet temperature.
- Control of the material problems. The main aspect to be considered is the change of material properties due to protons and neutrons. However, these problems must be solved for both the rotating wheel and the liquid metal target.

Two target versions complying with these requirements have been described in /2/. These are (Fig. 1):

- The cylindrical target: In a funnel-shaped nozzle the target material flows vertical downward as a liquid film. After leaving the nozzle the hollow jet coalesces to a free falling full cylindrical jet (point of coalescence) mainly by the effect of the forces of gravitation and surface tension. The proton beam hits the target surface vertically at the point of coalescence.
- The plate target: In a curved rectangular channel the liquid target material is pressed agains the outer curvature of the bended channel by the effect of centrifugal forces. At proper design of the channel the

fluid separates from the inner bend of the channel forming a free surface for the horizontally injected proton beam.

Both versions are suited for removing very high thermal powers. Compared with the operational data indicated in /2/ we have reduced:

- the thermal power to be removed from 4.2 to 2.8 MW in order to have values comparable with that of the rotating wheel /1/;
- the overall temperature level by 125 °C for the PbBi target, allowing a reduction of the inlet temperature from the previous value of 325 °C to 200 °C, implying that the release of radioactive materials for the proposed vacuum of 10^{-3} torr could be reduced by the factor 10^3 just above the liquid metal surface /3/.

The following operating parameters form the basis of the design:

- proton beam intensity	(E)	1100	MeV
current	(I)	5	mA
power	(Q)	2.8	MW
penetration	(R)	60	cm
- mean target diameter		10	cm
- PbBi temperature, target entrance		200	°C
- PbBi velocity (averaged)		3	m/s
- vacuum above free surface		10^{-3}	torr

With these data the flow passage through the target and the heat removal were investigated. The global values so calculated have also been entered in Fig. 1. The following statements relate to the determination of local values and shall prove that flow passage through the target does not bring about local temperatures which could adversely affect the safe removal of the heat.

2. THERMO- AND FLUIDDYNAMIC STUDIES OF THE VERTICAL CYLINDRICAL TARGET

2.1 Thermodynamic Computation

Consideration of the local temperature conditions in the target requires knowledge of the heat source distribution within the target. For the axial and radial power distributions the relationships given in /1/ are used. For 1.1 GeV proton intensity and 60 cm depth of penetration we obtain:

axial power distribution: $H(z) = 214 \cdot \exp(-\Sigma \cdot z)$ kW/cm
radial power distribution: $\emptyset(r,z) = (H(z)/\pi \cdot s^2) \cdot \exp(-r/s)^2$ kW/cm^3

where Σ = macroscopic inelastic cross section
z = distance from beginning of target
r = radius of proton beam (assumed value $r = 5$ cm)
s = variance ($s = r/2$)

If one uses the assumption made above on the flow condition and power distribution, the temperatures of the target in the axial and radial directions can be assessed for the following conditions:

- slug flow,
- only thermal conduction taken into account,
- constant material properties.

The results are indicated only for steady-state power operation. Pulsed operation averaged over the time produces the same heating up of the target material. Since the residence time of a fluid particle in the target zone amounts to about 200 ms, heating up takes place within 20 time intervals with a pulse repetition time of 10 ms. Related to the mean temperature increase of the target material of 84 °C, the mean temperature rise produced by one pulse thus becomes about 4 °C/pulse. If one calculates this heating up for the maximum calculated temperature rises in the center of the target, extreme values of about 15 °C/pulse are obtained. This is the maximum conceivable temperature variation of the axial temperature rise and it will be neglected here.

Regarding the target geometry the following two cases were distinguished:

- The simple version of a mere cylinder target. The funnel shaped entrance zone of the hollow jet target is neglected.
- The hollow jet target with the funnel shaped entrance geometry is taken into account.

The calculations were made with the HEATING 4 computer code /4/. The temperature distribution evaluated for mere cylinder geometry in the axial and radial directions and target powers of 4.2 MW and 2.8 MW has been represented in Fig. 2. The upper part shows the development of the maximum temperature along the target axis, the lower part the temperature in the hottest cross section for z = 60 cm. The following can be noticed:

- The temperature rises against the inlet temperature increase with growing distance from the target surface, corresponding to the axial heat release. The maximum temperature occurring on the target axis is about 635 °C for Q = 4.2 MW and not more than 480 °C for Q = 2.8 MW.
- The target periphery roughly stays at the level of the inlet temperature. Within the target length considered, it is therefore of no importance for heat transport. The upper diagram also shows data on the saturation pressures, which are identical with the admissible vacuum in case the evaporation of target material is to be avoided.
- If one compares the temperatures calculated for the target surface with the related saturation pressures, it can be recognized that here a much higher vaccum is admissible than the supposed vacuum of 10^{-3} torr.
- If one considers the maximum temperature occurring in the center of flow as the saturation value and compares it with the related saturation pressure, one finds that for a mere cylindrical target a vacuum of 10^{-3} torr is feasible even at the end of the target.

Some of the target material leaving the nozzle is hit by the proton beam even before it develops into the full jet. This means that heat is released in the entrance zone. The calculations performed show also for this example that a vacuum of 10^{-3}mm Hg is feasible. From the computations based on these very conservative assumptions, the evaporation of target material on the target surface can be ruled out. At the end of the target the saturation temperature corresponding to the 10^{-3} torr vacuum is attained by computation only for Q = 4.2 MW on the current filament running along the target axis. Thus, local boiling might occur as a mere hypothesis. Nevertheless, evaporation can be ruled out in practical application by:

- increase of the target flow rate,
- surface tension effects,

- slight flow congestion in the lower target zone (a suitable device has been tested),
- a different radial power distribution of the incoming proton beam.

2.2 Fluiddynamic Design Calculations

2.2.1 Theory of Flow Passage Through the Target /5,6/

The determination of the location where the hollow jet coalesces in a full, free falling jet is of main interest. The calculation model is devided in two parts. In the first part the flow in the nozzle is presumed to be friction dependent. In the calculation model of the second part, which describes the flow outside of the nozzle, the motion is assumed to be frictionless. Both models are coupled by the corresponding initial and boundary conditions.

The mathematical investigations base on the model shown in Fig. 3. The liquid flows under the angle α out of the ring gap with the width b_o and moves along the nozzle wall under the influence of the gravitation g. The fluid leaves the nozzle with the angle β; r_o is the inner radius at the inlet of the nozzle, r is the variable radius which has to be determined, c_r and c_x are the velocity components, b is the variable width of the liquid film, p signifies the pressure. It was the aim that the form of the nozzle should be determined in such a way that the contour would reflect the natural motion of the flow. That is, the form of the nozzle is not presupposed, but the contour and the hollow jet result from the influences of the pressures forces, the surface tension, the viscosity, the gravity and of the inertial forces.

The solution of this problem is given by the Navier-Stokes-Equations. In addition, the following assumptions are made:

- the fluid has Newtonian properties,
- stationary flow field,
- the material parameters, as the density g, the dynamic viscosity μ and the surface tension σ are constant,
- the radius of the nozzle inlet r_o is much greater than the width b_o of the gap.

With the assumption that the radius r_o is much greater than the width of the gap b_o, we reduce the problem to a boundary layer problem.

Usually, the problem is treated with dimensionless variables. The following combinations were chosen:

- radius ratio $R = r/r_o$: $R_1 = r/r_1$
- width of the liquid film $B = b/b_o$
- axial and radial velocity $C_x = c_x/c_{x_o}$; $C_r = c_r/c_{x_o}$
- axial coordinate $X = x/r_o$: $X_1 = x_1/r_1$
- the coordinate in normal direction $\eta = z/b$

After the introduction of these dimensionless parameters, the Navier-Stokes-Equations have the following integral form:

Radial Equation of motion

$$\frac{d}{dx}\left|\frac{dR}{dX}\int_o^1 C_x d\eta\right| + \frac{1}{We_0} = 0$$

Axial equation of motion:

$$\frac{d}{dX}\int_0^1 B\, C_x \left|C_x(\eta=1,X) - C_x\right| d\eta - \frac{dC_x}{dX}(\eta=1,X)\, B \int_0^1 C_x\, d\eta = \frac{r_o/b_o}{B}\cdot T - \frac{B}{Fr_o^2}$$

The equation of the conservation of mass is written as

$$RB \int_0^1 C_x\, d\eta = 1$$

So we are able to determine the three unknown variables: The radius ratio, the axial velocity and the width of the liquid film. Herein is T the wall shear stress, which is described by the law of Stokes for the laminar flow case:

$$T_\ell = \frac{1}{Re_0}\left.\frac{\partial C_x}{\partial \eta}\right|_{\eta=0}$$

In the turbulent case, T is described by the empirical friction law of Blasius:

$$T_t = \frac{0.03955}{(B\, Re_0)^{1/4}}\left(\int_0^1 C_x\, d\eta\right)^{7/4}$$

The dimensionless investigation produces a universal graph of the symmetrical nozzle wall, which can be described by the following characteristical parameters:

Geometric ratio r_o/b_o

Reynolds number $Re_o = \rho c_{x_o} b_o/\mu$

Weber number $We_o = \rho c_{x_o}^2 b_o/\sigma$

Froude number $Fr_o = \sqrt{c_{x_o}^2/r_o g}$

They represent the ratio of inertial forces to friction forces, of inertial forces to surface tension and of inertial forces to gravitation forces.

The problem to describe the flow outside of the nozzle is solved by the specification of a balance of forces for a mass element. The balance yields the equations for the motion in radial as well as in axial direction and for the conservation of mass.

Differential equation of motion in radial direction:

$$\frac{d^2r}{dt^2} = \frac{p_i - p_a}{\rho b} - 2\frac{\sigma}{\rho b r}$$

in axial direction:

$$\frac{d^2x_1}{dt^2} = g\ .$$

conservation of mass:

$$c_{x1} r_1 b_1 = c_x r b\ .$$

After the substitution of the time variable t by the parameter for the location x, we receive the differential equation for the form of the hollow jet:

$$\frac{d^2R_1}{dX_1^2} + \left(1+\frac{2}{Fr_1^2}X_1\right)^{-1}\frac{1}{Fr_1^2}\frac{dR_1}{dX_1} - \left(1+\frac{2}{Fr_1^2}X_1\right)^{-1/2}\left|Eu_1\frac{r_1}{b_1}R_1 - \frac{2}{We_1}\right| = 0\ .$$

Again we have the characteristic parameters refering to the coordinates: The Froude number and the Weber number. They are completed by the Euler number which is the ratio of pressure forces and inertial forces.

Euler number $Eu_1 = (p_i - p_a)/\rho c_{x_1}^2$

modified Froude number $Fr_1 = \sqrt{c_{x_1}^2/r_i g}$

modified Weber number $We_1 = \rho c_{x1}^2 \, b_1/\sigma$

Some theoretical results are shown in Fig. 4. In the graphs the mean contour of the jet R is plotted against the axial length X as function of the Reynolds number and the Euler number. We see that the contour of the nozzle is widened if the viscosity is reduced. For a reduction of the Froude number, for example by minimizing the flow rate, we also have a widening effect. If the surface tension increases the Weber number will decrease and the location of the contraction will move in upstream direction. For a given nozzle contour the location of coalescence moves also in upstream direction when the Euler number decreases.

2.2.2 Experimental Investigations into the Flow Behavior of the Hollow Jet Target

The theoretical investigations into hollow jet flow allow to evaluate the contour of the hollow jet and hence the size of the nozzle; besides, the axial location of coalescence can be determined where the hollow jet forms the full jet for given operating conditions. The theory does not provide any statement about the flow events occurring in detail at the location of coalescence, however, it assumes a stable flow in the direction of the target axis.

For this reason, the aims of the experimental investigations are:

- Validation of the theory concerning hollow jet flow. For technical application, the following items offer special interest:
  . the axial position of the location of coalescence
  . the stabilization of the full jet, and
  . the variations of the flow behavior in case of deviations from the point of operation.
- Investigations of the flow events around the location of coalescence. To support the thermodynamic calculations, the following items are of interest:
  . proof that no dead water zones will be formed
  . size of the local axial velocities, and
  . the turbulent fluctuations of velocity.

Water Tests on Hollow Jet Contour

The investigations were first made on 1 : 2.5 model scale with the H_2O test facility. The nozzle under investigation was connected to a cylinder shaped annular gap. The liquid surface within the nozzle and outside the full jet is exposed to atmospheric pressure, which means that the Euler number is Eu = 0. The nozzle in the H_2O-experiments are made from plexiglass so that the flow within the nozzle can be observed and the location of coalescence downstream of the end of the nozzle can be well determined.

The test facility with the true-scale nozzle was similar in design. The test rig and a test section of these experiments are represented in Fig. 5.

An optical impression of the flow phenomena occurring around the location of coalescence of the hollow jet into the full jet (x/r_o) is given by Fig. 6. With the nozzle geometry remaining unchanged (r_o/b_o; α), the flow (Froude number) was subject to variations. These photographic pictures show that with the Froude number getting greater the location of coalescence gets more and more approached to the end of the nozzle. The quantitative results have been entered in the diagram as $Fr = f(x/r_o)$ and compared with the theoretical values.

Summarizing, the following statements can be made on the basis of the previous H_2O experiments:

- The location of coalescence determined in the experiment are well consistent with the theoretical predictions in both test geometries.
- With the variation of the Froude number the location of coalescence is displaced. However, a variation of flow assumed for target operation of ±5 % of the nominal flow has practically no influence on the location of coalescence.
- Obstructions expressly introduced into the flow downstream of the end of the nozzle have no impact on the preceeding flow. By contrast, obstructions provided in the flow upstream of the nozzle exert an influence on the stability and conditions of the effluent portion of the full jet. Therefore, the development of the upstream flow and the 180°-flow reversal must be further studied with a view to their feasibility in order to optimize the dimensions of the target head.

Measurement of the Velocity Distribution and of the Turbulent Flow Fluctuations in the Zone of Full Jet Development

In the zone of full jet development flow conditions appear which cannot be recorded theoretically. Since at this point maximum heat releases take place at the same time, the flow passage must be studied in more detail in order to make a realistic thermodynamic design.

- Knowledge of the velocity distributions allow to draw conclusions regarding possible wakes or dead water zones, and above all to provide evidence for the perfect flow passage through this target area.
- Knowledge of the turbulent velocity fluctuations allow to derive indications of the degree of coolant cross mixing and hence of the turbulent heat exchange. These effects decisively contribute to reducing local temperature maxima and, in general terms, to the equalization of temperatures.

A picture of the actual flow conditions in H_2O flow was obtained by the following methods:

- First color tracers were introduced into the flow and their diffusion and transport followed up by a film camera. Then first measurements of the mean velocity distributions were made using Pitot probes. The measured velocity distributions are representative only at considerable distance from the location of full jet development.

On account of high flow turbulences consolidated statements are possible only by use of the Laser-Doppler Anemometry (LDA) allowing contactless and hence non-intrusive measurement of the longitudinal and transversal velocities and of the turbulent exchange variables /6/. Fig. 7 gives an impression of the whole facility. An important result from the comprehensive experiments is shown in Fig. 8. Measured axial velocities are represented as a function of the radial probe position for different distances z from the location of coalescence. It can be noted that for z = 4 mm a local flow reduction of about 20 - 30 % of the mean velocity can be expected on the flow axis and that this will be balanced out after about 15 mm of flow path. Consequently, the previous investigations have shown:

- At the point of coalescence a finite velocity component prevails which is not indicative of any reflows and dead water zones.

- The measurements yield intensive turbulent velocity fluctuations indicative of a high coolant cross mixing.

2.2.3 Investigations into Liquid Metal Flow

To guarantee the transferability of the results from H_2O experiments to the original PbBi fluid experiments are being performed in liquid metal flow on 1:2.5 and 1:1 target geometries. The transferability is examined here because the surface tension of PbBi is greater by about 40 times and the density by about 10 times than the values for water and since in PbBi tests at high vacuum can be performed. The test facilities used in these investigations must be so designed as to meet the requirements of a PbBi flow /7, 8/. Measurement of the liquid metal flow is possible via transit-time and orifice measurements. The outer contour of the target can be recorded via observation windows (saphire windows) and the inner contour of the flow by means of electrical scanning devices. Two PbBi-circuits will be provided for the investigations, both of them already operating. They consist of the storage tanks, the pumps, the test sections and the connecting pipe work with heating and insulation. Typical instrumentation for liquid metal systems is being installed and the loops are characterized as follows:

	PbBi Circuit I /7/	PbBi Circuit II /8/
Type of pump	Centrifugal	Centrifugal
- delivery $\lvert m^3/h \rvert$	5	100
- delivery head $\lvert m \rvert$	3	5
Scale of test section	1:2.5	1:1
Nominal pipe width $\lvert mm \rvert$	25	100

Circuit I (Fig. 9) mainly served to study the handling of PbBi and the eligible instrumentation; it was modified for accommodation of the test sections, scale 1:2.5. Circuit II (Fig. 11) serves to investigate the true-scale test section and, more generally, as a demonstration facility for operation with PbBi. So far two test sections have been designed and fabricated for use in PbBi. The test section I, scale 1:2.5, was already thoroughly examined in water flow and is presently being used in PbBi flow. The test section II, true scale, was likewise investigated in H_2O flow and is presently being adapted to operation in PbBi flow. The investigations have so far produced the following result:

- A stable hollow jet can be generated; this is shown by the photograph of the outside structure of the PbBi jet (Fig. 10).

- The location of the coalescence slightly differs from the results of H_2O experiments with the same test section for the Froude numbers under consideration, which can be explained by the higher Reynolds number and Weber number applicable here.

These first measurements in PbBi flow are supplemented by further parameter studies. They are primarily performed in the PbBi circuit II which allows flow passage through the target at the nominal flow aimed as for the spallation neutron source.

3. ALTERNATIVE CONCEPT OF A HORIZONTAL LIQUID METAL TARGET

3.1 Basic Concept and Problems Involved

The liquid metal concept with flowing PbBi eutectic or pure Pb discussed for the target station of the SNQ allows in principle different target geometries and hence the adaptation to the requirements on geometry resulting from neutron physics. The thermo- and fluiddynamic investigations described before primarily related to a target geometry shaped as a vertical upright cylinder target and the feasibility of the latter as a hollow jet target. However, the configuration of the target block linked to it gives rise to some drawbacks as regards the users requests. Therefore, the possibility was examined of realizing a liquid-metal target having the geometry of a wheel /2, 9/.

The fundamental concepts and the major aspects for design are:

- A target zone with flow passage is to be generated which is suited for horizontal proton injection. The target shall have a thickness of 10 cm normal to the proton beam and a depth of 60 cm along the proton beam axis. The free liquid surface is realized technically by a flow in a rectangular channel curved so as to form nearly a semicircle. The curvature generates centrifugal forces which detach the flow from the inner channel wall and press it to the outer channel walls. Thus, on the inner curved channel wall downstream of the point of detachment a proton beam inlet hole may be provided.

- Since no "window" shall be placed between the target and the proton beam, a vacuum exists above the target surface. It is assumed to be 10^{-3} torr in this case. Consequently, the transport energy can be obtained solely from the kinetic energy of the fluid itself. This leads to a continuous reduction of the flow velocity in the direction of flow. For reasons of continuity the flow channel downstream of proton beam inlet hole must be always widened

(diffuser) until the fluid flows into a storage tank and is returned from there to the side of inflow by means of a pump via a heat exchanger.

- The saturation temperature to be attributable to the pressure of 10^{-3} torr constitutes the maximum limit to be observed of local heating of the target material on the target surface.

- It seems necessary to close the proton inlet aperture for startup and shutdown operation in order to avoid the outflow of target material. This must be investigated by experiments and an engineered solution must be found, if necessary.

From these considerations the tasks are derived for the basic investigations which must precede thorough design activities for the liquid-metal target as a horizontal curved rectangular flow:

- calculation of the temperature distributions in the target.
- determination of the channel geometry required for suitable flow guidance
- determination of channel widening to ensure the axial fluid transport

Questions of circuit operation, cleaning and safety of the facility resemble those of the vertical cylindrical target.

3.2 Thermodynamic Computation

The investigation of the local coolant temperatures serves to prove that evaporation under vacuum of the target material on the target surface can be excluded. The computation models adopted include simplifications (slug flow, no radial heat exchange), so that the results determined must be termed "conservative". The minimum pressure and at the same time the maximum load occur on the target surface. Therefore, the maximum coolant temperature is investigated on the current filament directly on the target surface transversal to the beam axis (z = 0). The calculated maximum local temperatures have been represented as a function of the flow velocity in Fig. 13. At the same time we have entered the maximum coolant temperatures obtained for two possible given inlet temperatures of 200 °C (PbBi as the target material) and 400 °C (Pb as the target material), taking into account the calculated temperature rises, as well as the related saturation pressures. The 10^{-3} torr saturation pressure (corresponding to a saturation temperature of approx. 620 °C) marks the possible range of operation for the given inlet temperatures. Thus, a target of 10 cm diameter yields
- for the inlet temperature of 200 °C (PbBi) a flow rate of about 0.5 m/s and
- for the inlet temperature of 400 °C (Pb) a flow rate of about 1.0 m/s.

These velocities are exceeded in practical application. This means that the calculated admissible heating up levels can be observed without difficulties despite the conservative assumption.

These statements are valid for steady-state power operation and undergo but slight variations in pulsed operation. Each fluid particle is hit by a pulse about three times on its way through the target zone. Those particles which at the moment of proton pulse generation are present in the center of

the target surface are heated up most. These considerations provide as the results a maximum temperature increase and decrease, respectively, in pulsed operation, which on an average amounts to about $<\pm 10\ ^{o}C$. Consequently, pulsed operation does not affect the fundamental statements made about heat removal. The calculations show in addition that the fluid guiding channel walls within the target zone remain on entrance temperature.

3.3 Fluiddynamic Design Calculations

3.3.1 The Flow Contour on the Free Target Surface

It is purpose of these investigations to determine the flow contour as a function of the flow velocities for given channel curvatures. The channel curvatures are varied within a range delimited by a maximum outer diameter of 2 m and a minimum inner diameter of 0.2 m. The contour of the target surface was roughly estimated. The fluid is exposed to centrifugal and gravitational forces. The free surface of the fluid is obtained normal to the resultant of the attacking forces.

The surface contour is expressed here as the angel which gives the deviation of the contour from the proton beam axis. This computation model applies for a fluid velocity increasing proportional to the radius of curvature. Since this is not in conformity with reality, the radius of curvature for calculation of the surface contour is taken as the distance a between the center of curvature and the center of the fluid filled channel width (R). The results of this computation are shown in Fig. 12. The possible working range is characterized by the following variables:

- maximum external and minimum internal radius of curvature
- angle of the flow contour $\gamma > 50$ deg.
- maximum flow rate 7 m/s.

It appears that these requirements result in minimum velocities of about 2.0 m/s for the smallest inner diameter and 3.0 m/s for the greatest outer diameter of the channel.

3.3.2 Channel Widening for Axial Fluid Transport

The dependence of the axial reduction of velocity on the hydraulic data of the channel geometry was calculated from the equilibrium of frictional and inertial forces. After 2 m of flow path a reduction of velocity and, accordingly, an increase in the flow area of only about 10 % of the initial values is observed. Consequently, a very slim diffuser with little widening can be used which, practically, does not affect the horizontal extension of the target.

3.3.3 Investigations into the Flow Geometry

The previous investigations into the heat removal have shown that the admissible limit temperatures are observed. The considerations were based on simplified models and methods which have to be supported by experiments before a technically optimum solution can be realized. The said experiments primarily relate to the determination of the flow contour, which is not

possible theoretically for the time being.

For the purpose, the test section shown in Fig. 14 has been conceived and built. It is a 1:4 scale model and allows visual observation of the flow. By use of variable internals the question can be studied how to shape the point of detachment and an answer can be given as regards the most significant fluiddynamic variables exerting an influence on the realization of the free surface. The following parameters are being varied in these tests:

- the shape of the flow channel by variation of the outer and inner boundaries
- the location and geometry of the point of detachment by various internals provided at the inner curved channel wall.

In the experiments also variables of operation are investigated in addition to the fluiddynamic ones. They include above all the startup characteristic and the answer to the question whether and, if applicable, where a startup valve must be provided in the proton beam channel.

4. SUMMARY AND CONCLUSIONS

To ensure the safe removal of heat released in the target of a high-power spallation neutron source use of a liquid continuously circulated heavy metal would be eligible. The target may be designed on the principle of the hollow jet flow standing vertical as a cylindrical target with a free surface or lying horizontally as a curved rectangular channel to form a plate shaped target. Accordingly, the proton beam can be supplied vertically or horizontally. The studies have concentrated on global heat transport from the target zone and on the local temperature distributions and the local flow phenomena in the target zone.

The previous thermo- and fluiddynamic investigations into the hollow jet target have furnished the following results:

- By theoretical work a method has been made available which allows to calculate the hollow jet flow, especially the location of coalescense of the hollow jet into the full jet. Use of fluiddynamic characteristics enabled us to represent flow phenomena in a more general way. The theoretical predictions of the flow behavior were validated experimentally by water tests carried out on model and original geometries; they seem to be confirmed by first experiments also for liquid metal flows.

- In other experiments the flow phenomena were investigated at the location of coalescense which cannot be treated by the hollow jet theory, and evidence was provided that no dead water zones are formed and hence fluid evaporation on the surface can be ruled out. The measurements of turbulent variations of velocity indicate a very strong coolant cross mixing which contributes decisively to the radial equalization of temperatures and reduces local temperatures peaks.

- On the basis of knowledge so far gathered, we can make the following general statements:
  . The heat can be safely removed from the target zone.
  . Stable flow passage through the target is feasible.
  . The heat transport circuit and its components can be realized.

These global statements guarantee the basic feasibility of a liquid metal target. Further studies are being concentrated on the target geometries in PbBi flow so as to be able to include as well the range of high Weber and Reynolds numbers and to provide support for the comparison of the results with the theoretical predictions.

The preliminary thermo- and fluiddynamic computations relating to the realization of a liquid-metal target with the geometry of a horizontal, curved rectangular channel show:

- The flow velocity in a target formed by a rectangular channel should amount to about $\geq$2.0 m/s so as to enable the development of a sufficiently steep flow surface around the window.

- At this velocity safe heat removal without local superheat of the target material is guaranteed.

- The transport back of the liquid metal calls for a diffuser with about 10 % widening.

- From thermo- and fluiddynamics no indications have been derived which would raise doubts concerning the feasibility of the target geometry discussed in this paper.

However, more in-depth theoretical, experimental and design work will be required to optimize the system in technical terms; this concerns above all the following items:

- Geometry of the flow guidance within the zone of flow detachment upstream of the window.

- Flow phenomena and surface contour downstream of the target zone.

- Overall configuration of the design.

REFERENCES:

/1/ Bauer, G.S.; Sebening, H.; Vetter, J.E.; Willax, H.;
"Realisierungsstudie zur Spallations-Neutronenquelle, Teil I"
KfK 3175; Jül-Spez-113; (1981)

/2/ Hoffmann, H.J.; Huber, P.E.; Piesche, H.;
"Liquid Metal Target Development for the German Neutron Source (SNQ)"
ICANS-IV-Meeting, Oct. 1980, KENS report II, march 1981, KEK, Tsukuba

/3/ Hellwig, L.;
"Aktivitäten des PbBi-Targets: Auftreten und Verhalten"
in: Realisierungsstudie zur Spallations-Neutronenquelle, Teil II,
(1981), unpublished

/4/ Günther, C.; Hoffmann, H.;
"Stand der Temperaturfeldrechnungen zur Auslegung eines Flüssigmetalltargets mit freier Oberfläche für eine Spallations-Neutronenquelle"
in: Realisierungsstudie zur Spallations-Neutronenquelle, Teil III,
Annex E (1981), unpublished

/5/ Felsch, K.O.; Piesche, M.; Veith, W.;
"Theoretische Untersuchung der reibungsbehafteten Strömung in rotationssymmetrischen Düsen zur Auslegung eines Flüssigmetalltargets für eine Spallationsneutronenquelle";
KfK-3158, Kernforschungszentrum Karlsruhe (1981)

/6/ Piesche, M.; Veith, W.; Felsch, K.O; Hoffmann, H.;
"Fluiddynamische Untersuchungen zur Auslegung eines Flüssigmetalltargets für eine Spallationsneutronenquelle";
KfK-3171, Kernforschungszentrum Karlsruhe (1981)

/7/ Wild, E., Mack, K.J.; Gegenheimer, M.;
"Blei-Wismut-Kreislauf I-Beschreibung der Versuchseinrichtung";
in: Realisierungsstudie zur Spallations-Neutronenquelle, Teil III, Annex E. (1981), unpublished

/8/ Wild, E.; Hitzig, K.; Mack, K.J.; Gegenheimer, M.;
Blei-Wismut-Kreislauf II - Beschreibung der Versuchseinrichtung
in: Realisierungsstudie zur Spallations-Neutronenquelle, Teil III, Annex E, (1981) unpublished

/9/ Huber, P.E.; Hoffmann, H.J.;
Thermo- und fluiddynamische Untersuchungen am horizontal gekrümmten Rechteckkanal-Target;
in: Realisierungsstudie zur Spallations-Neutronenquelle, Teil III, Annex E, (1981), unpublished

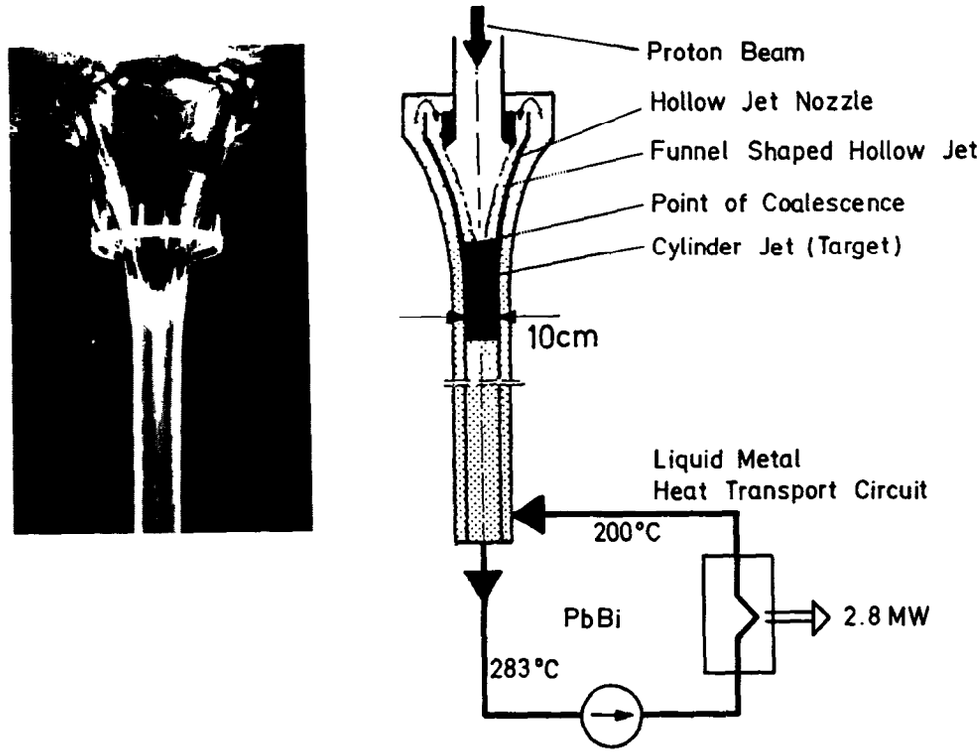

Hollow Jet Target - Cylinder Type

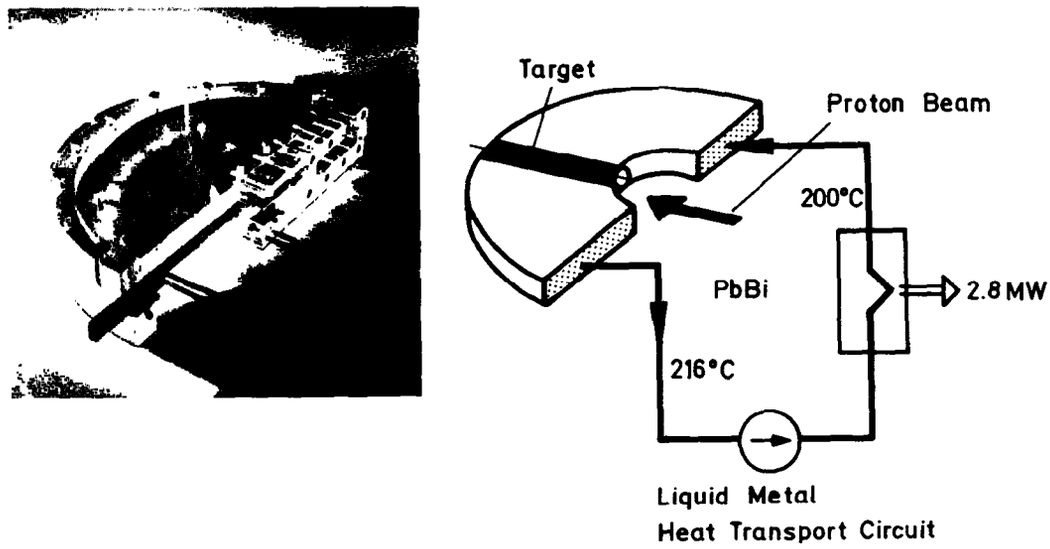

Flat Channel Target - Disc Type

Fig. 1 Liquid Metal Targets (LMT)

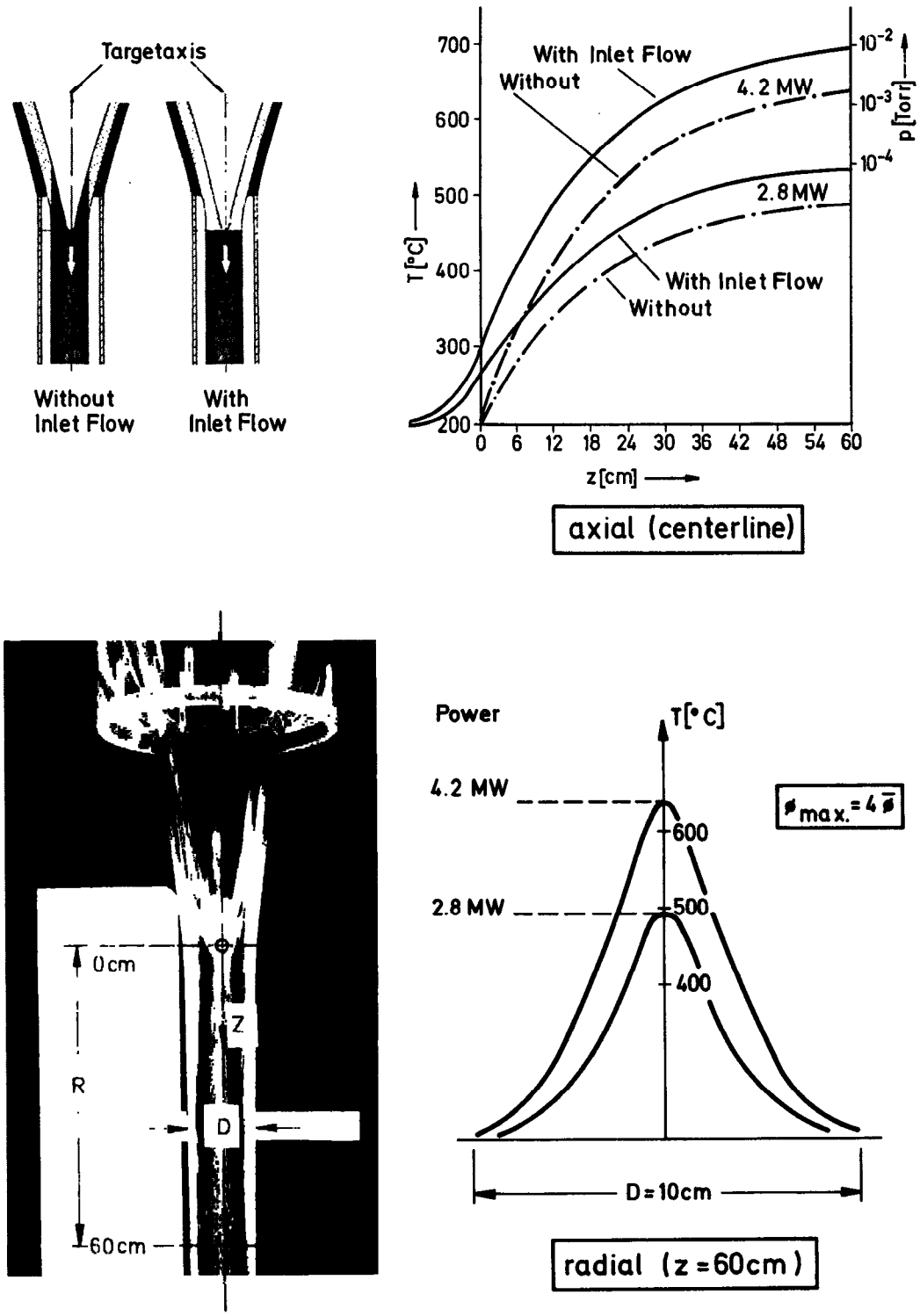

Fig. 2 Temperature Distribution in LMT - Cylinder Type

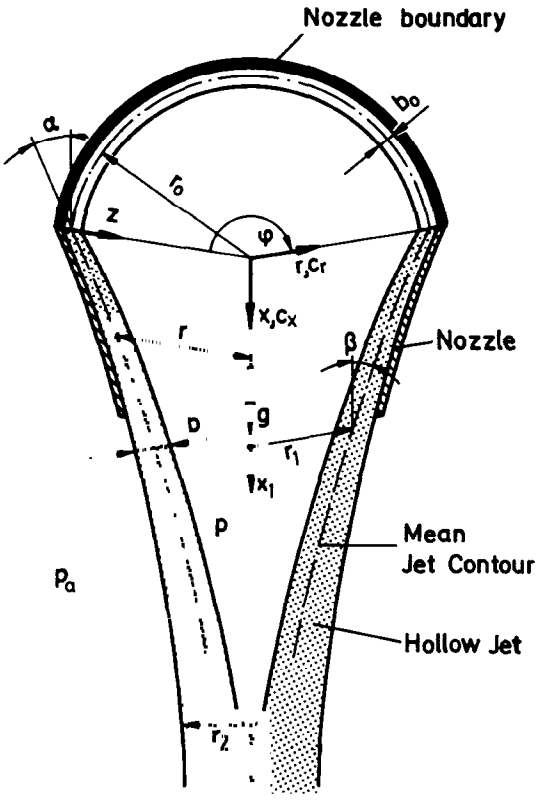

Fig. 3 Mathematical Model

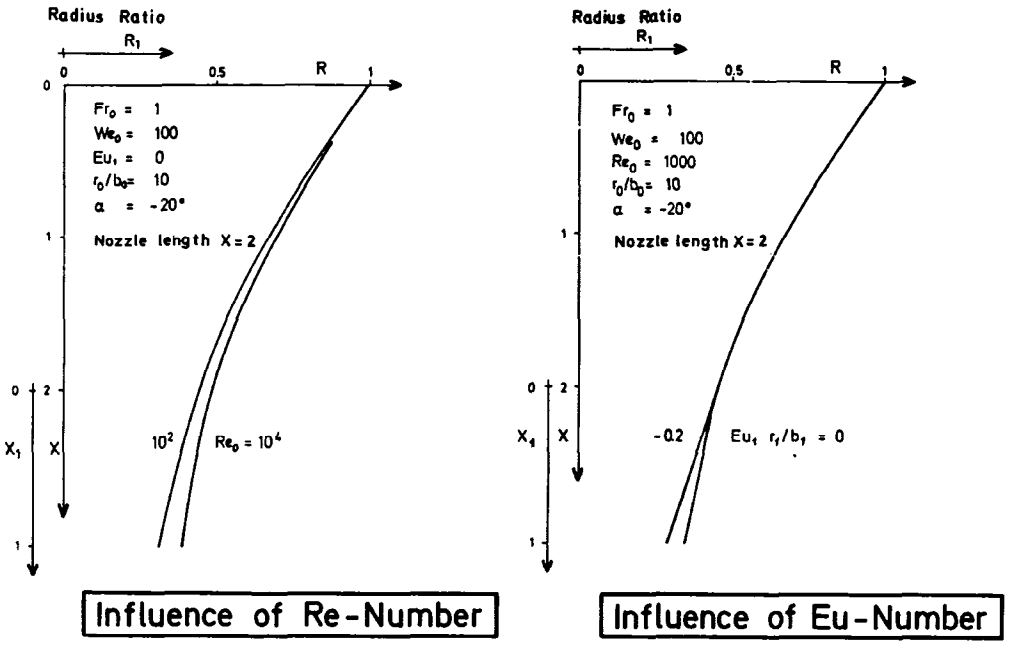

Fig. 4 Calculated Mean Nozzle Contours

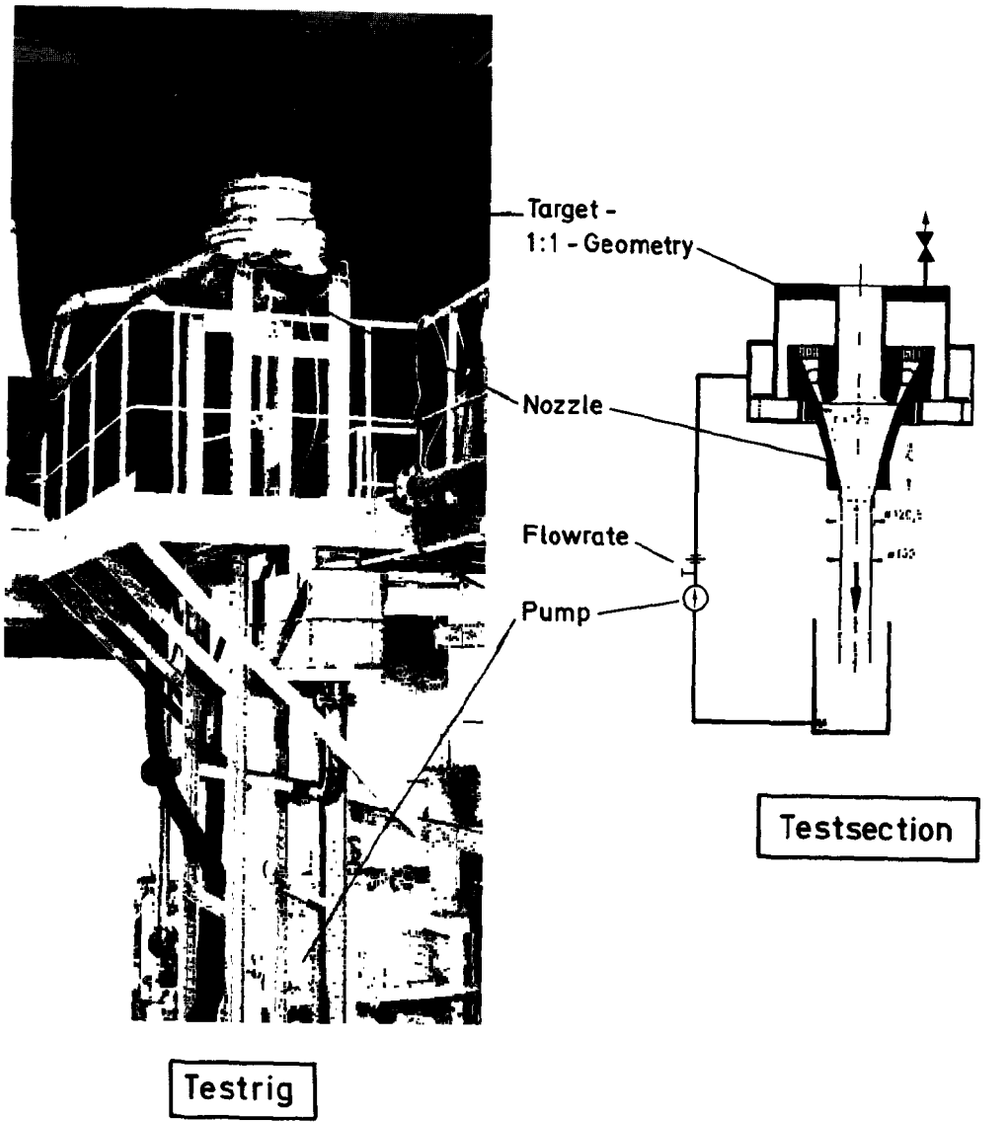

Fig.5 Experiments in H_2O Flow

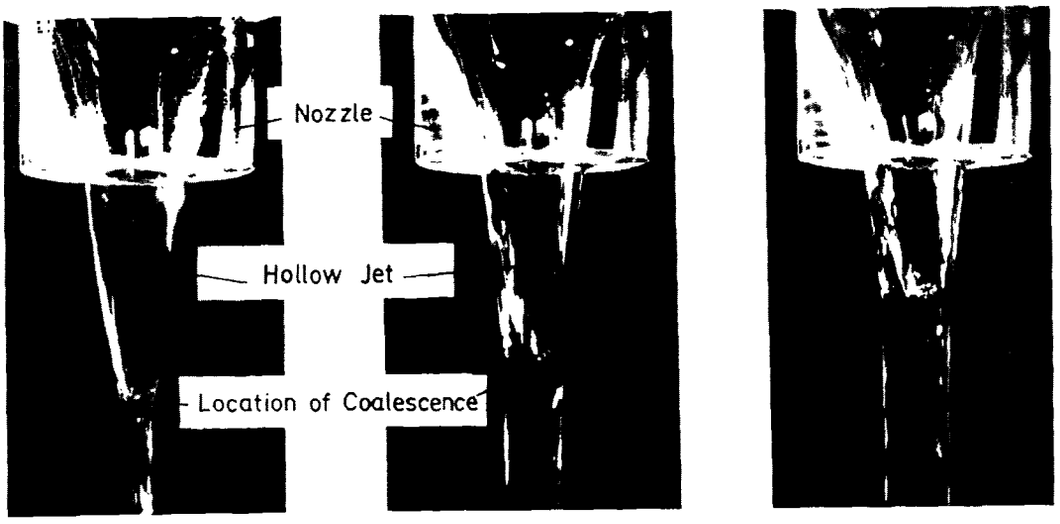

Fr = 0.4 1.15 1.6

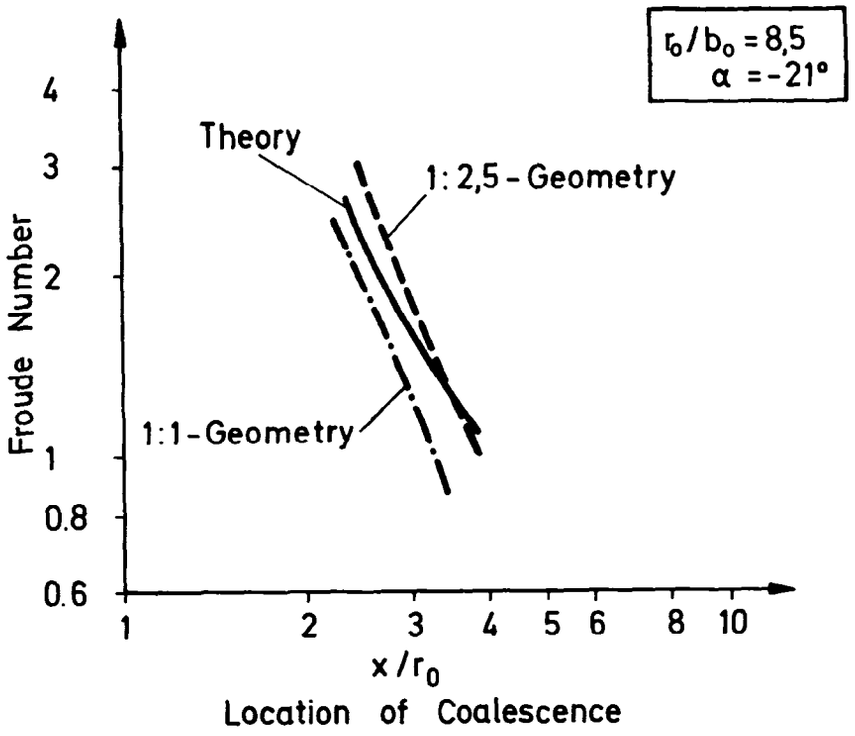

Fig. 6 Flow Behavior of Hollow Jet - Influence of Froude - Number on Location of Coalescence

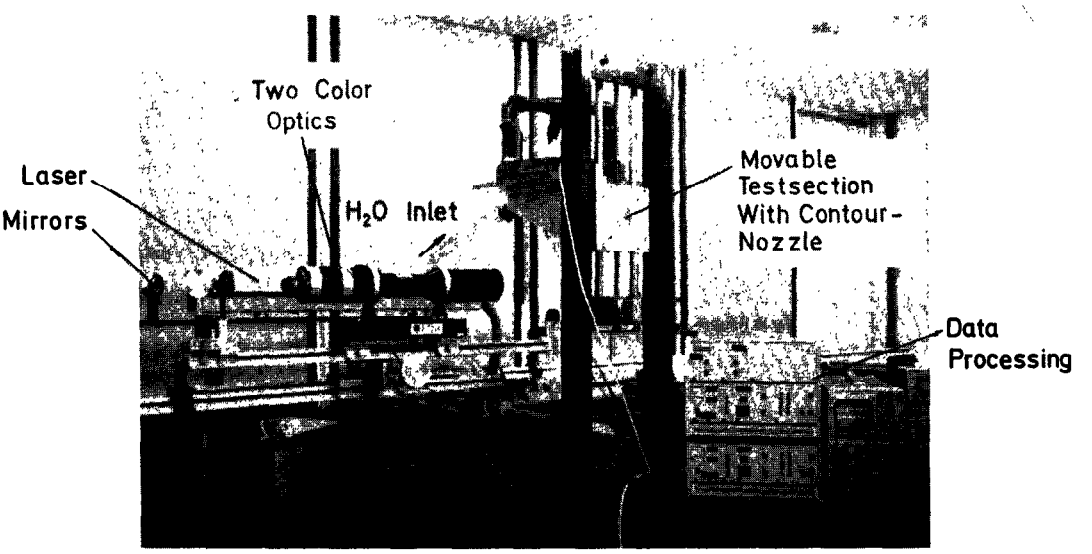

Fig.7 Laser Doppler Anemometry - Test Arrangement

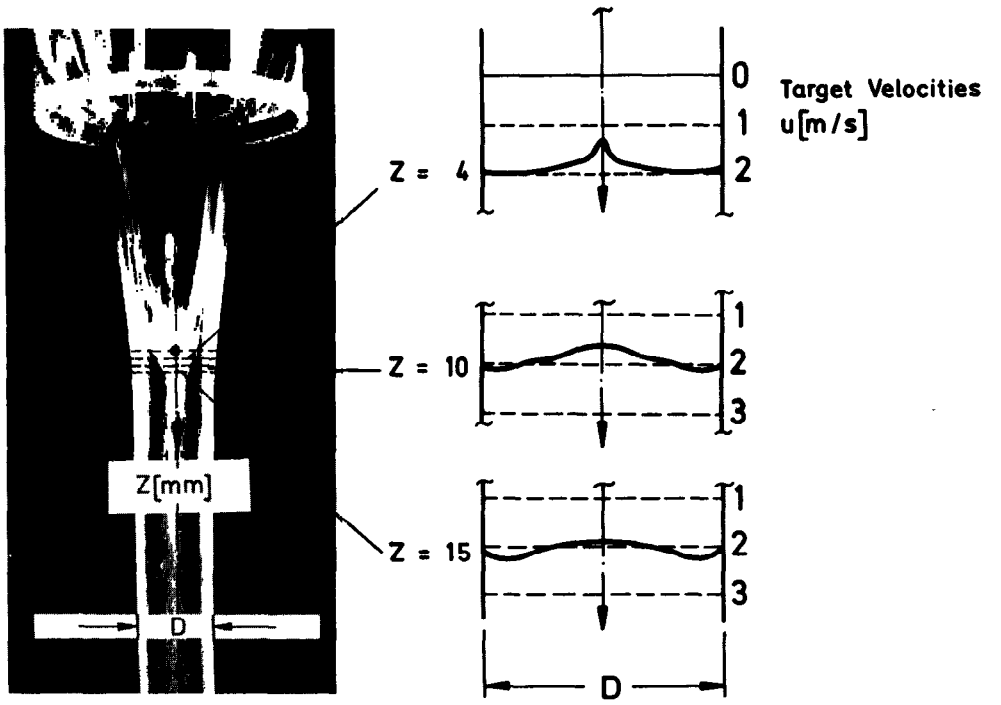

Fig.8 Local Velocity Distribution near the Point of Coalescence ($Fr = 1.4$; $r_0/b_0 = 5$; $\alpha = -21°$)

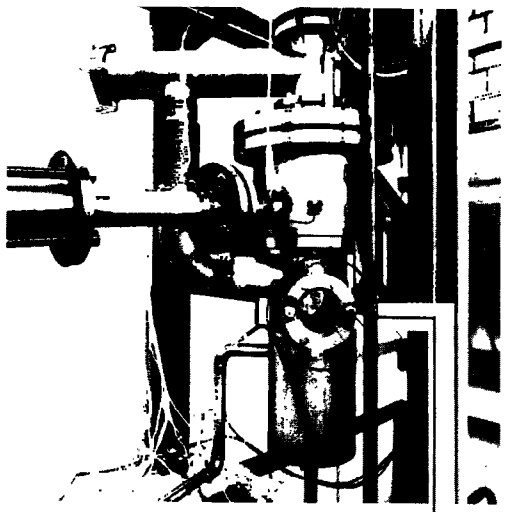

Testrig

Testsection

Fig.9 PbBi - Circuit I - Basic Experiments

Fig.10 Outer Contour of PbBi - Jet

PbBi - Testsection:
- Installed in H_2O -Rig -

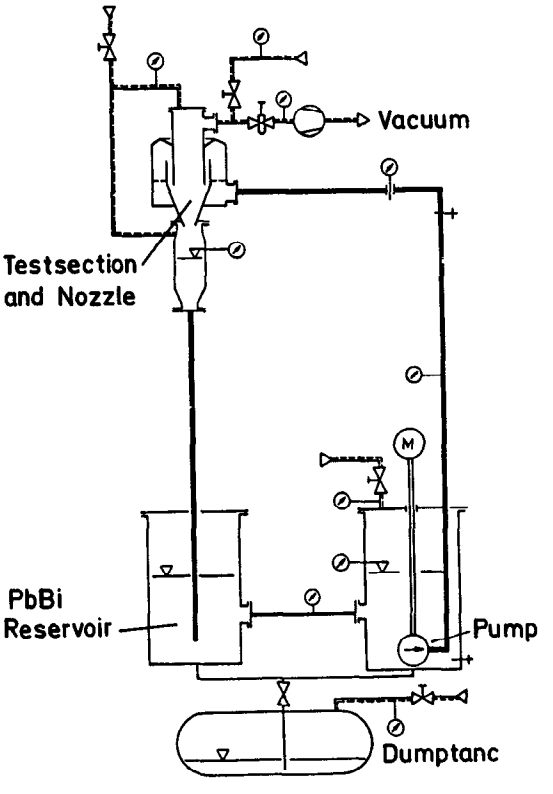

PbBi - Rig

Fig. 11 PbBi Circuit II - Demonstration

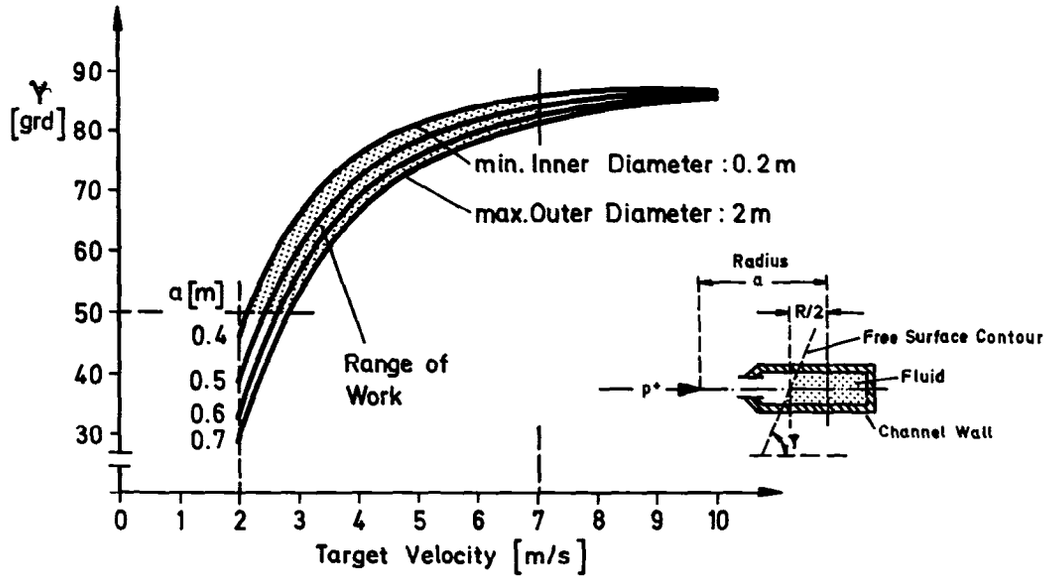

Fig. 12 Angle of Free Target Surface for Different Flat Channel Radia and Fluid Velocities

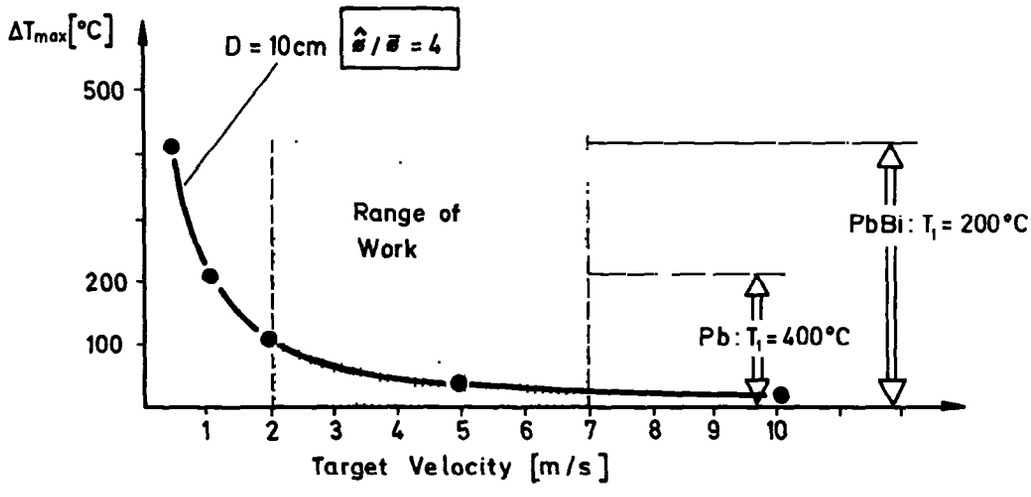

Fig. 13 Maximum Local Fluid Temperatures as Function of the Fluid Velocities (Q = 2.8 MW; z = 0 mm)

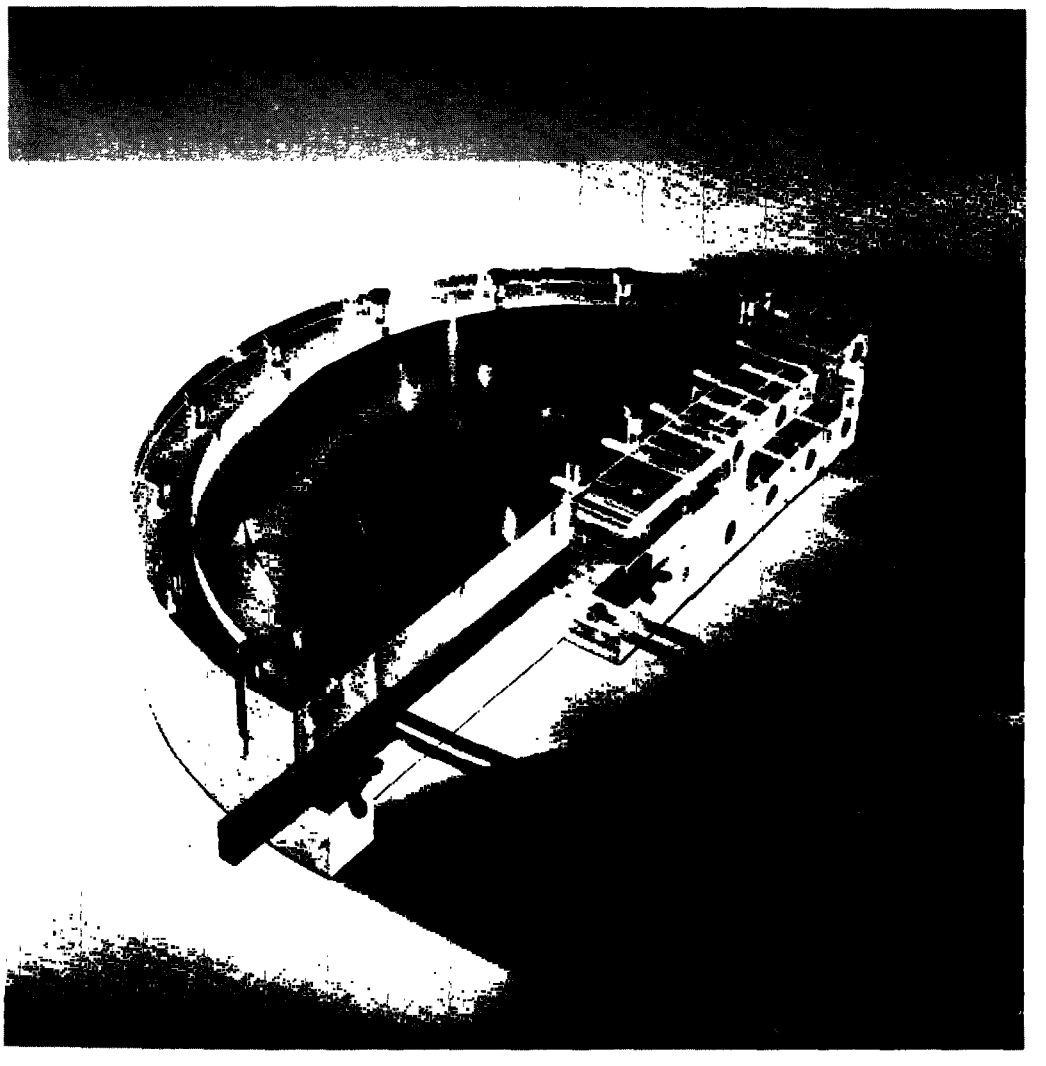

Fig.14 Experimental Proof of Flow Behavior in Flat - Channel Target - Testsection

Jül-Conf-45 D4-2

I C A N S - V

MEETING OF THE INTERNATIONAL COLLABORATION ON

ADVANCED NEUTRON SOURCES

June 22-26, 1981

at Kernforschungsanlage, Jülich

Vertical, Convective Spallation Target at SIN

C. Tschalär

Swiss Institute for Nuclear Research (SIN)
CH-5234 Villigen, Switzerland

Abstract

A new version of a spallation target for the SIN neutron source is presented. It consists of a vertical container filled with a eutectic mixture of Pb and Bi (LBE). The proton beam enters from the bottom through a window. The heat of 1 MW deposited by the beam is carried to a heat exchanger inside the LBE target by natural convection. Calculations for start-up and stationary flow of the LBE show stable thermodynamic behaviour with maximal temperatures well below 500° C. Problems of window materials and operational aspects are also discussed.

VERTICAL, CONVECTIVE SPALLATION TARGET AT SIN

1. Layout

The latest layout version for the spallation neutron source at SIN as mentioned in the survey talk is shown in figs. 1a and 1b. The proton beam is bent down into a ditch and subsequently deflected vertically upwards into a vertical, cylindrical target filled with a liquid entectic of lead and bismuth (LBE). The physical advantages of such an arrangement are a 360°-access to the source for the neutron users and optimal coupling of high-flux rectangular neutron tubes to the source. The technical advantages are a simple, highly symmetric structure of the entire source (modular shielding etc.) and the introduction of a simple target cooled by natural internal convection eliminating the need for expensive external cooling system carrying highly radioactive fluid.

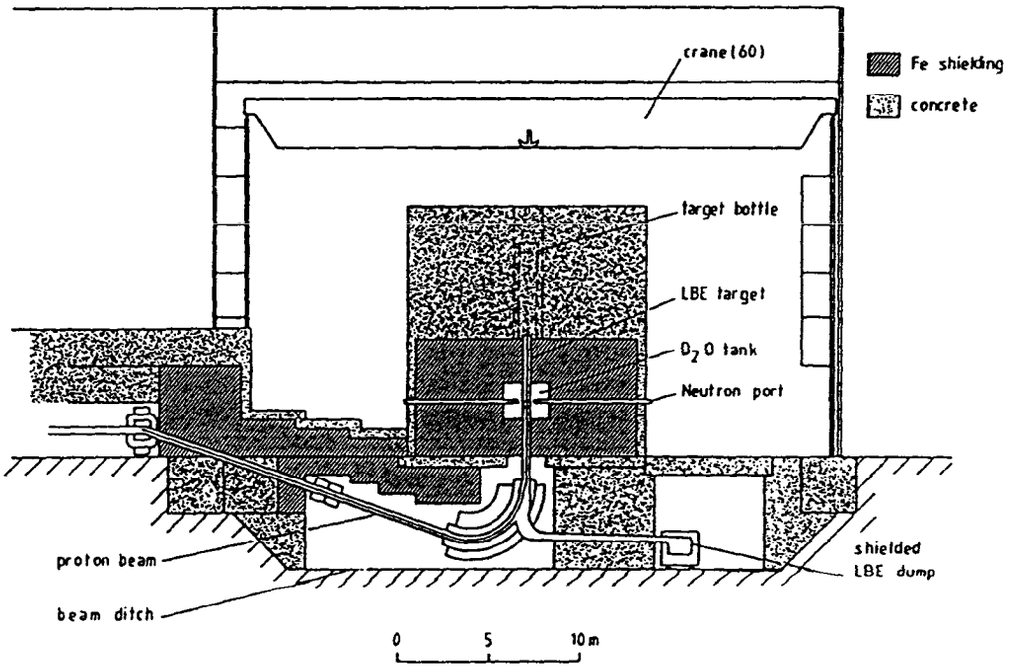

Fig. 1a

SIN neutron source: vertical cross section

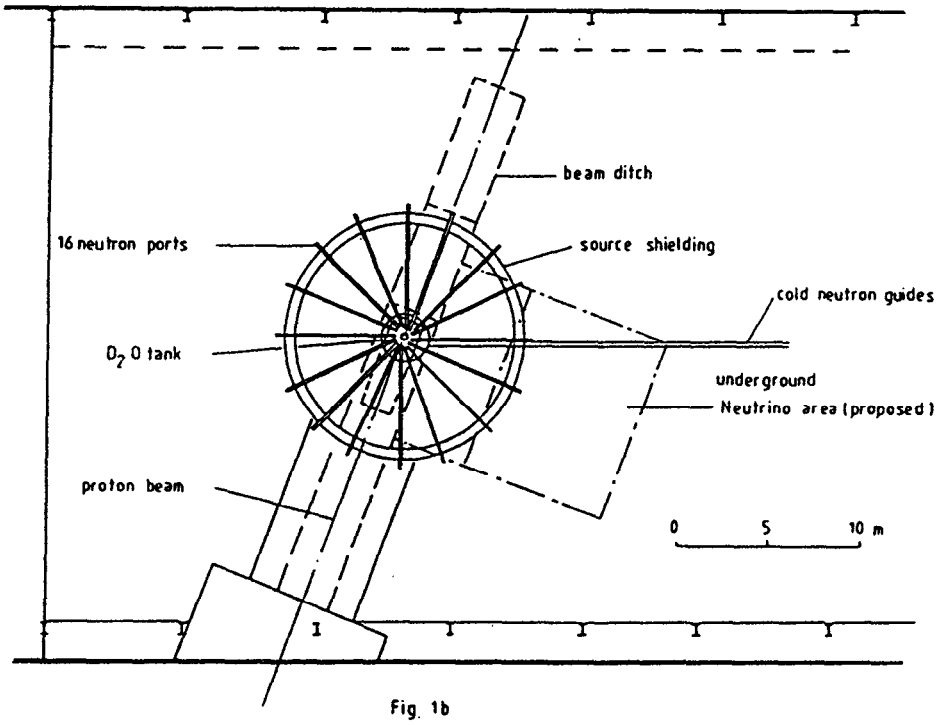

Fig. 1b

SIN neutron source: horizontal cross section

2. Convective Pb-Bi target

2.1 Description

The spallation target consists of a vertical, cylindrical vessel of about 20 cm diameter and a height of 3.5 m (fig. 2). The bottom end is closed off by a conical beam entrance window. The top is covered by flange carrying an array of cooling pipes which extend down by about 2 meters into the target vessel filled with liquid LBE. The proton beam entering the target deposits its energy near the entrance window. The hot LBE rises to the top where it is cooled on the cooling pipes and flows back along the wall of the target vessel. An internal coaxial guiding tube separates the hot and cold convective currents thereby preventing formation of "back water" pockets near the window and optimising the flow through the heat exchanger.

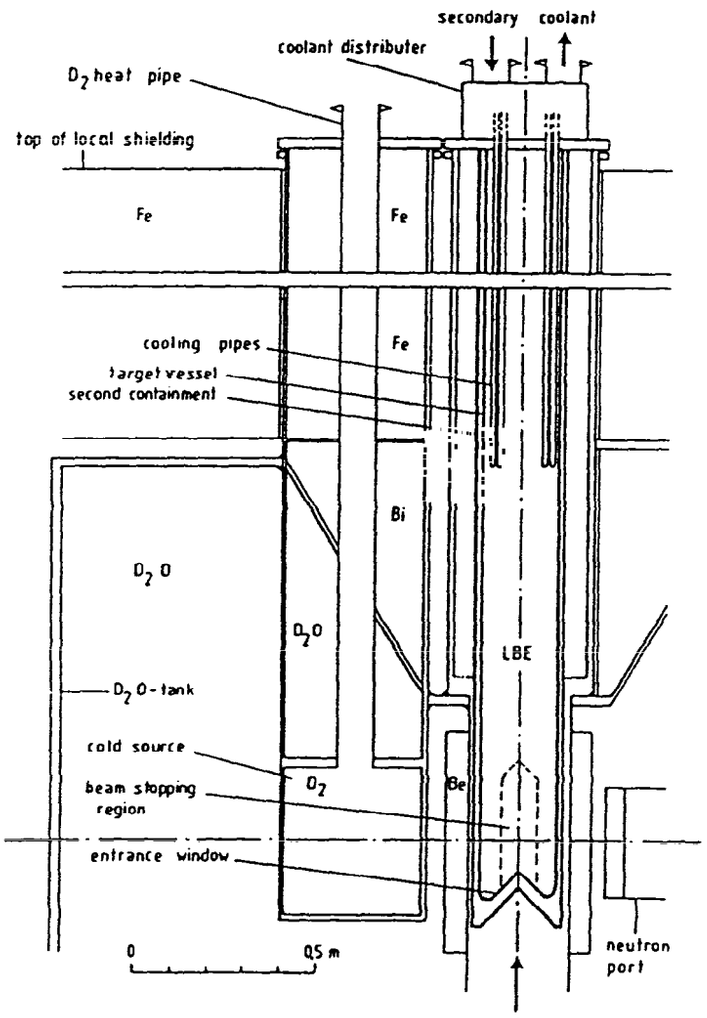

Fig 2

Spallation target region: vertical cross section

The inner target vessel is enclosed by a concentric outer vessel acting as a second containment fitted with a similar conical window cooled by radiation. Both vessels form an integrated target unit which is exchanged from the top in case of failure. The height of the target is designed such that the radiation level at the top flange allows simple manual coupling and decoupling of the target from the secondary cooling circuit and auxiliary connections.

2.2 Flow calculations

Calculations have been made of the convective flow of LBE in a vertical target . The stationary case can be described rather simply if we make the plausible assumption that the stationary flow can be represented as a sum of infinitesimal closed flow loops of volume flux $d\dot{V}$ which is constant over the loop, where the flow loops follow the direction of the flow velocity. Equilibrium between the buoyancy and the net frictional pressure drop Δp about each loop is expressed by the relation

$$\int_L d\dot{V}\cdot\Delta p = \int_L d\dot{V} \oint dz\cdot g\cdot\Delta\rho = \rho g\beta \int_L d\dot{V} \oint dz\cdot T$$

where

$\int_L$ = sum over all flow loops

$\oint$ = line integral over an individual loop

$\Delta\rho$ = change of density of LBE by heating

g = acceleration of gravity (= 981 cm/s^2)

β = volumeric thermal expansion coefficient of LBE

z = vertical coordinate

T = relative temperature of LBE

ρ = density of LBE at T = 0 (= 10 g/cm^3)

If the net rise of temperature in each flow loop by beam heating is ΔT, then the total beam power P is

$$P = c_p \int_L d\dot{V}\cdot\Delta T$$

where c_p is the heat capacity of LBE (=1.46 Ws/cm^3 K). We now define the mean difference of height between the area of heating and of cooling of the LBE as

$$\bar{h} = \frac{\int_L d\dot{V} \oint dz\, T}{\int_L d\dot{V}\cdot\Delta T} = \frac{\int_L d\dot{V} \oint dz\, T}{P/c_p}$$

As a final simplification we assume the mean pressure drop $\overline{\Delta p}$ over the flow loops to depend quadratically on the total volume flux $\dot{V}$:

$$\overline{\Delta p} \equiv \frac{1}{\dot{V}} \int_L d\dot{V}\, \Delta p = k \cdot \dot{V}^2$$

where $\dot{V} \equiv \int_L d\dot{V}$ and k is the constant of flow resistance.

Thus

$$k \dot{V}^3 = \rho g \beta \bar{h} P / c_p$$

or

$$\boxed{\dot{V} = \left[\frac{P \cdot \bar{h}}{k} \cdot \frac{\rho g \beta}{c_p} \right]^{1/3}} \qquad (1)$$

The mean temperature rise $\overline{\Delta T}$, defined as

$$\overline{\Delta T} \equiv \frac{1}{\dot{V}} \int_L d\dot{V} \cdot \Delta T = \frac{P}{c_p \dot{V}}$$

is then given by

$$\boxed{\overline{\Delta T} = \left[\frac{P^2 k}{\bar{h}} \cdot \frac{1}{\rho g \beta c_p^2} \right]^{1/3}} \qquad (2)$$

Two examples for convective LBE targets for proton beam powers of 1 MW and 10 MW resp. are shown schematically in fig. 3a and 3b. Both targets are cooled by an array of water pipes of 16 mm outer

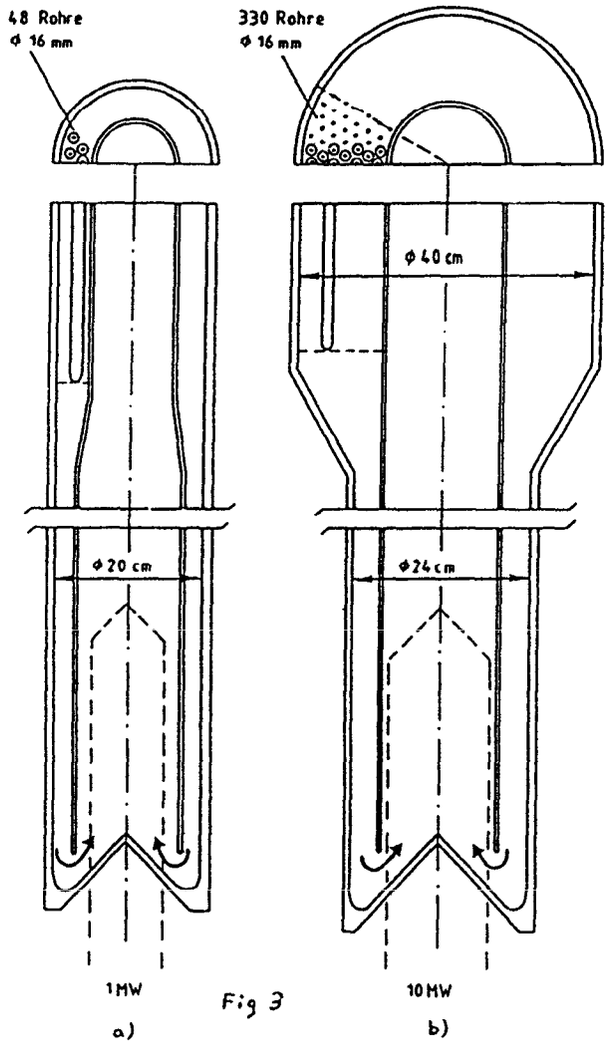

Fig 3

Convective spallation targets: conceptual layouts

diameter and 2 m length. The dimensions of these systems and the resulting characteristics of the stationary flow are shown in table 1:

Table 1

Target		I	II
Beam power	P	= 1	10 MW
Height of target	H	= 3.5	4.5 m
Effective convective height	$\bar{h}$	= 2	3 m

Number of cooling pipes	n =	48	330
Flow surface at heat exchanger	F_s =	100	400 cm^2
Total heat exchanger surface	F_k =	4.8	33 m^2
Water velocity	w =	2	3 m/s
Water flux	$\dot{V}_w$ =	4.8	54 l/s
Total heat transfer number water-LBE	α =	0.3	0.3 W/cm^2K
Theoretical flow resistance	k =	$2.3 \cdot 10^{-3}$	$2.3 \cdot 10^{-4}$ $bar/(l/s)^2$
Effective flow resistance	k_{eff} =	$3.4 \cdot 10^{-3}$	$3.4 \cdot 10^{-4}$ $bar/(l/s)^2$
LBE flux	$\dot{V}_p$ =	3.4	18 l/s
Mean frictional pressure drop	$\overline{\Delta p}$ =	40	110 mbar
Mean LBE temperature rise	$\overline{\Delta T}$ =	200	380 °C
Water inlet temperature	T_{ow} =	100	100 °C
Water outlet	T_{1w} =	150	145 °C
LBE inlet temperature	T_{op} =	375	540 °C
LBE outlet temperature	T_{1p} =	155	160 °C

The temperatures reached by the LBE even for the 10 MW example are still very manageable, especially since the only surfaces which are in contact with the LBE and which cannot be kept at low temperature are the window and the inner guiding tube which therefore have to be made of corrosion resistant materials e.g. graphite. The outer wall and the cooling pipes can probably be made of regular stainless steel since their temperature can be kept below 200 °C. Since the temperature rise ΔT calculated in these examples is proportional to only the power of 1/3 of the geometry factors h and k, the system temperatures will not vary much even if actual geometries turn out somewhat different from the simple-minded model described here.

In the start-up phase of the convective flow after the proton beam has been switched on, the LBE, initially at rest, has to be accelerated until the final stationary flow is achieved. In this phase the convective flow pattern is expected to change rapidly and local overheating of the LBE will occur.

In order to evaluate the behaviour of the system realistically, a computer programme for two-dimensional (cylindrical coordinates r, z), time dependent convective flow was written and used to compute the start-up phase of an LBE flow in a vertical cylindrical vessel in which the upper part of the side walls were held at constant temperature to simulate the heat exchanger and the lower part around the beam stopping region was insulated. For simplicity the frictional flow resistance in a realistic heat exchanger was neglected since in the start-up phase inertial forces in the LBE dominate. The basic Navier-Stokes equations were integrated using several suitable approximations especially that of constant density (exept for the buoyancy terms) and of low viscosity.

The temperature profiles in the flow at several heights z and times t after start-up are shown in fig.4. The cylindrical target vessel has a diameter of 20 cm and the r.m.s. diameter of the 600 MeV proton beam of power P is 5 cm and 10 cm resp. The target vessel is insulated over a height of 60 cm.

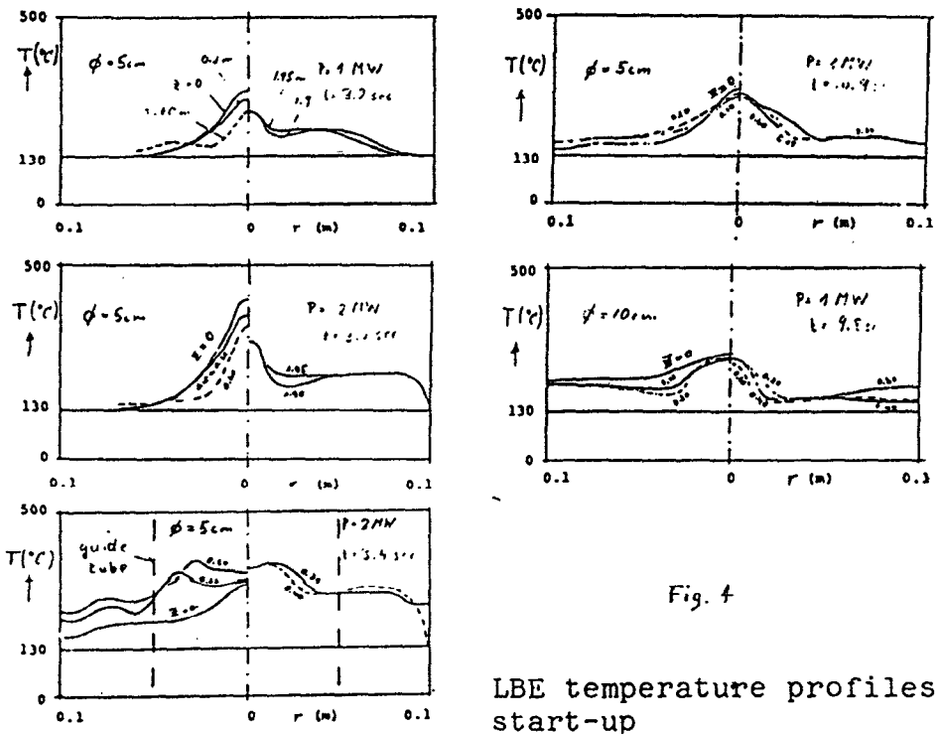

Fig. 4

LBE temperature profiles at start-up

In contrast to some earlier calculations for a target vessel and beam inclined at 20° to the horizontal, overheating in the vertical geometry is almost negligeable and the flow shows very stable behavior, especially if a concentric guiding tube is inserted into the heating region. The only condition for safe start-up is that the LBE be completely molten before the beam is switched on. However, the time structure and, within rather wide limits, also the diameter and shape of the proton beam does not critically affect the flow. Furthermore, an extension to higher beam power is easily possible by essentially beefing up the heat exchanger.

2.3 Beam window

The beam entrance window is obviously a crucial element since the entire lay out and target concept depends on its functioning. Besides questions of thermal and mechanical stress, the main uncertainty of window performance is still radiation damage by the proton beam. In order to minimize this problem, the design philosophy for the SIN spallation target calls for a proton beam as wide as possible even if it leads to a slightly larger source diameter. For beam powers above about 1 MW even tayloring of the beam profile to produce sharper edges and lower density at the centre for given source diameter would be considered. Widening of the beam in a given source will if anything in crease the neutron flux density at the neutron tube as long as the entire beam is still hitting the target. Flux calculations indicate that the flux reduction by going from a minimal source diameter of about 10 cm to about 20 cm is in the order of 10 %, a value which is probably reduced by reduced mutual flux depression through wider spacing of any given number of neutron ports. A further advantage of a larger source is the reduction of gamma heating in the surrounding structures and especially in a cold source. In view of these considerations, an r.m.s. beam diameter of 10 cm for a 1 MW beam (1.7 mA at 600 MeV; centre beam density = 20 A/cm2) and a LBE source diameter of 20 cm resulting in an inner D_2O tank diamter of 28 cm seemed quite acceptable.

In a radiation damage test at SIN, a disk of reactor graphite of 3 mm thickness and 3 cm diameter was exposed to the primary beam of 100 μA of 600 MeV protons

for 200 hours. The beam spot area was 0.3 cm^2 resulting in sample temperatures between 1100 and 1300 °C. After irradiation the disk showed no measurable swelling or visible cracks. A graphite window for the proposed neutron source with a peak load of 20 $\mu A/cm^2$ can therefore be expected live for several thousand hours or many months before radiation damage causes failure. In the case of a 10 MW source shown in fig. 3b assuming an r.m.s. beam diameter of 14 cm and a central beam density of 100 $\mu A/cm^2$, a window life time of several weeks can still be expected.

Three further examples of high intensity proton irradiations of target and win dow materials have been reported from LAMPF and TRIUMF and are listed below together with the SIN sample:

	LAMPF	LAMPF	SIN	TRIUMF	
sample material dimensions	pyro-graphite (A5 target)	inconel (A6 window)	reactor graphite	stainless steel	
	5 mm thick	3 mm thick	3 mm x 25 mm	3 mm thick	
beam energy	800	800	600	500	MeV
beam current	400	400	100	100	μA
spot size	< 0.5	10	0.3	10	cm^2
irrad. time	1000	10^4	200	5000	h
sample temp.	~ 1000	~ 500	~ 1200	~ 500	°C
equivalent dose	800	~ 400	60	50	mAh/cm^2

None of these samples showed any macroscopic damage but microscopic analysis is yet to be carried out. The evidence, however, points to possible life spans of several hundred mAh/cm^2 for some window materials.

Approximate calculations were made for the thermal strain $\varkappa$ and the compressive stress σ from the LBE pressure p on conical windows shown in fig. 3a and 3b.

The windows, made from reactor graphite (density 1.75 g /cm , minimal heat conductivity of 0.5 W/cm K, a thermal expansion coefficient of 3 ppm/K and a proton energy absorbtion of 6 MeV/cm), have a half opening angle of 45°, a thickness of 0.5 cm at the vertex and 1 cm at the base. For exponential beam profiles, the largest thermal strain $\varkappa_{max}$ occurs at about half the r.m.s. beam radius R. The largest compressive stress σ_{max} is found at the base. The calculated values for $\varkappa_{max}$ and σ_{max} and their relation to the limiting values break and break for graphite are shown in table 2:

Table 2

P	1	10	MW
$r_{r.m.s.}$	5	7	cm
$\varkappa_{max}$	$1.4 \cdot 10^{-4}$	$8 \cdot 10^{-4}$	
$\varkappa_{max}/\varkappa_{break}$	7 %	40 %	
σ_{max}/p	16	20	
σ_{max}	56	80	bar
$\sigma_{max}/\sigma_{break}$	11 %	15 %	

The radiation cooled window on the second containment of the same shape and ma terial would develop smaller thermal strains than the main window. In a 1 MW beam of 10 cm r.m.s. diameter it would heat up to about 1500 °C which is an acceptable operating temperature for graphite and still below the boiling point of LBE so that evaporation in the case of an LBE leak would be moderate. For a 10 MW beam at 14 cm r.m.s. diameter, however, temperatures of 2300 °C would be reached, therefore a thinner window may be a safer solution in this case.

2.4 Operation and safety

Flow calculations have shown that neither the time structure of the beam intensity nor the beam profile have a serious effect on the safe behaviour of the convective LBE flow and its temperature, provided the LBE is kept liquid at all times. Apart from considerations of life-time the same is true for the window performance within rather wide margins of beam variations.

If the exit temperature of the secondary coolant is kept at about 150 °C, the heating of the LBE by residual radioactivity will normally maintain a minimal convective current and prevent the LBE from freezing during stand-by. An electrical heating element of a few kW power inserted into the centre of the target near the top would have the same effect even in a fresh, non-activated LBE target. Should the LBE freeze accidentally or during a long shutdown, it could be melted by circulating hot gas between the target and secondary containment.

During normal operation, the space between target and second containment would be kept filled with helium at low pressure and monitored continuously for leaks from the the target. Gauges on the beam vacuum system would indicate any leaks form the secondary confinement.

The LBE target itself will have to be vented through an appropriate filtering system to prevent a major build up of gaseous spallation products in particular H_2 and He.

Leaks from the target would normally be contained within the target unit (second containment) which can be exchanged routinely. Should the windows of both containments break simultaneously, The LBE content would fall into a duct directly below the target at the "back" of the beam bending magnet where it will be slowed down and allowed to empty into a shielded dump at the end of the beam ditch. A fast closing vacuum valve placed suitably upstream in the proton beam line would localize contaminaton of the beam vacuum.

In case of stoppage or loss of secondary coolant the convective LBE current will continue automatically with the average temperature rising at about 450 °C /min allowing ample time to switch off the beam. The heat produced by the residual radioactivity ($\sim$1 % of beam power) can be radiated off through the target and vacuum vessels into the shielding. If the total emissivities of the vessel walls are above 0.5, the LBE temperature will stay below 800 °C.

3. Uranium target cooled be LBE convection

In order to boost the thermal neutron flux, concepts for a second generation target of uranium were studied. A simple proposal involves insertion of a bundle of cylindrical fuel rods filled with uranium carbide into a convective LBE target of the same dimensions as the one in fig. 3a exept that the heat exchanger would be enlarged to handle the power increase of a factor of 2 expected from a UC-target (see fig.5). The fuel rods would carry conical caps at both ends to reduce flow resistance and would be held by an appropriate matrix to allow the LBE to enter into the bundle from below and to ensure proper spacing of the rods.

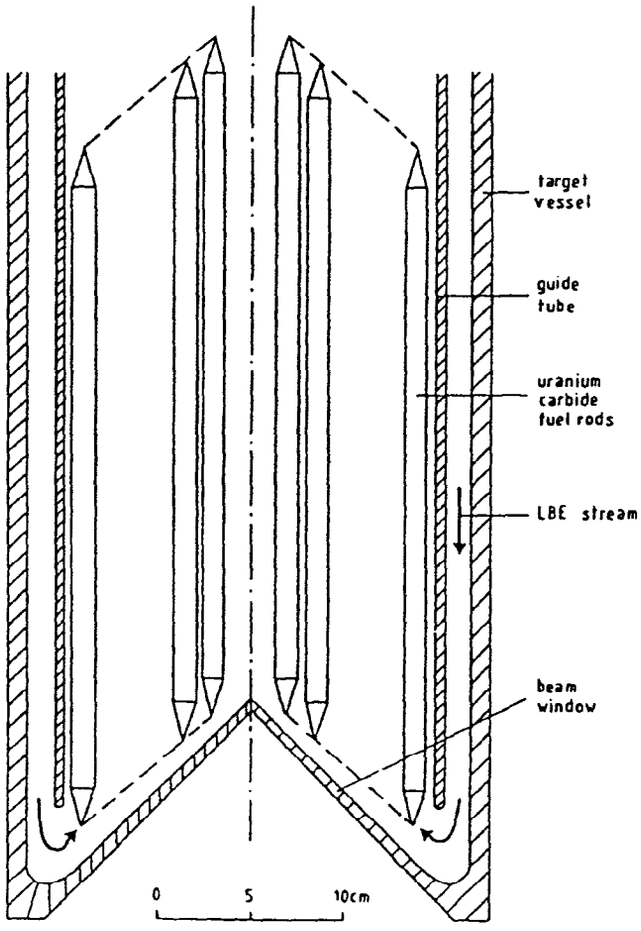

Fig 5

LBE target boosted by UC fuel rods

First approximate calculations for the stationary LBE flow through a bundle of fuel rods of 1.2 cm diameter and 35 cm length (beam stopping characteristics of a UC fuel rod with 80 % filling factor is about equal to that of LBE) have shown that by an appropriate spacing of the rods the maximum cladding temperature which is the critical temperature in view of the high melting point of UC (2300 °C) can be kept uniformly low for gaussian beams of r.m.s. diameter between 4 cm and 16 cm. The corresponding design figures and resulting thermodynamic flow values are shown in table 3. For simplicity the LBE flow resistance is assumed to be determined only by the flow resistance in the UC-bundle.

Table 3
---

beam current	1.7 mA
beam r.m.s.. diameter	10 cm
fuel rod diameter	d = 1.2 cm
beam power deposited	P = 1.5 MW
flow resistence through bundle	$k = 7.5 \cdot 10^{-4} \frac{bar}{(l/s)^2}$
flow rate	$\dot{V}$ = 6.5 l/s
pressure drop	$\overline{\Delta p}$ = 32 mbar
max. local temperature rise of LBE (same for beam diameters from 4 cm to 16 cm)	ΔT = 260 °C
effective relative density of UC	56 %
relative source strength compared to LBE (pure UC = 2.8)	2.0

If further flow resistences e.g. of the heat exchanger are significant, the flow rate $\dot{V}$ would be reduced by a factor of $(k_{total}/k)^{1/3}$ and the LBE temperature rises increased by the same factor.

For the start-up phase of the flow through a UC-bundle computer calculations are in progress.

Jül-Conf-45

D4-3

I C A N S - V

MEETING OF THE INTERNATIONAL COLLABORATION ON

ADVANCED NEUTRON SOURCES

June 22-26, 1981

Some Remarks Concerning the Use of a Rotating W-Target in a High Power Spallation Neutron Source

G.S. Bauer*, W. Lohmann* and F. Stelzer**

* Institut für Festkörperforschung

** Zentralabteilung für Allgemeine Technologie

Kernforschungsanlage Jülich

D-5170 Jülich, Fed. Rep. Germany

Abstract

In this paper we show that a rotating target for a high power spallation neutron source using tungsten as a target material can be built relatively easily and operated safely. According to experimental results we do not expect a significant disadvantage to result from the use of W instead of Pb even for the D_2O-tank of the hybrid moderator system proposed for the target station DIANE in the SNQ concept. We therefore conclude that the use of a rotating W-target is a viable backup solution for the SNQ target concept, avoiding practically all of the yet to investigate difficulties with a canned target material.

1. Introduction

For the spallation neutron source proposed in Germany, the initial moderator concept chosen consists of a D_2O-tank and an H_2O-moderator with lead reflector arranged above and below a rotating target /1/ as shown in Fig. 1. Since it was felt that the time average neutron flux in the D_2O depended quite critically on losses by absorption, a target concept was developed which allowed the use of the only weakly absorbing lead in conjunction with Al as structural material. Due to the thermal and thermomechanical properties of lead (low melting point, poor thermal conductivity, large differential expansion, low flow stress etc.) it was decided that the target should be built of about 9000 cylinders individually canned in aluminium /2/ and cooled by water flowing between them (see Fig. 1). Another incentive to choose this concept was - and still is - to make possible a later transition to uranium as target material and provide a safe containment for the then present fission products. Extensive studies /3/, /4/, /5/ have shown that such a concept should be feasible, but there remain a few problems which could not yet be investigated in sufficient detail to give a reliable estimate of the expected lifetime of such a target. Apart from this, the design has the following drawbacks:

- Difficult manufacturing procedure;
- dilution of target material by cooling channels and cladding material;
- need for a window to contain the coolant. This window, although rotating with the target, is the most heavily loaded part of the structure as far as radiation effects are concerned;
- mechanical load on the structure due to coolant pressure;
- part of the cooling water is hit by the proton beam, which may enhance corrosion effects.

These problems - and hence their possible effects on the target lifetime - can be avoided if tungsten is used as target material as shown in the present note. Table 1 summarizes some important properties of tungsten.

Density (g/cm²)	19.3
Hardness H_v (swaged material) (N/mm²)	4600 - 7500
Tensile strength (swaged material) (N/mm²)	1500 - 5000
*Young's modulus (20°C) (N/mm²)	400.000
Melting point (K)	3683
*Thermal conductivity (20°C) (W/cm K)	1.7
*Coefficient of thermal expansion (20K) (K^{-1})	$4.4 \cdot 10^{-6}$
Ductile-brittle transition (K)	400 - 700
Thermal neutron absorption cross section (barn)	19.2
Mean free path for protons of 1.1 GeV (cm)	9.8
Range of protons of 1.1 GeV (cm)	36

Table 1 Some properties of tungsten

*see also Figures

2. Design principle of the rotating tungsten target

As will be shown in section 3, it is sufficient to cool the upper and lower surface of a tungsten ring used as target with the SNQ-parameters[1] to remove the heat dissipated in the target even from the most highly loaded regions. This makes a target design possible, as sketched in Fig. 3. For manufacturing reasons and also to reduce internal stresses, the target consists of a large number of (almost) close packed hexagonal rods. (Of course it would be tolerable also to use square cross sections). Small gaps are left between the rods to accomodate lateral thermal expansion. In order to ensure good thermal contact, these rods are tightly bonded to the upper and lower support plates which contain the cooling channels. Since the coolant is flowing only in these bores, there results no bending stress on the support plates as in the design of Fig. 1. The proton beam does not hit the coolant directly and hence no window to contain the coolant is needed. A number of ways to arrange the coolant channels are conceivable in addition to the one shown in Fig. 3. It is possible to provide several separate sections which are only mechanically connected to one another, and thereby facilitate the manufacturing of the target wheel. Because of the short range of protons in tungsten, it is sufficient to have a target depth of 35 cm rather than 70 cm as required for the Pb-target of the reference concept, thereby reducing the number of target elements and hence the cost. According to manufacturers' quotes, one target element (rod) of the tungsten target would cost about as much as an Al-canned lead target element. Together with the much simpler manufacturing procedure of the whole target, this may result in considerable savings. The target has a high degree of mechanical rigidity due to the tight bonding between the target elements and the support structure.

3. Thermal and mechanical load on the rotating W-target

For the sake of simplicity, the geometry used earlier /3/ to calculate the temperatures and stresses in the lead target was also used for the W-target elements. This means, that a cylindrical rod of 24 mm diameter and 100 mm length, hit by a proton beam symmetrical to its centre plane once every two seconds (time of revolution of the target) was considered. The finite element method was used, and for symmetry reasons only one half of a rod at the outer periphery of the wheel was modelled. The grid of nodes and finite elements is shown in Fig. 2. For the sake of convergency it was necessary to use thin elements in the region of the heat sink. Within each nodal plane, a subdivision was made into 48 elements (65 nodal points) for which the time-dependent temperatures and stresses were computed. The heat deposition in the target was assumed to decrease purely exponentially along

---

[1] Outer target diameter 2,5 m; Height of target 10 cm; Frequency of rotation 0,5 Hz; Proton pulse repetition rate 100 Hz; Proton beam diameter 4 cm FWHM; Peak proton current 100 mA (1.1 GeV); Proton pulse duration 0,5 ms.

the proton beam with a decay constant given by the protons' mean free path (Table 1) and to follow in its lateral distribution the profile of the proton beam. This profile was assumed to be gaussian with a FWHM of 4 cm in both directions and truncated at 8 cm. The total heat deposition was assumed to be approximately the same as in a Pb-target /6/. The time-dependent temperature after startup is shown in Fig. 4 for the hot spot and for the first 30 revolutions of the target wheel. At this point equilibrium has almost been reached and the mean temperature can be seen to be about 350 K above the coolant temperature (i.e. about 680 K). The temperature cycling is 44 K once every two seconds.

For this first set of calculations the thermal conductivity and heat capacity have been assumed as temperature independent, using values of 1.5 W/cm•K and 130 J/kg•K respectively. From Figs. 7 and 8 it can be seen that this is not exact, but in view of the large distance of the operating temperature from the melting point, this is not very important. The distributions of reference stresses and maximum temperatures in the most highly stressed plane are shown in Figs. 5 and 6. The peak stress of 20.9 N/mm^2 is far below the tensile strength which is 3400 N/mm^2 (Fig. 9). Thus, even the fact that the operating temperature is above the ductile-brittle transition should not be important.

The maximum difference in thermal expansion (Fig. 10) between two target elements (separated by 4 cm, i.e. next nearest neighbours) is 0.01 mm on either side of the rods. There is no difficulty expected in accomodating this in the support plates.

From a thermomechanical point of view it seems that the use of a W-target as described here is absolutely without problems. All loads, at least in the unirradiated material, are far from any critical values.

4. Effect of irradiation on the performance of the rotating W-target

The kind and the amount of radiation damage in the rotating target is mainly determined by the intermittent proton irradiation and the time-averaged fast neutron flux. Table 2 shows some material parameters of W concerning the damage due to protons and neutrons.

	σ_{dpa} (barn)	σ_{He} (barn)	σ_H (barn)
Protons (800 MeV)	9100	0.58	5.13
Neutrons (E>0.1 MeV)	173 (fission spectrum)	$0.32 \cdot 10^{-3}$ (fusion spectrum)	$0.7 \cdot 10^{-3}$ (fusion spectrum)

Table 2 Radiation damage cross sections for proton- and neutron irradiation of W. The threshold energy for atomic displacement is assumed to be E_d = 65 eV.

The proton data are taken from calculations using a proton energy of 800 MeV. This does not seem to be very crucial for a first material assessment. The neutron data have been generated in the case of the dpa-damage by averaging over a FBR-spectrum, in the case of the gas production by averaging over a fusion reactor spectrum in order to take the harder spallation neutron spectrum into consideration. The latter values are therefore an upper limit for the expected damage.

Using the data from Table 2, values for the dpa-damage and the gas production under the SNQ operations conditions have been calculated and are given in Table 3. The spatial maximum of the time average fast neutron flux was estimated as $1.8 \cdot \hat{\Phi}$ (Pb)*, corresponding to the neutron yield ratio, Y(W)/Y(Pb) = 0.9 and the twofold shorter mean free path of protons in W.

	dpa-damage rate (dpa/sec)	He-production rate (appm He/sec)	H-production rate (appm H/sec)
Protons	$1.63 \cdot 10^{-7}$	$1.02 \cdot 10^{-5}$	$9 \cdot 10^{-5}$
Neutrons	$1.4 \cdot 10^{-8}$	$2.5 \cdot 10^{-8}$	$5.5 \cdot 10^{-8}$

Table 3 Radiation damage data for a rotating W-target.

Proton irradiation parameters: E_p = 800 MeV, $\bar{I}$ = 5 mA, FWHM = 4 cm

Neutron irradiation parameter: $\hat{\Phi}(W) = 7.9 \cdot 10^{13}$ $cm^{-2}s^{-1}$ (E>0.1 MeV)

Obviously, the damage created by the neutrons can be neglected nearly completely. Assuming - as for the SNQ reference design - a target working time of two years (12.000 h), the peak total damage is expected to be

7.6 dpa; 440 appm He; 3.900 appm H.

For proton irradiation of W, 1 mAh/cm² equals 0.21 dpa, 13 appm He and 115 appm H.

Furthermore, Re is created as a solid transmutation product from (n,γ)-reactions of the isotopes W^{184} and W^{186} with thermal neutrons. This Re-enrichment should give no problems because of the good alloyability of Re with W and several favourable properties of W-Re alloys (see below).

We are not aware of results from high energy proton irradiations of W. Therefore, for an assessment of the irradiation induced property changes, results from neutron irradiations were used. Because n-irradiated samples have a very low gas content, statements concerning the effects of the estimated He- and H-concentrations are not possible directly. As an outcome of the generally high H-mobility in metals, one can expect a noticeable H-release at the operating temperature level (section 3). For He, one has a quite different release behaviour. Thermal desorption measurements on He-implanted samples indicate the onset of He-release from surface layers (5 Å) at temperatures above 600°C,

* $\hat{\Phi}$(Pb) as calculated in ref. /6/ is $4.4 \cdot 10^{13}$ $cm^{-2}s^{-1}$ for E > 0.1 MeV

whereas He-release from the bulk is not observed below 1500-2100°C /7/. In order to estimate the possible He-induced material deteriorations like bubble swelling or embrittlement, an investigation of material containing roughly 500 appm He (cyclotron-injected) seems to be necessary. On the other hand, one can get - applying W made by powder metallurgical methods (product density below the theoretical density of W) - a product with a more open structure, providing a catching volume for the gaseous spallation products.

The findings concerning the void swelling are positive throughout. The SNQ-operating conditions will probably not lead into the void swelling region of W after two years of operation (Fig. 12). Even if this should occur, the amount of the void swelling will be very small. For pure W, only 0.25% after 9.5 dpa have been measured (Fig. 13). As can also be seen from Fig. 13, this may be diminished further by alloying. Higher, but absolutely tolerable void swelling values are reported for a n-irradiation of a W single crystal: after 3.9 dpa at 450-500°C a density of 1.2% is observed /10/.

The irradiation induced mechanical property changes of W have not been investigated in great detail. Results of tensile tests on wrought and stress-relieved material, which has been n-irradiated to 1.6 dpa at 385°C /11/, indicate trends which are typical of metals: with increasing dose the tensile strength increases, whereas the ductility decreases. Compared with the unirradiated condition, the gain in strength (expressed by the increase of the yield strength) at the SNQ-operating temperature of 400°C is about 57% after 1.6 dpa (Fig. 14, upper part). As a measure of the ductility loss, the total elongation decreases to roughly 45% of the unirradiated value (Fig. 14, lower part), which corresponds to absolutely about 4%.

Whereas the strength increase caused by the irradiation can be considered as very favorable, the drop in ductility might seem a serious problem at the first glance. Based on the magnitude of the thermomechanical stresses (section 3), the resulting strains are close to 10^{-3}, which lies far away from the critical limits. Furthermore, the intrinsically brittle behaviour of W has to be taken into account anyway in the design, especially because of the relatively high ductile-brittle transition temperature (DBTT). The DBTT values quoted in Table 1 can be lowered by alloying (e.g. with Re) or by a high degree of cold work (Fig. 15). These precautions may be necessary in order to keep the operating temperature within the ductile range, because the DBTT is shifted to higher temperatures under irradiation. In the paper mentioned above /11/, an DBTT-increase from -65°C to 230°C after 1.6 dpa is found. For W in the recrystallized condition, a DBTT-shift from 315°C to 793°C is observed already after 0.1 dpa /13/.

Summarizing, one can state, that the effects of the radiation damage after two years of operation are foreseeable and manageable. The void swelling can be neglected. The changes of the mechanical properties seem to be only weakly dose-dependent after about 0.5 dpa. The strength increase by irradiation hardening gives no problems. On the other hand, the accompanying ductility losses as well as irradiation-induced DBTT-increase should be investigated experimentally under damage conditions typical of the SNQ. Such data are necessary for a final materials selection, especially with regard to alloying and processing. In this context, a more detailed investigation of the change of the materials properties due to the relatively high He-concentration would also be desirable.

Based on the present knowledge, highly cold-worked W-products made by powder metallurgical methods - possibly alloyed with Re - offer the best characteristics for an application as SNQ target material.

5. Neutronic performance of a spallation neutron source with W-target

In order to get a feeling for the effect on the performance when replacing the lead target by a tungsten target in the target station DIANE of the SNQ-concept (i.e. with the hybrid moderator arrangement), a few measurements were carried out at the Swiss Institute of Nuclear research /14/. For a proton energy of 600 MeV, the following results were obtained:

(1) No difference was found for the thermal neutron leakage from the fast moderator. For this measurement both targets had been "diluted" by placing polyethylene sheets between the bricks from which they were put together (10% by volume). Omitting this dilution in the case of tungsten is expected to result in a 10 to 15% gain. Russell et al /15/ have found a 15% advantage for a small W-target over a lead target at 800 MeV.

(2) In a volume of D_2O (170x170x85 cm^3 LxWxH) located underneath the target, the thermal neutron flux distributions shown in Fig. 16 were found using Dy-foil activation. Obviously there is a much stronger flux depression near the target for tungsten, as expected from its high absorption cross section. On the other hand, the maximum flux value is reduced by 15% only and is shifted farer away from the target. For a cold neutron source of 30 cm height and located with its bottom about 10 cm above the bottom of the D_2O-tank /1/, the loss in time average flux will certainly be less than 10%. Also, it can be assumed that this loss in time average flux does not show up in the peak flux but only in a faster decay due to absorption.

These first results, although still incomplete and of preliminary nature, show, that the backup solution proposed here - although not applicable to a uranium target - is a viable one to ensure safe and reliable operation of the DIANE target station.

6. Use of the rotating W-target with a proton compressor for a pulsed source

As a second stage in the SNQ-concept it has been proposed to build a pulsed neutron source by introducing a proton pulse compressor. This compressor, called IKOR (isochronous compressor ring) /16/ is designed to deliver 0.7 μs long pulses of an integrated intensity ($2.7 \cdot 10^{14}$ protons) which amounts to 83% of that delivered in the basic concept within 500 μs. This results in extremely short heating times and hence is likely to lead to shock-waves in the target. According to a paper by Sievers /17/, a criterion as to whether or not such shock waves arise can be derived from the time a sound wave takes

to travel through the part of height 2B of the target element heated by the pulse of duration t_p. If

$$c \cdot t_p \leq 2B,$$

a temperature rise by ΔT_o results is a stress level

$$\sigma_o = E \cdot \alpha \cdot \Delta T_o$$

(E = Young's modulus, α = coefficient of thermal expansion).

If

$$c \cdot t_p \geq 2B,$$

one obtains

$$\sigma_{max} = \sigma_o \cdot \frac{2B}{c \cdot t_p} .$$

Making the simplifying assumption that the heat deposition is constant over a section 2B = 4 cm of the target rod, some data have been compiled in Table 4 for a Pb-target element with AlMg3-canning and for a W-target rod. The value of $3.6 \cdot 10^5$ N/cm² used for W corresponds to a temperature of 700 K (see Fig. 11).

Material	$\alpha(10^{-6}k^{-1})$	$E(\frac{N}{mm^2})$	$c \cdot t_p$(cm)	ΔT_o(K)	$\sigma_{max}(\frac{N}{mm^2})$	$\sigma_{zul}(\frac{N}{mm^2})$ *
Pb	29.1	$1.3 \cdot 10^4$	0.07	36	13.6	1-6
AlMg3	23.8	$7.1 \cdot 10^4$	0.43	21	35.5	60-120
W	4.6	$3.6 \cdot 10^5$	3.0	37	61.3	100-460**

* Endurance limit for alternating load

**Swaged material at 10^8 load cycles

Table 4 Data for the maximum stresses in the target of a pulsed source of the SNQ-concept

From Table 4 it can be seen, that in the case of a Pb-target the dynamic stresses are higher than the endurance limit under the assumed conditions, while there remains a clear safety margin in the case of tungsten. It should

be noted that this estimate is somewhat pessimistic on the one hand and that the stresses are of compressive nature on the other, which does relax the situation to some extent. Hence it may be concluded that a rotating W-target should also be applicable to a pulsed neutron source in the SNQ-concept.

7. Conclusions

The concept of a rotating W-target outlined in this paper is suitable for the basic intensity modulated SNQ concept (target station DIANE) as well as for a possible future pulsed source. The flux penalty in the D_2O-tank is acceptable, whilst it may be anticipated that, for 1.1 GeV proton energy, there is a gain in the H_2O-moderator due to the shorter range of the protons in tungsten relative to lead. This concept bypasses a number of difficulties present in the reference concept due to the fact that cooling of the upper and lower target surface alone is sufficient. Although not suited for a transition to uranium, it constitutes a viable backup solution for day one operation of a high power spallation neutron source.

References:

/1/ G.S. Bauer
"Layout of the Target Station for the German High Power Spallation Neutron Source Project"
Proc. ICANS IV-meeting, report KENS II (1981) pp. 156-180

/2/ H. Stechemesser and G.S. Bauer
"Engineering, Activity Handling and Emergency Considerations for a Rotating High Power Target"
Proc. ICANS IV-meeting, report KENS II (1981) pp. 313-322

/3/ E. Graudus, A. Sievers und F. Stelzer
"Temperaturen und Spannungen in den zylinderförmigen Protonentargets der Spallations-Neutronenquelle"
unpublished report KFA Jülich, ZAT-Bericht Nr. 110-II-22

/4/ E. Graudus, A. Sievers und F. Stelzer
"Berechnung und Optimierung des Targetradgehäuses der Spallations-Neutronenquelle"
unpublished report KFA Jülich, ZAT-Bericht Nr. 104-II-21

/5/ W. Lohmann
"Materials Problems in Beam Windows and Structural Compounts of the SNQ-Target"
Proc. ICANS IV-meeting, report KENS II (1981) pp. 323-332

/6/ G.S. Bauer, H. Sebening, J. Vetter and H. Willax, eds.
"Realisierungsstudie zur Spallations-Neutronenquelle"
Part I available as report Jül-Spez 113 and KfK 3175 (1981)

and

G.S. Bauer
"Einige Vorüberlegungen zur Targetstation einer Spallations-Neutronenquelle"
unpublished internal report KFA Jülich, KFA-PSN-IB 1/79 (1979)

/7/ G. Farrell and W.A. Grant
"Radiation Damage in Tungsten: Its Influence on the Trapping and Subsequent Thermal Desorption of Helium"
rad. eff. 3 (1970), 249

/8/ V.K. Sikka, J. Moteff
"Treshold Temperature for Void Formation in the Group VIa Metals"
Trans. Am. Nucl. Soc. 16 (1973), 97

/9/ J. Matolich, H. Nahm and J. Moteff
"Swelling in Neutron Irradiated Tungsten and Tungsten-25 Percent Rhenium"
Scr. Met. 8 (1974), 837

/10/ V.N. Bykov, G.A. Birzhevoi and M.I. Zakharova
"Change in the Density of Single-Crystal Tungsten During Neutron Irradiation"
At. Energ. (USSR) 32 (1972), 323

/11/ J.M. Steichen
"Tensile Properties of Neutron Irradiated TZM and Tungsten"
J. Nucl. Mat. 60 (1976), 13

/12/ W.D. Wilkinson, in
"Properties of Refractory Metals", New York (1969), p. 165

/13/ C.L. Younger and G.N. Wrights
"Effect of Reactor Irradiation on Ductile-Brittle Transition and Stress-Strain Behavior of Tungsten"
NASA-Report, Sept. 1970

/14/ G.S. Bauer, H.M. Conrad, F. Gompf, H. Spitzer und W. Reichardt
"Neutronenausflüsse aus wasserstoffhaltigen Moderatoren einer Spallations-Neutronenquelle für verschiedene Geometrien und Materialkombinationen des Target-Moderator-Reflektorsystems"
unpublished report in part III of the SNQ study

/15/ G.J. Russell, M.M. Meier, J.S. Gilmore, R.E. Prool, H. Robinson and A.D. Taylor
"Measurement of Spallation Target-Moderator-Reflector Neutronics at the Weapons Neutron Research Facility"
Proc. ICANS V-meeting, report KENS II (1981)

/16/ The IKOR study group:
"IKOR, An isochronous compressor ring for proton beams"
G. Schaffer, ed.
report Jül-Spez-114 (1981)

/17/ P. Sievers
"Elastic Stress Waves in Matter Due to Rapid Heating by an Intense High Energy Particle Beam"
unpublished internal report CERN (1976)

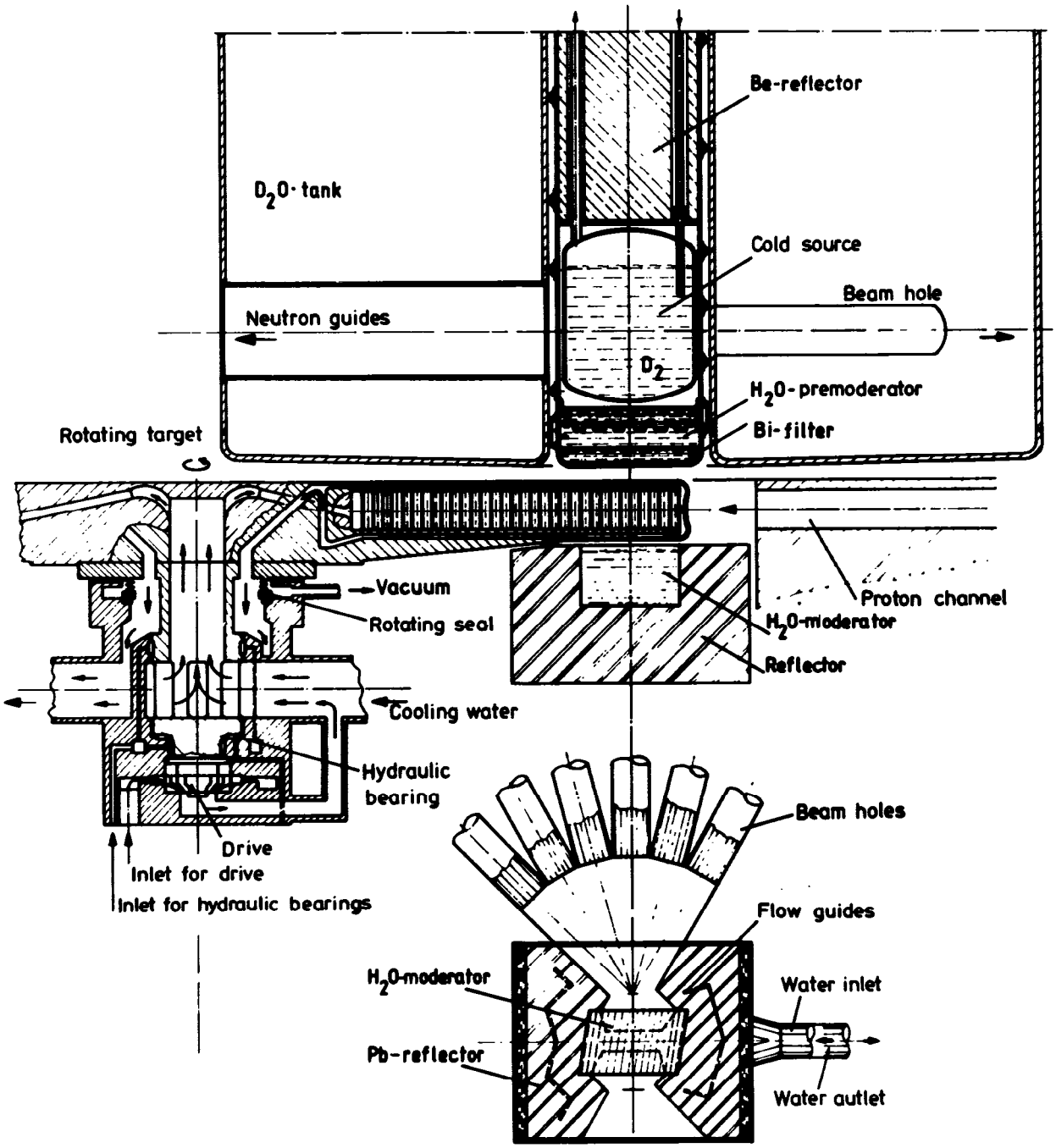

Fig. 1 Target-moderator arrangement as proposed for the SNQ target station DIANE. The individual target elements are directly cooled by water flowing between them and returning to the hub of the wheel through the upper and lower support structure.

Materials constant: Temperature independent thermal conductivity: 1.5 W/cmK

volume heat capacity: $\rho \cdot c = 2.5/J/cm^3K$

Young's modulus and thermal expansion temperature dependent

maximum heat density: 211 kW/cm^3 (during pulse)

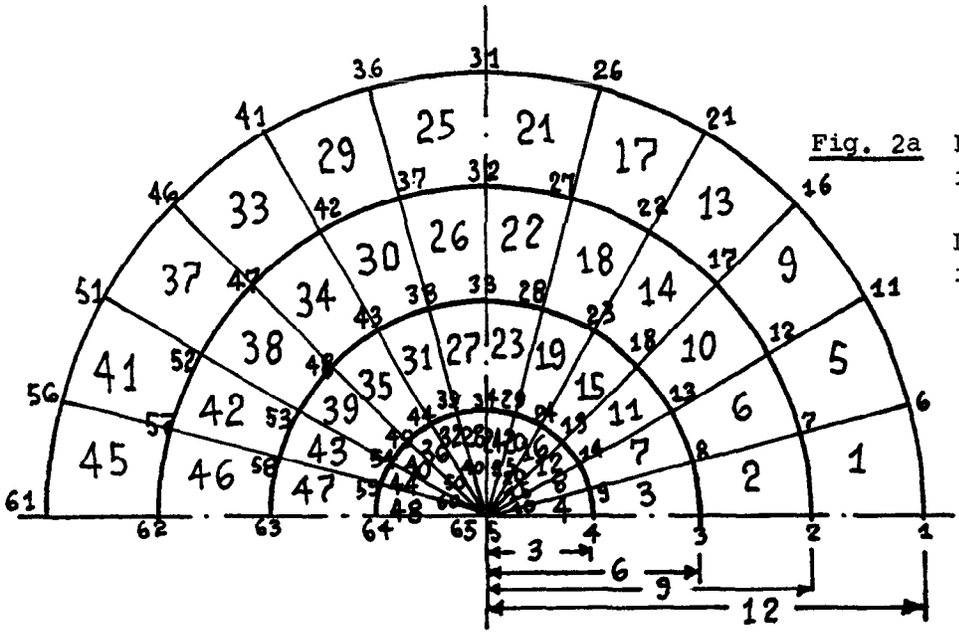

Fig. 2a Labelling of nodes in nodal plane 1

Labelling of elements in level 1

total of 288 elements and 455 nodes.

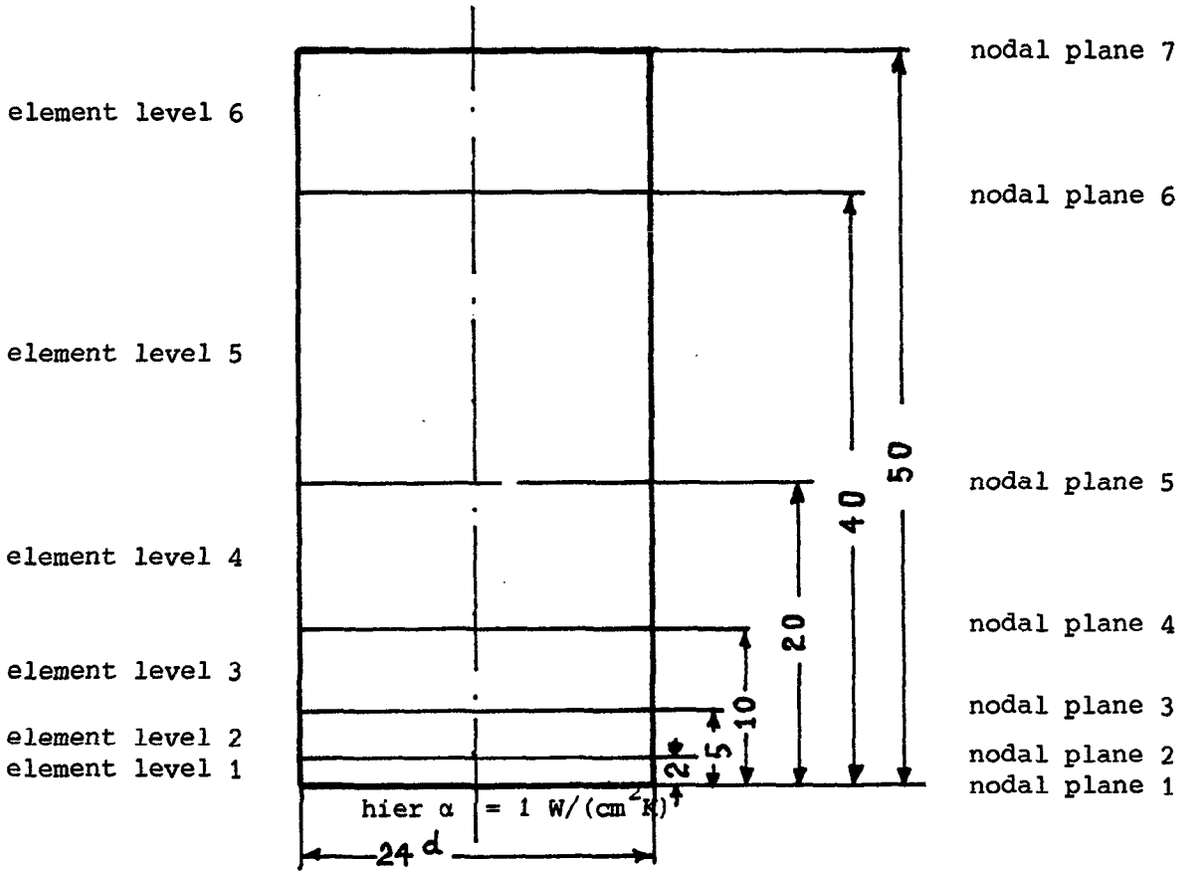

Fig. 2b Dimensions used for the mathematical model.

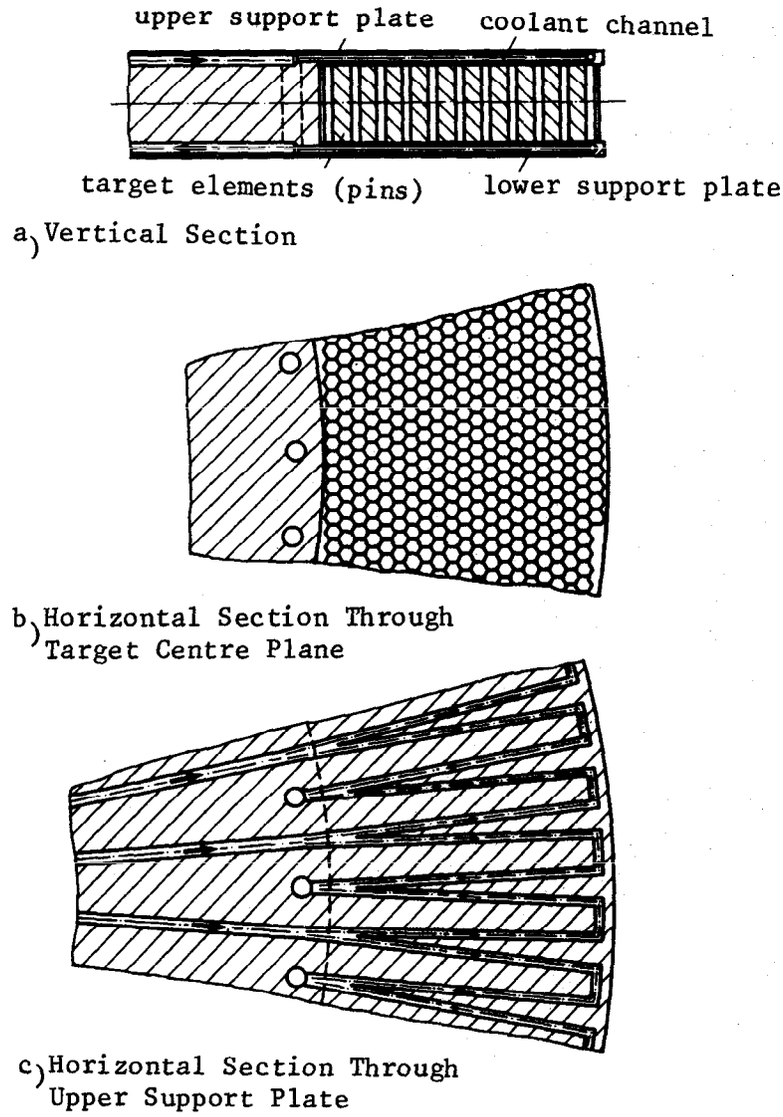

Fig. 3 Target region of a rotating W-target. Coolant flows only in the support structure, not between the hexagonal target elements.

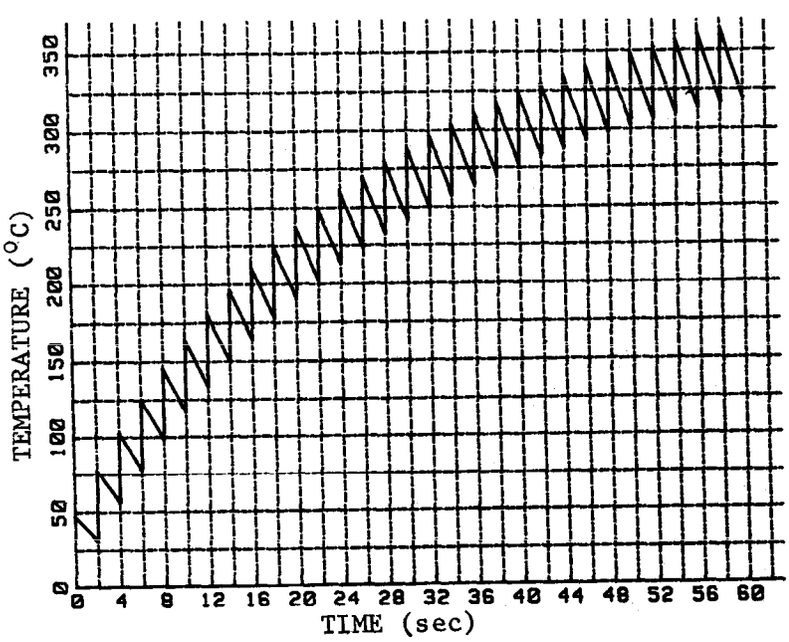

Fig. 4 Time dependence of temperature at the hot spot after start-up of the source at full power (node 391).

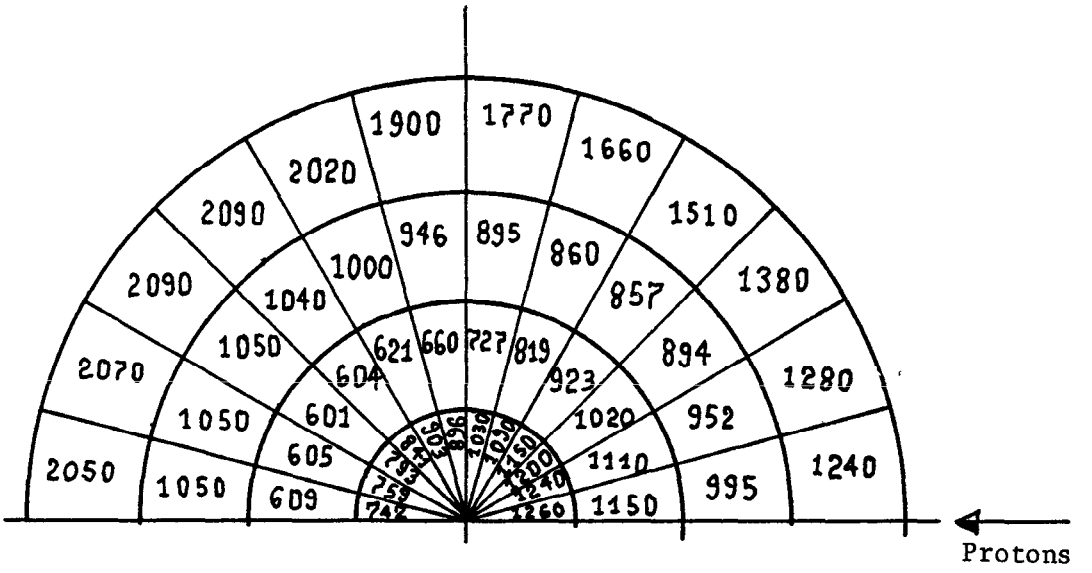

Fig. 5 Reference stresses in N/cm² in element level 6, the most highly stressed level, after 30 revolutions. The tensile strength of W at the temperature in question is about 340.000 N/cm².

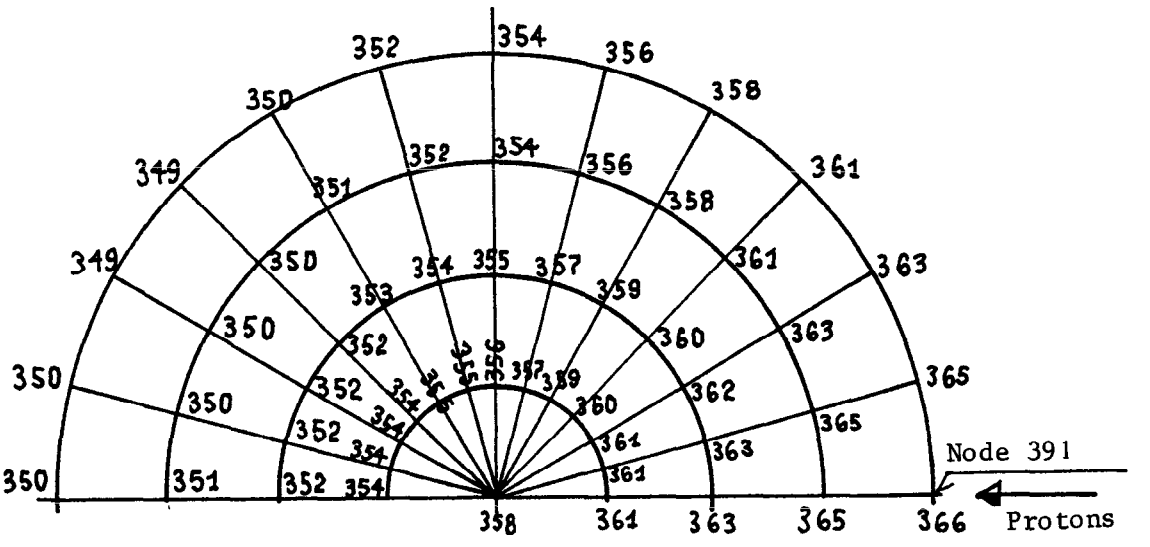

Fig. 6 Temperatures at the nodes of nodal plane 7 after 30 revolutions of the target wheel. This is the plane showing the highest temperatures.

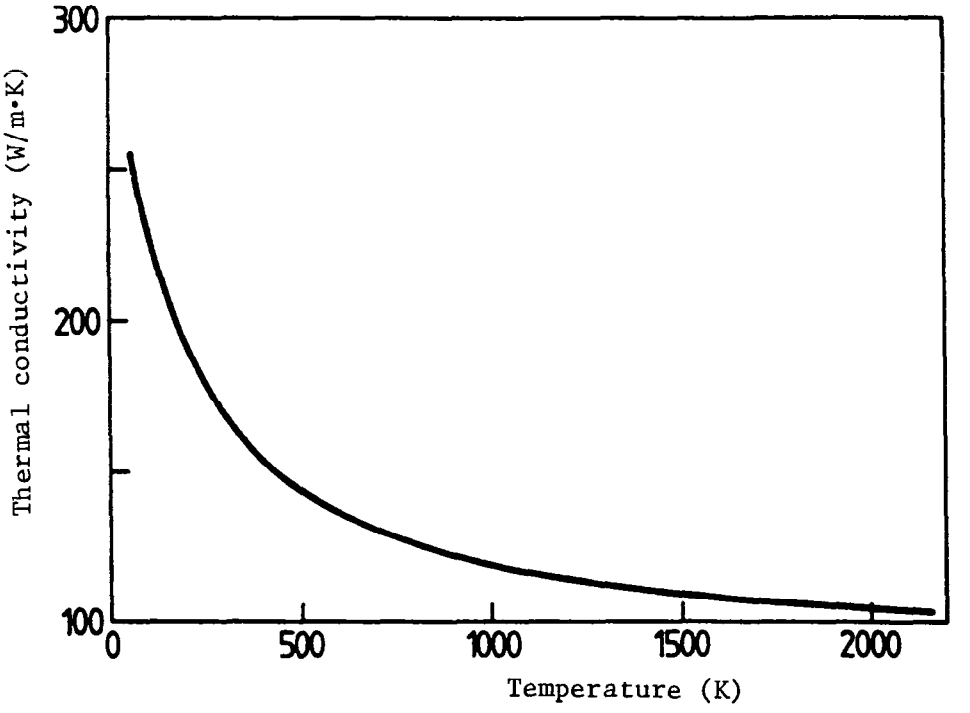

Fig. 7 Thermal conductivity of tungsten as a function of temperature.

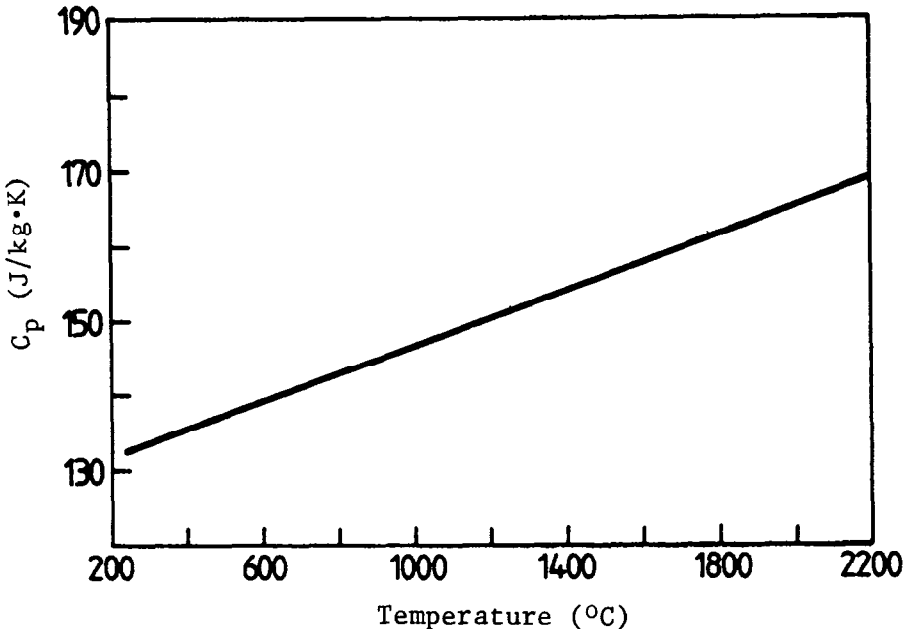

Fig. 8 Specific heat capacity of tungsten as a function of temperature.

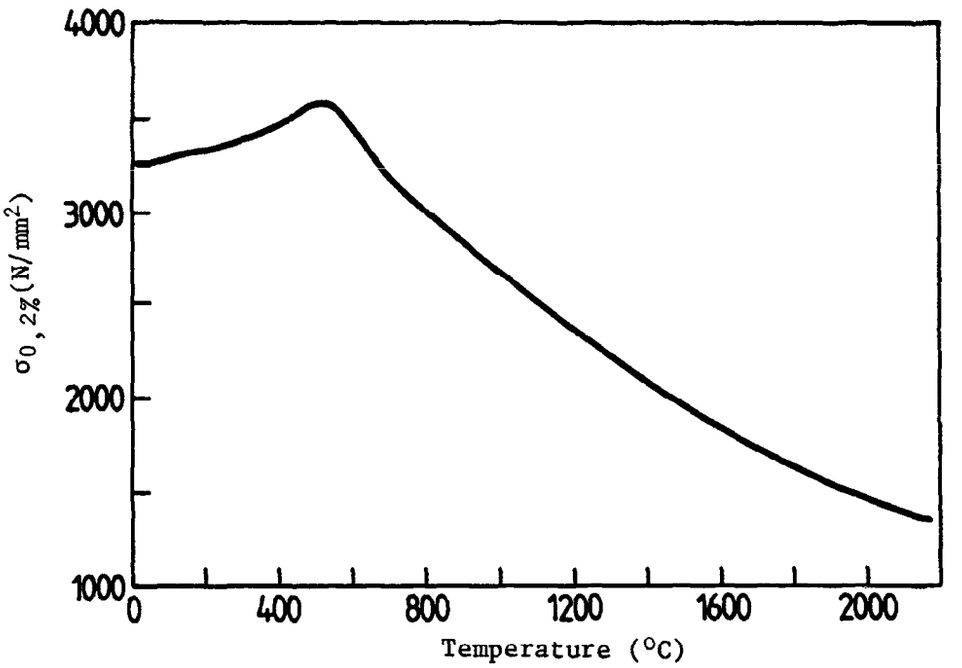

Fig. 9 Yield stress of tungsten as a function of temperature.

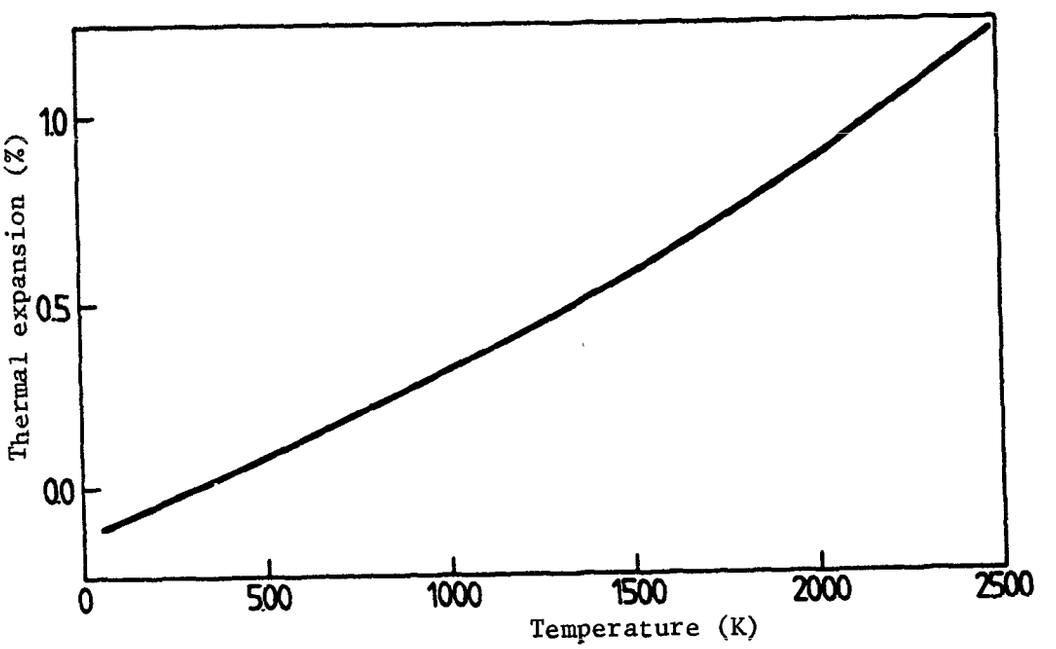

Fig. 10 Linear thermal expansion of tungsten between 0°C and T.

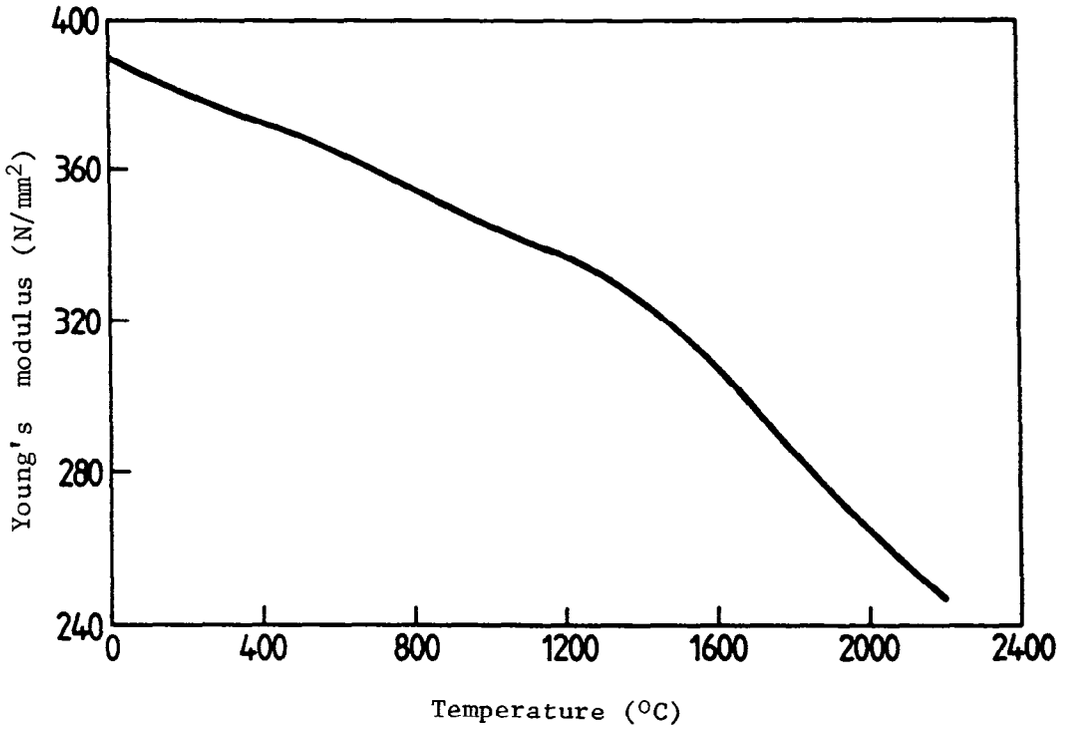

Fig. 11 Young's modulus of tungsten as a function of temperature.

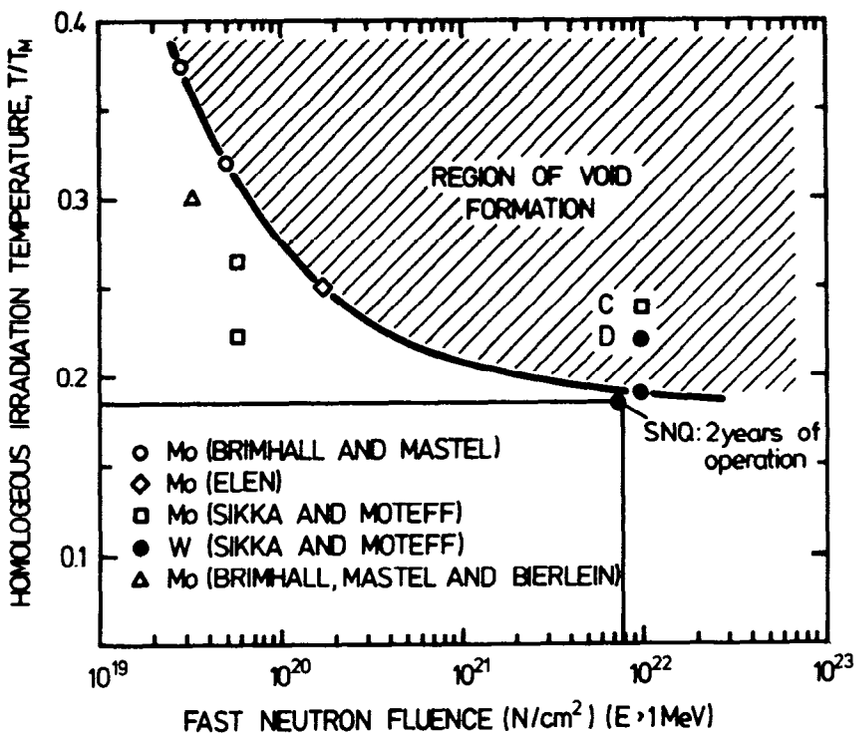

Fig. 12 Temperature- and fluence dependence of the void formation in the group VIa refractory metals /8/. The expected damage of 7.6 dpa after two years of operation corresponds to roughly $7.8 \cdot 10^{21}$ n/cm^2 (E > 1 MeV). For a temperature of 680 K = 0.18 • T_m, the region of void formation is not reached.

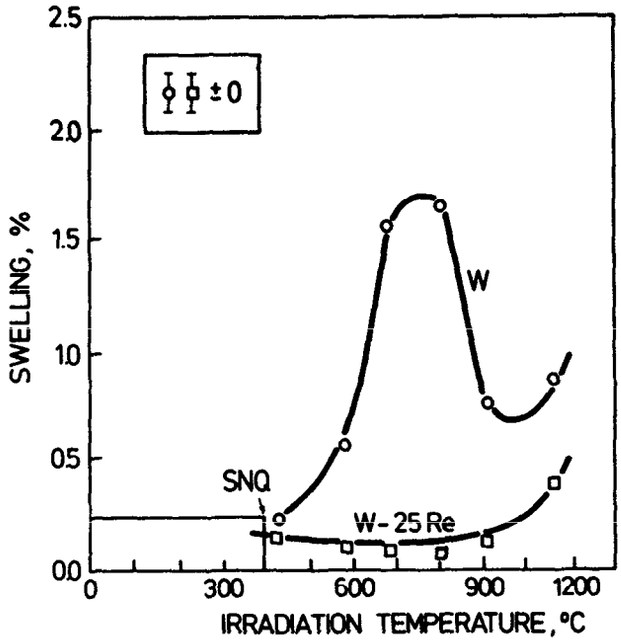

Fig. 13 Swelling of irradiated W (O) and W-25 Re (□) after 9.5 dpa as a function of temperature /9/. The SNQ operating temperature of about 410°C lies far away from the peak swelling temperature.

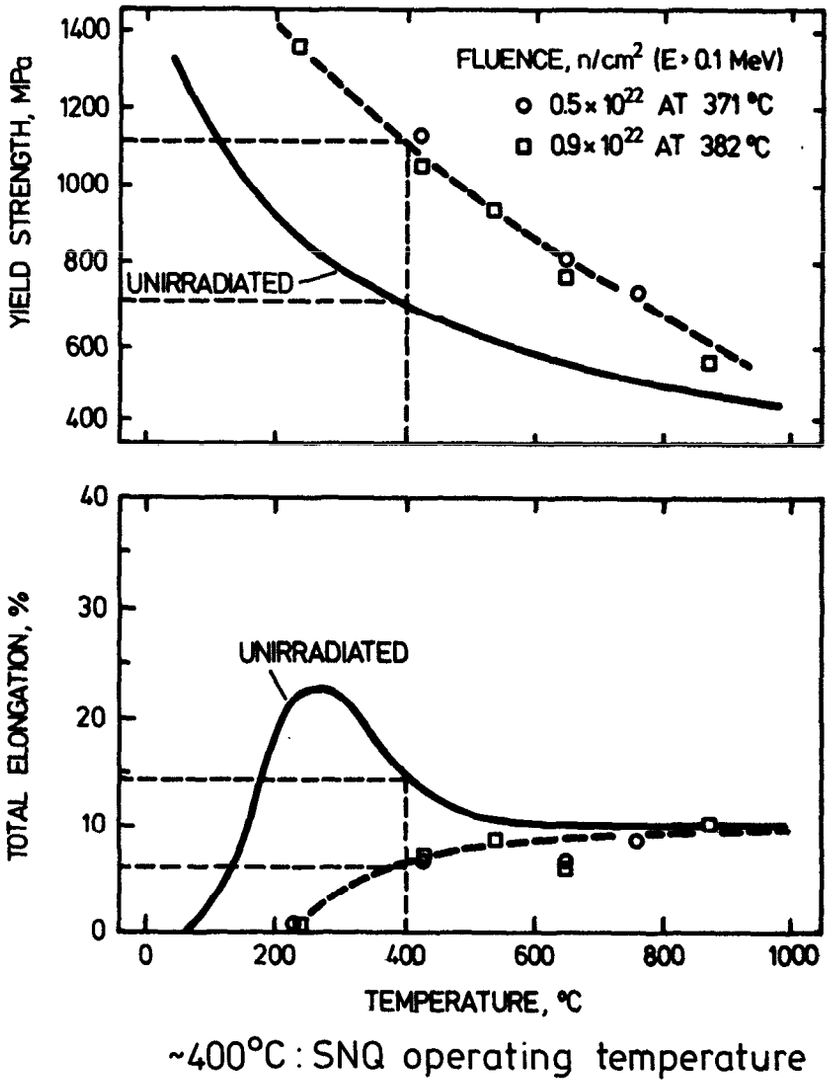

Fig. 14 Temperature dependence of strength (upper part) and ductility (lower part) of unirradiated and irradiated (1.6 dpa at 385°C) tungsten /11/.

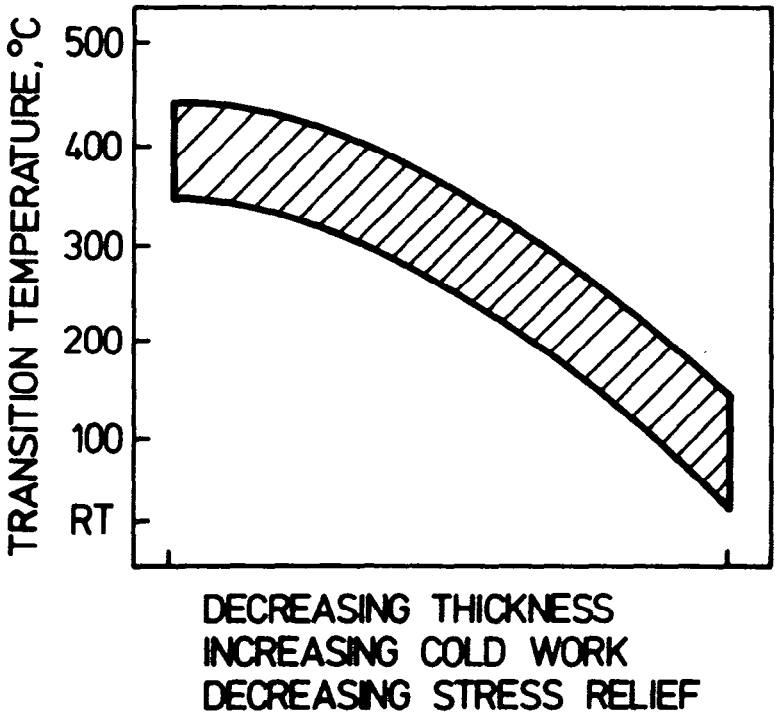

Fig. 15 Influence of processing parameters on the ductile-brittle transition temperature of flat-rolled, powder-metallurgy tungsten products /12/.

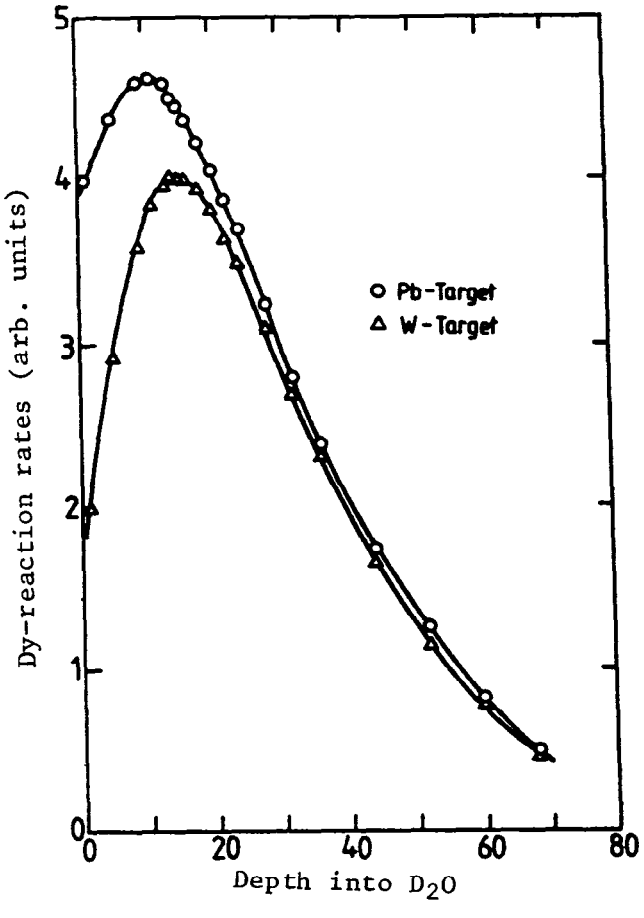

Fig. 16 Comparison of measured thermal neutron flux distribution in a D_2O-tank located below targets of Pb resp. W. Proton energy was 600 MeV.

Jül-Conf-45

D4-4

I C A N S - V

MEETING OF THE INTERNATIONAL COLLABORATION ON

ADVANCED NEUTRON SOURCES

June 22-26, 1981

REMARKS CONCERNING THE EFFICIENCY OF A BOOSTER NEUTRON SOURCE

W. Kley

Department of Natural Science and Physics
Commission of the European Communities
Joint Research Centre - Ispra Establishment
21020 Ispra (Va) - Italy

ABSTRACT

In the present paper criteria are defined for the comparison of the efficiency of a multiplying booster target with a non-multiplying accelerator target for different injection times and pulse widths. In order to obtain a "symmetric pulse" from the booster, the "Effective Figure of Merit": EFM = 0.75 A, where A stands for the multiplication of the booster. It is shown that for solid state physics scattering experiments using impinging neutrons in the energy range of $0.05 \leq E \leq 10$ eV, there exists a lower limit of one μsec for the pulse width and therefore a booster target with an amplification of A = 10, a generation time $\tau = 0.02$ μsec, has a "Figure of Merit": FM = 10 and for "symmetric pulses" an EFM = 7.5. For the epi-thermal energy region, an optimum slowing down flux is achieved for an effective water moderator thickness of 28 mm resulting in an energy dependent moderator pulse width: $\Delta t \cong 2/\sqrt{E}$ (μsec, E in eV). If the booster pulse is matched to the moderator response function, then the accelerator injection time $t_0 \cong \frac{1}{2}\Delta t$. This leads to an energy dependent figure of merit: FM(E), that is rapidly decreasing with energy and equal to one at 50 eV.

I. INTRODUCTION

The first powerful booster target has been constructed and operated by Pool[1] at Harwell. It was and it is used for neutron cross section work in the epithermal neutron energy range. In neutron "Time Of Flight" (TOF) experiments, the "Figure Of Merit" (FM)[2-8] is given by

$$FM = \frac{\int_0^\infty \phi(t)dt}{\sigma^n} \tag{1}$$

where σ^2 is the variance of the neutron pulse and given by

$$\sigma^2 = \frac{\int_0^\infty t^2 \phi(t)dt}{\int_0^\infty \phi(t)dt}. \tag{2}$$

In equation (1), "n" may vary[8,9] as

$$0 \leqslant n \leqslant 4. \tag{3}$$

For a simple transmission experiment and also for some scattering experiments, the figure of merit is given by

$$FM = \frac{\int_0^\infty \phi(t)dt}{\sigma^2}. \tag{4}$$

In the following considerations we limit ourselves to that definition of the figure of merit to be used to characterize the efficiency of a booster target.

II. COMPARISON OF THE EFFICIENCY OF A MULTIPLYING BOOSTER TARGET COMPARED TO A NON-MULTIPLYING ACCELERATOR TARGET

If ϕ_0 (n/sec) is the accelerator neutron source strength without multiplication, the neutron source strength of the booster target changes per unit time as follows[10]:

$$\frac{d\phi_B}{dt} = -\lambda\phi_B + \frac{\phi_0}{\tau} \tag{5}$$

where the decay constant is given by

$$\lambda = \frac{|\epsilon|}{\tau} = \frac{k(1-\beta)-1}{\tau} = \frac{1}{\tau A} \tag{6}$$

and where $A = \frac{1}{|\epsilon|}$ is the amplification, τ the generation time, the time between consecutive fissions, k is the multiplication factor and β the delayed neutron fraction in the booster target.
From equation (5) and (6) follows

$$\phi_B(t) = A\phi_0 + (1-A)\phi_0 e^{-\frac{t}{\tau A}} \tag{7}$$

In Fig. 1 the pulse shape is shown for a booster target pulse with amplification of 10 and different injection times $X = \frac{t_0}{\tau} = 1$, 6, 10 and ∞, where t_0 is the injection time in units of τ, the generation time. The figure of merit of the booster pulse compared to the respective accelerator input pulse is given by:

$$FM = FM(A, \tau_0, t_0) = \frac{FM\ (\text{Booster})}{FM\ (\text{Accelerator})} = \tag{8}$$

$$= \frac{[\int_0^\infty \phi_B(t)dt]^2 / \int_0^\infty t^2 \phi_B(t)dt \quad \text{Booster}}{[\int_0^{t_0} \phi_{Ac}(t)dt]^2 / \int_0^{t_0} t^2 \phi_{Ac}(t)dt \quad \text{Accelerator}}$$

$$FM(A, \tau, t_0) = \frac{A^2}{A - 3(1-A)e^{-\frac{X}{A}}\left(\frac{A}{X} + \frac{2A^2}{X^2}\right) + \frac{6A^3}{X^3}}$$

where $X = \frac{t_0}{\tau}$. This figure of merit, FM, has been plotted in Figs. 2 and 3 for an amplification of 5 and 10 respectively. Note that the injection time t_0/τ has to be 5 and 7 correspondingly in order to obtain the same performance characteristic as the accelerator itself. Only for longer injection times the maximum value of 5 and 10 can be reached.

III. THE "SYMMETRIC PULSE SHAPE CONDITION" FOR THE BOOSTER PULSE

For a number of reasons it is desirable to have a "symmetric pulse shape" also for the booster pulse. In order to achieve that we have to request that

$$\sigma_1^2 \equiv \sigma_2^2 \tag{9}$$

where

$$\sigma_1^2 = \frac{\int_0^{t_0} t^2 \phi_B(t)dt}{\int_0^{t_0} \phi_B(t)dt} \tag{10}$$

and

$$\sigma_2^2 = \frac{\int_{t-t_0}^{\infty} (t-t_0)^2 \phi_B(t_0) e^{-\lambda(t-t_0)}\, dt}{\int_{t-t_0}^{\infty} \phi_B(t_0)\, e^{-\lambda(t-t_0)}\, dt} \tag{11}$$

for $t \geqslant t_0$, as indicated in Fig. 4.

From equations (9), (10) and (11) follows

$$y = \frac{X^2}{3A} - (1-A)e^{-\frac{X}{A}} [\frac{X}{A} + 2] - 2A \overset{!}{\cong} 0 \tag{12}$$

From equation (12) and (8) follows the "Effective Figure of Merit (EFM)" which is plotted as a function of A in Fig. 5. It turns out that the EFM for a symmetric pulse shape is given approximately by

$$\text{EFM} \cong 0.75 \cdot A = 0.75 \text{ FM (maximum)}. \tag{13}$$

IV. THE ADVANTAGES OF A BOOSTER TARGET FOR NEUTRON SCATTERING EXPERIMENTS

For very general reasons such as intensity, moderator-, sample- and detector thickness, we have to match the time- and length of flight path resolution[10,11].

$$\frac{\Delta t}{t} = \frac{\Delta t}{\ell} v \equiv \frac{\Delta \ell}{\ell} \approx \frac{4 \times 10^{-2}}{40} = 10^{-3} \tag{14}$$

or

$$\Delta t \cong 10^{-6} \text{ sec} \tag{15}$$

where Δt is the full width at half maximum of the neutron pulse, t the flight time of neutrons with velocity v over a flight path of length ℓ and $\Delta \ell$ is its uncertainty.

Therefore, one μsec pulses are a lower limit in neutron scattering experiments. Considering a booster target with multiplication 10, we obtain according to Fig. 3 for a "symmetric pulse shape" an injection time of $t_0 \cong 22\tau$. Booster targets with a generation time of $\tau \cong 0.02$ μsec can be built leading to an injection time $t_0 \approx 0.5$ μsec and an effective multiplication of 7.5. The booster pulse shape is well matched with the moderator response function of heterogenously poisened moderators[7-11] and neutron energies $E_n \leqslant 10$ eV.

V. THE BOOSTER EFFICIENCY IN THE Epi-THERMAL ENERGY REGION

It has been shown[2-5,7-10] that for epithermal neutrons an optimum slowing down flux is obtained for an effective moderator thickness of 2.8 cm resulting in an energy dependent moderator pulse width of

$$\Delta t = \frac{d}{v} \cong \frac{2}{\sqrt{E}} \ (\mu\text{sec}) \tag{16}$$

where the neutron energy is given in eV.
If we want to match the accelerator booster pulse with the response function of the moderator then the accelerator injection time t_0 ought to be

$$t_0 \cong \tfrac{1}{2}\Delta t = \frac{1}{\sqrt{E}} \ (\mu\text{sec}) \tag{17}$$

or for

$$X = \frac{t_0}{\tau} = \frac{1}{\tau\sqrt{E}} \tag{18}$$

Using equation (8), the energy dependent Figure of Merit has been calculated for an amplification $A = 10$ and a neutron generation time $\tau = 20$ nanosec and the results are plotted in Fig. 6. As we can see from Fig. 6, the booster is only useful for neutron energies below about 50 eV. Around 10 eV, the FM ≈ 5. Therefore the use of booster targets in the epi-thermal energy range is rather limited. The best use of booster targets can be made for solid state physic scattering experiments using impinging neutrons with energies below 10 eV where the maximum Figure of Merit can be obtained.

VI. LITERATURE

1. Pool M.J., Wiblin E.R., Second General Conference on the Peaceful Uses of Atomic Energy, A/Conf. 15/P/59, and Proceedings "Intense Neutron Source", Santa Fe, New Mexico, 1966, pp.431-449, CONF-660925, U.S.A.E.C.-Report.
2. Michaudon A., Reactor Sci. Tech., 17, 165, 1963.
3. Day D.H., Sinclair R.N., Nucl. Inst. Methods, 72, 237, 1969.
4. Fluharty R.G., Simpson F.B., Russel G.J., Menzel J.H., Nucl. Sci. Eng., 35, 45, 1969.
5. Graham K.F., Carpenter J.M., Nucl. Fast. Meth., 85, 163, 1970.
6. Arcipiani B., Fraysse G., Menardi S., Riccobono G., Energia Nucleare, Vol. 14, No. 3, 151, 1967.
7. Rief H., Hartmann J., Annals of Nuclear Energy, Vol.2 pp.521-539, 1975.
8. Kley W., Proceedings of the Joint Meeting on Pulsed Neutrons and their Utilization, Ispra, September 17-18, 1971, EUR-Report 4954e, pp.379-424.
9. Watanabe N., Kimura M., Takahashi H., EUR-4934e, pp.255-291, 1971.
10. Kley W., European Applied Research Reports, Nuclear Science and Technology Section, in print [Remarks concerning the signal and signal to background ratio at pulsed spallation nuetron sources and their respective optimum target moderator-geometry].
11. Kley W., EuRoPean Applied Research Reports, Nuclear Science and Technology Section, in print [Time of Flight Spectrometry at pulsed spallation neutron sources].

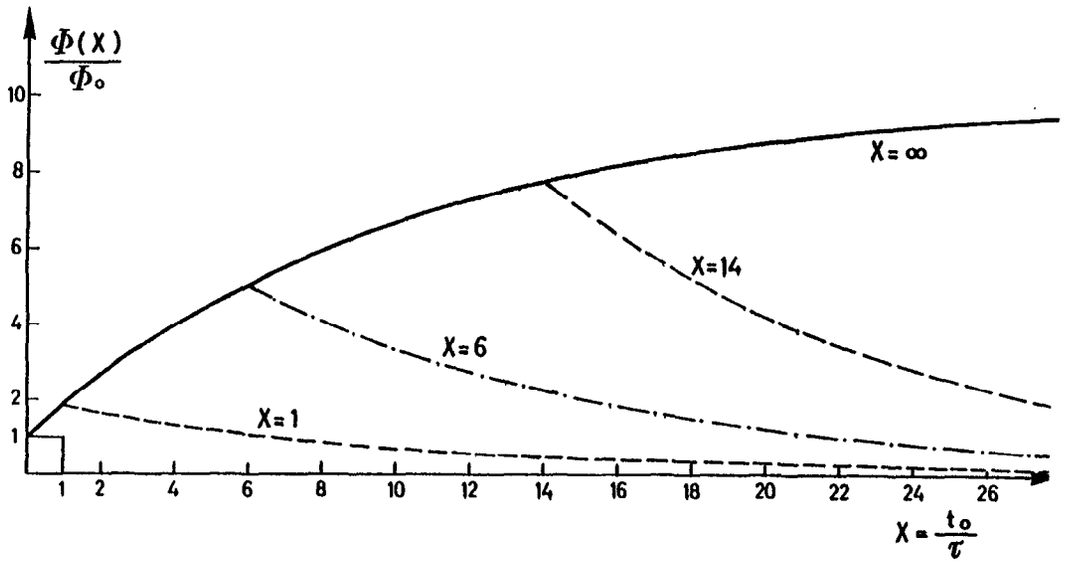

Fig. 1 - Pulseshape of a boosterpulse with amplification 10 and different injection times $X = \frac{t_0}{\tau} = 1, 6, 10$ and ∞

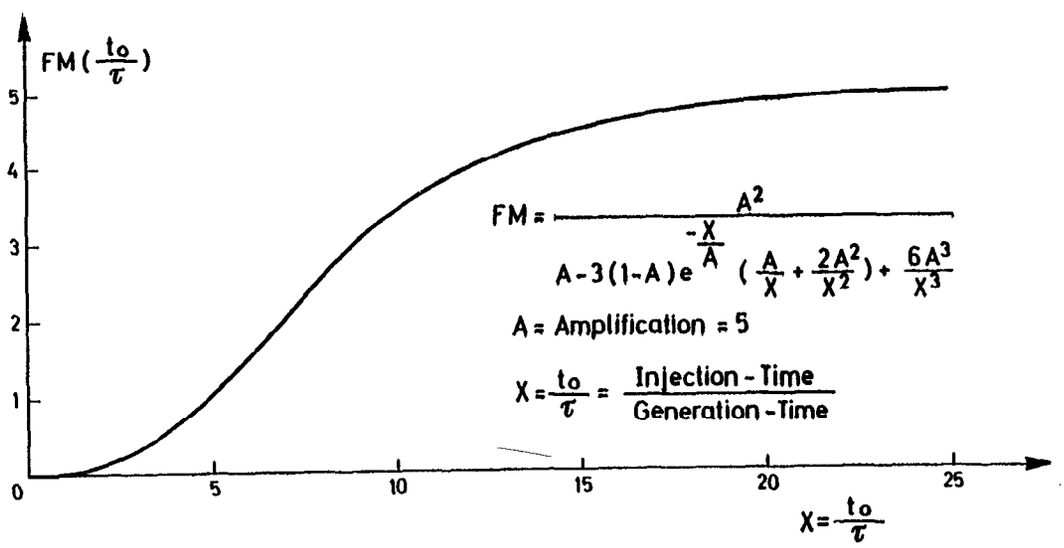

Fig. 2 - Figure of Merit for a Booster target with Amplification of 5

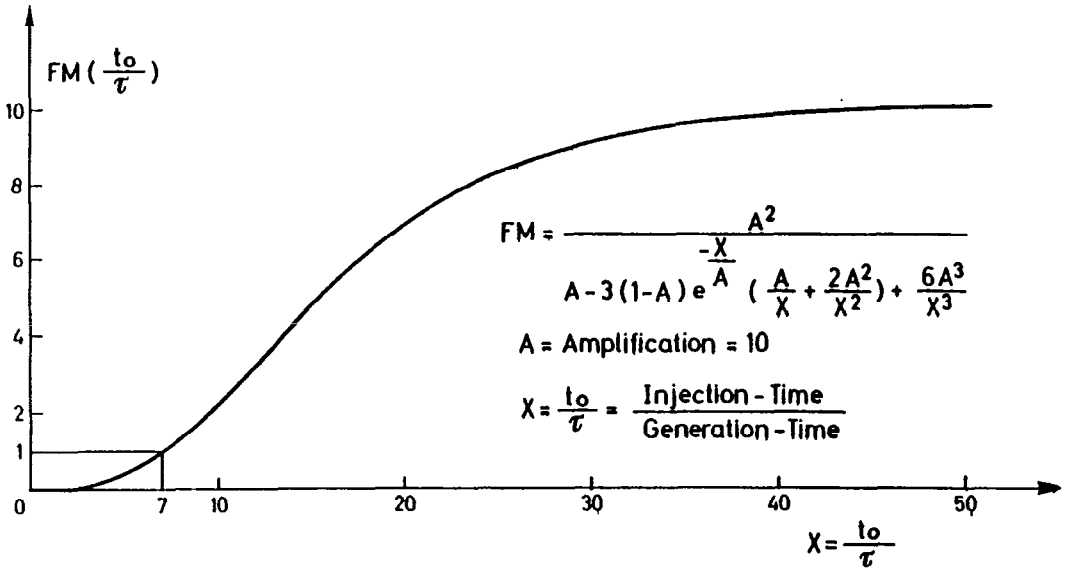

Fig. 3 - Figure of Merit for a Booster target with Amplification of 10

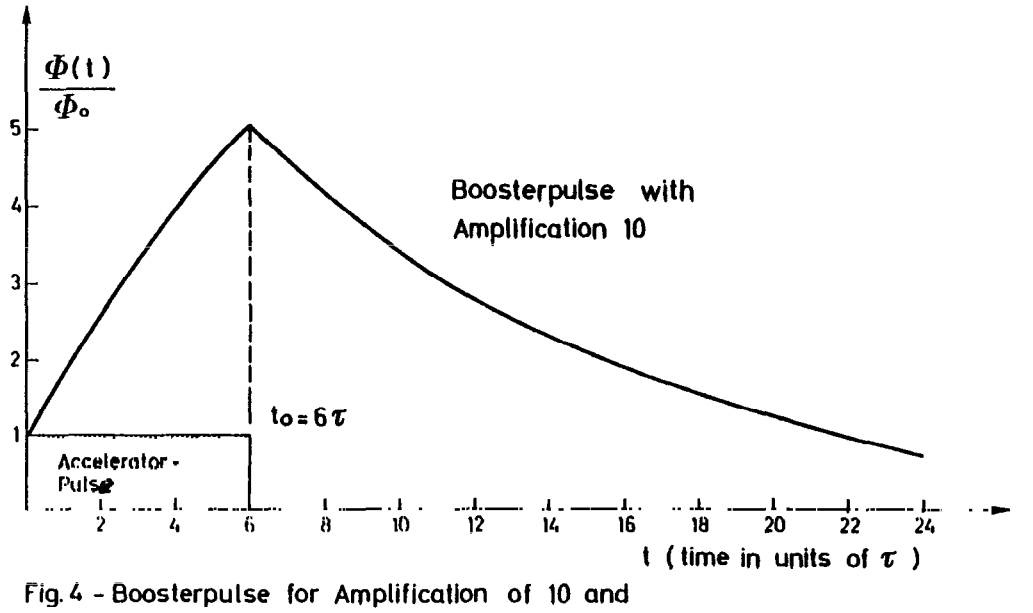

Fig. 4 - Boosterpulse for Amplification of 10 and Injection time : $t_o = 6\tau$

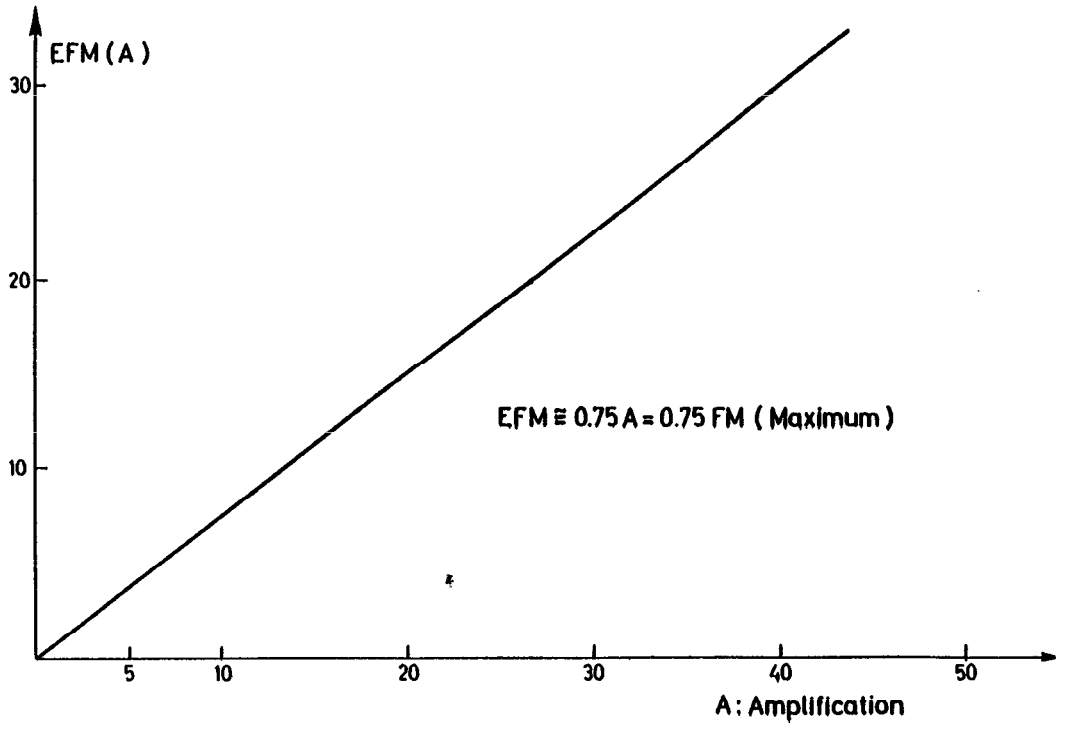

Fig. 5 = The Effective Figure of Merit for Symmetric Pulse- Shape

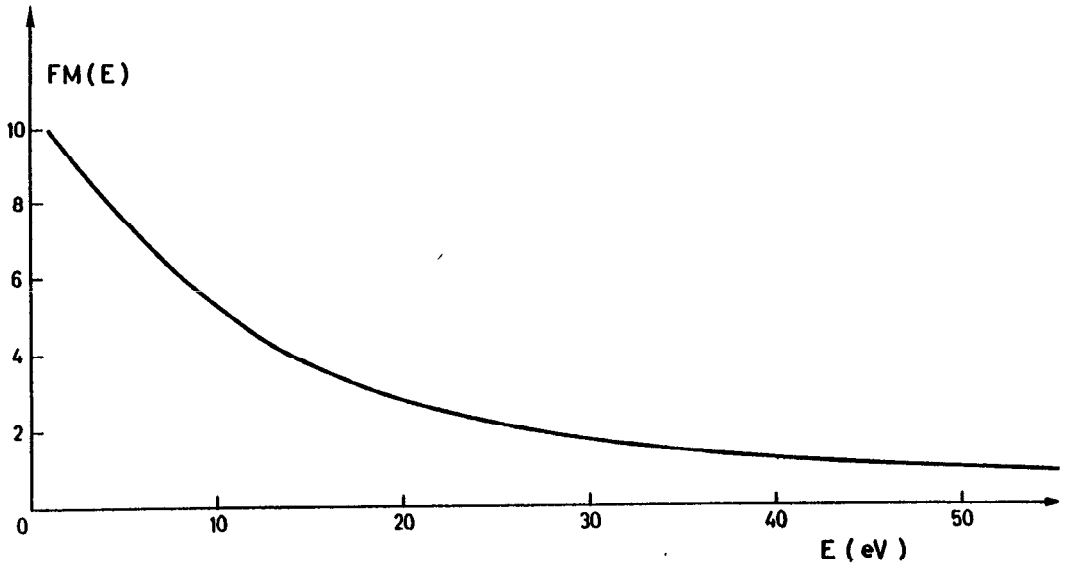

Fig. 6 - Figure of Merit for a Booster target as Function of Neutron energy with Amplification of 10 and generation time τ = 0.02 μsec

ICANS V

MEETING OF THE INTERNATIONAL COLLABORATION ON

ADVANCED NEUTRON SOURCES

June 22-26, 1981

Fertile-to-Fissile and Fission Measurements for Depleted Uranium Bombarded by 800-MeV Protons

G. J. Russell, J. S. Gilmore, H. Robinson, and R. E. Prael
Los Alamos National Laboratory
Los Alamos, New Mexico 87545, U.S.A.

ABSTRACT

Axial distributions of fertile-to-fissile conversions (^{238}U to ^{239}Pu) and fissions have been measured for a thick depleted uranium target bombarded by 800-MeV protons. We determine the ^{239}Pu production by measuring the amount of ^{239}Np produced. We integrate the axial distributions to get the total conversions and fissions occurring in the target. Our preliminary experimental results give 3.81 ± 0.19 ^{239}Np atoms produced per incident proton and 5.59 ± 0.56 fissions per incident proton. Corresponding calculated results are 3.46 ± 0.05 and 3.93 ± 0.06. The computations did not include the effects of high-energy fission competition with evaporation. We also report measured axial distributions of ^{237}U and eleven fission products produced in the target. Our preliminary experimental data give 0.95 ± 0.05 ^{237}U atoms made per incident proton.

INTRODUCTION

As part of the Fertile-to-Fissile Conversion (FERFICON) program[1,2] at the Los Alamos National Laboratory, we have measured (in a thick target of depleted uranium bombarded by 800-MeV protons): a) ^{239}Pu production, b) fission, and c) ^{237}U formation. We determine ^{239}Pu production by measuring the amount of ^{239}Np formed. Other laboratories[3,4] have made similar measurements (at proton energies < 800 MeV) by observing both the radial and axial distributions of the products of interest. Our experimental approach differs significantly (as suggested by one of the authors - J. S. Gilmore) in that we combined the depleted uranium foils to integrate the product formation radially, and only explicitly measured the axial distribution for the products of interest. This substantially reduced the number of samples to be counted, and the number of gamma-ray spectra to be analyzed. We integrate the measured axial distributions over the target to obtain the total number of each reaction.

The data described here are relevant to spallation neutron source development, accelerator breeder technology, and validating computer codes used in these applications (model evaluation). We will compare our experimental data with calculated predictions using the following Monte Carlo codes: a) the Oak Ridge National Laboratory (ORNL) code HETC[5] for particle transport $\gtrsim$ 20 MeV, and b) the Los Alamos code MCNP[6] for neutron transport $\lesssim$ 20 MeV. The present Los Alamos version of HETC does not include fission when predicting particle production from nucleon and pion collisions with a fissile nucleus. A version of HETC which accounts for this high-energy fission process in uranium will soon be released by ORNL[7]; Los Alamos has requested this version of HETC from ORNL.

The 800-MeV proton source is the Clinton P. Anderson Meson Physics Facility (LAMPF).[8] We conduct the experiments at the Weapons Neutron Research facility (WNR)[9] -- see Fig. 1. We describe here our experimental setup, show some preliminary results, and compare some of our data with calculated predictions.

EXPERIMENTAL SETUP AND PROCEDURES

The location of this 'conversion' experiment in the WNR beam channel is illustrated in Fig. 2. We used a 37-rod clustered target as shown in Fig. 3. The physical characteristics of the target are given in Table I. The axial distributions of ^{239}Np, 11 fission products, and ^{237}U (a spallation product) were determined from 171 (3.239-cm diam by 0.0062-cm thick) depleted uranium foils. Nineteen weighed and matched ($\sim$1 g) foils were placed in each of seven planes perpendicular to the target axis and on the front and back target faces (see Fig. 4). Each of the 9 planes contained one foil in the central rod and 18 foils loaded symmetrically in 3 of the 6 target sectors (see Fig. 3). We chose this loading for mechanical reasons and to minimize any effects from misaligning the proton beam, which was focused on the central rod.

After an irradiation of 4.3×10^{15} protons, we prepared nine solutions for counting by dissolving the foils in hydrochloric and nitric acids. For each plane, a representative sample was obtained by mixing one-half the solution of the central-rod foil with the solution of the remaining eighteen foils. Five percent (5.00 ml) of each combined solution was used for gamma-ray counting.

To determine the number of protons striking the target, we placed a 0.0254-cm-thick Al monitor foil (sandwiched between two 0.00254-cm-thick Al guard foils to compensate for recoil losses) ~ 65 cm in front of the target. We used the number of $^{27}Al(p,x)^{7}Be$, $^{27}Al(p,x)^{22}Na$, and $^{27}Al(p,3pn)^{24}Na$ reactions occurring in the monitor foil to determine the incident proton dose. The guard foils were sufficiently thick (~ 7 mg/cm^2) to compensate for ^{7}Be, ^{22}Na, and ^{24}Na recoil losses from the central monitor-foil.[10] The number of protons determined from each of these reactions is given in Table II; we ultimately use the $^{27}Al(p,3pn)^{24}Na$ reaction in our normalizations because the cross section for this reaction is known best.[10] We located the proton beam center from the discoloration of a cellophane foil that covered one of the Al guard foils, and measured the proton beam profile by counting concentric rings cut from one of the guard foils (see Fig. 5).

All samples were counted using a Ge(Li) detector and associated pulse height analyzer, which had been calibrated against a mixed radionuclide gamma-ray reference standard.* The gamma-ray spectra were analyzed by the GAMANAL computer program.[11] After combining data from five or more counts by the CLSQ computer code,[12] we calculated the atoms of each nuclide formed using the specific gamma-rays, absolute intensities, and half-lives listed in Table III. Two of the isotopes (^{105}Rh and ^{147}Nd) had to be resolved from interfering activities by decay. We corrected all nuclide production for decay during irradiation and for gamma-ray attenuation in the sample.

EXPERIMENTAL RESULTS AND CONCLUSIONS

In Figs. 6-8, we show the measured number of atoms produced per proton per gram of uranium for eleven fission products. The shape of these (unnormalized) fission mass-yield curves do not change appreciably from front to back of the target. This latter point is further illustrated in Fig. 9 where we show the ratio of each fission product to ^{99}Mo as a function of axial position.

As shown in Fig. 10, the apparent fission-yield curve from this experiment resembles the known ~14.7-MeV-neutron fission of ^{238}U.[13] In Fig. 10, we compare this latter curve with our (average) measured value for each fission product. We obtained our yields by ratioing our measured

* Amersham Corporation solution number R9/270/46.

values to that of ^{99}Mo; our 'best' estimate of the ^{99}Mo absolute yield is (5.7 ± 0.5)%. We selected our ^{99}Mo yield by envisioning curves whose summation would be noticeably greater or lower than 200% if the ^{99}Mo yield were as high as 6.2% or as low as 5.2%, respectively.
The axial distributions of the fissions (based on a ^{99}Mo yield of 5.7%), ^{239}Np (^{239}Pu precursor), and ^{237}U are shown in Fig. 11 and tabulated in Table IV. The axial fission distribution is an important practical consideration (from an energy deposition viewpoint) when designing a uranium target for a spallation neutron source,[14] while the peak in the axial distribution of ^{239}Np is an aid in locating moderators to maximize low-energy ($\lesssim 1$ eV) neutron production from a uranium target.

The total number (per proton) for each reaction is

$$\text{Total}_i = \frac{M}{\ell \cdot p} \int N_i(z)dz \quad , \tag{1}$$

where M is the mass of the target in grams, ℓ is the target length in cm, p is the number of protons, and N_i is the number of atoms produced per gram of uranium. We evaluated the integral (over the target volume) using Simpson's rule. Table V lists the measured ^{239}Np, fission, and ^{237}U production per incident proton from the 30.46-cm-long target. In Table V, we also show some calculated predictions for two target lengths; the longer target was used in the Los Alamos FERFICON water-bath measurements.[1,2] In these preliminary computations, we mocked-up the rod geometry of the target exactly (exclusive of the Al target canister, etc.), and used a Gaussian proton beam spot with a standard deviation of 0.35 cm and 0.26 cm for the shorter and longer targets, respectively. When high-energy fission[15] is neglected in the computation, our preliminary comparisons between experiment and calculation show: a) that neutron production is underestimated by ~10%, and b) that the number of fissions is underestimated by ~42%. Note that the calculated quantities do not change appreciably for the 40.64-cm target compared to the 30.46-cm target. We are still evaluating our data and hope to report a few more fission and spallation product distributions in a final publication. For comparison with experimental data, we will calculate the axial distribution of the various products and the total product formation in the target. We will make a similar measurement using a thorium target in the near future.

ACKNOWLEDGEMENTS

This work was performed under the auspices of the U. S. Department of Energy. We would like to acknowledge the support and encouragement of R. Woods, and useful discussions with I. M. Thorson, A. J. Miller, and J. H. Cook. We appreciate the help of J. R. Baldonado and K. J. Hughes in setting up the experiment and of R. D. Ryder and H. M. Howard for beam tuning and assistance during the irradiation. The target canister was remotely disassembled by A. G. Nicol and F. H. Newbury. We acknowledge the help of G. W. Knobeloch and J. Drake for preparing samples, G. W.

Butler for advice and assistance in counting and the use of GAMANAL and CLSQ computer programs, I. Binder for processing the Al monitor foils, and all the counting room personnel in the Los Alamos Nuclear Chemistry group. E. R. Whitaker's help in preparing the illustrations is greatly appreciated.

REFERENCES

1. G. J. Russell, et al., "Spallation Target-Moderator-Reflector Studies at the Weapons Neutron Research Facility," Symp. on Neutron Cross Sections from 10-50 MeV, Brookhaven National Laboratory, Upton, NY, May 12-14, 1980, BNL-NCS-51245, Vol. I, pp. 169-192.

2. G. J. Russell, et al., "Measurements of Spallation Target-Moderator-Reflector Neutronics at the Weapons Neutron Research Facility," Proc. of the 4th Meeting of the International Collaboration on Advanced Neutron Sources (ICANS-IV), National Laboratory for High Energy Physics (KEK), Tsukuba, Japan, October 20-24, 1980, KENS report II (March 1981).

3. R. G. Vasil'kov, et al., "Neutron Multiplication in Uranium Bombarded with 300-600-MeV Protons," Atomnaya Energiya, 44, No. 4, pp. 329-335 (1978).

4. I. M. Thorson, private communication.

5. K. C. Chandler and T. W. Armstrong, "Operating Instructions for the High Energy Nucleon Meson Transport Code HETC," Oak Ridge National Laboratory report ORNL-4744 (January 1972).

6. W. L. Thompson, ed., "MCNP - A General Monte Carlo Code for Neutron and Photon Transport," Los Alamos Scientific Laboratory report LA-7396-M (November 1979).

7. F. S. Alsmiller, et al., "A Phenomenological Model for Particle Production from the Collisions of Nucleons and Pions with Fissile Elements at Medium Energies," Oak Ridge National Laboratory report ORNL/TM-7528 (March 1981).

8. M. S. Livingston, "LAMPF A NUCLEAR RESEARCH FACILITY," Los Alamos Scientific Laboraotory report LA-6878-MS, UC-28 and UC-34 (September 1977).

9. G. J. Russell, et al., "The WNR Facility -- A Pulsed Spallation Neutron Source at the Los Alamos Scientific Laboratory," Intl. Conf. on Neutron Physics and Nucl. Data for Reactors and Other Applied Purposes, Harwell, England (1978).

10. J. B. Cumming, et al., "Absolute Cross Sections for the $^{27}Al(p,3pn)^{24}Na$ Reaction at 28 and 0.8 GeV," Nucl. Inst. and Meth., 180, pp. 37-44 (1981).

11. R. Gunnink and J. B. Niday, "Computerized Qualitative Analysis by Gamma-Ray Spectrometry," University of California NTIS, USAEC report UCRL-51061 (1972).

12. J. B. Cumming, "Applications of Computers to Nuclear and Radiochemistry," National Academy of Sciences National Research Council report NAS-NS-3107, pp. 25-33 (1962).

13. B. F. Rider and M. E. Meek, "Compilation of Fission Product Yields," Vallecitor Nuclear Center report NEDO-12154-2E (1978).

14. Y. Ishikawa, et al., "Proceedings of the 4th Meeting of the International Collaboration on Advanced Neutron Sources (ICANS-IV)," Tsukuba, Japan, 20-24 October 1980, National Laboratory for High Energy Physics report KENS-II (March 1981).

15. E. K. Hyde, The Nuclear Properties of Heavy Elements (Prentice-Hall, Inc., Englewood Cliffs, New Jersey, 1964) Vol. III, Ch. 11.

TABLE I
PHYSICAL CHARACTERISTICS OF DEPLETED URANIUM TARGET

DENSITY (g/cm^3)	DIAMETER (cm)	LENGTH (cm)	^{235}U CONTENT (wt %)
19.04	19.704[a]	30.460	0.251

[a]Effective diameter ($D = d\sqrt{n}$) for a 37-rod clustered target with an individual rod diameter of 3.2393 cm.

TABLE II
Al MONITOR FOIL DATA

REACTION	CROSS SECTION USED (mb)	MEASURED NUMBER OF PROTONS	STATISTICAL COUNTING ERROR (%)
$^{27}Al(p,x)^{7}Be$	5.7	4.25×10^{15}	±0.9
$^{27}Al(p,x)^{22}Na$	13.6	4.30×10^{15}	±1.1
$^{27}Al(p,3pn)^{24}Na$	10.8	4.32×10^{15}	±0.3

TABLE III
NUCLEAR PARAMETERS USED TO CALCULATE NUCLIDE YIELDS

ISOTOPE	HALF LIFE (DAYS)	GAMMA ENERGY (keV)	INTENSITY (γ/d)
^{95}Zr	64.05	756.71	0.546
^{97}Zr	0.704	743.36	0.926
^{99}Mo	2.767	140.51	0.8014
^{103}Ru	39.45	497.08	0.8637
^{105}Rh	1.473	319.4	0.1960
^{112}Pd	0.838	617.4	0.4289
^{115}Cd	2.208	336.23	0.459
^{132}Te	3.25	954.56	0.1659
^{140}Ba	12.8	487.03	0.4463
		1596.18	0.9540
^{143}Ce	1.375	293.26	0.4130
^{147}Nd	11.04	531.10	0.1310
^{237}U	6.75	208.0	0.2170
^{239}Np	2.35	277.6	0.1387
^{7}Be	53.29	477.6	0.103
^{22}Na	949.6	1274.6	0.9995
^{24}Na	0.625	1389.2	1.000

TABLE IV
MEASURED ^{239}Np AND ^{237}U PRODUCTION AND NUMBER OF FISSIONS IN THE DEPLETED URANIUM TARGET

FOIL POSITION	DISTANCE FROM TARGET FRONT FACE (cm)	^{239}Np PRODUCTION (ATOMS/PROTON·GRAM)[a]	^{237}U PRODUCTION (ATOMS/PROTON·GRAM)[a]	NUMBER OF FISSIONS (FISSIONS/PROTON·GRAM)[b]
1	0.00	1.69×10^{-5}	6.75×10^{-6}	3.65×10^{-5}
2	2.51	2.78×10^{-5}	1.07×10^{-5}	5.76×10^{-5}
3	5.01	3.40×10^{-5}	1.08×10^{-5}	6.04×10^{-5}
4	7.52	3.49×10^{-5}	9.62×10^{-6}	5.55×10^{-5}
5	10.02	3.19×10^{-5}	7.82×10^{-6}	4.63×10^{-5}
6	13.03	2.84×10^{-5}	6.08×10^{-6}	3.75×10^{-5}
7	17.04	2.16×10^{-5}	4.00×10^{-6}	2.59×10^{-5}
8	22.54	1.26×10^{-5}	2.04×10^{-6}	1.38×10^{-5}
9	30.46	4.23×10^{-6}	4.79×10^{-7}	3.24×10^{-6}

[a]Nominal estimated error is ±5%.

[b]Nominal estimated error is ±10%.

TABLE V
PRELIMINARY EXPERIMENTAL DATA COMPARED WITH CALCULATED RESULTS

	EXPERIMENT	CALCULATION[a]	
	TARGET LENGTH (30.46 cm)	TARGET LENGTH (30.46 cm)	TARGET LENGTH (40.64 cm)
^{239}Np PRODUCTION (atoms/protons)	3.81±0.19	3.46±0.05	3.71±0.05
NUMBER OF FISSIONS (fissions/proton)	5.59±0.56	3.93±0.06	4.09±0.06
^{237}U PRODUCTION (atoms/proton)	0.95±0.05	----	----

[a]The effects of fission competing with evaporation were not included in the calculations.

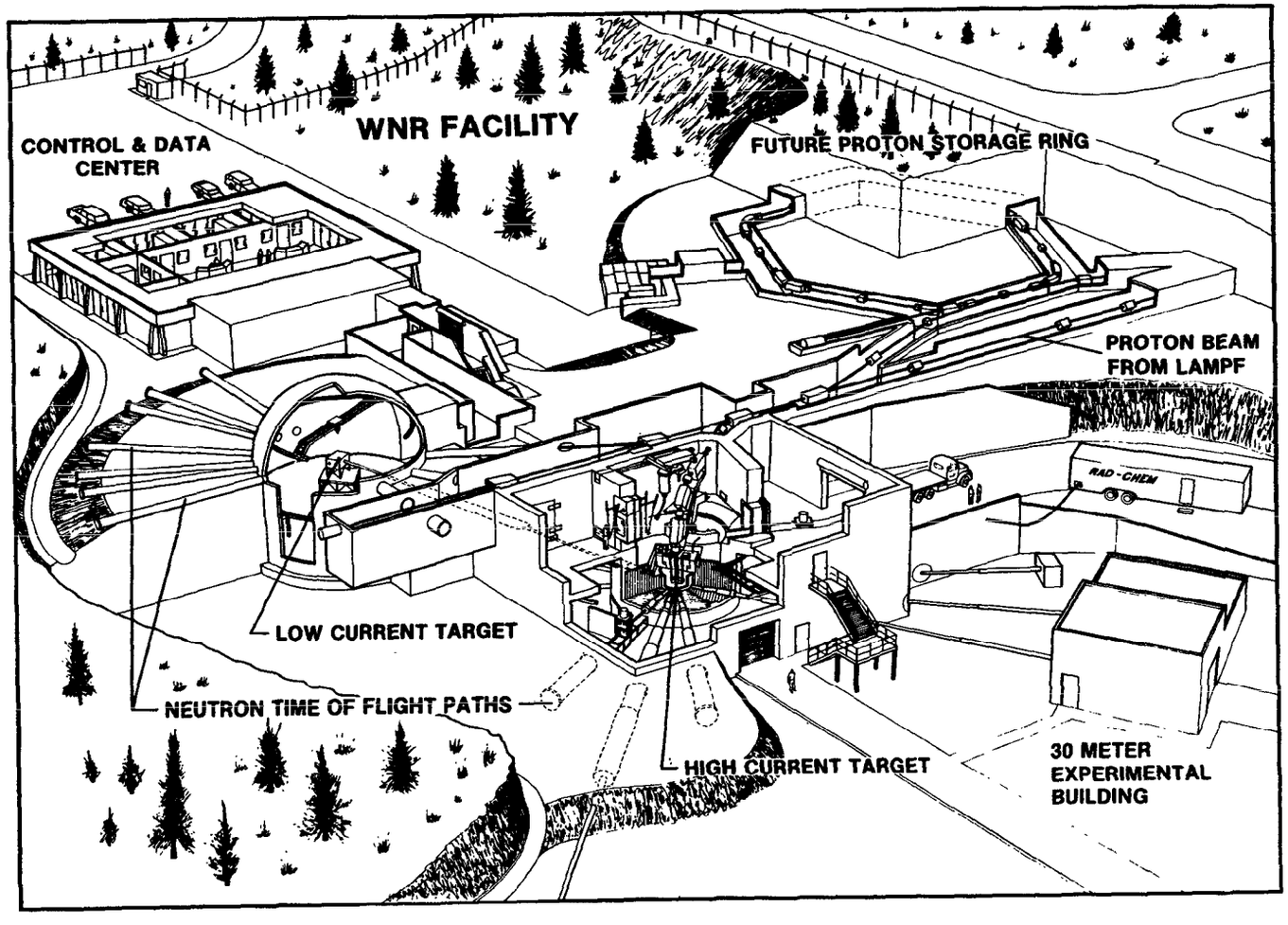

Fig. 1. General layout of the WNR showing the two target areas. The high-current target is located in a vertical proton beam and is viewed by 11 horizontal flight paths. The low-current target is located in a horizontal proton beam and viewed by 11 horizontal flight paths and one vertical flight path.

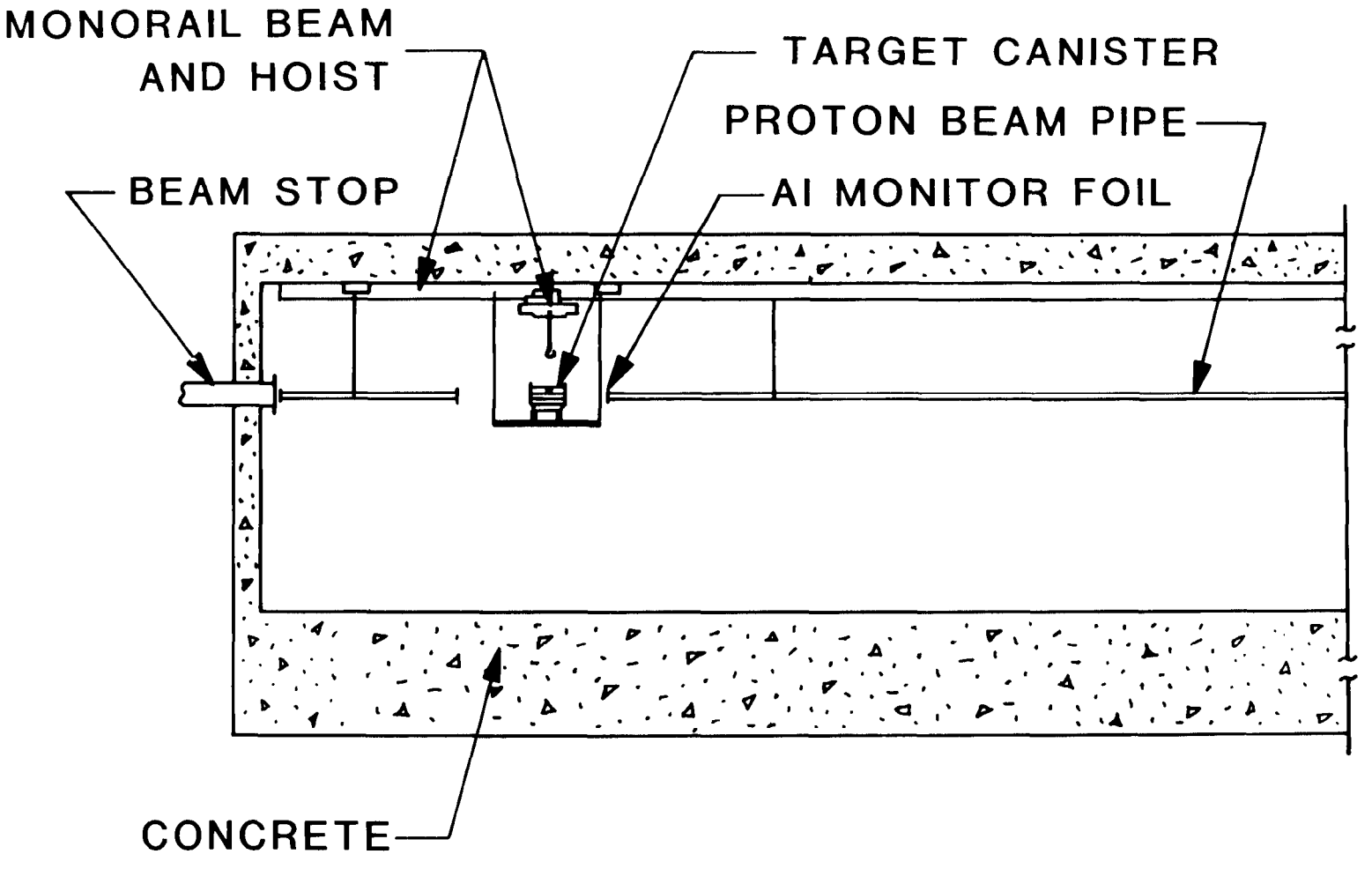

Fig. 2. Section thru the WNR beam channel showing the location of the FERFICON conversion experiment.

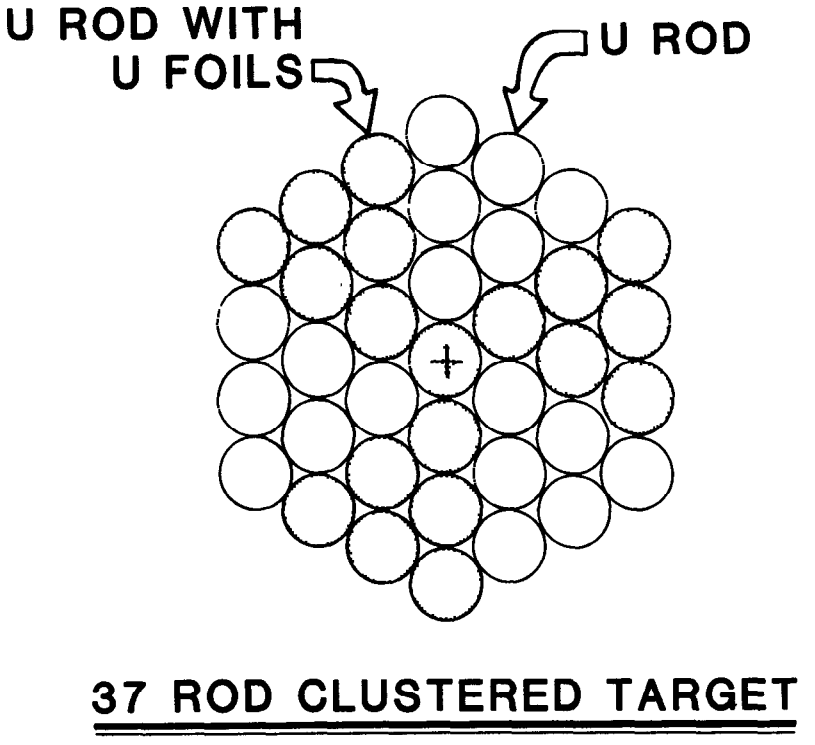

Fig. 3. Illustration of the 37-rod clustered target and the location of the foils in the array.

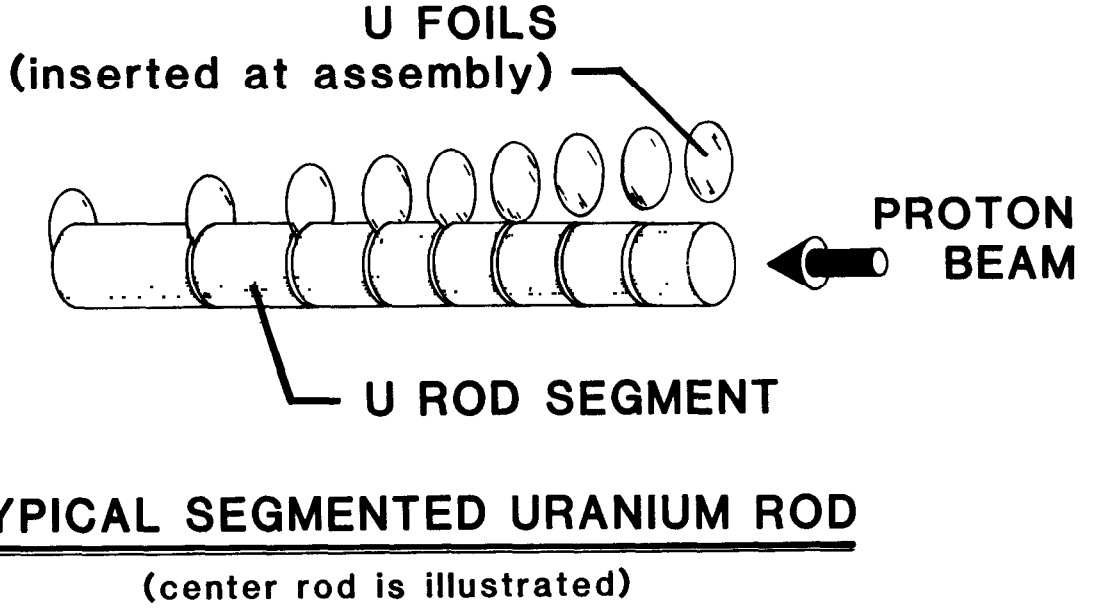

Fig. 4. Illustration showing the foil positions within a rod.

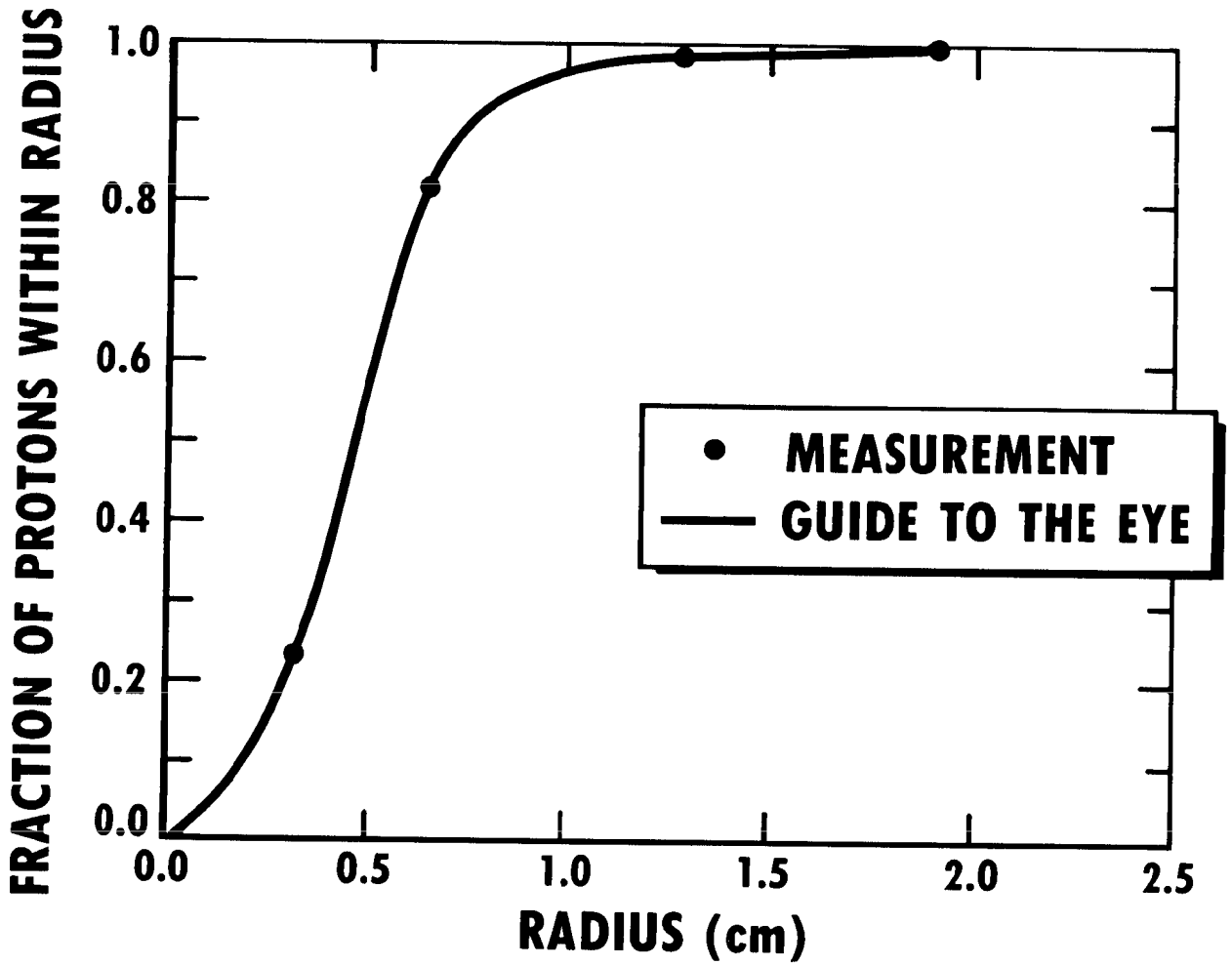

Fig. 5. Measured spatial distribution of the proton beam. The radius of the individual uranium rods was 1.62 cm.

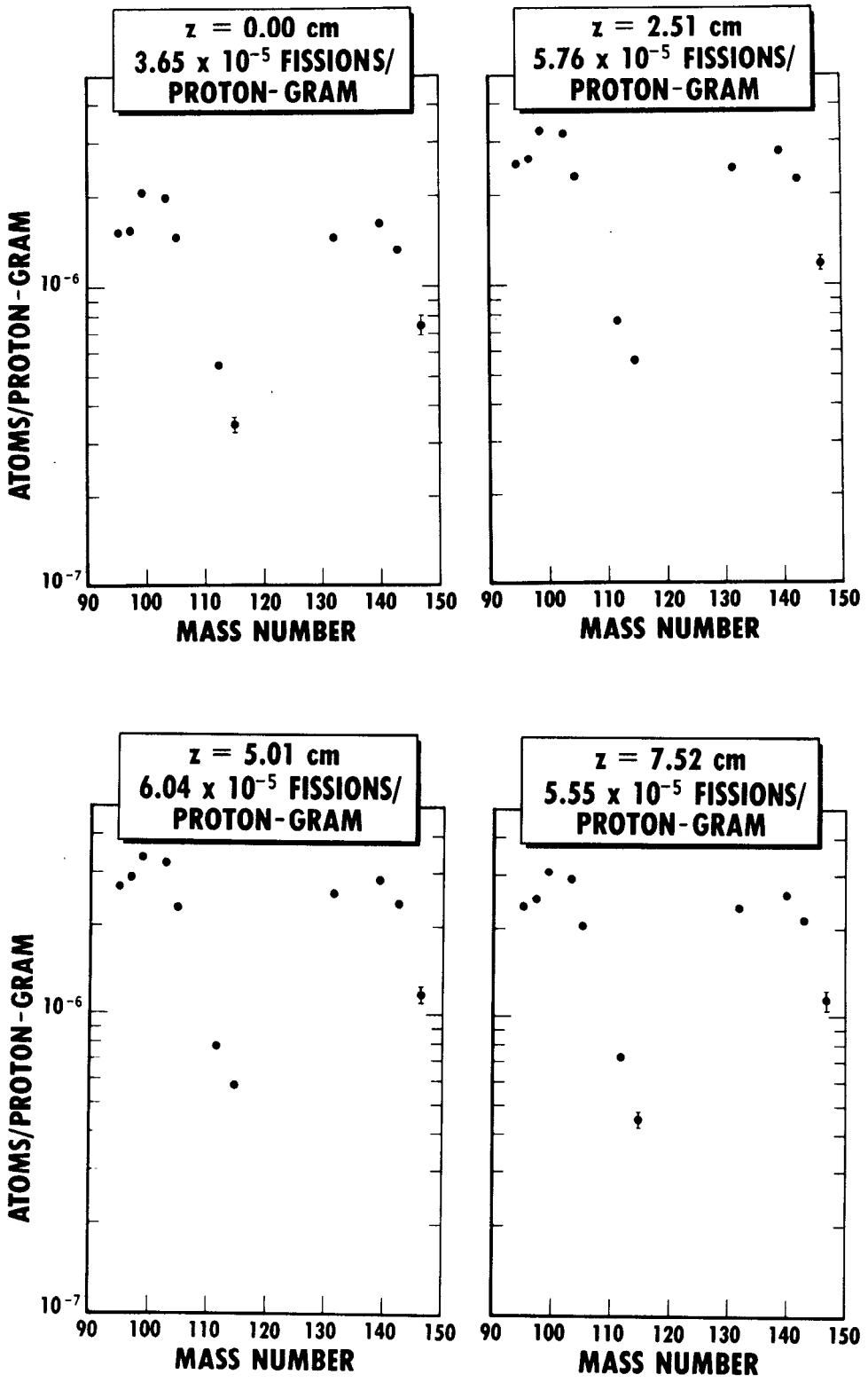

Fig. 6. Measured production of various atoms as a function of target axial position. The position z = 0.00 cm is the front target face where the 800-MeV protons were incident.

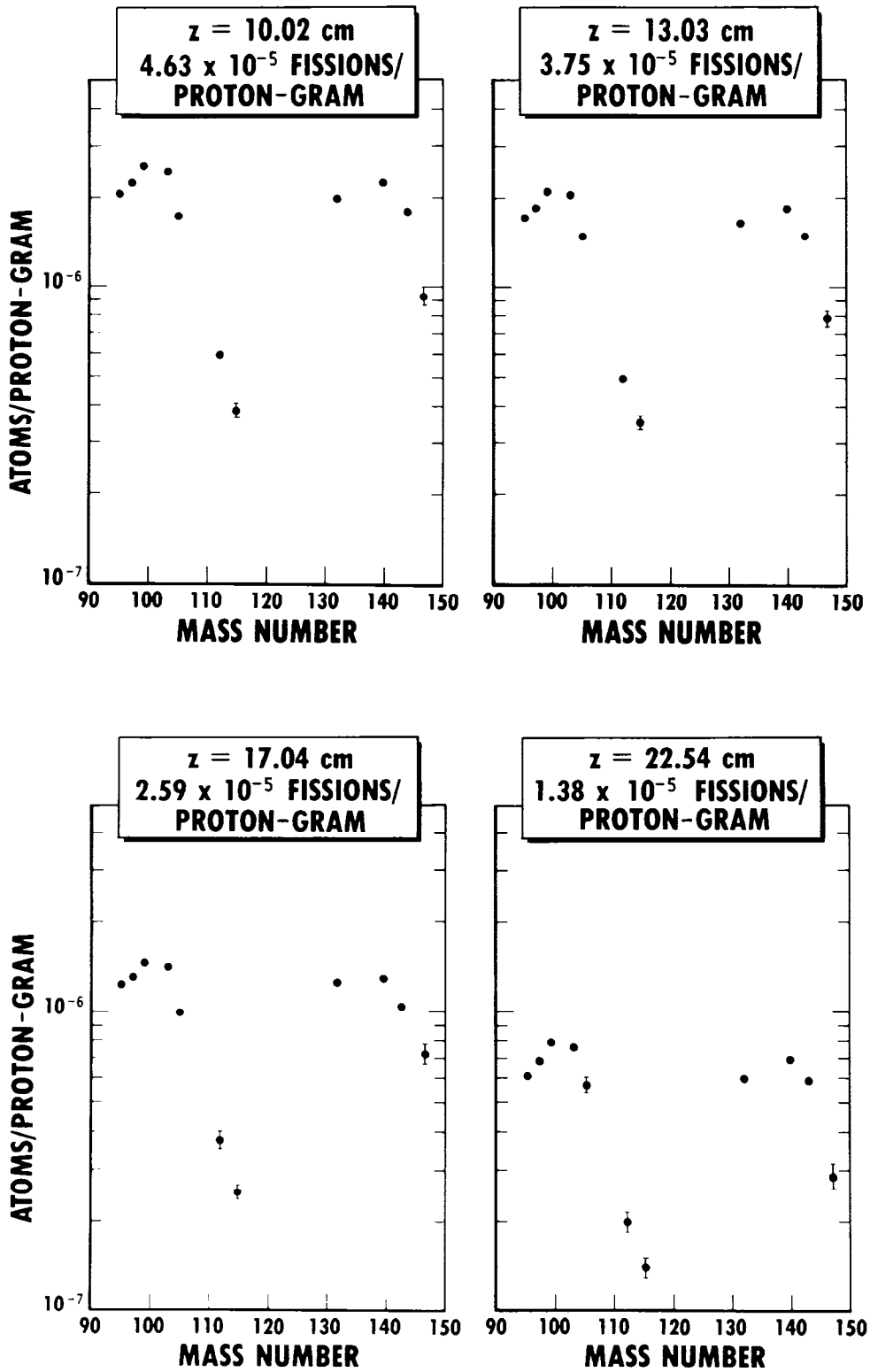

Fig. 7. Measured production of various atoms as a function of target axial position. The position z = 0.00 cm is the front target face where the 800-MeV protons were incident.

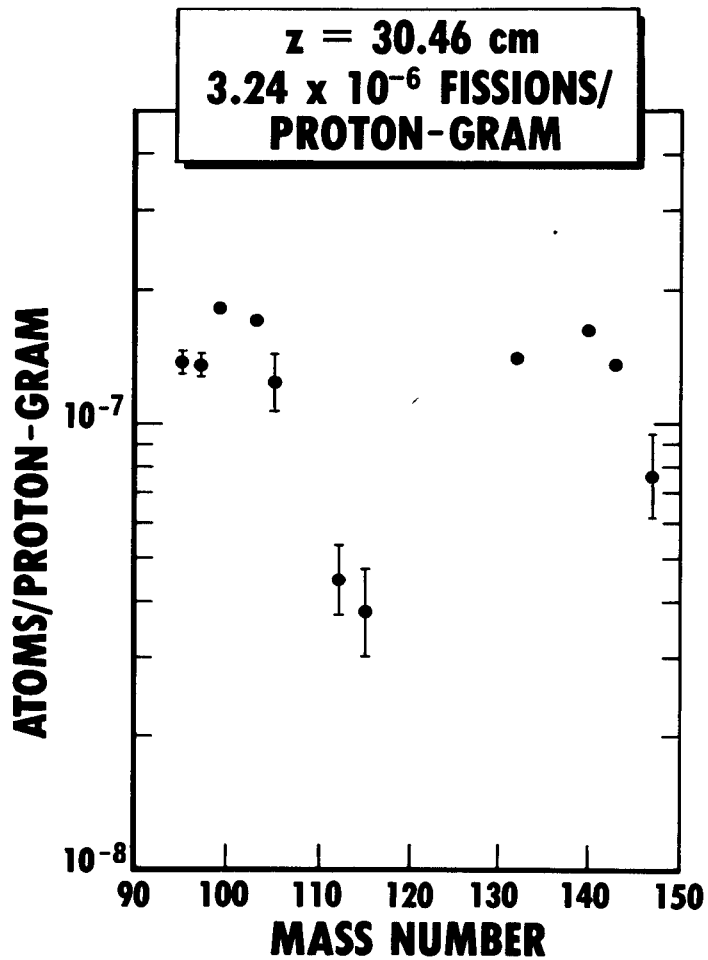

Fig. 8. Measured production of various atoms as a function of target axial position. The position z = 0.00 cm is the front target face where the 800-MeV protons were incident.

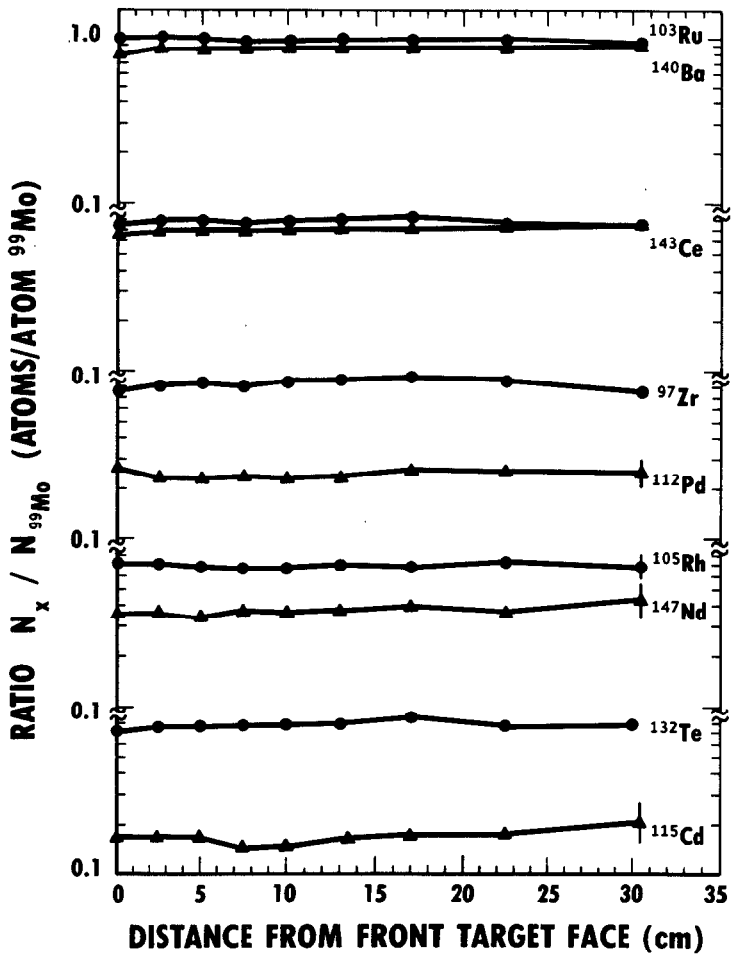

Fig. 9. Ratio of measured fission product formation to that of ^{99}Mo as a function of target axial-position.

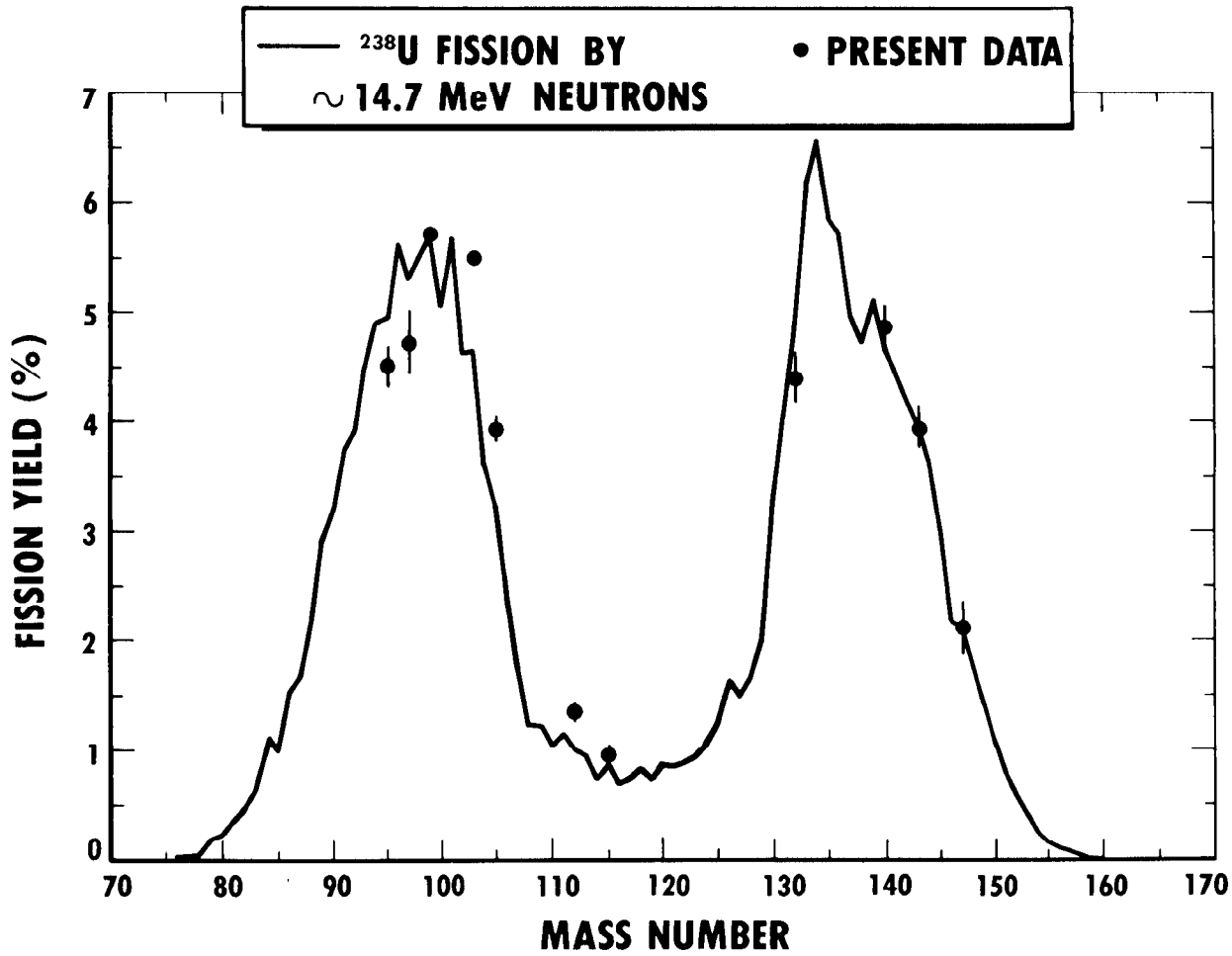

Fig. 10. Present normalized fission product yields versus mass number compared to ~14.7-MeV-neutron fission of ^{238}U (Ref. 13).

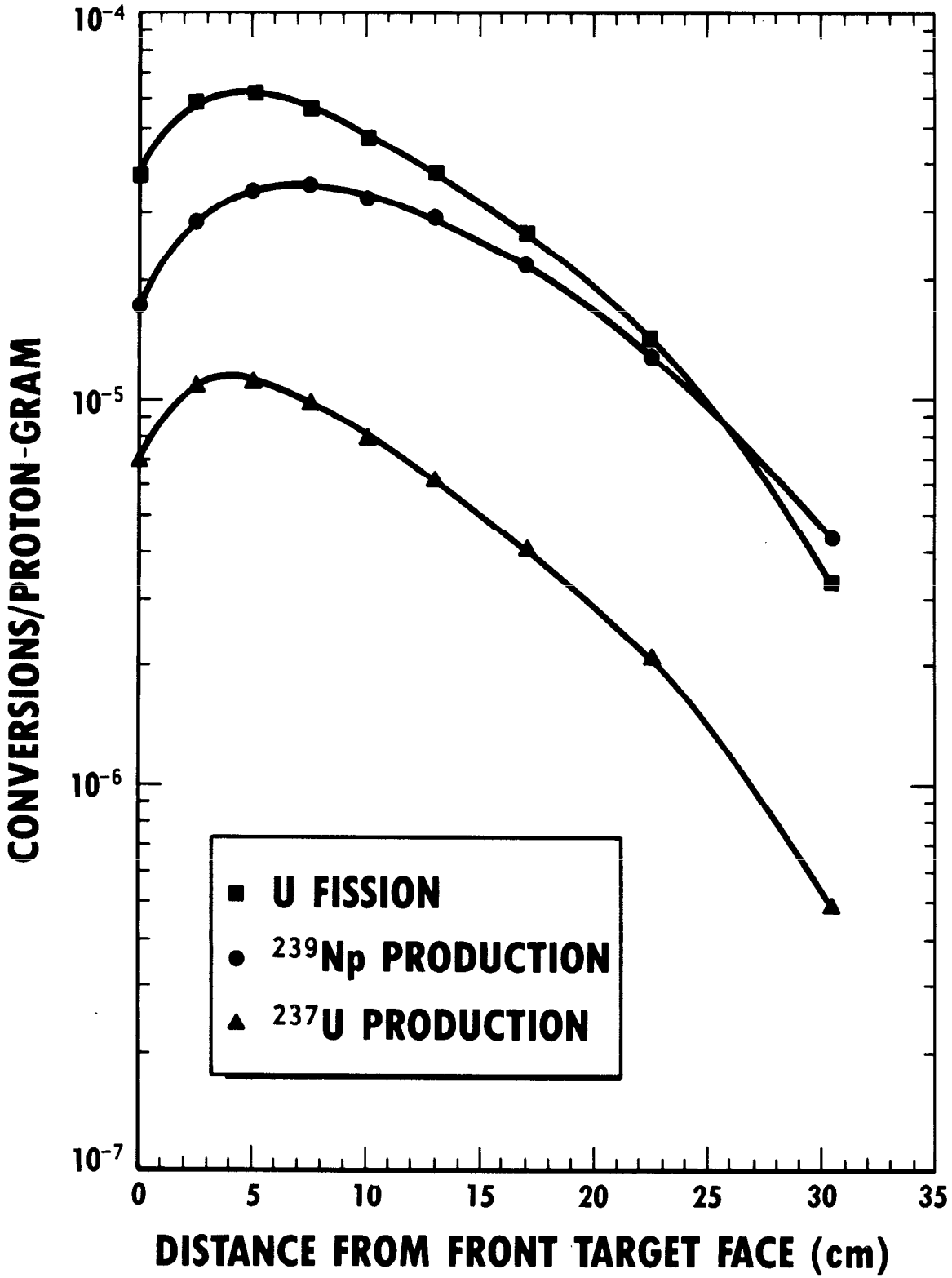

Fig. 11. Axial distribution of fissions, ^{239}Np, and ^{237}U in the depleted uranium target.

Jül-Conf-45

D5-2

I C A N S - V

MEETING OF THE INTERNATIONAL COLLABORATION
ON ADVANCED NEUTRON SOURCES

June 22-26, 1981

Spallation in a Nuclear Energy System

Manfred Heindler

Institute for Theoretical Physics
Technical University of Graz,
Graz, Austria

Abstract

There is a prospect that intense spallation neutron sources may become an efficient tool in alleviating some crucial problems troubling the fission reactor economy. However, the recent concept promotion seems to be based on fragmentary design and engineering considerations and inadequate system characterization. Premature claims may serve short term interests, but may also increase the chance that spallation research be eventually hit by public acceptance problems, if perceived as closely associated with the deployment of fission reactors. Therefore, a careful investigation of the actual benefits of associating fission reactors with intense spallation neutron sources is required. As an illustrative example for a static and dynamic impact assessment, the merits of intense spallation neutron sources as fissile fuel factories for fission converter reactors are investigated and numerical results are presented for typical design proposals.

Spallation in a Nuclear Energy System

M. Heindler

I. Introduction

While most contributions to ICANS meetings view spallation as a neutron source to be developed to serve fundamental research, there is a renewed interest in the potential role of spallation neutron sources in a nuclear energy economy (see Refs. 1 to 8 and papers quoted therein).

To a great extent this interest is motivated by the increasing recognition that external intense neutron sources could potentially represent a solution to those fission related problems which call in question both the public acceptance and the long-term prospect of the fission reactor economy. Also the accelerator community partly joins in the promotion of this new field of application for their technology, and weapons programs (Ref.9) as well as the initial fuel requirements for a DT-based fusion energy program may call for spallation as a future source for tritium.

This interest is also based on the promise that intense spallation neutron sources can be developed as a straight-forward extension of present spallation neutron source projects, such as those discussed at this and previous ICANS meetings; it has been claimed that there is no technological quantum jump required for the transition to high power designs as a result of the experience with advanced accelerators accumulated in high energy physics research (Ref.4) and of the benefit that can be taken from proven fission reactor technology. However, some requirements are recognized to be beyond the present experience in thermal and fast fission reactors (Ref.3) and may be closer to those associated with a fusion reactor (Ref.1o).

In a time period in which the fission reactor industry of important countries suffers from an unprecedented stalemate, there seems to be only modest tendency to be critical with respect to the apparent tension between "vision" and "realism" in dealing with emerging concepts. Hence, the ICANS community may wish to consider seriously the proper assessment of the spallation-fission synergism ideas,even if the near-term application of spallation neutron sources as research tool dominates its interest.

II. Spallation-Fission Synergetics

The idea to link spallation and fission goes back to the post-World War II period when fissile material needed for the US weapons program was thought to be in short supply. The MTA project was established in the US with the

goal of producing spallation neutrons via the high-energy proton induced reaction

$$p + (\text{high Z nuclei}) \rightarrow \nu_{sp} n + (\text{residual nuclei}) \qquad (1)$$

and to use the emerging ν_{sp} neutrons to transmute fertile into fissile fuel,

$$^{232}Th + n \rightarrow \ldots \rightarrow {}^{233}U$$

$$^{238}U + n \rightarrow \ldots \rightarrow {}^{239}Pu \qquad (2)$$

With the discovery of ample resources of natural uranium and the successful development of the fission reactor technology, the MTA project was terminated.

Until recently, no need for non-fission neutron sources was perceived for the civilian application of nuclear power. This resulted from the firm belief in the early market penetration of fast fission breeder reactors and of the associated fuel cycle which would make full use of the natural fissile and fertile fuel resources. Only Canada has been showing a continued interest in spallation neutron induced fertile-to-fissile conversion for their CANDU program (Ref.8).

This situation has significantly changed in view of the actual development of the nuclear energy technology and economy which is far from meeting original expectations. Problems plaguing the fission reactor community are, amongst others, (i) the broadened insight into the consequences of a large scale deployment of nuclear energy based on low-converter reactors such as the LWR, showing the threat of local or even global unvailability of cheap fissile fuel as a consequence of the delayed market introduction, the economy and the marginal breeding capacity of fast breeder reactors; (ii) the growing concern regarding the link between nuclear weapons proliferation and the civilian nuclear fuel cycle, which motivated the International Nuclear Fuel Cycle (INFCE) studies and the Nonproliferation Alternative Systems Assessment Program (NASAP); (iii) the lack of public acceptance of specific aspects of the nuclear energy program, such as fission reactor safety and the nuclear waste management program.

To a great extent these problems can be seen as symptoms of the scarcity of neutrons in the fission cycle. This scarcity has been defining by and large the current nuclear energy program, which aims at stand-alone fission reactors. Therefore intense external neutron sources -- such as spallation or fusion -- may offer an answer to the above problems, as they potentially offer the following novel options:
(i) Intense spallation neutron sources as an alternative to the introduction of fast breeder reactors, or as a means to accelerate their introduction by providing for the initial fissile fuel requirement. In both cases this is based on the extension of the fissile fuel resources by

neutron induced transmutation of plentiful fertile material into fissile fuel, Eq. (2).
(ii) Intense spallation neutron sources as enricher and rejuvenator of fuel contained in fission reactor fuel elements. These novel options for the nuclear fuel cycle are based on the in situ enrichment of fresh fuel elements and the rejuvenation, or re-enrichment, of spent fuel elements respectively, in high-flux neutron fields with appropriately tailored spectral distribution (Refs. 11,12,13). Thus the proliferation resistance may be increased by reduction or even elimination of the need for fissile enrichment in isotopic separation plants and for reprocessing of spent fuel elements.
(iii) Intense spallation neutron sources also offer novel options for the nuclear waste management by their potential to reduce the amount of radioactive waste by neutron induced transmutation of hazardous radioisotopes into less hazardous, or even stable ones in high-flux neutron fiels (Ref.4). With respect to nuclear waste incineration, the spallation source seems to be unrivaled as very high neutron fluxes are essential to its successful application.
(iv) The availability of external neutron sources could change the design requirements for advanced fission reactors by shifting the emphasis from neutron balance to safety considerations. This may point to a long-term deployment of fission power with high-converter reactors, offering safety features that may be superior to those achievable with fast breeder reactors.

III. Towards a World of Neutron Abundance ?!

This potential beneficial role of intense external neutron sources in a fission reactor economy gave rise to a wealth of ideas on how to combine various nuclear processes -- such as fission, spallation, fusion, breeding, transmutation, etc. -- in novel ways to yield a synergetic nuclear energy system that might be more acceptabele than current stand-alone fission reactors (Refs. 14,15).

However, many of the ideas promoted have enjoyed limited or only fragmentary investigation. A number of crucial factors remain to be demonstrated under realistic conditions and technical feasibility as well as engineering practicality has not yet been tackled seriously for various systems components, such as the high power target/blanket unit of an intense spallation neutron source, to name one example of interest here (Refs. 3,1o). It seems therefore important to note that the traditional approach in selecting crucial design parameter -- such as beam power and intensity, target power multiplication, etc. -- is to "adjust" these data within "reasonable" limits to yield an overall spallation source performance which seems desirable.

Scepticism is occasionally expressed with respect to the question whether intense spallation neutron sources should be and could be developed for

integration into the fission reactor economy. However, little attention has been paid to a realistic examination of the impact of spallation-fission systems on the future nuclear power market in the event that the various system components can eventually be built and operated as proposed. This criticism equally applies to other emerging energy concepts such as fusion-fission systems (Ref.17).

In our analyses (Refs. 18 to 21) we take the following approach:
We assume the feasibility of intense spallation neutron sources as described in various design proposals and evaluate the actual impact which such spallation sources would have on the fuel and power market. Clearly this impact will not only depend on the performance of the spallation neutron source, but also on the performance of the companion fission reactors, on the associated fuel cycle and on the rate at which the energy system is assumed to grow. The impact is evaluated in terms of appropriately chosen system merit parameters which directly reflect the "price" to pay for the introduction of spallation sources into a fission reactor economy per unit energy supplied to external costumers, depending on their use as fuel producer, enricher, rejuvenator and/or waste incinerator. This price will here be expressed in physical units such as energy efficiency of the system, beam power requirement per unit net power to the grid, etc. Based on these results an economic analysis can be undertaken, translating our physical units into any currency, such as constant Dollars. This then can be used to define cost break-even points (e.g. mined vs. spallation produced fissile fuel), but also to formulate requirements which spallation neutron sources will have to meet in any nuclear energy scenario.

In particular we emphasize here the role of spallation neutrons in breeding fissile fuel for use in fission converter reactors such as LWRs, HTGRs, HWRs. The possible role of spallation neutrons for the incineration of nuclear waste and for the full of partial replacement of chemical reprocessing by rejuvenation of spent fuel elements in a spallation neutron field will be touched upon only qualitatively in this paper.

IV. Static Analysis of Spallation Breeders

We first consider a zero growth nuclear energy system in its operational equilibrium. This system is conceived to consist of fission converter (FC) reactors which receive their fuel requirement from an associated spallation breeder (SB). In some cases only "topping enrichment" will be provided by the spallation breeder with some fissile fuel supplied from external sources, e.g. in the form of natural uranium (Ref. 8). It is common practice to characterize the breeding performance of the spallation breeder in terms of static support ratios, such as (i) the "number" support ratio defined as the number of fission reactors supported by one spallation breeder, or (ii) the "electrical" support ratio, that is the number of GWe fission power supported per GW beam power, etc.

In order to evaluate these support ratios, we need to know the specific fissile fuel requirement of a fission converter reactor described in tons of fissile fuel per year per GWe installed capacity; typical values found in the literature are

$$y_{FC} = \begin{cases} 1.2 & ; \text{ LWR-OT (Pu)} \\ 0.8 & ; \text{ LWR-OT, HWR-OT (U3,U5)} \\ 0.48 & ; \text{ LWR (U5,Pu)} \\ 0.3 & ; \text{ LWR, HTGR (U3)} \\ 0.1 & ; \text{ HWR, advanced HTGR (U3)} \end{cases} ; \quad [\text{t/a/GWe}] \tag{3}$$

As indicated these values apply to various fuel cycles -- reprocessing and full recycle in general, once through if labeled "OT" -- and to various types of fissile fuel. Some of the above combinations of reactor types, fuel types and fuel cycles are being deployed, such as LWR-OT (U5,Pu) and HWR-OT (U5), others are more or less remote options envisaged for the future.

Concurrently, the breeding performance of a spallation source is here characterized by the specific breeding capacity in tons per year per GW beam power. Typical values for lead-bismuth targets are

$$y_{SB} = \begin{cases} 2.5 & ; \text{ (Pu)} \\ 1.5 & ; \text{ (U3)} \end{cases} ; \quad [\text{t/a/GW beam}] \tag{4}$$

This fissile fuel yield is quite insensitive to the proton energy, but may considerably vary depending on the blanket and target design. Recently, considerably higher breeding capacities have been predicted for uranium targets (Ref. 4). Note, however, that the data available for y_{SB} result generally from one-dimensional calculations with computational models and data files that have yet to be checked against experimental results. Therefore this parameter is still subject to much uncertainty; it will eventually have to be established from space and time dependent isotopic built-up and burn-up calculations, which account for the spectral and density variation with space and time of the neutron flux and of the isotopic concentrations, and for the actual fuel management scheme.

The steady state fissile fuel balance equation

$$y_{SB}P_p - (1-f_{ext})y_{FC}P_{FC,e} = 0 \tag{5}$$

then provides the coupling condition between the spallation and the fission component of the synergetic system. In Eq.(5) f_{ext} is taken to be the fraction of fuel provided from sources external to the synergetic spallation-fission system, P_p and $P_{FC,e}$ is the nameplate power of the accelerator beam and of the fission converter reactor, respectively.

The electrical support ratio results immediately from Eq.(5):

$$P_{FC,e}/P_p = (1-f_{ext})^{-1} y_{SB}/y_{FC} \tag{6}$$

As an illustrative example let us consider two proposals by the Brookhaven National Laboratory, the LAFER (Linear Accelerator Fuel Enricher and Regenerator, Ref.13) and the most recent design proposal, the ASR (Accelerator Spallation Reactor, Ref.4). The former has a liquid lead-bismuth target, the latter a metallic uranium target making the ASR power-self-sufficient. The reported and derived characteristics of these two spallation breeder proposals are listed in Table I.

Reported Data			
Parameter	Unit	LAFER	ASR
proton energy	GeV	1.5	2.0
beam power	GW	0.45	0.60
beam current	A	0.3	0.3
accelerator efficiency	-	0.5	0.5
Pu production	t/a	1.2	3.7
thermal power generated	GWt	1.35	3.6
net thermal-to-electric eff'y	-	0.33	0.33
power required for acc.	GWe	0.9	1.2
Derived Parameters			
specific breeding capacity	t/a/GW	2.67	6.17
Q-value (electric-to-electr.)	-	0.50	1.00

Table I: Spallation breeder parameters

The number of fission reactors that can be supported with one LAFER and one ASR, resp., is calculated from these data and shown in Table II.

Fission Converter Reactor	Fuel	Fuel Cycle	Number Support Ratios LAFER	ASR
LWR	Pu	OT	1.0	3.1
LWR, HWR	U3	OT	0.9	2.8
LWR	Pu	rec.	2.5	7.7
LWR, HTGR	U3	rec.	2.4	7.4
HWR, adv. HTGR	U3	rec.	7.2	22.2

Table II: Number support ratios obtained with two typical spallation breeder designs.

As can be seen, one spallation breeder supports one to three LWRs if re-

processing is prohibited, and two to eight LWRs if fissile fuel contained in spent fuel elements is fully recycled.

As is evident from Eq.(5), the support ratio can be considerably increased if one does not impose the condition of complete fuel self-sufficiency, $f_{ext} > 0$; this then explains the higher support ratios abtained in Ref.4. Clearly this "improvement" severely reduces the fuel resource utilization, that is the fission power that can ultimately be achieved from existing fissile and fertile fuel resources.

At this point in the analysis, the physics assessment of a spallation breeder design proposal typically ends, followed by an economic assessment yielding, for example, the break even price for yellow cake (U_3O_8), for which the spallation breeder starts to be competitive.

V. The Power Cycle of Spallation Breeders

The analysis in the previous section yields a characterization of the performance of the breeder in terms of tons of Pu or U3 bred per year. However, it does not respond to the question for the impact of a synergetic spallation-fission system on the external fuel and power market.

As an illustrative example let us consider one LAFER-type spallation breeder, Table I, supporting 2.5 Pu-fulled 1 GWe-LWRs, Table II. Out of the 2.5 GWe produced in these fission reactors, only 2 GWe reach external customers; the rest is required as make-up power for the accelerator and for operation and control of the spallation breeder. Since the quantity of interest is clearly the electric power available to the consumers rather than the power produced in the system, the conventional support ratios should be replaced by system parameters which describe the system-consumer interface rather than system components. For instance we may define a "net" support ratio by

$$\frac{P_{o,e}}{P_p} = \frac{\text{electric power to the grid}}{\text{beam power}} \qquad (7)$$

Table III shows this parameter for a synergetic system in which a LAFER-type spallation breeder supports various fission reactors and compares it to the corresponding conventional support ratio, Eq.(6). Only for self-powered breeders -- such as the ASR -- do the two support ratios merge. This illustrates that the power going to the grid may be considerably smaller than the power produced in the supported fission reactors; the difference will increase with decreasing breeding capacity, decreasing reliance on natural fissile fuel resources and increasing power requirement of the accelerator.

It is a particular feature of spallation neutron sources -- in which

Fission Converter Reactor	Fuel	Fuel Cycle	Electrical Support Ratio conventional $\frac{(GWe)_{FC}}{(GW\ beam)}$	Electrical Support Ratio net $\frac{(GWe)_{grid}}{(GW\ beam)}$
LWR	Pu	OT	2.2	1.1
LWR, HWR	U3	OT	2.0	0.8
LWR	Pu	rec.	5.6	4.4
LWR, HTGR	U3	rec.	5.3	4.2
HWR, adv. HTGR	U3	rec.	16.0	14.8

Table III: Conventional and net electrical support ratios for LAFER-type spallation breeders.

they contrast with fusion neutron sources -- that the circulating energy invariably proceeds via the thermal conversion cycle (electrical to rf to kinetic to thermal to electrical) and that the basic nuclear reaction itself is endoergic. Thus the spallation source is inherently an energy sink unless an exoergic reaction is concurring. By choosing a fissionable target material (Th, U8, Unat,...) and/or by admitting an appreciable fissile concentration in the blanket, the proton and neutron induced fission reactions will improve the overall energy balance of the spallation breeder. In principle the breeder can be made energy self-sufficient or even a net energy producer, just by allowing enough fission reactions to occur, e.g. in a near-critical blanket, in which case the spallation breeder would be better described as spallation neutron driven fission reactor (Ref.22), or an Accelerator Spallation Reactor (Ref.4).

However, the problems anticipated for fissionable targets (power density, radioactive load, structural integrity,...) and for high-power blankets (high peak average power ratio, non-uniform fuel built-up, complex fuel management, ...) are considered to be far beyond currently existing engineering and operating experience from fission power reactors, including that with the liquid metal cooled fast breeder. Furthermore a serious deficiency of definitive design calculations and engineering considerations concerning the power cycle is recognized by the authors of breeder proposals (e.g.Ref.23).

This suggests that power-cycle-related design data, in particular the thermal power deposition in the target and the blanket, reflect the wish of their authors to minimize the net power requirement of the breeder, rather than thorough engineering studies. It is worth noting in this context that blanket studies performed for fusion-fission hybrids have recently been tending to minimize the power production in the blanket for technological reasons; this lead to the so-called fission-suppressed blankets (Ref.24). Since many more blanket design studies have been per-

formed for fusion breeders than for spallation breeders, there is reason to believe that more thorough spallation blanket studies will point in the same direction. Thus we consider power self-sufficient spallation breeders to be very remote options.

In view of these tremendous power cycle uncertainties we will characterize the power cycle associated with the spallation breeder by a set of parameters identified in Fig. 1 for which values may be chosen, in a specific analysis, according to one's preference:

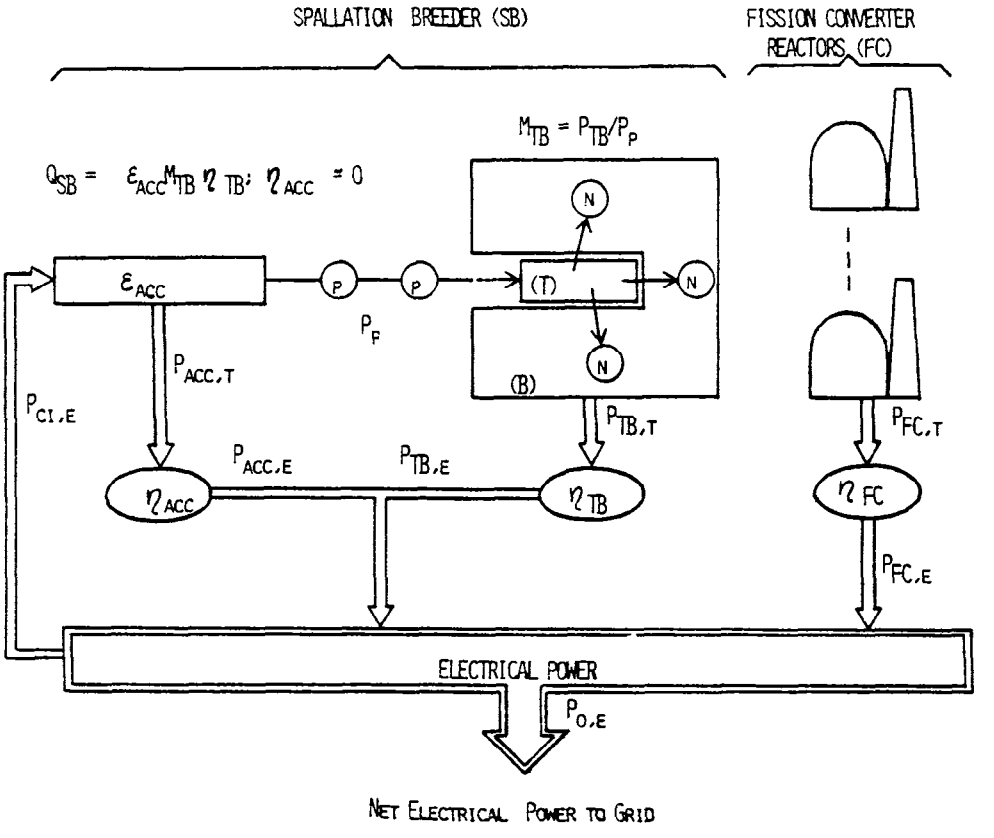

Fig. 1: Power flow in a synergetic spallation-fission system.

(i) Accelerator efficiency ε_{acc} (electric to beam). Typical values are

$$\varepsilon_{acc} = \begin{cases} 0.2 \text{ to } 0.3; & \text{current proposals for next generation of spallation sources for fundamental research;} \\ 0.5 & \text{current proposals for high-intensity spallation sources for energy systems;} \\ 0.7 \text{ to } 0.8; & \text{optimistic estimates based on novel technology.} \end{cases} \quad (8)$$

It is assumed that the lost power fraction is rejected as low grade heat, which will not be converted into electricity.

(ii) Thermal-to-electrical conversion efficiency of the heat deposited in the target and blanket of the breeder. The similarity to fission power reactors suggests

$$\eta_{TB} \simeq 0.3 \text{ to } 0.35. \quad (9)$$

Just as the anlogous efficiency η_{FC} for the fission power conversion, η_{TB} is taken to be a net efficiency, accounting for the power requirement for operation and control of the breeder.

(iii) The power multiplication of the target/blanket station, M_{TB}, defined as the amount of thermal power deposited in the target and blanket per unit beam power; this parameter depends on the target material and on the power production in the blanket which, in turn, is determined by the blanket design and the fission fuel concentration. Reasonable values seem to be

$$M_{TB} = \begin{cases} 2 \text{ ; non-fissionable target, fission-suppressed blanket;} \\ 3 \text{ ; non-fissionable target, blanket with moderate enrichment;} \\ 6 \text{ ; fissionable target and for near-critical blanket.} \end{cases} \quad (10)$$

This results in an overall electric-to-electric Q value of the breeder,

$$Q_{SB} = \varepsilon_{acc} M_{TB} \eta_{TB} \quad (11)$$

of the order of

$$Q_{SB} = \begin{cases} 0.1 \text{ ; low-efficiency accelerator, non-fissionable target, fission-suppressed blanked;} \\ 0.3 \text{ ; average design value;} \\ 0.5 \text{ ; high-efficiency accelerator, non-fissionable target, blanket with moderate fissile concentration.} \end{cases} \quad (12)$$

The value $Q_{SB} = 1$ may be used as an upper bound characterizing a breeder with fissionable target and near-critical blanket. The heat production associated with power self-sufficiency,

$$P_{TB,t} \simeq \begin{cases} 2.7 \text{ GWt ; LAFER-type breeder} \\ 3.6 \text{ GWt ; ASR-type breeder} \end{cases} \quad (13)$$

compares to that achieved in the most recent generation of LWRs, yet it presents an incomparable challenge, due to the considerably higher power densities in the target and to the higher peak-to-average power ratios in the blanket.

VI. Static Impact Analysis of Synergetic Spallation-Fission Systems

We have identified two fundamental system merit parameters, the electrical energy efficiency ε_E and the overall energy conversion efficiency η_o of the system. Another fundamental merit parameter not considered here is the fuel efficiency defined as the fraction of nuclear energy content of natural fertile and fissile fuel transformed, by a given system into useful energy.

The energy efficiency was originally introduced by R.W. Hardie (Ref.25) and is defined as that fraction of the electric power generated in the system which ultimately becomes available to external consumers:

$$\varepsilon_E = \frac{\text{electric power to grid}}{\text{electric power generated in the system}} \quad (14)$$

Note that $\varepsilon_E = 0$ indicates that the synergetic system circulates internally all the electric power generated in the system; this apparently constitutes a lower bound for a system which may be termed an "energy" system. On the other hand $\varepsilon_E = 1$ constitutes the theoretical upper bound, which is approached as Q_{SB} and/or y_{SB} approach infinity.

Other merit parameters can be easily derived from ε_E to characterize the size of various system components on a per-unit-power-to-the-grid basis, such as the specific beam power requirement,

$$P_p/P_{o,e} = \varepsilon_{acc}(1-\varepsilon_E)\varepsilon_E^{-1} \tag{15}$$

and the specific circulating power,

$$P_{ci,e}/P_{o,e} = (1-\varepsilon_E)\varepsilon_E^{-1} \tag{16}$$

The second fundamental system-merit-parameter is the overall energy conversion efficiency, defined by

$$\eta_o = \frac{\text{electric power to grid}}{\text{thermal power generated in system}} \tag{17}$$

The inverse of this parameter characterizes the amount of thermal energy that must be handled and, consequently, the amount of fissionable nuclei consumed and of nuclear waste produced per unit electric energy supplied to the grid.

Both system merit parameters can be described in terms of the previously defined fuel and power flow parameters,

$$\varepsilon_E = 1 - \left(\frac{\varepsilon_{acc}}{1-f_{ext}} \frac{y_{SB}}{y_{FC}} + Q_{SB}\right)^{-1} \tag{18}$$

and

$$\eta_o = \eta_{FC}\, \varepsilon_E \{1+(1-\varepsilon_E)[\, Q_{SB}(\eta_{FC}/\eta_{TB}-1)-(1-\varepsilon_{acc})\eta_{FC}]\} \tag{19}$$

As can be seen from these equations, the energy efficiency of a system with self-powered spallation breeders does not reach unity. In fact, this corrects the common viewpoint that a self-powered system component is energetically "free"; apparently ε_E, η_o and all derived parameters correctly account for the fact that circulating energy is never "free", neither fuel-wise, nor with respect to the associated thermal and radioactive waste.

For our previously discussed examples, LAFER and ASR assisted fission reactors, Table IV displays a few results which clearly show the effect of the spallation breeder on the overall system performance. Note that ASR-type breeders are taken to be power self-sufficient.

Fission Converter Reactor	Fuel	Fuel Cycle	LAFER ε_E	LAFER η_o	LAFER $\frac{P_{ci}}{P_{o,e}}$	ASR ε_E	ASR η_o	ASR $\frac{P_{ci}}{P_{o,e}}$
LWR	Pu	OT	0.38	0.10	1.63	0.72	0.21	0.39
LWR, HWR	U3	OT	0.33	0.08	2.00	0.70	0.20	0.43
LWR	Pu	rec.	0.70	0.20	0.44	0.87	0.27	0.16
LWR, HTGR	U3	rec.	0.68	0.20	0.46	0.86	0.27	0.16
HWR, adv. HTGR	U3	rec.	0.88	0.28	0.13	0.95	0.31	0.05
Stand-alone FC	any	any	1.0	0.33	0.0	1.0	0.33	0.0

Table IV: System merit parameters for a LAFER and ASR supported fission reactor economy, resp.; for comparison the last row gives the corresponding values for stand-alone fission reactors.

It becomes apparent that any type of fission reactor associated with a once-through fuel management yields unsatisfactory system performance, even if combined with high-yield self-powered ASR-type spallation breeders. With LAFER-type breeders, only high converting reactors in a closed fuel cycle display attractive features, whereas ASR-type spallation breeders may also favourably combine with moderately-converting fission reactors if the fuel cycle is closed.

As previously noted, there is much uncertainty about the eventual power multiplication of the target/blanket unit of spallation breeders. In order to evaluate the sensitivity of power cycle parameters, we elaborate in Fig. 2 on a medium gain LAFER-type breeder associated with various fission reactors; we take the electrical-out to electrical-in power-ratio Q_{SB} as variable, with the accelerator efficiency being constant. In the case of a system based on LWRs or HTGRs with closed fuel cycles, the sensitivity to the accelerator efficiency is also indicated. Note that a breeder with a low-efficiency accelerator requires a high power multiplication M_{TB} in the target/blanket unit to yield the same Q_{SB} as a breeder with a more efficient accelerator. The achievable limit in Q_{SB} is indicated for M_{TB} = 3 and 6 by asterisks and crosses respectively.

The description of the energy system by the merit-parameters defined in this section constitutes an essential improvement with respect to the conventional support-ratio-parameters, as they give information that is relevant to the assessment of the system-consumer interface rather than of internal performance parameters.

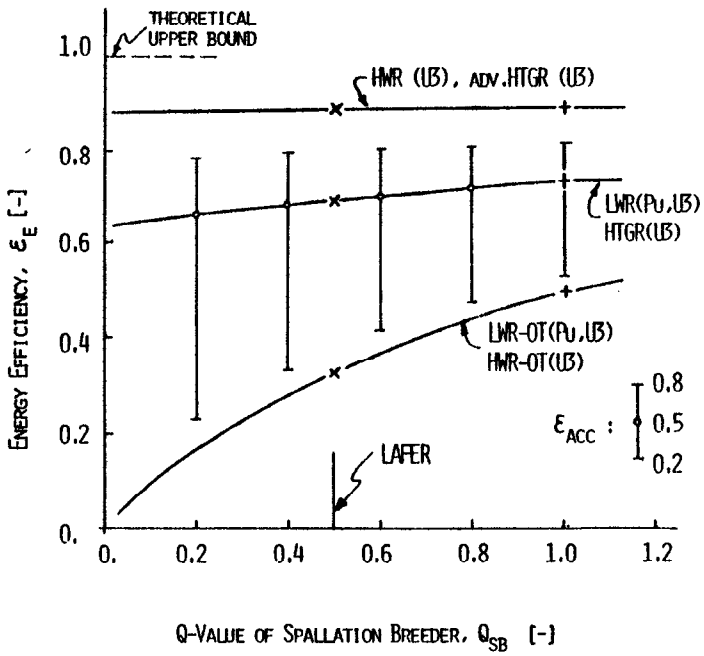

Fig. 2: The energy efficiency of a LAFER-type spallation breeder supporting various types of fission reactors as a function of the electric-to-electric Q value of the breeder. For details see the text.

VII. Dynamic Impact Analysis of Synergetic Spallation-Fission Systems

So far we have considered energy systems in their operational equilibrium, with all fuel flows to be taken constant with time. However both the past development and future expectations show nuclear energy in expansion. Growth rates of the installed nuclear capacity were of the order of 27.5 % from 1968 to 1978 and only little less between then and now (Ref.26). In this case, not only the operating, but also the embodied energy and fuel requirements are of importance; for high expansion rates, the latter may even dominate.

By embodied energy we here mean the energy that has been required to build the energy system. Information on this subject (e.g. Refs.27 and 28 and references therein) is both scarce and vague, in particular in as far as the quality profile of the invested energy compared to that of the energy supplied by the system is concerned. Much uncertainty also surrounds the definition of the system boundary,e.g. whether the power

transmission is included or not, whether today's high-grade or tomorrow's low grade ore should be considered, etc. It is also to be noted that the net thermal-to-electrical energy conversion efficiencies η_{TB} and η_{FC} should not only account for operational and control power requirements but also for the energy annually invested into the fuel cycle from mining to reprocessing and disposal, except for initial inventories. In the same realm the embodied fuel is taken here to represent that amount of fissile fuel which has to be accumulated in a device to make it operational.

In a detailed analysis the net amount of fuel and energy made available to or required by each component of the expanding nuclear energy system has to be described as a function of time, accounting for the energy investment during construction, for initial fuel inventories due at time of startup, for pre-equilibrium and eventually equilibrium characteristics. To each of the system components a fuel trajectory $M_i(t)$ (Refs. 29 to 31) and an energy trajectory $E_i(t)$ can be associated, describing the cumulative amount of fuel and energy, resp., that has been made available to or has been required by this system component up to the point in time t. The expanding nuclear energy system -- consisting of an increasing number of fission reactors, accelerator breeders etc. -- may then be described by a system fuel trajectory

$$M_o(t) = \sum M_i(t) = \sum \int y_i(t-t_i)P_i(t-t_i)dt \qquad (2o)$$

and a system energy trajectory

$$E_o(t) = \sum E_i(t) = \sum \int P_i(t-t_i)dt \qquad (21)$$

where y_i is the specific fuel yield (>0) or requirement (<0), Eqs.(3) and (4), P_i represent the respective power terms and t_i the time of startup of the i-th system component. The time-dependence of y_i and P_i accounts for pre-startup and pre-equilibrium features. As has been shown in Ref.3o, these trajectories are "functions-of-merit" which replace, in a non--steady-state analysis, the usual single-valued merit parameters and yield a compact and adequate system description.

In order to simplify the analysis of an expanding spallation-fission system in a first approach, we here replace the exact trajectory by the following quasi-dynamic model:
(i) At time of startup the asymptotic -- rather than the initial -- fuel inventory is loaded, defining the specific fuel inventory.
(ii) The energy required for construction and lower-than-asymptotic thermal energy production during pre-equilibrium operation (e.g. during fissile fuel build-up in the blanket) is accounted for in a single energy investment at time of startup, defining the specific energy inventory.

With these approximations, both the fuel and the energy yield/requirement of a system component can be taken to assume its constant equilibrium value from the very beginning of its operation, as all pre-startup and pre-equilibrium features are embodied in the fuel and energy investments taken to occur at time of startup.

Note that in this model no distinction is made between fuel that is externally supplied and fuel that is breed in situ. As a matter of fact, we have shown in Ref. 3o, taking the fast fission breeder reactor with its loaded core-inventory and its in-situ bred blanket-inventory as an illustrative example, that the cumulative fuel yield/requirement is independent of the way the fuel was originally provided for, as soon as the associated fuel flow reaches its equilibrium.

Let us assume an exponentially growing system taken to consist of spallation breeders and partially or fully supported fission converter reactors. Let us also smooth out the discontinuities due to the actual size of each unit going into operation. This then translates into a growing installed proton beam and electric fission power as described by

$$\frac{d}{dt}P_i = GP_i \quad ; \quad i = p \text{ and } FC,e \tag{22}$$

Here G is the fractional annual system growth rate, with the associated doubling time $\tau = \ln 2/G$.

As previously indicated, we define specific fuel inventories of fission converter reactors and spallation breeders, in units of tons per GW of electric fission power and beam power, respectively. Again taking typical design values from the literature, we find for the various fission reactors

$$\mu_{FC} = (1+Z_{FC})\cdot\begin{cases} 3.5 \; ; \; \text{HWR(U5),LWR(Pu)} \\ 2.4 \; ; \; \text{LWR(U3,U5)} \\ 1.8 \; ; \; \text{HTGR(U3),HWR(U3)} \end{cases} ; \quad [\text{t/GWe}] \tag{23}$$

and for spallation breeders

$$\mu_{SB} = (1+Z_{SB})(m_B Q_{SB} \varepsilon_{acc}^{-1} \varepsilon_{SB}) \quad ; \quad [\text{t/GW beam}] \tag{24}$$

Here Z is the amount of fuel accumulated in the fuel cycle, expressed in units of the asymptotic inventory of the fission reactor and breeder respectively, with $Z_{FC} = 0$ for OT-cycles; otherwise we assume $Z_{SB} = 0.5$ and, perhaps too optimistically, $Z_{FC} = 0.5$. Furthermore, m_B is the specific

blanket inventory per percent enrichment in the blanket and per GWe power obtained from the target/blanket unit; clearly, this value is strongly design dependent, with typically $m_B = 0.9$ [t/GWe] .

In addition, we define a specific energy requirement for the fission reactors, π_{FC}, in units of equivalent GWe years per GWe fission power, and for the spallation breeders, π_{SB}, in units of equivalent GWe per GW beam power. The term "equivalent" here alludes to the quality profile of the invested vs. supplied power. We here take $\pi_{FC} = 0.3$ [GWe-years per GWe] corresponding to an energy pay-back time of 0.3 years; we will also assume that, for the same electric power generated, the spallation breeder requires twice as much embodied energy as does the fission reactor, $\lambda_{SB/FC} = 2$:

$$\pi_{SB} = \lambda_{SB/FC} \cdot Q_{SB} \varepsilon_{acc}^{-1} \pi_{FC} \qquad \text{[GWe per GW beam]} \quad (25)$$

In the quasi-dynamic model, the coupling equation which replaces Eq.(5) now reads

$$(y_{SB} - G\mu_{SB})\ P_p(t) = (1-f_{ext})(y_{FC} + G\mu_{FC}) P_{FC,e}(t) \qquad (26)$$

This then defines, in turn, the exponentially growing power which the system makes available to external customers:

$$P_{o,e}(t) = P_{FC,e}(t)(1-G\pi_{FC}) - P_p(t)\{\ \varepsilon_{acc}^{-1}(1-Q_{SB}) + G\pi_{SB}\} \qquad (27)$$

From these equations, the electrical energy efficiency, Eq.(14), can again be calculated:

$$\varepsilon_E(G) = (1-G\pi_{FC}) - \frac{1+G\pi_{FC} Q_{SB}(\lambda_{SB/FC}-1)}{\varepsilon_{acc}(1-f_{ext})^{-1}(y_{SB}-G\mu_{SB})(y_{FC}+G\mu_{FC})^{-1} + Q_{SB}} \qquad (28)$$

Again for the design proposals for LAFER and ASR as typical examples, we show in Table V the dependence of the energy efficiency on the growth rate for the various reactor types and fuel cycles. Throughout these calculations we have used the design parameters displayed in Table I; furthermore we have assumed an asymptotic fuel enrichment in the breeding blanket of 2 % for LAFER and 4 % for the self-powered ASR, independently of the type of fuel.

Fission Component	LAFER				ASR			
	G = 0.	.05	.10	.20	0.	.05	.10	.20
LWR-OT(Pu)	.38	.28	.17	<0	.72	.65	.58	.42
LWR-OT(U3)	.33	.21	.08	<0	.70	.61	.51	.28
LWR-rec.(Pu)	.70	.53	.37	.08	.87	.77	.68	.48
LWR-rec.(U3)	.68	.49	.30	<0	.86	.75	.62	.34
HTGR-rec.(U3)	.68	.52	.36	.03	.86	.77	.66	.39
HWR-rec.(U3)	.88	.71	.53	.16	.95	.85	.74	.46

Table V: Growth dependence of the electrical energy efficiency of the spallation-fission system.

From these results it becomes obvious that even for low-inventory high-converting fission reactors, such as the HWR(U3) with full fissile fuel recycle, the energy efficiency drops considerably with increasing growth rate. For growth rates as low as 10 %, LAFER-type spallation breeders yield energy efficiencies below 5o % -- corresponding to specific circulating power fractions, Eq.(17), of more than 5o % -- with one single exception, that is if they are associated with U-233 fuelled HWRs; for self-powered high-yield ASR-type breeders the energy efficiency ranges from 5o to 75 % for the various fission reactors and fuel cycles, dropping well below 5o % in all cases for growth rates in excess of 2o %.

It is interesting to study the sensitivity of the results to parameters which describe the various fuel cycles and system components. Figure 3 illustrates, for Pu-239 fuelled LWRs with full fissile recycle in association with LAFER-type spallation breeders, the sensitivity of the growth rate dependence of the energy efficiency on the accelerator efficiency, the specific embodied energy, the fissile inventory of the breeding blanket and the fuel cycle inventory fraction; upper and/or lower bounds of the respective parameters are thereby considered, all the other parameters taken to assume the standard values in each case. It becomes obvious that the single most important parameter is the accelerator efficiency which will determine to a great extent the attractiveness of spallation-fission synergetic systems.

VII. Nuclear Fission Waste Incineration and Rejuvenation

Without attempting a numerical analysis of the spallation breeder as nuclear waste incinerator and spent fuel rejuvenator, we may readily gain a qualitative appraisal of the effect of these fuel cycle options on the system merit parameters such as the energy efficiency.

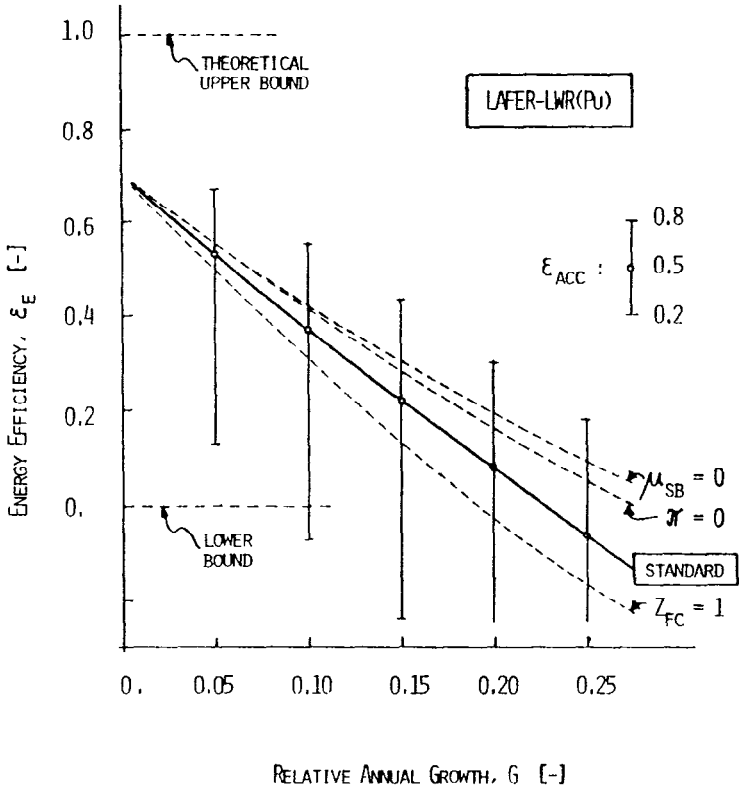

Fig.3: Growth dependence of the energy efficiency of Pu-fuelled LWRs supported by LAFER-type accelerator breeders. For details see text.

The incineration of hazardous radioisotopes produced in fission reactors can be envisaged through beam and spallation proton induced as well as through spallation neutron induced reactions. In particular the latter case, which will invariably occur in the presence of absorbing waste isotopes, will reduce the number of neutrons available for breeding purposes. Also side reactions, reactions with transmuted waste nuclei and the appearance of unstable spallation reaction products will counteract the incineration process, increasing the energy cost of the radiological hazard-reduction of nuclear waste. To include nuclear waste incineration via spallation induced reactions, therefore means necessarily to reduce further the energy efficiency of the synergetic system. The question therefore arises to what extent nuclear waste incineration can be performed before an intolerable fraction of the fission energy is reinvested therein.

The same is true for the rejuvenation of spent fuel as an alternative to chemical reprocessing. The accumulation of fission products in the fuel elements will necessarily have a deteriorating effect on the neutron

balance, resulting both in parasitic neutron absorptions and the necessity to achieve increasingly high enrichment in order to compensate for the adverse reactivity effect of the fission and activation products. Preliminary studies show that the fissile fuel breeding requirement will be close to that for a once-through fuel management starting from purely fertile fuel.

In addition, the breeding requirement per unit net power output will clearly increase -- and the energy efficiency accordingly decrease -- with an increasing number of rejuvenation cycles.

Thus the previously discussed use of the spallation neutron sources as fissile fuel factory only, combined with spent fuel reprocessing, definitively yields the most favourable merit parameters for a spallation fission system. The deployment of any supplementary option offered by the physics of spallation processes will invariably tend to adversely affect the system performance and may be justified for reasons other than energy-physics related ones only.

VIII. Conclusions and Implications

This analysis reveals the invariable role of energy and fissile mass as "endowments" towards more secure and complete nuclear energy options. For example, the consideration of the initial fuel requirement of a fission reactor and of the complementary initial power requirement of a spallation breeder, makes fissile fuel and energy sustainability the limits to growth of a spallation-fission based nuclear economy.

The electric-energy efficiency and the energy conversion efficiency of a synergetic system have been shown to describe adequately the system performance with respect to the system-consumer interface, that is with respect to its actual impact on external fuel and power markets. It accounts for all fuel and power flows occuring from the beginning of construction to equilibrium operation of each of the system components, while simultaneously incorporating the effect of a system expansion. A straightforward extension to economic analyses is possible.

The implications of this analysis identify the parameter ranges and system options of interest. The results demonstrate that there is no clear-cut answer to the question of the desirability of the various spallation-fission synergism options. They indicate that, in any event, only high-performance accelerators associated with fuel-efficient fission converter reactors and with a closed fuel cycle show the prospect of an attractive systems performance.

In a steady state operation, the power requirement of a spallation breeder is of minor concern if the breeder is associated with high-converter low-inventory fission reactors.

This aspect changes drastically for an expanding economy, even for expansion rates well below historical growth rates for installed nuclear capacities. In this case there are growth rate dependent trade-offs between the effect of increasing power production and decreasing fuel availibility with increasing blanket enrichment, between invested vs. annual fuel requirements of the associated fission reactors, etc., which require a careful analysis before the question of the feasibility of spallation-fission synergisms can be answered.

The implications of this analysis point also strongly to the fact that a fundamental and engineering analysis needs to be undertaken in order to identify the actual fuel breeding and power amplification potentials of spallation breeders and to realistically estimate the duty factor and the efficiency of high power high-intensity proton accelerators. Only then will a full appraisal of the potential of spallation-fission synergisms be possible.

Acknowledgement

Computational assistance for this work has been provided by Maria Böhm and Karl Niederl.

Bibliography

1. H.J.C.Kouts, Ed., Proc. of an Information Meeting on Accelerator Breeding, Upton, Jan. 1977, CONF-770107.

2. G.Kessler and P.J.Jansen: Accelerator Breeders and Fission Converter Reactors, Proc. IIASA Conf., Ref. 16.

3. J.S.Fraser: Accelerator Breeder Applications, Proc. IIASA Conf., Ref. 16.

4. M.Steinberg: Accelerator Spallation Reactors for Breeding of Fissile Fuel and Transmuting Fission Products, Proc. IIASA Conf., Ref. 16.

5. Special Session on the Physics of Accelerator Breeding, Transactions of the American Nuclear Society 28 (1978) 754 - 6o.

6. A.A.Harms and C.W.Gordon: A Parametric Analysis of the Spallation Breeder, Nucl.Sci.Eng. 63 (1977) 336 - 41.

7. T.J.Burns, D.E.Bartine and J.P.Renier: Concept Evaluation of a Nuclear Design for Electronuclear Fuel Production; ORNL/TM-6828 (1979).

8. G.A.Bartholomew: Research Opportunities with Prototype Accelerators for an Accelerator Breeder. Proceedings of this Meeting, ICANS-V (1981).

9. Nucleonics Week 22, No. 8, Feb. 26 (1981).

1o. S.O.Schriber: Electronuclear Fuel Production using High-Intensity Accelerators; Proc. First Int. Conf. Advanced Nuclear Energy Systems, Graz, March 1978, Atomkernenergie 32 (1978) 49 - 55.

11. A.A.Harms, W.J.Hartmann: Spent Nuclear Fuel Re-enrichment without Reprocessing; Annals of Nuclear Energy 5 (1978) 213 - 4.

12. J.Dorning and F.Gunnison: On the Feasibility of an Accelerator-Driven Rejuvenator for Light-Water-Reactor Fuel; Transactions of the A.N.S. 32 (1979) 799 - 8oo.

13. P.Grand, H.J.Kouts, J.R.Powell, M.Steinberg and H.Takahashi: Conceptual Design and Economic Analysis of a Light-Water-Reactor Fuel Enricher/Regenerator; Brookhaven National Laboratory, USA, Report BNL 5o838 (1978).

14. A.A.Harms: The Nuclear Energy Continuum and its Spectrum of Choices, Proc. IIASA Conf., Ref. 16.

15. A.A.Harms, W.Haefele: Nuclear Synergism: An Emerging Framework for Energy Systems; American Scientist 69 (1981) 1 - 8.

16. A Perspective on Adaptive Nuclear Energy Evolutions: Towards a World of Neutron Abundance; Workshop of the International Institute for Applied Systems Analysis, Laxenburg, Austria, May 25-27, 1981; Proceedings to be published by IIASA.

17. S.I.Abdel-Khalik, P.Jansen, G.Kessler, P.Klumpp: Impact of Fusion-Fission Hybrids on World Nuclear Future; University of Wisconsin Report UWFDM-333 (198o), Kernforschungszentrum Karlsruhe, Report KfK 2998 (198o).

18. K.F.Schöpf, M.Heindler and A.A.Harms: Energy Production in Stand-Alone and Interactive Fission and Fusion Systems: Proceedings Jahrestagung Kerntechnik, Düsseldorf, March 1981, pp. 621 - 624.

19. M.Heindler, K.F.Schöpf, A.A.Harms: The Effective Breeding Capacity of Spallation Breeders; Proceedings Jahrestagung Kerntechnik, Düsseldorf, March 1981, pp. 625 - 628.

2o. M.Heindler, A.A.Harms: Efficiency Merit Assessment of Emerging Synergetic Nuclear Energy Systems; Proc. 2nd Int. Conf. Emerging Nuclear Energy Systems, Lausanne, April 198o, Atomkernenergie-Kerntechnik 36 (198o) 7 - 12.

21. M.Heindler, K.F.Schöpf: A Dynamic Analysis of the Breeding and Expansion Capacity of Spallation Breeders; in preparation (1981).

22. E.Greenspan: Preliminary Report on tne Promise of Accelerator-Driven Natural-Uranium-Fueled Light-Water-Moderated Breeding Power Reactors; Oak Ridge National Laboratory, ORNL/TM-6138.

23. M.Steinberg, J.R.Powell, H.Takahashi, P.Grand, H.J.C.Kouts: The Linear Accelerator Fuel Enricher Regenerator (LAFER) and Fission Product Transmuter (APEX); Proc. 2nd Int.Conf. Emerging Nuclear Energy Systems, Lausanne, April 198o, Atomkernenergie-Kerntechnik 36 (198o) 42 - 46.

24. R.W.Moir: Hybrid Reactors; Lawrence Livermore Laboratory, UCRL-84826 (1981), presented at Jahrestagung Kerntechnik '81, Düsseldorf, March 1981.

25. R.W.Hardie, R.J.Barrett, J.G.Freiwald: Comparative Assessment of Nuclear Fuel Cycles; Los Alamos Scientific Laboratory, LA-8291-MS, June 198o.

26. Another Year of Lost Opportunities, Nuclear News, Aug. 198o, p.73.

27. H.J.Wagner: Der Energieaufwand zum Bau und Betrieb ausgewählter Energieversorgungstechnologien, eine nettoenergetische Analyse; Kernforschungsanlage Jülich, Jül-1561 (1978).

28. C.Held, G.Moraw, M.Schneeberger, A.Szeless: Energy Analysis of Nuclear Power Plants and Their Fuel Cycle; Proc.Int.Conf. on Nuclear Power and its Fuel Cycle, IAEA, Salzburg, May 1977, paper IAEA-CN-36/145, Vol.I, 723 - 29.

29. A.A.Harms, M.Heindler: Life-Time Fuel Trajectories for Fission Reactors, Transactions of the A.N.S. 33 (1979) 125 - 7.

3o. A.A.Harms, M.Heindler: Theory and Application of the Nuclear Fuel Trajectory Concept, Nuclear Technology 53 (1981) 267 - 79.

31. J.K.Presley, A.A.Harms, M.Heindler: Nuclear Fuel Trajectories of Fusion-Fission Symbionts, Nucl.Sci.Eng. 74 (198o) 193 - 8.

I C A N S - V

MEETING OF THE INTERNATIONAL COLLABORATION ON ADVANCED NEUTRON SOURCES

June 22-26, 1981

Program of the Plenary Sessions

June 22-23, 1981

22.6.	8^{30}	Opening of Conference Desk in the foyer of the KFA central library Coffee served
	$10^{00}-10^{30}$	Welcome Address (H. Stiller)
	$10^{30}-12^{30}$	Status Reports I Chairman W. Klose
	$10^{30}-11^{15}$	(1) R. Woods, LASL WNR
	$11^{15}-11^{45}$	(2) R. Cooper, LASL PSR
	$11^{45}-12^{30}$	(3) N. Watanabe, KENS
	$12^{30}-14^{00}$	Lunch break
	$14^{00}-16^{15}$	Status Reports II Chairman G. z. Putlitz
	$14^{00}-14^{45}$	(1) J.M. Carpenter IPNS
	$14^{45}-15^{30}$	(2) D.A. Gray SNS
	$15^{30}-16^{15}$	(3) W.E. Fischer SIN
	$16^{15}-17^{00}$	Coffee break

$17^{00}-18^{30}$	Status Reports III Chairman H. Stiller	
$17^{00}-17^{45}$	(1) H.H. Hennies	SNQ
$17^{45}-18^{30}$	(2) G. Bartholomew:	"Neutron Research Opportunities offered by the Accelerator-Breeder Development Program at CRNL"
19^{00}	Reception at the "Waldcasino" of KFA Jülich	

23.6. $9^{00}-10^{30}$	"Research Opportunities offered by Spallation Neutron Sources I" Chairman W. Schmatz	
	(1) R. Scherm:	Neutron Scattering
	(2) R. Golub:	Ultracold Neutrons
$10^{30}-11^{00}$	Coffee break	
$11^{00}-12^{30}$	"Research Opportunities offered by Spallation Neutron Sources II" Chairman R. Hecker	
$11^{00}-11^{45}$	(1) A. Seeger:	Application of Muons to Solid State Research
$11^{45}-12^{30}$	(2) B. Zeitnitz:	Neutrino Physics
$12^{30}-13^{30}$	Lunch break	
$13^{30}-15^{00}$	"Target physics" Chairman J.M. Carpenter	
$13^{30}-14^{15}$	(1) T.W. Armstrong and D. Filges:	Models and Computational Methods in the theoretical treatment of Spallation Neutron Sources
$14^{15}-15^{00}$	(2) S. Cierjacks:	High Energy Particle Spectra from Spallation Targets

$15^{00}-15^{30}$	Coffee break
$15^{30}-17^{45}$	"Layout Problems" Chairman A. Carne
$15^{30}-16^{15}$	(1) P. Jung: Radiation Effects in Targets and Structural Components
$16^{15}-17^{00}$	(2) G.J. Russell and A.D. Taylor: Moderator and Reflector Layout and Spectral Tailoring
$17^{00}-17^{45}$	(3) M. Reiser: Advanced High Intensity Accelerator Concepts

I C A N S V

MEETING OF THE INTERNATIONAL COOPERATION ON ADVANCED NEUTRON SOURCES

Plenary sessions and target workshops at Kernforschungsanlage Jülich

June 22-26, 1981

List of Participants

Ali-Khan, I.	Institut für Plasmaphysik Kernforschungsanlage Jülich GmbH Postfach 1913 D-5170 Jülich
Amian, Winfried	Institut für Reaktorentwicklung Kernforschungsanlage Jülich GmbH Postfach 1913 D-5170 Jülich
Anderko, Kurt	Institut für Material- und Festkörperforschung II Kernforschungszentrum Karlsruhe GmbH Postfach 3640 D-7500 Karlsruhe 1
Armstrong, T.	SAI Science Applications Inc. PO Box 2807 1200 Prospectstr. La Jolla, Calif. 92038
Bartholomew, Gilbert A.	Atomic Energy of Canada Limited Chalk River, Ontario KOJ 1JO Canada
Bauer, Günter	Institut für Festkörperforschung Kernforschungsanlage Jülich GmbH Postfach 1913 D-5170 Jülich
Bedau, J.	Brüker Analytische Messtechnik GmbH Am Silberstreifen D-7512 Rheinstetten
Böhne, Dieter	Gesellschaft für Schwerionenforschung GSI Postfach 110541 D-6100 Darmstadt
Böning, Klaus	Reaktorstation Techn. Universität München D-8046 Garching

Carne, Alan	Rutherford & Appleton Laboratories Chilton Didcot, Oxon OX11 England
Carpenter, J.M.	Argonne National University Bldg. B 72 Argonne, Illinois 60439 U.S.A.
Chidley, Bruce	Atomic Energy of Canada Limited Chalk River, Ontario KOJ 1JO Canada
Citron, A.	Institut für Kernphysik Kernforschungszentrum Karlsruhe Postfach 3640 D-7500 Karlsruhe 1
Cloth, Peter	Institut für Reaktorentwicklung Kernforschungsanlage Jülich GmbH Postfach 1913 D-5170 Jülich
Conrad, Harald	Institut für Festkörperforschung Kernforschungsanlage Jülich GmbH Postfach 1913 D-5170 Jülich
Corsten, C.J.A.	Techn. Hogescholl Cycl. Lab. Eindhoven Netherlands
Cooper, Richard K.	Los Alamos National Laboratory P.O. Box 1663 Los Alamos, N.M. 87545 U.S.A.
Deyda, Hartmut	Der Bundesminister für Forschung und Technologie Postfach 200706 D-5300 Bonn 2
Drüke, Volker	Institut für Reaktorentwicklung Kernforschungsanlage Jülich GmbH Postfach 1913 D-5170 Jülich
Filges, Detlef	Institut für Reaktorentwicklung Kernforschungsanlage Jülich GmbH Postfach 1913 D-5170 Jülich

Fischer, Walter E.	Swiss Institut for Nuclear Research SIN CH-5234 Villingen Switzerland
Gear, Peter E,	S.R.C. Rutherford & Appleton Labs. Chilton, Didcot, Oxon England
Golub, Robert	T.U.M. Reaktorstation Physik Department D-8046 Garching
Grand, Pierre	Brookhaven National Lab. Blg. 129 Upton, N.Y. 11973 U.S.A.
Gray, David A.	Rutherford & Appleton Laboratories Chilton, Didcot, Oxon OX11 OQX England
Heck, Eva-Maria	Gesellschaft für Schwerionenforschung GSI Postfach 110541 D-6100 Darmstadt
Hecker, H.	Leiter des Instituts für Reaktorentwicklung Kernforschungsanlage Jülich GmbH Postfach 1913 D-5170 Jülich
Heidenreich, Gerd	Swiss Institute for Nuclear Research SIN CH-5234 Villigen Switzerland
Heil, Jura	Bundesministerium für Forschung und Technologie Postfach 200906 D-5300 Bonn 2
Heindler, Manfred	Technische Universität Graz Petersg. 16 A-8010 Graz Austria
Hellwig, Lutz	Kernforschungszentrum Karlsruhe PS2 Postfach 3640 D-7500 Karlsruhe
Hietschold, R.	Kernforschungszentrum Karlsruhe Postfach 3640 D-7500 Karlsruhe
Hoffmann, H.	Kernforschungszentrum Karlsruhe Postfach 3640 D-7500 Karlsruhe

Jason, Andrew J.	Los Alamos National Laboratory MS 808 Los Alamos, N.M. 87545 U.S.A.
Kiöe. Willard E.	New England Nuclear 601 Treble Cove Rd. No. Billerica, Mass. 02173 U.S.A.
Kley, Walter	EURATOM-ispra 21020 Ispra Italy
Klose, W.	Vorstand des Kernforschungszentrums Karlsruhe Weberstr. 5 D-7500 Karlsruhe 1
Kühn, Werner	Kernforschungszentrum Karlsruhe Postfach 3640 D-7500 Karlsruhe
Lohmann, W.	Institut für Festkörperforschung Kernforschungsanlage Jülich GmbH Postfach 1913 D-5170 Jülich
Macek, Robert I.	Los Alamos National Laboratory MS-838 Los Alamos, N.M. 87545 U.S.A.
Mittag, K.	Kernforschungszentrum Karlsruhe Postfach 3640 D-7500 Karlsruhe
Müller, O.	Kernforschungszentrum Karlsruhe Postfach 3640 D-7500 Karlsruhe
Neef, Ralf-Dieter	Institut für Reaktorentwicklung Kernforschungsanlage Jülich GmbH Postfach 1913 D-5170 Jülich
Nücker, Nikolaus	Kernforschungszentrum Karlsruhe IAK 1 / PSQ Postfach 3640 D-7500 Karlsruhe 1
Peek, N.F.	Physics Department University of California Davis, Ca 95616 U.S.A.

Piesche	Kernforschungszentrum Karlsruhe Postfach 3640 D-7500 Karlsruhe
Piosczyk, B.	Kernforschungszentrum Karlsruhe Postfach 3640 D-7500 Karlsruhe
Potts, Charles W.	Argonne National Laboratory 9700 S. Cass Ave. Argonne, Il. 60439 U.S.A.
Planner, C.W.	Rutherford Lab. Chilton Didcot, Oxon OX11 England
Pugh, V.T.	Rutherford Lab. Chilton, Didcot, Oxon OX11 England
zu Putlitz, G.	Gesellschaft für Schwerionenforschung GSI Postfach 11541 D-6100 Darmstadt
Rees, Grahame H.	Rutherford Lab. Chilton, Didcot, Oxon OX11 OQX England
Reich, K.H.	C E R N CH-1211 Genf 23 Switzerland
Reichardt, w.	Kernforschungszentrum Karlsruhe Postfach 3640 D-7500 Karlsruhe
Reiser, M.	University of Maryland Dept. Physics & Astronomy College Park, MD 20742 U.S.A.
Russell, Gary J.	Group P-9, Physics Division Los Alamos National Laboratory P.O. Box 1663 Los Alamos, N.M. 87545 U.S.A.
Seeger, A.	Max-Planck-Institut für Metallforschung Postfach 800665 D-7000 Stuttgart
Sigg, B.	Institut für Reaktortechnik ETH CH-5303 Würenlingen Switzerland

Subbutkutty, K.	Institut für Reaktorentwicklung Kernforschungsanlage Jülich GmbH Postfach 1913 D-5170 Jülich
Sebening, H.	Kernforschungszentrum Karlsruhe PSQ Postfach 3640 D-7514 Leopoldshafen
Schaal, H.	Institut für Reaktorentwicklung Kernforschungsanlage Jülich GmbH Postfach 1913 D-5170 Jülich
Schaffer, G.	Kernforschungszentrum Karlsruhe KfK - IK, Bau 416 Postfach 3640 D-7500 Karlsruhe 1
Scherm, R.	Physikalisch-Technische Bundesanstalt Bundesallee 100 D-3300 Braunschweig
Schmatz, W.	Kernforschungszentrum Karlsruhe Institut für Angewandte Kernphysik I Postfach 3640 D-7500 Karlsruhe 1
Schmidt-Rohr, U.	Max-Planck-Institut für Kernphysik Postfach 103980 D-6900 Heidelberg
Stanco, L.	Institut für Festkörperforschung Kernforschungsanlage Jülich GmbH Postfach 1913 D-5170 Jülich
Stiller, H.H.	Institut für Festkörperforschung Kernforschungsanlage Jülich GmbH Postfach 1913 D-5170 Jülich
Stirling, G.C.	Rutherford & Appleton Laboratories Didcot, Oxon OX11 OQX England
Stöver, Detlev	Institut für Reaktorentwicklung Kernforschungsanlage Jülich GmbH Postfach 1913 D-5170 Jülich
Strehl, Peter	Gesellschaft für Schwerionenforschung GSI Postfach 11541 D-6100 Darmstadt

Taylor, A.D.	Los Alamos National Laboratory P.O. Box 1663 Los Alamos, N.M. 87545 U.S.A.
Thorson, Ian	Physics Dept. Simon Fraser University Burnaby, B.C. V5A-156 Canada
Tschalär, Ch.	Schweizerisches Institut für Nuklearforschung CH-5234 Villigen Switzerland
Uhlhorn,	Bundesministerium für Forschung und Technologie Ref. 211 Postfach 200706 D-5300 Bonn 2
Utsuro, M.	Research Reactor Institute Kyoto University Kumatori-cho, Sennan-gun, Osaka 590-04 Japan
Vetter, J.E.	Kernforschungszentrum Karlsruhe Postfach 3640 D-7500 Karlsruhe 1
Watanabe, N.	National Laboratory for High Energy Physics Oho-machi, Tsukuba-gun, Ibaraki-ken 305 Japan
Woods, R.	Los Alamos National Laboratory P.O. Box 1663 MS 480 Los Alamos, N.M. 87545 U.S.A.
Wüstefeld, G.	Institut für Festkörperforschung Kernforschungsanlage Jülich GmbH Postfach 1913 D-5170 Jülich
Zeitnitz, B.	Institut für Kernphysik Kernforschungszentrum Karlsruhe Postfach 3640 D-7500 Karlsruhe